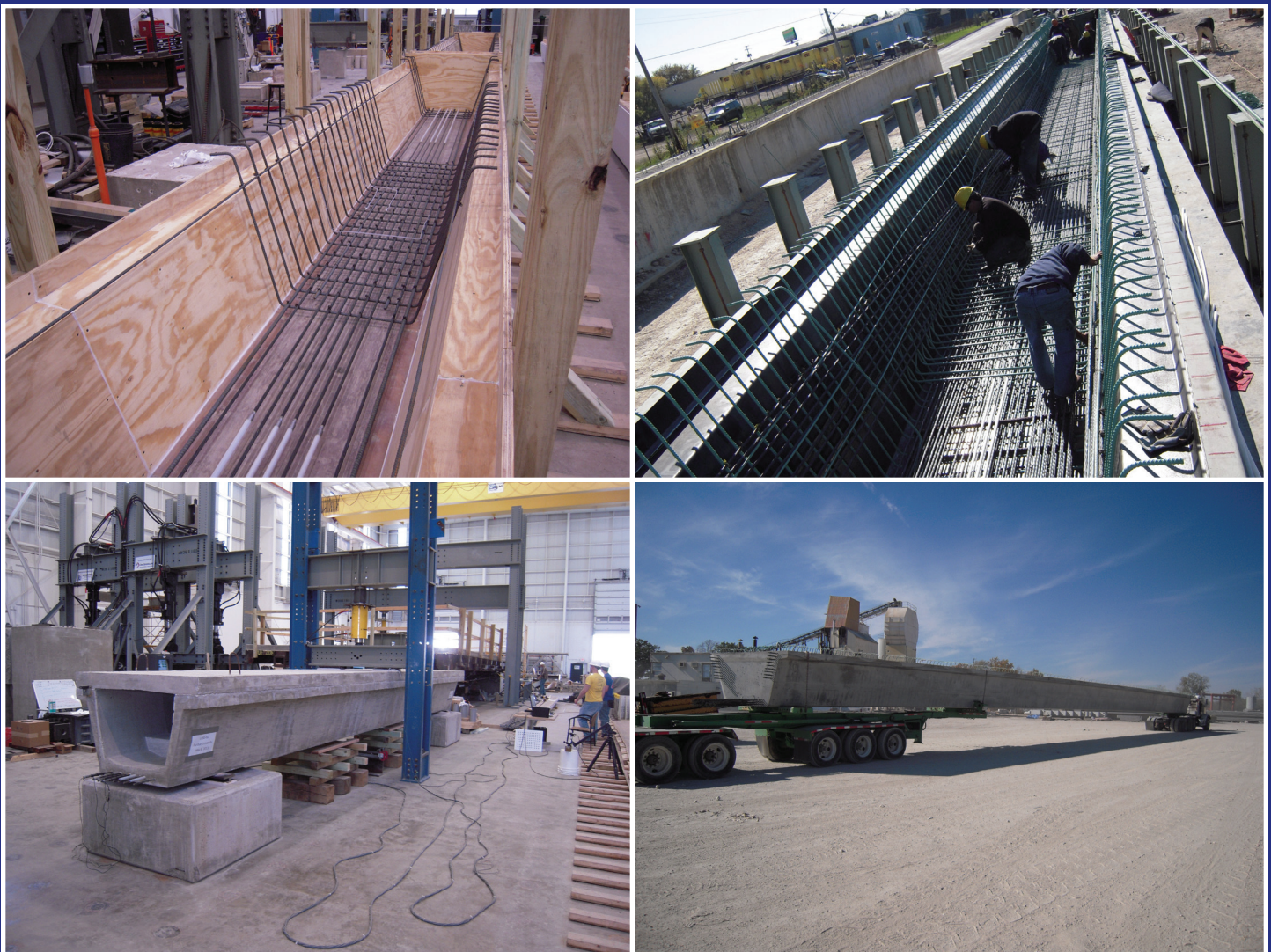


JOINT TRANSPORTATION RESEARCH PROGRAM

INDIANA DEPARTMENT OF TRANSPORTATION
AND PURDUE UNIVERSITY



Improving the Design of U-Beams for Indiana



Michael D. Wesson, Matthew A. Pavelchak, Robert J. Frosch, Michael E. Kreger

RECOMMENDED CITATION

Wesson, M. D., Pavelchak, M. A., Frosch, R. J., & Kreger, M. E. (2014). *Improving the design of U-beams for Indiana* (Joint Transportation Research Program Publication No. FHWA/IN/JTRP-2014/07). West Lafayette, IN: Purdue University. <http://dx.doi.org/10.5703/1288284315501>

AUTHORS

Michael D. Wesson

Graduate Research Assistant
Lyles School of Civil Engineering
Purdue University

Matthew A. Pavelchak

Graduate Research Assistant
Lyles School of Civil Engineering
Purdue University

Robert J. Frosch, PhD

Professor of Civil Engineering
Lyles School of Civil Engineering
Purdue University
(765) 494-5904
frosch@purdue.edu
Corresponding Author

Michael E. Kreger, PhD

Professor of Civil Engineering
Lyles School of Civil Engineering
Purdue University

JOINT TRANSPORTATION RESEARCH PROGRAM

The Joint Transportation Research Program serves as a vehicle for INDOT collaboration with higher education institutions and industry in Indiana to facilitate innovation that results in continuous improvement in the planning, design, construction, operation, management and economic efficiency of the Indiana transportation infrastructure. https://engineering.purdue.edu/JTRP/index_html

Published reports of the Joint Transportation Research Program are available at: <http://docs.lib.purdue.edu/jtrp/>

NOTICE

The contents of this report reflect the views of the authors, who are responsible for the facts and the accuracy of the data presented herein. The contents do not necessarily reflect the official views and policies of the Indiana Department of Transportation or the Federal Highway Administration. The report does not constitute a standard, specification, or regulation.

COPYRIGHT

Copyright 2014 by Purdue University. All rights reserved.
Print ISBN: 978-1-62260-305-3
ePUB ISBN: 978-1-62260-306-0

1. Report No. FHWA/IN/JTRP-2014/07	2. Government Accession No.	3. Recipient's Catalog No.	
4. Title and Subtitle Improving the Design of U-Beams for Indiana		5. Report Date June 2014	6. Performing Organization Code
7. Author(s) Michael D. Wesson, Matthew A. Pavelchak, Robert J. Frosch, Michael E. Kreger		8. Performing Organization Report No. FHWA/IN/JTRP-2014/07	
9. Performing Organization Name and Address Joint Transportation Research Program Purdue University 550 Stadium Mall Drive West Lafayette, IN 47907-2051		10. Work Unit No.	11. Contract or Grant No. SPR-3144
12. Sponsoring Agency Name and Address Indiana Department of Transportation State Office Building 100 North Senate Avenue Indianapolis, IN 46204		13. Type of Report and Period Covered Final Report	
15. Supplementary Notes Prepared in cooperation with the Indiana Department of Transportation and Federal Highway Administration.		14. Sponsoring Agency Code	
16. Abstract <p>The use of prestressed U-beams, developed as an economical and aesthetic alternative to traditional I-beams, is becoming increasingly common. While U-beams are seeing increased use, questions have arisen in the design of bridges utilizing this girder type. Specific issues include live load distribution, bridge deck behavior, and debonding limits. First, since the U-beam is a new girder type, limited guidance exists for the live load distributions to be used in design. Second, due to the increased stiffness and strength of this girder, fewer girder lines are required resulting in increased deck spans. Finally, current AASHTO debonding limits severely restrict the efficiency and economy of the section. The objective of this research program is to develop design strategies to improve the efficiency and optimize the design of the Indiana modified U-beam with a focus on the concerns related to the design of U-beams. In particular, this research program will evaluate the live load distribution appropriate for the design of U-beams, assess the behavior and design of the bridge deck when supported by U-beams, and evaluate both the shear strength and shear design of the composite U-beam system. It is important that the strength strength of pretensioned concrete beams with debonded strand be fully evaluated. Five phases of research were conducted. The first phase consisted of evaluation of a U-beam bridge constructed in Indianapolis, Indiana to assess the live load distribution factors and flexural deck behavior of this bridge. The second phase evaluated the effectiveness of debonding sheathing to ensure that proper debonding is being achieved. The third phase evaluated the influence of the percentage of debonded strands on shear strength using rectangular and I-shaped cross sections to investigate flexure-shear and web-shear strengths, respectively. While this phase concentrated on the shear strength resisted by the concrete, the influence of transverse reinforcement was also evaluated. The fourth phase evaluated the influence of varying strength concretes, which are commonly used in composite sections, on shear strength. Finally, the fifth phase evaluated the shear strength of a 50% debonded U-beam both with and without transverse reinforcement. From the results, an improved understanding of the influence of debonding on shear strength is obtained. Recommendations are provided to improve the analysis, design, and construction of U-beams as well as the design and construction of girders utilizing debonded strand in general.</p>			
17. Key Words U-beam, prestressed concrete, structural concrete, shear strength, debonding, debond sheathing, live load distribution factors, bridge deck design		18. Distribution Statement No restrictions. This document is available to the public through the National Technical Information Service, Springfield, VA 22161.	
19. Security Classif. (of this report) Unclassified	20. Security Classif. (of this page) Unclassified	21. No. of Pages 198	22. Price

EXECUTIVE SUMMARY

IMPROVING THE DESIGN OF U-BEAMS FOR INDIANA

Introduction

Many state agencies are faced with the challenge of improving deteriorating bridges while increasing roadway capacity and meeting aesthetic requirements of adjacent communities. These challenges have led to increased interest in bridges utilizing U-beams. The U-beam is a pretensioned concrete, open top, trapezoidal-shaped beam that was developed as an economical and aesthetic alternative to traditional I-beams. Bridges designed with U-beams typically require only one-half to two-thirds as many beams as compared to a traditional I-beam bridge. Additionally, U-beams have fewer horizontal break lines per beam. This combination of reduction in the number of girders and break lines leads to a greatly streamlined aesthetic.

While the use of the U-beam section is becoming more common, there are some design concerns and code limitations restricting their efficiency. Questions have arisen regarding how live load is distributed in a U-beam bridge as well as how the bridge deck behaves in flexure. Additionally, code limits on debonding of prestressing strand have been found in practice to limit both the efficiency and economy of this girder section.

The objective of this research program is to develop design strategies to improve the efficiency and optimize the design of the Indiana modified U-beam with a focus on the concerns related to the design of U-beams. In particular, this research program evaluated the live load distribution appropriate for the design of U-beams, assessed the behavior and design of the bridge deck when supported by U-beams, and evaluated both the shear strength and shear design of the composite U-beam system. It is important that the strength of pretensioned concrete beams with debonded strand be fully evaluated.

The research was completed in five major phases. Phase 1 consisted of the field instrumentation of the 21st Street Bridge, which is the first U-beam bridge to be built in Indiana. Phase 2 consisted of an experimental investigation of the effectiveness of debond sheathing. Phase 3 evaluated the influence of strand debonding on the shear strength of pretensioned beams. Phase 4 evaluated the effect of different concrete strengths in a composite section on shear strength. This is important considering that pretensioned girders are typically constructed as composite members using different concrete strengths. Finally, Phase 5 combined the results of Phases 2 through 4 to test scaled U-beams with and without transverse reinforcement to evaluate the applicability of the previous conclusions on this section shape and access overall system behavior.

Findings

Field Evaluation

The load test of the 21st Street Bridge allowed for measurement of the live load distribution factors for this bridge. Upon comparison of the measured live load distribution factors with those calculated based on the AASHTO LRFD Bridge Design Specifications, it appears that the expression for interior girder distribution factors is slightly nonconservative, but reasonable. The exterior girder live load distribution factor computed based on AASHTO was extremely conservative based on the testing performed. While the measured live load distribution factors are

only applicable to this bridge deck and girder configuration, the results of this study indicate that a simple spring beam model can be used to closely and conservatively determine the live load distribution factors for interior and exterior girders.

The flexural behavior of the bridge deck between the interior and exterior girder lines exhibited a moment distribution with positive moment in the middle of the span and negative moment over the girder lines. The development of negative moment over the exterior girder lines is expected due to the continuity of the deck over the girder lines. The results of both a simple beam and shell model of the bridge deck indicate that the strains in the bridge deck can be accurately determined using simple finite element models. The shell model also indicates that the strip width values calculated according to the AASHTO LRFD Bridge Design Specifications are both reasonable and conservative.

Debond Sheathing Effectiveness

The type of debonding product used can have a significant impact on the effectiveness of strand debonding. While some of the split sheathing types tested showed acceptable performance, effective debonding can be ensured through the use of un-split sheathing or by sealing slit sheathing along its entire length. It was discovered that paste infiltration as a result of openings in the sheathing reduced the effectiveness of the un-taped, split sheathing, allowing for force transfer inside the debonded region. The amount of overlap the sheathing provides did not influence the results; however, tight-fitting split sheathing products perform better than looser-fitting products. To ensure effective debonding, sealing of split sheathing is strongly recommended.

Influence of Debonding on Shear Strength

As the percentage of debonding increased from 0% to 75%, shear strengths decreased. For V_{ci} at the end of the debonded region, a 35% reduction in shear strength (at formation of primary shear crack) was observed in the specimen with 50% debonding relative to the specimen with 0% debonding. In increasing the debonded strand to 75%, a 61% reduction in shear strength (at formation of primary shear crack) occurred. For V_{cw} within the debonded region, a 16% reduction in shear strength (at formation of primary shear crack) was observed in the specimen with 50% debonding relative to the specimen with 0% debonding. Where V_{ci} cracks formed outside the debonded region, an 8% reduction in shear strength (at formation of primary shear crack) was observed in the specimen with 50% debonding relative to the specimen with 0% debonding. This minor reduction is within the scatter expected in shear test results.

The modulus of rupture was observed to be lower at the end of the debonded region than at midspan (fully bonded region). Values as low as $3\sqrt{f'_c}$ were observed for the Series II specimens with 75% debonding. This corresponds to a 53% reduction in the modulus of rupture relative to midspan. It is theorized that these reduced modulus of rupture values result from damage sustained at the end of the debonded region at transfer (when the strands were cut). As the number of debonded strands increased, the modulus of rupture at the end of the debonded region decreased.

Composite Section Shear Strength

The concrete compressive strength was observed to have almost no impact on the shear strength of the specimens tested in this experimental program. The small differences in test results (8% for the specimens with 0.48% reinforcement and 12% for the specimens with 2.40% reinforcement) are within the scatter expected in the shear test results.

U-Beam Shear Strength

Overall, shear strengths developed by these specimens were as expected based on the test results from the previous phases. Low

modulus of rupture values were also observed for these specimens, especially at the end of the debonded region. On average, the modulus of rupture was $4.6\sqrt{f'_c}$ at midspan and $2.1\sqrt{f'_c}$ at the end of debonding. Therefore, debonding 50% of the strand resulted in a 54% reduction in the modulus. This was higher than observed for the rectangular section where 50% debonding resulted in a 26% reduction in the modulus. Adding transverse reinforcement in the debonded region provided additional shear capacity as well as improved ductility. With the addition of #3 at 12 in., the shear capacity was increased 20% beyond the shear at the formation of the primary shear crack. Shear crack widths were controlled and failure was not brittle. The transverse reinforcement also forced the shear failure to occur outside of the debonded region.

Implementation

The following recommendations are provided for implementation by INDOT to improve the efficiency and economy of girders utilizing debonded strands. These recommendations can be incorporated into the INDOT Design Manual as well as the standard construction specifications.

1. The percentage of debonded strands should not be limited. However, debonding of strands can have a significant influence on shear strength. Therefore, the concrete contribution to shear strength (V_c) must be calculated in the debonded region. Web-shear strength (V_{cw}) can control throughout the debonded region while flexure-shear strength (V_{ci}) will control at the end of debonding. For the calculation of shear strength of beams with debonded strand, the modulus of rupture should be assumed as zero ($f_r = 0\sqrt{f'_c}$) in the debonded regions to account for the reduced moduli that can occur at the ends of debonded regions. The lower limits for flexure-shear strength in AASHTO as well as ACI 318 are not appropriate and should not be used. In considering the composite section, the concrete strength in the compression zone of composite beams should be used to calculate flexure-shear strength. Conservatively, the section can be assumed as homogenous using the lower strength concrete.
2. Debond sheathing should be staggered so that all debonded strands do not begin transfer at the same location. A significant reduction (54%) in the modulus of rupture was observed when increased numbers of strands were transferred at the same location. The AASHTO LRFD Bridge Design Specifications provide recommendations regarding staggering that are considered reasonable to assist in minimizing this phenomenon.
3. All openings in debonding sheathing should be sealed to ensure effective debonding. Sealing can be achieved using a flexible adhesive tape such as duct tape. Alternately, un-split sheathing should be used.

CONTENTS

1. INTRODUCTION	1
1.1 Background	1
1.2 Design Concerns	1
1.3 Strand Debonding	2
1.4 Current Standards	3
1.5 Previous Research	4
1.6 Objective and Scope	5
2. FIELD EVALUATION OF A U-BEAM BRIDGE	5
2.1 Research Summary	5
2.2 Conclusions.	6
3. EVALUATION OF DEBOND SHEATHING EFFECTIVENESS	6
3.1. Research Summary	6
3.2 Evaluation of Debond Sheathing Products.	6
3.3 Evaluation of Debond Sheathing Installation Techniques	7
4. INFLUENCE OF STRAND DEBONDING ON SHEAR STRENGTH	7
4.1 Research Summary	7
4.2 Conclusions.	8
5. COMPOSITE SECTION EFFECTS ON SHEAR STRENGTH	9
5.1 Research Summary	9
5.2 Conclusions.	9
6. INFLUENCE OF U-SHAPE ON SHEAR STRENGTH	9
6.1 Research Summary	9
6.2 Conclusions.	9
7. CONCLUSIONS	10
7.1 Bridge Deck Bending Behavior	10
7.2 Live Load Distribution Factors.	10
7.3 Debond Sheathing	10
7.4 Shear Strength.	10
7.5 Debonding Limit	11
7.6 Expected Benefits.	11
REFERENCES	11
APPENDICES	
Appendix A. Field Evaluation of a U-Beam Bridge	13
Appendix B. Evaluation of Debond Sheathing Products.	43
Appendix C. Evaluation of Debond Sheathing Installation Techniques	67
Appendix D. Influence of Strand Debonding on Shear Strength	83
Appendix E. Composite Section Effects on Shear Strength	148
Appendix F. Influence of U-Shape on Shear Strength	159

LIST OF TABLES

Table	Page
Table 1.1 Debonding Limits for DOTs	4
Table 1.2 Longitudinal Stiffness vs. Shear Strength	4
Table 4.1 Comparison of Shear Strength Ratios for Series I, II, and III	8
Table A.1 Summary of U-Beam Trial Batch Results	17
Table A.2 U-Beam Design Mix	17
Table A.3 U-Beam Compressive Strength Data	18
Table A.4 U-Beam Modulus of Elasticity Data	19
Table A.5 Cast-in-Place Deck Concrete Mix Design	19
Table A.6 Cast-in-Place Deck Trial Batch Results	20
Table A.7 Cast-in-Place Deck INDOT Test Results	21
Table A.8 Cast-in-Place Deck Purdue Test Results	21
Table A.9 Cast-in-Place Deck Modulus of Elasticity Data	22
Table A.10 Prestressing Strand Tensile Strength	22
Table A.11 Reinforcing Steel Tensile Strength	23
Table A.12 Series S1-X Strains	32
Table A.13 Series S2-X Strains	33
Table A.14 Transverse Deck Gage Strains	34
Table A.15 Distribution Factors One Truck Loading at 1/4 Span	36
Table A.16 Distribution Factors One Truck Loading at 1/2 Span	36
Table A.17 Distribution Factors One Truck Loading at 3/4 Span	37
Table A.18 Distribution Factors One Truck Loading at 3/2 Span	37
Table A.19 Distribution Factors Two Truck Loading at 1/2 Span, Edge of Deck	38
Table A.20 Distribution Factors Two Truck Loading at 1/2 Span, Middle of Deck	38
Table A.21 Distribution Factors Two Truck Loading at 3/2 Span, Edge of Deck	39
Table A.22 Distribution Factors Two Truck Loading at 3/2 Span, Middle of Deck	39
Table A.23 Load Distribution Factors S1-X Series	40
Table A.24 Load Distribution Factors S2-X Series	40
Table A.25 Live Load Distribution Factors—SAP Model	41
Table A.26 Flexural Deck Strains—SAP Model	42
Table B.1 Debonding Agents	44
Table B.2 Test Specimen Layout	45
Table B.3 Concrete Mix Design Weights per Cubic Yard	45
Table B.4 Concrete Mix Batch Weights per Cubic Yard	46
Table B.5 Concrete Compressive Strength Data	46
Table B.6 Prestressing Strand Tensile Strength	47
Table B.7 Specimen Designations	51
Table B.8 Transfer Lengths	66
Table C.1 Test Matrix	68
Table C.2 Concrete Mix Design Weights per Cubic Yard	69

Table C.3 Final Concrete Mix Batch Weights per Cubic Yard	69
Table C.4 Concrete Compressive Strength Data	70
Table D.1 Test Matrix	91
Table D.2 Predicted Shear Strengths	100
Table D.3 Concrete Mix Design Weights per Cubic Yard	100
Table D.4 Concrete Mix Batch Weights per Cubic Yard for Series I (V_{ci-in})	101
Table D.5 Concrete Mix Batch Weights per Cubic Yard for Series II (V_{ci-out})	101
Table D.6 Concrete Mix Batch Weights per Cubic Yard for Series III (V_{cw})	101
Table D.7 Concrete Mix Batch Weights per Cubic Yard for Series IV	102
Table D.8 Concrete Strengths on Test Day	103
Table D.9 Prestressing Strand Tensile Strengths	103
Table D.10 #3 Stirrup Tensile Properties	104
Table D.11 Curing and Transfer	106
Table D.12 Test Results at Formation of Primary Shear Crack	109
Table D.13 Test Results at Ultimate Failure	110
Table D.14 Comparison of Shear Strengths for Series I	121
Table D.15 Comparison of Shear Strength Ratios for Series I	121
Table D.16 Measured Modulus of Ruptures for Series I	122
Table D.17 Comparison of Shear Strengths for Series II	126
Table D.18 Comparison of Shear Strength Ratios for Series II	127
Table D.19 Measured Modulus of Ruptures for Series II	127
Table D.20 Comparison of Shear Strengths for Series III	131
Table D.21 Comparison of Shear Strength Ratios for Series III	131
Table D.22 Measured Modulus of Ruptures for Series III	132
Table D.23 Comparison of Shear Strengths for V_{ci-in} -50- V_s	134
Table D.24 Comparison of Shear Strength Ratios for V_{ci-in} -50- V_s	134
Table D.25 Measured Modulus of Ruptures for Series IV	134
Table D.26 Comparison of Shear Strength Ratios for Series I, II, and III	134
Table D-2.1 Average Concrete Compressive Strength Data for Series I (V_{ci-in})	143
Table D-2.2 Average Concrete Compressive Strength Data for Series II (V_{ci-out})	143
Table D-2.3 Average Concrete Compressive Strength Data for Series III (V_{cw})	143
Table D-2.4 Average Concrete Compressive Strength Data for Series IV	144
Table D-2.5 Average Concrete Split Tensile Strength Data for All Series	144
Table E.1 Test Matrix	148
Table E.2 Concrete Mix Design Weights per Cubic Yard	150
Table E.3 Concrete Mix Batch Weights per Cubic Yard	150
Table E.4 Concrete Strengths During Test Phase	151
Table E.5 Concrete Age on Test Day	151
Table E.6 Longitudinal Reinforcement Ultimate Stress (Tested at Bowen Lab)	151
Table E.7 Longitudinal Reinforcement Yield Stress (Tested by MMFX)	151
Table E.8 Longitudinal Reinforcement Tensile Properties (Mill Certification)	152

Table E.9 Test Results	154
Table E.10 Comparison of Shear Strengths	156
Table E.11 Comparison of Shear Strength Ratios	156
Table E-1.1 Average Concrete Strength Data for 4,000 psi Concrete Mix	158
Table E-1.2 Average Concrete Strength Data for 10,000 psi Concrete Mix	158
Table F.1 Test Matrix	159
Table F.2 Predictions	164
Table F.3 Concrete Mix Design Weights per Cubic Yard	165
Table F.4 Final Concrete Mix Batch Weights per Cubic Yard for Trial Batch	165
Table F.5 Final Concrete Mix Batch Weights per Cubic Yard for U-Beams	167
Table F.6 Final Concrete Mix Batch Weights per Cubic Yard for U-Beam Decks	167
Table F.7 Concrete Strengths on Test Day	168
Table F.8 Longitudinal Reinforcement Tensile Properties	168
Table F.9 #3 Stirrup Tensile Properties	169
Table F.10 #4 Stirrup Tensile Properties	170
Table F.11 Test Results at Formation of Primary Shear Crack	177
Table F.12 Test Results at Ultimate Failure	177
Table F.13 Comparison of Shear Strengths for U-50	180
Table F.14 Comparison of Shear Strength Ratios for U-50	180
Table F.15 Comparison of Shear Strengths for U-50-V _s	183
Table F.16 Comparison of Shear Strength Ratios for U-50-V _s	183
Table F.17 Measured Modulus of Ruptures for U-Beams	183
Table F-1.1 Average Concrete Strength Data for Trial Batch	184
Table F-1.2 Average Concrete Strength Data for U-Beams	184
Table F-1.3 Average Concrete Strength Data for U-Beam Decks (One Truck)	184

LIST OF FIGURES

Figure	Page
Figure 1.1 U-beam cross section	1
Figure 1.2 Accelerate I-465 project limits	2
Figure 1.3 Concrete spalling around debonded strand	2
Figure 1.4 Debond sheathing	3
Figure A.1 U-beam dimensions	13
Figure A.2 21 st Street Bridge cross section	14
Figure A.3 U-beam prestressing layout	14
Figure A.4 Gage layout for live load distribution	15
Figure A.5 Vertical gage layout for live load distribution	16
Figure A.6 Gage layout for deck bending behavior	16
Figure A.7 Girder concrete strength growth curves	17
Figure A.8 Lot and subplot layout	20
Figure A.9 Cast-in-place deck concrete compressive strength	21
Figure A.10 Prestressing strand grip setup	22
Figure A.11 Mild steel extensometer stress-strain curves	22
Figure A.12 U-beam outer form	23
Figure A.13 U-beam inner form	23
Figure A.14 Concrete surface mounted strain gage	24
Figure A.15 Typical rebar strain gage installation	24
Figure A.16 Typical U-beam side-wall strain gage installations	25
Figure A.17 Typical U-beam floor strain gage installation	25
Figure A.18 Deck PVC conduit	25
Figure A.19 Typical deck form penetration	25
Figure A.20 Deck placement at center of bridge	26
Figure A.21 Deck placement at sidewalk	26
Figure A.22 Load test truck dimensions	27
Figure A.23 Truck scale measurements	27
Figure A.24 Test load distributions	28
Figure A.25 Dual truck load test S2-1	28
Figure A.26 Series S2-X load test	29
Figure A.27 Series S1-X load test	30
Figure A.28 Series D load test layout	31
Figure A.29 Location of wheel loads for S1-2 load case	34
Figure A.30 Use of load test symmetry	35
Figure A.31 Girder identification	35
Figure A.32 Example of distribution factor calculation	35
Figure A.33 Transverse layout of trucks for S1-X and S2-X series	40
Figure A.34 Beam model	41
Figure A.35 Lever rule for exterior girder	41

Figure A.36 Deck behavior flexural strains	42
Figure B.1 Prestressed specimen cross section	43
Figure B.2 Prestressed specimen layout	44
Figure B.3 Sheathing termination detail	45
Figure B.4 Concrete strength growth curves	46
Figure B.5 Prestressing strand tensile test specimens	47
Figure B.6 Prestressing abutment	47
Figure B.7 Formwork	48
Figure B.8 End forms	48
Figure B.9 Prestress jacking apparatus	48
Figure B.10 Specimen casting	48
Figure B.11 Prestressing strand release	49
Figure B.12 Use of DEMEC layout bar	49
Figure B.13 DEMEC mechanical strain gage	49
Figure B.14 DEMEC measurements	50
Figure B.15 Strain distribution —PSI split sheathing (14 ft)	51
Figure B.16 Strain distribution —PSI split sheathing (10 ft)	52
Figure B.17 Strain distribution—Fister split sheathing (14 ft)	53
Figure B.18 Strain distribution—Fister split sheathing (10 ft)	54
Figure B.19 Strain distribution—fully bonded specimen, Cast #1 (14 ft)	55
Figure B.20 Strain distribution—DuraJoint split sheathing un-taped (14 ft)	55
Figure B.21 Strain distribution—DuraJoint split sheathing (14 ft)	56
Figure B.22 Strain distribution—DuraJoint split sheathing (10 ft)	57
Figure B.23 Strain distribution—fully bonded specimens, Cast #2 (14 ft)	58
Figure B.24 Strain distribution— fully bonded specimens, Cast #2 (10 ft)	59
Figure B.25 Strain distribution—PVC pipe (14 ft)	60
Figure B.26 Strain distribution—PVC pipe (10 ft)	61
Figure B.27 Strain distribution—DuraJoint un-split sheathing (14 ft)	62
Figure B.28 Strain distribution—DuraJoint un-split sheathing (10 ft)	63
Figure B.29 Strain distribution— fully bonded specimens, Cast #3 (10 ft)	64
Figure B.30 PSI split sheathing effectiveness comparison	64
Figure B.31 Fister split sheathing effectiveness comparison	64
Figure B.32 DuraJoint un-split sheathing effectiveness comparison	65
Figure B.33 DuraJoint split sheathing effectiveness comparison	65
Figure B.34 Debonding effectiveness comparison tapped vs. un-taped	65
Figure B.35 Average maximum strain (AMS) method	66
Figure C.1 Cross section	67
Figure C.2 DuraJoint un-split sheathing comparison	67
Figure C.3 DuraJoint split sheathing comparison	68
Figure C.4 Profile	68
Figure C.5 Sheathing installation details	69

Figure C.6 Compressive strength	70
Figure C.7 Pretensioning abutments	70
Figure C.8 Prestress jacking assembly	71
Figure C.9 Side forms	71
Figure C.10 Formwork termination	71
Figure C.11 Casting	72
Figure C.12 Strand release	72
Figure C.13 DEMEC layout bar	72
Figure C.14 DEMEC mechanical strain gage	73
Figure C.15 DEMEC measurements	73
Figure C.16 Boundary specimens	74
Figure C.17 Un-split sheathing	74
Figure C.18 Split sheathing	74
Figure C.19 Strain profile over time—fully bonded	75
Figure C.20 Strain profile over time—PVC pipe sheathing (taped)	75
Figure C.21 Strain profile over time—un-split sheathing (un-taped)	75
Figure C.22 Strain profile over time—un-split sheathing (taped)	76
Figure C.23 Strain profile over time—split sheathing (un-taped)	76
Figure C.24 Strain profile over time—split sheathing (taped)	76
Figure C.25 Un-split (un-taped) sheathing effectiveness	77
Figure C.26 Un-split (taped) sheathing effectiveness	78
Figure C.27 Split (un-taped) sheathing effectiveness	78
Figure C.28 Split (taped) sheathing effectiveness	78
Figure C.29 Autopsy of un-split sheathing with taped ends	79
Figure C.30 Autopsy of un-split sheathing without taped ends	79
Figure C.31 Autopsy of taped, split sheathing	79
Figure C.32 Autopsy of un-taped, split sheathing—solid paste	80
Figure C.33 Autopsy of un-taped, split sheathing—paste infiltration seam	80
Figure C.34 Autopsy of un-taped, split sheathing—end of solid paste	81
Figure C.35 Un-split vs. split sheathing (un-taped)	81
Figure C.36 Un-split vs. split sheathing (taped)	82
Figure C.37 Autopsy of un-taped sheathing	82
Figure C.38 Autopsy of taped sheathing	82
Figure D.1 Stress-strain comparison for concrete in compression	84
Figure D.2 Stress-strain comparison for mild steel in tension	85
Figure D.3 Stress-strain comparison for Grade 270 prestressing steel in tension	85
Figure D.4 Discretization of beam section	86
Figure D.5 Internal forces in prestressed beam	86
Figure D.6 Effective area of flanged section	87
Figure D.7 Distribution of web-shear strengths through depth of I-beam	87
Figure D.8 Strain profiles at transfer for V_{ci} -in-00 and V_{ci} -in-75	89

Figure D.9 Strain profiles at transfer for $V_{ci-in-25}$ and $V_{ci-in-50}$	90
Figure D.10 Strain profiles at transfer for $V_{ci-out-00}$ and $V_{ci-out-75}$	90
Figure D.11 Support and loading conditions	91
Figure D.12 Series I specimens (V_{ci-in})	92
Figure D.13 Transverse reinforcement details for rectangular beams	92
Figure D.14 Predicted shear strength profile for $V_{ci-in-00}$	93
Figure D.15 Predicted shear strength profile for $V_{ci-in-25}$	93
Figure D.16 Predicted shear strength profile for $V_{ci-in-50}$	94
Figure D.17 Predicted shear strength profile for $V_{ci-in-75}$	94
Figure D.18 Series II specimens (V_{ci-out})	95
Figure D.19 Predicted shear strength profile for $V_{ci-out-00}$	95
Figure D.20 Predicted shear strength profile for $V_{ci-out-25}$	96
Figure D.21 Predicted shear strength profile for $V_{ci-out-50}$	96
Figure D.22 Predicted shear strength profile for $V_{ci-out-75}$	97
Figure D.23 Series III specimens (V_{cw})	97
Figure D.24 Transverse reinforcement details for I-beams	98
Figure D.25 Predicted shear strength profile for V_{cw-00}	98
Figure D.26 predicted shear strength profile for V_{cw-25}	98
Figure D.27 Predicted shear strength profile for V_{cw-50}	99
Figure D.28 Predicted shear strength profile for V_{cw-75}	99
Figure D.29 $V_{ci-in-50}$ - V_s profile	99
Figure D.30 Predicted shear strength profile for $V_{ci-in-50}$ - V_s	100
Figure D.31 Compressive strength growth	102
Figure D.32 Split tensile strength growth	102
Figure D.33 Prestressing steel test sample	104
Figure D.34 Stress-strain response of transverse reinforcement	105
Figure D.35 Transverse reinforcement test sample	105
Figure D.36 Formwork	105
Figure D.37 Concrete transport during casting operations	105
Figure D.38 Strand release	106
Figure D.39 Test setup	106
Figure D.40 Supports	107
Figure D.41 Load pin	107
Figure D.42 Strain gage installation	108
Figure D.43 Strand slip instrumentation	108
Figure D.44 Support deformation instrumentation	108
Figure D.45 Instrumentation at midspan	109
Figure D.46 Shear due to self-weight	110
Figure D.47 Load-deflection behavior—Series I (V_{ci-in})	111
Figure D.48 Primary shear cracks—Series I (V_{ci-in})	111
Figure D.49 Load-deflection behavior—Series II (V_{ci-out})	112

Figure D.50 Primary shear cracks—Series II (V_{ci-out})	112
Figure D.51 Load-deflection behavior— $V_{ci-out-75}$	113
Figure D.52 Primary shear cracks— $V_{ci-out-75}$	113
Figure D.53 Load-deflection behavior— $V_{ci-out-75}$ and $V_{ci-out-75-2}$	114
Figure D.54 Primary shear cracks— $V_{ci-out-75}$ and $V_{ci-out-75-2}$	114
Figure D.55 Load-deflection behavior—Series III (V_{cw})	115
Figure D.56 Primary shear cracks—Series III (V_{cw})	115
Figure D.57 Load-deflection behavior— $V_{ci-in-50}$ and $V_{ci-in-50-V_s}$	115
Figure D.58 Primary shear cracks— $V_{ci-in-50}$ and $V_{ci-in-50-V_s}$	116
Figure D.59 Ultimate failure— $V_{ci-in-50-V_s}$	116
Figure D.60 Shear strength profile for $V_{ci-in-00}$	118
Figure D.61 Shear strength profile for $V_{ci-in-25}$	119
Figure D.62 Shear strength profile for $V_{ci-in-50}$	119
Figure D.63 Shear strength profile for $V_{ci-in-75}$	120
Figure D.64 Shear strength profile for $V_{ci-out-00}$	123
Figure D.65 Shear strength profile for $V_{ci-out-25}$	124
Figure D.66 Shear strength profile for $V_{ci-out-50}$	124
Figure D.67 Shear strength profile for $V_{ci-out-75}$	125
Figure D.68 Shear strength profile for $V_{ci-out-75-2}$	125
Figure D.69 Shear strength profile for V_{cw-00}	128
Figure D.70 Shear strength profile for V_{cw-25}	129
Figure D.71 Shear strength profile for V_{cw-50}	129
Figure D.72 Shear strength profile for V_{cw-75}	130
Figure D.73 Shear strength profile for $V_{ci-in-50-V_s}$	132
Figure D.74 Stirrup locations for $V_{ci-in-50-V_s}$	133
Figure D.75 Shear strength profile for $V_{ci-in-50-V_s}$; $V_{s,INT}$	133
Figure D-1.1 Strain profile over time— $V_{ci-in-00}$	135
Figure D-1.2 Strain profile over time— $V_{ci-in-75}$	135
Figure D-1.3 Strain profile over time— $V_{ci-in-25}$	136
Figure D-1.4 Strain profile over time— $V_{ci-in-50}$	136
Figure D-1.5 Strain profile over time— $V_{ci-out-00}$	137
Figure D-1.6 Strain profile over time— $V_{ci-out-75}$	137
Figure D-2.1 Compressive strength for $V_{ci-in-00}$ and $V_{ci-in-75}$	138
Figure D-2.2 Compressive strength for $V_{ci-in-25}$ and $V_{ci-in-50}$	138
Figure D-2.3 Compressive strength for $V_{ci-out-00}$ and $V_{ci-out-75}$	139
Figure D-2.4 Compressive strength for $V_{ci-out-25}$ and $V_{ci-out-50}$	139
Figure D-2.5 Compressive strength for V_{cw-00} and V_{cw-75}	139
Figure D-2.6 Compressive strength for V_{cw-25} and V_{cw-50}	140
Figure D-2.7 Compressive strength for $V_{ci-in-50-V_s}$ and $V_{ci-out-75-2}$	140
Figure D-2.8 Split tensile strength for $V_{ci-in-00}$ and $V_{ci-in-75}$	140
Figure D-2.9 Split tensile strength for $V_{ci-in-25}$ and $V_{ci-in-50}$	141

Figure D-2.10 Split tensile strength for $V_{ci-out-00}$ and $V_{ci-out-75}$	141
Figure D-2.11 Split tensile strength for $V_{ci-out-25}$ and $V_{ci-out-50}$	141
Figure D-2.12 Split tensile strength for V_{cw-00} and V_{cw-75}	142
Figure D-2.13 Split tensile strength for V_{cw-25} and V_{cw-50}	142
Figure D-2.14 Split tensile strength for $V_{ci-in-50-V_s}$ and $V_{ci-out-75-2}$	142
Figure D-3.1 Ultimate failure— $V_{ci-in-00}$	145
Figure D-3.2 Ultimate failure— $V_{ci-in-25}$	145
Figure D-3.3 Ultimate failure— $V_{ci-in-50}$	145
Figure D-3.4 Ultimate failure— $V_{ci-in-75}$	145
Figure D-3.5 Ultimate failure— $V_{ci-out-00}$	145
Figure D-3.6 Ultimate failure— $V_{ci-out-25}$	145
Figure D-3.7 Ultimate failure— $V_{ci-out-50}$	146
Figure D-3.8 Ultimate failure— $V_{ci-out-75}$ (south shear span)	146
Figure D-3.9 Ultimate failure— $V_{ci-out-75}$ (north shear span)	146
Figure D-3.10 Ultimate failure— $V_{ci-out-75-2}$	146
Figure D-3.11 Ultimate failure— V_{cw-00}	146
Figure D-3.12 Ultimate failure— V_{cw-25}	146
Figure D-3.13 Ultimate failure— V_{cw-50}	147
Figure D-3.14 Ultimate failure— V_{cw-75}	147
Figure D-3.15 Ultimate failure— $V_{ci-in-50-V_s}$	147
Figure E.1 Support and loading conditions	149
Figure E.2 Specimen designs	149
Figure E.3 Compressive strength	151
Figure E.4 Split tensile strength	151
Figure E.5 Stress-strain response of longitudinal reinforcement	152
Figure E.6 Formwork	152
Figure E.7 Concrete casting operations	153
Figure E.8 Test setup	153
Figure E.9 Supports	153
Figure E.10 Load pin	153
Figure E.11 Instrumentation	154
Figure E.12 Load-deflection behavior	155
Figure E.13 Primary shear cracks—Series I (4,000 psi)	155
Figure E.14 Primary shear cracks—Series II (10,000 psi)	155
Figure E.15 Primary shear cracks—Series III (composite)	156
Figure E-2.1 Ultimate failure—Series I (4,000 psi)	158
Figure E-2.2 Ultimate failure—Series II (10,000 psi)	158
Figure E-2.3 Ultimate failure—Series III (composite)	158
Figure F.1 Support and loading conditions	160
Figure F.2 U-50 specimen	160
Figure F.3 Effective shear area of U-beam	161

Figure F.4 Predicted shear strength profiles for U-50	162
Figure F.5 U-50- V_s specimen	163
Figure F.6 Predicted shear strength profiles for U-50- V_s	164
Figure F.7 Compressive strength of trial batch	165
Figure F.8 Split tensile strength for trial batch	166
Figure F.9 Slump flow for U-50- V_s	166
Figure F.10 Slump flow for U-50	166
Figure F.11 Compressive strength	167
Figure F.12 Split tensile strength	168
Figure F.13 Stress-strain response of longitudinal reinforcement	169
Figure F.14 Longitudinal reinforcement test sample	169
Figure F.15 Stress-strain response of transverse reinforcement for #3 stirrups	170
Figure F.16 Stress-strain response of transverse reinforcement for #4 stirrups	171
Figure F.17 Transverse reinforcement test sample	171
Figure F.18 Prestressing outrigger assembly	171
Figure F.19 Interior and exterior formwork	172
Figure F.20 Foam cut-out for concrete diaphragm	172
Figure F.21 Lateral force resisting system for exterior formwork	172
Figure F.22 Placing interior formwork	172
Figure F.23 Buoyancy force resisting system for interior formwork	172
Figure F.24 Detail of buoyancy force resisting system for interior formwork	172
Figure F.25 Stirrup layout	173
Figure F.26 Concrete placement operations for U-beams	173
Figure F.27 U-beams after transfer and form removal	173
Figure F.28 Deck shoring and formwork	173
Figure F.29 Deck shoring and formwork detail	173
Figure F.30 Lateral force resisting system for deck side panels	174
Figure F.31 Deck reinforcement	174
Figure F.32 Concrete placement operations for U-beam decks	174
Figure F.33 Deck shoring and formwork before removal	174
Figure F.34 Deck shoring removal	175
Figure F.35 Test setup	175
Figure F.36 Supports	176
Figure F.37 Load pins	176
Figure F.38 Strand slip instrumentation	176
Figure F.39 Support deformation instrumentation	176
Figure F.40 Instrumentation at midspan	176
Figure F.41 Load-deflection behavior—U-beams	177
Figure F.42 Primary shear cracks—U-beams	178
Figure F.43 Complete failure—U-50	178
Figure F.44 Cracks at conclusion of test—U-50- V_s	178

Figure F.45 Shear strength profile for U-50	179
Figure F.46 Shear strength profile for U-50- V_s	181
Figure F.47 Stirrup locations for U-50- V_s	181
Figure F.48 Shear strength profile for U-50- V_s ; $V_{s,INT}$	182

1. INTRODUCTION

1.1 Background

Many state agencies are faced with the challenge of improving deteriorating bridges while increasing roadway capacity and meeting aesthetic requirements of adjacent communities. These challenges have led to increased interest in bridges utilizing U-beams. The U-beam is a pretensioned concrete, open top, trapezoidal shaped beam that was developed as an economical and aesthetic alternative to traditional I-beams. A typical U-beam cross section is shown in Figure 1.1. Bridges designed with U-beams typically require only one-half to two-thirds as many beams as compared to a traditional I-beam bridge. Additionally, U-beams have fewer horizontal break lines per beam. This combination of reduction in the number of girders and break lines leads to a greatly streamlined aesthetic.

The U-beam section was originally developed and deployed in Texas by the Texas Department of Transportation (TxDOT). It has subsequently been used in bridge projects in a number of Southern states including Louisiana and Arizona. As the Indiana Department of Transportation (INDOT) planned the Accelerate I-465 project, they were encouraged to incorporate innovative materials and methods to meet aesthetic and economic concerns. The Accelerate I-465 team consisting of INDOT and consulting design firms led by HNTB was tasked with increasing the main line capacity of an 11-mile stretch of I-465 originally constructed in the late 1950's and early 1960's, as well as improving deteriorating bridges and pavements. The roadway improvements extend from 56th Street to just south of the I-465/I-70 interchange as shown in Figure 1.2. The roadway widening and realignment necessitated the replacement of a significant number of mainline and highway overpass bridges within the project scope. The Accelerate I-465 team targeted the use of U-beams for these bridge replacements to meet aesthetic and economic constraints.

1.2 Design Concerns

While the use of the U-beam section is becoming more common, there are some design concerns and

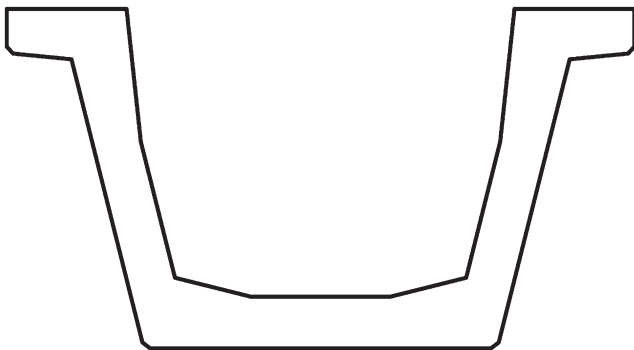


Figure 1.1 U-beam cross section.

code limitations restricting their efficiency. Some questions have arisen regarding how live load is distributed in a U-beam bridge as well as how the bridge deck behaves in flexure. Additionally, code limits on debonding of prestressing strand have created problems for designers.

1.2.1 Live Load Distribution

The live load distribution for U-beam bridges currently prescribed by the American Association of State Highway and Transportation Officials (AASHTO) LRFD Bridge Design Specifications, 6th Edition (AASHTO, 2012a) is the same as that for spread concrete box beams. This method is being used in the absence of any experimental data on the live load distribution for this girder section. The distribution factor for interior girders is determined using Equation 1.1 for one design lane loaded or Equation 1.2 for two design lanes loaded (AASHTO Section 4.6.2.2.2b). The exterior girder distribution factors are to be determined by use of the lever rule (AASHTO Section 4.6.2.2.2d). The lever rule assumes a hinge develops at the center of the first interior girder and moments are summed about this hinge. Two design loads are placed on the deck, the first design load is to be placed 2 ft from the edge of the driving surface and the second load is offset by 6 ft from the first. The ratio of the resulting reaction at the exterior girder to the applied load yields the exterior girder distribution factor. Due to the high torsional stiffness of the U-beam, it is expected that the actual live load distribution for these sections will be more favorable than that specified by AASHTO. Quantifying the live load distribution has the potential of providing future cost savings in the deployment of bridges utilizing this beam cross section.

One Design Lane Loaded:

$$\left(\frac{S}{3.0}\right)^{0.35} + \left(\frac{Sd}{12.0L^2}\right)^{0.25} \quad (1.1)$$

Two Design Lanes Loaded:

$$\left(\frac{S}{6.3}\right)^{0.60} + \left(\frac{Sd}{12.0L^2}\right)^{0.125} \quad (1.2)$$

where:

S : girder or web spacing, ft

d : girder depth, in.

L : span length, ft

1.2.2 Bridge Deck Behavior

Questions have arisen regarding the behavior of bridge decks when supported on U-beams. U-beam bridges have longer transverse deck spans due to the decrease in the overall number of girder lines for the same roadway width. Consequently, it is assumed that flexure will dominate the response of the deck. Current guidance regarding design strip widths (AASHTO

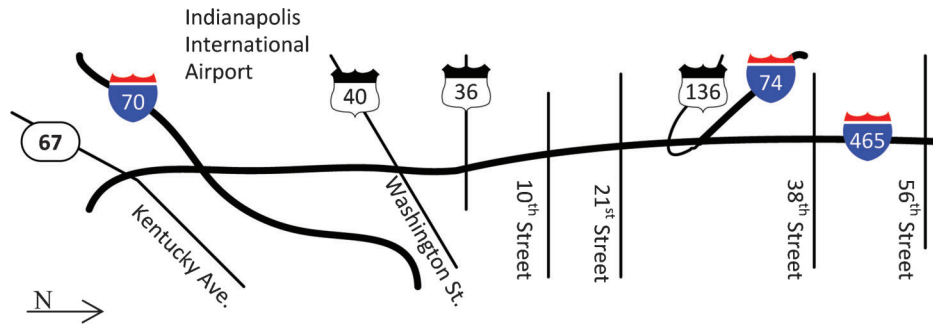


Figure 1.2 Accelerate I-465 project limits.

Section 4.6.2.1.3) may not be applicable as loads may distribute differently due to the long spans. Additionally, it is presumed that the U-beam will provide greater restraint at the girder line than a traditional I-beam. More understanding of this behavior is needed to properly design these bridge decks.

1.2.3 Strand Debonding Limitations

Perhaps the most significant issue identified by the design firm for the I-465 U-beams is the issue of prestressing strand debonding limitations. Chapter 5 of the AASHTO LRFD Bridge Design Specifications (AASHTO Section 5.11.4.3) places several restrictions on the use of partial strand debonding. The number of debonded strands is limited to 25% of the total number of strand, and no more than 40% of one row of strand may be debonded. These debonding limits greatly limit the efficiency of U-beam sections. U-beams require large quantities of prestressing steel due to their large size, yet they have very limited draping capacity. Draping is limited due to the narrow and sloped webs, requiring the majority of the prestressing steel to be placed in the bottom flange.

The AASHTO limits on debonding so greatly reduce the efficiency of the U-beam section, that TxDOT has relaxed the AASHTO limits to improve U-beam efficiency. TxDOT now allows designers to debond up to 75% of the strand in a section (TxDOT, 2013). The AASHTO limit of 25% strand debonding was incorporated into the specification out of concerns related to shear strength (Shahawy et al., 1993). The limitation on debonding essentially ensures that substantial pre-compression will occur at beam ends where shear is primarily of concern. When designing U-beams for TxDOT, designers typically limit the principle web tensile stress to $3\sqrt{f'_c}$ at the centroid of the section to prevent shear problems (He, 2007). Other states such as Indiana have chosen to maintain the AASHTO limits until further study has been conducted about the influence of partial debonding on shear strength. Designing U-beams to meet the AASHTO limitations reduces their efficiency and in the case of Accelerate I-465, necessitated an increase in web thickness of the standard TxDOT section. Designers increased the web thickness from 5-1/2" to 7-1/2" to

accommodate additional draped strands due to limitations on debonding.

1.2.4 Strand Debonding Effectiveness

While questions have arisen about the AASHTO limits on strand debonding, questions have also arisen regarding the effectiveness of common debonding products. Some designers and precasters avoid the use of debonding because of concerns about concrete spalling and strand wedging at release. Spalling around debonded strand can be quite significant, greatly reducing the available concrete cover for the reinforcement in the girder and potentially resulting in durability issues. The severity of this spalling can be seen in Figure 1.3, which shows a cluster of debonded strand at the end of a U-beam produced for the 21st Street Bridge crossing I-465 in Indianapolis. The conditions shown in Figure 1.3 were typical for the beams used in this bridge. In addition, there is concern that wedging forces actually reduce the effectiveness of debonding. Consequently, strands may not be properly debonded as assumed in design.

1.3 Strand Debonding

Debonding strands in pretensioned beams is common in the prestressing industry. Debonding is typically accomplished by shielding (also known as blanketing) the strand with a thin plastic sheathing (split or un-split



Figure 1.3 Concrete spalling around debonded strand.

as shown in in Figure 1.4), preventing bond between the strand and the concrete. Split sheathing, as its name suggests, is plastic sheathing with a longitudinal slit down its length which allows for the sheathing to be installed over a tensioned strand. It can be installed after tensioning has occurred and can be replaced if damaged. Un-split sheathing must be installed prior to tensioning by slipping it over the end of the strand. Therefore, the use of un-split sheathing requires additional care and planning and is rarely used unless specified in the construction documents.

According to Horn and Preston (1981), other debonding techniques such as grease, chemical retarders, and tape have been employed by precasters. Grease and chemical retarders are generally not recommended because they can easily be spilled in areas not intended to be debonded (Kose, 1999). The use of tape as a debond sheathing is also not recommended because the pressures during casting clamp the thin tape around the strand. After the concrete sets and the strands are released, friction forces develop which leads to bond transfer (Kose, 1999).

Designers usually take advantage of debonding at the ends of pretensioned beams where stresses at transfer might otherwise present a flexural cracking problem due to the lack of dead load flexural stresses. An alternative to debonding is to harp (drape) some of the strands up in the end regions. Draping strands reduces the eccentricity at the ends of beams, providing another method of reducing stresses at transfer. However, due to economic reasons, and safety concerns, debonding is often used in conjunction or completely in place of draping (PCI, 2004). Section geometry also can necessitate the use of debonding over draping such as in U-beams where strand are “trapped” in the bottom flange.

The first design guidelines for debonding limits were presented in the third edition of the AASHTO LRFD Bridge Design Specifications (2004). The AASHTO LRFD specifications (2004) limited the percentage of debonded strand based on a series of tests conducted by the Florida Department of Transportation. These tests indicated that the anchored strength of strands is one of the primary contributors to shear strength in the end zone of pretensioned beams (Shahawy et al., 1993).

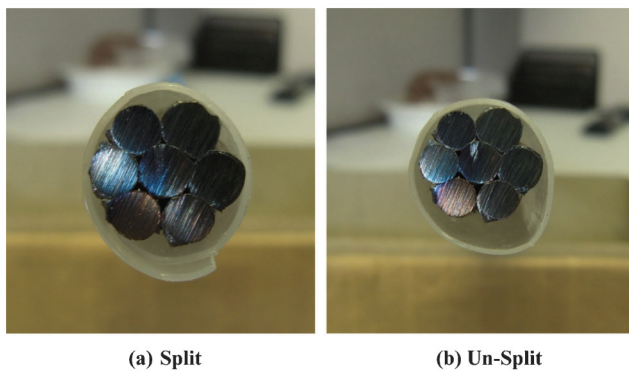


Figure 1.4 Debond sheathing.

There was concern that shear strength may be inadequate when 40% of the strands are debonded. Conservatively, a 25% limit per section and a 40% limit per row were specified. This limit significantly impacts the efficiency of sections such as U-beams and box beams. Furthermore, there is a lack of data regarding this issue which is leading to variations in design limits across the county. An example of this variation among state DOTs is provided in Table 1.1. Ultimately the lack of experimental data has allowed the original AASHTO debonding provisions to remain unchanged since 2004.

Based on recent research at Purdue University on the shear strength of pretensioned beams (Wolf & Frosch, 2007), the real issue may not be the use of debonded strands but rather the influence of the loss of stiffness of the longitudinal reinforcement in the debonded region. This influence of the longitudinal reinforcement stiffness on shear strength was recently tested by Saqan and Frosch (2009). Nine rectangular beams without transverse reinforcement with the same concrete cross-section, prestressing force, and concrete strength were constructed and tested in the Bowen Laboratory at Purdue University. All of the beams were simply supported, loaded at midspan, and designed to have the same shear capacity according to the ACI 318 (2011) design provisions. The amount of prestressing steel and mild steel was varied in each series resulting in different expected shear strengths according to Equation 1.3. According to this equation, the shear strength is directly related to the compressive area at the section in question ($b_w c$). The calculated and actual capacities for the nine beams in the 2009 study are shown in Table 1.2.

$$V_c = 5\sqrt{f'_c} b_w c \quad (1.3)$$

where:

b_w : web width, in.

c : depth to neutral axis, from moment-curvature analysis, in.

f'_c : concrete compressive strength, psi.

The test results in Table 1.2 clearly show the influence of the total area of steel, A_{tot} , (directly related to longitudinal reinforcement stiffness) on shear strength. As the reinforcement area increases, the neutral axis depth and compressive area increases, thus increasing the shear strength according to Equation 1.3. It is important to note that the beams with the same (or close to the same) amounts of total reinforcement (prestressing and mild steel) had similar shear strengths. Consequently, this approach predicts a reduction of shear strength in a debonded region.

1.4 Current Standards

Current practice pertaining to strand debonding is addressed in the AASHTO LRFD Bridge Design Specifications (6th Edition) (2012a), PCI Design Handbook (2010), and ACI 318-11 (2011).

TABLE 1.1
Debonding Limits for DOTs

State	Limiting Percentage per Section	Limiting Percentage per Horizontal Row
Indiana (INDOT, 2012)	25*	40*
California (Caltrans, 2011)	33	50
Texas (TxDOT, 2013)	75	75

*Applies to bulb-tees; limit for AASHTO I-beams and box beams is 50%.

1.4.1 AASHTO LRFD Bridge Design Specifications, 6th Edition (2012a)

AASHTO adopted the limiting percentage of debonded strand per section (25%) following the study by Shahawy et al. (1993). The provisions for debonding (AASHTO Section 5.11.4.3) also limit the percentage of debonded strand per horizontal row to 40%. Debond sheathing terminations are required to be staggered in groups no greater than 40% of the total number of debonded strand, or four strands, whichever is greater. The debonded strand should be distributed symmetrically about the centerline of the beam section in terms of position and length. Exterior strands in each horizontal row are required to be fully bonded. In addition, the development length of debonded strand (measured from the end of sheathing) is required to be doubled where tension exists in the precompressed tensile zone.

1.4.2 PCI Design Handbook, 7th Edition (2010)

PCI recommends the following guidelines (PCI, 2010, Section 5.2.3.1) when debonding is used. All of the strands in the bottom row should not be debonded. The debonding should be staggered at transfer length increments while avoiding debonding adjacent strands. It is also recommended to not debond more than 50% of the strands below a dapped end. Finally, at least the minimum amount of transverse reinforcement should be provided in the debonded region.

TABLE 1.2
Longitudinal Stiffness vs. Shear Strength—Saqa and Frosch (2009)

Series	Specimen	f'_c (psi)	F_c (kip)	A_{ps} (in. ²)	A_s (in. ²)	A_{tot} (in. ²)	V_{ACI} (kip)	V_{calc} (kip)	V_{test} (kip)	Failure Mode
1	V-4-0	7550	108.0	0.61	0.00	0.61	49.6	38.1	46.0	Y-DT
	V-4-0.93	7650	108.0	0.61	0.93	1.54	50.0	46.7	59.5	Y-DT
	V-4-2.37	7750	108.0	0.61	2.37	2.98	50.3	55.5	66.5	DT
2	V-7-0	7900	110.3	1.07	0.00	1.07	50.8	43.2	57.5	DT
	V-7-1.84	7700	110.3	1.07	1.84	2.91	50.1	55.4	67.0	DT
	V-7-2.37	7700	110.3	1.07	2.37	3.44	50.1	58.0	68.5	DT
3	V-10-0	7500	111.1	1.53	0.00	1.53	49.5	46.5	64.5	DT
	V-10-1.51	7500	111.1	1.53	1.51	3.04	49.5	55.7	67.5	DT
	V-10-2.37	7500	111.1	1.53	2.37	3.90	49.5	59.7	72.5	DT

1.4.3 ACI 318-11 (2011)

There is no limiting percentage of debonded strand given in ACI 318-11. In fact, the only requirement for debonded strand is to double the development length (ACI 318-11 Section 12.9.3). The commentary in the same section (ACI 318-11 Section R12.9.3) states that both the transfer length and development length are assumed to be doubled when analyzing sections where strand is not fully developed. The provision in ACI 318-11 Section 11.3.5, however, states that the transfer length of debonded strand is to be taken as 50 strand diameters which is the same as that assumed for fully bonded strand.

1.5 Previous Research

The following studies provided the basis on which several of the current provisions on debonded strand were founded. Studies by Ken and Magura (1965) and Pensinger and Sutton (1987) provided the basis for doubling the development length. The basis for limiting the percentage of debonded strand in the AASHTO LRFD Bridge Design Specifications is Shahawy et al. (1993).

1.5.1 Karr and Magura (1965)

Karr and Magura tested five pretensioned T-beams with and without debonded strand. The beams were loaded in fatigue before being statically loaded to complete failure. The development length required by the 1963 ACI Building Code was found not to be adequate for debonded strand with an embedment length of 1.0 times the development length. It should be noted that the equation for development length in the 1963 ACI Building Code is effectively the same equation as in the current codes (ACI 318-11, 2011; AASHTO, 2012a). It was concluded that the development length for debonded strand should be double that of fully bonded strand after specimens with embedment lengths twice that required by the code performed similarly to a specimen without debonded strand. Only

specimens with embedment lengths of 1.0 and 2.0 times the development length were tested in this study.

1.5.2 Pensinger and Sutton (1987)

Pensinger and Sutton tested six pretensioned box beams with and without debonded strand and with varying embedment lengths of debonded strand. The beams were fatigue tested before being loaded to complete failure under a static loading. It was concluded that doubling the development length of debonded strand suggested by Karr and Magura (1965) was overly conservative. Instead, it was determined that a specimen with an embedment length for debonded strand of 1.5 times the development length resulted in similar behavior as specimens with longer embedment lengths. It should be noted that this conclusion has not been implemented by ACI 318 or AASHTO.

1.5.3 Shahawy et al. (1993)

As previously discussed, the 25% limit implemented by AASHTO originated from the study conducted by Shahawy et al. in 1993 for the Florida Department of Transportation. In this study 32 AASHTO Type II simply supported beams with a cast-in-place deck were tested. The beams were tested with a concentrated load in a manner that produced unequal shear spans. Of these 32 beams, 7 contained debonded strand. Each beam was tested twice by using two setups. After the initial failure, the support was moved in beyond the failure location and then retested. Therefore, each specimen was typically tested with two different span lengths, and thus, two different shear span to depth (a/d) ratios.

Two nominal percentages of debonded strand were used (25% and 50%). Out of the seven specimens with debonded strand, there were three sets of companion specimens each with the two nominal percentages of debonded strand. However, two of these sets of specimens failed in flexure; therefore, they are not relevant to shear strength. Furthermore, none of the fully bonded specimens were tested with the same a/d ratio as their companion specimens. These variations make relative behavioral comparisons not possible.

A 3.7% shear strength reduction was observed in a specimen with 45.5% debonding compared to the companion specimen with 27.3% debonding. These two specimens were reported as identical except for the percentage of debonded strand. Given the results from these two specimens, Shahawy et al. (1993) give the following explanation for a limit on debonding:

Shielding of prestressing strands reduces shear capacity in the end regions of a girder. Girders with 50% of the strands shielded and loaded at 140 inches from the ends exhibited a shear mode of failure with decreased ductility when compared to girders with 25% shielding. Therefore limiting the percentage of shielded strands to 25% appears to be reasonable.

Confinement steel was also studied as a separate variable in this study. It was concluded that the

reduction in shear strength due to the absence of confinement steel in the end regions was greater than the shear strength reduction due to debonding.

1.6 Objective and Scope

The objective of this research program is to develop design strategies to improve the efficiency and optimize the design of the Indiana modified U-beam with a focus on the concerns related to the design of U-beams. In particular, this research program will evaluate the live load distribution appropriate for the design of U-beams, assess the behavior and design of the bridge deck when supported by U-beams, and evaluate both the shear strength and shear design of the composite U-beam system. It is important that the strength of pretensioned concrete beams with debonded strand be fully evaluated.

This research was completed in five major phases:

- Phase 1 consisted of the field instrumentation of the 21st Street Bridge, which is the first U-beam bridge to be built in Indiana. In this phase, the live load distribution and flexural deck behavior of a U-beam bridge are assessed. This phase of research is presented in Chapter 2.
- Phase 2 consisted of an experimental investigation of the effectiveness of debond sheathing. This phase was separated into two parts. Part 1 investigated the effectiveness of a variety of commercially available debond sheathing products while Part 2 focused on the sheathing installation techniques. It is essential that the materials and installation techniques used to debond the strand in this study as well as in the field provide effective debonding. This phase of research is presented in Chapter 3.
- Phase 3 evaluated the influence of strand debonding on the shear strength of pretensioned beams. Considering flexure-shear and web-shear failure modes, a full range of debonding from 0% to 75% is evaluated. This phase of research is presented in Chapter 4.
- Phase 4 evaluated the effect of different concrete strengths in a composite section on shear strength. This is important considering that pretensioned girders are typically constructed as composite members using different concrete strengths. This phase of research is presented in Chapter 5.
- Phase 5 combined the results of Phases 2 through 4 to test scaled U-beams with and without transverse reinforcement to evaluate the applicability of the previous conclusions on this section shape and access overall system behavior. This phase of research is presented in Chapter 6.

2. FIELD EVALUATION OF A U-BEAM BRIDGE

2.1 Research Summary

The 21st Street Bridge over I-465 was instrumented during construction to assess the live load distribution and bridge deck behavior for this U-beam bridge. Strain gages were placed throughout the depth of the composite section on one of the two spans at the 1/4, 1/2, and 3/4 span locations to allow for determination of the live load distribution under applied loading. Additionally, a series of strain gages were placed on the transverse deck reinforcement to measure the

response of the bridge deck under applied loading. After completion of the bridge, two loaded dump trucks were strategically placed in a number of load configurations to allow for measurement of the live load distribution. One of the trucks was also positioned to apply load to the center of the instrumented deck region to allow for assessment of the bridge deck behavior. The results of the live load distribution testing, and bridge deck behavior were compared with the values determined based on the current AASHTO provisions as well as with values obtained from simple, analysis models. Complete details of the experimental program are provided in Appendix A.

2.2 Conclusions

Based on these results of the experimental program, the following conclusions are provided.

2.2.1 Interior Girder Live Load Distribution Factors

- The interior girder live load distribution factor was experimentally determined to be 0.45 for this bridge configuration. This value corresponds to trucks placed at the centerline of the bridge (directly above the interior girder) and was measured at the location of load application (1/2 span).
- The AASHTO equation for one lane loaded on an “Open Steel or Precast Concrete Box” girder bridge yields a distribution factor of 0.41 for this bridge configuration. The value for one lane loaded was selected because load was applied to only one lane of the bridge at a time during load testing.
- Analysis of a beam model also produced a live load distribution factor of 0.41. The model was developed by supporting a beam on three elastic springs which were located at the girder centerlines with each stiffness based on the individual girder stiffness at midspan. The beam element representing the bridge deck was modeled based on a 10 ft strip width. The model results were found to be fairly insensitive to the assumed deck width, and 10 ft was selected because the rear axle loads were applied over approximately a 10 ft width.
- Both the AASHTO and simple analytical model are in reasonable agreement with the measured test results, and distribution factors calculated using these methods should be considered appropriate for design purposes.

2.2.2 Exterior Girder Live Load Distribution Factors

- The exterior girder live load distribution factor was experimentally determined to be 0.48 for this bridge configuration. This value corresponds to trucks being placed at the edge of the driving surface and was measured at the location of load application (1/2 span).
- The results of a lever rule analysis of the bridge as prescribed by AASHTO for an exterior girder yields a live load distribution factor of 0.70. The results of this testing indicate that use of the lever rule is very conservative for this bridge configuration.

- Analysis of a beam model produced a live load distribution factor of 0.58. While the beam model is also conservative, it provides more reasonable results and should be considered suitable for use in design.

2.2.3 Bridge Deck Bending Behavior

- The flexural behavior of the bridge deck between the interior and exterior girder lines exhibited a moment distribution consistent with general flexural behavior; positive moment in the middle of the span and negative moment over the girder lines.
- The magnitude of the reinforcement strains were in general agreement with the analytical results from both a beam and finite element model of the bridge deck. Due to the length of the deck span, flexural behavior appears to dominate its response.
- Strip widths provided for design of bridge decks by AASHTO Section 4.6.2.1.3 were found to be both reasonable and conservative based on the results of finite element modeling.

3. EVALUATION OF DEBOND SHEATHING EFFECTIVENESS

3.1 Research Summary

To evaluate the effectiveness of commercially available prestressing strand debonding products, an experimental investigation was conducted. It was important to examine the effectiveness of debonding products prior to studying the influence of debonding on shear strength to determine which debonding product is most effective and which should be used in the shear strength investigation. The research was separated into two phases. The first phases evaluated the effectiveness of a variety of commercially available debond sheathing products. Based on the results from these phases, it is clear that installation technique is an important component related to the performance of the split sheathing products. Therefore, the second phase evaluated the influence of installation technique of the performance of sheathing.

3.2 Evaluation of Debond Sheathing Products

A series of 27 concentrically prestressed specimens were constructed to evaluate the effectiveness of four commercially available prestress strand debonding products. In addition fully bonded specimens as well as specimens debonded with oversized PVC pipe were constructed as control specimens. Three split sheathing products were tested along with one un-split sheathing. The split sheathing products tested were selected to represent the extremes of slit overlap and snugness of fit of the sheathing samples collected. Use of a mechanical strain gage allowed for assessment of concrete strain distributions along the length of each specimen. Strain measurements were recorded immediately after release and at 14 and 28 days after release. These strain distributions allowed for direct visual comparison of

the debonding effectiveness as well as determination of the transfer length for each specimen. Complete details of the experimental program are provided in Appendix B.

3.2.1 Conclusions

Based on the experimental program, the following conclusions are made:

1. Un-split sheathing provides excellent debonding performance. This product can be used where control of release stresses in the debonded regions is essential.
2. Split sheathing can also be used to achieve effective debonding; however, the performance of this sheathing is product specific. The effectiveness of the split sheathing products varied significantly ranging from full debonding to transfer of approximately 60% of the prestress force over a 4 ft debond length.
3. The length of overlap at the slit in the sheathing is of little importance to the performance of the product. The product with the most overlap at the slit (13/16 in.) performed adequately, the product with the least overlap (3/16 in.) performed excellently, and the third product with an intermediate amount of overlap (3/8 in.) performed poorly.
4. The tightness of the split sheathing impacts its performance. The tightest fitting sheathing product (PSI) performed the best of the three, the loosest product (DuraJoint) had the worst performance, and the product with intermediate tightness (Fister) performed adequately.

Limited testing was conducted on the impact that taping the termination of split debond sheathing has on the performance of the sheathing. One specimen was produced using DuraJoint split sheathing without tape placed at the terminations. Comparison of the results of the taped and un-taped specimens for this product indicate no benefit from providing tape at the termination. However, this type of sheathing performed poorly in all the specimens, likely due to paste infiltration from the slit. Therefore, any impact from potential paste infiltration from the end of the sheathing may be overshadowed by the paste infiltration from the slit in this product. The influence of taping is further investigated in the next section.

3.3 Evaluation of Debond Sheathing Installation Techniques

Six concentrically prestressed concrete prisms were constructed to evaluate the effectiveness of two different types of debond sheathing (split and un-split) as well as alternative taping (sealing) techniques. Two prisms were designed as boundary specimens. One of these boundary specimens was designed to exhibit no debonding (fully bonded), and the other was designed to demonstrate perfect debonding (PVC pipe debonded with ends sealed). Commercially available debond sheathing was used in the remaining four specimens: two with split sheathing and two with un-split sheathing. The effects of sealing (or not sealing) the openings in the specimens with split and un-split sheathing was evaluated by

comparing their debonding effectiveness to that of the PVC pipe debonded specimen. A mechanical strain gage provided means for assessing the debonding effectiveness by using the strain data to construct concrete surface strain profiles for each specimen at transfer, 14 days, and 28 days after casting. The concrete surface strains are directly correlated to the stress in the concrete, and therefore, to the bond between the strand and the surrounding concrete. Strain measurements were recorded over time to determine if the debonding effectiveness is time dependent. Complete details of the experimental program are provided in Appendix C.

3.3.1 Conclusions

Based on the experimental program, the following conclusions are made:

1. The majority of the specimens performed well in terms of debonding effectiveness. However, it was discovered that paste infiltration as a result of openings in the sheathing reduced the effectiveness of the un-taped, split sheathing allowing for force transfer inside the debonded region. The impact of paste infiltration on debonding effectiveness also depends on the length over which the paste covered the strand inside the sheathing. It was determined that un-taped, split sheathing performed the worst due to the fact that paste infiltrated along the entire length of the sheathing.
2. No noticeable difference was observed in the transfer lengths at the cut ends and the dead ends. All transfer lengths were observed to be approximately 2 ft (48d_s).
3. The transfer lengths remained unchanged over time. Measurements were taken at transfer, 14 days after the cast, and 28 days after the cast.

4. INFLUENCE OF STRAND DEBONDING ON SHEAR STRENGTH

4.1 Research Summary

Fourteen pretensioned beams were constructed and tested to better understand the influence of strand debonding on shear strength. It was hypothesized that the shear strength would only be reduced in the debonded regions due to the reduced prestressing force and longitudinal reinforcement stiffness. Therefore, these beams were separated into four series. Series I specimens were rectangular beams designed to fail in flexure-shear (V_{ci}) inside (at the end of) the debonded region. Specimens in Series II were rectangular beams designed to fail in flexure-shear (V_{ci}) outside the debonded region. The specimens in Series III were designed as I-beams to enhance the likelihood of web-shear failures (V_{cw}) inside the debonded region. Specimens in these series were designed to include one specimen of each of the following percentages of debonded strand: 0, 25, 50, and 75. The specimens in these first three series were also constructed without transverse reinforcement in the debonded region to better understand the influence of the debonding on shear strength. Series IV, however, consisted of one

rectangular beam with 50% debonding designed to investigate the effect of transverse reinforcement in the debonded region. Complete details of the experimental program are provided in Appendix D.

4.2 Conclusions

Based on the experimental program, the following conclusions are made:

1. As the percentage of debonding increased from 0% to 75%, shear strengths decreased. For V_{ci} at the end of the debonded region (Series I), a 35% reduction in shear strength (at formation of primary shear crack) was observed in the specimen with 50% debonding relative to the specimen with 0% debonding. In increasing the debonded strand to 75%, a 61% reduction in shear strength (at formation of primary shear crack) occurred. For V_{cw} within the debonded region (Series III), a 16% reduction in shear strength (at formation of primary shear crack) was observed in the specimen with 50% debonding relative to the specimen with 0% debonding. Where V_{ci} cracks formed outside the debonded region (Series II), an 8% reduction in shear strength (at formation of primary shear crack) was observed in the specimen with 50% debonding relative to the specimen with 0% debonding.
2. The modulus of rupture was observed to be lower at the end of the debonded region than at midspan (fully bonded region). Values as low as $3\sqrt{f'_c}$ were observed for the Series II specimens with 75% debonding. This corresponds to a 53% reduction in the modulus of rupture relative to midspan. It is theorized that these reduced modulus of rupture values result from damage sustained at the end of the debonded region at transfer (when the strands were cut). As the number of debonded strand increased, the modulus of rupture at the end of the debonded region decreased. In addition, a larger modulus reduction (53%) was observed in the Series II specimens with 75% debonding compared to the Series I

specimen with 75% debonding (38%). The shorter debonded length likely resulted in less friction in the sheathing at transfer; therefore, increasing damage.

3. Using the shear model to analyze the beams with a modulus of rupture assumed to be zero throughout the beam (debonded and fully bonded regions) resulted in conservative and consistent calculations of the concrete contribution to shear strength. As shown in Table 4.1 the shear model provided an average shear strength ratio of 1.10 and a standard deviation of 0.09 when the modulus was taken as zero ($f_r = 0\sqrt{f'_c}$). Using a modulus of rupture of zero is conservative and allows for variations of the modulus as well as effects of debonding.
4. The ACI 318 and AASHTO approaches provided conservative calculations for web-shear strength (V_{cw}). However, these approaches are unconservative for flexure-shear (V_{ci}) as shown in Table 4.1 ($f_r = 0\sqrt{f'_c}$, Limit). There are two problems. First, the lower bound limits are not appropriate for lightly reinforced sections such as what occurs with debonding. Second, the use of a modulus of rupture of $6\sqrt{f'_c}$ is too high for sections with debonded strand. These results indicate that current design expressions cannot be safely used with a high percentage of debonded strand.
5. The ACI 318 and AASHTO approaches for the calculation of flexure-shear strength can be significantly improved if slightly modified. First, the lower bound limits should not be used for sections with debonded strand. Second, the modulus of rupture should be set as $0\sqrt{f'_c}$. Results of this approach are provided in Table 4.1 ($f_r = 0\sqrt{f'_c}$, No Limit). It should be noted that the code estimates (using these modifications) for the flexure-shear strength of V_{ci} -in-75 are still unconservative (Table 4.1). Therefore, these modifications do not completely solve the problems with these expressions.
6. Transverse reinforcement (#3 at 9 in.) placed in (and surrounding) the debonded region (V_{ci} -in-50- V_s) resulted in a higher shear capacity with more ductility compared to the specimen without transverse reinforcement in the debonded region (V_{ci} -in-50). The shear carried beyond

TABLE 4.1
Comparison of Shear Strength Ratios for Series I, II, and III

Specimen ID	$f_r = 6\sqrt{f'_c}$					$f_r = 0\sqrt{f'_c}$				
	Model	ACI 318		AASHTO		Model	ACI 318		AASHTO	
		Limit	N.L.*	Limit	N.L.*		Limit	N.L.*	Limit	N.L.*
V_{ci} -in-00	1.11	1.01	1.01	1.02	1.02	1.12	1.07	1.30	1.02	1.31
V_{ci} -in-25	1.04	0.96	0.96	0.96	0.96	1.05	1.01	1.23	0.97	1.23
V_{ci} -in-50	0.94	0.67	0.67	0.67	0.67	0.96	0.71	0.97	0.68	0.96
V_{ci} -in-75	0.78	0.42	0.47	0.40	0.47	0.96	0.42	0.80	0.40	0.78
V_{ci} -out-00	1.19	0.95	1.16	0.90	1.16	1.19	0.95	1.45	0.90	1.46
V_{ci} -out-25	1.18	0.99	1.18	0.96	1.19	1.19	0.99	1.47	0.96	1.48
V_{ci} -out-50	1.12	0.93	1.11	0.89	1.12	1.12	0.93	1.38	0.89	1.40
V_{ci} -out-75	0.84	0.67	0.82	0.64	0.82	1.09	0.67	0.96	0.64	0.94
V_{ci} -out-75-2	0.85	0.70	0.84	0.67	0.85	1.11	0.70	0.99	0.67	0.97
V_{cw} -00	0.99	1.33	1.33	1.82	1.82	0.99	1.33	1.33	1.82	1.82
V_{cw} -25	1.00	1.25	1.25	1.94	1.94	1.11	1.25	1.25	1.94	1.94
V_{cw} -50	0.98	1.18	1.18	1.90	1.90	1.15	1.36	1.36	1.90	1.90
V_{cw} -75	0.92	0.95	0.95	1.61	1.61	1.28	1.65	1.65	1.63	1.63
Average:	1.00	0.92	0.99	1.11	1.19	1.10	1.00	1.24	1.11	1.37
Std. Dev:	0.13	0.26	0.25	0.53	0.48	0.09	0.34	0.24	0.53	0.39

*N.L.=No limit.

the formation of the primary shear crack in V_{ci} -in-50- V_s was increased by 64%. In addition, cracks widths were controlled until complete failure. For comparison, shear beyond the primary shear crack in V_{ci} -in-50 was increased by 44%. However, extremely wide shear crack widths occurred after primary shear crack formation.

7. The steel contribution to shear capacity (V_s) for V_{ci} -in-50- V_s was overestimated when using the ACI 318 and AASHTO equations which are smeared stirrup approaches (Table 4.1). Test results indicate that only 2 stirrups were effective while the equations suggest 3.6. An equation proposed by Frosch (2000), however, provided a conservative representation of the stirrup contribution by calculating a discrete number of stirrups that a shear crack would likely cross. Using this approach, 2 stirrups are calculated as effective which is in agreement with the test results. This approach is of increased importance when a large stirrup spacing is used such that a small number of stirrups are expected to cross a shear crack.

5. INFLUENCE OF COMPOSITE SECTION ON SHEAR STRENGTH

5.1 Research Summary

Six rectangular, reinforced concrete beams were constructed and tested to evaluate the influence of different concrete strengths used in composite members. It was hypothesized that the shear strength of these specimens is dependent on the concrete provided in the compression zone. The experimental program was divided into three series (two beams each) based on the concrete strengths. Each series included a beam with a low longitudinal reinforcement ratio (0.48%) and a beam with a high longitudinal reinforcement ratio (2.40%). Series I specimens were constructed with normal strength concrete (4,000 psi) as typically used in bridge decks. Series II specimens were constructed with high strength concrete (10,000 psi) as typically found in pretensioned beams. Series III specimens were constructed as composite beams using high strength concrete (10,000 psi) in the bottom portion (representing the beam) and normal strength concrete (4,000 psi) in the top portion (representing the deck). Complete details of the experimental program are provided in Appendix E.

5.2 Conclusions

Based on the experimental program, the following conclusions are made:

1. The load-deflection behavior of the specimens tested are clearly distinguished by the amount of longitudinal reinforcement. The average shear capacities of the specimens with a high reinforcement ratio (2.40%) were double that of the specimens with a low reinforcement ratio (0.48%).
2. The concrete compressive strength was observed to have almost no impact on the shear strength of the specimens tested in this experimental program. The small differences in test results (8% for the specimens with 0.48% reinforcement and 12% for the specimens with 2.40%

reinforcement) are within the scatter expected in the shear test results.

3. The shear model and MCFT conservatively estimated the shear capacity of almost every specimen (Table E.11). It should be noted that the MCFT yielded a slightly unconservative shear strength for D10-B10-0.48. The shear model and MCFT are the only two of the four approaches that incorporate the longitudinal reinforcement stiffness in the calculation of shear strength. The importance of the longitudinal reinforcement ratio is clearly visible in the test results.
4. The effect of the concrete compressive strength in the shear model is also shown to have a reduced impact on shear strength as compared with other methods such as ACI 318. The test results support this minimal influence of the concrete strength on shear strength.
5. Both the ACI 318 and AASHTO simplified approach were unable to conservatively calculate the shear strength of the specimens with a low reinforcement ratio (0.48%) because these code equations do not account for the longitudinal reinforcement. Shear strength estimates were unconservative in all cases. For the nominal 10,000 psi specimen, V_{test}/V_{calc} ratios of 0.53 for ACI 318 and 0.58 for AASHTO were obtained.
6. The AASHTO simplified approach as discussed in Section D.2.3.2.3 conservatively estimated the shear capacity of every specimen when the lower bound limit was ignored. However, for the specimens with a reinforcement ratio of 2.40%, extremely conservative results are obtained with an average $V_{test}/V_{calc}=2.8$.

6. INFLUENCE OF U-SHAPE ON SHEAR STRENGTH

6.1 Research Summary

Two pretensioned U-beams were constructed and tested to evaluate the effects of strand debonding and shape on shear strength. The U-beam sections were half scale and designed to evaluate the applicability of the findings from the previous three phases on this cross section. Furthermore, this phase allowed for assessment of analytical models to accurately capture the shear strength of a section with a complex geometry. The two U-beams were only differentiated in design by the transverse reinforcement. One specimen was designed without transverse reinforcement in the debonded region while the other specimen was designed with transverse reinforcement throughout the span length. A cast-in-place deck was constructed on both U-beams after transfer to reflect bridge construction sequencing and common practice. Complete details of the experimental program are provided in Appendix F.

6.2 Conclusions

Based on the experimental program, the following conclusions are made:

1. Low modulus of rupture values were observed for these specimens, especially at the end of the debonded region. On average, the modulus of rupture was $4.6\sqrt{f'_c}$ at midspan and $2.1\sqrt{f'_c}$ at the end of debonding. Therefore,

debonding 50% of the strand resulted in a 54% reduction in the modulus. This was higher than observed for the rectangular section in Appendix D, where 50% debonding resulted in a 26% reduction in the modulus.

2. The shear model was shown to be capable of conservatively estimating the concrete contribution to shear strength of U-beams regardless of its complex geometry. The model resulted in a $V_{\text{test}}/V_{\text{calc}}$ ratio of 1.05 using $f_r = 0\sqrt{f'_c}$. The shear funnel approach using 45 degree angles captured the overall shear behavior.
3. The ACI 318 and AASHTO approaches to calculate the concrete contribution to shear capacity provided conservative estimates of shear strength when the modulus of rupture was taken as zero ($f_r = 0\sqrt{f'_c}$) in the debonded region. $V_{\text{test}}/V_{\text{calc}}$ ratios of 1.05 for ACI 318 and 1.47 for AASHTO were computed.
4. Adding transverse reinforcement in the debonded region provided additional shear capacity as well as improved ductility. With the addition of #3 at 12 in., the shear capacity was increased 20% beyond the shear at the formation of the primary shear crack. Shear crack widths were controlled and failure was not brittle. The transverse reinforcement also forced the shear failure to occur outside the debonded region. Shear beyond the primary shear crack (9% increase) was also carried in the specimen without transverse reinforcement in the debonded region. An extremely brittle failure, however, was observed for this specimen.
5. The wide stirrup spacing led to unconservative estimates of the stirrup contribution to shear capacity when using code expressions which use the smeared stirrup approach. This approach estimated 2.5 stirrups would cross the shear crack while the test results indicate only 1 stirrup crossed the crack. The integer stirrup approach, on the other hand, provided accurate estimates of the stirrup contribution indicating that only 1 stirrup would be effective.

7. DESIGN RECOMMENDATIONS

7.1 Bridge Deck Bending Behavior

When designing a bridge deck on a U-beam bridge with long transverse deck spans, it is recommended that the provisions of AASHTO Section 4.6.2.1.3 be followed for computing effective deck strip widths. Deck design should be based on commonly assumed flexural theory.

7.2 Live Load Distribution Factors

7.2.1 Interior Girder

When proportioning an interior girder on a U-beam bridge, it is recommended that either the AASHTO Section 4.6.2.2b for "Open Steel or Precast Concrete Boxes" provisions or a beam model be used to determine the live load distribution factor. When calculating the distribution factors using a beam model, the girders are modeled as support springs and the deck is modeled as the beam. The spring stiffness is determined based on the midspan stiffness of each girder. The beam stiffness is determined based on bridge deck thickness assuming

an effective deck strip width consistent with that used in bridge deck design. Alternatively, a 10 ft deck strip can be assumed. Analysis results indicate that the distribution factor is not highly sensitive to the assumed deck width.

7.2.2 Exterior Girder

When proportioning an exterior girder on a U-beam bridge it is recommended that the beam model previously discussed for the interior girders be used to determine the live load distribution factor. While the lever rule as prescribed by AASHTO Section 4.6.2.2.d provides conservative results, improvements in economy can be achieved through improved modeling that is only slightly more complicated. The beam model provides a consistent approach where both interior and exterior girder distribution factors can be determined using the same model.

7.3 Debond Sheathing

- All openings in debonding sheathing should be sealed with a flexible adhesive tape such as duct tape to ensure effective debonding. Alternately, un-split sheathing should be used.
- Debond sheathing should be staggered so that all debonded strand do not begin transfer at the same location. A significant reduction (54%) in the modulus of rupture was observed when increased numbers of strand were transferred at the same location. The AASHTO LRFD Bridge Design Specifications provide recommendations regarding staggering that are considered reasonable to assist in minimizing this phenomenon.

7.4 Shear Strength

7.4.1 Flexure-Shear Strength (V_{ci})

- The concrete strength in the compression zone of composite beams should be used to calculate flexure-shear strength. Conservatively, the section can be assumed as homogenous using the lower strength concrete.
- For the calculation of shear strength of beams with debonded strand, the modulus of rupture should be assumed as zero ($f_r = 0\sqrt{f'_c}$) in the debonded regions to account for the reduced moduli that can occur at the ends of debonded regions.
- **Shear model:** Taking the modulus of rupture as zero throughout the beam can be used to conservatively and consistently estimate the flexure-shear strength of beams with or without debonded strand. It should be noted that the modulus only needs to be taken as zero in the debonded region; however, assuming the modulus as zero throughout the beam simplifies analysis. It is recommended that a 45° shear funnel be used to provide the effective shear area used in the shear model. To simplify analysis, the effective shear area can conservatively be based on the web width. Therefore, the flexure-

shear strength can be calculated as $V_{ci} = 5\sqrt{f'_c}b_wc$ and the location of cracking determined based on $f_r = 0\sqrt{f'_c}$.

- **ACI 318 and AASHTO:** The lower limits for flexure-shear strength in ACI 318 and AASHTO are not appropriate and should not be used. In addition, a modulus of rupture of zero should be assumed in the debonded region as previously discussed. Assuming the modulus as zero throughout the beam further increases the conservatism. It is important to note, however, that the flexure-shear strength of V_{ci} -in-75 was underestimated (V_{test}/V_{calc} of 0.80 for ACI 318 and 0.78 for AASHTO) using these modifications to the code approaches. The flexure-shear strength in ACI 318 should be calculated using Equation 7.1 and Equation 7.2, and the expressions in AASHTO should be substituted with Equation 7.3 and Equation 7.4.

$$V_{ci} = 0.6\sqrt{f'_c}b_wd_p + V_d + \frac{V_iM_{cre}}{M_{max}} \quad (7.1)$$

$$M_{cre} = \frac{I}{y_t}(f_{pe} - f_d) \quad (7.2)$$

$$V_{ci} = 0.02\sqrt{f'_c}b_vd_v + V_d + \frac{V_iM_{cre}}{M_{max}} \quad (7.3)$$

$$M_{cre} = S_c \left(f_{pe} - \frac{M_{dnc}}{S_{nc}} \right) \quad (7.4)$$

7.4.2 Web-Shear Strength (V_{cw})

- The web-shear strength can accurately be calculated using a principal stress analysis approach with the split tensile strength assumed to be $6\sqrt{f'_c}$. However, the ACI 318 required concrete tensile strength of $4\sqrt{f'_c}$ should be used for conservatism.
- **ACI 318 and AASHTO:** Although the existing web-shear strength expressions in ACI 318 and AASHTO provide conservative estimates, it is recommended that a principal stress analysis be conducted when more accurate estimates are required. It is recommended to use a concrete tensile strength of $4\sqrt{f'_c}$.

7.4.3 Shear Strength Provided by Transverse Reinforcement (V_s):

The integer stirrup approach (Equation 7.5 through Equation 7.7) should be used to calculate the steel contribution to shear strength, especially in beams with widely spaced stirrups.

$$V_s = A_v f_y N_v \quad (7.5)$$

$$N_v = INT \left(\frac{d - l_{dv}}{s} \right) \quad (7.6)$$

$$l_{dv} = \left(\frac{0.02f_y}{\sqrt{f'_c}} \right) d_b \quad (7.7)$$

7.5 Debonding Limit

It is recommended that the 25% debonding limit be removed. The concrete contribution to shear strength (V_c) must be calculated in the debonded region as outlined above. Web-shear strength (V_{cw}) can control throughout the debonded region while flexure-shear strength (V_{ci}) will control at the end of debonding.

7.6 Expected Benefits

It is anticipated that these design and construction recommendations will enable designers to more economically utilize the capabilities of U-beams. More importantly, the recommendations regarding debonding are applicable not only for U-beams, but prestressed girders in general. Therefore, improved efficiency and economy can be achieved for the various girders types used across the state. Through the improved understanding of behavior provided by this research and the improved design methods provided, not only is more economic design possible, improved safety of the traveling public can be provided.

REFERENCES

- AASHTO. (2004). *AASHTO load resistance factor design (LRFD) bridge design specifications* (3rd ed.). Washington, DC: American Association of State Highway and Transportation Officials.
- AASHTO. (2012a). *AASHTO load resistance factor design (LRFD) bridge design specifications* (6th ed.). Washington, DC: American Association of State Highway and Transportation Officials.
- AASHTO. (2012b). *Standard specification for steel strand, uncoated seven-wire for concrete reinforcement* (M203). Washington, DC: American Association of State Highway and Transportation Officials.
- ACI 318. (2011). *Building code requirements for structural concrete (ACI 318-11) and commentary*. Farmington Hills, MI: American Concrete Institute.
- ACI 363. (1992). *Guide to quality control and testing of high-strength concrete*. Farmington Hills, MI: American Concrete Institute.
- ASTM. (2002). *Standard test method for static modulus of elasticity and Poisson's ratio of concrete in compression* (ASTM-C469). West Conshohocken, PA: ASTM International.
- ASTM. (2011). *Standard test method for splitting tensile strength of cylindrical concrete specimens* (ASTM-C496). West Conshohocken, PA: ASTM International.
- ASTM. (2012). *Standard specification for steel strand, uncoated seven-wire for prestressed concrete* (ASTM-A416). West Conshohocken, PA: ASTM International.
- ASTM. (2012). *Standard test method for compressive strength of cylindrical concrete specimens* (ASTM-C39). West Conshohocken, PA: ASTM International.
- ASTM. (2012). *Standard Test Methods and Definitions for Mechanical Testing of Steel Products*. ASTM-A370. West Conshohocken, PA: ASTM International.
- ASTM (2013). *Standard practice for making and curing concrete test specimens in the laboratory* (ASTM-C192). West Conshohocken, PA: ASTM International.
- Barnes, R. W., Burns, N. H., & Kreger, M. E. (1999). *Development length of 0.6-inch prestressing strand in*

- standard I-shaped pretensioned concrete beams. Austin: Center for Transportation Research, Bureau of Engineering Research, University of Texas at Austin.
- Caltrans. (2011). *California amendments to AASHTO LRFD Bridge Design Specifications* (4th ed). Sacramento, CA: California Department of Transportation.
- FDOT. (2014). *Standard specifications for road and bridge construction*. Tallahassee, FL: Florida Department of Transportation.
- Frosch, R. J. (2000). Behavior of large-scale reinforced concrete beams with minimum shear reinforcement. *ACI Structural Journal*, 97(6), 814–820.
- He, E. (2007). Personal correspondence regarding precast U girder study topics from E. He of HNTB Corporation, Indianapolis, IN.
- Horn, D. G., & Preston, H. K. (1981). Use of debonded strands in pretensioned bridge members. *PCI Journal*, 26(4), 42–58.
- INDOT. (2012). *Design manual*. Indianapolis, IN: Indiana Department of Transportation.
- Karr, P. H., & Magura, D. D. (1965). Effect of strand blanketing on performance of pretensioned girders. *PCI Journal*, 10(6), 20–34.
- Kose, M. M. (1999). *Statistical evaluation of transfer and development length of low-relaxation prestressing strands in standard I-shaped pretensioned concrete beams* (Doctoral dissertation). Lubbock: Texas Tech University.
- PCI. (2004). *PCI design handbook—Precast and prestressed concrete* (6th ed.). Chicago, IL: Precast/Prestressed Concrete Institute.
- PCI. (2010). *PCI design handbook—Precast and prestressed concrete* (7th ed.). Chicago, IL: Precast/Prestressed Concrete Institute.
- Pensinger, K. L., & Sutton, C. D. (1987). *A fatigue study of debonded strands in pretensioned prestressed members* (Report CE-STR-87-23). West Lafayette, IN: Purdue University. Retrieved from https://engineering.purdue.edu/CE/Academics/Undergraduate/Groups/Structural/Details/CE691S-Seminar/CE691S_Fall08/ReportSeries/ReportSeries/1987/ReportSeries/1987/CE-STR-87-23.pdf
- Saqan, E. I., & Frosch, R. J. (2009). Influence of flexural reinforcement on shear strength of prestressed beams without web reinforcement. *ACI Structural Journal*, 106(1), 60–68.
- Sargin, M. (1971). *Stress-strain relationship for concrete and the analysis of structural concrete sections*. Waterloo, Ontario, Canada: Solid Mechanics Division, University of Waterloo.
- Shahawy, M., Robinson, B., & Batchelor, B. deV. (1993). *An investigation of shear strength of prestressed concrete AASHTO type II girders*. Tallahassee, FL: Structures Research Center, Florida Department of Transportation.
- Sozen, M. A., Zwoyer, E. M., & Siess, C. P. (1959). *Investigation of prestressed concrete for highway bridges, part 1: Strength in shear of beams without web reinforcement* (Engineering Experiment Station Bulletin No. 452). Urbana: University of Illinois.
- Thorenfeldt, E., Tomaszewicz, A., & Jensen, J. J. (1987). Mechanical properties of high strength concrete and application to design. *Proceedings of the Symposium: Utilization of High-Strength Concrete* (pp. 149–159). Trondheim, Norway: Tapir Academic Press.
- Tompos, E. J., & Frosch, R. J. (2002). Influence of beam size, longitudinal reinforcement, and stirrup effectiveness on concrete shear strength. *ACI Structural Journal*, 99(5), 559–567.
- Tureyen, A. K., & Frosch, R. J. (2003). Concrete shear strength: Another perspective. *ACI Structural Journal*, 100(5), 609–615.
- Tureyen, A. K., Wolf, T. S., & Frosch, R. J. (2006). Shear strength of reinforced concrete T-beams without transverse reinforcement. *ACI Structural Journal*, 103(5), 656–663.
- TxDOT. (2013). Chapter 3: Superstructure design. In *TxDOT bridge design manual*, Austin, TX: Texas Department of Transportation.
- Wang, P. T., Shah, S. P., Naaman, A. E. (1978). High strength concrete in ultimate strength design. *ASCE Journal of the Structural Division*, 104(11), 1761–1773.
- Wight, J. K., & MacGregor, J. G. (2009). *Reinforced concrete mechanics and design* (5th ed.). Upper Saddle River, NJ: Pearson Education, Inc.
- Wolf, T. S., & Frosch, R. J. (2007). Shear design of prestressed concrete: A unified approach. *ASCE Journal of Structural Engineering*, 133(11), 1512–1519.
- Zwoyer, E. M., & Siess, C. P. (1954). Ultimate strength in shear of simply-supported prestressed concrete beams without web reinforcement. *Journal of the American Concrete Institute*, 51(2), 181–200.

APPENDICES

APPENDIX A. FIELD EVALUATION OF A U-BEAM BRIDGE

A.1 INTRODUCTION

The field evaluation portion of this study focused on IB-30026, the first U-beam bridge to be constructed in the state of Indiana. The bridge carries 21st Street in Indianapolis, Indiana over I-465 and was replaced as part of the Accelerate I-465 project. The field evaluation focused on experimentally determining the live load distribution as well as the bridge deck flexural behavior. This chapter describes the bridge, materials testing, the instrumentation program, data collection, and analysis.

A.2 BRIDGE OVERVIEW

A.2.1 General

The 21st Street Bridge was designed by HNTB in their Indianapolis, Indiana office. The bridge consists of two 116 ft spans made continuous for live load with an overall width of 51 ft. A modified 54 in. Texas U-beam was selected for the spans and made continuous with the cast-in-place deck. The bridge has a skew of 18 degrees and utilizes integral abutments. The overall dimensions of the girders used in this bridge are shown in Figure A.1. Each span has three girder lines as shown in Figure A.2. The low number of girder lines emphasizes one of the key benefits of the U-beam. The bridge consists of two 12 ft lanes, two 6 ft shoulders, and two 6 ft sidewalks.

The girders are typical 54 in. Texas U-beams with several modifications for use in Indiana. The thickness of the webs was increased from 5-1/2 in. to 7-1/2 in. to allow for additional strand draping. Due to concerns about long term inspections of the girders to assess their condition, INDOT requested that an access hatch be added to each girder for inspection purposes. In response, HNTB added 3 ft x 1.5 ft access hatches to both ends of each girder. Additionally, lighting and electrical outlets were installed inside the girders to aid in future inspection work. These provisions aided in instrumentation of the precast girders after erection. As previously mentioned in Section 1.2.3, TxDOT has

eased the 25% debonding limit imposed by AASHTO and replaced it with a limit of 75%. Absent additional studies on the implications of increasing the percentage of debonded strand, Indiana maintained the AASHTO limits. Therefore, in the design of the 21st Street girders, the percentage of debonding was a key limiting factor. The final design maximized debonding within these limits.

A.2.2 Girder Prestressing

A total of 93-0.6 in. diameter uncoated seven-wire, low-relaxation, Grade 270 prestressing strands, conforming to ASTM A416, and AASHTO M203 were specified for each girder. Debonding was specified for selected strand placed in the bottom flange while other strands located in the webs were draped. Strand was debonded in six groups with a total of 21 debonded strands. Draping was performed for 18 strands in each web for a total of 32 strands per girder. The location of the draped and debonded strands is shown in Figure A.3. The designers were constrained by the AASHTO limits for both overall debonding percentage (25%) as well as the percentage of strand which may be debonded in each row (40%).

The design jacking force for each 0.6 in. strand was 43,900 lbs to develop a stress of 202,500 psi ($0.75f_{pu}$). A final total prestress loss of 12,900 psi was assumed. The effective prestress for each strand is therefore estimated to be 189,600 psi.

A.3 INSTRUMENTATION DESIGN

The objective of the field instrumentation of the 21st Street Bridge was to provide experimental data to access the live load distribution and deck behavior of U-beam bridges. Several constraints and limitations influenced the design of the instrumentation. It was of primary importance that the research instrumentation of the bridge not cause any damage or harm to the structure in the short or long term. Additionally, it was important that research activities not delay or impede construction activities. Due to the fast pace of girder construction at the precast yard, it was decided that no instrumentation would be placed within the girders. This decision allowed for more timely production of the girders. Instead gages were installed on the interior surface of the girders after girder erection.

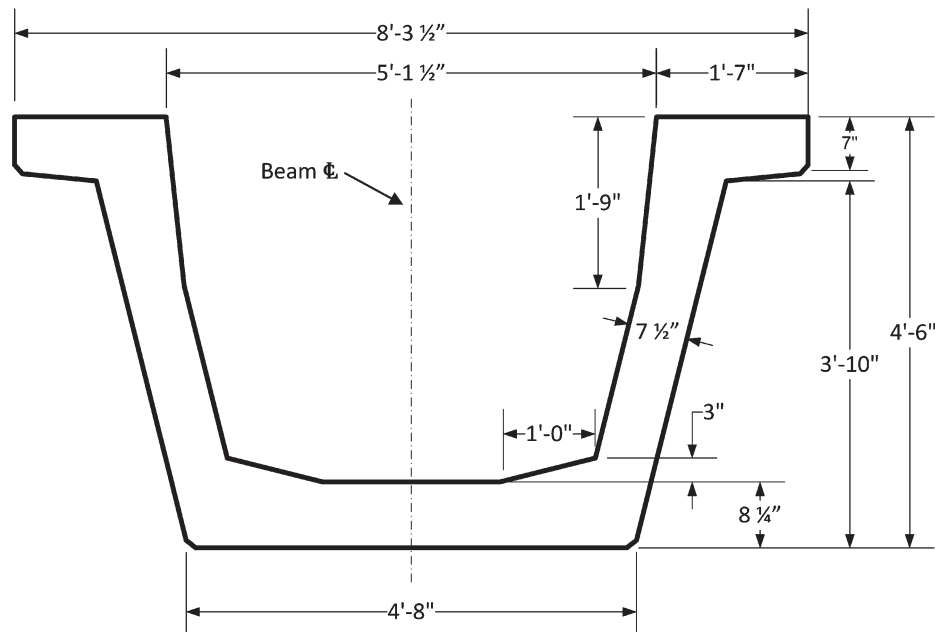


Figure A.1 U-beam dimensions.

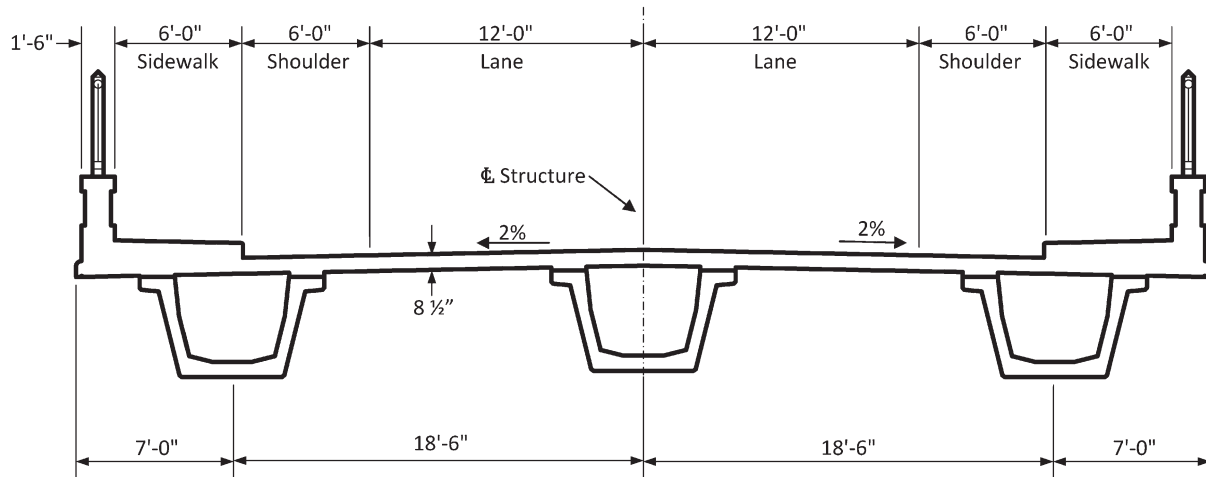
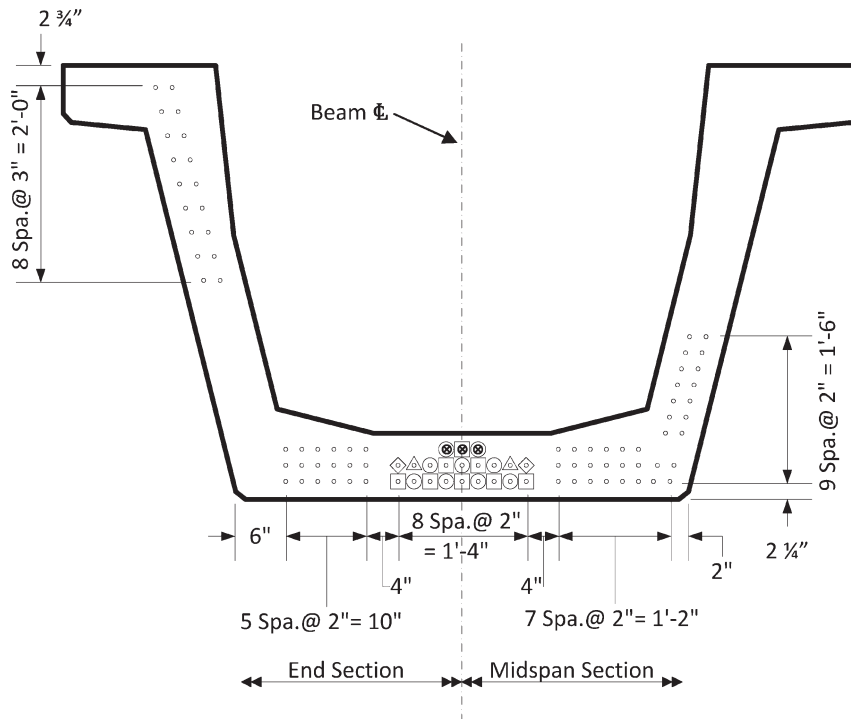


Figure A.2 21st Street Bridge cross section.



- - Fully Bonded Strand
- ◻ - Strands debonded 9'-0" from end of beam.
- ⊙ - Strands debonded 12'-0" from end of beam.
- △ - Strands debonded 15'-0" from end of beam.
- ◇ - Strands debonded 18'-0" from end of beam.
- ⊞ - Strands debonded 21'-0" from end of beam.
- ⊗ - Strands debonded 24'-0" from end of beam.

Figure A.3 U-beam prestressing layout.

A.3.1 Gage Layout

The 21st Street Bridge was selected for instrumentation because it was the first U-beam bridge to be built in the state of Indiana. As previously mentioned, the bridge has two 116 ft spans and three girder lines. To reduce field installation time and conserve resources, the strain gage layout makes extensive use of symmetries. It was determined that only one of the two spans would be instrumented. Due to the equal spans, symmetry about the intermediate pier could be used to assess the behavior of both spans. Additionally, the bridge is essentially symmetric about the centerline of the middle girder line other than the skew of 18°. Therefore, only two of the girder lines, one exterior as well as the interior girder line, were instrumented. A total of 44 strain gages were installed on the 21st Street Bridge; 30 gages were used to investigate the live load distribution with the other 14 devoted to the investigation of the flexural behavior of the bridge deck.

The strain gage layout was controlled by the two primary goals of the field evaluation, assessing bridge deck behavior and determining the live load distribution factors. Strain gages were placed at 1/4, 1/2, and 3/4 of the girder span for both the interior and exterior girder. At each of these six locations, five strain gages were placed throughout the depth of the composite section. A schematic of these six locations can be found in Figure A.4. One strain gage was installed on the top as well as the bottom mat of longitudinal reinforcement in the deck. Three strain gages were surface mounted inside the U-beam cavity. These gages were distributed vertically, with one gage installed 4 in. from the top of the web, one at approximately mid-height of the web, and one on the bottom flange. The vertical distribution of the strain gages is shown in Figure A.5. This layout enables measurement of the strain profile through the depth of the section at these six locations. The placement of the surface mounted gage 4 in. from the top of the web was controlled by steel angles installed as part of the stay-in-place formwork for the cast-in-place deck. Placing two gages in the deck primarily provided built-in redundancy. Due to the harsh environment created during concrete placement of the cast-in-place deck, it was anticipated that several gages might be lost. Therefore, redundancy was important.

Strain gages were also installed to assess the flexural behavior of the bridge deck. These gages were installed at mid span between the interior and exterior girders. Seven locations were selected with two gages at each location, one on the top mat of transverse reinforcement and the other on the bottom mat. The gage locations are shown schematically in Figure A.6. Placement of two gages at each location provides a view of the strain profile within the deck and also provides redundancy for potential gages lost during construction.

A.4 MATERIALS

A.4.1 Girder Concrete

The prestressed concrete U-beams were constructed by Stress Con Industries, Inc. in the Kalamazoo, Michigan plant in October of 2008. The design concrete strength of the U-beams was 10,000 psi with a minimum release strength of 8,000 psi. The concrete mix design was primarily controlled by the prestressing

plant's desire to quickly turn over the formwork. Therefore, the mix was targeted to obtain 8,000 psi within 24 hours to allow for quick prestress force transfer. Another key consideration for the prestressing yard was the workability of the mix. The mix needed to be pumped between the inside and outside forms with minimal internal vibration.

A.4.1.1 Trial Batches

Three distinct concrete mixes were submitted to INDOT for approval. INDOT approved these mixes for use in a trial batch. Standard 6 × 12 in. cylinders were made for each batch and were tested by both INDOT as well as by the prestressing plant. All three mixes were batched and tested at both 24 hours and 7 days as shown in Table A.1. The compressive strength data are based on the average of two 6 × 12 in. cylinder breaks. The mix designated SIKA #1 was the only mix of the three which achieved the prestress plant goal of meeting the release strength within 24 hours by both test labs. This mix also reached the design strength within 7 days. Therefore, the 28-day concrete strength was expected to well exceed the design strength of 10,000 psi. Due to an accelerated time frame for girder construction, the decision was made to use mix SIKA #1 to construct the beams and discontinue further testing of the trial batch cylinders.

A.4.1.2 Concrete Mix Design

The mix design for the SIKA #1 mix is provided in Table A.2. Both mid-range and high-range water reducing admixtures were used in conjunction with an air entraining admixture. The target slump was 8–9 in.

A.4.1.3 Concrete Compressive Strength

The prestressed U-beams were produced in six separate casts during October of 2008. INDOT field inspectors were onsite for all six placements and cast 6 × 12 in. cylinders for each beam. A number of cylinders were produced for INDOT internal testing purposes, and an additional 21 cylinders were produced by INDOT for the use of Purdue researchers. Additionally, Stress Con produced cylinders for internal testing purposes. The cylinders produced for Purdue were brought to the Bowen Laboratory for testing after completion of the U-beam casts. Testing within the first 28 days was performed by INDOT and Stress Con to establish acceptance of the girders based on the concrete reaching the design concrete strength of 10,000 psi. Once each mix reached the design strength, INDOT and Stress-Con discontinued cylinder testing.

Cylinder testing was performed at the Bowen Laboratory at 112, 180, and 280 days as well as on the week of the bridge load testing which was at approximately 300 days. The cylinders were tested in accordance with ASTM C39 at a loading rate of 60,000 lb per minute, using 70 durometer elastomeric pads. Compressive strength values from Purdue are the average result of three 6 × 12 in. cylinders. Compressive strength values from Stress-Con and INDOT are the average result of two 6 × 12 in. cylinders. The compressive strength growth curves are shown in Figure A.7, and a summary of the strength results is presented in

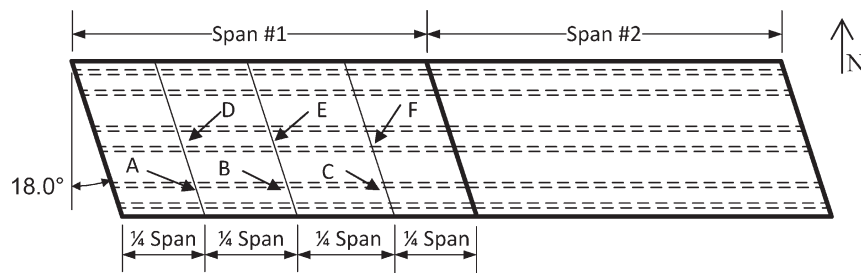


Figure A.4 Gage layout for live load distribution.

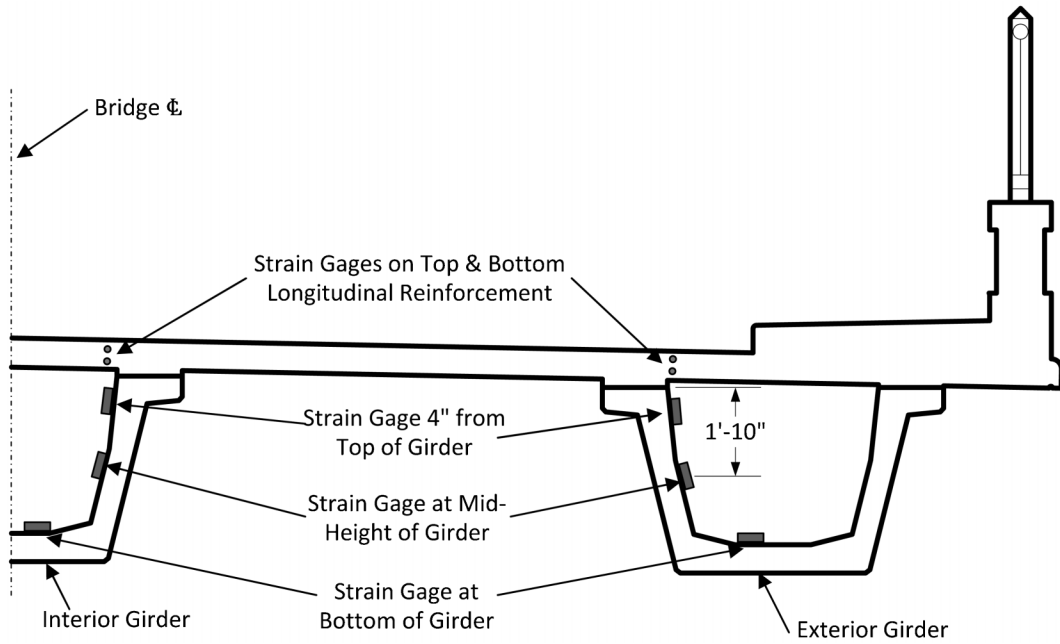


Figure A.5 Vertical gage layout for live load distribution.

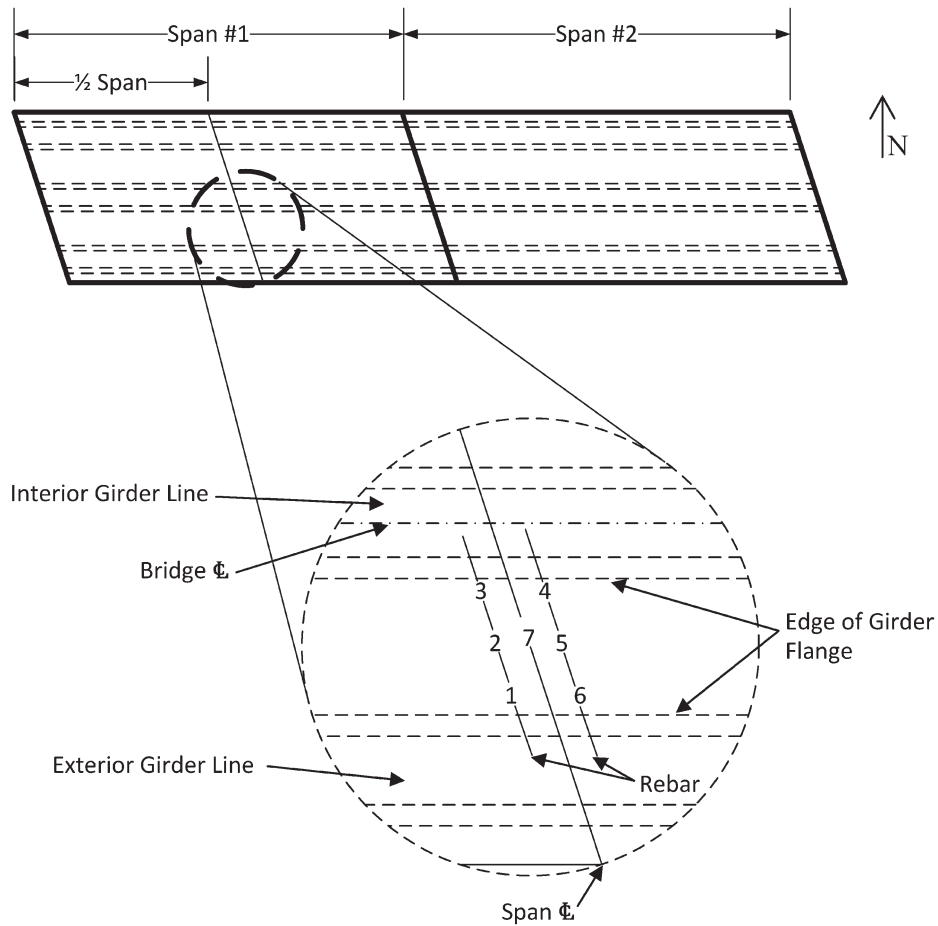


Figure A.6 Gage layout for deck bending behavior.

TABLE A.1
Summary of U-Beam Trial Batch Results

Mix Designation	Compressive Strength (psi)			
	24-Hour		7-Day	
	INDOT	Stress Con	INDOT	Stress Con
Sika #1	8,100	9,020	10,780	10,870
Sika #2	7,370	8,530	9,710	9,650
BASF #1	5,030	4,940	6,090	—

TABLE A.2
U-Beam Design Mix

Material	Design Weights Per Yard
Cement (lb)	800
Silica Fume (lb)	50
Coarse Aggregate (lb)	1,770
Fine Aggregate (lb)	1,056
Water (lb)	28
SIKA PLAST-500 Mid-Range Water Reducer (oz)	12
SIKA VISC-4100 High-Range Water Reducer (oz)	13
SIKA AEA-15 Air Entraining Admixture (oz)	3

Table A.3. When testing was performed by both Stress-Con and INDOT on the same day, the results have been averaged as presented in Table A.3. The compressive strengths of the six casts ranged from 13,000 psi to 14,800 psi at the time of the bridge load test.

A.4.1.4 Concrete Modulus

Concrete cylinders taken during the U-beam girder casts were also used to determine the modulus of elasticity of the concrete. These tests were performed in accordance with ASTM C469 (2002) using a loading rate of 35 psi/sec. An ELE International

Inc. CT-170 Concrete Cylinder Compressometer was used to measure the deformation over the middle 6 in. of the specimen. The dial indicator has a resolution of 0.00005 in. Devices such as the CT-170 have lever action which amplifies displacements by a factor of two. The stress corresponding to a strain of 0.00005 was recorded and loading was continued until the applied stress corresponded to 50% of the ultimate stress. The modulus of elasticity can then be determined using Equation A.1. Testing was performed in accordance with ASTM C469 with the exception of the maximum level of stress induced. ASTM C469 specifies 40% of the ultimate stress; however, 50% of the ultimate stress was induced.

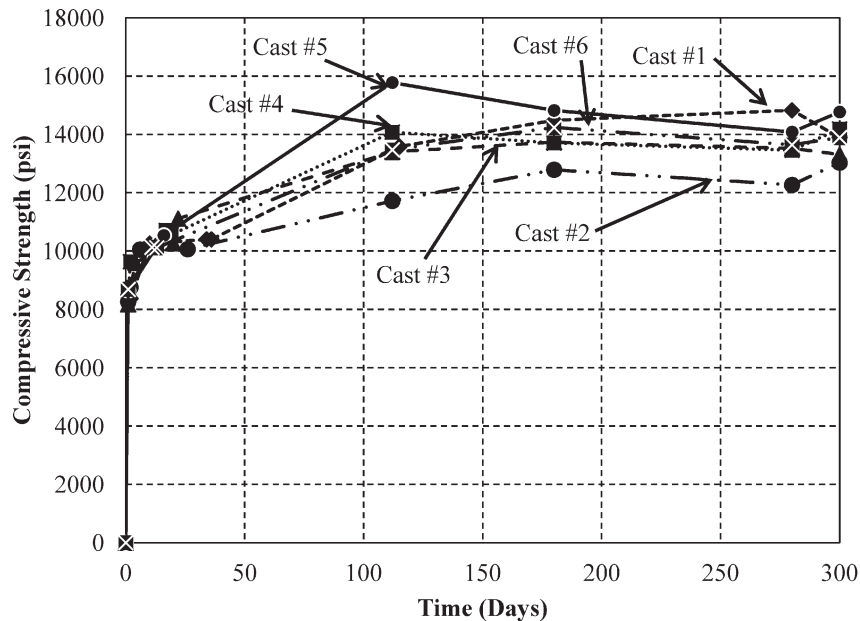


Figure A.7 Girder concrete strength growth curves.

TABLE A.3
U-Beam Compressive Strength Data

Cast	Slump (in.)	Age (Days)	Test Performed By	f_c (psi)
1	8.5	1	Stress-Con	8,483
		2	INDOT	8,366
		10	Stress-Con	10,256
		36	Stress-Con/INDOT	10,399
		115	Purdue	13,581
		180	Purdue	14,480
		280	Purdue	14,825
		300	Purdue	13,889
2	7	1	Stress-Con/INDOT	8,261
		2	Stress-Con	8,756
		6	Stress-Con	10,049
		26	INDOT	10,062
		112	Purdue	11,718
		180	Purdue	12,785
		280	Purdue	12,264
		300	Purdue	13,029
3	8.5	1	Stress-Con/INDOT	8,168
		4	Stress-Con	9,598
		20	Stress-Con	10,262
		22	Stress-Con/INDOT	11,113
		112	Purdue	13,402
		180	Purdue	13,731
		300	Purdue	13,522
4	8.75	1	Stress-Con/INDOT	8,428
		2	Stress-Con	9,632
		17	Stress-Con	10,705
		19	Stress-Con/INDOT	10,553
		112	Purdue	14,076
		180	Purdue	13,704
		280	Purdue	13,455
		300	Purdue	14,183
5	8	1	Stress-Con/INDOT	8,651
		14	Stress-Con	10,272
		16	Stress-Con/INDOT	10,532
		112	Purdue	15,775
		180	Purdue	14,820
		300	Purdue	14,080
6	8	1	Stress-Con/INDOT	8,687
		11	Stress-Con	10,129
		13	Stress-Con/INDOT	10,112
		112	Purdue	13,467
		180	Purdue	14,237
		300	Purdue	13,641

$$E_c = \frac{(S_2 - S_1)}{(\epsilon_2 - 0.00005)} \quad (\text{A.1})$$

where:

S_1 : stress corresponding to a longitudinal strain of 50 millionths, psi

S_2 : stress corresponding to 40% of ultimate stress or load, psi

ϵ_2 : longitudinal strain produced by stress S_2

In determining the modulus of elasticity for each cast, two cylinders were tested. Each cylinder was loaded four times, with

the first test being primarily to seat the testing apparatus, and this data was not used. The calculated modulus was computed as the average modulus from the six loadings performed on two different cylinders.

The measured modulus of elasticity for the six concrete casts are provided in Table A.4, along with the measured concrete compressive strength. Also provided in Table A.4 are the calculated moduli of elasticity from both ACI 318-11 (2011) and ACI 363R-92 (1992). The expression from ACI 318-11 (Equation A.2) does not have an upper limit placed on the value of concrete compressive strength, however ACI 363-92 suggests that the ACI 318-11 expression will tend to over predict for compressive

TABLE A.4
U-Beam Modulus of Elasticity Data

Cast	Compressive Strength at Time of Testing, f'_c (psi)	Experimental Modulus (ksi)	Calculated E_c (ksi)	
			ACI 318-11	ACI 363R-92
1	13,890	6,510	6,720	5,710
2	13,030	6,860	6,510	5,570
3	13,310	6,800	6,580	5,620
4	14,180	6,300	6,790	5,760
5	14,770	6,220	6,930	5,860
6	13,890	6,050	6,720	5,710

strengths greater than 6,000 psi. The ACI 363R-92 expression (Equation A.3) is intended for concrete with compressive strength between 3,000–12,000 psi. Clearly the ACI 363R-92 expression is not designed for use on concrete with compressive stresses between 13,000–14,800 psi. The ACI 318-11 expression does a good job of approximating the measured moduli but is generally a little bit high. The ACI 363R-92 expression is conservative across the board but does not come close to approximating the measured values.

$$E_c = 57,000\sqrt{f'_c} \quad (\text{A.2})$$

$$E_c = 40,000\sqrt{f'_c} + 1,000,000 \quad (\text{A.3})$$

A.4.2 Cast-In-Place Deck Concrete

The cast-in-place concrete deck was placed on March 17, 2009 by Walsh Construction, Inc. The concrete was supplied by Prairie Concrete, Inc. from their Kentucky Ave. ready mix plant in Indianapolis, Indiana. Purdue researchers were on-site to collect concrete samples from the deck cast. In addition, both Prairie Concrete, Inc. and INDOT collected cylinders. The deck concrete was a QA/QC deck mix with a design concrete strength of 5,000 psi.

A.4.2.1 Trial Batch

A trial batch was produced on January 22, 2009 at the Prairie Concrete, Inc. Kentucky Avenue ready mix plant. While the concrete design strength was 5,000 psi due to the QA/QC provisions which would monetarily penalize Walsh Construction for failure to achieve the design strength within 28 days, the mix was engineered to well exceed the design strength. The concrete mix design used for the trial batch as well as for the actual deck placement is provided as Table A.5. The results obtained from the trial batch by both INDOT and Prairie Concrete are shown in

TABLE A.5
Cast-in-Place Deck Concrete Mix Design

Material	Design Weights Per Yard
Cement (lb)	455
Fly Ash Class C (lb)	125
Silica Fume (lb)	32
Coarse Aggregate (lb)	1,752
Fine Aggregate (lb)	1,232
Water (lb)	239
BASF Micro-Air Air Entraining Admixture (oz)	14
BASF Glenium 3030 NS Full Range Water Reducer (oz)	336
BASF Pozzolith 100XR Set Retarding Admixture (oz)	26

Table A.6. These test results are the average values obtained by testing two 6 × 12 in. cylinders.

A.4.2.2 Concrete Compressive Strength

The concrete bridge deck was cast during a night time placement between 10 PM on March 16, 2009 and 4 AM on March 17, 2009 using the same mix used in the trial batch (Table A.5). The cool weather necessitated the use of thermal blankets during the curing process. After finishing, the bridge deck was covered in wet burlap, thermal blankets, and plastic tarps. This wet curing process was continued for 14 days. During the deck placement, both INDOT and Purdue made 6 × 12 in. cylinders. The cylinders produced by INDOT were taken at regular predetermined intervals along the bridge, broken into lots and sublots since this was a QA/QC mix. Each subplot consisted of 50 cubic yards of concrete and the sampling location within each lot was determined randomly. The extents of the lots and sublots are shown in Figure A.8. Additionally, the approximate locations where INDOT sampled within each subplot are indicated in Figure A.8 by a dashed line. Samples were taken at approximately the middle of the deck when the concrete placement reached the predetermined sampling locations. The INDOT cylinders were cured in curing tanks onsite for 1-week before being moved to INDOT's testing facility. A summary of INDOT's test results are provided in Table A.7. Please note that INDOT only conducted 28-day tests for acceptance purposes. Purdue's cylinders on the other hand were cured consistent with the bridge deck. The cylinders were coated by burlap, blankets, and plastic tarps. Walsh Construction, Inc. wet the burlap over the cylinders each time they wet the burlap on the bridge. Concrete cylinders were tested by Purdue researchers at the Bowen Laboratory at 7, 14, and 28 days after casting as well as on the day of load testing. The concrete strength growth curve for the cast-in-place deck is shown in Figure A.9, and the results are tabulated in Table A.8. The Purdue samples were taken from lot 1, subplot 3. Comparing the 28-day cylinder breaks conducted by Purdue to the corresponding cylinder tested by INDOT shows the values differ by only 134 psi.

TABLE A.6
Cast-in-Place Deck Trial Batch Results

Age (Days)	Testing Lab	Average Compressive Strength (psi)
7	INDOT	5,588
	Prairie Concrete	5,554
28	INDOT	7,210
	Prairie Concrete	7,656

A.4.2.3 Concrete Modulus

Concrete cylinders taken by Purdue were also used to determine the modulus of elasticity of the deck concrete. The test was performed according to ASTM C-469 as discussed for the U-beam concrete. The test results along with the values calculated by Equations A.2 and A.3 are presented in Table A.9. It may be noted that the experimentally determined modulus well exceeds the modulus computed by both equations.

A.4.3 Prestressing Steel

Representative samples from the U-beam prestressing steel were obtained from Stress Con Industries, Inc. The prestressing steel strand was Grade 270, uncoated, seven-wire, low relaxation strand with a 0.6 in. nominal diameter. The nominal cross-sectional area of the strand is 0.217 in.²

Samples of the prestressing strand used in the U-beams for the 21st Street Bridge were tested to failure in a universal testing machine. Testing was performed in accordance with ASTM A370. Gripping of the strands was accomplished using prestressing chucks for 0.6 in. strand. Standard commercially available aluminum foil was used at the gripping locations to reduce notching at the teeth of the grips. The aluminum foil was wrapped around the strand before installation of the chuck teeth. It was found that five

wrappings of the aluminum foil was the maximum that would fit within the chuck assembly. Using more wraps caused the teeth to protrude outward preventing the body of the chuck from fitting snugly over the teeth. Figure A.10 shows a prestressing strand specimen after failure with the prestressing chucks installed over aluminum foil. Three specimens each with a test length of approximately 2 ft were tested. A summary of the test results is provided in Table A.10. The average tensile strength of the strand based on the nominal strand cross-sectional area was 281.2 ksi exceeding the nominal strength of 270 ksi. All the strands tested failed due to simultaneously rupture of the entire cross section of the seven strands.

A.4.4 Reinforcing Steel

Representative samples of each bar size used in the construction of the cast-in-place deck for the 21st Street Bridge were collected from Walsh Construction, Inc. The bridge deck was constructed with Grade 60 steel in five sizes ranging from #4 to #8 produced by Gerda Ameristeel. Reinforcement samples were not collected from the steel used in the construction of the U-beams as these bars were used for stirrups and not primary reinforcement.

The reinforcing steel was tested in tension in accordance with ASTM A370 in a universal test machine using standard V-grips. A test length of approximately 2 ft was maintained for all the tests. Three samples of each rebar size were tested to determine the average tensile strength, and an extensometer was used to record the stress - strain behavior of the bars. The extensometer was removed at a strain of 0.04 to prevent damage to the instrument during bar rupture. A representative stress-strain curve for a #4 and #8 US bar is shown in Figure A.11.

Both the yield and rupture stress were recorded for each specimen tested. The triplicate values for each bar size were then averaged. The bars had yield stresses in the range of 74.1-85.6 ksi, and rupture stresses in the range of 92.0-104.6 ksi. A summary of the tensile testing results is included as Table A.11.

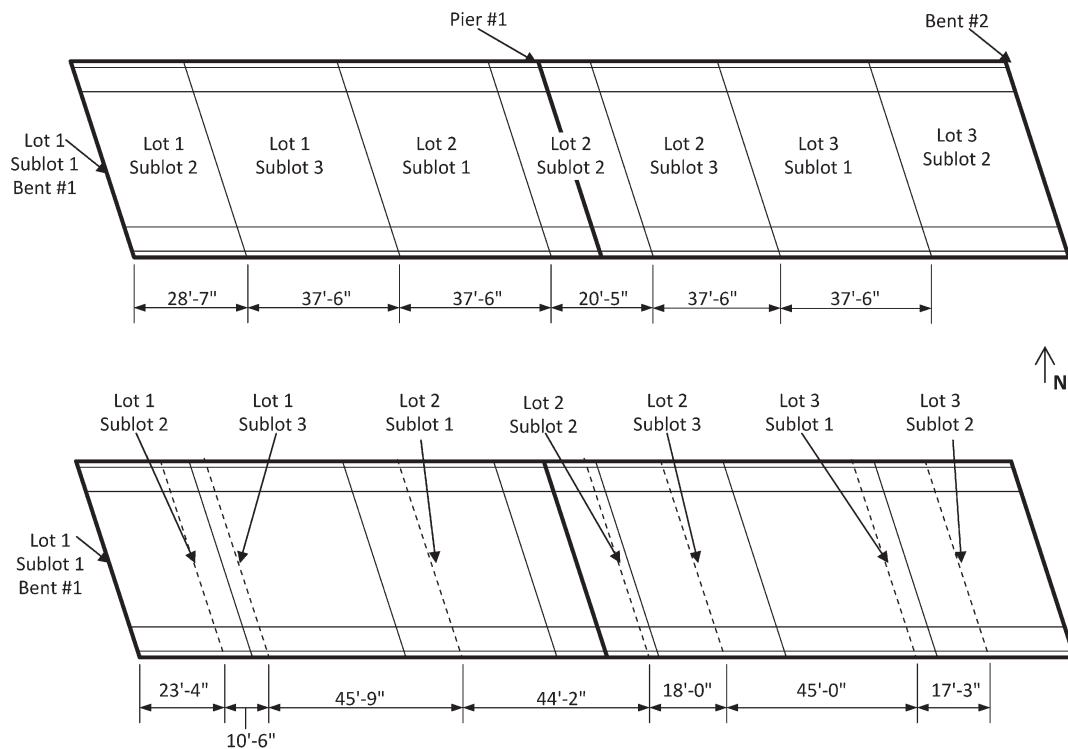


Figure A.8 Lot and subplot layout.

TABLE A.7
Cast-in-Place Deck INDOT Test Results

Lot	Sublot	28-Day Concrete Compressive Strength (psi)
1	1	7,880
	2	7,855
	3	9,215
2	1	6,230
	2	7,670
	3	8,175
3	1	8,260
	2	8,215

TABLE A.8
Cast-in-Place Deck Purdue Test Results

Date Tested	Age (days)	Concrete Compressive Strength (psi)
3/24/2009	7	6,090
3/31/2009	14	8,180
4/14/2009	28	9,080
8/5/2009	141	9,500

A.5 INSTRUMENTATION AND CONSTRUCTION

A.5.1 Girder Construction

As previously mentioned, the U-beam girders were constructed by Stress Con Industries, Inc. in October of 2008. The girders were cast individually between outer and inner formwork to achieve the desired shape. The outer forms are shown in Figure A.12 during the placement of mild shear reinforcement. The inner form which was lifted by a crane and placed over the outer forms prior to casting is shown in Figure A.13. The inner form has cross beams at regular intervals along its length which match up with columns on the outer forms. Once in place, the cross beams are bolted to the outer form columns to prevent movement of the inner form and to resist the inner form's buoyancy during concrete placement.

A.5.2 Strain Gage Selection

Electrical resistance strain gages were selected to instrument the bridge. Due to their small size they could be installed on the deck rebar as well as on the surface of the girders to measure strain profiles throughout the composite section depth. Installation on the deck reinforcement necessitated small strain gages which could be installed with the removal of only one or two bar deformations.

Accordingly, a Vishay Micro-Measurements EA-06-250BF-350 strain gage was selected. This gage has a gage length of 0.25 in. and a gage width of 0.125 in. Installation on the surface of the concrete girders required a gage with a long gage length. Because concrete is not homogenous, a long gage length is desirable to average strain over a large sample of the concrete. Shorter gages may be unacceptably affected by individual aggregate. The Vishay Micro-Measurements EA-06-40CBY-350 strain gage was selected for use on the U-beam girders. This gage has a gage length of 4 in. and a gage width of 0.125 in.

The strain gage designations for Vishay Micro-Measurements are composed of four hyphenated parts. The first two letters indicate the backing material of the gage. Both gages selected for this project are designated EA, which is a constantan foil in combination with a tough, flexible, polyimide backing. The polyimide backing leads to a thin and flexible gage appropriate for most general purpose applications. The constantan foil makes the gage self-temperature-compensating. The second part of the designation is the S-T-C number, or the Self Temperature Correction. This parameter is selected based on the material which the gage is to be installed upon. In the case of concrete and steel, 06 is the recommended general application designation. The third portion of the name designates the model of the gage which defines the size and shape. The final portion of the designation specifies the resistance of the gage. Generally, there are only two options for resistance 120 ohm or 350 ohm. Selection of the 350 ohm gages was based on a threefold reduction in heat generation at the gage as compared to 120 ohm gages excited with the same voltage. Additionally, the higher voltage reduces lead wire effects such as gage desensitization due to lead wire

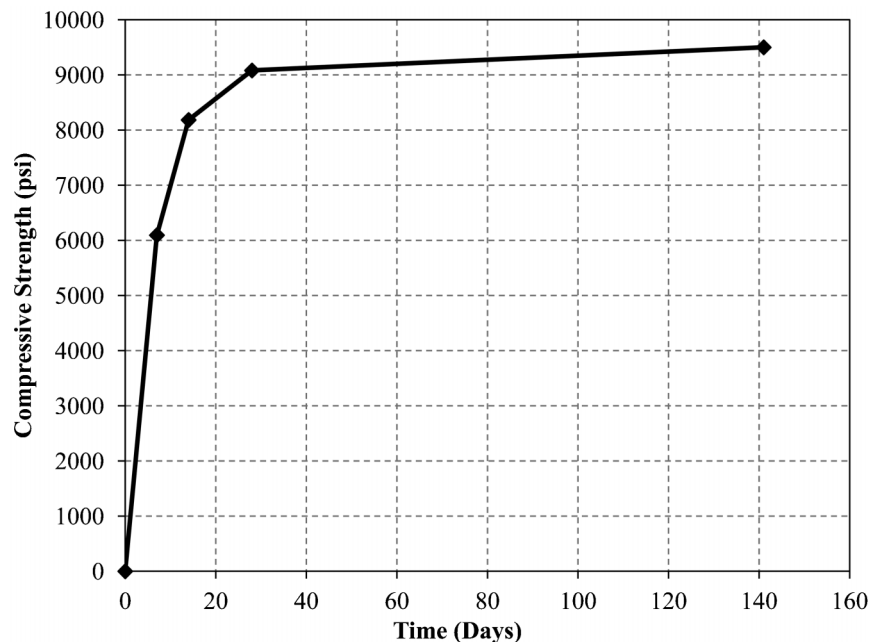


Figure A.9 Cast-in-place deck concrete compressive strength.

TABLE A.9
Cast-in-Place Deck Modulus of Elasticity Data

Cast	Compressive Strength at Time of Testing, f'_c (psi)	Experimental Modulus (ksi)	Calculated E_c (ksi)	
			ACI 318-11	ACI 363R-97
Deck	9,501	6,160	5,560	4,900



Figure A.10 Prestressing strand grip setup.

resistance. The gages were purchased with pre-attached lead wires to aid in quick field installation under adverse conditions.

A.5.3 Substrate Surface Preparation

To achieve good bond between the strain gages and the substrate, the substrate surface must first be prepared by mechanical and chemical means. The locations where rebar mounted gages were to be installed needed to be prepared to produce a smooth, clean surface. A high speed rotary tool with an abrasive ceramic disk was used to grind the surface of the steel rebar to produce a flat bonding site. The coarse abrasive disk was

used to remove the surface deformations as well as to remove enough of the bar to create a flat region large enough for the strain gages. Once the bulk material was removed using the rotary tool, 220 and 320-grit sand papers were used to produce a smooth mirrored finish.

Grinding of the rebar surface was generally completed days or weeks prior to gage installation. Immediately prior to gage installation additional preparatory steps were taken to ensure a strong bond. The surface was first treated with Vishay's CSM-2 Degreaser, a tough aerosol degreaser which removes oils and lubricants. The degreaser was applied liberally and wiped off with disposable gauze pads. After degreasing, Vishay Conditioner A, a mild phosphoric acid solution was applied to the surface. The acid solution removes any rust or surface scale which may be present on the surface. The acid solution is worked into the surface with 220-grit sandpaper to increase its effectiveness. The surface is then wiped with a disposable gauze pad to remove any remaining solution and any particles. After conditioning, Vishay Neutralizer 5A, an ammonia-based solution was applied to the surface. The Neutralizer 5A solution neutralizes any chemical reaction produced by the conditioner and creates a neutral pH for strain gage bonding. The Neutralizer was worked into the surface with a disposable cotton swab, and then the surface was wiped dry with a

TABLE A.10
Prestressing Strand Tensile Strength

Test No.	Failure Distance From Grip (in.)	Peak Load (lb)	Max Stress (ksi)
1	6	61,106	281.6
2	7	60,979	281.0
3	13	60,977	281.0
Average:		61,021	281.2

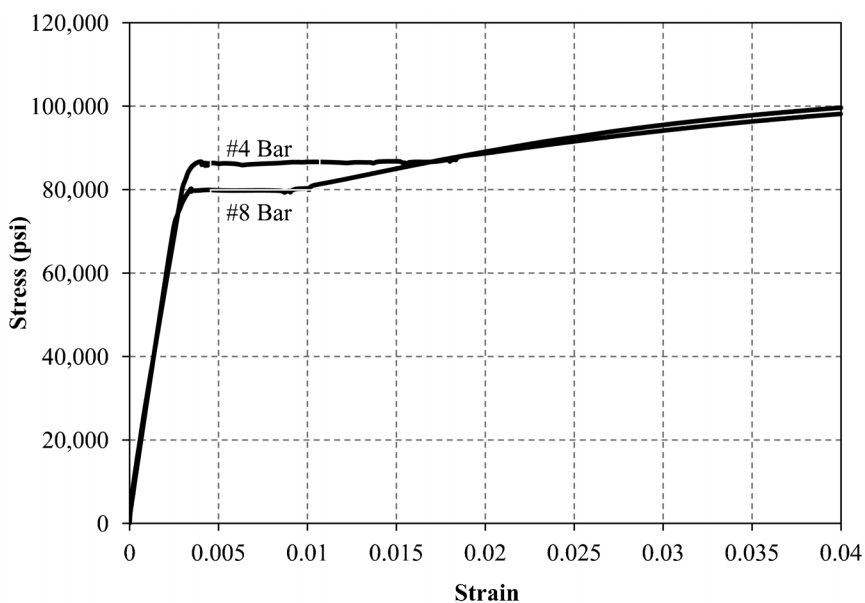


Figure A.11 Mild steel extensometer stress-strain curves.

TABLE A.11
Reinforcing Steel Tensile Strength

Bar Size (US)	Yield		Fracture	
	Load (lb)	Stress (psi)	Load (lb)	Stress (psi)
4	16,901	85.6	20,331	103.5
5	25,669	83.7	30,572	99.6
6	34,364	77.9	43,880	99.3
7	44,889	74.7	55,347	92.0
8	62,151	79.1	82,190	104.6

disposable gauze pad. Once surface preparation concluded, the gage was immediately installed to ensure a clean bonding surface.

Similarly, installation of the gages on the interior walls of the U-beams required a smooth bonding surface. Concrete typically has an irregular, rough surface which also contains some surface voids or “bug holes.” To create an appropriate bonding surface, a bed of epoxy was first placed at the locations of the gage installations. Vishay M-Bond AE-10 epoxy, a two-component, 100%-solids epoxy was used for these locations. Prior to epoxy placement, the concrete surface was first wiped clean with cotton cloths, and then treated with Vishay Conditioner A. The conditioner was worked into the concrete with a wire brush. After treatment with the conditioner, Vishay Neutralizer 5A was applied liberally. The concrete surface was then blotted with cotton clothes and allowed to air dry prior to epoxy application. The epoxy was applied to the surface of the concrete taking great care to produce an even level surface and to fill any voids which may have existed. The epoxy was then allowed to cure for approximately one week prior to gage installation. After curing, the epoxy was then sanded with both a 220 and a 320-grit sand paper to ensure a smooth bonding surface. The epoxy surface was then treated with the Vishay Neutralizer 5A to ensure a proper pH for bonding and to remove any remnants from sanding. The neutralizer was wiped off with a disposable gauze pad. Gage installation proceeded immediately after surface preparation.



Figure A.12 U-beam outer form.



Figure A.13 U-beam inner form.

A.5.4 Strain Gage Installation

Strain gages must be securely fastened to the substrate surface to produce accurate readings. Several methods are available including welding, epoxies, and fast setting glues. All gages used on the 21st Street Bridge had to be installed in the field under less than ideal conditions. Therefore ease and speed of installation were important factors when selecting the gage installation procedure. The strain gages also needed to be adequately protected from the environment to prevent short circuiting. This was especially important for the rebar mounted strain gages which had to survive placement of the deck concrete.

Vishay M-Bond 200 quick setting cyanoacrylate adhesive was selected for the installation of the strain gages. This is a general purpose adhesive appropriate for strain readings in temperate environmental conditions (−25° to 150°C), and is capable of achieving greater than 5% elongation. M-Bond 200 uses a catalyst to produce a nearly instant cure under light thumb pressure.

Installation was achieved through the use of Vishay PTC-2M Installation Tape. A piece of tape approximately 3–4 in. longer than each gage was used. The gage to be installed was placed bonding side down on a clean surface and the installation tape was placed over the gage. The installation tape was then peeled back at a shallow angle so that the strain gage would remain adhered to the tape. The gage/tape assembly was then placed over the desired bonding location and light pressure was used to affix the tape. One end of the tape was then peeled back at a shallow angle until the entire gage was lifted off of the bonding surface. The M-Bond 200 accelerant was then sparingly brushed onto the bonding surface of the strain gage. Two drops of the M-Bond 200 adhesive was placed on the specimen surface at the junction of the specimen surface and installation tape. The installation tape was then quickly rotated onto the specimen surface, in one quick stroke; then the adhesive was forced along the length of the gage with thumb pressure. Firm thumb pressure was then applied to each gage for approximately 2 minutes while the M-Bond 200 set up. Thumb pressure ensures a firm and uniform adhesive line. Additionally, the body heat provided by the thumb speeds the curing process. Following the 2 minute cure time, the installation tape was peeled back at a 180° angle (directly over itself) to prevent damage to the gage or surface bond. The installation tape was then discarded. A concrete mounted strain gage can be seen in Figure A.14 immediately after installation over the bed of epoxy.

A.5.5 Strain Gage Waterproofing

The electrical resistance strain gages selected for the bridge instrumentation are susceptible to short circuiting when exposed to moisture; therefore, the gages had to be properly waterproofed. Special care had to be taken for the strain gages that were installed inside the bridge deck. These gages had to survive the placement of the cast-in-place deck and therefore needed to be protected against both the moisture in the wet concrete as well as mechanical disturbance from placement activities. A multipart waterproofing system was implemented to prevent the loss of gages during



Figure A.14 Concrete surface mounted strain gage.

concrete placement. The concrete surface mounted gages were also waterproofed. Due to their semi-protected environment, a less intensive regime was employed.

The waterproofing of the rebar mounted deck gages will be addressed first. After gage installation, a series of three coats of Vishay M-Coat D, a solvent thinned acrylic waterproofing agent was applied to the gage. M-Coat D has a white pigment to allow for visual inspection of proper coverage. Care was taken to apply M-Coat D not only to the back of the strain gage, but to also cover the entire area of the reinforcing bar where the epoxy coating had been removed during surface preparation. This was done to help prevent accelerated corrosion in these areas where the factory applied coating had been removed. After the M-Coat D had been allowed to dry which takes several minutes, Vishay M-Coat F was applied. M-Coat F is a multipart protective coating system designed to provide environmental and mechanical protection to gages in adverse environments. The M-Coat F kit consists of five materials, M-Coat FB butyl rubber sealant, M-Coat FN neoprene rubber sheets, M-Coat FA aluminum foil tape, M-Coat B nitrile rubber coating and M-Coat FT Teflon Tape. As the result of four lab mockups of the rebar gage installations waterproofed using different procedures, it was determined that only the M-Coat FB and M-Coat FN were required to achieve the desired results. The aluminum tape and Teflon tape were found to have poor adhesion to the epoxy coating on the rebar, and the nitrile rubber coating had high viscosity at room temperature and was difficult to place.

A piece of the M-Coat FB butyl rubber was cut for each gage location. The butyl rubber was sized to cover the entire gage as well as any surrounding areas where the epoxy coating had been removed. The butyl rubber served a dual purpose of providing waterproofing as well as mechanical shock absorption. The butyl rubber sheets are extremely sticky and easily adhere to the surface of the rebar. At each location, an M-Coat FN neoprene sheet of equal size was cut and placed over the butyl rubber, adhered primarily by the stickiness of the butyl rubber. Additionally, cable ties were placed around the bar over the rubber coatings to ensure they stayed in place. The neoprene sheets were intended to aid in gage survival during concrete placement and vibration. As an additional protection, the edges of the rubber coatings were sealed with a bead of silicone caulk to further prevent moisture infiltration. A typical strain gage installation can be seen in Figure A.15, which shows two gages mounted on the top and bottom mats of the longitudinal deck reinforcement.

Despite the environmental and mechanical protection applied to each gage, concern remained about the ability of the gages to withstand the direct impact of pumped concrete or a mechanical concrete vibrator. To address this concern, plywood markers were placed over locations of strain gage installations to identify them to the construction crew. Purdue researchers also conducted a pre-placement briefing with the crew to explain the procedure to be followed when a gage location was encountered. Researchers were also on hand during the cast to provide guidance when gage locations were encountered. The construction crew was asked to place concrete in a 6 to 12 in. diameter around the gages and



Figure A.15 Typical rebar strain gage installation.

vibrate the concrete from this distance to ensure proper consolidation without harming the gages. Due to these precautions, only one deck strain gage was lost during the deck placement.

As previously mentioned, the protection of the surface mounted gages within the U-beams was of considerably less concern. These gages did not have to withstand additional construction operations and are in a semi controlled environment. The gages were coated with three coats of the M-Coat D, acrylic coating. Additionally, the gages were covered with M-Coat FB butyl rubber sheets. The M-Coat FN, neoprene rubber sheets were excluded from the gages installed on the sidewalls since there was no expectation of the gages being mechanically disturbed. The neoprene rubber sheets, however, were installed over the gages on the floor of the U-beam tub. Additionally, a section of rubber floor mat material was placed over the area and taped to the floor of the tub. These additional precautions were taken to prevent damage to the gages due to someone walking on them in the future. A typical sidewall installation within the U-beams is shown in Figure A.16. As evident, the wax paper on the backside of the M-Coat FB is still intact as no additional mechanical protection was placed over this rubber layer. Figure A.17 shows a typical U-beam floor gage installation with the floor mat taped over the installation site.

A.5.6 Strain Gage Wiring

As previously mentioned, the strain gages selected for this study all had pre-attached lead wires, which eliminated the need for soldering lead wires to the gage terminals in the field. The lead wires were then spliced with wires which ran to the data collection unit. The number of wire runs required was reduced through the use of 22-gauge wire bundles. The use of bundles reduced the 132 individual wires to six bundles which were then run to the data collector. The data collection unit was placed in a traffic control cabinet adjacent to the western abutment. The contractor provided PVC conduit from the control cabinet through the abutment to the bottom of the bridge deck at the southwestern corner of the bridge. The wire bundles were run from the edge of the deck down through the PVC conduit to the control cabinet. Additional PVC conduit was installed to run the cables through the deck to the centers of the two instrumented girder lines as shown in Figure A.18. The bundles were then dropped into the interior of the U-beams through the deck forms. The bundles then ran inside the girders to the gage installation locations. The PVC installed in the bridge deck was installed between the two reinforcement mats to prevent issues with the placement of the deck concrete.

The lead wires for each gage were fed through holes drilled in the steel deck forms into the interior cavity of the U-beams. The lead wires were placed inside clear plastic tubing to eliminate direct bonding of the wires with the concrete to reduce the likelihood of wire fracture during concrete cracking. Grommets were installed in the holes drilled in the steel forms to prevent



Figure A.16 Typical U-beam side-wall strain gage installations.

damage to the wires, and the holes were sealed with putty to prevent concrete seepage during placement. This typical detail is shown in Figure A.19. Once inside the U-beam cavity, each lead wire was soldered to the appropriate bundle wire. Each connection was soldered, coated with Vishay M-Coat D acrylic waterproofing, and then wrapped with electrical tape. These steps were taken to ensure a clean electrical signal without the potential for short circuiting due to moisture infiltration.

A.5.7 Deck Casting

As previously mentioned, the concrete bridge deck was cast during a night time cast between 10 PM on March 16, 2009 and 4 AM on March 17, 2009. The placement began at the western abutment and proceeded towards the eastern abutment. The concrete was pumped into place as illustrated in Figure A.20 with concrete pumps located on both approach slabs. Two pumps were used because each pump was only able to reach approximately mid-span. Therefore, the western span was cast with concrete pumped from the western approach and the east span was cast with concrete pumped from the eastern approach. The sidewalks and barrier rail were placed in a separate cast after the deck had cured. The contractor placed approximately the same thickness of concrete across the whole bridge deck leaving the sidewalk reinforcement exposed as shown in Figure A.21. The surface of



Figure A.17 Typical U-beam floor strain gage installation.



Figure A.18 Deck PVC conduit.

the concrete within the confines of the sidewalks was intentionally left unfinished to provide a roughened surface to bond with the concrete from the sidewalk cast.

A.5.8 Data Collection

The selection of a data acquisition unit was primarily controlled by the requirement of collecting both static and dynamic load cases using loaded dump trucks. While many data acquisition units were adequate to collect the data from the static load cases, the dynamic loading posed a problem. If the loaded truck was to travel at a speed close to the posted speed limit of 45 mph, the data acquisition unit would have to read all the gages fifty or more times per second to capture the bridge response. A Campbell Scientific CR-9000 was selected for its ability to record each of the 44 gages 56 times per second. The CR-9000 was programmed using Campbell Scientific's RTDAQ software package. A switched excitation of 5 volts was used. Two programs were developed, one for static loadings and one for dynamic loadings. The dynamic program read each gage five times and averaged the result for each time step, while the static program averaged 125 readings per time step. Averaging of consecutive readings is one of the best ways to prevent noise and variability in the strain readings. A larger number of readings were averaged for the static program due to the longer scan interval. The static program recorded each gage once per second while the dynamic program recorded each gage 56 times per second.

A.6 LOAD TESTING

The objective of the load testing was to determine the live load distribution factors for a wide array of load placements to compare the experimental results to the design expressions for load distribution factors provided by the AASHTO LRFD Bridge Design Specifications. A series of one and two truck static load



Figure A.19 Typical deck form penetration.



Figure A.20 Deck placement at center of bridge.

placements were performed to determine the live load distribution factors. Additionally, dynamic load tests were performed with one truck to allow for comparison with the results of the one-truck static load placements.

A.6.1 Test Load Vehicles

The test load was applied by positioning loaded dump trucks on the bridge at various locations. Preliminary analysis of the bridge using SAP2000 revealed that the anticipated weight of one loaded dump truck might not produce significant, measurable strains at the gage locations under all anticipated truck placements. To ensure measurable strains for the live load distribution testing, two dump trucks were used for some of the load placements. The dump trucks were supplied by INDOT and were identical tandem axle trucks. During loading configurations requiring both trucks, the trucks were placed back-to-back to concentrate the applied load over the desired location. The dimensions of the trucks used can be found in Figure A.22 along with configuration used for loading with both trucks.

The trucks were loaded to capacity with wet sand to maximize their weight. A portable vehicle scale was used onsite immediately prior to load testing to measure the wheel load from each set of wheels as shown in Figure A.23. Care was taken to center the wheel(s) being measured over the load plate of the scale, and measurements were only taken after the reading had stabilized. The two trucks are identified by their INDOT vehicle numbers. Truck No. 63700 had a total vehicle weight of 50,870 lbs and Truck No. 63701 had a total vehicle weight of 47,500 lbs at the time of testing. The distribution of the wheel loads for both trucks is identified in Figure A.24.



Figure A.21 Deck placement at sidewalk.

A.6.2 Static Test Load Configurations

Placement of the test load trucks was designed to maximize the moments at the instrumented locations and to provide sufficient data to assess the live load distribution as well as the deck bending behavior. Two series of static load tests were performed on the bridge. The first series of tests were performed using both loaded trucks back-to-back as shown in Figure A.25. This series of tests are designated S2-X where S indicates static loading, 2 indicates the number of trucks and X indicates the individual test loading. This series included six truck placements as illustrated in Figure A.26. These tests were designed primarily to measure the live load distribution among the three girder lines under the statically applied test load. These tests included placement of the trucks about the two span centerlines at the two edges of the driving surface as well as at the center of the bridge. The individual trucks are identified by their vehicle numbers in Figure A.26 to fully define the load pattern. Placement of the trucks was confined to the normal driving surface to prevent damage to the sidewalks.

The second series of static tests utilized only one truck placed within the two driving lanes. Tests within this series have the designation S1-X. These tests served the dual purpose of further analyzing the live load distribution as well as loading the instrumented portion of the bridge deck to analyze the deck bending behavior. Truck No. 63700 was used exclusively for the second series of tests due to its larger vehicle weight. This series consisted of eight truck placements centering the rear axles over the 1/4, 1/2 and 3/4 span locations of the first span as well as the 1/2 span location of the second span in both driving lanes. The truck configurations for the second series of tests are shown in Figure A.27. The second series of tests was also designed to provide a reference to the dynamic truck loadings. Both the static and dynamic loadings were conducted such that the trucks were located in approximately the same transverse location of the bridge deck.

A.6.3 Dynamic Test Load Configurations

A series of dynamic load tests were also conducted on the bridge, primarily to compare the live load distribution measured on the basis of static loading to that measured under dynamic loading. These tests were conducted by driving one dump truck across the bridge within the designated driving lanes. As in the S1 static series, Truck 63700 was used for all the tests in this series due to the larger weight of this vehicle. The truck was positioned at the extents of the approaches to the bridge and accelerated to the test speed prior to reaching the bridge. This series of tests are designated DX-Y where D identifies the test as dynamic, X designates the loading configuration, and Y designates the number of the test run. A total of four loading configurations were performed in this series as illustrated in Figure A.28. The four conditions tested represent the truck driving both east and west in each of the two lanes.

Load tests D1 and D2 were repeated in triplicate, and loadings D3 and D4 were each completed once. The target speed for the truck was set at 35 mph. This target speed was less than the posted speed limit of 45 mph and was selected to work well with the maximum speed capabilities of the data acquisition system as well as the acceleration capabilities of the dump truck. The target speed for the D1 and D2 tests was achieved on the bridge approach and maintained over the length of the bridge. The target speed could not be achieved in the D3 and D4 tests due to the shorter length of the eastern bridge approach. In the case of test D3, a speed of 30 mph was achieved, and a speed of 33 mph was achieved for test D4. The truck was maintained approximately in the center of the marked lanes for each of the tests.

A.6.4 Data Collection

A Campbell Scientific CR-9000 was used to collect data during the load testing. As mentioned earlier (Section A.5.8), two

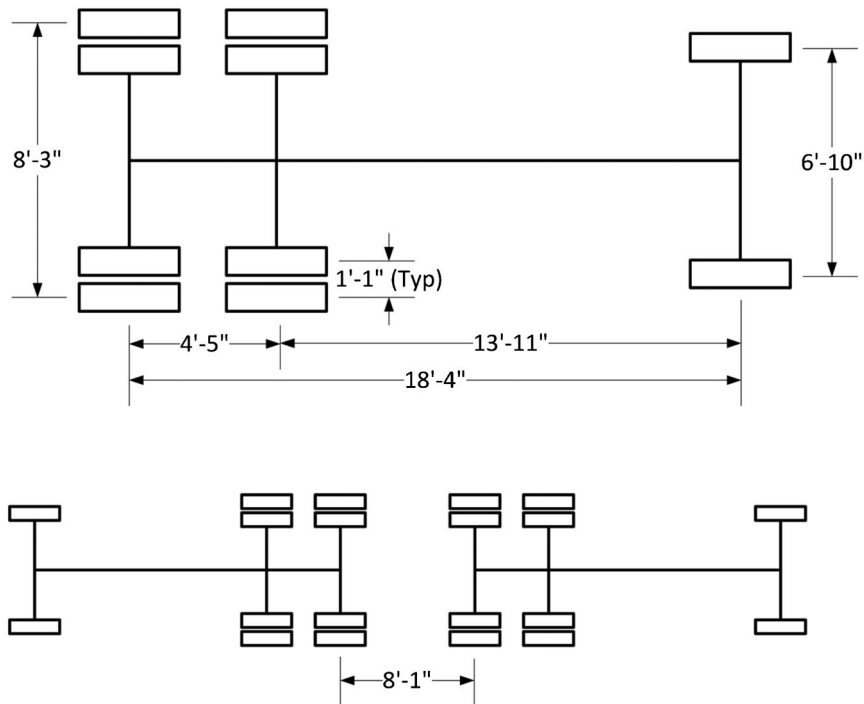


Figure A.22 Load test truck dimensions.

different programs were developed for reading the strain gages. One program was developed for the static loading cases, recording one data point per gage each second. The second program, developed for the dynamic loadings recorded each gage 56 times per second which corresponds to the maximum practical speed for recording 44 strain gages with the CR-9000.

During the static loadings, the datalogger was manually triggered after the trucks were in place and allowed to record for approximately two minutes, providing approximately 120 readings to be averaged. During the dynamic loadings, the program was manually triggered during truck acceleration and was discontinued after the truck had driven over the bridge.

Due to an unforeseen problem, the dynamic program had to be altered in the field and the datalogger was reprogrammed with the altered program onsite. The resulting readings taken during the dynamic readings were inconsistent with the static readings and

showed great variability. This was caused by an error in programming and operation of the data collection unit rendering the dynamic data useless.

A.7 RESULTS

Data were collected for approximately two minutes for each of the static load cases in both the S1-X and S2-X load cases. Additionally, a two minute reference strain gage reading was taken while no vehicles were on the bridge. The sample rate for static loadings and the reference reading was one record per second. The resulting data set for each static loading and reference sample were averaged. The static readings were very stable with typical readings varying by ± 1 micro-strain. The reference value for each gage was then subtracted from the average value for that gage under each loading condition. It should be noted that a total of two reinforcement mounted strain gages were lost prior to testing. These gages are noted as such in the results summary. One gage was lost during deck placement and the other gage was lost between the time of deck placement and load testing. The resulting strain values for the live load distribution are reported in Table A.12 and Table A.13 for the S1-X and the S2-X series respectively.

The gages installed at mid-span to assess the flexural bridge deck behavior were similarly recorded and averaged. The S1-2 load placement was designed to place the rear axle of the load vehicle over the instrumented deck region as shown in Figure A.29. Note that the transverse location of the truck is approximate due to field conditions. The transverse deck strains resulting from the S1-2 load case are presented in Table A.14 with the positions of the gages referenced to Figure A.6.

A.8 ANALYSIS

A.8.1 Measured Live Load Distribution Factors

A procedure was developed to utilize the strain data obtained from the load test to determine the live load distribution factors for each load case. To accomplish this, strains measured in each of the girder lines were compared. Since only two of the three girder



Figure A.23 Truck scale measurements.

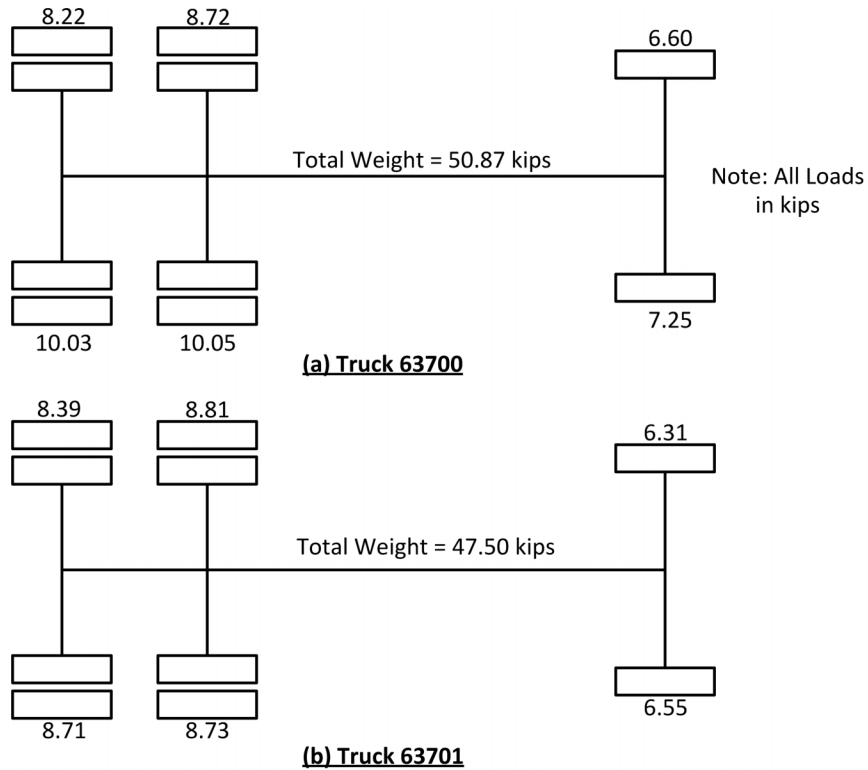


Figure A.24 Test load distributions.

lines were instrumented, data from two load cases was required for non-symmetric loadings. For instance, data from the S2-1 load case and S2-5 load case were combined to provide the strains for all three girder lines. As shown in Figure A.30, these two loadings are approximately symmetric about the centerline of the bridge. Therefore, the strain measured at the exterior girder (Girder 1) under loading S2-5 provides the data for the un-instrumented girder (Girder 3) for loading S2-1. This logic was repeated for all load tests except for the tests where the truck(s) were positioned about the bridge centerline. For these centerline loadings, the two exterior girders were assumed to develop the same strain.

The use of symmetry to determine the strains in each of the girder lines produced two values for the strain in the interior girder, one reading for each of the two load cases. These two interior strain readings do not necessarily agree, in part because

the gages on the interior girder are installed on one of the two beam webs (Figure A.5) and are therefore not completely symmetric about the beam centerline. Several algorithms for determining the load distribution factors were explored and compared. The method which produced the most consistent results and was considered as fairly weighting the results from both loadings is presented as Equation A.4 to Equation A.6. This method also considers that the truck may not be in exactly the correct location along the span for each loading. This method expresses each exterior girder strain as a fraction of the interior girder strain from the same load test. In this way, differences in the interior girder measurements can be normalized. The nomenclature for identifying each girder is shown in Figure A.31 and an example calculation for the determination of the distribution factors for load cases S2-1 and S2-5 for the top rebar is included as Figure A.32.



Figure A.25 Dual truck load test S2-1.

$$DF_{Ext-S} = \frac{\frac{E_S}{I_S}}{\frac{E_N}{I_N} + 1 + \frac{E_S}{I_S}} \quad (A.4)$$

$$DF_{Int} = \frac{1}{\frac{E_N}{I_N} + 1 + \frac{E_S}{I_S}} \quad (A.5)$$

$$DF_{Ext-N} = \frac{\frac{E_N}{I_N}}{\frac{E_N}{I_N} + 1 + \frac{E_S}{I_S}} \quad (A.6)$$

where:

DF_{Ext-S} : live load distribution factor for southern exterior girder line

DF_{Int} : live load distribution factor for interior girder line

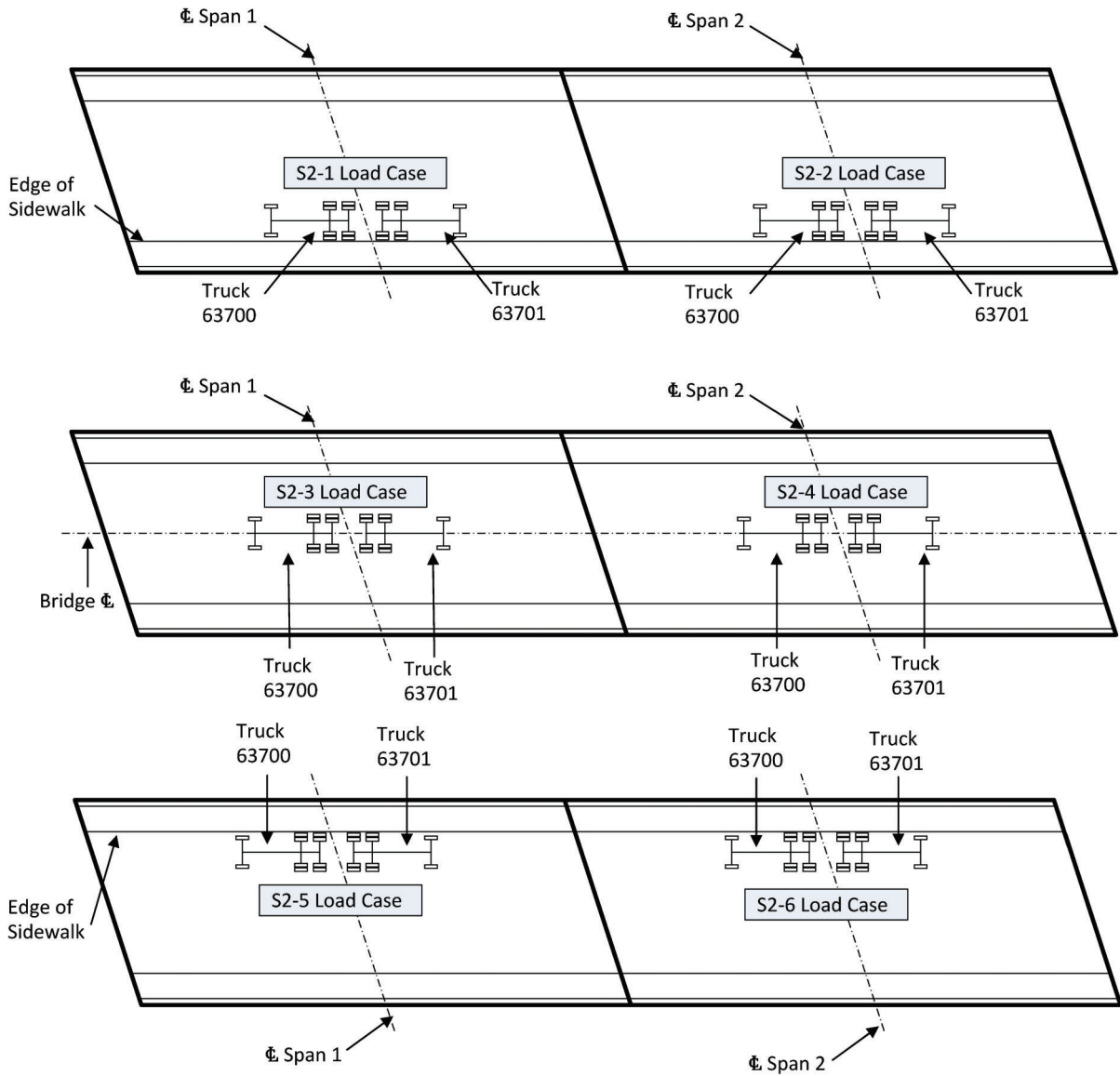


Figure A.26 Series S2-X load test.

DF_{Ext-N} : live load distribution factor for northern exterior girder line

E_S : strain measured in southern exterior girder

E_N : strain measured in northern exterior girder

I_S : strain measured in interior girder corresponding to E_S

I_N : strain measured in interior girder corresponding to E_N

$$DF_{Ext-S} = \frac{29.83}{\frac{15.15}{16.15} + 1 + \frac{29.83}{22.39}} = 0.41$$

$$DF_{Int} = \frac{1}{\frac{15.15}{16.15} + 1 + \frac{29.83}{22.39}} = 0.31$$

$$DF_{Ext-N} = \frac{15.15}{\frac{15.15}{16.15} + 1 + \frac{29.83}{22.39}} = 0.29$$

As previously mentioned, 30 strain gages were installed to assess the live load distribution. These gages were installed in six

locations with five gages distributed through the depth of the composite section at each location. As a result, at each location five sets of distribution factors could be developed using the method outlined. These distribution factors are presented in Table A.15 through Table A.22 for both the S1-X (one truck) and S2-X (two truck) series. Please note that the one truck loadings were at different transverse locations on the bridge than the two truck loadings. Therefore, due to the different positions, different distribution factors are expected.

Several different methods were explored for combining the five individual distribution factors for each location. It was desired to develop a methodology which provided a consistent basis for inclusion or exclusion of the data. For instance, the data for the strain at the top of the U-beams tends to be small for most loadings since the elastic neutral axis of the composite section is located near the top of the girder. Also when strain gages were located distant from the test load placement, strains tended to be small. It was observed that outliers in the data tended to correspond to locations where small strains were measured. Therefore, all data sets where none of the strain readings exceeded 5 micro-strains or one strain reading was less than 1 micro-strain were excluded. These exclusions are indicated by shading in

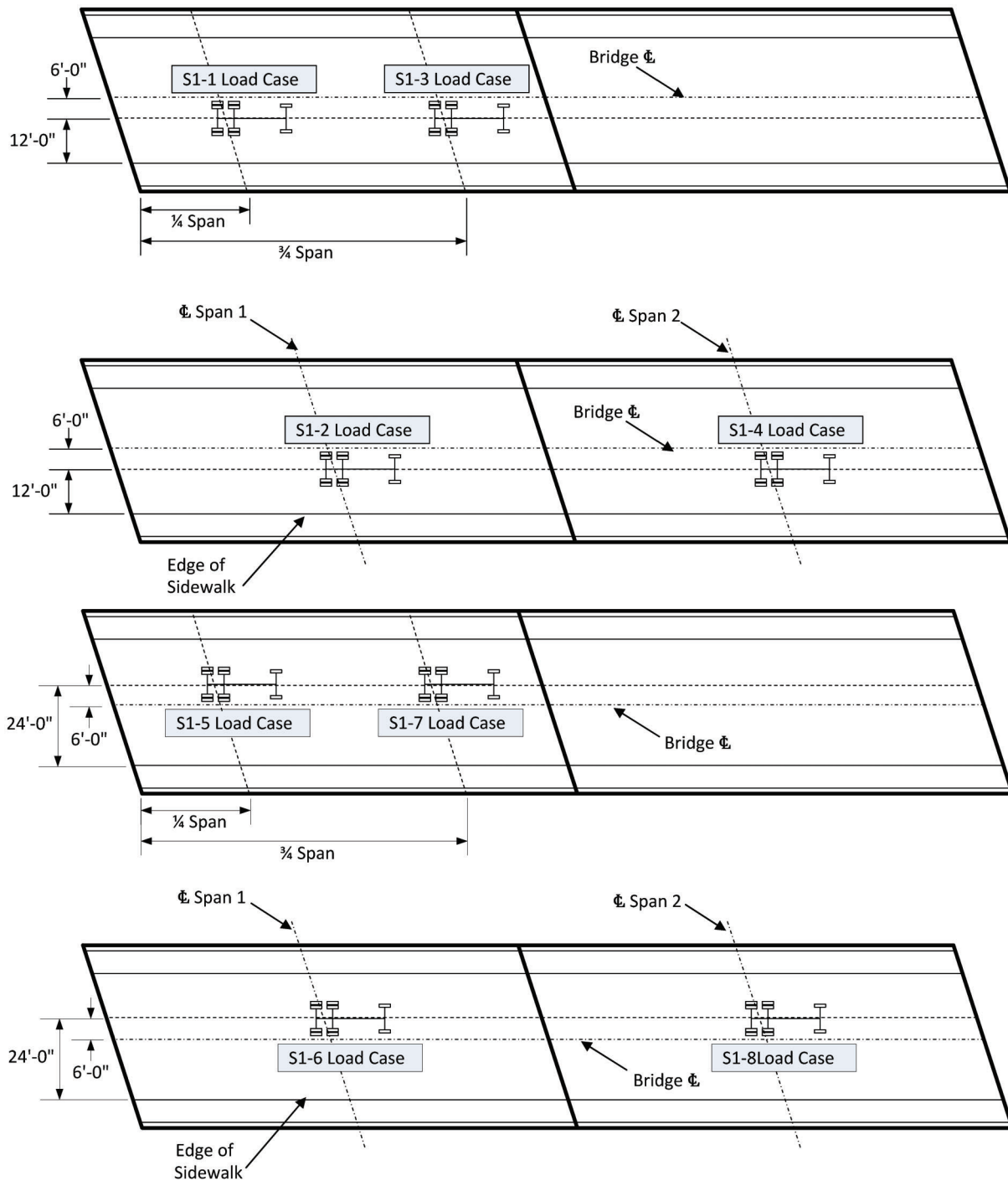


Figure A.27 Series S1-X load test.

Table A.15 through Table A.22. It may be noted that in the case of the S1-X series (Table A.18) none of the strains measured at the 1/2 and 1/4 spans during tests S1-4 and S1-8 exceeded the thresholds set. This is not surprising since the load is remote from the gages during these tests.

The remaining distributions factors which were of sufficient magnitude were then averaged to determine the distribution factor for a given loading at a given location. The resulting distribution factors are presented in Table A.23 and Table A.24 for the S1-X and S2-X series respectively. The distribution factors measured at the location of the loading have been bolded for emphasis. In examining the distribution factors, often the largest distribution

factor for a girder under a given loading occurs at gages which are distant from the applied load. At gages distant from the applied load, the measured strains are smaller than those measured at the area of load application. As a result, the distribution factors measured at the location of load application are presumed to more accurately reflect the behavior of the bridge. The following discussion analyzes only the distribution factors measured at the location of truck placement. The calculated distribution factors for the S1-X series provide a maximum value of 0.42 for the exterior girder and 0.48 for the interior girder. Looking at the three values for the interior girder distribution factor (0.37, 0.46, and 0.48) indicates that the maximum value of 0.48 is likely high.

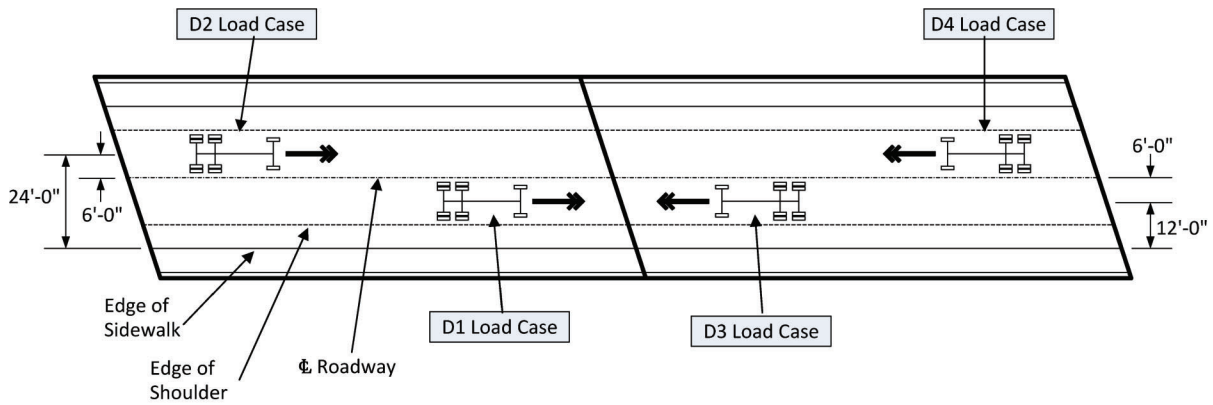


Figure A.28 Series D load test layout.

Given the location of the truck between the interior and exterior girder lines, the distribution factors for the interior and exterior girders would be expected to be similar. The average of the interior girder distribution factors for the S1-X series is 0.44. Also note that for the S1-X series, the northern exterior girder, which was distant from the load, always carried approximately 20% of the load. Similar analysis of the S2-X series data shows a maximum calculated distribution factor of 0.48 for the exterior girders and 0.45 for the interior girder. The higher distribution factors for the S2-X series make sense as this series placed the loading more directly over both the interior and exterior girders while the S1-X series placed the trucks in the driving lanes which are between girder lines. The approximate transverse placement of the trucks for the two series is provided in Figure A.33.

A.8.2 Beam Model Live Load Distribution Factors

To provide confirmation of the live load distribution experimental results, a simple beam model of the bridge was developed in SAP 2000. This model was designed to represent the approximate stiffness of the girders and bridge deck. In developing the model, a 10 ft strip of the bridge deck was isolated. This deck width was selected because the load of the dump truck rear axles was applied over approximately a 10 ft length. It should be noted that the deck width was varied and had only a small influence on the resulting live load distribution factors. Alternately, it would be appropriate to use the deck strip width calculated using the AASHTO LRFD Bridge Design Specifications Section 4.6.2.1.3 provisions for deck design. The bridge deck was supported by a series of three springs located at the centerline of each girder as illustrated in Figure A.34. The stiffness of the springs was equivalent to the flexural stiffness of the girders calculated using Equation A.7. In calculating the stiffness of the exterior girders, the sidewalk was included but the barrier rail was not assumed to act with the composite section. A series of three load cases were explored. These load cases represented to three load conditions tested in the field (edge loading, centerline loading and lane loading). In each case, a unit load was applied in a location corresponding to the center of the truck and the resulting reactions at each spring were recorded. The results of the model analysis are presented in Table A.25.

$$k_{eq} = \frac{48EI}{L^3} \quad (A.7)$$

where:

- E : modulus of elasticity (6,200 ksi)
- I : composite moment of inertia (interior = 1,672,000 in.⁴, exterior = 1,886,000 in.⁴)
- L : span length (116 ft)

Based on the model, the maximum interior live load distribution factor for the interior girder is 0.41 and 0.58 for the exterior girder. Inspection of the model results shows good overall agreement with the experimentally measured values. In general, the model under-predicted the load which was transmitted to the northern exterior girder which is most remote from the applied load. The centerline loading model (0.30, 0.41, 0.30) produced the best agreement with the experimental results (0.27, 0.45, 0.27). The edge loading and centerline loading models produced results which were within the high end of the range of the experimental data for the interior and southern exterior girder. The results for the northern exterior girder are under-estimated for these loading conditions.

A.8.3 AASHTO LRFD Live Load Distribution Factors

The AASHTO LRFD Bridge Design Specifications provide for the determination of the live load distribution factors for interior beams in Section 4.6.2.2b and for exterior beams in Section 4.6.2.2d. The U-beam bridge with composite concrete deck is classified as "Open Steel or Precast Concrete Boxes." The design formula for one lane loaded for determining the live load distribution factor for an interior girder is shown as Equation A.8. Use of this expression yields a distribution factor of 0.41 given the geometric properties of the bridge ($S=12$ ft, $d=54$ in., $L=116$ ft). The distribution factor for the exterior girder is to be determined through use of the lever rule where a hinge is assumed to develop at the first interior girder (in this case the center of the deck) and two design loads are placed on the deck. The first design load is to be placed 2 ft from the edge of the driving surface and the second load is offset by 6 ft from the first. Use of the lever rule produces a distribution factor of 0.70. Application of the lever rule for this bridge is shown in Figure A.35.

$$\left(\frac{S}{3.0}\right)^{0.35} + \left(\frac{Sd}{12.0L^2}\right)^{0.25} \quad (A.8)$$

where:

- S : girder or web spacing, ft
- d : girder depth, in.
- L : span length, ft

Based on the testing performed on the 21st Street Bridge, the AASHTO design distribution factors are very conservative for the exterior girders and slightly unconservative for the interior girder. The interior girder had a maximum measured live load distribution factor of 0.45 which exceeds the 0.41 prescribed by AASHTO. The exterior girder, however, had a maximum measured distribution factor of 0.48 but AASHTO calculates 0.70. The maximum distribution factor for the interior girder from the beam model agrees exactly with that calculated according to AASHTO. The distribution factors for the

TABLE A.12
Series S1-X Strains

Location			Load Case							
			S1-1	S1-2	S1-3	S1-4	S1-5	S1-6	S-7	S1-8
1/4 Span	Exterior	TR	-15.53	-11.08	-8.04	-4.54	-6.55	-5.20	-1.94	-2.49
		BR	-13.77	-10.05	-8.00	-6.15	-7.32	-5.16	-1.59	-4.32
		TG	-2.56	-1.14	-1.35	-1.40	-2.81	-1.97	-0.16	-1.53
		MG	-2.68	-2.29	-3.60	-3.86	-1.97	-0.41	0.77	1.85
		BG	4.93	2.93	-0.90	-3.19	1.09	2.68	2.53	-3.37
	Interior	TR	-16.45	-9.13	-6.70	-4.98	-9.88	-4.66	-1.89	-2.30
		BR	Lost Gage							
		TG	-8.71	-5.23	-4.02	-3.01	-4.01	-2.22	-0.92	-2.92
		MG	-4.20	-5.12	-4.51	-3.69	1.03	-0.53	-0.67	-2.24
		BG	1.52	-5.12	-5.57	-4.74	8.72	2.25	0.05	-3.52
1/2 Span	Exterior	TR	-10.98	-12.52	-7.43	-3.72	-5.25	-5.40	-3.61	-1.46
		BR	-3.92	-5.66	-2.58	-0.12	-1.44	-2.72	-1.99	-1.54
		TG	2.24	0.20	2.04	2.55	1.26	-0.52	-0.66	-0.88
		MG	3.44	4.89	3.72	0.76	1.95	1.93	1.63	-1.04
		BG	8.37	12.75	7.15	-0.18	5.27	6.83	5.36	-0.39
	Interior	TR	-9.44	-15.08	-4.83	-1.39	-4.21	-9.28	-3.50	-1.88
		BR	-5.70	-8.99	-2.52	-0.24	-2.74	-6.62	-2.67	-0.60
		TG	1.14	-0.88	1.31	2.00	0.14	-2.14	-0.73	-1.24
		MG	2.96	6.73	2.84	0.74	2.53	5.12	2.46	-1.05
		BG	9.43	16.26	6.31	1.26	7.71	16.08	6.88	0.42
3/4 Span	Exterior	TR	-11.63	-11.38	-12.57	-6.40	-6.44	-5.00	-3.47	-4.17
		BR	-13.75	-13.00	-13.49	-8.37	-8.20	-6.14	-3.48	-6.12
		TG	-2.66	-2.62	-3.94	-2.20	-2.40	-1.69	-0.98	-3.81
		MG	-3.92	-2.34	-2.02	-5.14	-2.87	-0.76	1.03	-4.93
		BG	-3.43	0.12	2.76	-6.49	-1.24	1.73	4.02	-4.89
	Interior	TR	-12.21	-12.75	-16.27	-6.13	-5.90	-5.84	-7.63	-5.56
		BR	-10.08	-11.03	-13.96	-4.97	-5.22	-5.68	-7.43	-4.27
		TG	-3.56	-4.34	-4.45	-2.10	-2.16	-2.18	-2.40	-4.64
		MG	-4.25	-2.09	0.77	-2.22	-0.46	0.60	3.05	-4.85
		BG	-4.58	0.57	7.04	-3.62	0.43	3.73	11.20	-7.19

Key: TR = Top Longitudinal Rebar; BR = Bottom Longitudinal Rebar; TG = Top of Girder; MG = Mid-Height of Girder; BG = Bottom of Girder.

exterior girders from the beam model also indicate that the AASHTO modeling technique is conservative.

A.8.4 Flexural Behavior of the Bridge Deck

As previously discussed, a series of 14 strain gages were installed on the transverse reinforcement at mid-span between the exterior and interior girder to assess the flexural behavior of the deck. These gages were positioned in seven locations as previously outlined (Figure A.6). One of the gages installed on the transverse reinforcement was lost during deck placement. The strains on the two lines of reinforcement are shown in Figure A.36. The first line of gages (Line A) indicates negative moment over each of the girder lines with positive moment in the center of the deck span. This arrangement of flexural stresses makes sense given the continuity of the deck over the U-beam girders. The second line of gages (Line B) is missing a strain measurement due to the lost gage, but shows a trend in stress distribution which indicates negative moment at the girder lines. However, these gages did not appear to provide reliable data.

A simple model of the bridge deck was developed in SAP 2000 to explore the distribution of forces induced in the deck by the applied loading. This model isolated a strip of the deck and

treated it as a beam element, with supports located at the location of the six beam webs. The moments from the model were then used to calculate the strains at the gage levels. The strains were calculated assuming a tributary deck width equal to the strip widths calculated according to the AASHTO LRFD Bridge Design Specifications Section 4.6.2.1.3. The tributary deck widths for the negative moment regions (84 in.) and the positive moment regions (105 in.) were calculated for a cast-in-place concrete deck. Consideration was given to the effect of the stay-in-place forms when calculating the section properties. While block outs were used at the deck ribs, the cross-sectional area of the decking provides additional capacity to the deck section. The strains calculated by the SAP model are presented in Table A.26. It is of note that the negative moment at the face of the interior girder from the model is substantially higher than the negative moment at the exterior girder. This is due to the applied load pattern (Figure A.29). While one of the truck wheels was placed over the center of the main deck span, the other set of rear wheels was located over the interior girder and also induced negative moment at the location of the beam webs.

Comparison of the measured strains in Rebar A in Figure A.35 with those calculated based on the model shows close agreement for the top transverse reinforcement strains. The bottom transverse reinforcement strains do not show close agreement with the

TABLE A.13
Series S2-X Strains

Location			Load Case					
			S2-1	S2-2	S2-3	S2-4	S2-5	S2-6
1/4 Span	Exterior	TR	-25.88	-16.92	-19.95	-11.97	-15.40	-10.58
		BR	-22.89	-14.55	-16.84	-9.52	-12.03	-9.45
		TG	3.58	3.76	-0.52	1.31	-0.38	-0.54
		MG	0.96	-5.54	-2.22	-5.16	-3.47	-5.88
		BG	11.55	-4.58	6.73	-3.67	2.65	-4.98
	Interior	TR	-24.62	-18.73	-21.56	-13.99	-18.42	-10.11
		BR				Lost Gage		
		TG	-9.32	-7.42	-10.07	-7.71	-9.21	-6.14
		MG	-10.27	-11.41	-8.29	-10.30	-6.64	-8.02
		BG	-10.47	-16.13	-5.05	-14.12	-2.53	-11.01
1/2 Span	Exterior	TR	-29.83	-13.99	-19.81	-10.20	-15.15	-7.87
		BR	-10.87	-0.50	-6.34	-0.57	-4.85	-0.71
		TG	9.25	11.31	5.62	7.20	3.31	4.83
		MG	17.28	4.97	8.20	2.71	4.17	1.46
		BG	32.28	-0.34	15.81	-0.99	8.13	-0.77
	Interior	TR	4.35	10.25	0.45	6.11	0.54	4.57
		BR	8.14	4.12	11.37	2.03	7.55	1.13
		TG	19.65	2.11	30.39	0.65	19.02	-0.36
		MG	-36.92	-44.32	-34.75	-32.14	-30.08	-22.31
		BG	-0.33	-10.75	-12.76	-7.25	-6.27	-4.38
3/4 Span	Exterior	TR	-22.58	-15.72	-17.13	-11.13	-13.71	-10.55
		BR	-21.82	-14.84	-16.14	-11.26	-13.80	-12.22
		TG	6.64	5.99	2.77	2.18	0.36	-1.26
		MG	5.62	-1.80	2.04	-2.92	-0.37	-5.33
		BG	6.81	-10.04	3.53	-7.91	0.32	-8.10
	Interior	TR	-23.88	-15.21	-18.94	-13.09	-17.61	-10.55
		BR	-17.10	-10.14	-15.54	-9.69	-15.15	-7.75
		TG	1.23	3.65	-0.62	-1.21	-3.46	-2.30
		MG	3.85	-0.59	-0.36	-5.69	-3.39	-5.80
		BG	9.48	-3.61	3.01	-10.42	-0.77	-10.42

Key: TR = Top Longitudinal Rebar; BR = Bottom Longitudinal Rebar; TG = Top of Girder; MG = Mid-Height of Girder; BG = Bottom of Girder.

experimental results at all sections. The model strain for the bottom reinforcement at the deck centerline (between girders) agrees well with the measured value, however, the strains for the bottom reinforcement adjacent to the girders do not agree well with the measured values. It should also be noted that the strains in Rebar B from Figure A.35 do not agree well with the calculated strains. This was expected as the strains measured on that bar seemed unusual.

Additionally, a shell model of the bridge deck was constructed to model the bridge deck behavior under the applied load. The deck was modeled using shell elements with the same dimensions as the instrumented bridge span. The model provided displacement restraint at the locations of each of the six beam webs and the truck loads were applied at the centroid of the wheels. This model produced stress levels at the top and bottom of the slab which agree with strains from the simple beam model (Table A.26). Also of note, the flexural stresses were distributed over approximately a 10 ft slab strip. This is consistent with the strip width used earlier for the beam model (Section A.8.2). In addition, the results indicate that the AASHTO strip widths are conservative.

A.9 CONCLUSIONS

The load test of the 21st Street Bridge allowed for the measurement of the live load distribution factors for this bridge.

Additionally, a simple beam model of the bridge was developed for the loading conditions considered. The results of the beam model were within the range of the experimental results. Upon comparison of the measured live load distribution factors with those calculated based on the AASHTO LRFD Bridge Design Specifications, it appears that the expression for interior girder distribution factors is slightly unconservative but reasonable. The exterior girder live load distribution factor computed based on AASHTO was extremely conservative based on the testing performed. While the measured live load distribution factors are only applicable to this bridge deck and girder configuration, the results of this study indicate that a simple spring beam model can be used to closely and conservatively determine the live load distribution factors for interior and exterior girders.

The flexural behavior of the bridge deck between the interior and exterior girder lines exhibited a moment distribution with positive moment in the middle of the span and negative moment over the girder lines. The development of negative moment over the exterior girder lines is expected due to the continuity of the deck over the girder lines. The results of both a simple beam and shell model of the bridge deck indicate that the strains in the bridge deck can be accurately determined using simple finite element models. The shell model also indicates that the strip width values calculated according to the AASHTO LRFD Bridge Design Specifications are both reasonable and conservative.

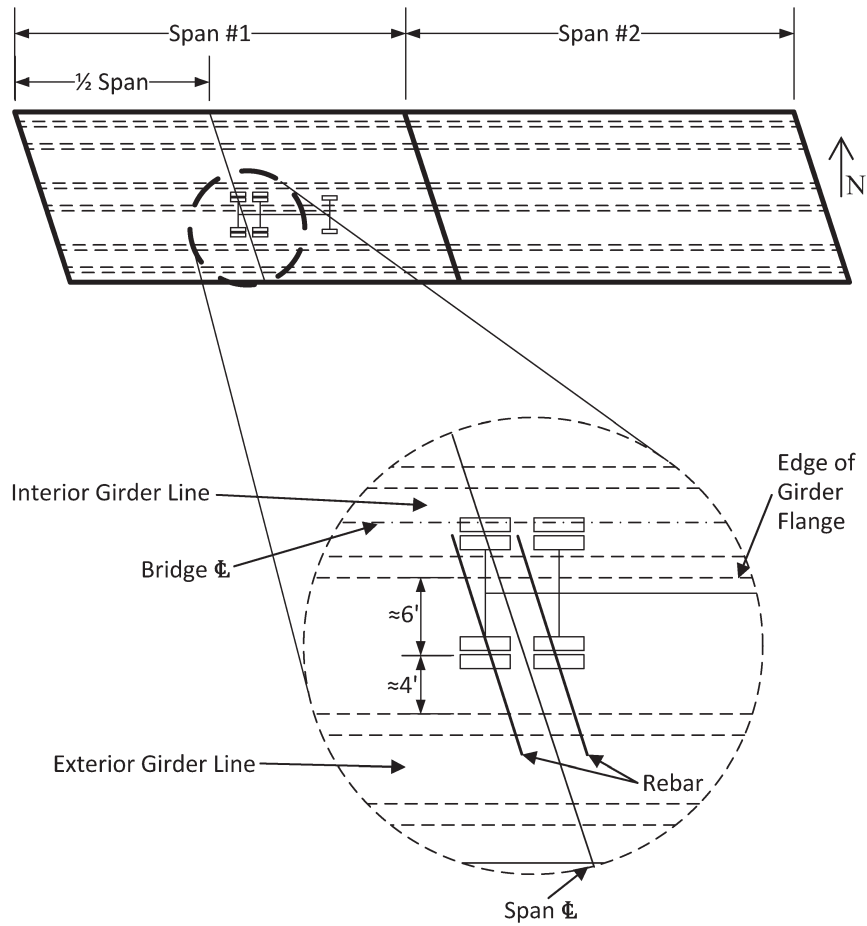


Figure A.29 Location of wheel loads for S1-2 load case.

TABLE A.14
Transverse Deck Gage Strains

Location		
Position	Rebar	Strain
1	Top	6.93
	Bottom	-4.31
2	Top	-14.52
	Bottom	15.35
3	Top	17.14
	Bottom	-1.09
4	Top	-1.83
	Bottom	-2.42
5	Top	Lost Gage
	Bottom	-32.14
6	Top	-0.11
	Bottom	-9.04
7	Top	-123.30
	Bottom	-4.25

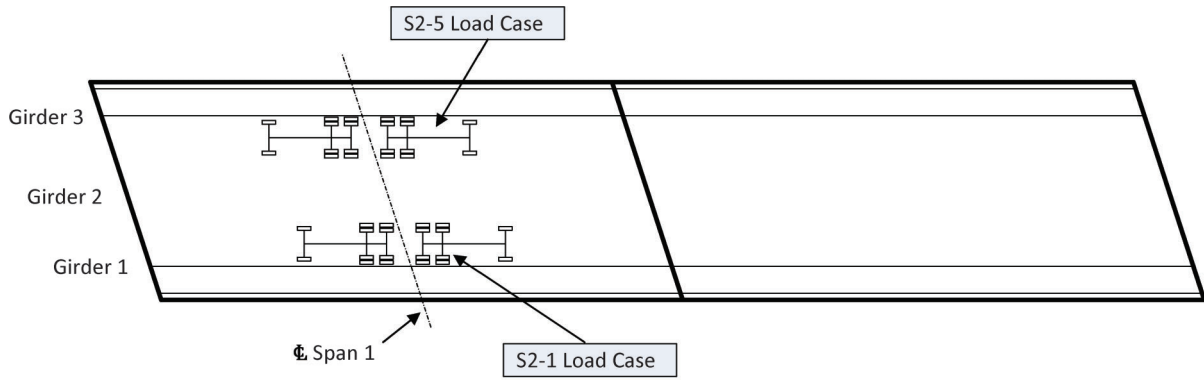


Figure A.30 Use of load test symmetry.

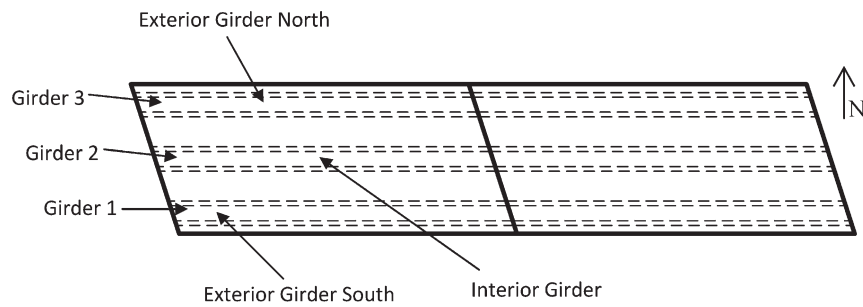
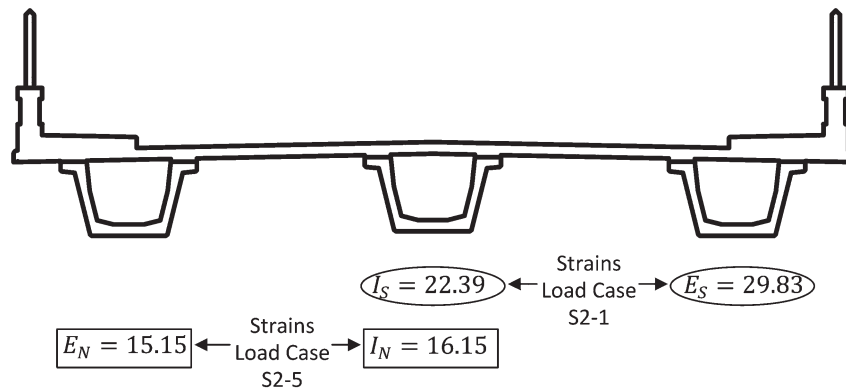


Figure A.31 Girder identification.



$$DF_{Ext-S} = \frac{\frac{29.83}{22.39}}{\frac{15.15}{16.15} + 1 + \frac{29.83}{22.39}} = 0.41$$

$$DF_{Int} = \frac{1}{\frac{15.15}{16.15} + 1 + \frac{29.83}{22.39}} = 0.31$$

$$DF_{Ext-N} = \frac{\frac{15.15}{16.15}}{\frac{15.15}{16.15} + 1 + \frac{29.83}{22.39}} = 0.29$$

Figure A.32 Example of distribution factor calculation.

TABLE A.15
Distribution Factors One Truck Loading at 1/4 Span

Gage Location		S1-5 Strains		S1-1 Strains		Distribution Factors		
		Ext.-N	Int.-N	Int.-S	Ext.-S	Ext.-N	Int.	Ext.-S
1/4 Span	TR	-6.55	-9.88	-16.45	-15.53	0.25	0.38	0.36
	BR	Lost Gage						
	TG	-2.81	-4.01	-8.71	-2.56	0.35	0.50	0.15
	MG	-1.97	1.03	-4.20	-2.68	0.54	0.28	0.18
	BG	1.09	8.72	1.52	4.93	0.03	0.23	0.74
1/2 Span	TR	-5.25	-4.21	-9.44	-10.98	0.37	0.29	0.34
	BR	-1.44	-2.74	-5.70	-3.92	0.24	0.45	0.31
	TG	1.26	0.14	1.14	2.24	0.75	0.09	0.17
	MG	1.95	2.53	2.96	3.44	0.26	0.34	0.40
	BG	5.27	7.71	9.43	8.37	0.27	0.39	0.35
3/4 Span	TR	-6.44	-5.90	-12.21	-11.63	0.36	0.33	0.31
	BR	-8.20	-5.22	-10.08	-13.75	0.40	0.25	0.35
	TG	-2.40	-2.16	-3.56	-2.66	0.39	0.35	0.26
	MG	-2.87	-4.67	-4.25	-3.92	0.24	0.39	0.36
	BG	-1.24	4.32	-4.58	-3.43	0.14	0.49	0.37

NOTE: Shaded region indicates data excluded from distribution factor calculations.

TABLE A.16
Distribution Factors One Truck Loading at 1/2 Span

Gage Location		S1-6 Strains		S1-2 Strains		Distribution Factors		
		Ext.-N	Int.-N	Int.-S	Ext.-S	Ext.-N	Int.	Ext.-S
1/4 Span	TR	-5.20	-4.66	-9.13	-11.08	0.34	0.30	0.36
	BR	Lost Gage						
	TG	-1.97	-2.22	-5.23	-1.14	0.42	0.48	0.10
	MG	-0.41	-0.53	-5.12	-2.29	0.20	0.45	0.35
	BG	2.68	2.25	-5.12	2.93	0.21	0.36	0.43
1/2 Span	TR	-5.40	-9.28	-15.08	-12.52	0.24	0.41	0.34
	BR	-2.72	-6.62	-8.99	-5.66	0.20	0.49	0.31
	TG	-0.52	-2.14	-0.88	0.20	0.17	0.68	0.16
	MG	1.93	5.12	6.73	4.89	0.18	0.48	0.35
	BG	6.83	16.08	16.26	12.75	0.19	0.45	0.36
3/4 Span	TR	-5.00	-5.84	-12.75	-11.38	0.31	0.36	0.32
	BR	-6.14	-5.68	-11.03	-13.00	0.33	0.31	0.36
	TG	-1.69	-2.18	-4.34	-2.62	0.33	0.42	0.25
	MG	-0.76	0.60	-2.09	-2.34	0.37	0.30	0.33
	BG	1.73	3.73	0.57	0.12	0.28	0.60	0.12

NOTE: Shaded region indicates data excluded from distribution factor calculations.

TABLE A.17
Distribution Factors One Truck Loading at 3/4 Span

Gage Location		S1-7 Strains		S1-3 Strains		Distribution Factors		
		Ext.-N	Int.-N	Int.-S	Ext.-S	Ext.-N	Int.	Ext.-S
1/4 Span	TR	-1.94	-1.89	-6.70	-8.04	0.32	0.31	0.37
	BR				Lost Gage			
	TG	-0.16	-0.92	-4.02	-1.35	0.12	0.66	0.22
	MG	0.77	-0.67	-4.51	-3.60	0.39	0.34	0.27
	BG	2.53	0.05	-5.57	-0.90	0.98	0.02	0.00
1/2 Span	TR	-3.61	-3.50	-4.83	-7.43	0.29	0.28	0.43
	BR	-1.99	-2.67	-2.52	-2.58	0.27	0.36	0.37
	TG	-0.66	-0.73	1.31	2.04	0.26	0.29	0.45
	MG	1.63	2.46	2.84	3.72	0.22	0.34	0.44
	BG	5.36	6.88	6.31	7.15	0.27	0.34	0.39
3/4 Span	TR	-3.47	-7.63	-16.27	-12.57	0.20	0.45	0.35
	BR	-3.48	-7.43	-13.96	-13.49	0.19	0.41	0.40
	TG	-0.98	-2.40	-4.45	-3.94	0.18	0.44	0.39
	MG	1.03	3.05	0.77	-2.02	0.09	0.25	0.66
	BG	4.02	11.20	7.04	2.76	0.20	0.57	0.22

NOTE: Shaded region indicates data excluded from distribution factor calculations.

TABLE A.18
Distribution Factors One Truck Loading at 3/2 Span

Gage Location		S1-8 Strains		S1-4 Strains		Distribution Factors		
		Ext.-N	Int.-N	Int.-S	Ext.-S	Ext.-N	Int.	Ext.-S
1/4 Span	TR	-2.49	2.30	-4.98	-4.54	0.36	0.33	0.30
	BR				Lost Gage			
	TG	-1.53	2.92	-3.01	-1.40	0.26	0.50	0.23
	MG	1.85	-2.24	-3.69	-3.86	0.29	0.35	0.36
	BG	-3.37	-3.52	-4.74	-3.19	0.36	0.38	0.26
1/2 Span	TR	-1.46	-1.88	-1.39	-3.72	0.18	0.22	0.60
	BR	-1.54	-0.60	-0.24	-0.12	0.64	0.25	0.12
	TG	-0.88	-1.24	2.00	2.55	0.24	0.34	0.43
	MG	-1.04	-1.05	0.74	0.76	0.33	0.33	0.34
	BG	-0.39	0.42	1.26	-0.18	0.45	0.49	0.07
3/4 Span	TR	-4.17	-5.56	-6.13	-6.40	0.27	0.36	0.37
	BR	-6.12	-4.27	-4.97	-8.37	0.35	0.24	0.41
	TG	-3.81	-4.64	-2.10	-2.20	0.29	0.35	0.37
	MG	-4.93	-4.85	-2.22	-5.14	0.23	0.23	0.53
	BG	-4.89	-7.19	-3.62	-6.49	0.20	0.29	0.52

NOTE: Shaded region indicates data excluded from distribution factor calculations.

TABLE A.19
Distribution Factors Two Truck Loading at 1/2 Span, Edge of Deck

Gage Location		S2-5 Strains		S2-1 Strains		Distribution Factors		
		Ext.-N	Int.-N	Int.-S	Ext.-S	Ext.-N	Int.	Ext.-S
1/4 Span	TR	-15.40	-18.42	-24.62	-25.88	0.29	0.35	0.36
	BR				Lost Gage			
	TG	-0.38	-9.21	-9.32	3.58	0.03	0.70	0.27
	MG	-3.47	-6.64	-10.27	0.96	0.32	0.62	0.06
	BG	2.65	-2.53	-10.47	11.55	0.33	0.32	0.35
1/2 Span	TR	-15.15	-16.15	-22.39	-29.83	0.29	0.31	0.41
	BR	-4.85	-9.31	-10.65	-10.87	0.21	0.39	0.40
	TG	3.31	0.54	4.35	9.25	0.66	0.11	0.23
	MG	4.17	7.55	8.14	17.28	0.15	0.27	0.58
	BG	8.13	19.02	19.65	32.28	0.14	0.33	0.54
3/4 Span	TR	-13.71	-17.61	-23.88	-22.58	0.29	0.37	0.35
	BR	-13.80	-15.15	-17.10	-21.82	0.29	0.31	0.40
	TG	0.36	-3.46	1.23	6.64	0.02	0.15	0.83
	MG	-0.37	-3.39	3.85	5.62	0.04	0.39	0.57
	BG	0.32	-0.77	9.48	6.81	0.19	0.47	0.34

NOTE: Shaded region indicates data excluded from distribution factor calculations.

TABLE A.20
Distribution Factors Two Truck Loading at 1/2 Span, Middle of Deck

Gage Location		S2-3 Strains				Distribution Factors		
		Ext.-N	Int.-N	Int.-S	Ext.-S	Ext.-N	Int.	Ext.-S
1/4 Span	TR	-19.95	-21.56	-19.95	-19.95	0.32	0.35	0.32
	BR				Lost Gage			
	TG	-0.52	-10.07	-0.52	-0.52	0.05	0.91	0.05
	MG	-2.22	-8.29	-2.22	-2.22	0.17	0.65	0.17
	BG	6.73	-5.05	6.73	6.73	0.36	0.27	0.36
1/2 Span	TR	-19.81	-23.85	-19.81	-19.81	0.31	0.38	0.31
	BR	-6.34	-14.87	-6.34	-6.34	0.23	0.54	0.23
	TG	5.62	0.45	5.62	5.62	0.48	0.04	0.48
	MG	8.20	11.37	8.20	8.20	0.30	0.41	0.30
	BG	15.81	30.39	15.81	15.81	0.25	0.49	0.25
3/4 Span	TR	-17.13	-18.94	-17.13	-17.13	0.32	0.36	0.32
	BR	-16.14	-15.54	-16.14	-16.14	0.34	0.32	0.34
	TG	2.77	-0.62	2.77	2.77	0.45	0.10	0.45
	MG	2.04	-0.36	2.04	2.04	0.46	0.08	0.46
	BG	3.53	3.01	3.53	3.53	0.35	0.30	0.35

NOTE: Shaded region indicates data excluded from distribution factor calculations.

TABLE A.21
Distribution Factors Two Truck Loading at 3/2 Span, Edge of Deck

Gage Location		S2-6 Strains		S2-2 Strains		Distribution Factors		
		Ext.-N	Int.-N	Int.-S	Ext.-S	Ext.-N	Int.	Ext.-S
1/4 Span	TR	-10.58	-10.11	-18.73	-16.92	0.28	0.27	0.45
	BR	Lost Gage						
	TG	-0.54	-6.14	-7.42	3.76	0.05	0.59	0.36
	MG	-5.88	-8.02	-11.41	-5.54	0.30	0.41	0.29
	BG	-4.98	-11.01	-16.13	-4.58	0.24	0.54	0.22
1/2 Span	TR	-7.87	-3.56	-7.40	-13.99	0.31	0.14	0.55
	BR	-0.71	-0.36	-0.21	-0.50	0.45	0.23	0.32
	TG	4.83	4.57	10.25	11.31	0.23	0.22	0.55
	MG	1.46	1.13	4.12	4.97	0.19	0.15	0.66
	BG	-0.77	-0.36	2.11	-0.34	0.52	0.24	0.23
3/4 Span	TR	-10.55	-10.55	-15.21	-15.72	0.29	0.29	0.43
	BR	-12.22	-7.75	-10.14	-14.84	0.35	0.22	0.43
	TG	-1.26	-2.30	3.65	5.99	0.13	0.24	0.63
	MG	-5.33	-5.80	-0.59	-1.80	0.41	0.45	0.14
	BG	-8.10	-10.42	-3.61	-10.04	0.28	0.36	0.35

NOTE: Shaded region indicates data excluded from distribution factor calculations.

TABLE A.22
Distribution Factors Two Truck Loading at 3/2 Span, Middle of Deck

Gage Location		S2-4 Strains				Distribution Factors		
		Ext.-N	Int.-N	Int.-S	Ext.-S	Ext.-N	Int.	Ext.-S
1/4 Span	TR	-11.97	-13.99		-11.97	0.32	0.37	0.32
	BR	Lost Gage						
	TG	1.31	-7.71		1.31	0.13	0.75	0.13
	MG	-5.16	-10.30		-5.16	0.25	0.50	0.25
	BG	-3.67	-14.12		-3.67	0.17	0.66	0.17
1/2 Span	TR	-10.20	-6.12		-10.20	0.38	0.23	0.38
	BR	-0.57	-1.01		-0.57	0.27	0.47	0.27
	TG	7.20	6.11		7.20	0.35	0.30	0.35
	MG	2.71	2.03		2.71	0.36	0.27	0.36
	BG	-0.99	0.65		-0.99	0.38	0.25	0.38
3/4 Span	TR	-11.13	-13.09		-11.13	0.31	0.37	0.31
	BR	-11.26	-9.69		-11.26	0.35	0.30	0.35
	TG	2.18	-1.21		2.18	0.39	0.22	0.39
	MG	-2.92	-5.69		-2.92	0.25	0.49	0.25
	BG	-7.91	-10.42		-7.91	0.30	0.40	0.30

NOTE: Shaded region indicates data excluded from distribution factor calculations.

TABLE A.23
Load Distribution Factors S1-X Series

Loading	Location	Ext.-N	Int.	Ext.-S
Driving Lane	1/4 Span	0.21	0.37	0.42
1/4 Span	1/2 Span	0.29	0.38	0.33
S1-1, S1-5	3/4 Span	0.38	0.29	0.33
Driving Lane	1/4 Span	0.32	0.38	0.30
1/2 Span	1/2 Span	0.20	0.46	0.34
S1-2, S1-6	3/4 Span	0.32	0.34	0.34
Driving Lane	1/4 Span	0.32	0.31	0.37
3/4 Span	1/2 Span	0.28	0.31	0.41
S1-3, S1-7	3/4 Span	0.20	0.48	0.32
Driving Lane	1/4 Span			—
Adjacent Span	1/2 Span			—
S1-4, S1-8	3/4 Span	0.26	0.28	0.46

TABLE A.24
Load Distribution Factors S2-X Series

Loading	Location	Ext.-N	Int.	Ext.-S
Edge Loading	1/4 Span	0.31	0.33	0.36
S2-1, S2-5	1/2 Span	0.20	0.32	0.48
	3/4 Span	0.29	0.34	0.37
Centerline Loading	1/4 Span	0.29	0.42	0.29
S2-3	1/2 Span	0.27	0.45	0.27
	3/4 Span	0.34	0.33	0.34
Adjacent Span	1/4 Span	0.28	0.41	0.32
Edge Loading	1/2 Span	0.25	0.17	0.58
S2-2, S2-6	3/4 Span	0.26	0.28	0.46
Adjacent Span Centerline Loading	1/4 Span	0.25	0.50	0.25
S2-4	1/2 Span	0.37	0.27	0.37
	3/4 Span	0.32	0.36	0.32

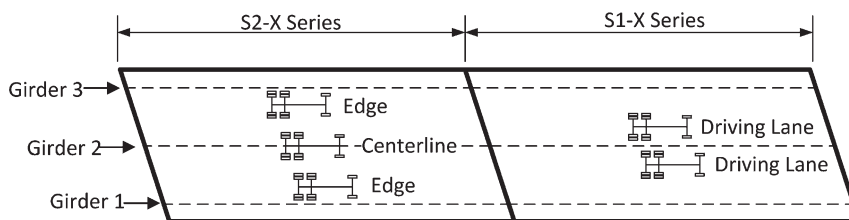


Figure A.33 Transverse layout of trucks for S1-X and S2-X series.

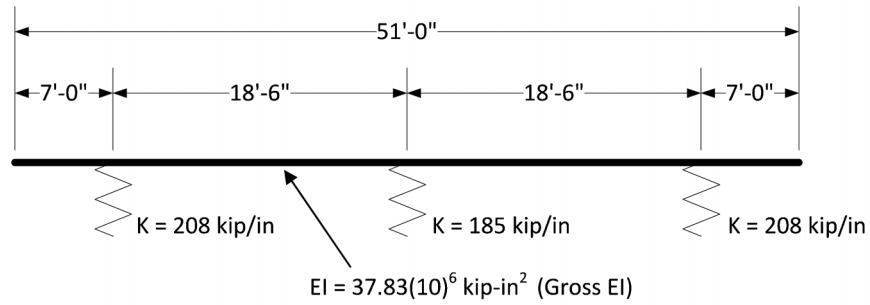


Figure A.34 Beam model.

TABLE A.25
Live Load Distribution Factors—SAP Model

Load Case	Ext.-N	Int.	Ext.-S
Edge	0.10	0.32	0.58
Lane	0.13	0.38	0.48
Centerline	0.30	0.41	0.30

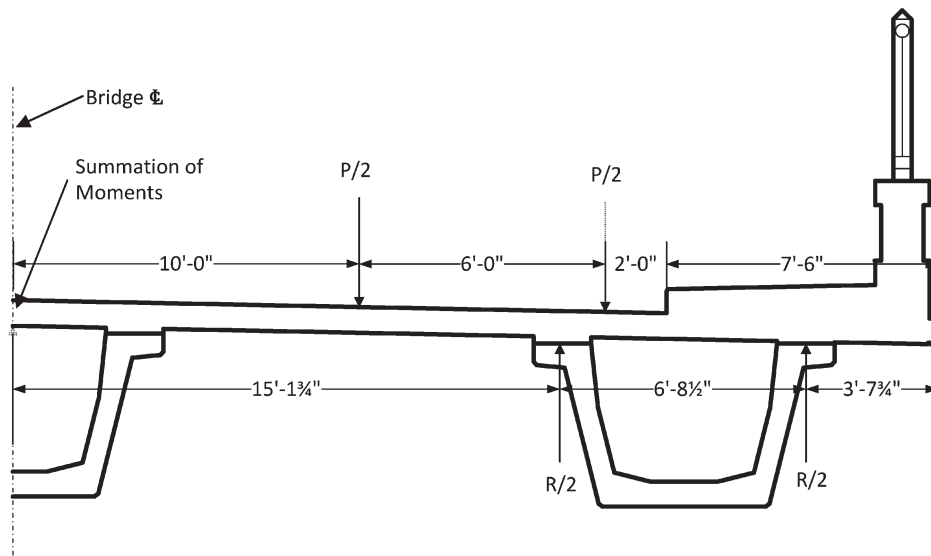


Figure A.35 Lever rule for exterior girder.

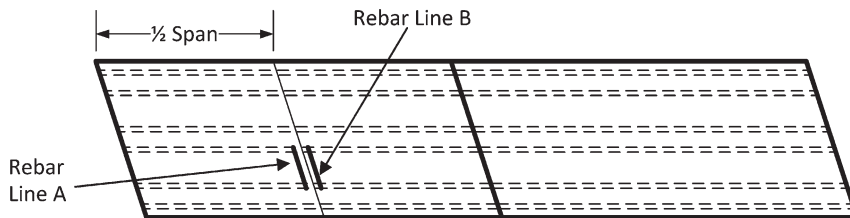
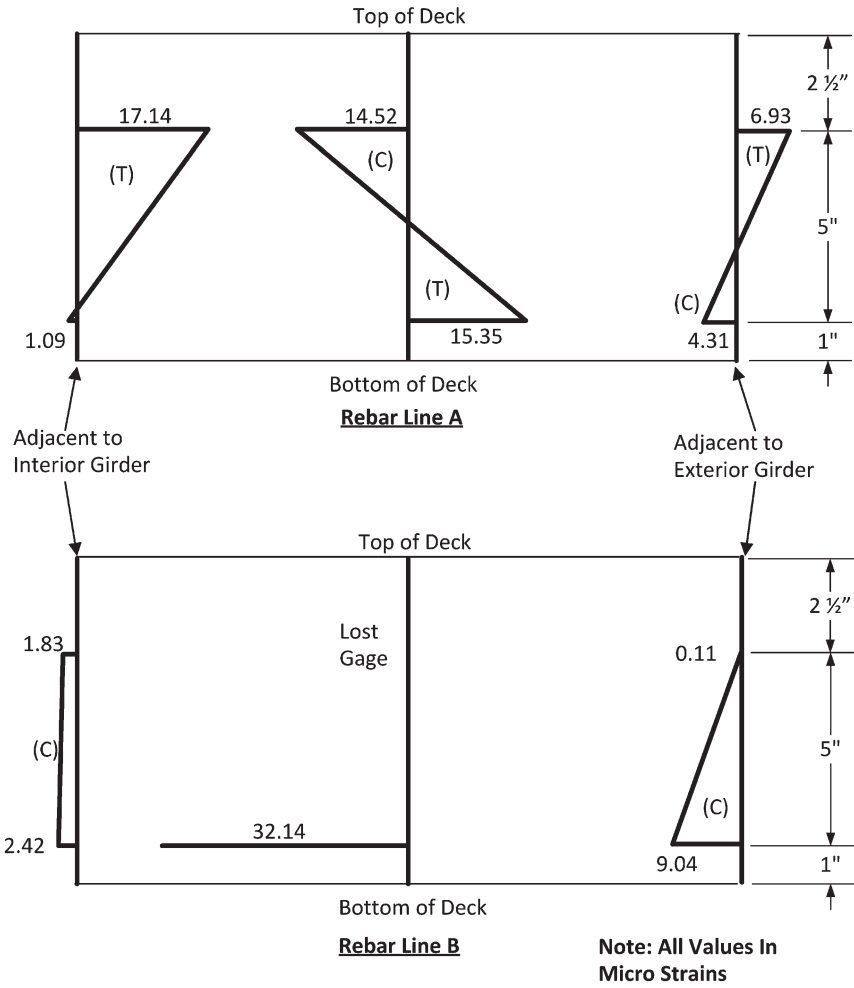


Figure A.36 Deck behavior flexural strains.

TABLE A.26
Flexural Deck Strains—SAP Model

Location	Adjacent to Interior Girder	Centerline of Deck	Adjacent to the Exterior Girder
	Strain ($\mu\epsilon$)		
Top of Deck	38.0	28.2	18.0
Top Transverse Reinforcement	17.7	13.2	8.4
Bottom Transverse Reinforcement	22.6	16.8	10.7
Bottom of Deck	24.5	22.8	11.6

APPENDIX B. EVALUATION OF DEBOND SHEATHING PRODUCTS

B.1 INTRODUCTION

An experimental program conducted at the Bowen Laboratory investigated the effectiveness of commercially available prestressing strand debonding products. A series of prismatic, symmetrically prestressed specimens were constructed with debonded regions of varying length at each end. The experimental program included specimens with varying lengths of debond and different debonding products. This chapter describes the design, construction, and testing of these specimens as well as the results.

B.2 SPECIMEN DESIGN

The objective of the laboratory evaluation was to assess the effectiveness of some of the more common, commercially available, prestressing strand debonding products. It was determined that strains in the concrete before and after prestress force transfer would be used to assess the effectiveness of the products. Ease of measuring these strains was of primary importance in the design of the member cross section.

B.2.1 Specimen Cross Section

The specimen cross section was selected to be 4 in. square with one 1/2 in. prestressing strand placed in the center of the member as shown in Figure B.1. This cross section was selected because prestressing strands are typically placed on a 2 in. grid within prestressed members. Therefore this section isolates one strand and provides typical edge cover. Having only one prestressing strand in each specimen reduces the complexity of analysis and the number of variables for which to account. Keeping the specimen size to a minimum in turn maximizes the induced concrete strains making them easier to measure. The specimens were also concentrically prestressed, further simplifying the strain profile in the concrete cross section by eliminating applied moments. No additional mild steel was added to the specimens because compression is induced throughout the specimens by the concentric prestressing.

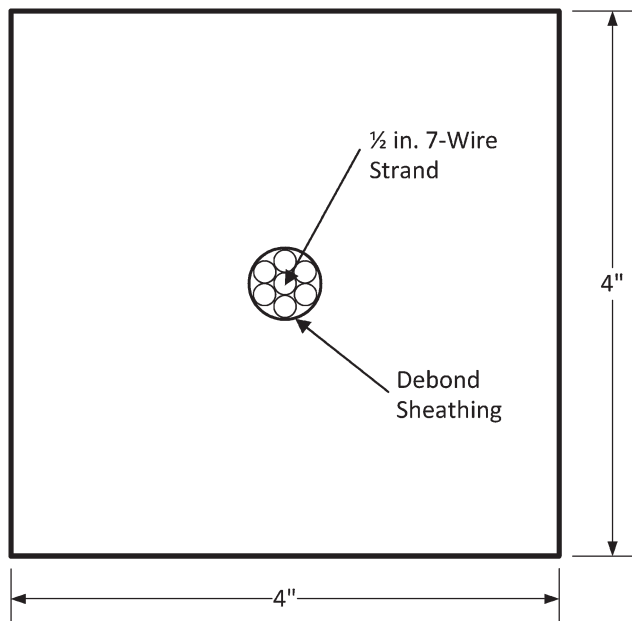


Figure B.1 Prestressed specimen cross section.

B.2.2 Prestressing Strand

Each specimen was concentrically prestressed with one 1/2 in. diameter uncoated seven-wire, low-relaxation, Grade 270 prestressing strand, conforming to ASTM A416 (2012) and AASHTO M203 (2012b). Maximizing the total prestressing force was desired to maximize the concrete strains and aid in measurement of the strain profile along the specimens. The release stress was limited to 75% (202.5 ksi) of the ultimate strength of the prestressing strands (270 ksi). A prestressing loss due to slip in the chucks was calculated based on a 0.25 in. slip over a bed length of 51 ft. This resulted in a calculated loss due to slip of 11.6 ksi. Therefore, a jacking stress of 214.1 ksi ($0.79f_{pu}$) was used for a total jacking force of 32.8 kips. The prestressing force at transfer was calculated to induce an axial compressive stress of 1.94 ksi in the concrete specimens.

B.2.3 Debonding Products

Debonding is generally performed by placing a plastic tubing product over the portion of the prestressing strand where debonding is specified. The plastic sheathing is intended to prevent the development of bond between the surrounding concrete and the prestressing strand. Commercially available debonding products generally fall into one of two main classifications, split and un-split. It is uncommon for designers to specify the type of debonding product to be used on a given project. Therefore, split sheathing has become the predominant form of debonding used by most prestressing yards. The ease of installation before or after stressing of the strands is the main reason for its popularity. Generally, un-split sheathing is only used when specified as part of the member design or by client specific requirements. As an example, the Florida Department of Transportation (FDOT) requires use of un-split sheathing (FDOT, 2014). Because it is uncommon for the sheathing type to be specified, the use of un-split sheathing is rare. Consequently, many sheathing suppliers do not stock un-split sheathing in their inventory.

In designing the experimental program, the main goal was to test sheathing products that are widely used in industry. To accomplish this goal, extensive outreach to prestressing plants and concrete accessory producers and retailers was conducted. No discussion about debonding material is provided in the Precast/Prestressed Concrete Institute (PCI) Design Handbook (2010), the ACI 318-11 Building Code (2011), or the American Association of State Highway and Transportation Officials (AASHTO) LRFD Bridge Design Specifications (2012a). In the absence of national guidelines governing the composition of debond sheathing, provisions required for use on FDOT projects have become the defacto standards. FDOT currently requires that debond sheathing be composed of high density plastic with a minimum wall thickness of 0.025 in. (FDOT, 2014). As previously mentioned, they require un-split sheathing for use on their projects with an inside diameter exceeding the outside diameter of the strand by 0.025–0.14 in. While the use of un-split sheathing is rare, the FDOT wall thickness has become fairly standard throughout the industry.

Samples of seven commonly used split sheathing products were procured and examined. The various products varied mainly in their length of overlap at the location of the split. All sheathing products had a wall thickness of 0.025 in. and were designed for use on 1/2 in. seven wire strand. From the sample products, three were selected for testing. These products were selected to represent the bounds of the samples examined. Two samples of un-split sheathing were obtained and found to be nearly identical. One of these products was selected for testing based on availability. The debond sheathing products selected for testing are listed in Table B.1. The split sheathing distributed by DuraJoint Concrete Accessories, Inc. was selected to provide a direct comparison to the un-split sheathing of the same composition also being tested. The Fister, Inc. and Prestressed Supply, Inc. (PSI) split sheathing products were selected for having the largest and smallest amount of overlap of the sample products respectively. Included along with the commercially available debonding products was 1/2 in.,

TABLE B.1
Debonding Agents

Supplier	Sheathing Type	Overlap at Split (in.)
DuraJoint Concrete Accessories, Inc.	Split	3/8
Fister, Inc.		13/16
Prestressed Supply, Inc.		3/16
DuraJoint Concrete Accessories, Inc.	Un-Split	—
1/2" PVC Pipe		—

Schedule 40 PVC pipe. The PVC pipe was included for several reasons. First, its inside diameter of 0.721 in. is sufficiently large that wedging of the strand would not be anticipated. Second, the wall thickness of 0.119 in. should prevent damage, crimping or other defects during concrete placement. Finally, this product could be considered a best-case scenario.

B.2.4 Specimen and Debond Length

The specimen length was controlled by two main factors, the desired length of debonding and the transfer length for the strand to develop the full prestress force. The length of each member would have to be long enough to encompass the debond length on each end, the transfer length on each end, and a region in the center of the specimen with the full prestress force. The transfer length was taken as 60 times the strand diameter, d_b , as provided in the AASHTO LRFD Bridge Design Specifications, 6th Edition Section 5.11.4.1. Consequently, a transfer length of 2.5 ft for each side of the prism was needed.

Selection of the length of debond was primarily controlled by practical considerations of keeping the specimens economical and manageable. Two different debond lengths of 2 ft and 4 ft were selected to allow for comparison of the effectiveness of the products over two different lengths. Providing a 1 ft fully bonded region resulted in overall specimen lengths of 10 ft and 14 ft, respectively, as shown in Figure B.2. Debonding at both ends of each specimen, allowed for each specimen to demonstrate any difference in behavior between the end of the specimen where the strand is released (cut end) and the other end (dead end). In addition, duplicate specimens for each product and debond length were constructed. Fully bonded specimens of 10 ft and 14 ft were also produced to provide comparisons to the debonded specimens.

B.2.5 Sheathing Installation

Most debond sheathing suppliers suggest that flexible adhesive tape be used to seal the termination of the sheathing to prevent paste infiltration. While this procedure is suggested for both split

and un-split sheathing, it is likely more critical for un-split sheathing which may have a large annulus space between the strand and sheathing. Observations at several prestressing plants indicate that this practice is not commonly conducted in the industry. However, in the interest of evaluating the products under their recommended use, the termination of the debonding products in this experiment were sealed with duct tape. A typical termination in the interior of one of the specimens is shown in Figure B.3.

B.2.6 Test Specimens

A summary of the test specimens is provided in Table B.2, which provides the debonding manufacturer and debonding length of each specimen. The specimen IDs are composed of three hyphenated parts. The first letter indicates the debonding manufacturer, the second letter indicates split or un-split sheathing, and the number indicates the length of debond. In the case of the bonded specimens the specimen IDs are of the form B-X-Y where B stands for fully bonded, X is a number indicating the length of debonding, and Y is a number which indicates the cast number. It was decided to construct one fully bonded specimen in each concrete cast to provide a direct comparison between that specimen and the debonded specimens of the same cast. All debonding products were taped at their termination except for the specimen D-S-4T where T indicates un-taped debond sheathing.

B.3 MATERIALS

B.3.1 Concrete

The concrete mix design was selected primarily based on the desired release strength. As previously mentioned, the calculated compressive stress induced in the concrete at release was 1.94 ksi. Due the induced compressive stress, a concrete strength of 4 ksi at the time of release was desired. Additionally, in keeping with the fast paced nature of the prestressed industry, it was desired to transfer the prestress force within 48–72 hours from casting. The

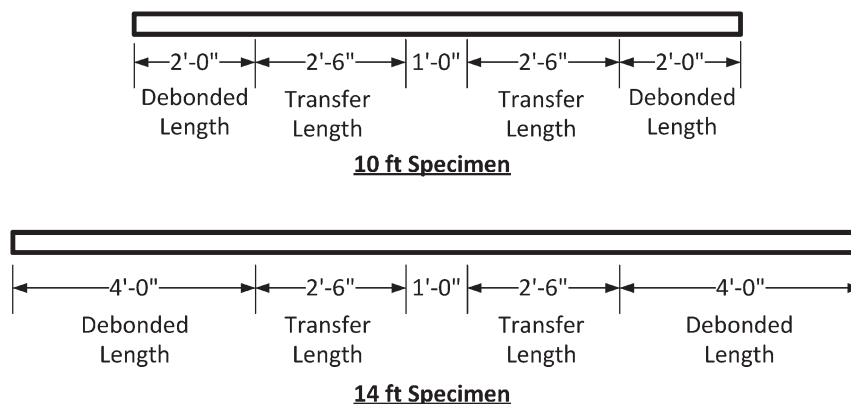


Figure B.2 Prestressed specimen layout.



Figure B.3 Sheathing termination detail.

mix was selected based on strength growth curves generated during previous unrelated research.

The concrete was ordered from Irving Materials, Inc. (IMI), a ready-mix concrete supplier located approximately 1.5 miles from the Bowen Laboratory. The selected mix was a seven bag mix with a full range water reducing admixture as shown in Table B.3. The specimens were cast in three separate casts which required less than one cubic yard each. To ensure a quality well blended mix, two cubic yards were ordered for each cast. A slump of 5 in. was requested for each of the casts and was measured upon arrival at the laboratory. The slump for each cast was 5 in. \pm 0.25 in. and no water was added to the trucks onsite. The batch weights for the three casts are included in Table B.4.

The compressive strength of the each concrete cast was monitored by testing three standard 6 \times 12 in. cylinders at regular intervals up to 28 days. Compressive tests were also performed prior to prestress transfer to ensure sufficient strength at the time of release. The cylinders were tested in accordance with ASTM C39 (2012). A loading rate of 60,000 lb per minute was used during the compressive cylinder tests along with 70 durometer elastomeric pads. A total of 15 cylinders were cast during each cast and were cured in the same manner as the test specimens. After the concrete surface hardened, the specimens and cylinders were covered with wet burlap and plastic sheathing to prevent moisture

loss. The curing of the cylinders was discontinued at the same time that curing of the specimens was discontinued. Additionally, the cylinders molds were removed when the side forms of the specimens were removed. The compressive strength growth curves for each cast are shown in Figure B.4, and a summary of the results is provided in Table B.5.

B.3.2 Prestressing Steel

The prestressing strand used in the laboratory specimens was obtained from Prestressed Services Industries, LLC (PSI), Decatur, Indiana. The prestressing steel strand was Grade 270, uncoated, seven-wire, low relaxation strand with a 1/2 in. nominal diameter. The nominal cross-sectional area of the strand was 0.153 in².

Samples of the prestressing strand used in the laboratory specimens were tested to failure in a universal testing machine. Testing was performed in accordance with ASTM A370 (2012). Gripping of the strands was accomplished using prestressing chucks for 1/2 in. strand. Standard aluminum foil was used in the grips as described previously in Section 2.4.3.

Four specimens, each with a test length of approximately 2 ft were tested. A summary of the test results is provided in Table B.6. The average tensile strength of the strand was 282.4 ksi exceeding the nominal strength of 270 ksi. All strands tested failed due to rupture of an individual wire near the gripping location as shown in Figure B.5.

B.4 SPECIMEN CONSTRUCTION

B.4.1 Production

The prestressed specimens were constructed in the Bowen Laboratory in three separate concrete casts. This was necessitated by limits on the length of the casting bed as well as the overall length of the specimens to be cast. A total of 27 specimens were

TABLE B.2
Test Specimen Layout

Specimen ID	Manufacturer	Split/Un-Split	Debond Length (ft)	Specimen Length (ft)
P-S-2	Prestressed Services, Inc.	Split	2	10
P-S-4			4	14
F-S-2	Fister, Inc.	Split	2	10
F-S-4			4	14
D-S-2	DuraJoint, Inc.	Split	2	10
D-S-4			4	14
D-S-4T			4	14
D-U-2			Un-Split	2
D-U-4	4	14		
V-U-2	PVC Pipe	Un-Split	2	10
V-U-4			4	14
B-2	Fully Bonded	—	2	10
B-4			4	14

TABLE B.3
Concrete Mix Design Weights per Cubic Yard

Material	Design Weights Per Yard
Cement (lbs)	658
Coarse Aggregate (lbs)	1850
Fine Aggregate (lbs)	1360
Water (lbs)	240
BASF Glenium 3030 NS Full Range Water Reducer (oz)	10

TABLE B.4
Concrete Mix Batch Weights per Cubic Yard

Material	Cast 1	Cast 2	Cast 3
Cement (lbs)	657.5	660	657.5
Coarse Aggregate (lbs)	1830	1870	1830
Fine Aggregate (lbs)	1410	1400	1410
Water (lbs)	185	169	192
BASF Glenium 3030 NS Full Range Water Reducer (oz)	13	12.5	12.5

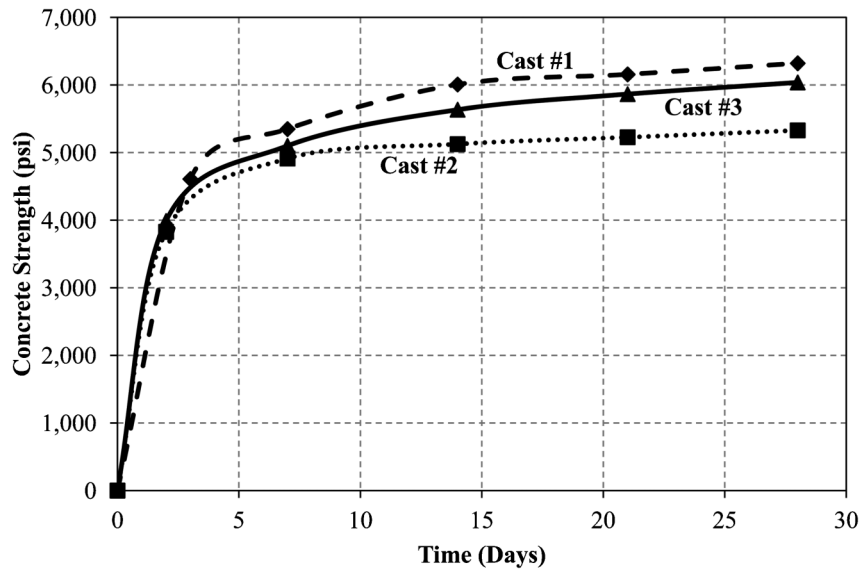


Figure B.4 Concrete strength growth curves.

TABLE B.5
Concrete Compressive Strength Data

Cast	Debonding Types	Specimen ID	Slump (in.)	Age (Days)	f_c (psi)
1	PSI Split Sheathing Fister Split Sheathing	P-S-2	5	3	4,609
		P-S-4		7	5,348
		F-S-2		14	6,007
		F-S-4		21	6,157
		B-4-1		28	6,321
2	DuraJoint Split Sheathing Fully Bonded	D-S-2	5	2	3,828
		D-S-4		7	4,912
		D-S-4T		14	5,126
		B-2-2		21	5,227
		B-4-2		28	5,329
3	DuraJoint Un-Split Sheathing 1/2" PVC Pipe	D-U-2	5.25	2	3,988
		D-U-4		7	5,100
		V-U-2		14	5,635
		V-U-4		21	5,865
		B-2-3		28	6,038

TABLE B.6
Prestressing Strand Tensile Strength

Test No.	Failure Distance From Grip (in.)	Peak Load (lb)	Max Stress (ksi)
1	2	43,395	283.6
2	3	43,045	281.3
3	2	43,114	281.8
4	1.5	43,297	283.0
Average:		43,213	282.4

produced in the laboratory with a total specimen length of 326 ft. The prestressing bed was 40 ft in length but allowed for three sets of forms during each cast.

B.4.2 Prestressing Bed

The prestressing abutments used for this project were designed for use with the Bowen Laboratory strong floor. The abutments, as shown in Figure B.6, were designed to resist the pretensioning force applied to the prestressing strand and transfer the force through horizontal friction to the strong floor. A coefficient of friction of 0.4 was assumed to act between the steel abutment and the smooth finished concrete floor. A normal force was applied at the interface of the floor and abutment through the use of six Grade 150, 1-3/4 in. diameter threaded Dywidag bars. Each bar was stressed to 200 kips for a total of 1,200 kips. The vertical plates of the abutments have holes drilled on a 2 in. grid spacing to make them versatile for different prestressing configurations. The lower plate is 3 in. in thickness with the upper plate being 1.5 in. thick. The prestressing chucks bear on the vertical plate to maintain the prestress force.

B.4.3 Formwork

The formwork for the specimens was constructed from plywood and dimensional lumber. Base forms were constructed from 2x4s and plywood to isolate the concrete from the laboratory floor as well as to provide a uniform surface. Side forms for the specimens were also constructed from plywood and 2x4s and were secured to the base forms. Three sets of forms were constructed so that multiple lines of specimens could be produced in parallel during each cast. The three sets of forms were configured as shown in Figure B.7, with two sets of forms directly on the base forms and the final set of forms elevated. This formwork configuration was designed to take advantage of the prestressing abutments at the Bowen Laboratory. The side forms were installed after the prestressing strands were in place to ensure that the forms were centered around the prestressing strands. The side forms extended the full 40 ft length of the prestressed bed and were divided by end pieces to achieve the desired specimen lengths as shown in Figure B.8.

B.4.4 Pretensioning

Jacking of the prestressing strands was completed in two phases. Initially, the prestressing strands were jacked to a load of 8-9 kips.



Figure B.5 Prestressing strand tensile test specimens.

The initial prestressing was necessary to keep the strand taught and straight so that the side forms could be installed around them. A wooden spacer with a groove cut in it to accommodate the prestressing strand was used to align the forms to maintain the 2 in. of cover on each side of the strand. The final stressing took the strands to their jacking force of 32.8 kips. Final stressing was performed the morning of each cast. During stressing operations, all personnel were cleared from the laboratory floor, and the jacking crew was sheltered behind a masonry wall.

The jacking of the strand was performed with the assembly shown in Figure B.9, which consisted of two prestressing chucks, a load cell, hydraulic ram, and steel plates. In order from the face of the abutment, the system was assembled as follows. The first prestressing chuck was placed against the abutment to grip the strand and remain in place after jacking. A plate was placed after the chuck to distribute the load evenly, followed by the load cell, hydraulic ram and another plate. Finally, the second prestressing chuck gripped the strand so that it could be pulled. The load cell was connected to a data collection system, and the load was monitored in real-time during stressing operations. The hydraulic ram was connected to a hand operated hydraulic jack. After the jacking force of 32.8 kips was developed for each strand, the hydraulic ram was slowly released to gradually transfer the load to the prestressing chuck adjacent to the abutment face. The strands were also marked prior to stressing so that the approximate elongation could be measured afterward to check that proper seating of the chuck had occurred.

B.4.5 Specimen Casting

The debonding specimens were constructed in three distinct casts. Upon arrival of the concrete truck, a small sample was taken to perform a concrete slump test to ensure proper workability of the mix. Once the mix was approved, the forms were filled manually with shovels from a series of wheelbarrows as shown in Figure B.10. The forms were filled with shovels due to their small size which made the use of a chute difficult.



Figure B.6 Prestressing abutment.

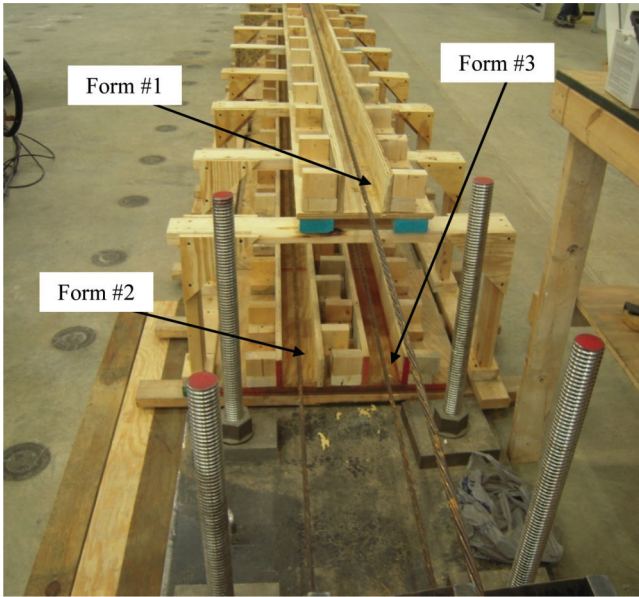


Figure B.7 Formwork.

Additionally, the overall volume of concrete to be placed was small making manual placement practical. Mechanical concrete vibrators were used to consolidate the concrete with care taken not to damage the debonding products with prolonged exposure to the vibrator. Once the concrete had been placed, the top surface was screeded to remove excess concrete. The surface was then smoothed with a magnesium hand float.

The specimens were wet cured for a total of two days. Wet curing was accomplished through the use of saturated burlap which was placed over the specimens and covered with plastics tarps to reduce evaporation. The burlap was removed after approximately 16 hours to facilitate removal of the formwork and installation of mechanical strain gage locating disks. As soon as work on the specimens was complete, the burlap and tarps were placed back over the specimens until prestress transfer. The small size of the specimens made it possible to easily cover all the exposed sides with burlap after form removal.

Standard 6 × 12 in. concrete cylinders were cast simultaneously with the specimens. Consolidation of the cylinders was performed using mechanical concrete vibrators in accordance with ASTM C192 (2013). The procedure for curing of the cylinders was the same as that used for the specimens. The cylinder molds were removed two days after casting to coincide with the end of the wet curing process.

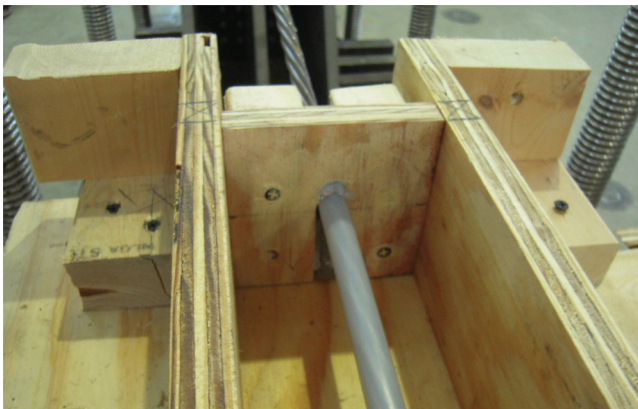


Figure B.8 End forms.

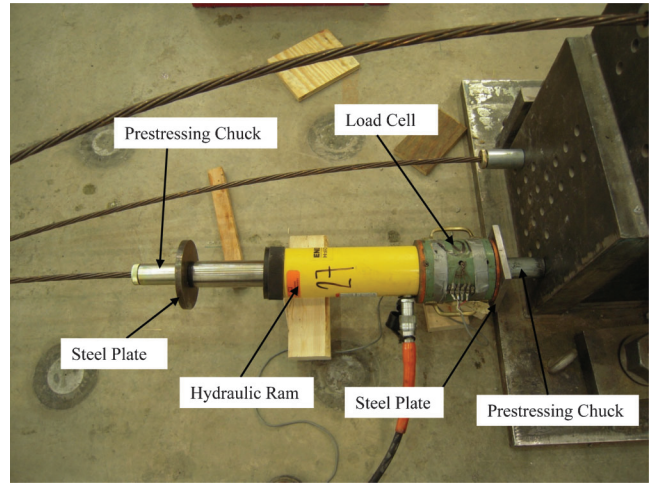


Figure B.9 Prestress jacking apparatus.

B.4.6 Strand Release

The prestressing strands were released on the third day after casting for the first cast and on the second day for the remaining two casts. There were two main factors governing the timing of strand release, concrete strength and instrumentation. In the case of the first cast, delays in the instrumentation process dictated release on day three rather than day two.

The prestressing strands were released by torching them between the end of the specimens and the abutment. A slow release procedure was used to gradually transfer the prestressed force to the specimens. Each strand was gradually heated over approximately a 1 ft length to allow the individual wires of the seven-wire strand to break separately. The use of this method generally resulted in the wires breaking in pairs with the last three wires generally breaking simultaneously. The failure of the last wires caused the specimens to slide away from the release location because of the small specimen size and use of only one prestressing strand. The process of strand release is shown in Figure B.11. Once all three strands had been released gradually on one end of the prestressing bed, an oxy-acetylene torch was used to cut the strand on the other end of the bed. An angle grinder was used to cut the strand between each of the individual specimens. The angle grinder was used to reduce the risk of igniting the wooden formwork and to minimize heat effects on the strand.



Figure B.10 Specimen casting.



Figure B.11 Prestressing strand release.

B.5 TEST SETUP AND PROCEDURE

B.5.1 Instrumentation

To assess the effectiveness of the various debonding products to be tested, strain profiles along the length of the specimens were needed. The DEMEC Mechanical Strain Gage system manufactured by Mayes Instruments Limited located in Berkshire, England was selected. The system consists of a series of DEMEC locating disks which are installed on the specimen surface as well as the DEMEC gage which measures the relative distance between adjacent locating disks. Collecting distance measurements between the locating disks before and after prestress transfer allows for determination of average concrete strains induced by prestressing over the gage length.

B.5.1.1 DEMEC Locating Disks

The DEMEC locating disks are 6.3 mm in diameter, composed of stainless steel, and are machined with a small conical hole drilled in the disk center. The machined hole is designed to mate with the conical locating points found on the DEMEC gages. The locating disks were installed on one side of each specimen at mid-height. This corresponded with the approximate level of the prestressing strand. The disks were laid out with a 50 mm center-to-center spacing along the length of each specimen. Use of a DEMEC layout bar composed of invar, a metal alloy used for its low coefficient of thermal expansion, aided in laying out the disks. The layout bar consists of an invar beam with two conical locating points, which ensures appropriate placement of the disks. Use of the layout bar is shown in Figure B.12.

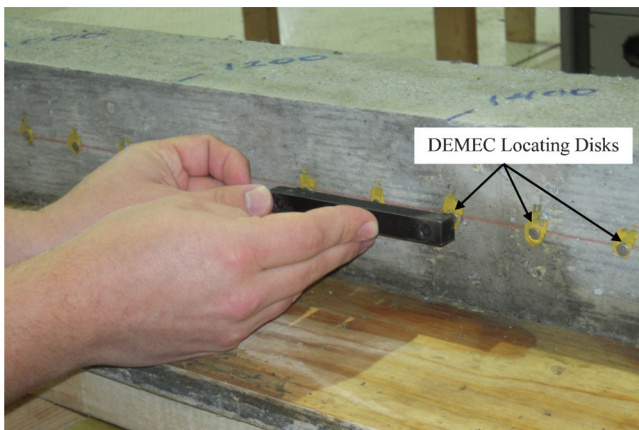


Figure B.12 Use of DEMEC layout bar.

The disks were attached to the surface of the specimens with a two part epoxy from the BondAway series produced by Fielco Adhesives. The BondAway 2011A/2012B system was selected for its pot life, viscosity, and signature bond removal capacity. Once cured, the BondAway epoxy will debond with the surfaces to which it is affixed if subjected to boiling water for approximately 1 min. The epoxy does not dissolve, but rather loses all adhesion with foreign surfaces while maintaining its shape and continuity. This product was selected for use in this project to aid in the recovery of the DEMEC locating disks. After testing of each specimen was complete, the disks and epoxy were chipped off the concrete surface and subjected to a boiling water bath. Easy removal of the epoxy eliminated the painstaking process of grinding epoxy off the locating disks after testing.

B.5.1.2 DEMEC Mechanical Strain Gage

The 100 mm digital version of the DEMEC Demountable Mechanical Strain Gage was used for this investigation and was selected because it is the smallest gage currently available. The DEMEC gage as shown in Figure B.13 consists of one fixed and one pivoting locating point mounted to an invar beam. The dial is a Mitutoyo 543 digital indicator with an accuracy of $\pm 5 \times 10^{-6}$ in. The gage is used by placing the pivoting point in one locating disk and then placing the fixed point in the second disk. Care must be taken to keep the points well seated within the locating disks without producing lateral thrust within the device. Additionally, the gage must be approximately parallel to the plane on which the disks are located to produce an accurate reading.

Changes in the distance between the locating disks are transmitted to the digital indicator through a pivot. This pivot lever has a nominal ratio of 0.81:0. Therefore, a change in distance of 0.8 will be measured as 1.0 by the pivot mechanism. As a result, all measurements must first be reduced by 20% before calculating the strain values. The average strain between any two locating points is simply the extension of the gage corrected for the pivot lever divided by the gage length (100 mm).

B.5.2 Procedure

After casting each set of specimens, the DEMEC locating disks were installed as described previously. After installation of the locating disks, the epoxy was allowed to cure overnight to prevent movement of the disks during measurements. The distance between each set of locating disks was recorded prior to strand release, immediately following strand release, and 14 and 28 days after strand release. The difference in the pre and post release measurements allowed for the construction of concrete strain profiles along the length of each specimen.

The strain gage measurements were all taken by the same operator throughout the duration of the laboratory investigation. Mechanical strain gage measurements can be sensitive to the

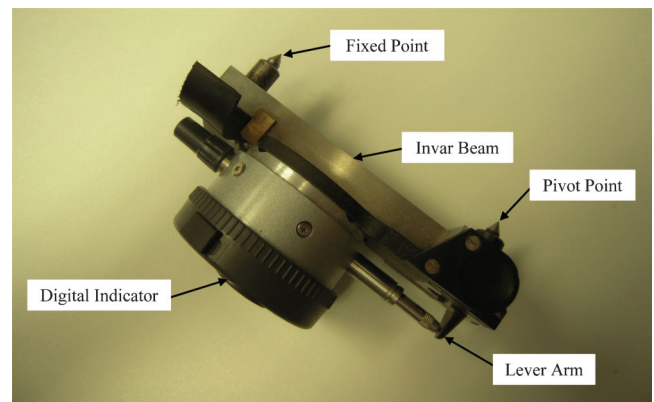


Figure B.13 DEMEC mechanical strain gage.

operator, and maintaining a consistent operator was intended to eliminate any errors due to this sensitivity. Readings were taken only when the gage reading was stable. Instability in the display measurement is typically an indication of improper seating of the points within the locating disks. At regular intervals, duplicate measurements were taken between points to confirm the repeatability of the measurements.

As previously mentioned, the locating disks were installed at 50 mm on center along the length of each specimen, while a 100 mm mechanical strain gage was used. As a result, each measurement was made not between consecutive disks but between alternate disks (disk (i) and a disk (i+2)) as shown in Figure B.14. In this way, the distance between two consecutive points was included in two measurements. The strain between any two consecutive points was taken as the average of the strain calculated for the two intervals to which it belonged.

The strain for each measurement was determined using the pre-release distance measurement as well as the appropriate post-release measurement using the procedure presented as Equation B.1. The strain between any two consecutive locating disks was then taken as the average of the strain for the two measurements.

$$\epsilon_n = \frac{d_t - d_0}{l_g + d_0} \quad (\text{B.1})$$

where:

- ϵ_n : concrete strain over measurement n, mm/mm
- d_t : gage extension at time, t, corrected for lever action, mm
- d_0 : gage extension prior to transfer corrected for lever action, mm
- l_g : gage length of the device (100 mm)

B.6 RESULTS

During each cast, two debonding conditions were tested. A total of four specimens were constructed for each debonding product, two 10 ft specimens and two 14 ft specimens. This accounts for eight specimens per cast. The size of the casting bed and formwork, however, allowed for the production of nine specimens per cast. Therefore, during the first and third casts, an additional fully bonded specimen was produced, and during the second cast a specimen was produced using DuraJoint Split sheathing that was un-taped. The inclusion of the extra fully bonded specimens allowed for direct comparison with the debonded specimens from each cast. As previously mentioned, most precast yards do not tape the ends of the debond sheathing to prevent concrete paste infiltration. The additional debonded specimen allowed for comparison with the taped specimens. A summary of the test specimens produced is provided in Table B.7. The strain profiles for the specimens are presented in Figure B.15 through Figure B.29. Comparison of the replicate specimens reveals that strains within the debonded regions tend to agree closely while the strain profiles within the strain plateaus tend to have greater variability.

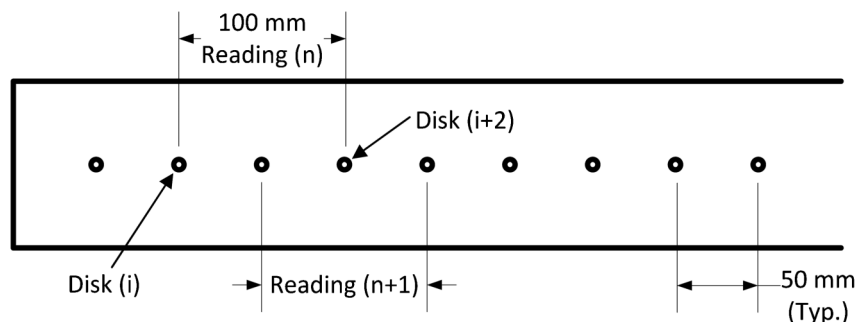


Figure B.14 DEMEC measurements.

B.7 ANALYSIS

There are several methods which may be used to evaluate the effectiveness of the various debonding agents. The simplest method of evaluation is visual inspection of the strain profiles at release, and at 14 and 28 days. In the case of a 100% effective debonding product, the strain profile within the debonded region should remain close to zero. In the case of an ineffective debonding product, the strain profile would have an upward trend over the debonded region. An alternate method of evaluation is comparison of the transfer lengths for the various specimens. Using the Average Maximum Strain (AMS) method as defined by Barnes, Burns, and Kreger (1999), it is possible to define the region over which the full prestress force acts. The region of prestress transfer is then bounded by the debonded and fully bonded regions. Comparison of the transfer lengths for the different debonding products also allows for comparison of relative effectiveness.

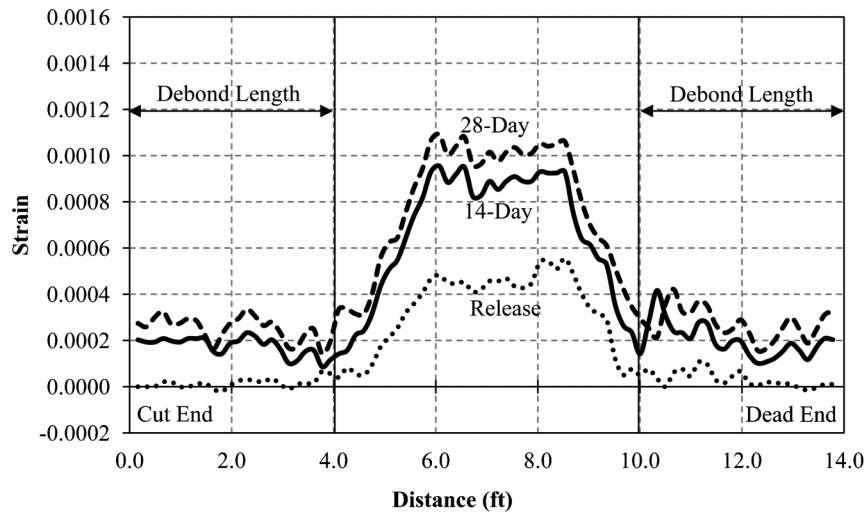
The strains were measured along the length of each specimen immediately after release, at 14 days, and at 28 days. The strain profiles clearly show an increase in strain over time. This phenomenon can be attributed to two main causes; shrinkage and creep within the concrete specimens. Inspection of the strain profiles reveals that the debonded regions tend to have a smaller increase in strain over time than the fully bonded regions. In the regions where the full prestress force acts, creep increases the measured strains, while shrinkage acts over the entire specimen length.

B.7.1 Strain Profile Analysis

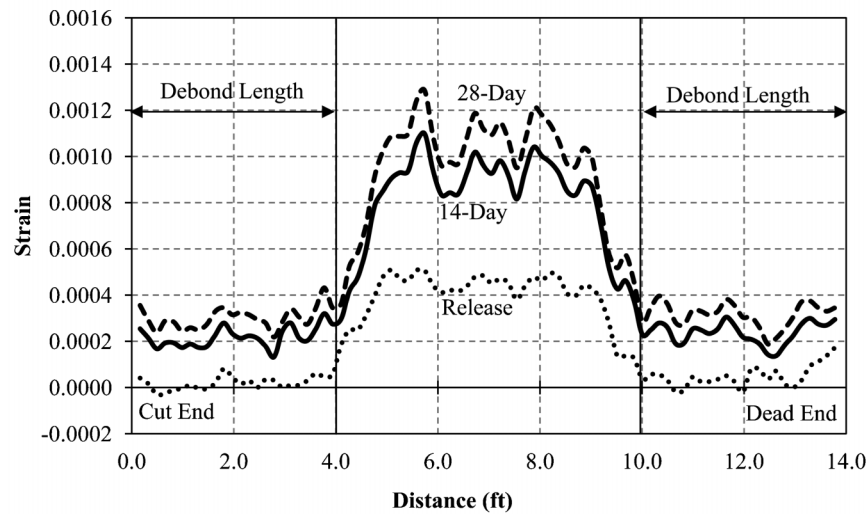
By comparison of the strain profiles presented as Figure B.15 through Figure B.29, the effectiveness of the various debonding products can be assessed. All the products exhibited good performance in the 10 ft specimens. It appears that the 2 ft debond length was not sufficient to develop any significant stress over the debonded region. Therefore, the following analysis will focus on the 14 ft specimens. The majority of the products tested appear to provide effective debonding for the 14 ft specimens. The PSI Split Sheathing (Figure B.15 and Figure B.16), DuraJoint Un-split Sheathing (Figure B.27 and Figure B.28) and PVC pipe (Figure B.25 and Figure B.26) appear to provide very good debonding. Over the debonded region, the strain profiles remain close to zero after release indicating that minimal stress has developed in the concrete. The Fister split sheathing (Figure B.17 and Figure B.18) showed good performance, with a slight increasing trend in strain over the last 4 to 8 in. of the debonding length for some of the specimens. The DuraJoint Split sheathing (Figure B.21 and Figure B.22) exhibited very poor performance in preventing stress development in the 14 ft specimens. The strain profile over the debonded length for these specimens clearly shows an increasing trend. To clearly show the different levels of effectiveness, Figure B.30 to Figure B.33 include the strain distributions for both a PVC pipe and a fully bonded specimen alongside one of the commercially available prestressing products.

TABLE B.7
Specimen Designations

Cast	Specimen ID	Debonding Type	Debonding Length (ft)	Specimen Length (ft)
1	P-S-4	PSI—Split	4	14
	P-S-2	PSI—Split	2	10
	F-S-4	Fister—Split	4	14
	F-S-2	Fister—Split	2	10
	B-4-1	Fully Bonded	—	14
2	B-4-2	Fully Bonded	—	14
	B-2-2	Fully Bonded	—	10
	D-S-4	DuraJoint—Split	4	14
	D-S-2	DuraJoint—Split	2	10
	D-S-4T	DuraJoint—Split—No Tape	4	14
3	V-U-4	PVC Pipe	4	14
	V-U-2	PVC Pipe	2	10
	D-U-4	DuraJoint—Un-Split	4	14
	D-U-2	DuraJoint—Un-Split	2	10
	B-2-3	Fully Bonded	—	10

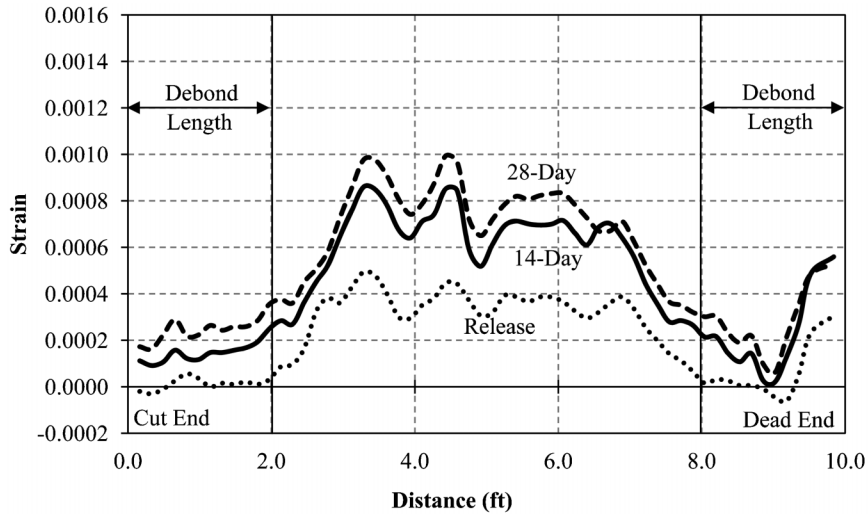


(Specimen A)

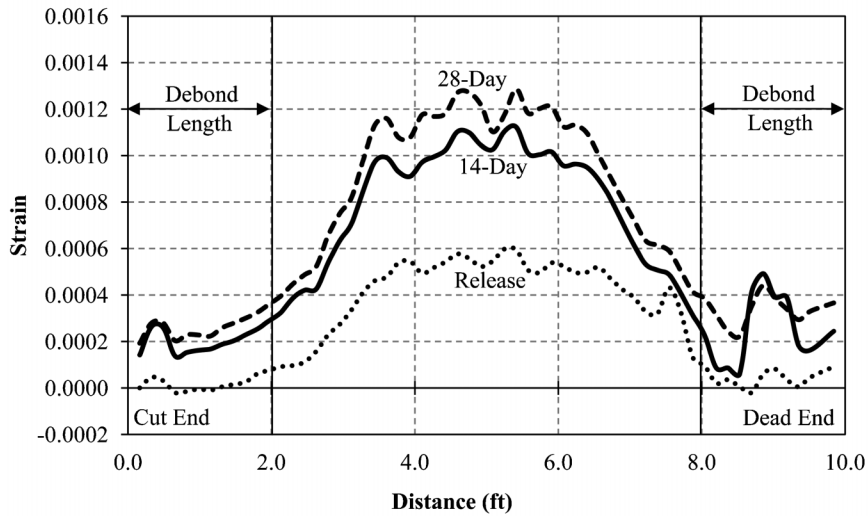


(Specimen B)

Figure B.15 Strain distribution —PSI split sheathing (14 ft).



(Specimen A)



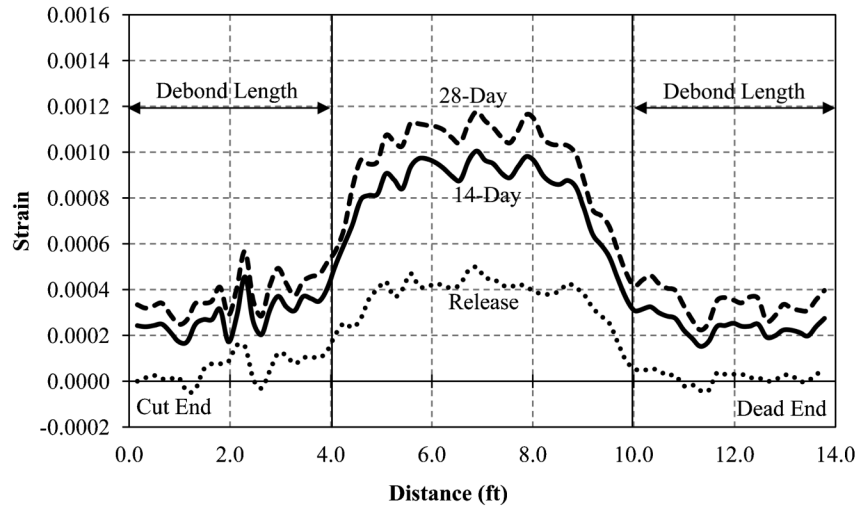
(Specimen B)

Figure B.16 Strain distribution —PSI split sheathing (10 ft).

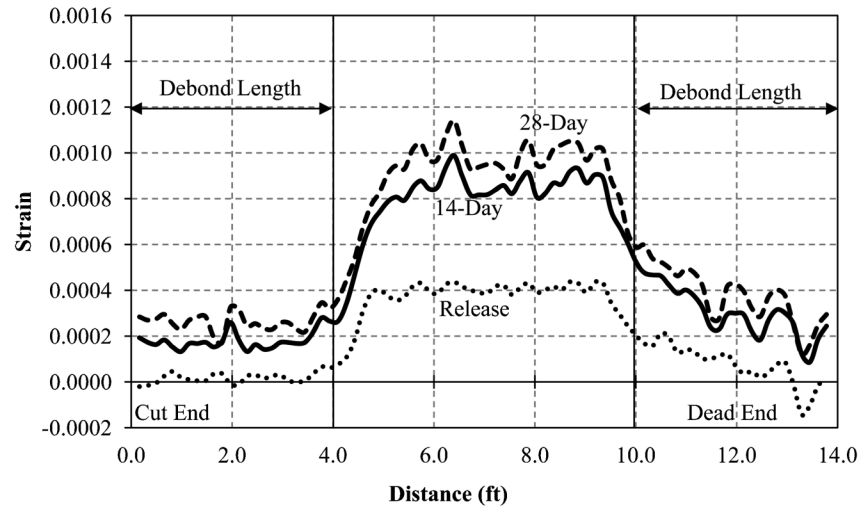
The PVC pipe and fully bonded specimens were designed to represent the two extremes of strand bonding and provide context to the results from the commercially available products. The strain distributions presented in Figure B.30 to Figure B.33 represent one of the replicate 14 ft specimens produced to provide ease in comparison. The PSI Split Sheathing (Figure B.30) provided very effective debonding with the strain distribution remaining close to that of the PVC pipe along the entire specimen length. The Fister Split Sheathing (Figure B.31) appears to provide overall good debonding performance with no clear increasing trend over the debonded region, although there are local areas of high strain within the profile. The DuraJoint Un-Split Sheathing (Figure B.32) provides very effective debonding with the strain profile showing very close agreement with the PVC pipe over the entire specimen length. The DuraJoint Split Sheathing (Figure B.33) has a clear and consistent trend of increasing strain over the intended debonding region which corresponds with transfer of the prestress force. In the case of this product, approximately half of the plateau strain is developed over the debonded region. The strain profile is approximately linear with a positive slope over the debonded region. Therefore, it could be expected that given a longer length of debonding, perhaps as much

as the full prestress force could be developed prior to termination of debonding.

A direct comparison can also be made between the DuraJoint Split Sheathing Specimens which were sealed with duct tape at their termination and the specimen where tape was not used. The two strain distributions for the taped specimens are shown alongside the strain distribution for the un-taped specimen in Figure B.34. Since the tape is placed at the end of the debonded length, it would be expected that any influence on debonding efficiency would be apparent at the end of the debonded length. Close examination of Figure B.34 reveals that for the dead end of the specimens the un-taped strain distribution falls in between the strain distributions for the two taped specimens. On the cut end of the specimens, the un-taped specimen exhibits a higher strain over approximately the last 4 in. of debonding. While the strains on the cut end of the specimens were slightly higher for the un-taped specimen, this is within the typical scatter observed in the series. Therefore, there does not appear to be a large benefit to providing flexible tape at the sheathing termination for this sheathing. It is important to note that this product exhibited poor performance, possibly due to paste infiltration along the slit which may obscure any impact from leaving the terminations un-taped.



(Specimen A)



(Specimen B)

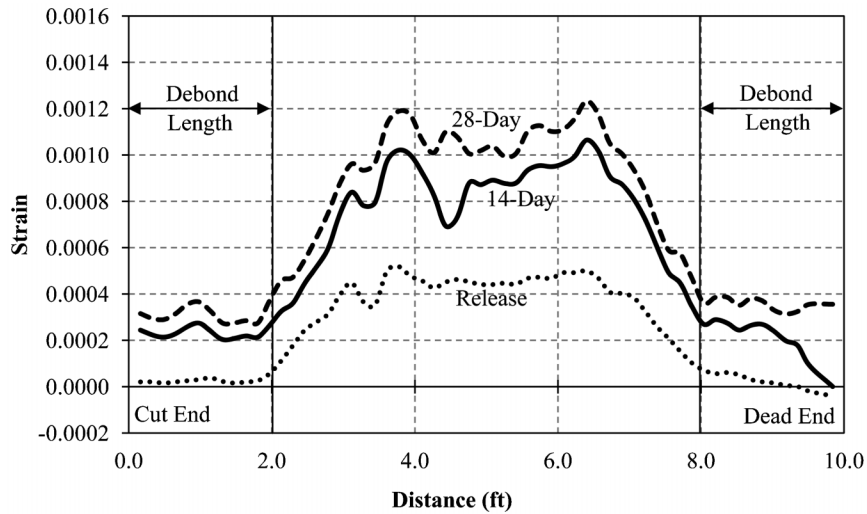
Figure B.17 Strain distribution—Fister split sheathing (14 ft).

B.7.2 Transfer Length Analysis

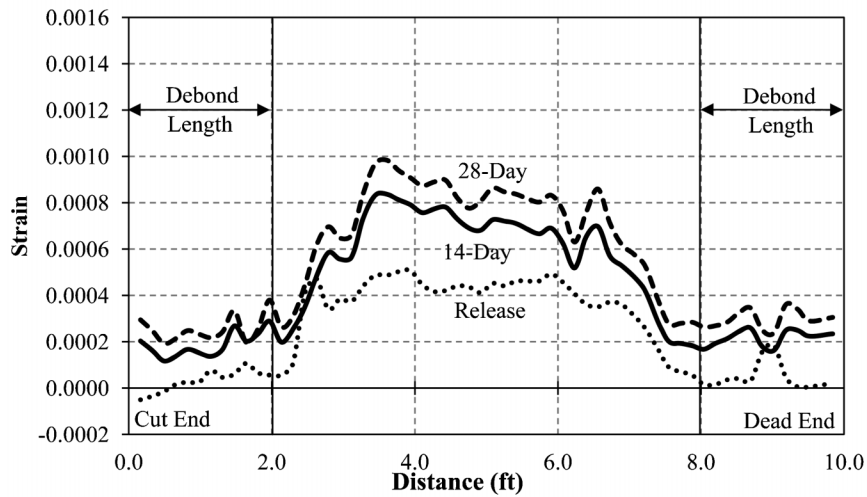
The transfer length for each of the debonded specimens can be determined using the 95% AMS procedure (Barnes, Burns, & Kreger, 1999). First the strain plateau which defines the fully bonded region is identified by visual inspection. The average of the strain measurements within the plateau is taken and reduced by 5%. This value of 95% of the average maximum strain is then compared to the points on the edges of the strain plateau previously selected. The range of the plateau is then adjusted to include points equal to or exceeding the 95% AMS value and excluding those below. Once the plateau has been redefined, the 95% AMS is recalculated to reflect the new boundaries, and the plateau is readjusted as needed. The transfer length was then taken as the distance between the end of debonding and the beginning of the fully bonded region as defined by the 95% AMS procedure. Figure B.35 provides an example of the 95% AMS method applied to a fully bond strain distribution. The transfer lengths computed with this method are shown in Table B.8. The strain distribution was measured using a 50 mm disk spacing. As a result, the transfer lengths reported in Table B.8 were determined to the nearest 50 mm (1.96 in.). Also note that the values

presented in Table B.8 are based on the average of the two replicate specimens made for each condition. It should also be noted that the transfer lengths for duplicate specimens were very consistent.

Analysis of the transfer lengths shows that, in general, the transfer length for each specimen did not vary significantly over the duration of the testing period. It is noteworthy that there is great variability in the measured transfer lengths for the different specimens. Additionally, there was generally a large difference between the transfer length on the cut and dead ends of the specimen. The transfer lengths on the cut end of the specimen were generally shorter than that for the dead end. The calculated transfer length of 60 times the strand diameter from Section 5.11.4.1 of the AASHTO LRFD Bridge Design Specifications, 6th Edition yields a predicted transfer length of 30 in. This value provides an upper bound to the measured data which exhibited a maximum transfer length of 27.5 in. In general, transfer lengths were much less than the calculated value. It is also noteworthy that the transfer lengths for the effective debonded products were similar to the transfer lengths for the fully bonded specimens from the same concrete pour. Therefore, no increase in transfer length was caused by debonding of the strand.



(Specimen A)



(Specimen B)

Figure B.18 Strain distribution—Fister split sheathing (10 ft).

Comparing the measured transfer lengths of the 14 ft specimens for the DuraJoint Split Sheathing (Specimens D-S-4) to the fully bonded specimens from the same concrete cast (Specimens B-4-2) confirms the earlier observation. The average transfer length on the cut end for the 14 ft fully bonded specimens from Cast #2 was 23.62 in. while the average transfer length for the DuraJoint Split Sheathing was only 9.84 in. This reduction in length shows that the prestressing force was partially developed over the debonded region leading to a shortened apparent transfer length. Analysis of the comparable data for the 10 ft members does not show a reduction in the transfer length from the debonded specimen. It appears that the 2 ft length of debonding was not sufficient to develop adequate friction to transfer the prestressing force. As the length of debonding is increased, the effectiveness of the debonding appears to decrease. Additionally, comparison can be made between the taped and un-taped specimens as was previously made visually. The un-taped specimen has a slightly smaller transfer length of 7.87 in. as compared to 9.84 in. on the cut end for the taped specimens. Note that due to the 50 mm (1.96 in.) spacing of the locating disks, this difference in transfer length is only one disk spacing increment.

It is also possible to calculate the average bond rate over the transfer length for the fully bonded specimens. Inspection of the fully bonded strain distributions (Figure B.19, Figure B.23, Figure B.24, and Figure B.29) indicates that the strain in the concrete increases linearly over the transfer length. Therefore, it is appropriate to use an average bond rate over the debonded region. The average bond rate can be calculated by dividing the prestress force at transfer (31.0 kips) by the transfer length. The average bond rate for the 14 ft specimens constructed in Cast #2 is 1.31 kips per in. Inspection of Figure B.30 shows that the slope of the strain distribution for the DuraJoint split sheathing between the debonding termination and strain plateau is approximately the same as the slope for the fully bonded specimen. Therefore, the average bond rate (1.31 kips per in.) and the effective cut end transfer length for the 14 ft DuraJoint split sheathing specimen (9.84 in.) can be used to determine the level of force in the prestressing strand at the debonding termination (18.1 kips). Based on a 48 in. length of debond, it is then possible to calculate the average bond rate for strand debonded with DuraJoint split sheathing which is 0.38 kips per in. Assuming that this average bond rate can be extended to

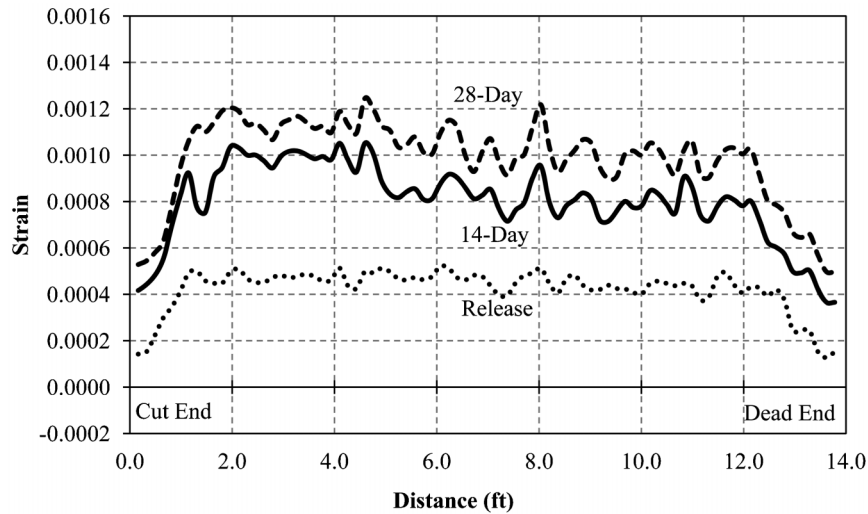


Figure B.19 Strain distribution—fully bonded specimen, Cast #1 (14 ft).

longer lengths of debond, strand debonded with DuraJoint split sheathing would achieve the full prestress force over a debond length of 6.8 ft.

B.8 Conclusions

The results of the laboratory evaluation have shown that the type of debonding product used can have a significant impact on the effectiveness of strand debonding. While some of the split sheathing types tested showed acceptable performance, the best way to ensure effective debonding is to use un-split sheathing. When split sheathing is used, the amount of overlap the sheathing provides does not appear to be an important parameter given that sheathing with more and less overlap than the DuraJoint Split Sheathing performed much better. It appears that tight fitting split sheathing products perform better than looser fitting products. This may be due to paste infiltration through the slit in loose fitting split sheathing products. Comparison of the results of the taped and un-taped specimens for

DuraJoint Split Sheathing indicate no benefit from providing tape at the termination. However, this type of sheathing performed poorly in all the specimens, likely due to paste infiltration from the split. Therefore, any impact from potential paste infiltration from the end of the sheathing may be overshadowed by the paste infiltration from the split in this product.

B.9 Recommendations

When effective strand debonding is important to the performance of a prestressed element, the best way to ensure proper performance is to specify and use un-split sheathing. In testing, the commercially available un-split sheathing performed as well as the over-sized PVC pipe. If it is costly or impractical to use un-split sheathing, then tight fitting split sheathing will provide the best performance. It is recommended that flexible adhesive tape be used on the terminations of sheathing products to prevent possible paste infiltration.

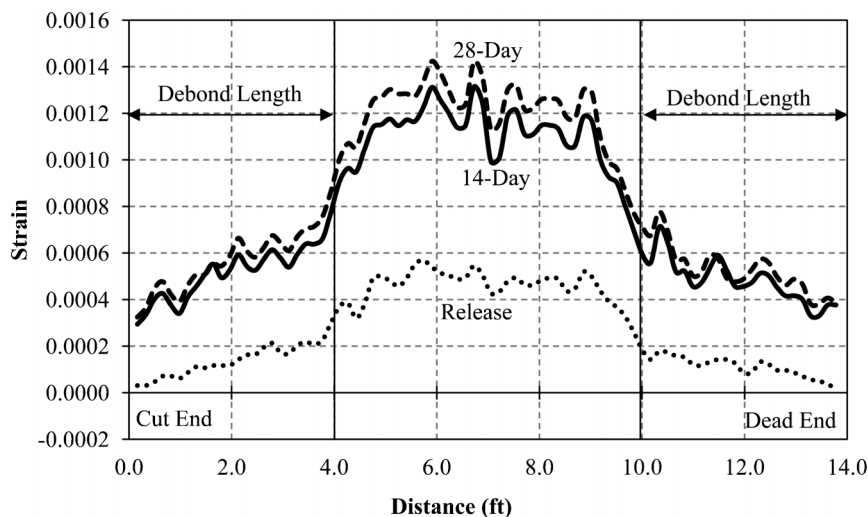
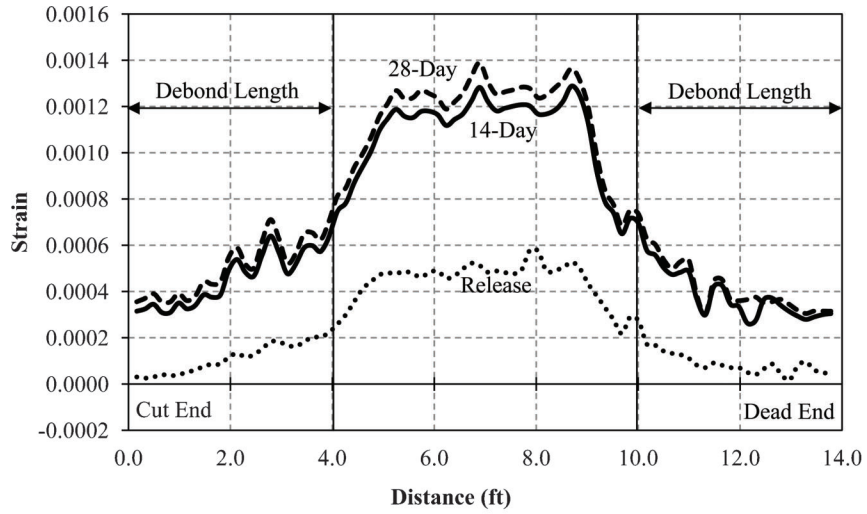
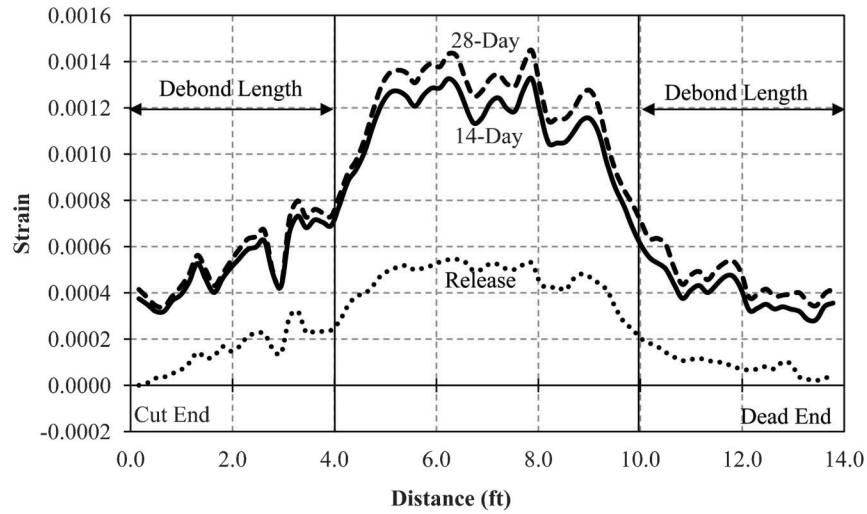


Figure B.20 Strain distribution—DuraJoint split sheathing un-taped (14 ft).

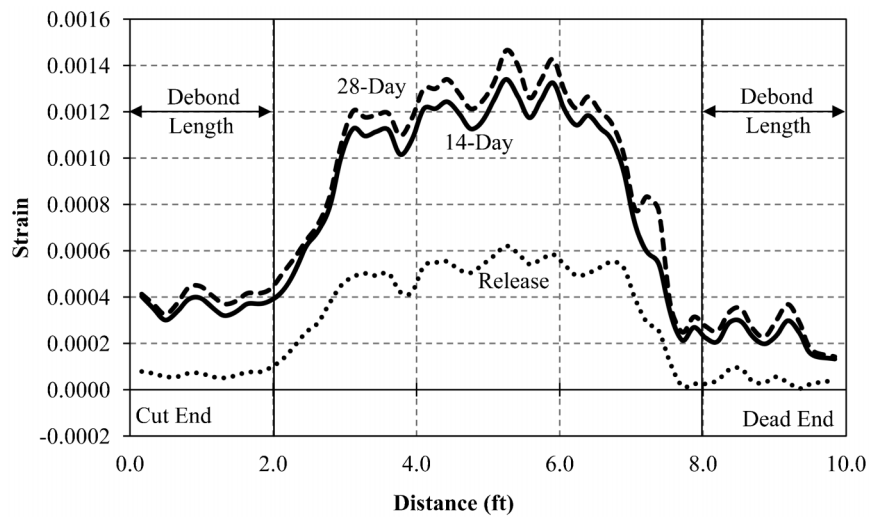


(Specimen A)

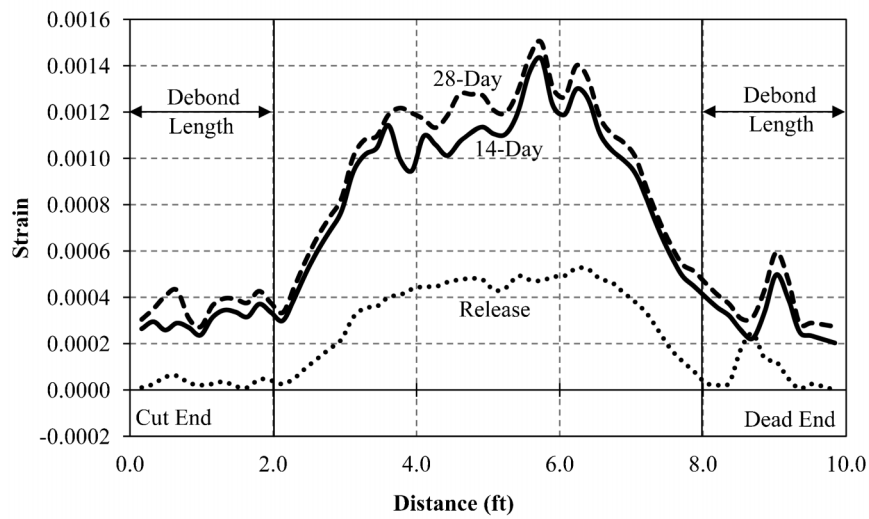


(Specimen B)

Figure B.21 Strain distribution—DuraJoint split sheathing (14 ft).

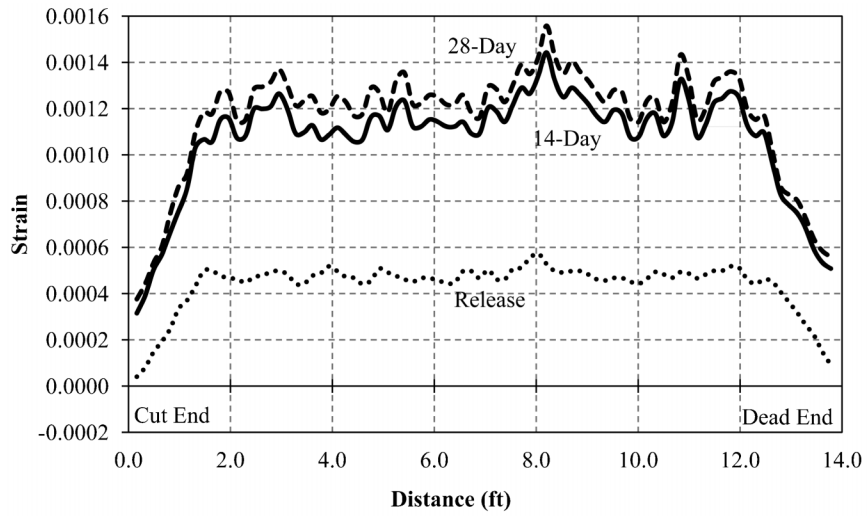


(Specimen A)

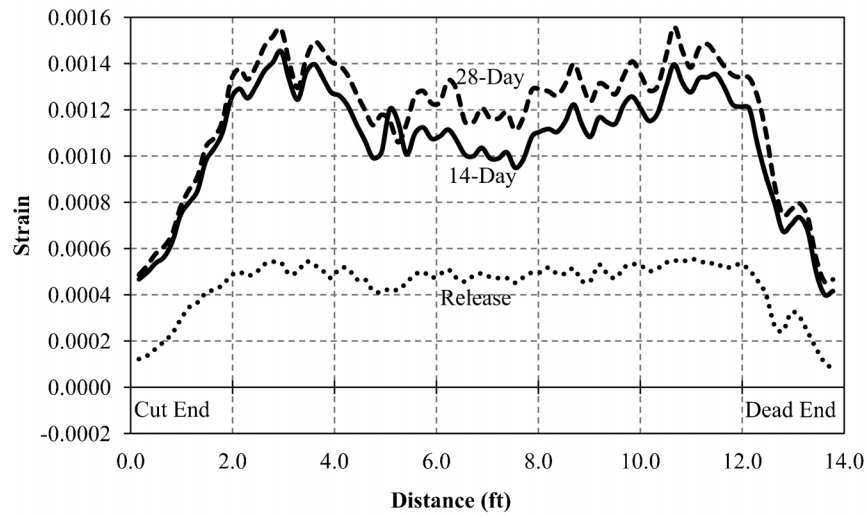


(Specimen B)

Figure B.22 Strain distribution—DuraJoint split sheathing (10 ft).

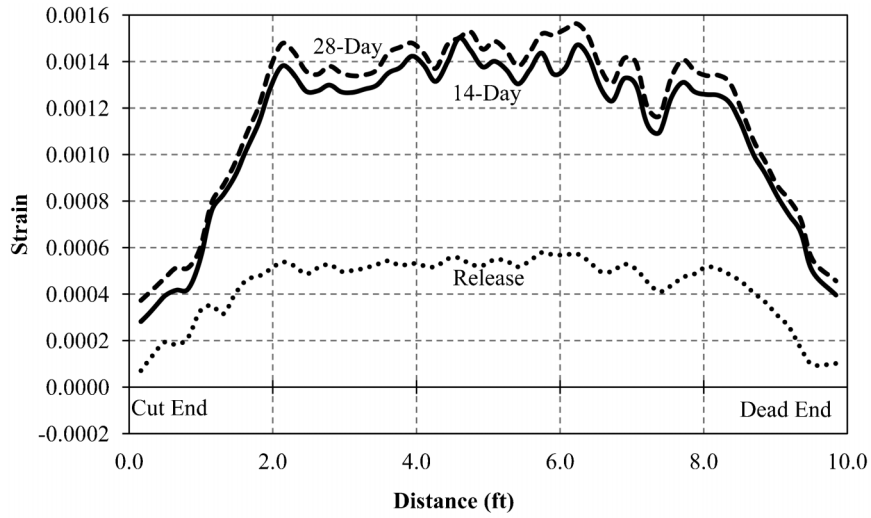


(Specimen A)

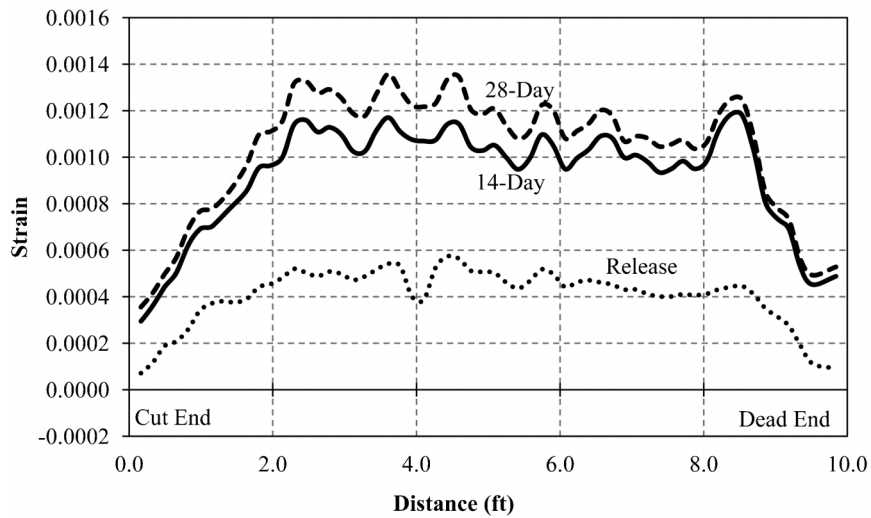


(Specimen B)

Figure B.23 Strain distribution—fully bonded specimens, Cast #2 (14 ft).

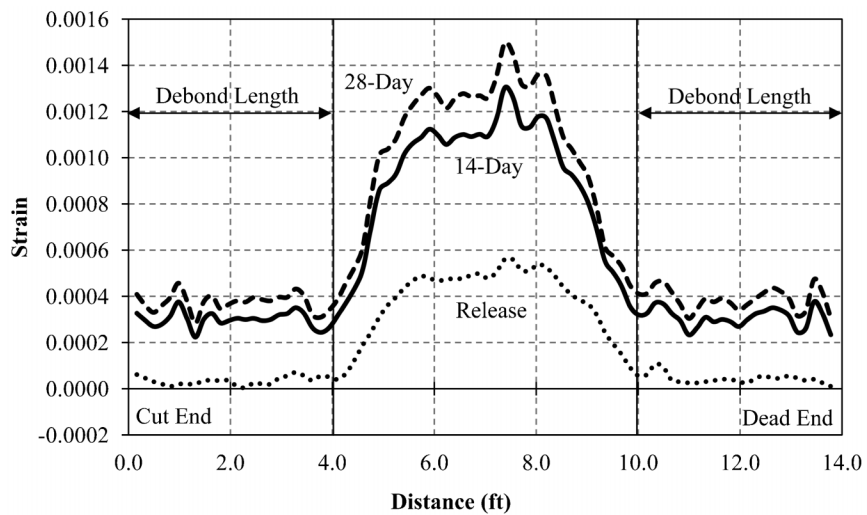


(Specimen A)

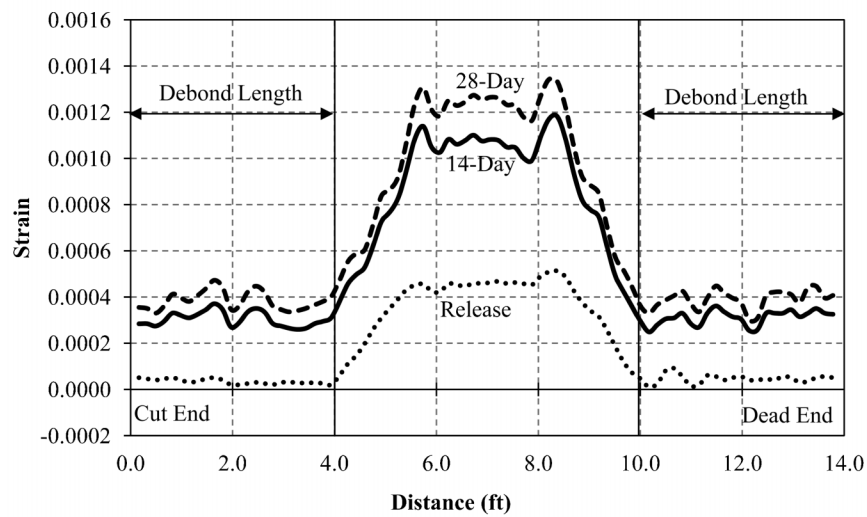


(Specimen B)

Figure B.24 Strain distribution—fully bonded specimens, Cast #2 (10 ft).

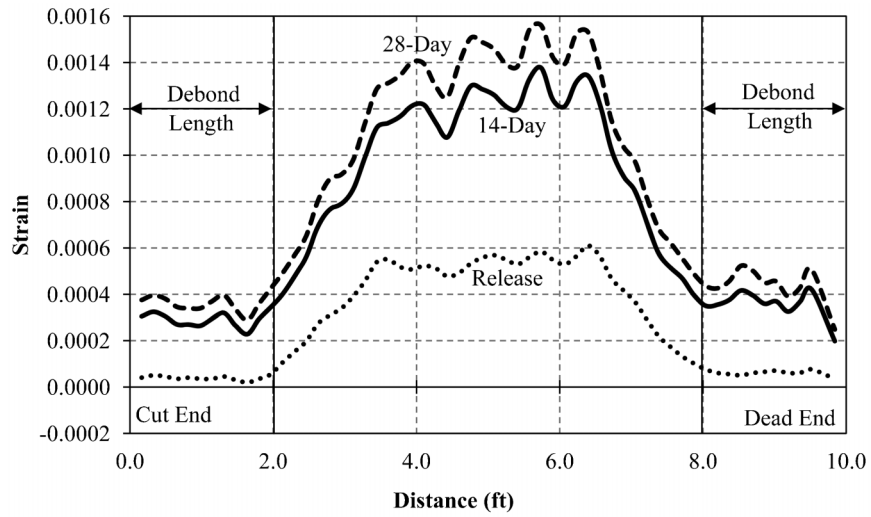


(Specimen A)

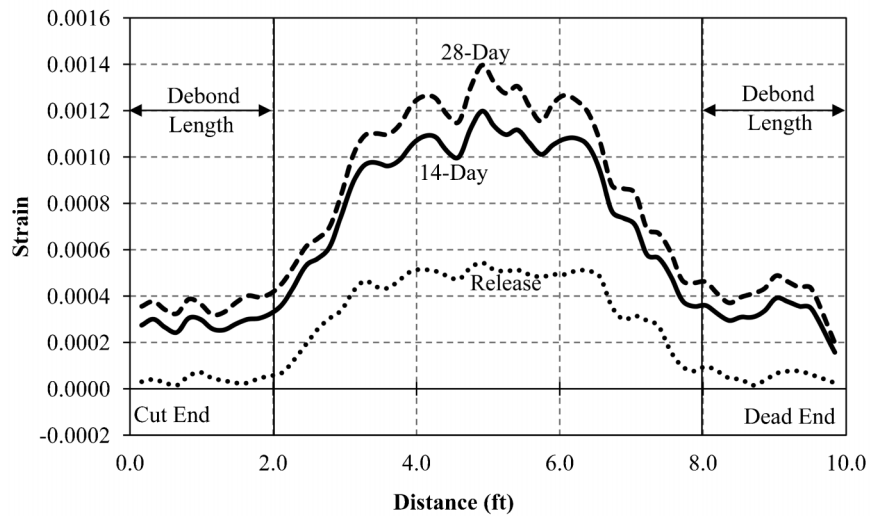


(Specimen B)

Figure B.25 Strain distribution—PVC pipe (14 ft).

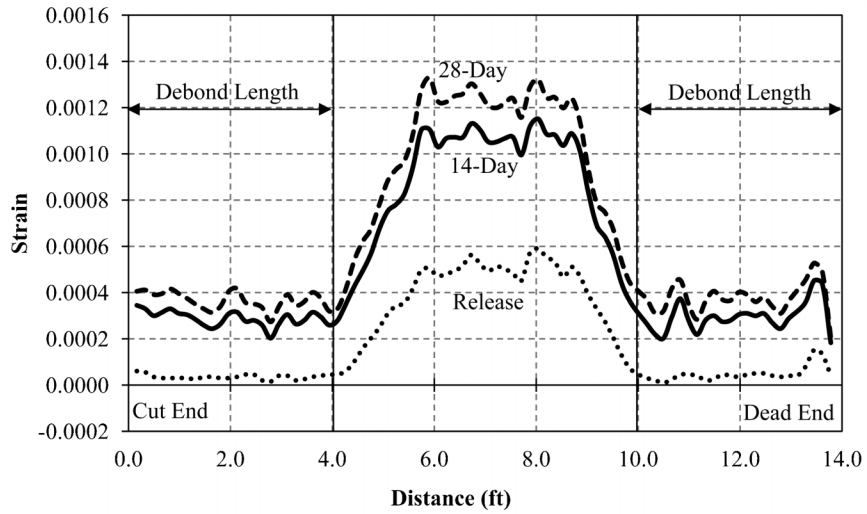


(Specimen A)

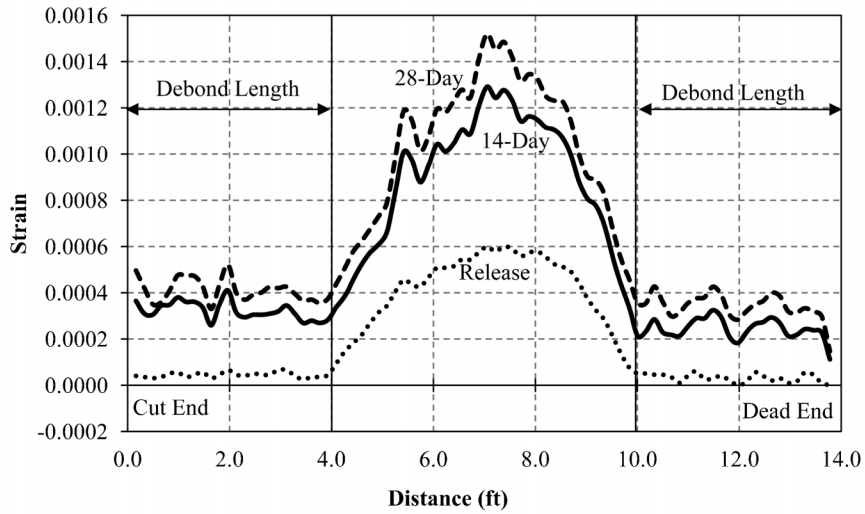


(Specimen B)

Figure B.26 Strain distribution—PVC pipe (10 ft).

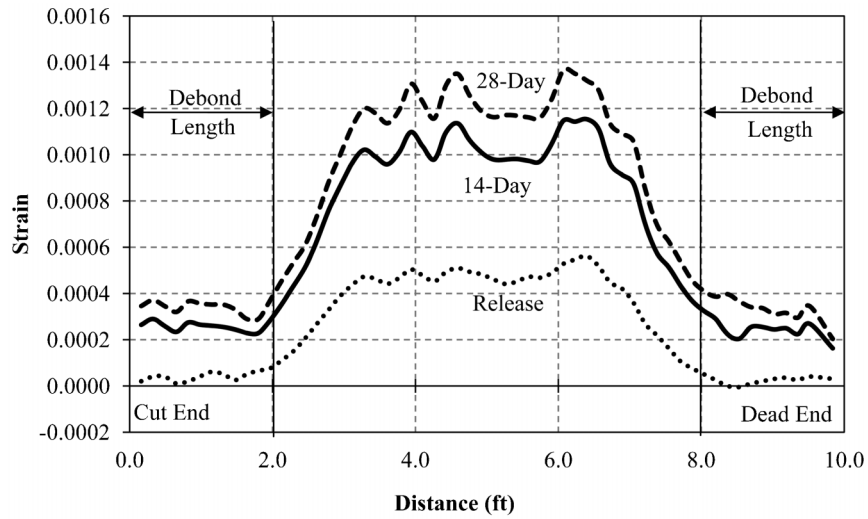


(Specimen A)

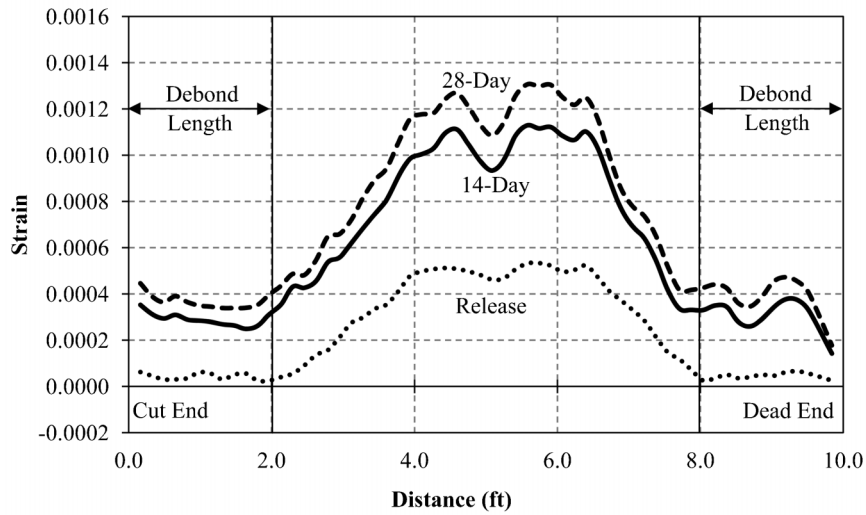


(Specimen B)

Figure B.27 Strain distribution—DuraJoint un-split sheathing (14 ft).



(Specimen A)



(Specimen B)

Figure B.28 Strain distribution—DuraJoint un-split sheathing (10 ft).

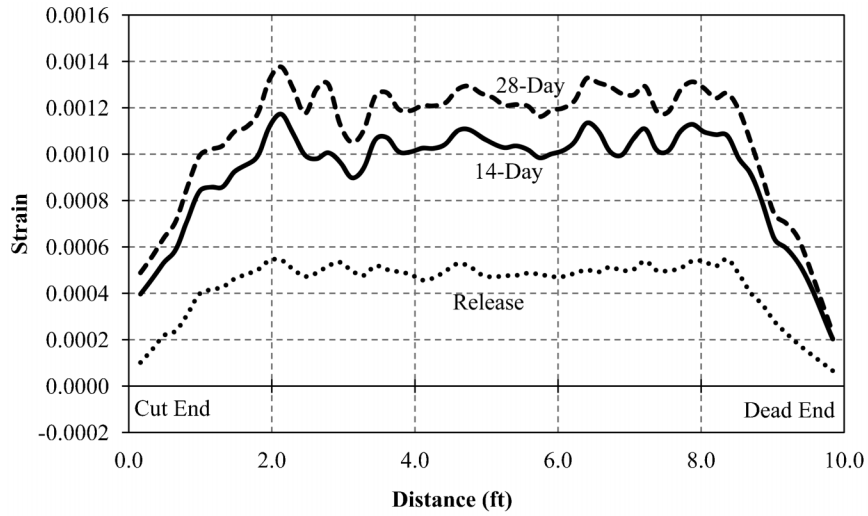


Figure B.29 Strain distribution—fully bonded specimens, Cast #3 (10 ft).

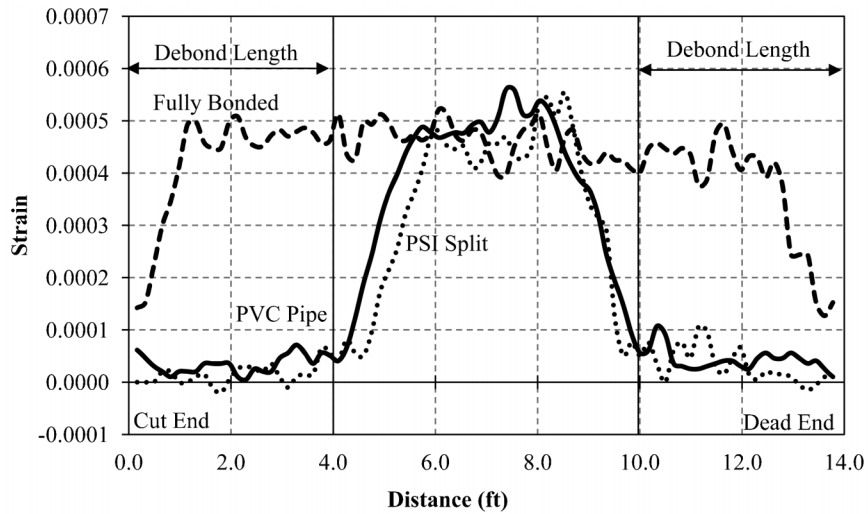


Figure B.30 PSI split sheathing effectiveness comparison.

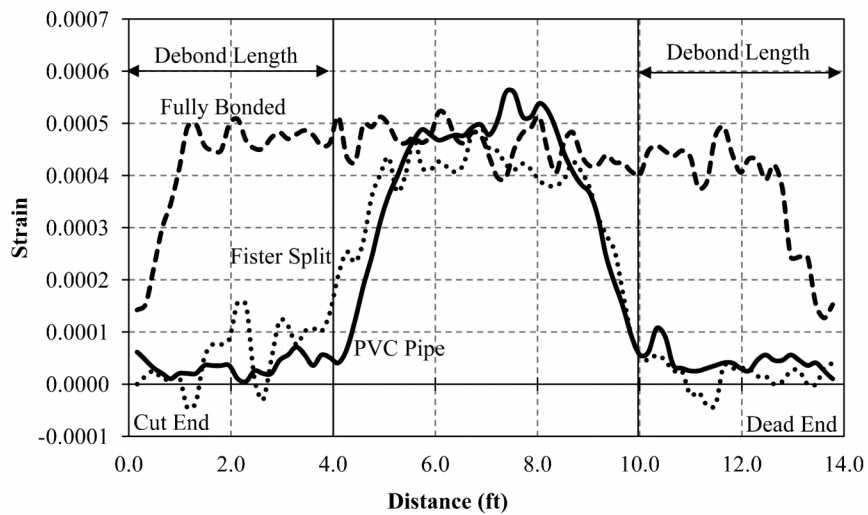


Figure B.31 Fister split sheathing effectiveness comparison.

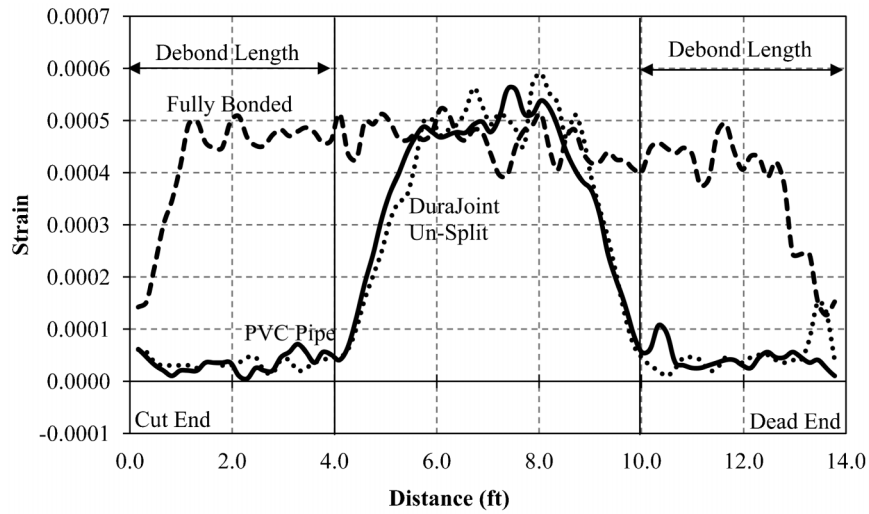


Figure B.32 DuraJoint un-split sheathing effectiveness comparison.

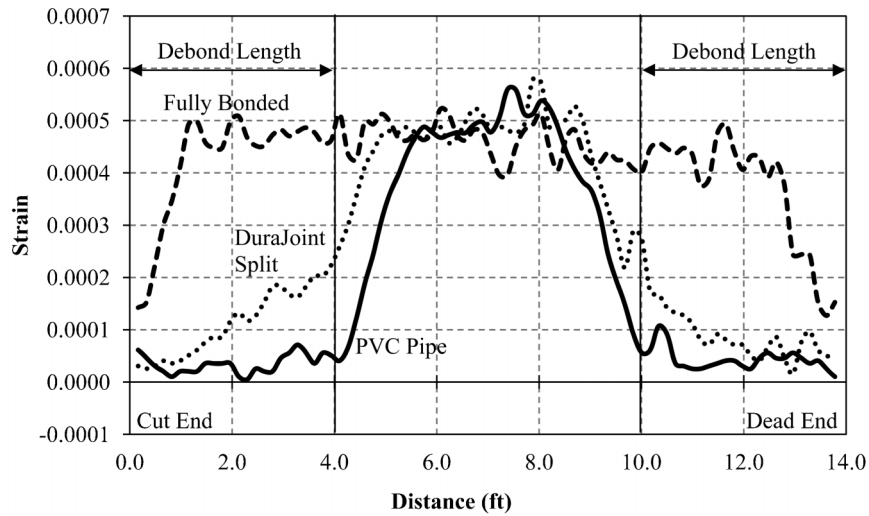


Figure B.33 DuraJoint split sheathing effectiveness comparison.

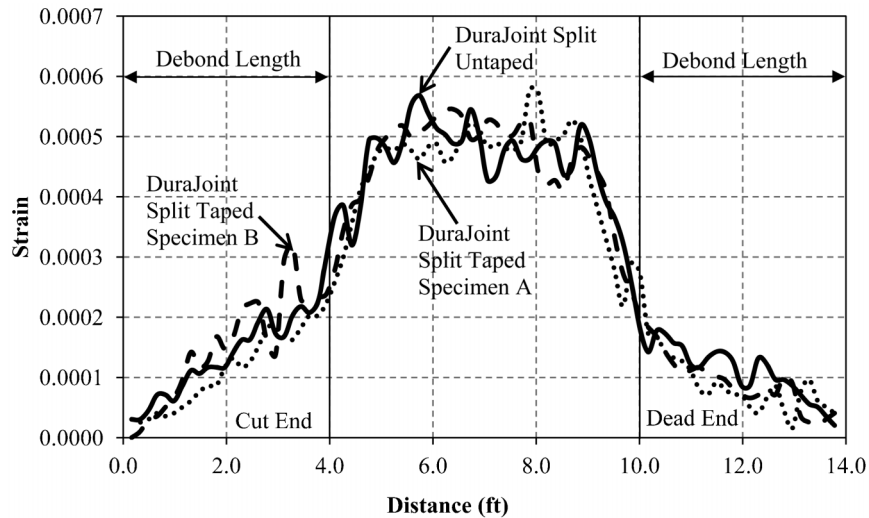


Figure B.34 Debonding effectiveness comparison tapped vs. un-taped.

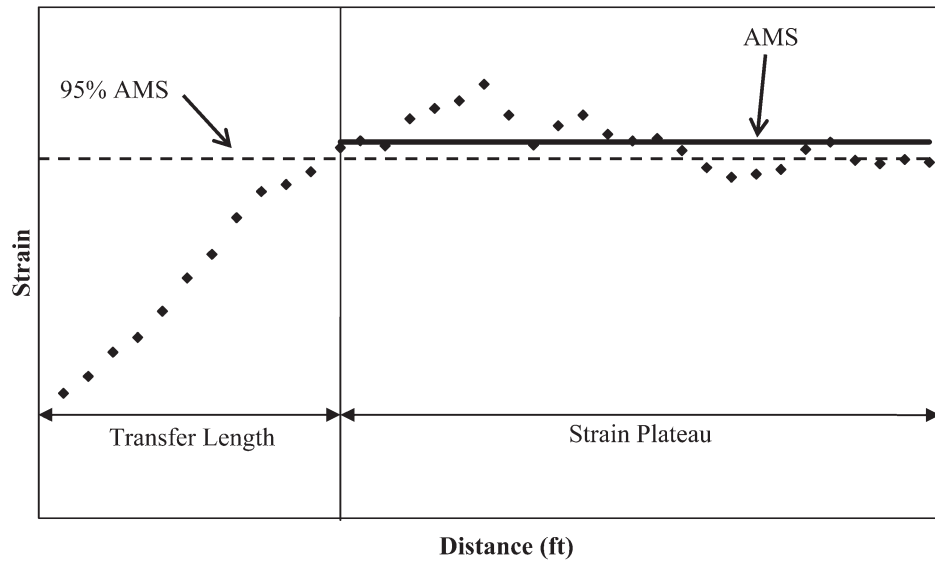


Figure B.35 Average maximum strain (AMS) method.

TABLE B.8
Transfer Lengths

Debond Product	Length (ft)	Specimen ID	Measured Transfer Length (in.)					
			Release		14 Day		28 Day	
			Cut End	Dead End	Cut End	Dead End	Cut End	Dead End
PSI Split Sheathing	10	P-S-2	15.75	23.62	15.75	21.65	15.75	21.65
	14	P-S-4	17.72	13.78	17.72	13.78	17.72	13.78
Fister Split Sheathing	10	F-S-2	19.69	21.65	17.72	17.72	17.72	19.69
	14	F-S-4	9.84	11.81	11.81	11.81	11.81	11.81
DuraJoint Split Sheathing	10	D-S-2	23.62	15.75	19.69	17.72	19.69	19.69
	14	D-S-4	9.84	11.81	9.84	9.84	9.84	9.84
	14	D-S-4T	7.87	9.84	7.87	9.84	7.87	9.84
DuraJoint Un-Split Sheathing	10	D-U-2	17.72	19.69	17.72	19.69	19.69	19.69
	14	D-U-4	27.56	17.72	27.56	17.72	27.56	17.72
PVC Pipe	10	V-U-2	25.59	17.72	23.62	17.72	23.62	17.72
	14	V-U-4	17.72	15.75	17.72	15.75	17.72	17.72
Fully Bonded	10	B-2-2	21.65	19.69	25.59	17.72	23.62	17.72
	10	B-2-3	19.69	17.72	23.62	17.72	23.62	17.72
	14	B-4-1	13.78	25.59	13.78	27.56	13.78	21.65
	14	B-4-2	23.62	21.65	21.65	21.65	23.62	21.65

APPENDIX C. EVALUATION OF DEBOND SHEATHING INSTALLATION TECHNIQUES

C.1 INTRODUCTION

To evaluate the effectiveness of commercially available prestressing strand debonding products, an experimental investigation was conducted. It was important to examine the effectiveness of debonding products prior to studying the influence of debonding on shear strength to determine which debonding product is most effective and which should be used in the shear strength investigation. This investigation builds on the study discussed in Appendix B from which it was determined that certain products are not as effective at debonding as others.

The debonding effectiveness experimental program consisted of six concentrically prestensioned concrete prisms with different types of debond sheathing and sealing techniques. All six specimens were designed to have the same concrete strength and prestressing force. This chapter discusses the design, materials, construction, testing, and results of the experimental program.

C.2 SPECIMEN DESIGN

The specimens were designed to allow evaluation of the difference between the two types of debond sheathing, split and un-split. In addition, different sealing (taping) methods were examined.

C.2.1 Specimen Cross Section

The specimen cross section was selected on the basis of the study discussed in Appendix B. The specimens in that study consisted of one strand concentrically prestressed in a 4 in. \times 4 in. cross section. After that study, it was questioned whether depth (hydraulic pressure) influenced debonding effectiveness. To assist in answering this question, the cross section was selected to be a 4 in. \times 8 in. slice of a typical prestensioned member. This section allows a vertical arrangement of three prestressing strands, each with debond sheathing, with a 2 in. spacing and a 2 in. cover from center of strand as shown in Figure C.1. The three strands were designed to be concentrically prestressed to eliminate moment.

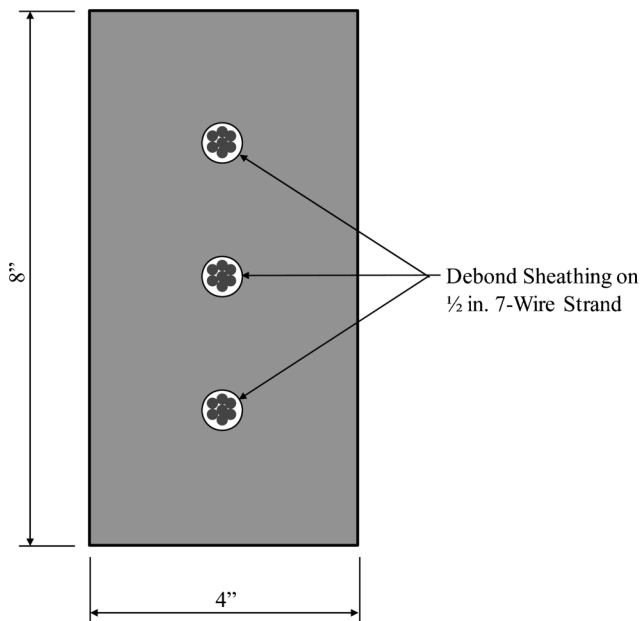


Figure C.1 Cross section.

C.2.2 Prestressing Strand

Standard 1/2 in. uncoated seven-wire, low-relaxation, Grade 270 strand, conforming to ASTM A416 and AASHTO M203 was selected for its common usage in the prestressing industry.

C.2.3 Debonding Products

Debonding strands in prestensioned beams is common in the prestressing industry. Debonding is typically accomplished by shielding (also known as blanketing) the strand with a thin plastic sheathing, preventing bond between the strand and the concrete. Designers usually take advantage of debonding at the ends of prestensioned beams where stresses at transfer might otherwise present a flexural cracking problem due to the lack of dead load stresses. The two main types of sheathing to debond the strands are split and un-split. As its name implies, split sheathing has a split down the entire length, while un-split does not. Due to the physical nature of the different sheathing types, precast plants often use split sheathing over un-split because split sheathing can be applied over the strand before or after stressing. On the other hand, un-split sheathing requires the precaster to thread the strands through each sheath. Un-split sheathing is typically only used on client specific projects. For instance, the Florida Department of Transportation (FDOT, 2014) requires the use of un-split sheathing.

There are several commercially available debonding products currently on the market. However, after reviewing the results from the study discussed in Appendix B, it was decided to use the sheathing products from DuraJoint Concrete Accessories, Inc. DuraJoint's un-split sheathing performed well in the study discussed in Appendix B. On the other hand, DuraJoint's split sheathing was the least effective in terms of debonding. Limiting the products in the current study to DuraJoint's un-split and split sheathing provide upper and lower bounds in terms of debonding effectiveness.

It should be noted that the DuraJoint un-split and split sheathing used for this investigation was different in appearance to those used in the study discussed in Appendix B as illustrated in Figure C.2 and Figure C.3, respectively. The un-split sheathing from this investigation (labeled "DuraJoint 2013" in Figure C.2) has a larger diameter (3/4 in.) compared with the 5/8 in. diameter un-split sheathing from the Appendix B study (labeled "DuraJoint 2009" in Figure C.2). In addition, the un-split sheathing from the Appendix B study is translucent, while the un-split sheathing from this study is not. The split sheathing from this investigation (labeled "DuraJoint 2013" in Figure C.3) has a larger overlap at the slit (1/2 in.) compared with the 3/8 in. overlap in the split sheathing from the Appendix B study (labeled "DuraJoint 2009" in Figure C.3). Furthermore, the split sheathing from this study is noticeably tighter fitting than the split sheathing from the Appendix B study. The differences in the sheathing from 2009 to 2013 might be due to changing the design or manufacturing process (all products were manufactured by DuraJoint).

C.2.4 Specimen and Debond Length

Specimen length was controlled by the debond length and the total casting bed length. It was decided to increase the debond length on either end from a maximum of 4 ft in the study discussed in Appendix B to 6 ft in the current study. The increased debond length was chosen to accentuate any potential issues with debonding effectiveness. Using the same debond length on both



Figure C.2 DuraJoint un-split sheathing comparison.



Figure C.3 DuraJoint split sheathing comparison.

ends allowed a comparison between the cut end and the other end (dead end). Considering a debond length of 6 ft and a transfer length of 2.5 ft (assuming 60 bar diameters according to AASHTO Section 5.11.4.1), the specimens were designed to be 18 ft long as shown in Figure C.4. The 18 ft length also provides a 1 ft region of full prestress in the middle of each specimen.

C.2.5 Sheathing Installation Technique

Most debond suppliers recommend that flexible adhesive tape be used to seal the open ends of the sheathing to prevent paste infiltration. However, it should be noted that many precast plants do not follow these recommendations, leaving the ends un-taped. Furthermore, no recommendations are given to seal the longitudinal slit on the split sheathing. Considering that the split sheathing was not fully effective in debonding the strand in the study discussed in Appendix B, it was decided to test the difference between taping the slit and leaving it un-taped. The objective was to determine if taping the slit and end of the split sheathing results in similar debonding effectiveness as the un-split sheathing with taped ends. It was also of interest to determine the effectiveness of taping the ends of un-split sheathing. Therefore, the ends of one specimen with un-split sheathing were taped while the ends of the other specimen with un-split sheathing were left un-taped. Duct tape was selected as the flexible adhesive tape for sealing.

C.2.6 Test Specimens

The test matrix for the debonding effectiveness prisms is given in Table C.1. Traditional sheathing was used in four of the six specimens. The other two specimens were constructed as controls. One control specimen was debonded using 1/2 in., Schedule 40 PVC pipe because of its rigidity and annular space (0.6 in. inside diameter). This specimen, with the pipes taped at their ends, is considered a bounding condition where perfect debonding can be achieved. The other control specimen was fully bonded and provided the other extreme (no debonding). Installation details for each specimen are shown in Figure C.5.

C.3 MATERIALS

C.3.1 Concrete

The concrete mix design was selected based on the desired strength at release (f_{ci}^r). It was desired to limit the concrete compressive stress at release to $0.6f_{ci}^r$ to maintain the concrete in essentially its elastic range. Although not a requirement, this also served to satisfy ACI 318-11 Section 18.4.1. With three strands released at 202.5 ksi ($0.75f_{pu}$) inducing an immediate compressive stress of approximately 2900 psi (not considering elastic and relaxation losses), the minimum required compressive strength at

TABLE C.1
Test Matrix

Sheathing Type	Taping Scenario
Fully Bonded	—
Sch. 40 PVC Pipe	Taped Ends
Un-Split Plastic (DuraJoint Concrete Accessories, Inc.)	Un-Taped Ends Taped Ends
Split Plastic (DuraJoint Concrete Accessories, Inc.)	Un-Taped Slits and Ends Taped Slits and Ends

transfer was approximately 4850 psi. The mix used in the Appendix B study provided compressive strengths of approximately 4,600 psi at 3 days, and over 5,000 psi at 7 days. With the compressive strength history already known for that particular mix, it was ultimately selected. In addition, using the same mix as that used in the Appendix B study provided another level of consistency between the two investigations.

The concrete was ordered from Irving Materials, Inc. (IMI), a ready-mix concrete supplier located approximately 1.5 miles from the Bowen Laboratory. The selected mix was a seven sack mix with a full range water reducing admixture as given in Table C.2. This mix contained 3/4 in. maximum aggregate size (gravel). In addition, while the required quantity of concrete was less than one cubic yard, two cubic yards were ordered to ensure a well-blended mix. The slump was initially measured as 4 in. To improve workability of the mix, two gallons of water were added to the truck onsite. This increased the slump to 5.5 in. The final batch weights including the additional two gallons of water added onsite are presented in Table C.3.

Standard 6 × 12 in. cylinders were cast in plastic molds and cured in the same manner as the test specimens. After the concrete surface hardened, the specimens and cylinders were covered with wet burlap and plastic to prevent moisture loss. Curing of the cylinders was discontinued at the same time that the curing of the specimens was discontinued. Additionally, the cylinder molds were removed when the specimen forms were removed.

Compressive strength was monitored by testing three cylinders at regular intervals up to 28 days in accordance with ASTM C39. A loading rate of 50,000 lb per minute was used during the compressive cylinder tests along with 70 durometer elastomeric pads. The compressive strength gain is shown in Figure C.6, and a summary of the compressive strength results is provided in Table C.4.

C.3.2 Prestressing Steel

It should be noted that the prestressing steel properties are given in Chapter 3. The debonding effectiveness study is not dependent on the prestressing steel properties.

C.4 CONSTRUCTION

The pretensioned specimens were constructed in the Bowen Laboratory in one cast. A 56 ft casting bed was used such that two rows of three specimens were cast adjacent to each other. Constructing all the specimens from the same cast eliminated concrete as a variable.

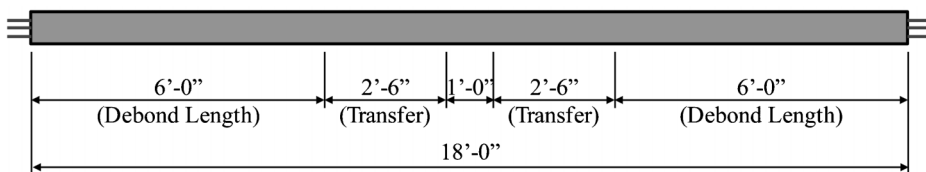


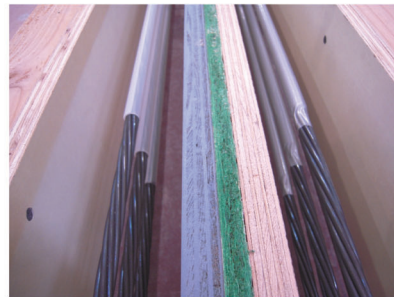
Figure C.4 Profile.



Fully Bonded PVC Pipe



**Un-Taped Taped
Un-Split Sheathing**



**Un-Taped Taped
Split Sheathing**

Figure C.5 Sheathing installation details.

TABLE C.2
Concrete Mix Design Weights per Cubic Yard

Material	Design Weights Per Cubic Yd
Type I Cement (lbs)	658
3/4" Coarse Aggregate (lbs)	1850
Fine Aggregate (lbs)	1360
Water (lbs)	235
BASF Glenium 3030 NS Full Range Water Reducer (oz)	10

TABLE C.3
Final Concrete Mix Batch Weights per Cubic Yard

Material	Batch Weights Per Cubic Yd
Type I Cement (lbs)	657.5
3/4" Coarse Aggregate (lbs)	1830
Fine Aggregate (lbs)	1410
Water (lbs)	175
BASF Glenium 3030 NS Full Range Water Reducer (oz)	12.5

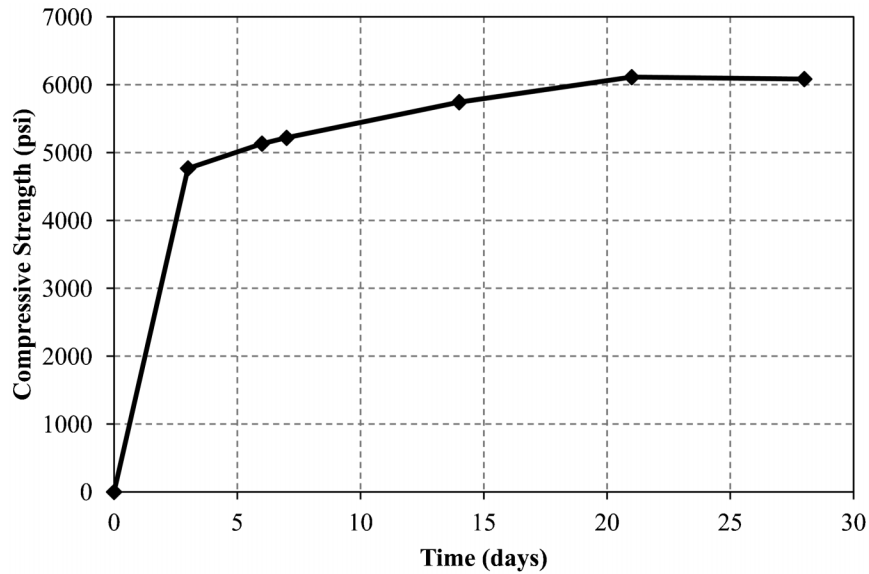


Figure C.6 Compressive strength.

C.4.1 Prestressing Bed

The pretensioning abutments used in this study were designed to be anchored to the strong floor. The abutments, as shown in Figure C.7, resist the pretensioning force through friction of the abutment against the strong floor. Six, Grade 150, 1-3/4 in. diameter threaded Dywidag bars were stressed to approximately 190 kips, resulting in a normal force of 1,140 kips. Assuming a coefficient of friction between the steel abutment and the concrete strong floor of 0.4, the resisting force is 456 kips. The abutment face has holes drilled on a 2 in. grid to accommodate different prestressing configurations. The lower plate of the abutment (where all the strands were placed) is 3 in. thick, providing a rigid contact surface to anchor the prestressing chucks.

C.4.2 Pretensioning

Jacking of the prestressing strands was carried out in two phases. The first phase included pulling the strands to 2 kips. This initial pull kept the strands taut which allowed strain gages to be installed. Three strain gages were installed on both center strands (one per specimen), resulting in six strain gages total. After strain gage installation, the second phase began. In this phase, the stressing crew tensioned each strand to the full jacking stress. The release stress was targeted at 75% (202.5 ksi) of the ultimate nominal strength of the strands (270 ksi) which corresponds to a release force of 31 kips per strand. However, due to seating losses, a jacking stress of 209.2 ksi (0.77 f_{pu}) was initially selected. This jacking stress was determined by estimating a strand slip (seating in the chuck) of 0.2 in. over a bed length of 70 ft. The jacking stress estimation was confirmed by monitoring the strain gage and load cell measurements during stressing operations through the

following procedure. While stressing the first strand (one of the two center strands), the strain measurements at 31 kips (0.75 f_{pu}) were noted. The jacking force was subsequently increased to 32 kips (0.77 f_{pu}) to account for the seating losses as previously mentioned. The jacking force was then slowly released, allowing the strand to slowly and completely seat into the chuck. As the strand was seating into the chuck, the strain measurements continued to drop until the jacking force was zero. At this point, the final strain measurements were compared to the strains noted at 31 kips. The strains were in close agreement (within 2%); therefore, the force in the strand after seating losses was approximately 31 kips. The remaining strands were tensioned to 32 kips as well. It should be noted that dial gages (stationed at both pretensioning abutments) recorded a maximum total movement of 0.016 in. This resulted in a negligible loss of approximately 85 lbs per strand.

The jacking assembly consisted of two prestressing chucks, pipe, load cell, ram, steel plates, and washers. The entire assembly is shown in Figure C.8. The order of the assembly from the abutment face is as follows. First, one of the prestressing chucks bears directly against the abutment face. This chuck remains in place and is the final anchor holding the strand in its stressed state. Against the chuck rests a steel washer to create a standoff so that

TABLE C.4
Concrete Compressive Strength Data

Age (days)	f_c (psi)
3	4,770
6	5,130
7	5,220
14	5,740
21	6,110
28	6,080



Figure C.7 Pretensioning abutments.

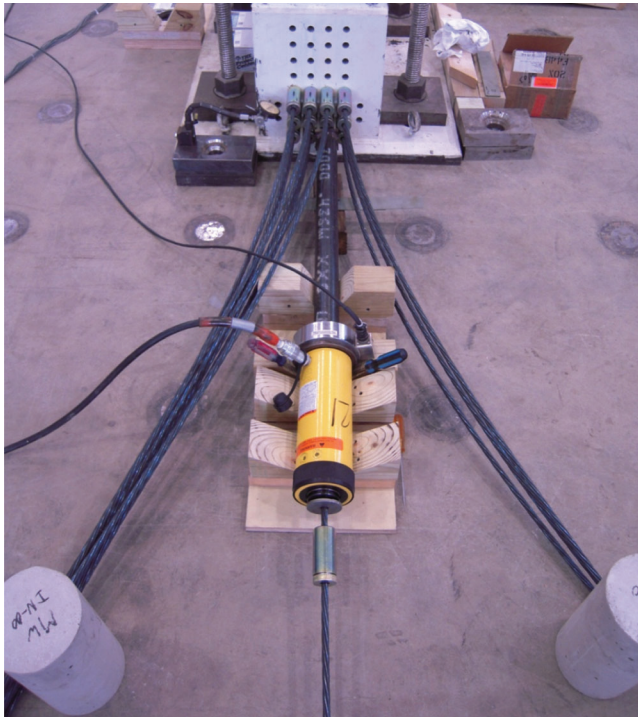


Figure C.8 Prestress jacking assembly.

only the designated chuck is in contact with the jacking assembly. After the washer is a double, extra strong steel pipe. The purpose of the pipe is to move the load cell and ram far enough away from the abutment face to allow the strands to be bent out of the way. A steel plate washer was welded to the end of the pipe to bear on the load cell in the proper location. The load cell was connected to a data acquisition system allowing real time viewing of the force and strain in each strand. The load cell is followed by a circular steel plate which transfers the load from the ram (controlled by a pneumatic pump) to the load cell. On the other side of the ram is another steel plate washer which bears against the second prestress chuck. This chuck is removed with the rest of the assembly from strand to strand until stressing is completed. The entire jacking assembly rests on a custom made wood stand with inserts to accommodate raising and lowering to three different levels of strands. It should be noted that Figure C.8 is from another test series, which uses more strands. However, the jacking assembly is identical.

C.4.3 Formwork

The formwork (side forms and base) was constructed from plywood and 2×4 s. Exterior side forms were attached to the base with lag screws to ensure no side form movement at the base. The use of two adjacent lines of forms was possible due to the tight formwork configuration as shown in Figure C.8. A central panel consisting of two $3/4$ in. pieces of plywood sandwiching a $1/2$ in. piece of plywood was used. The center plywood simply acted as a spacer to provide the correct side cover. However, this setup prevents direct attachment of the middle panel to the base. Therefore, top link beams (2×4 s) as shown in Figure C.9, as well as a threaded rod and coupling nut spacer system were installed. Coupling nuts were threaded onto the ends of short pieces of $1/4$ in. diameter threaded rods. Next, the coupling nuts were adjusted against the protective padding of weather-stripping to ensure the correct side cover. The weather stripping prevented the small coupling nuts from punching into the side forms while being tightened. These threaded spacer rods were used throughout the length of each form. The formwork was discontinued at each

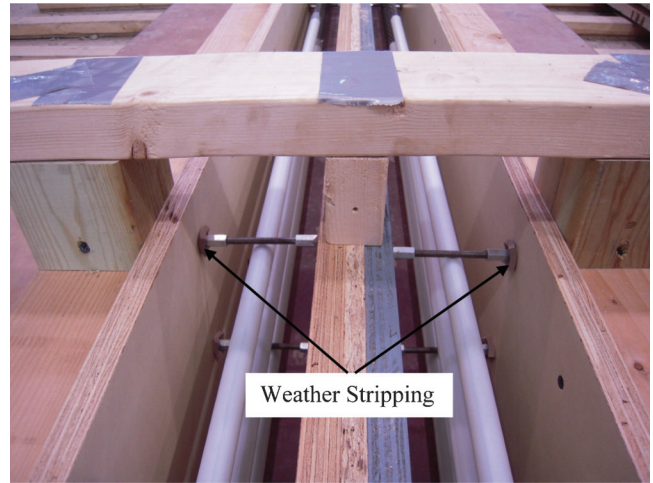


Figure C.9 Side forms.

specimen end as shown in Figure C.10 for ease of cutting the strands at transfer.

C.4.4 Casting

The debonding effectiveness prisms were constructed in one cast. Due to the small specimen size and their location on the laboratory floor, a one cubic yard concrete bucket was used to transport the concrete from the truck to the specimens as shown in Figure C.11. As the concrete was being placed, internal vibrators were used to consolidate the mix. After vibrating, the top surface was screeded to the proper level followed by finishing with magnesium hand floats.

The specimens were wet cured for three days. This was accomplished by covering the surface with wet burlap and plastic to prevent moisture loss. In addition, the burlap was re-wetted every 12–24 hours to maintain wet curing. Curing was discontinued after three days, at which time, the side forms and plastic cylinder molds were removed.

Standard 6×12 cylinders were cast alongside the specimens. The cylinders were consolidated using a small internal vibrator according to ASTM C192. The cylinders were wet cured in the same manner and for the same duration as the specimens.



Figure C.10 Formwork termination.



Figure C.11 Casting.

C.4.5 Strand Release

The prestressing strands were released on the sixth day after casting. The timing was controlled by wet curing and instrumentation that needed to be installed prior to release. Each strand was gradually released by heating approximately a 1 ft length back and forth with a torch until all of the seven wires were cut as shown in Figure C.12. The individual wires typically broke two or three at a time, and the specimens slid on the smooth base after each of the three strands were cut. The order of strand release was top, bottom, and middle for each of the two columns of strands. After all six strands were cut at the live end (jacking end), they were cut at the other abutment (dead end), and finally in between the specimens which were in the casting line.

C.5 TEST SETUP AND PROCEDURE

C.5.1 Instrumentation

To determine the debonding effectiveness of each debonding system, the concrete strain profile was measured. The strains were measured using a DEMEC Mechanical Strain Gage, manufactured by Mayes Instruments Limited located in Berkshire, England. This strain measurement system consists of installing



Figure C.12 Strand release.

metal locating disks on the concrete surface and measuring displacements with the DEMEC gage. Taking distance measurements along the length of each specimen, before and after transfer, allows for the calculation of an average concrete strain over the gage length.

C.5.1.1 DEMEC Locating Disks

The DEMEC locating disks are 6.3 mm diameter, stainless steel disks with a small conical hole machined in the middle. The hole in each disk is identical and is machined to perfectly fit with the conical tip of the DEMEC strain gage. A single line of these locating disks were installed on one side of each specimen at mid-height, the centroid of the prestressing force. The disks were installed at a 50 mm spacing with a DEMEC layout bar composed of Invar, a metal alloy used for its low coefficient of thermal expansion, which has conical tips at both ends to aid in disk placement. Figure C.13 illustrates installing the disks with the layout bar.

The DEMEC locating disks were attached to the concrete surface by means of a special two-part epoxy made by Fielco Adhesives. The BondAway 2011A/2012B system was selected due to its unique bond removal capabilities. This epoxy is designed to fall off of the substrate when immersed in boiling water for one minute. After finishing all of the measurements, the disks were scraped off the concrete surface and placed in boiling water to allow the remaining epoxy to fall off. This bonding system provides a simple and efficient method to reuse the disks.

C.5.1.2 DEMEC Mechanical Strain Gage

The DEMEC Mechanical Strain Gage that was used has a 100 mm gage length and is equipped with a digital indicator. The 100 mm gage length was selected because it was the shortest gage length at the time of purchase. As shown in Figure C.14, the DEMEC gage consists of a small Invar beam with a conical tip at either end, one fixed and one on a pivot. The gage is equipped with a Mitutoyo 543 digital indicator with a resolution of $\pm 5 \times 10^{-6}$ in. The gage functions by inserting the pivoting conical tip in one locating disk and then placing the fixed end in the



Figure C.13 DEMEC layout bar.

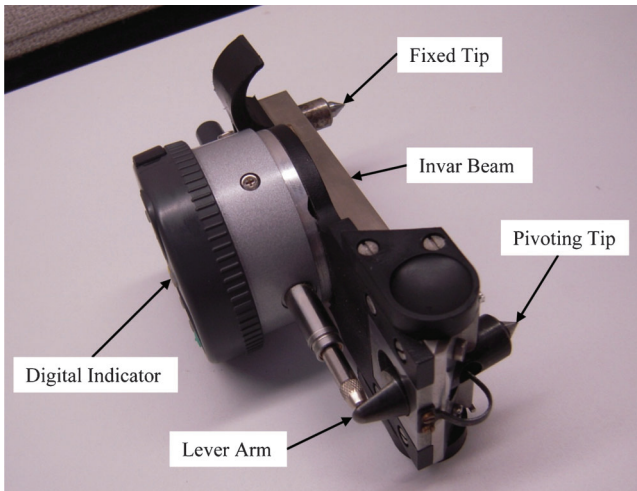


Figure C.14 DEMEC mechanical strain gage.

second disk. It is important to note that care must be taken while using the gage to ensure accurate and consistent measurements. The conical tips must be well seated in the disks, and the gage should be held parallel to the measuring plane.

A change in distance between two disks is transmitted to the digital indicator through a pivot. The lever arm pivots on a 0.81:0 ratio. This means that a distance of 8 mm will be measured as 10 mm due to the pivot. Therefore, all of the measurements must first be reduced by 20% before calculating strains.

C.5.2 Procedure

After removing the side forms, the locating disks were installed. The disks were left to cure overnight to prevent any disk movement while taking measurements. Measurements were taken before strand release, immediately after release, 14 days after casting, and 28 days after casting. Strains were then calculated using the pre-release measurements along with the post-release measurements.

Measurements were taken with the DEMEC gage by the same operator throughout the investigation. The measurements can be operator sensitive; therefore, it was important that this error be eliminated. In addition, only stable readings were recorded (unstable measurements are indicative of gage pins not being properly seated in the disks). It should be noted that duplicate measurements were taken at several locations in each specimen to ensure repeatability.

The strains were calculated using Equation C.1 with the pre-release measurements and their corresponding post-release measurements.

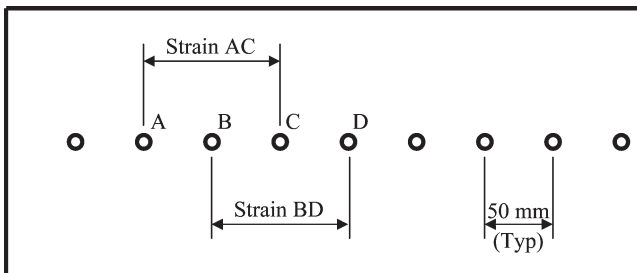


Figure C.15 DEMEC measurements.

$$\varepsilon_n = \frac{d_t - d_0}{l_g + d_0} \quad (C.1)$$

where:

ε_n : Concrete strain over measurement, n

d_0 : Gage extension prior to transfer, corrected for lever action (mm)

d_t : Gage extension at time, t, corrected for lever action (mm)

l_g : Gage length of the device (100 mm)

As mentioned previously, the locating disks were spaced at 50 mm while the gage length of the DEMEC gage was 100 mm. This meant that measurements were taken between every other disk as shown in Figure C.15. The strain between any two consecutive disks is taken as the average strain calculated for the two gage length intervals to which it belonged. For example, the strain between “BC” in Figure C.15 is calculated as the average of “Strain AC” and “Strain BD.”

C.6 RESULTS

The data is plotted as the concrete surface strain at the centroid of the prestressing force versus the distance along each specimen. It should be noted that the horizontal axis is the distance from the cut end (end closer to the location where the strands were cut with the torch).

C.6.1 Transfer Behavior

Figure C.16 illustrates the two extremes in terms of debonding. The fully bonded specimen has no debonding sheathing and therefore, simply begins transferring stress from the strands to the concrete immediately from each end. The specimen with PVC pipe debond sheathing, however, is considered a perfect form of debonding as evidenced by zero strain in the debonded regions.

Figure C.17 and Figure C.18 compares the debonding effectiveness of taped versus un-taped sheathing for both commercially available sheathing types, un-split and split, respectively. The only opening on un-split sheathing is at the end. Split sheathing, on the other hand, has a longitudinal slit down the length, as well as an opening at the end. The end opening on split sheathing, however, is much smaller than un-split sheathing due to the tighter fitting split sheathing. It is important to note that the specimens with taped sheathing have all openings sealed with duct tape to prevent paste infiltration. Specimens with un-taped sheathing do not include tape.

Figure C.17 indicates that the specimens with un-split sheathing (taped and un-taped) performed similarly and produced zero strain over the debonded regions. The lack of strain in this region indicates effective debonding. Figure C.18, however, shows that an increase in concrete compressive strains occurred in the debonded region for the specimen with un-taped, split sheathing. The specimen with taped, split sheathing, on the other hand, performed similar to the specimens with un-split sheathing (zero strain in the debonded regions).

C.6.2 Behavior Over Time

Figure C.19 through Figure C.24 illustrate change in the strain profiles over time for each specimen. The compressive strains over the length of each specimen are shown to increase with time. Compressive strains increase throughout the specimen due to shrinkage and creep strains. The debonded regions are primarily subjected to shrinkage strains, while the middle regions (with prestress forces) are subjected to shrinkage and creep strains. For this reason, the magnitude of the strain increase is seen to be different in these regions.

Transfer lengths are observed to remain approximately constant over time. In addition, the transfer lengths do not appear to be dependent on the end (cut or dead). The transfer length of all the

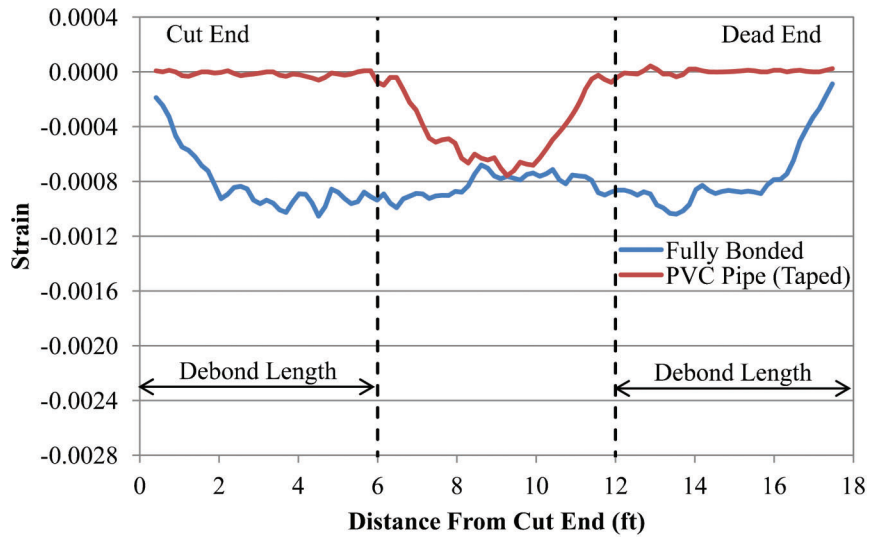


Figure C.16 Boundary specimens.

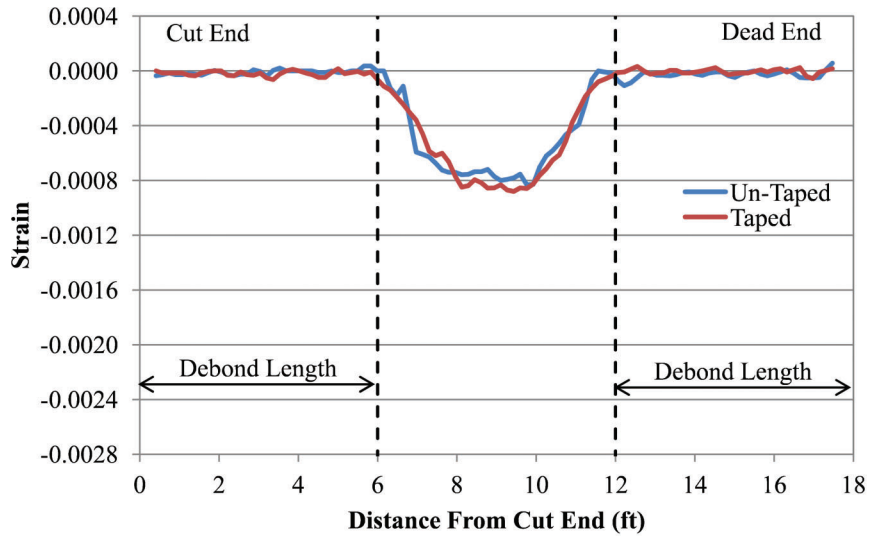


Figure C.17 Un-split sheathing.

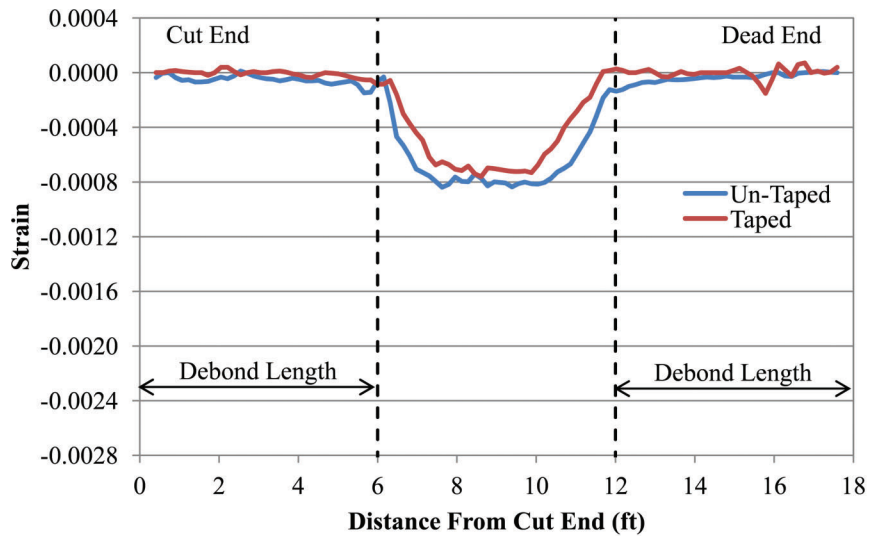


Figure C.18 Split sheathing.

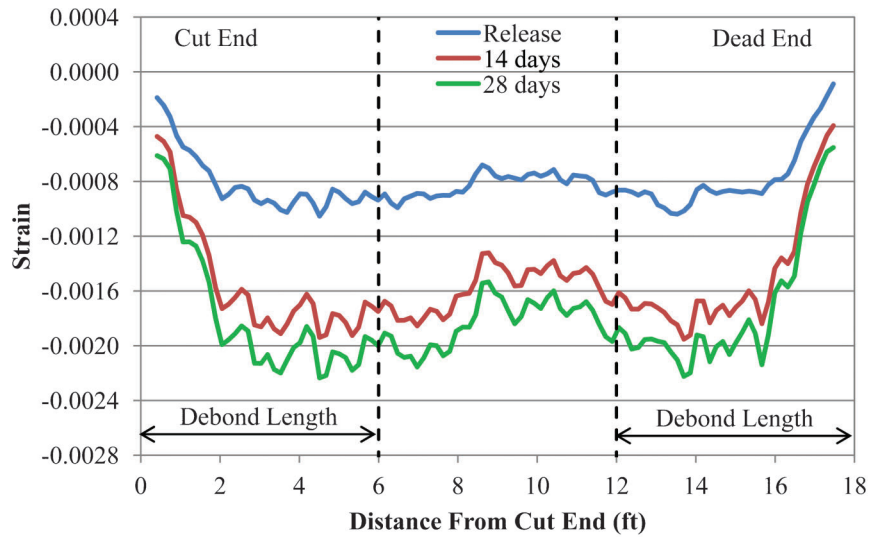


Figure C.19 Strain profile over time—fully bonded.

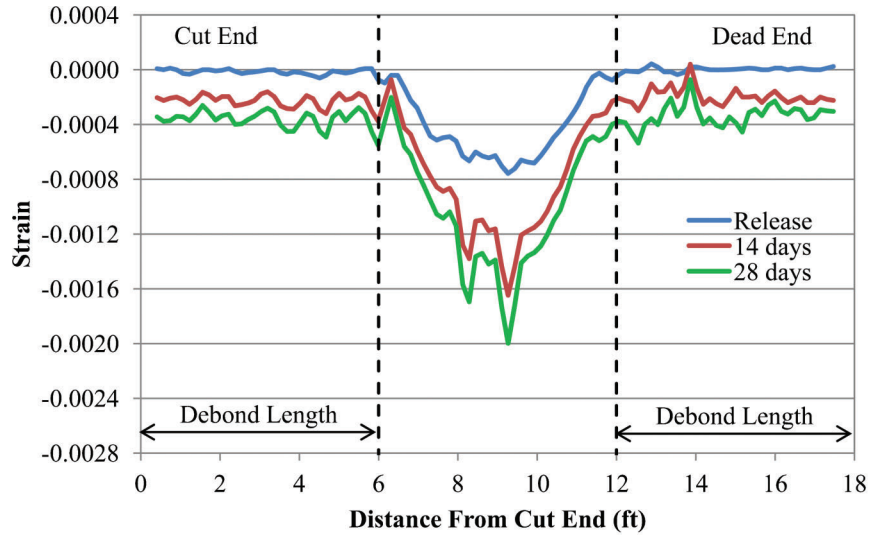


Figure C.20 Strain profile over time—PVC pipe sheathing (taped).

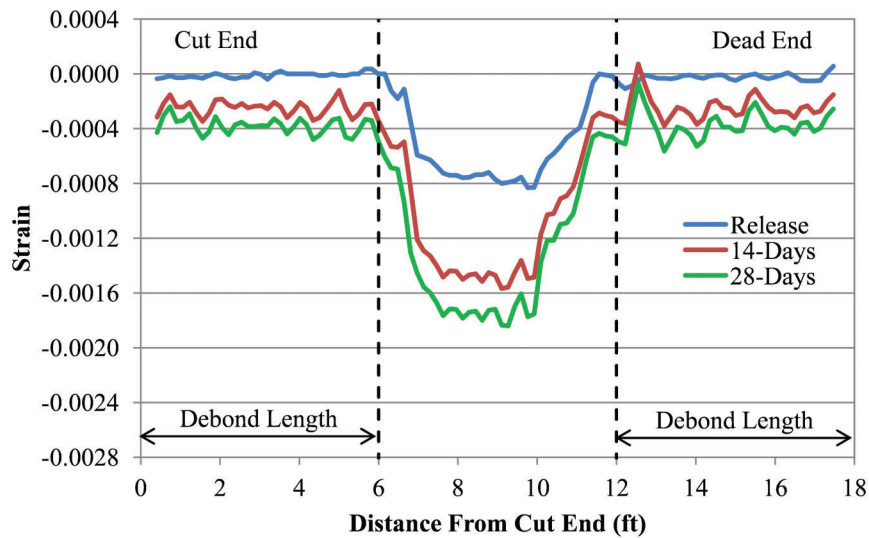


Figure C.21 Strain profile over time—un-split sheathing (un-taped).

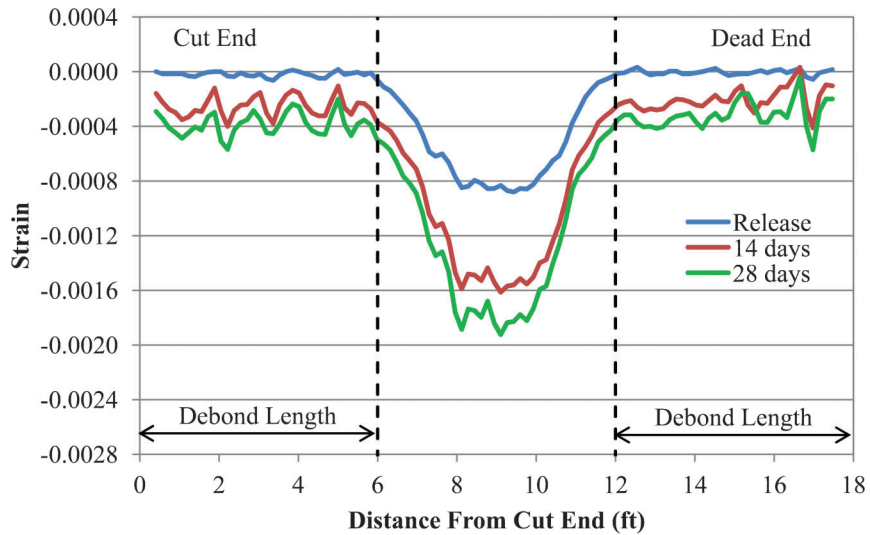


Figure C.22 Strain profile over time—un-split sheathing (taped).

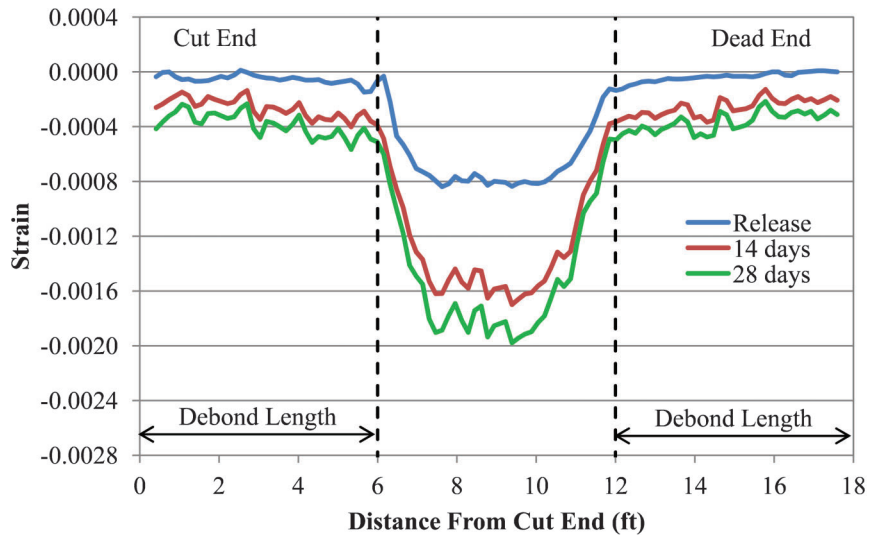


Figure C.23 Strain profile over time—split sheathing (un-taped).

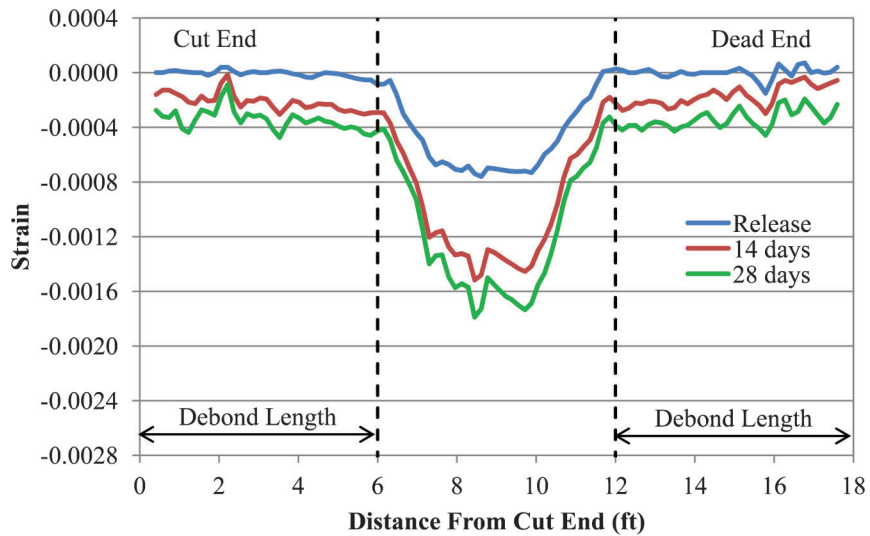


Figure C.24 Strain profile over time—split sheathing (taped).

specimens over time is observed to be approximately 2 ft (48d_b), regardless of the end (cut or dead).

C.7 ANALYSIS

The strain profiles were analyzed visually to determine the effectiveness (or ineffectiveness) of a debonding system. Strain profiles with zero concrete strain over the entire debond length are considered to be fully debonded. On the other hand, when the strains fall below zero (compressive strains), the strands are bonding to the concrete; therefore, they are no longer debonded. If bonding takes place within the debonded length, the assumption of strand debonding made in a prestress transfer analysis is incorrect and may lead to unexpected behavior within the debonded region due to unexpected prestress forces.

Figure C.25 through Figure C.28 compare the results of the specimens with commercially available debond sheathing and taping combinations to those of the control specimen with PVC pipe sheathing. This comparison is provided to evaluate the effectiveness of each debonding system.

All of the strain profiles, except one, shown in Figure C.25 through Figure C.28 match the strain profile of the perfectly debonded control specimen. The one exception is the specimen with un-taped, split sheathing. In this specimen, the strain profile begins diverging from zero in the debonded region. This behavior is evidence of strands beginning to bond to the surrounding concrete in the debonded regions, resulting in a system that is not truly debonded.

To understand the reason for this difference in behavior, each specimen with commercially available debond sheathing was cut open in the debonded region. Of particular interest was to determine if paste infiltration had occurred. Paste infiltration can provide an explanation of poor debonding performance. It should be noted that all three sheaths at both ends were inspected to determine if there was any effect from strand depth or transfer location (cut end versus dead end).

C.7.1 Taping Ends of Un-Split Sheathing

Figure C.17 illustrates the effect of taping and not taping the ends of un-split sheathing on the strain profile. As shown, there was no noticeable difference between the strain profiles of both specimens. In addition, both specimens exhibited excellent debonding characteristics when compared to the specimen with PVC pipe sheathing as shown in Figure C.25 and Figure C.26.

Both specimens were opened to determine if there was any paste infiltration in either specimen. Figure C.29 illustrates the autopsy of the specimen with taped ends, while Figure C.30 shows the autopsy of the specimen without taped ends.

There was an obvious difference when both specimens (un-split sheathing with and without taped ends) were opened. Absolutely no paste infiltration was found in the specimen with the taped ends (Figure C.29). On the other hand, paste infiltration was discovered at all of the sheathing ends of the un-taped specimen (Figure C.30). Approximately 6 in. of paste was observed from the end of the sheathing. Nevertheless, the strain profiles did not appear to reflect this difference in paste infiltration which may be explained as follows. First, only a minimum amount of paste entered the ends of the sheathing; therefore, the force when the strand tension was released could have partially broken through that paste. Again, only 6 in. of material was observed. Second, an increase in strain may have been difficult to measure due to the disk spacing (2 in.) relative to this small length of bonding (6 in.).

It should be emphasized that the results (and analysis of those results) are for the specific set of specimens that were evaluated as part of this study. The objective was to better understand the differences in behavior of several debonding systems. However, these results should not be extrapolated for every member with every concrete mix. For instance, higher slump mixes may increase the distance of paste infiltration. There are likely several other parameters that may affect the performance of any given debonding system. Therefore, it is always recommended to seal the ends of un-split sheathing with a flexible adhesive tape, such as duct tape.

C.7.2 Taping Slits and Ends of Split Sheathing

The effect of taping the slits and ends of split sheathing is illustrated in Figure C.18 by comparing it to the specimen with un-taped, split sheathing. A definite difference in the debonded region of the strain profile is observed. The un-taped specimen's strain profile diverges from zero in the debonded regions, while the taped specimen follows the behavior of the specimen with PVC pipe sheathing (Figure C.28).

Both specimens were opened to determine if paste infiltration occurred which could explain the poor debonding performance of the un-taped specimen. Figure C.31 illustrates the autopsy of the specimen with taped sheathing, while Figure C.32 shows the autopsy of the specimen with un-taped sheathing.

The autopsy of the specimen with taped, split sheathing as shown in Figure C.31 is in stark contrast with the autopsy of the

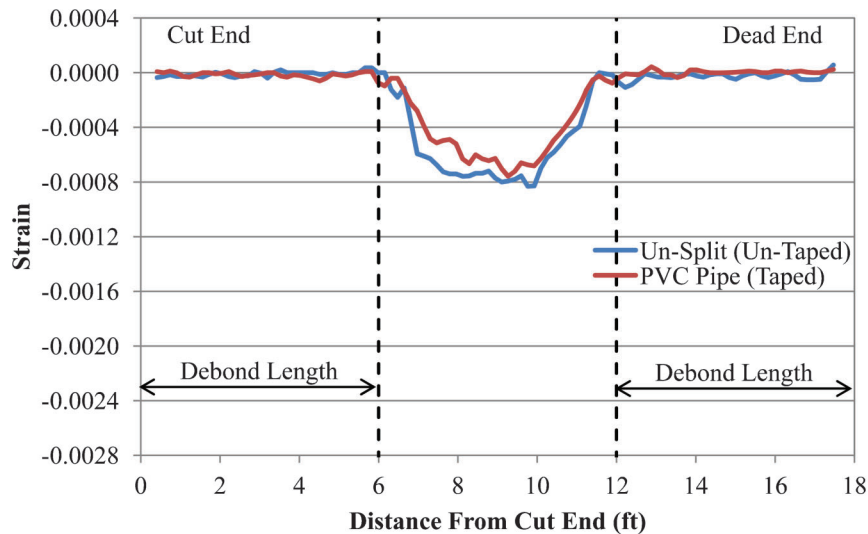


Figure C.25 Un-split (un-taped) sheathing effectiveness.

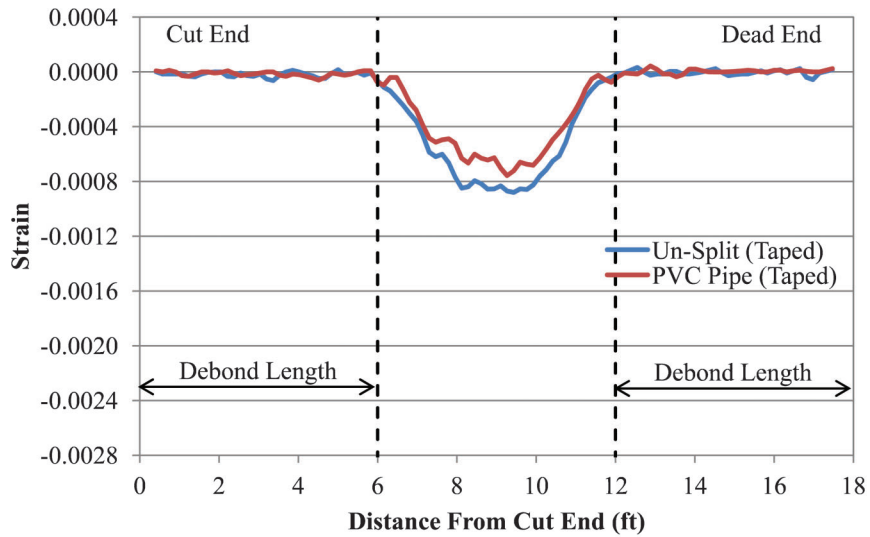


Figure C.26 Un-split (taped) sheathing effectiveness.

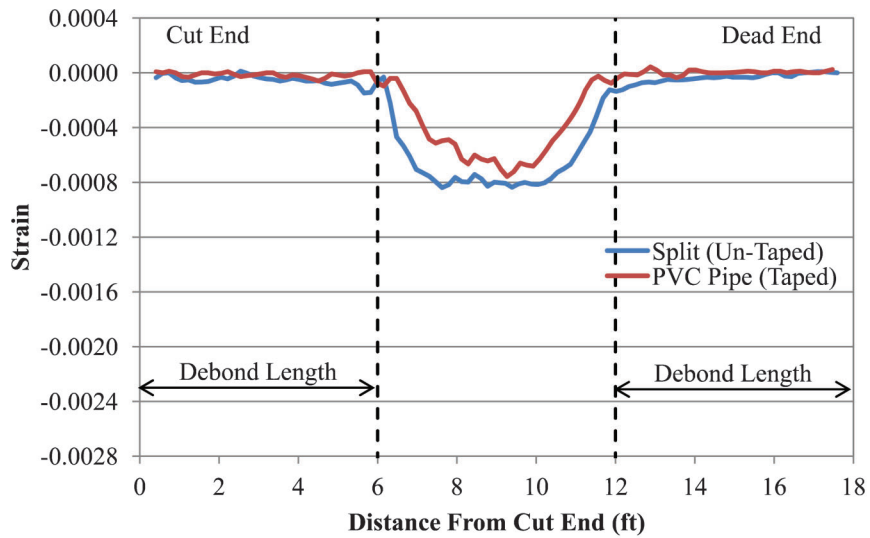


Figure C.27 Split (un-taped) sheathing effectiveness.

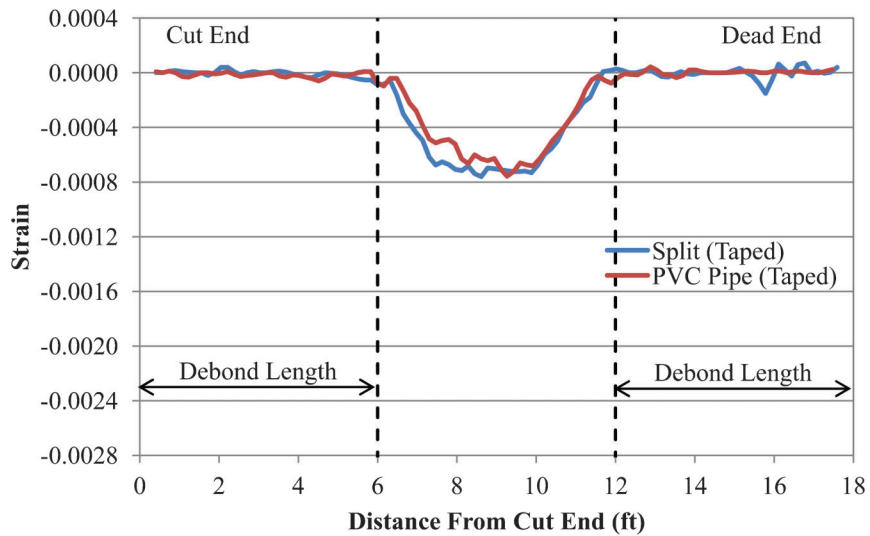


Figure C.28 Split (taped) sheathing effectiveness.



Figure C.29 Autopsy of un-split sheathing with taped ends.

specimen with un-taped, split sheathing illustrated in Figure C.32. It was immediately apparent that there was no paste infiltration when the specimen with taped sheathing was cut open. No paste fell out when the sheathing was peeled open. In addition, as illustrated in Figure C.31, the strands in the debonded region were completely clean, containing no sign of paste residue. The specimen without tape, on the other hand, contained obvious evidence of paste infiltration (Figure C.32). As shown in Figure C.33, paste infiltration occurred along the entire debonded region as evidenced by the distinct seam along the length where split (un-taped) sheathing was located.

A distinct point was observed where the paste was no longer solid within the sheathing as shown in Figure C.34. Solid paste is present to the left while no paste is visible to the right. Although there was paste along the entire length, it fell out of the sheathing to the right of the line in Figure C.34 once the specimen was opened. The photograph in Figure C.32 was taken immediately adjacent to the end of the debonded region, while the photograph in Figure C.34 was taken approximately 18 in. from the end of the debonded region. Both photographs show the same strand. This length of solid paste from the end of the debonded region (18 in.)

is in close agreement with the strain profiles for the specimen with un-taped, split sheathing (Figure C.18). As shown, compression strains developed approximately 18–24 in. from the end of debonding.

Although paste infiltration was observed throughout the debond length, only about 2 ft of bonding at the end of the debonded region is evident in the strain profile of Figure C.18. One likely explanation for this phenomenon is that the strand, when cut, released significant energy that was partially absorbed by the paste in the sheathing. As the stand tension was released, it is likely that the tension was transferred directly to the paste, breaking up along the length, until it was slowed to the point of not incurring damage to the paste at the end of the debonded region.

C.7.3 Un-Split vs. Split Sheathing

To illustrate the difference in debonding effectiveness between un-split and split sheathing, two classifications are made. First, and most obvious, is the distinction between un-split and split



Figure C.30 Autopsy of un-split sheathing without taped ends.



Figure C.31 Autopsy of taped, split sheathing.



Figure C.32 Autopsy of un-taped, split sheathing—solid paste.

sheathing. Second, is the distinction between un-taped and taped sheathing. Figure C.35 illustrates the difference between un-taped, un-split sheathing and un-taped, split sheathing. The difference between taped, un-split sheathing and taped, split sheathing is shown in Figure C.36.

The obvious difference in the strain profiles of Figure C.35 is the divergence from zero of the specimen with un-taped, split sheathing. Not only does this specimen's strain profile diverge from zero, but it also diverges from the other specimen's (un-taped, un-split) strain profile. Figure C.35 illustrates that the un-taped, un-split sheathing is noticeably more effective, in terms of debonding performance, than the specimen with un-taped, split sheathing. Therefore, given a choice between un-split and split sheathing, un-split sheathing is preferable.

There are no obvious differences in the strain profiles of Figure C.36 when comparing taped, un-split sheathing to taped, split sheathing. In fact, both are effective debonding systems as

evidenced by the strain profile comparisons against the PVC pipe debonded specimen as shown in Figure C.26 and Figure C.28. While paste was discovered in both un-taped specimens (Figure C.37), no paste infiltration was found in either of the taped specimens (Figure C.38). Considering the strain behavior shown in Figure C.36, and the fact that no paste was observed inside the sheathing of both specimens with taped sheathing, it appears that a successful method of ensuring effective debonding is to prevent paste infiltration by sealing all of the openings in the sheathing. Therefore, it is recommended to seal all openings in the debond sheathing with a flexible adhesive tape.

C.8 CONCLUSIONS

Six concentrically prestressed concrete prisms were constructed to evaluate the effectiveness of commercially available debond sheathing using different sealing techniques. The following conclusions are made based on the experimental program:

1. The majority of the specimens performed well in terms of debonding effectiveness. However, it was discovered that paste infiltration as a result of openings in the sheathing reduced the effectiveness of the un-taped, split sheathing allowing for force transfer inside the debonded region. The impact of paste infiltration on debonding effectiveness also depends on the length over which the paste covered the strand inside the sheathing. It was determined that un-taped, split sheathing performed the worst due to the fact that paste infiltrated along the entire length of the sheathing.
2. No noticeable difference was observed in the transfer lengths at the cut ends and the dead ends. All transfer lengths were observed to be approximately 2 ft (48d_b).
3. The transfer lengths remained unchanged over time. Measurements were taken at transfer, 14 days after the cast, and 28 days after the cast.

C.9 RECOMMENDATIONS

Either split or un-split sheathing can be effectively used to provide debonding of prestressing strand. To be effective, however, all openings including the slit and ends must be sealed. A flexible adhesive tape, such as duct tape, can be used for this purpose.



Figure C.33 Autopsy of un-taped, split sheathing—paste infiltration seam.



Figure C.34 Autopsy of un-taped, split sheathing—end of solid paste.

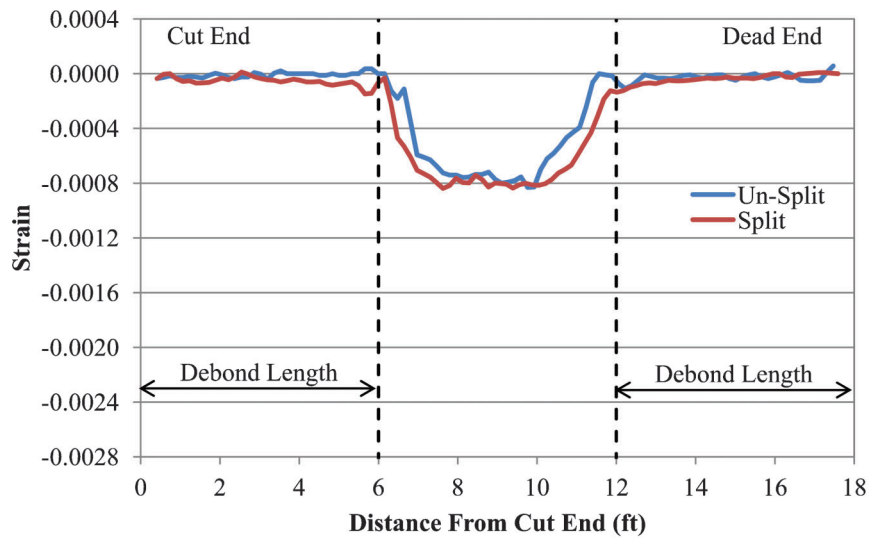


Figure C.35 Un-split vs. split sheathing (un-taped).

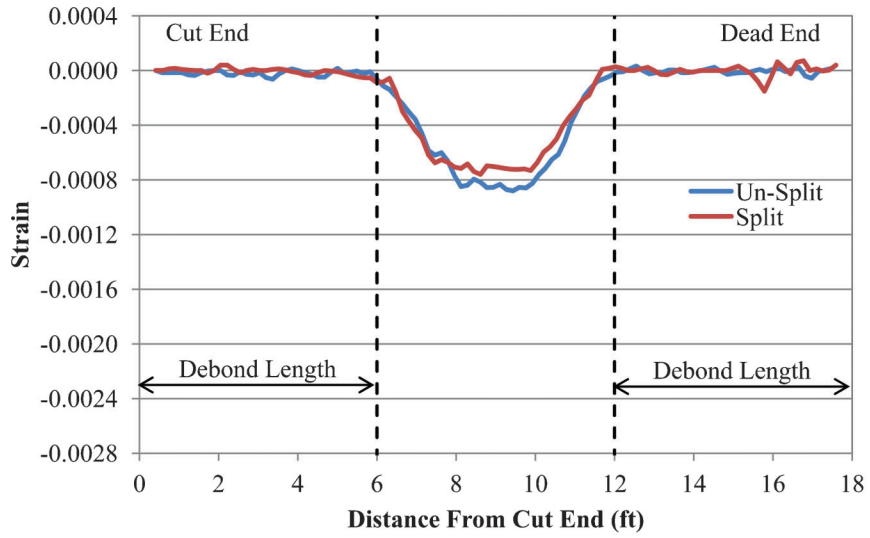


Figure C.36 Un-split vs. split sheathing (taped).

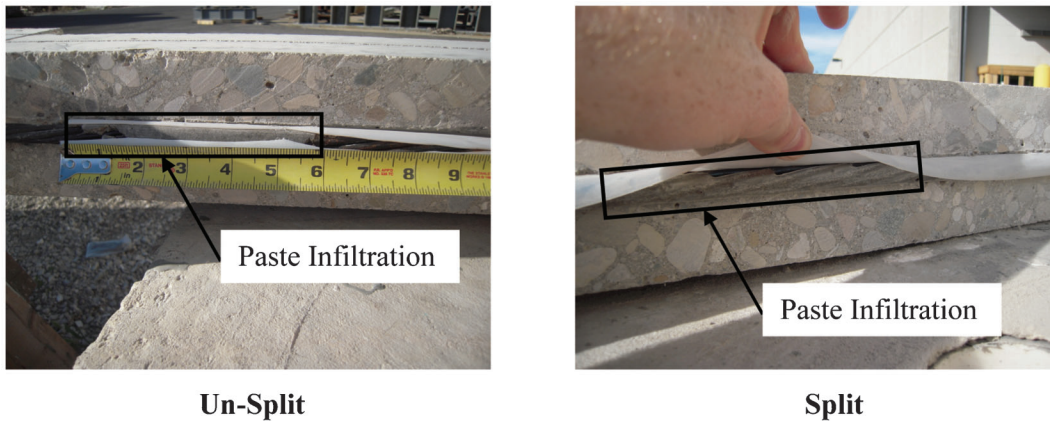


Figure C.37 Autopsy of un-taped sheathing.



Figure C.38 Autopsy of taped sheathing.

APPENDIX D. INFLUENCE OF STRAND DEBONDING ON SHEAR STRENGTH

D.1 INTRODUCTION

To evaluate the influence of strand debonding on shear strength, an experimental investigation consisting of fourteen large-scale pretensioned concrete beams with different percentages of debonded strand was conducted. The experimental program was divided into three primary series. Each series included specimens containing 0, 25, 50, and 75% debonded strand. These specimens were designed to evaluate the influence of percentage of debonded strand on shear strength. It was hypothesized that strand debonding would have an effect on shear strength only in the debonded region due to the reduction of prestressing force and longitudinal reinforcement stiffness.

In addition to these tests, two additional specimens were tested. One of these specimens was designed to evaluate the influence of transverse reinforcement on the shear strength of a beam with 50% debonded strand. The other specimen was a duplicate of one of the beams with 75% debonded strand. This specimen was retested to gain insight regarding the influence of prestress transfer delays on shear strength.

All fourteen specimens were designed to have the same dimensions, concrete strength, prestressing force (in fully bonded region), and prestressing eccentricity. This chapter discusses the analysis, design, materials, construction, testing, and results of the experimental program.

D.2 ANALYTICAL EVALUATION

A computer program, written in Visual Basic with output in Excel, was developed to assist in the design of the specimens. The program was developed to analyze the behavior of reinforced and pretensioned concrete beams (rectangular beams, I-beams, and U-beams) and in particular the flexural and shear behavior of structural concrete beams (with or without strand debonding). The main functions of the program include a moment-curvature analysis as well as a shear strength analysis. Additional features include: material model options for concrete and mild reinforcement, beam cross section schematic, moment-curvature checks at ultimate, and the distribution of web-shear strengths through the beam depth. The program's material models, variables, and operating procedure are discussed in the following sections.

D.2.1 Material Models

The following material models were selected due to their general acceptance among the engineering community.

D.2.1.1 Concrete Models

Two different concrete material models were considered. The first concrete model is the Hognestad stress distribution provided by Equation D.1. This model is recommended for concrete with compressive strengths up to 6,000 psi (Wight & MacGregor, 2009). It should be noted that ε_0 was selected such that the stress-strain curve intersects with the secant modulus (using E_c) at $0.5f'_c$.

$$f_c = f'_c \left[\frac{2\varepsilon_c}{\varepsilon_0} - \left(\frac{\varepsilon_c}{\varepsilon_0} \right)^2 \right] \quad (D.1)$$

where:

ε_c : strain in concrete

ε_0 : strain in concrete at peak strength, Eq. D.2

f_c : stress in concrete, psi

f'_c : concrete compressive strength, psi

$$\varepsilon_0 = 1.71 \left(\frac{f'_c}{E_c} \right) \quad (D.2)$$

The second concrete model is the stress-strain relationship developed by Thorenfeldt, Tomaszewics, and Jensen (1987) (Equation D.3) and will be referred to as the Thorenfeldt model. This model is applicable for concrete compressive strengths up to 18,000 psi (Wight & MacGregor, 2009). Due to the relatively high compressive strengths of the specimens (approximately 7,000 psi), the Thorenfeldt model was used throughout this study. A comparison of stress-strain curves for 7,000 psi concrete is presented for both concrete models in Figure D.1.

$$f_c = f'_c \left[\frac{n \left(\frac{\varepsilon_c}{\varepsilon_0} \right)}{n-1 + \left(\frac{\varepsilon_c}{\varepsilon_0} \right)^{nk}} \right] \quad (D.3)$$

where:

ε_0 : strain in concrete at peak strength, Eq. D.4

k : non-dimensional constant, Eq. D.5

n : non-dimensional constant, Eq. D.6

$$\varepsilon_0 = \frac{n}{n-1} \left(\frac{f'_c}{E_c} \right) \quad (D.4)$$

$$k = \begin{cases} 1 & \frac{\varepsilon_c}{\varepsilon_0} \leq 1 \\ 0.67 + \frac{f'_c}{9000} \frac{\varepsilon_c}{\varepsilon_0} & \frac{\varepsilon_c}{\varepsilon_0} > 1 \end{cases} \quad (D.5)$$

$$n = 0.8 + \frac{f'_c}{2500} \quad (D.6)$$

The stress-strain relationship is nearly identical in the elastic range of behavior for both concrete material models (Figure D.1). However, the peak stress is reached in the Thorenfeldt curve before the Hognestad curve. In addition, the descending portion (strain softening) of the Hognestad curve is abbreviated in comparison to the Thorenfeldt curve. Finally, the descending portion of the Thorenfeldt curve is more abrupt which more closely represents the actual behavior of high strength concrete (compressive strengths greater than 6,000 psi).

Regardless of model selection, the concrete modulus of elasticity, E_c (in psi), is calculated as $57,000\sqrt{f'_c}$ (AASHTO Section C5.4.2.4 and ACI 318-11 Section 8.5.1), and the modulus of rupture, f_r (in psi), is assumed to be $7.5\sqrt{f'_c}$ (AASHTO Section 5.4.2.6 and ACI 318-11 Section 9.5.2.3). It should be noted that f'_c used to calculate the modulus of elasticity, E_c , and the modulus of rupture, f_r , is in psi units.

D.2.1.2 Mild Steel Longitudinal Reinforcement Models

Two models for the mild steel longitudinal reinforcement were also considered. The first is Sargin's model (1971) which includes a yield plateau followed by strain hardening. The expression used is provided by Equation D.7. This model follows the general trend of traditional (Grade 60) mild steel reinforcement. The four parameters used to characterize the stress-strain relationship of the mild steel are calculated with regression equations (Equation D.8 through Equation D.11) developed by Wang, Shah, and Naaman (1978).

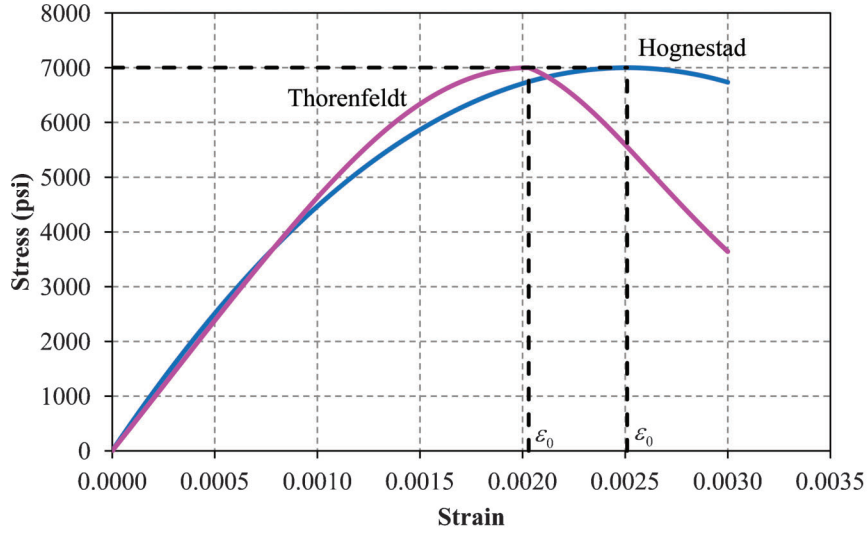


Figure D.1 Stress-strain comparison for concrete in compression.

$$f_s = \begin{cases} \varepsilon_s E_s & \varepsilon_s \leq \varepsilon_y \\ f_y & \varepsilon_y < \varepsilon_s \leq \varepsilon_{sh} \\ f_y + E_{sh}(\varepsilon_s - \varepsilon_{sh}) \left[1 - \left(\frac{E_{sh}(\varepsilon_s - \varepsilon_{sh})}{4(f_{su} - f_y)} \right) \right] & \varepsilon_{sh} < \varepsilon_s \leq \varepsilon_{su} \end{cases} \quad (D.7)$$

where:

ε_{sh} : strain in mild steel at onset of strain hardening, Eq. D.8

ε_{su} : ultimate tensile strain of mild steel, psi, Eq. D.9

E_{sh} : shape factor for strain hardening portion, psi, Eq. D.10

f_{su} : ultimate tensile strength of mild steel, psi, Eq. D.11

$$\varepsilon_{sh} = -0.00009 \left(\frac{f_y}{1000} \right) + 0.0145 \quad (D.8)$$

$$\varepsilon_{su} = -0.00023 \left(\frac{f_y}{1000} \right) + 0.0867 \quad (D.9)$$

$$E_{sh} = \left[-9.44 \left(\frac{f_y}{1000} \right) + 1788 \right] 1000 \quad (D.10)$$

$$f_{su} = \left[0.523 \left(\frac{f_y}{1000} \right) + 73.2 \right] 1000 \quad (D.11)$$

The second is the elastic, perfectly plastic model provided by Equation D.12. This model is simple and conservative for design purposes, but may not capture behavior as well as other models that describe the full range of steel behavior. Both models assume the modulus of elasticity of mild steel to be 29,000,000 psi. While a general elastic-plastic model does not specify the ultimate tensile strain, the ultimate strain from Equation D.9 was used for consistency of the models. The elastic-plastic model was used throughout this study due to the intentions of maintaining the longitudinal mild steel stresses within the elastic range. Figure D.2 illustrates the stress-strain curves for both mild steel material models.

$$f_s = \begin{cases} \varepsilon_s E_s & \varepsilon_s \leq \varepsilon_y \\ f_y & \varepsilon_y < \varepsilon_s \leq \varepsilon_{su} \end{cases} \quad (D.12)$$

where:

ε_s : strain in mild steel

ε_y : yield strain of mild steel, Eq. D.13

f_s : stress in mild steel, psi

f_y : yield stress of mild steel, psi

$$\varepsilon_y = \frac{f_y}{E_s} \quad (D.13)$$

The stress-strain relationships shown in Figure D.2 are identical up to the onset of strain hardening (captured by the Sargin (1971) model). The difference in the two curves is clearly evident after the onset of strain hardening, ε_{sh} . At this point, the stress in the Sargin curve quickly begins increasing towards the ultimate stress while the stress in the elastic-plastic curve remains constant (at the yield stress). Both curves continue this trend until the ultimate tensile strain, ε_{su} , is reached.

D.2.1.3 Prestressing Steel Model

Although there are several available models for prestressing steel, the one selected for use in this study is the widely accepted PCI Design Handbook expression provided by Equation D.14. It should be noted that this equation is only intended for Grade 270, uncoated, seven-wire, low relaxation strand. This model assumes the modulus of elasticity of prestressing steel to be 28,500,000 psi and the strain at ultimate to be 0.05. The stress-strain relationship for Grade 270, seven-wire, low relaxation strand is illustrated in Figure D.3. All prestressing losses were calculated in accordance with the procedure in the PCI Design Handbook (2004, Section 4.7.3).

$$f_{ps} = \begin{cases} \varepsilon_{ps} E_{ps} & \varepsilon_{ps} \leq \varepsilon_{y,ps} \\ f_{pu} - \left(\frac{40}{\varepsilon_{ps} - 0.007} \right) & \varepsilon_{ps} > \varepsilon_{y,ps} \end{cases} \quad (D.14)$$

where:

ε_{ps} : strain in prestressing steel

$\varepsilon_{y,ps}$: yield strain of prestressing steel, 0.0086

f_{ps} : stress in prestressing steel, psi

f_{pu} : ultimate tensile strength of prestressing steel, 270,000 psi

D.2.2 Variables

The computer program was written to be flexible to allow any structural concrete rectangular beam, I-beam, or U-beam to be analyzed. Variables considered are listed below.

- Cross Section Dimensions
- Beam Span

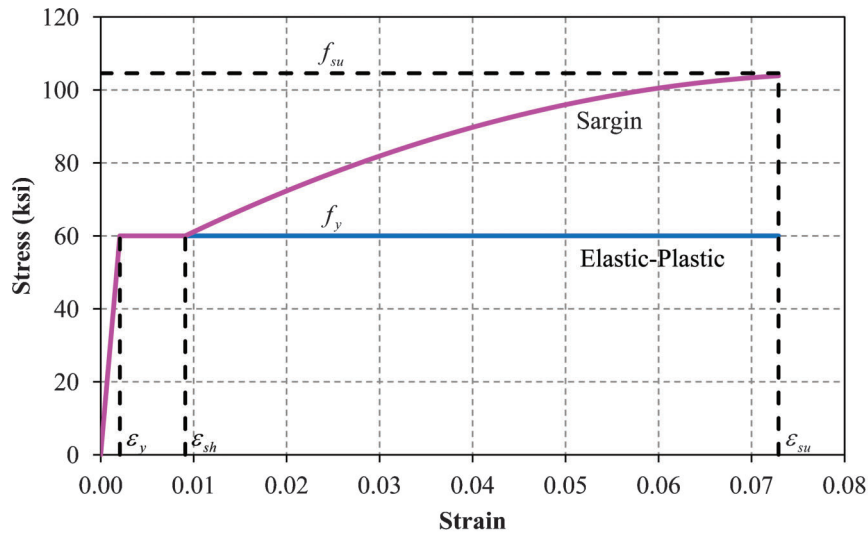


Figure D.2 Stress-strain comparison for mild steel in tension.

- Shear Span
- Optional Deck
- Concrete Strength
- Initial Prestress
- Effective Prestress
- Prestress Loss Variables
- Number of Strands
- Position of Strands
- Diameter of Strands
- Number of Debonded Strands
- Position of Debonded Strands
- Debond Length
- Number of Mild Bars
- Position of Mild Bars
- Diameter of Mild Bars
- Spacing of Stirrups
- Location of Stirrups
- Diameter of Stirrups

D.2.3 Procedure

D.2.3.1 Moment-Curvature Analysis

Moment-curvature analysis provides the foundation of the analytical approach. This analysis is accomplished by cutting the cross section into discrete slices as illustrated in Figure D.4 (of equal thickness, dy), and calculating the area of each material in that slice (concrete, mild steel, prestressing steel).

After section properties and stresses due to prestressing are calculated, a moment-curvature analysis is performed. First, provided an extreme fiber compression strain, a trial neutral axis is initially selected as one quarter of the section depth. Using the extreme fiber compression strain, trial neutral axis, selected material models, and the assumption that plane sections remain plane, the stresses are calculated in each slice for each material (Figure D.5). Then the forces are calculated from the stresses for

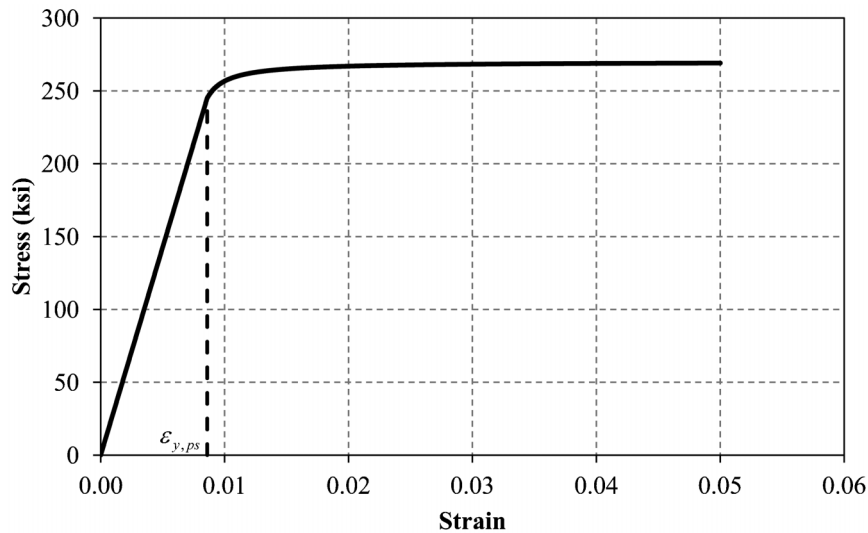


Figure D.3 Stress-strain comparison for Grade 270 prestressing steel in tension.

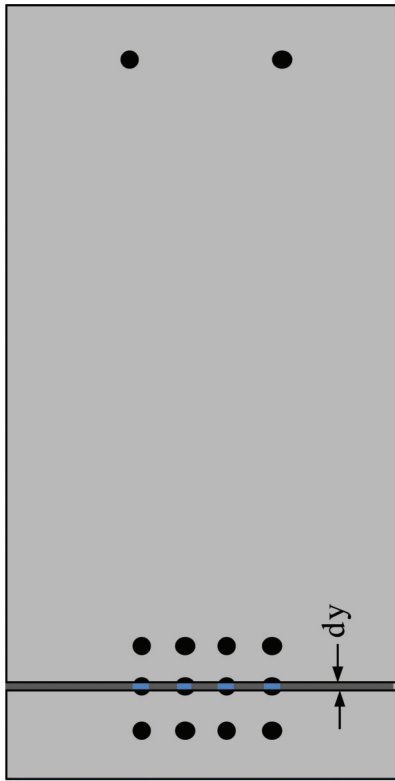


Figure D.4 Discretization of beam section.

each material present in the given slice. Once the forces in each slice are determined, force equilibrium is checked using Equation D.15 through Equation D.17. If force equilibrium is satisfied (within ± 1 kip), the process is repeated with a larger extreme fiber compression strain. However, if force equilibrium is not achieved, the neutral axis is adjusted accordingly until force equilibrium is satisfied.

$$\sum C = C_c + C_s \quad (D.15)$$

$$\sum T = T_{ps,1} + T_{ps,2} + T_{ps,3} \quad (D.16)$$

$$\sum C \cong \sum T \quad (D.17)$$

where:

C_c : resultant compressive force in concrete, lbs

C_s : compressive force in mild steel, lbs

$\sum C$: summation of compressive forces, lbs

$T_{ps,1}$: tensile force in bottom row of prestressing steel strand, lbs

$T_{ps,2}$: tensile force in middle row of prestressing steel strand, lbs

$T_{ps,3}$: tensile force in top row of prestressing steel strand, lbs

$\sum T$: summation of tensile forces in prestressing steel strand, lbs

The internal moment is then calculated from the forces multiplied by the moment arms, which are calculated as the distances from the center of each slice to the neutral axis as illustrated in Figure D.5. Moment equilibrium is satisfied when the internal moment is equal to the external moment necessary to create that particular stress state in the beam (Equation D.18). This process is repeated until the ultimate compressive strain in the concrete is reached (0.003), or until the tension steel ruptures, whichever occurs first.

$$M = T_{ps,1}(d_{ps,1}) + T_{ps,2}(d_{ps,2}) + T_{ps,3}(d_{ps,3}) + C_c(d_c) + C_s(d_s) \quad (D.18)$$

where:

d_c : distance from neutral axis to resultant force in concrete, in.

$d_{ps,1}$: distance from neutral axis to force in bottom row of strand, in.

$d_{ps,2}$: distance from neutral axis to force in middle row of strand, in.

$d_{ps,3}$: distance from neutral axis to force in top row of strand, in.

d_s : distance from neutral axis to compressive force in mild steel, in.

If there is a debonded region, two moment-curvature analyses are performed. The first moment-curvature analysis is for the fully bonded region of the beam. This analysis is used for sections in the region of the beam where all strands are bonded. The second analysis covers sections in the end regions of the beam, where debond sheathing is placed.

The concrete compressive stresses are calculated using one of the two models provided in Section D.2.1.1. Concrete tensile stresses are calculated using straight line theory, with the slope equal to the modulus of elasticity of concrete, up to the modulus of rupture, $f_r = 7.5\sqrt{f'_c}$.

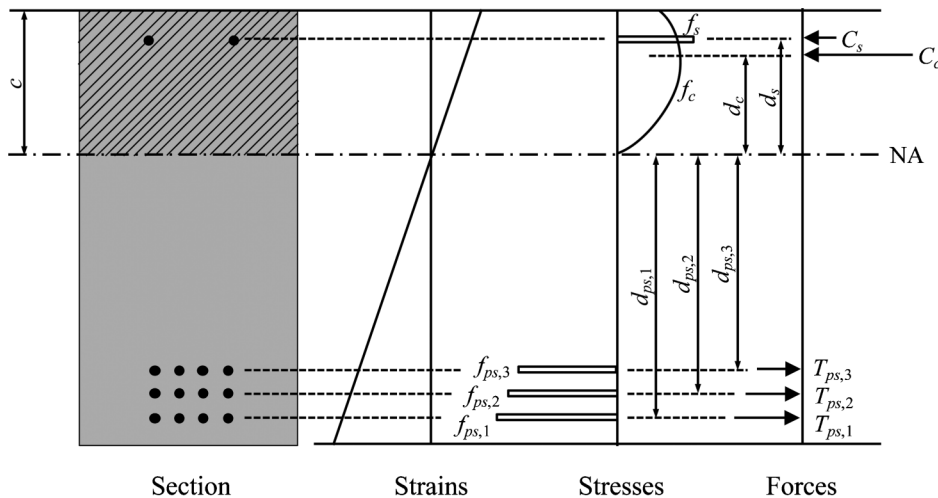


Figure D.5 Internal forces in prestressed beam.

D.2.3.2 Shear Analysis

After the moment-curvature analysis is completed, the shear strength analysis commences. Shear strengths are calculated using three approaches: a shear model, the ACI 318 approach, and the AASHTO LRFD approach.

D.2.3.2.1 Shear model The concrete contribution to shear strength is taken to be the web-shear strength (V_{cw}) in an uncracked section and is taken as the flexure-shear strength (V_{ci}) in a cracked section. Flexure-shear strength is calculated using Equation D.19.

$$V_{ci} = 5\sqrt{f'_c}A_{eff} \quad (D.19)$$

This equation was selected due to its capability to analyze most slender structural concrete beams by directly relating the flexure-shear strength, V_{ci} , to the compressive area, A_{eff} , at each section. Therefore, the flexure-shear strength is controlled by the neutral axis (at each section) as well as the compressive strength of the concrete. The neutral axis is governed by the longitudinal reinforcement stiffness, prestress force, concrete strength, and section geometry. Accounting for the reduced prestress force and longitudinal reinforcement stiffness in debonded regions made this equation an excellent shear model for this study.

The original form of this equation (Equation 1.1) was developed by Tureyen and Frosch (2003) as an alternative method of calculating the concrete contribution to shear strength in slender reinforced concrete beams. Wolf and Frosch (2007) showed that the same equation can be used for prestressed beams as well. Tureyen, Wolf, and Frosch (2006) modified the equation to include A_{eff} as the effective shear area in the compression zone to account for flanged sections as well as other cross sections that are not rectangular. In addition, Saqan and Frosch (2009) presented the influence of flexural reinforcement on the shear strength of prestressed concrete beams. One of the major findings from the Saqan and Frosch (2009) study is that the longitudinal reinforcement stiffness controlled the shear strength more than any other factor. The dependence of the longitudinal reinforcement stiffness is recognized by Equation D.19 through the neutral axis (compressive area). The variables in Saqan and Frosch's testing program included the area of prestressing steel and mild longitudinal reinforcement, as well as the prestressing stress.

The effective shear area in the compression zone (A_{eff}) is calculated using the shear funnel approach developed by Tureyen et al. (2006). This effective shear area is computed for each neutral axis depth from the moment-curvature analysis. Typically, the angle of the shear funnel in a flanged section with respect to the horizontal is assumed to be 45° as shown in Figure D.6. However, this angle can be adjusted to any value.

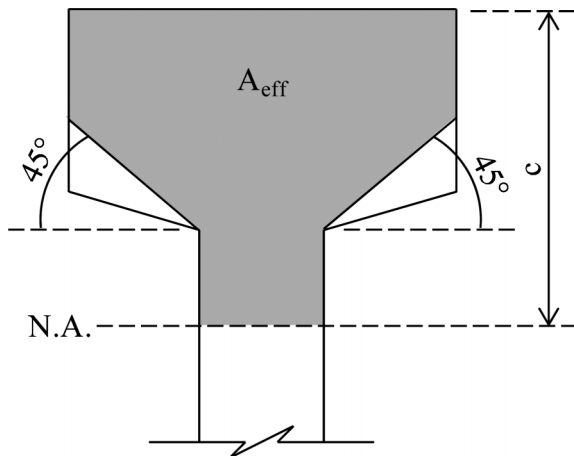


Figure D.6 Effective area of flanged section.

The web-shear strength is calculated using the alternative method in ACI 318-11 Section 11.3.3.2 in which a principal stress analysis is conducted. A principal stress analysis was chosen over the simplified method in ACI 318 Section 11.3.3.2 and AASHTO Section 5.8.3.4.3 to more accurately estimate the web-shear capacity of the specimens. A concrete tensile strength of $6\sqrt{f'_c}$ is used instead of the design value of $4\sqrt{f'_c}$ as recommended in ACI 318 to more closely represent actual beam behavior. It should be noted that the web-shear strength is only applicable in uncracked sections.

The distribution of web-shear strengths through the beam depth is calculated. This distribution illustrates the weakest location, where a web-shear crack is most likely to initiate within the section. Figure D.7 shows an example of a web-shear strength distribution at the critical section of one of the I-beams tested as part of this research program. The web-shear strengths are cut off at 400 kips at the bottom and top flanges for purposes of clarity. However, the strengths continue to increase, approaching infinite web-shear strength, at the top and bottom fibers of the beam.

The steel contribution to shear capacity (V_s) is calculated the same way as the ACI approach in ACI 318-11 Section 11.4.7.2. It should be noted that this calculation assumes a smeared stirrup contribution where fractions of a stirrup are considered in the calculation.

The shear strength is calculated over the shear span of the beam. These shear strengths are then compared to the shear forces due to the dead load and applied load. If at any load stage, and at any location, the applied shear force (including shear from dead load) exceeds the shear strength, the beam has reached analytical failure. However, if no shear failure occurs before the flexural capacity is reached, the beam is considered to fail in flexure.

D.2.3.2.2 Shear analysis with ACI 318 The concrete contribution to shear strength, according to ACI 318, is taken to be the lesser of flexure-shear strength (V_{ci}) and web-shear strength (V_{cw}), regardless of whether the section cracked or not. The flexure-shear strength equation (ACI 318-11 Section 11.3.3.1) is given by Equation D.20 and is based on experimental evidence (Zwoyer & Siess, 1954; Sozen, Zwoyer, & Siess, 1959). The web-

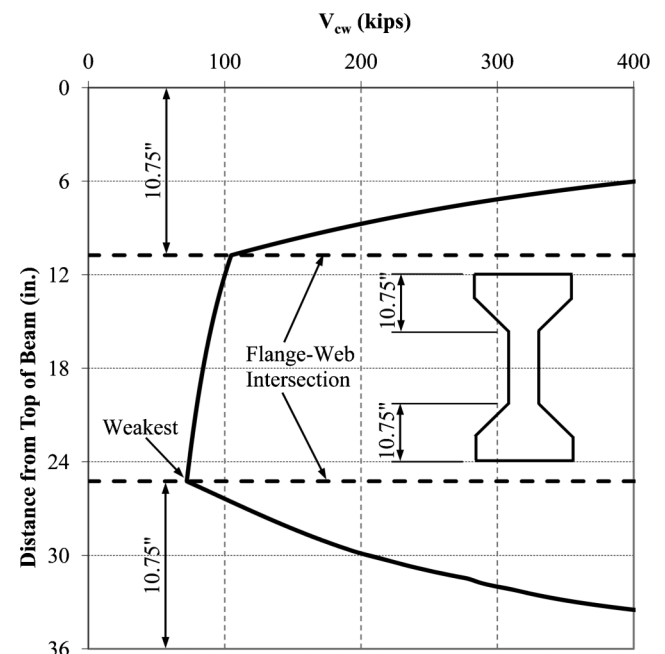


Figure D.7 Distribution of web-shear strengths through depth of I-beam.

shear strength is provided by Equation D.22. The contribution of transverse reinforcement to shear strength, V_s , is accounted for by ACI 318 Section 11.4.7.2 using Equation D.24. It is important to note that these ACI equations (Equation D.20 through Equation D.24) calculate shear strengths using parameters in lb-in. units (lb, psi, in.).

$$V_{ci} = 0.6\sqrt{f'_c}b_wd_p + V_d + \frac{V_iM_{cre}}{M_{max}} \geq 1.7\sqrt{f'_c}b_wd \quad (D.20)$$

where:

b_w : web width, in.

d : distance from extreme compressive fiber to centroid of reinforcement, in.

d_p : distance from extreme compressive fiber to centroid of strands, in.

M_{cre} : cracking moment due to externally applied loads, lb-in., Eq. D.21

M_{max} : maximum factored moment due to externally applied loads, lb-in.

V_d : shear force at section due to unfactored dead load, lb

V_i : factored shear force at section due to externally applied loads, lb

$$M_{cre} = \frac{I}{y_t} \left(6\sqrt{f'_c} + f_{pe} - f_d \right) \quad (D.21)$$

where:

f_d : stress at tension face due to unfactored dead loads, psi

f_{pe} : compressive stress in concrete due to effective prestress only (after allowance for all prestress losses) at extreme fiber of section where tensile stress is caused by externally applied loads, psi

I : moment of inertia of gross section, in.⁴

y_t : distance from centroidal axis of gross section to tension face, in.

$$V_{cw} = \left(3.5\sqrt{f'_c} + 0.30f_{pc} \right) b_wd_p + V_p \quad (D.22)$$

where:

f_{pc} : compressive stress in concrete (after allowance for all prestress losses) at centroid of cross section resisting externally applied loads, psi

V_p : vertical component of effective prestress force, lb

$$V_c = \left\{ \begin{array}{ll} V_{cw} & V_{cw} < V_{ci} \\ V_{ci} & V_{ci} < V_{cw} \end{array} \right\} \leq 5\sqrt{f'_c}b_wd \quad (D.23)$$

$$V_s = \frac{A_vf_ytd}{s} \leq 8\sqrt{f'_c}b_wd \quad (D.24)$$

where:

A_v : area of transverse reinforcement within a distance s , in.²

f_y : yield strength of transverse reinforcement, psi

s : spacing of transverse reinforcement, in.

D.2.3.2.3 Shear analysis with AASHTO Similar to the ACI approach, the concrete contribution to shear strength according to AASHTO is taken to be the lesser of the flexure-shear strength (V_{ci}) and web-shear strength (V_{cw}), regardless of whether the section is cracked or not. The simplified flexure-shear strength equation (AASHTO Section 5.8.3.4.3) is given by Equation D.25, and the web-shear strength is provided by Equation D.27. The contribution of transverse reinforcement to shear strength, V_s , is accounted for by AASHTO Section 5.8.3.3 using Equation D.28. It is important to note that these AASHTO equations (Equation D.25 through Equation D.30) calculate shear strengths using parameters in kip-in. units (kip, ksi, in.). These equations are essentially identical to the ACI 318 equations with the following exceptions. First, the coefficients were adjusted because ACI uses lb-in. units (lb, psi, in.). Second, the effective depth is defined differently. Finally, the steel contribution to shear

capacity (V_s) in the AASHTO approach (Equation D.28) includes the angle of the compressive stresses (θ).

$$V_{ci} = 0.02\sqrt{f'_c}b_vd_v + V_d + \frac{V_iM_{cre}}{M_{max}} \geq 0.06\sqrt{f'_c}b_vd_v \quad (D.25)$$

where:

b_v : minimum web width measured parallel to neutral axis, in.

d_v : distance between tensile and compressive resultant forces, in.

$$M_{cre} = S_c \left(f_r + f_{pe} - \frac{M_{dnc}}{S_{nc}} \right) \quad (D.26)$$

where:

f_r : modulus of rupture of concrete, psi

M_{dnc} : total unfactored dead load moment acting on non-composite section, lb-in.

S_c : section modulus for extreme fiber of composite section where tensile stress is caused by externally applied loads, in.³

S_{nc} : section modulus for extreme fiber of noncomposite section where tensile stress is caused by externally applied loads, in.³

$$V_{cw} = \left(0.06\sqrt{f'_c} + 0.30f_{pc} \right) b_vd_v + V_p \quad (D.27)$$

$$V_s = \frac{A_vf_yd_v \cot \theta}{s} \quad (D.28)$$

where:

θ : angle of diagonal compressive stresses from horizontal, deg

$\cot \theta$: cotangent of θ , Eq. D.29

$$\cot \theta = \left\{ \begin{array}{ll} 1 & V_{ci} < V_{cw} \\ 1.0 + 3 \left(\frac{f_{pc}}{\sqrt{f'_c}} \right) \leq 1.8 & V_{ci} > V_{cw} \end{array} \right\} \quad (D.29)$$

$$V_n = V_c + V_s \leq 0.25\sqrt{f'_c}b_vd_v \quad (D.30)$$

The AASHTO approach, like the ACI approach, includes a lower limit on V_{ci} . There is an upper limit for the total shear capacity (V_n) in AASHTO while ACI applies upper limits to the concrete contribution (V_c) and the steel contribution (V_s).

D.2.3.3 Development Length

Regardless of the type of failure (flexure-shear, web-shear, or flexure) the required development length is calculated using Equation D.31 (AASHTO Section 5.11.4.2 and ACI 318-11 Section 12.9.1), and compared to the available embedment length. The first term in Equation D.31 refers to the transfer length, and the second term accounts for the additional length necessary to develop stresses greater than f_{pe} . The development length check is completed for the fully bonded strands at the end of the debonded region, as well as for all of the strands at the section of maximum moment. It should be noted that the required development length was not doubled during the design for debonded strands as required by ACI 318 and AASHTO for design purposes.

$$l_d = \left(\frac{f_{pe}}{3000} \right) d_s + \left(\frac{f_{ps} - f_{pe}}{1000} \right) d_s \quad (D.31)$$

where:

d_s : diameter of prestressing strand, in.

f_{pe} : effective stress in prestressing steel after losses, psi

f_{ps} : stress in prestressing steel, psi

l_d : length required to develop stress in prestressing steel, in.

Transfer lengths are calculated using the first term of Equation D.31 which yields a transfer length of approximately 19 in. for the beams in this testing program. The more conservative estimate

given by AASHTO of $60d_b$, which results in a transfer length of 30 in. for 1/2" strand was not used. The decision to use the first term of Equation D.31 to calculate the transfer length is supported by the strain profiles at transfer shown in Figure D.8 through Figure D.10 (in addition to the relatively low prestressing stress discussed in Section D.3.1.4). These strain profiles were developed from surface strain measurements at the centroid of the prestressing force for six of the specimens in this testing program. The same instrumentation (DEMEC disks) and procedure as described in Chapter 2 were used to obtain these measurements.

The average transfer length of the fully bonded strand observed in the strain profiles of Figure D.8 through Figure D.10 is 16.3 in. (measurements range from 12.8 in. to 20.1 in.). The average transfer length of the debonded strand observed in the strain profiles of Figure D.8 through Figure D.10 is 17.6 in. (measurements range from 13.3 in. to 21.2 in.). All transfer lengths were measured from the free end of the strand (for fully bonded and debonded strand) to the strain plateau (determined by visual inspection). However, due to the 50 mm (1.97 in.) disk spacing, the accuracy of the average transfer length is one disk spacing (1.97 in.). Therefore, the average transfer length (considering the disk spacing) for the fully bonded strand is 14.3 in. to 18.3 in., and the average transfer length for the debonded strand is 15.6 in. to 19.6 in. This suggests that the 19 in. approximation given by Equation D.31 is sufficient for analysis purposes.

It is clear that the average transfer lengths of the debonded strand are nearly identical to the transfer lengths of the fully bonded strand. This is contradictory to ACI 318-11 Fig. R9.3.2.7(b) which suggests that the transfer length (in addition to the entire development length) of debonded strand should be doubled. Furthermore, AASHTO Section 5.11.4.3 and ACI 318-11 Section 12.9.3 state that the development length (which includes the transfer length) of debonded strand is required to be doubled. It is important to note, however, that these transfer length results may not reflect the effects of debonded strand on the development length (particularly the second term of Equation D.31). The strain profiles shown in Figure D.8 through Figure D.10 represent the surface strains measured immediately after transfer. Additional strain profiles (Appendix D-1) were constructed at 28 days after casting to determine if time affected the transfer behavior. These strain profiles clearly illustrate that the transfer length is unaffected by time. Creep and shrinkage, however, contribute to increased strains after transfer. The increased strains illustrated in the strain profiles of Appendix D-1 closely resemble the behavior observed in the strain profiles over time in Chapter 2.

D.3 SPECIMEN DESIGN

The beams were designed to test the hypothesis presented in Section D.1. Several variables controlled the beam designs and include: length of debonded region (relative to shear span), percentage of debonding, prestressing force, prestressing eccentricity, concrete strength, and transverse reinforcement. The primary variables for the testing program are listed in Table D.1. The designs also considered cost, construction, and applicable design provisions. It was decided that the test setup would consist of a simply supported beam with a concentrated load at midspan as shown in Figure D.11. This setup afforded a simplified analysis by providing constant and equal shear in both shear spans.

D.3.1 Series I: Flexure-Shear — Inside Debonded Region (V_{ci} -in)

Beams in this series were designed to fail in flexure-shear inside the debonded region. Therefore, the expectation of the specimens in Series I is that the shear strength would decrease as the percentage of debonded strand increased. The type and location of shear failure, as well as the percentage of debonded strand, is specified within the specimen identifications. The identifier for the 25% debonded specimen, for example, is V_{ci} -in-25, where the "25" specifies the percentage of strand debonded. The " V_{ci} " indicates that the beam is designed for a flexure-shear failure, and the "in" denotes that the shear failure is designed to occur inside the debonded region. A rectangular cross section was selected to isolate debonding as the primary variable so that shape did not complicate the behavior. The rectangular shape also served to simplify both analysis and construction. Design details for Series I specimens are shown in Figure D.12 while transverse reinforcement details are shown in Figure D.13.

D.3.1.1 Length of Debonded Region and Shear Span

The debonded region was designed to be long enough to ensure that at the end of the debonded region, the flexural stresses were sufficiently large and the neutral axis was small enough to initiate a flexure-shear crack at that section. The length of the debonded region was designed to be 7'-6" from the beam ends. Consideration was also given to developing the fully bonded strands assuming failure initiated at the end of the debonded region. The strands were also designed to be fully developed at midspan. The shear span was adjusted to satisfy these criteria.

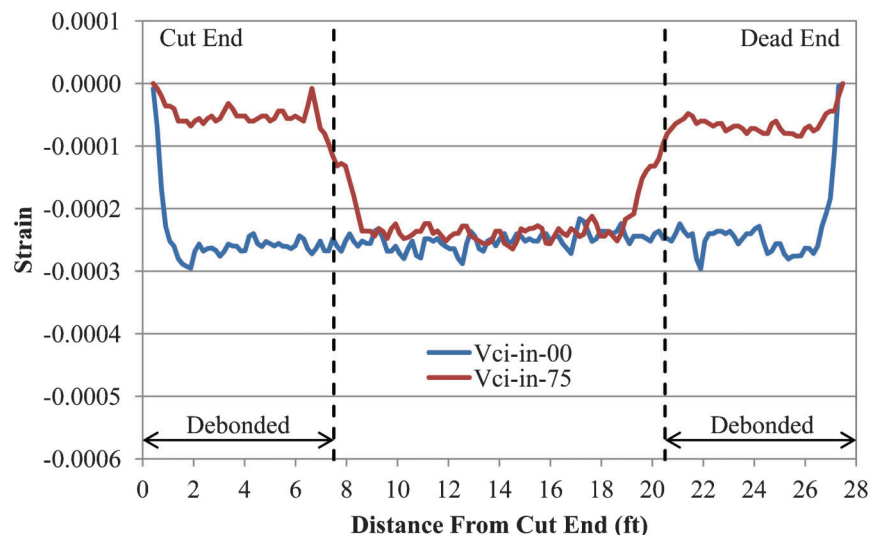


Figure D.8 Strain profiles at transfer for V_{ci} -in-00 and V_{ci} -in-75.

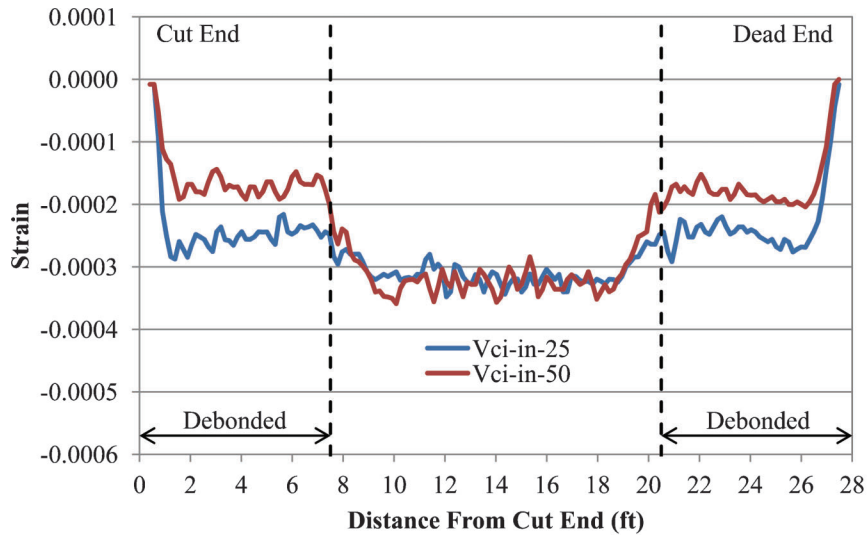


Figure D.9 Strain profiles at transfer for $V_{ci-in-25}$ and $V_{ci-in-50}$.

D.3.1.2 Cross Section

Rectangular cross section dimensions were controlled by several variables. The most important cross section dimension is the beam depth which was governed by the limiting concrete stresses due to prestressing transfer and the a/d ratio. The section depth is directly related to the prestressing eccentricity and the shear span. Ultimately, a depth was selected that promoted the beam to fail in shear while keeping the transfer stresses below allowable levels. Also, it was desired to make the a/d ratio greater than 3.0 to ensure slender beam behavior. The beam width also affects the concrete stresses at transfer as well as the shear capacity, although the degree of effect is much less than the influence of the beam depth. Therefore, the width was primarily selected to result in a 21 beam depth to width ratio. This resulted in an 18 in. wide \times 36 in. deep cross section.

D.3.1.3 Strand Pattern

The strand pattern was selected for two main reasons. First, selecting a strand pattern that would accommodate the desired

percentages of debonding was essential. The goal was to be able to debond 0, 25, 50, and 75% of the total number of strands without changing the effective depth, d . A strand pattern consisting of three rows of four strands met this criterion. This resulted in twelve strands per section. To debond 25%, one strand per row can be debonded. Debonding two strands per row results in the 50% debonded specimen. The 75% debonded specimen requires debonding three strands per row. These twelve strands also provide a wide range of potential prestress forces.

D.3.1.4 Jacking Force

As mentioned in Section D.3.1.3, the twelve strands per section allowed a variety of potential prestress forces. The prestress force was selected based on analytical results and ACI 318-11 provisions. This force needed to be small enough to prevent cracking or crushing at transfer. On the other hand, the force was selected to be large enough to allow the beams to behave like typical prestressed beams. ACI 318-11 requires that the effective prestress force be at least 40% of the total strength of all tension reinforcement (ACI 318-11 Section 11.3.2). In addition, the prestress force was adjusted

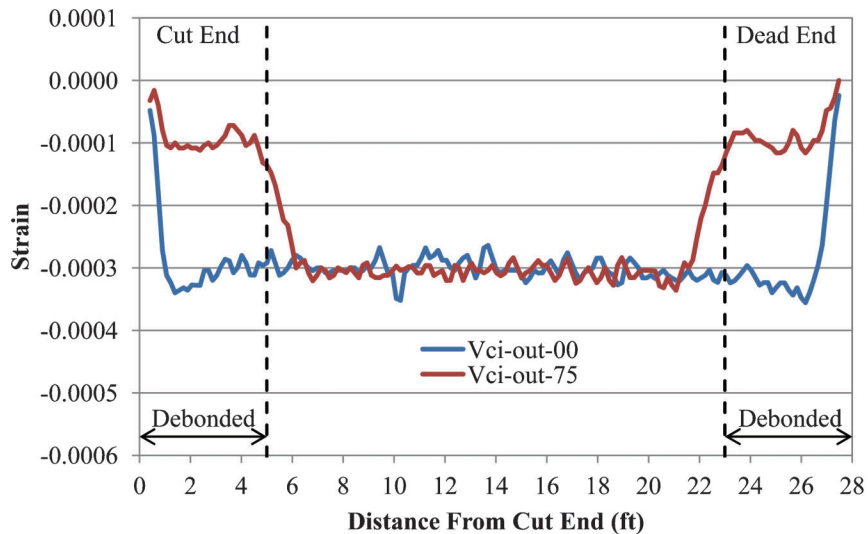


Figure D.10 Strain profiles at transfer for $V_{ci-out-00}$ and $V_{ci-out-75}$.

TABLE D.1
Test Matrix

Series	Specimen ID	Debonded Strand (%)	Debond Length (ft)
I	V _{ci} -in-00	0	—
	V _{ci} -in-25	25	7.5
	V _{ci} -in-50	50	7.5
	V _{ci} -in-75	75	7.5
II	V _{ci} -out-00	0	—
	V _{ci} -out-25	25	5
	V _{ci} -out-50	50	5
	V _{ci} -out-75	75	5
III	V _{cw} -00	0	—
	V _{cw} -25	25	6
	V _{cw} -50	50	6
	V _{cw} -75	75	6
IV	V _{ci} -in-50-V _s	50	7.5

to provide the beams the best chance to fail in the flexure-shear mode. The jacking stress was selected to be 139 ksi (after seating losses) which results in a total prestress force of 255 kips.

D.3.1.5 Concrete Compressive Strength

The concrete compressive strength was selected to maintain stresses below the allowable limits at transfer. Analysis also aided the choice of concrete compressive strength by selecting a strength that best promoted a flexure-shear failure. This resulted in the strength being high enough for the transfer stress limits, but low enough to ensure the shear capacity is less than the flexural capacity. These conditions resulted in a design compressive strength of 5,500 psi.

D.3.1.6 Transverse Reinforcement

The location and quantity of transverse reinforcement was selected to promote flexure-shear failures inside the debonded region. To accomplish this, the middle region of the beam (fully bonded region) was reinforced with transverse reinforcement to force the failure to occur outside the fully bonded region and inside the debonded region. The outermost stirrup was designed to be one beam depth outside the debonded region to permit a flexure-shear crack to develop without crossing a stirrup. Ultimately, #4 closed stirrups spaced at 6 in. were selected.

D.3.1.7 Predicted Shear Strengths

The following analytical results represent the predicted shear strengths using the shear model discussed in Section D.2.3.2.1. These calculated shear strengths for each specimen, V_n , were

plotted against the total applied shear (dead plus superimposed), V_u as shown in Figure D.14 through Figure D.17. Due to symmetry, each figure presents the shear over half the beam which is the shear span. The applied load was analytically increased for each beam until $V_u \geq V_n$ at any location along the span. The location at which this occurs is the location of failure (formation of primary shear crack) and is labeled " $V_{u,fail}$ " in each shear strength profile. The flexure-shear strengths are combined with the web-shear strengths for both the bonded and debonded regions to create one comprehensive shear strength profile for each specimen. The analyses assume the design concrete strength of 5,500 psi.

The shear strength profiles (for all series) illustrate several important aspects of the analytical model used throughout this study. First, the profiles indicate where the beam is cracked and uncracked which directly corresponds to the controlling shear strength type, V_{ci} and V_{cw} , respectively. The only region not labeled as cracked or uncracked is the transfer region (in beams with debonded strand). In this region, the shear strength at the end of the debonded region to the shear strength at the end of the transfer length (Section D.2.3.3) is connected with a straight line. It is important to note that the 2 ft of beam length overhanging each support is long enough to transfer all of the prestressing force into the beam according to Section D.2.3.3 ($l_{transfer} = 19$ in.). The shear strength profiles also locate the debonded region as well as the area reinforced with stirrups. Finally, the profiles specify the location and shear at the calculated failure.

The predicted shear strength profiles for Series I (Figure D.14 through Figure D.17) illustrate that the failure mode (primary shear crack) for each specimen is flexure-shear (V_{ci}). The profiles also show that the primary shear crack in V_{ci}-in-25 should form outside the debonded region while the primary cracks in the other two debonded specimens (V_{ci}-in-50 and V_{ci}-in-75) are shown to form at the end of the debonded region. In addition, as the percentage of debonded strand increases, the shear strength decreases. These predictions are in agreement with the hypothesis that the shear strength will be affected in the debonded region.

It was not possible to design all of the specimens with debonded strand in this series to fail inside (at the end of) the debonded region without compromising the bond strength of the strand in V_{ci}-in-25 or lengthening the beams which promotes flexural failures. Although the debonded region could have been lengthened to analytically promote a shear failure inside the debonded region for V_{ci}-in-25, this would have resulted in inadequate development length for the debonded strand in the middle of the beam. Furthermore, the total moment at the end of the debonded region at the expected failure load is 435 kip-ft which is only slightly less than the cracking moment of 455 kip-ft in the debonded region. Therefore, it was expected that failure could occur at the end of the debonded region if failure did not first occur outside the debonded region at the predicted load.

The shear capacity falls below the total applied shear at the failure location for V_{ci}-in-50 and V_{ci}-in-75 in Figure D.16 and Figure D.17, respectively, because of the relatively high percentage of debonding. This high percentage of debonding directly corresponds to low neutral axis depths at cracking in the debonded region which results in large shear strength reductions once cracking occurs. These large shear strength reductions cause the shear capacity to fall below the total applied shear in

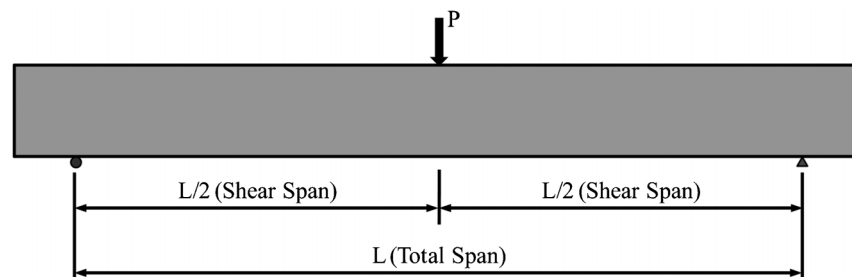


Figure D.11 Support and loading conditions.

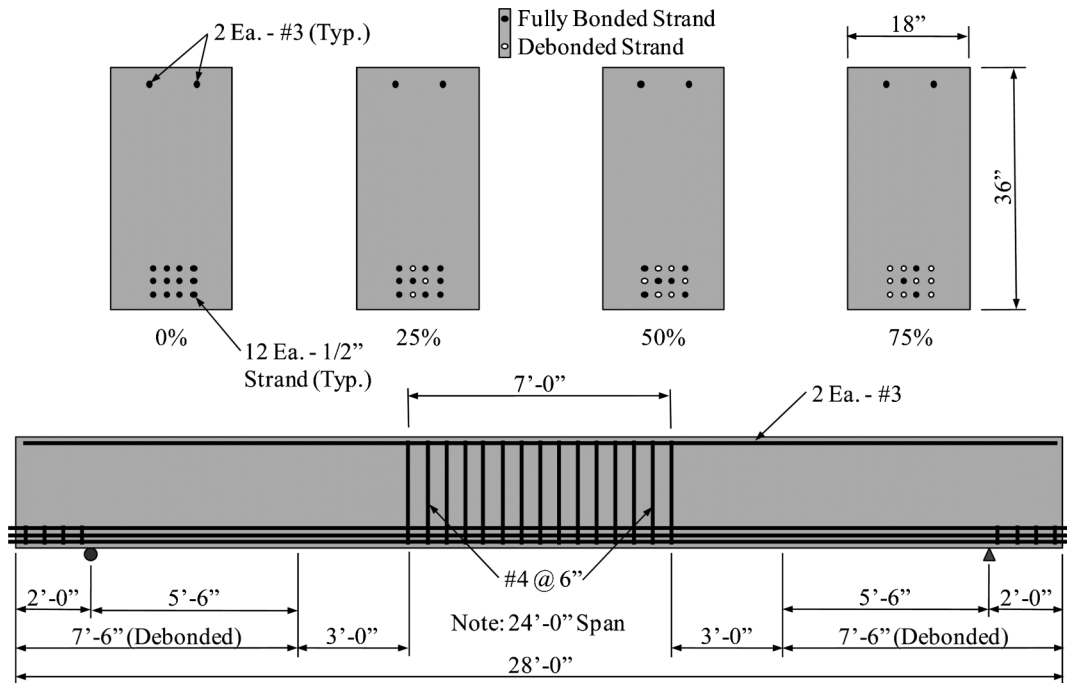


Figure D.12 Series I specimens (V_{ci-in}).

Figure D.16 and Figure D.17. For both of these beams, the failure load occurs at first cracking. At loads below this value, the beams were uncracked with significant shear strength at the predicted failure location.

D.3.2 Series II: Flexure-Shear — Outside Debonded Region (V_{ci-out})

Beams in this series were designed to fail in flexure-shear outside the debonded region. Therefore, the expectation of the specimens in Series II is that the shear strength would be unaffected as the percentage of debonded strand increased. The type and location of shear failure, as well as the percentage of debonded strand, is specified within the specimen identifications. The identifier for the 25% debonded specimen, for example, is $V_{ci-out-25}$, where the “25” specifies the percentage of strand

debonded. The “ V_{ci} ” indicates that the beam is designed for a flexure-shear failure, and the “out” denotes that the shear failure is designed to occur outside the debonded region. Again, the cross section was selected to be rectangular to isolate debonding as the primary variable so that shape did not complicate the behavior. Furthermore, the only difference between this series of specimens and those in Series I is the length of the debonded region and the presence of transverse reinforcement. All other variables were held constant to allow for comparisons between Series I and Series II. Design details for Series II specimens are provided in Figure D.18.

D.3.2.1 Length of Debonded Region and Shear Span

The debonded region was designed so that it was located away from areas with high flexural stresses. This resulted in a length of the debonded region of 5'-0" from the beam ends. Consideration was also given to developing the fully bonded strands assuming that failure initiated at the end of the debonded region. The strands were also designed to be fully developed at midspan. The shear span was designed to be identical to Series I.

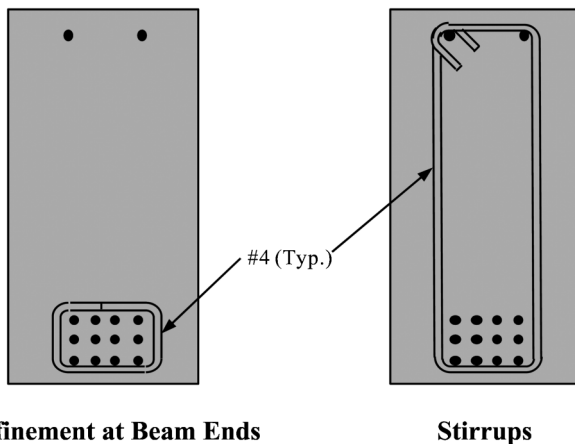
D.3.2.2 Transverse Reinforcement

Series II specimens were designed without transverse reinforcement to promote flexure-shear failures outside the debonded region.

D.3.2.3 Predicted Shear Strengths

The predicted shear strengths based on the shear model are illustrated in Figure D.19 through Figure D.22. The analyses assume the concrete strength is 5,500 psi.

The predicted shear strength profiles for Series II (Figure D.19 through Figure D.22) illustrate that the failure mode (primary shear crack) for each specimen is flexure-shear (V_{ci}). The profiles also show that the primary shear cracks for all four specimens should form outside the debonded region at the same shear. These predictions are also in agreement with the hypothesis that the shear strength should only be affected in the debonded region.



Confinement at Beam Ends

Stirrups

Figure D.13 Transverse reinforcement details for rectangular beams.

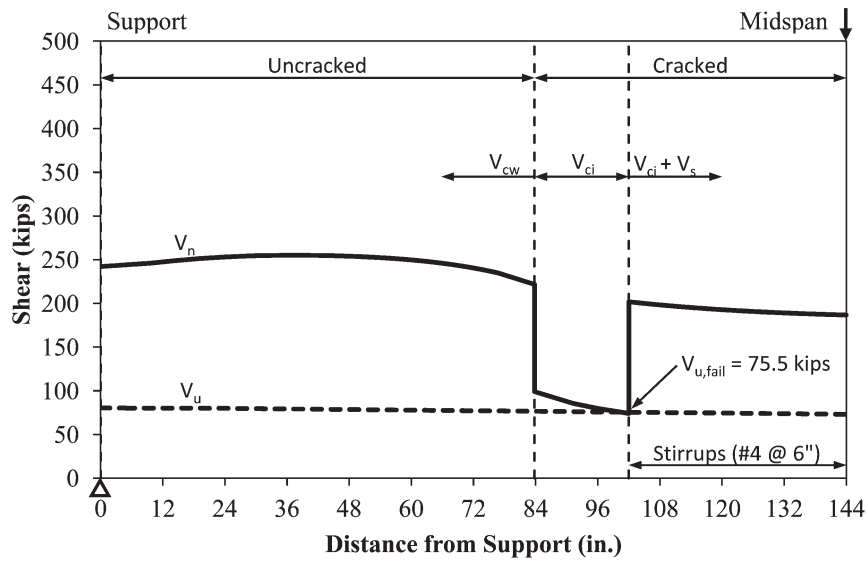


Figure D.14 Predicted shear strength profile for V_{ci} -in-00.

D.3.3 Series III: Web-Shear (V_{cw})

Beams in this series were designed to fail in web-shear inside the debonded region. Therefore, the expectation of the specimens in Series III is that the shear strength would decrease as the percentage of debonded strand increased. The type and location of shear failure, as well as the percentage of debonded strand, is specified within the specimen identifications. The identifier for the 25% debonded specimen, for example, is V_{cw} -25, where the “25” specifies the percentage of strand debonded. The “ V_{cw} ” indicates that the beam is designed for a web-shear failure. The cross section was selected to be an I-shape to promote a web-shear failure. This series of specimens was included in the testing program to incorporate both major types of shear failures (flexure-shear and web-shear) that can be influenced by strand debonding. Design details for Series III specimens are provided in Figure D.23, and the transverse reinforcement details are shown in Figure D.24.

D.3.3.1 Length of Debonded Region and Shear Span

The debonded region was designed to be long enough to produce flexural stresses that reduced the web-shear strength, but also short enough to prevent flexural cracking at the end of the debonded region. This resulted in a debonded length of 6'-0" from the beam ends. Consideration was also given to developing the fully bonded strands assuming failures initiated at the end of the debonded region. The strands were also designed to be fully developed at midspan. The shear span used in Series I and II was maintained.

D.3.3.2 Cross Section

The I-shape cross section dimensions were controlled by several variables. The critical cross section dimension was the web width

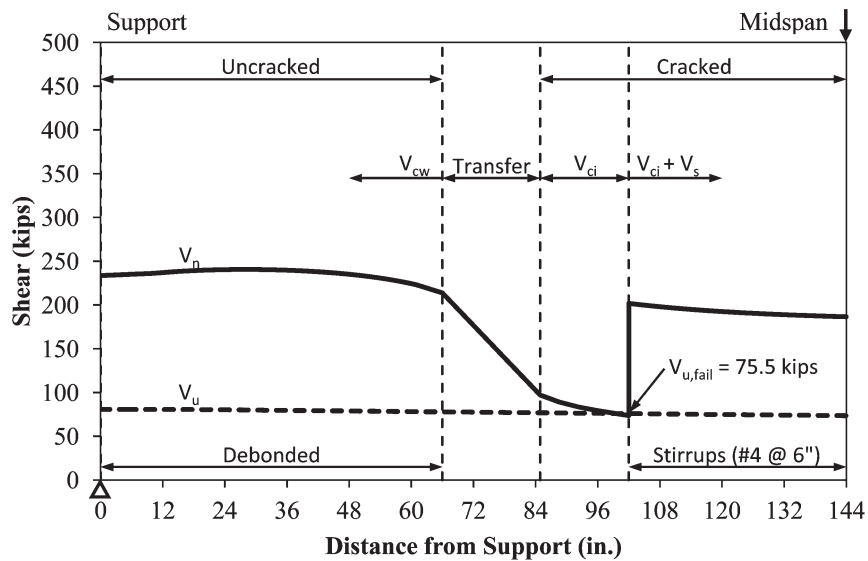


Figure D.15 Predicted shear strength profile for V_{ci} -in-25.

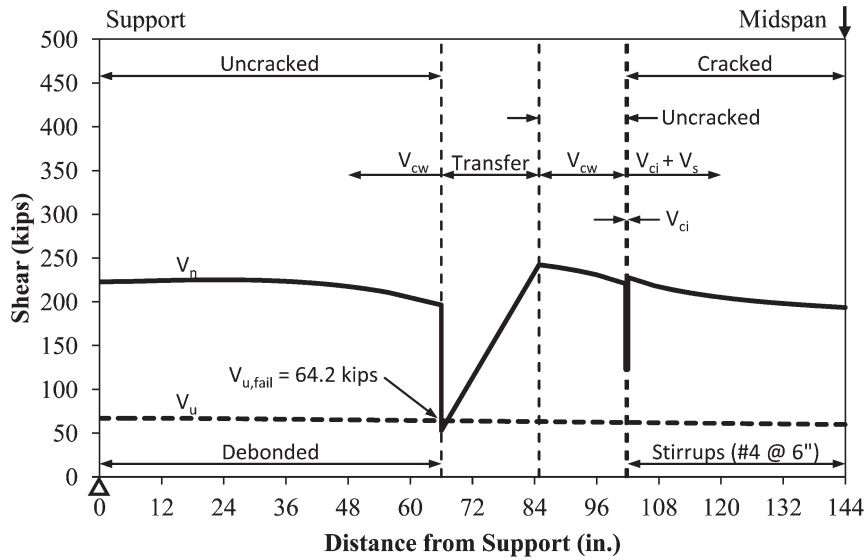


Figure D.16 Predicted shear strength profile for V_{ci} -in-50.

which directly affects the web-shear capacity. Therefore, the web width was selected as 5.5 in. to promote web-shear failures. The beam depth and flange widths were selected to be identical to the Series I and II specimens for consistency and to allow comparison of results. It should be noted that the final cross section dimensions limited the flexural stresses at transfer below allowable levels.

D.3.3.3 Jacking Force

The jacking stress was slightly altered relative to the Series I and II specimens to compensate for the increased losses with the I-beams and still maintain the same effective prestress as the rectangular specimens. This resulted in a jacking stress of 149.5 ksi (after seating losses) which produces a total prestress force of 274 kips.

D.3.3.4 Transverse Reinforcement

The location and quantity of transverse reinforcement was selected to promote web-shear failures inside the debonded region. To accomplish this, the middle region (fully bonded region) was reinforced with transverse reinforcement to force the failure to occur outside the fully bonded region and inside the debonded region. Ultimately, transverse reinforcement consisting of two #4 stirrups with 90 degree bends at both ends and spaced at 6 in. was selected.

D.3.3.5 Predicted Shear Strengths

The predicted shear strength profiles based on the shear model are illustrated in Figure D.25 through Figure D.28. The analyses assume the concrete strength is 5,500 psi.

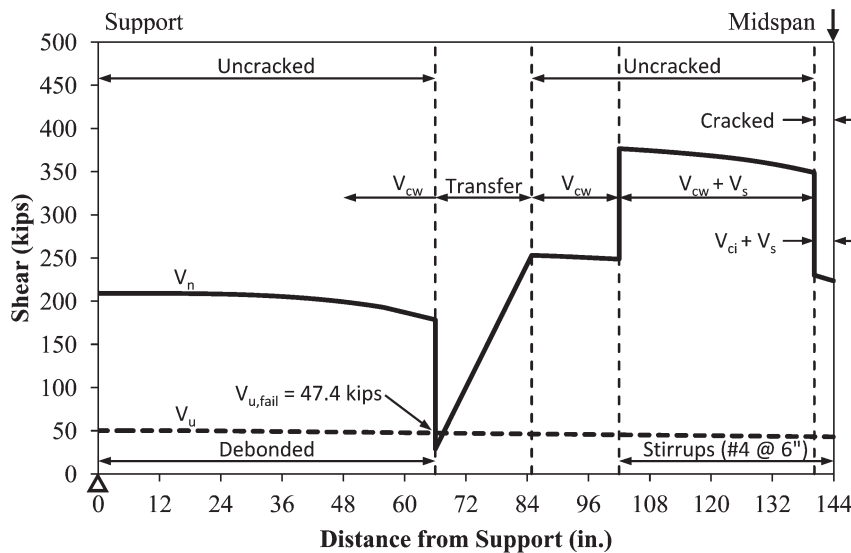


Figure D.17 Predicted shear strength profile for V_{ci} -in-75.

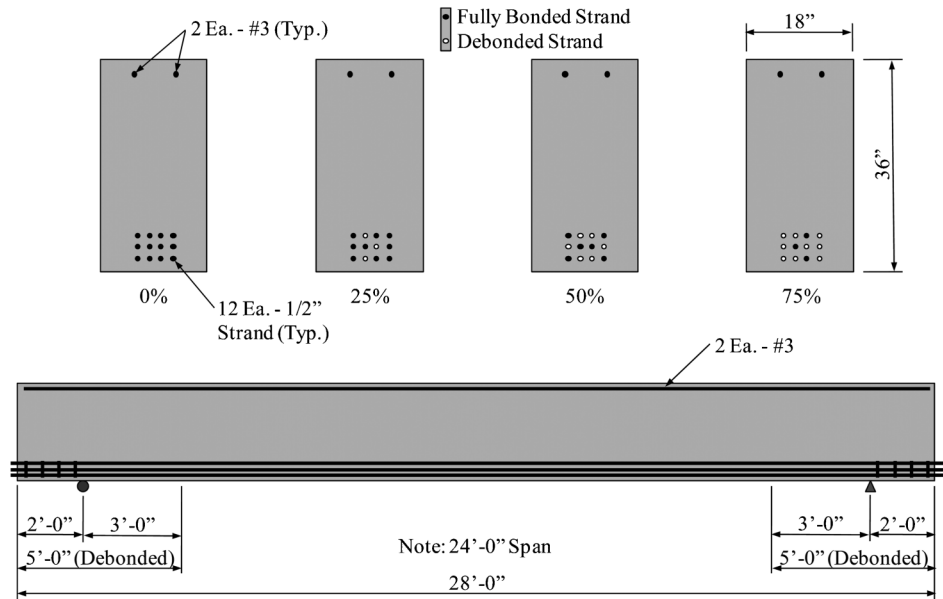


Figure D.18 Series II specimens (V_{ci} -out).

The predicted shear strength profiles for Series III (Figure D.25 and Figure D.28) illustrate that the failure mode (primary shear crack) for each specimen is web-shear (V_{cw}). The profiles also show that the primary shear crack in the first two specimens (V_{cw} -00 and V_{cw} -25) should form near the support while the primary cracks in the other two specimens (V_{cw} -50 and V_{cw} -75) should form at the end of the debonded region. It should be noted that although the predicted failure in V_{cw} -25 occurs near the support, the total shear at the end of the debonded region (84.2 kips) is only slightly less than the shear capacity (V_n) at that point (84.9 kips) at the predicted failure load. Therefore, the failure could form near the support or at the end of the debonded region. As shown, it is expected that the shear strength will decrease as the percentage of debonded strand is increased.

D.3.4 Series IV: Transverse Reinforcement

A beam was designed to better understand the effect of transverse reinforcement in the debonded region and to evaluate the analytical procedure for beams that include transverse reinforcement in the expected failure region. Therefore, the contribution of both concrete and steel to the overall shear capacity can be evaluated. The V_{ci} -in-50 beam was selected for this purpose. The only difference is in the inclusion of transverse reinforcement in the debonded region. The beam is identified as V_{ci} -in-50- V_s to indicate that transverse reinforcement (V_s) is added to the original V_{ci} -in-50 beam. The beam profile, illustrating the transverse reinforcement, is shown in Figure D.29. The cross section, as well as position and number of debonded strands, remain the same as the comparison beam, V_{ci} -in-50, illustrated in

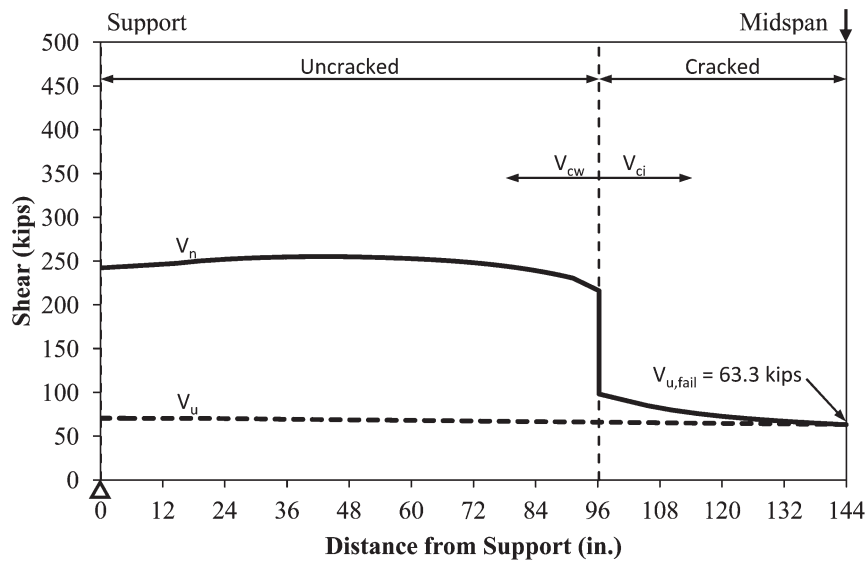


Figure D.19 Predicted shear strength profile for V_{ci} -out-00.

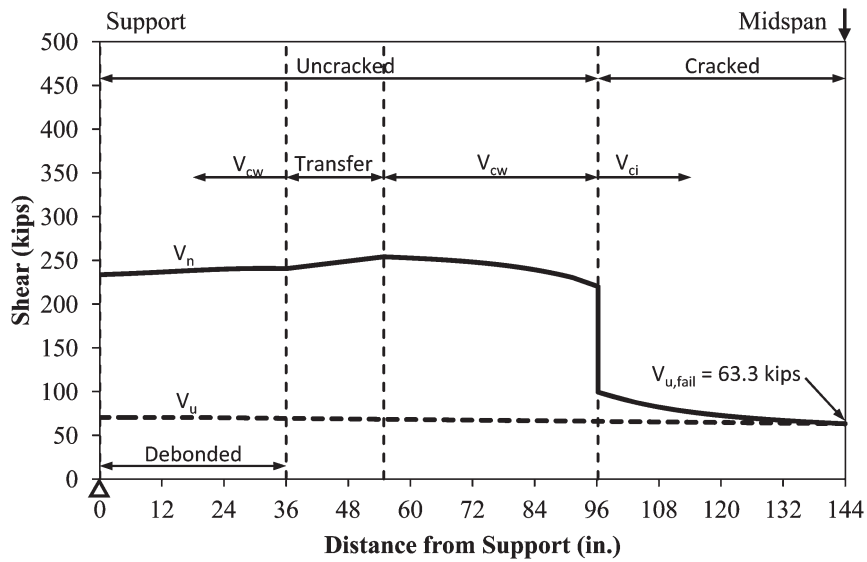


Figure D.20 Predicted shear strength profile for V_{ci} -out-25.

Figure D.12. The predicted shear strength profile is illustrated in Figure D.30 which can be compared with the predicted shear strength profile of its counterpart, V_{ci} -in-50, in Section D.3.1.7 (Figure D.16). The analysis assumes the concrete strength is 5,500 psi.

The failure predicted for V_{ci} -in-50- V_s is a flexure-shear crack that ultimately leads to yielding of stirrups. The profile also shows that, like the profile of V_{ci} -in-50, the primary shear crack should form at the end of the debonded region. The difference between the two specimens (V_{ci} -in-50- V_s and V_{ci} -in-50) is that V_{ci} -in-50- V_s is predicted to show increased load capacity after the formation of the primary shear crack because of the transverse reinforcement throughout the span length.

D.3.5 Test Series Summary

The capacities predicted by the shear model, V_{pred} , are provided in Table D.2. The predicted shear capacities consist of the shear due to applied load, $V_{applied}$, and the shear due to self-weight, $V_{self-weight}$, at each failure location. A uniform load of

675 lb/ft for rectangular beams and 405 lb/ft for I-beams was used to calculate $V_{self-weight}$. The predicted shear failure mode and failure location (where “In” indicates inside the debonded region and “Out” indicates outside the debonded region) are also listed in Table D.2.

D.4 MATERIALS

D.4.1 Concrete

The concrete mix design was selected based on the desired strength at release and at the time of testing. The latter was controlled by the optimized compressive strength from the analytical stage. Due to the allowable stress limits, a compressive strength of 4,500 psi was desired at the time of release. The strength at the time of testing was targeted to be 5,500 psi. To achieve this minimum difference in strength, a lower cement content mix was needed as compared to that typically used in the precast industry. Therefore, it was expected that release strengths would need several days after casting to be achieved. In precast

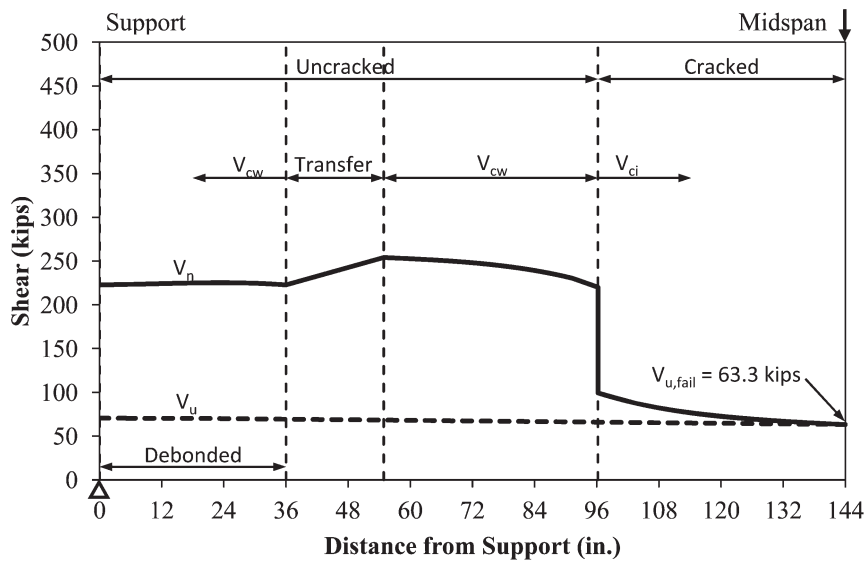


Figure D.21 Predicted shear strength profile for V_{ci} -out-50.

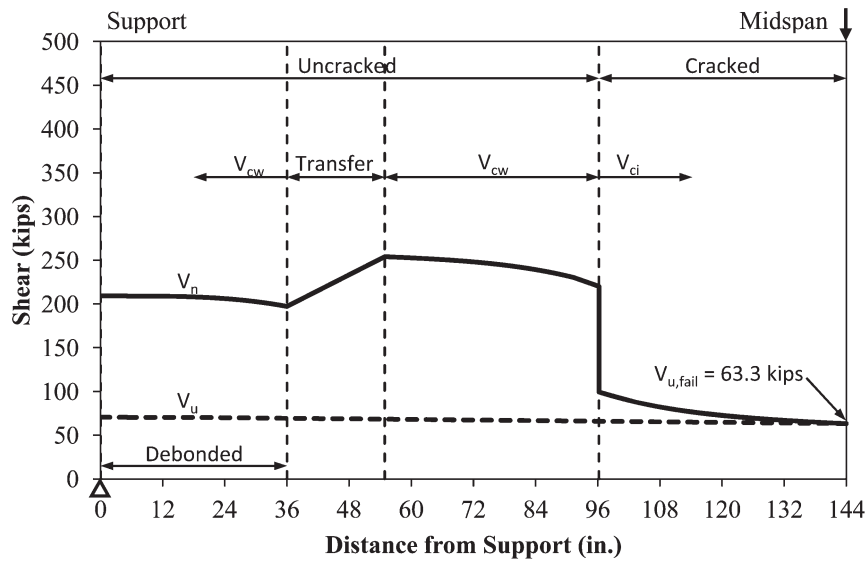


Figure D.22 Predicted shear strength profile for V_{ci} -out-75.

products, early release is achieved with high cement mixes as the final compressive strength is easily achieved, and over strength concrete is typically not a problem.

The concrete was ordered from Irving Materials, Inc. (IMI). The selected mix was a cement and fly ash mix with a full range water reducing admixture as shown in Table D.3. The selected mix contained 3/4 in. maximum aggregate size gravel. The specimens were cast in seven separate casts, each yielding two beams. A slump of 6 in. was requested for each cast and was measured upon arrival at the laboratory. The batch weights and slump for each of the seven casts are included in Table D.4 through Table D.7. No water was added to the trucks onsite.

Standard 6 × 12 in. cylinders were cast in plastic molds and cured in the same manner as the test specimens. After the concrete surface hardened, the specimens and cylinders were covered with wet burlap and plastic to prevent moisture loss. Curing of the cylinders was discontinued at the same time that curing of the

specimens was discontinued. Additionally, the cylinder molds were removed when the specimen forms were removed.

Compressive strength was monitored by testing three cylinders in accordance with ASTM C39 at regular intervals up to 28 days and including each specimen test day. In addition, split tension cylinders were tested in accordance with ASTM C496 (2011) at the time of release, 28 days, and the test day. A loading rate of 50,000 lb per minute was used during the compressive cylinder tests along with 70 durometer elastomeric pads. A loading rate of 15,000 lb per minute was used for the split tension cylinder tests. The compressive and split tensile strength growth curves for each cast (one beam from each cast) are shown in Figure D.31 and Figure D.32, respectively. The concrete strengths presented in Figure D.31 and Figure D.32 are from Truck 1 cylinders. A reduced number of cylinders were cast from Truck 2 to determine the strength at transfer, 28 days, and test day. A summary of the compressive and split tensile strength results on the test day for

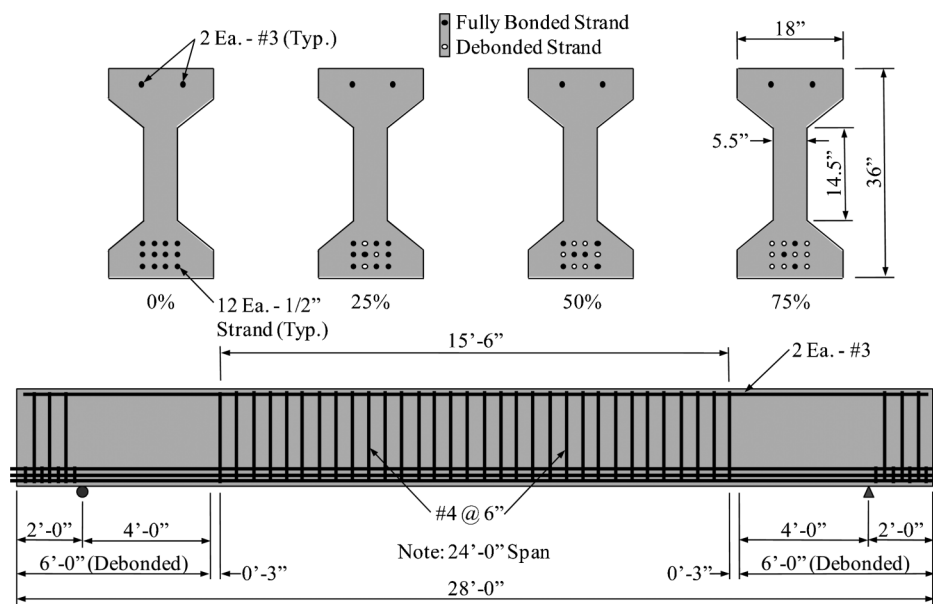


Figure D.23 Series III specimens (V_{cw}).

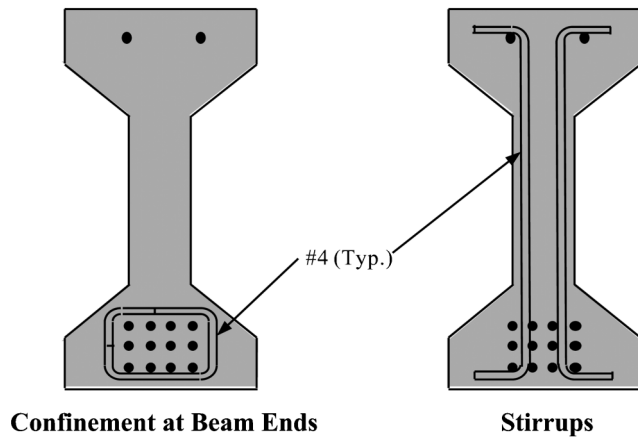


Figure D.24 Transverse reinforcement details for I-beams.

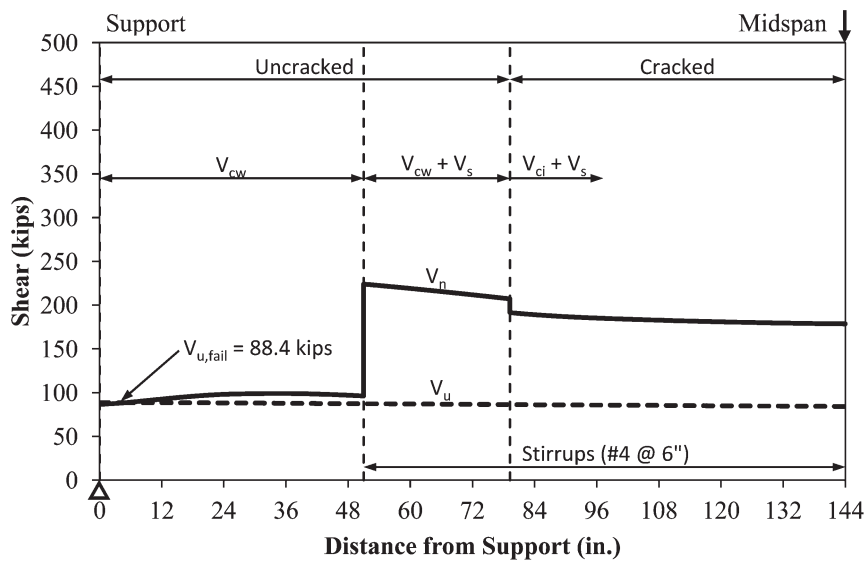


Figure D.25 Predicted shear strength profile for V_{cw-00} .

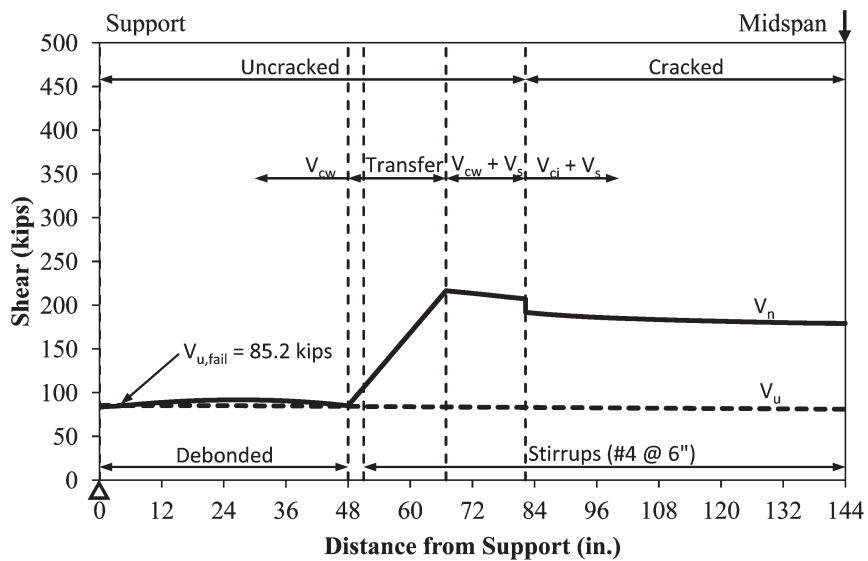


Figure D.26 predicted shear strength profile for V_{cw-25} .

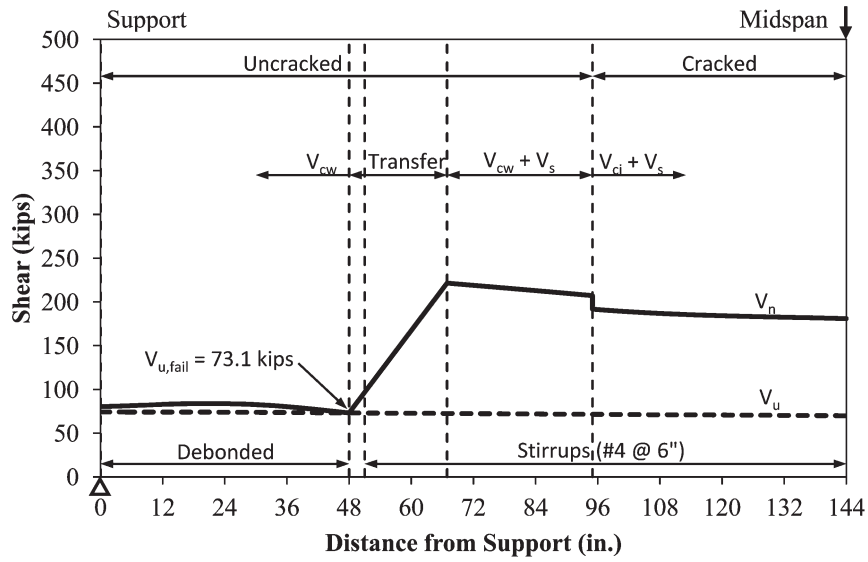


Figure D.27 Predicted shear strength profile for V_{cw-50} .

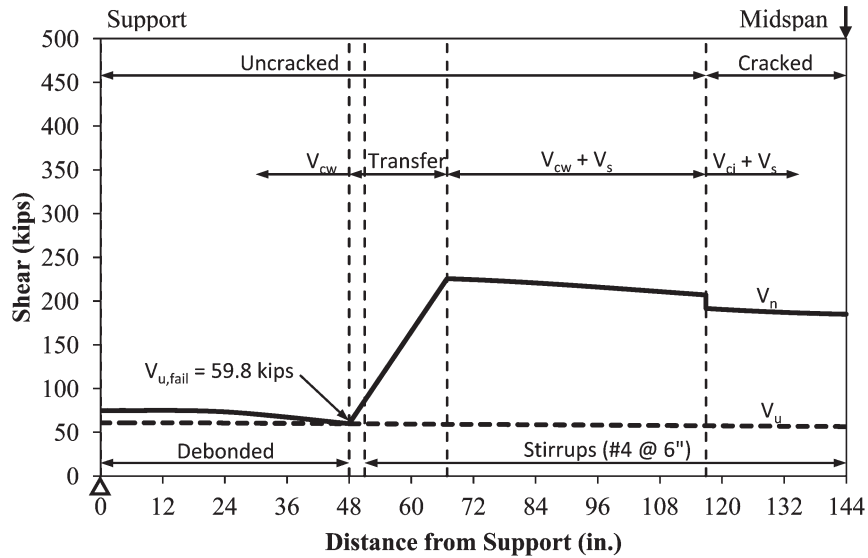


Figure D.28 Predicted shear strength profile for V_{cw-75} .

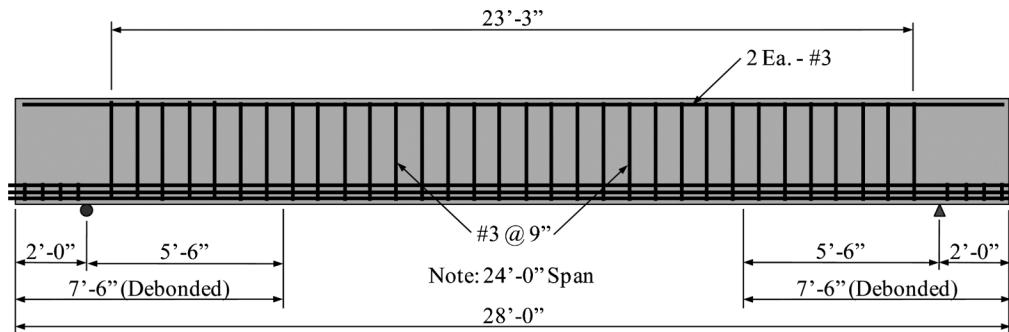


Figure D.29 $V_{ci-in-50-V_s}$ profile.

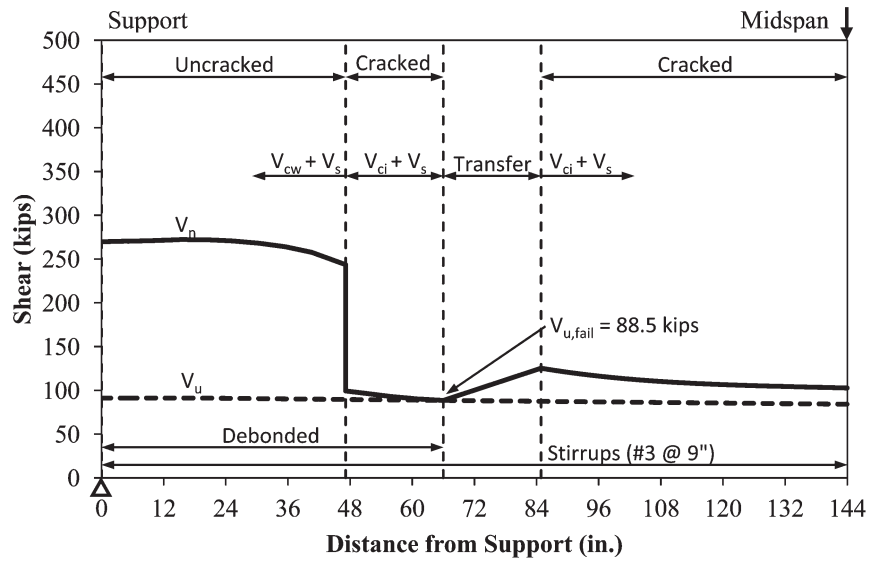


Figure D.30 Predicted shear strength profile for V_{ci} -in-50- V_s .

TABLE D.2
Predicted Shear Strengths

Series	Specimen ID	P_{applied} (kip)	V_{applied} (kip)	$V_{\text{self-weight}}$ (kip)	V_{pred} (kip)	Failure Mode	Failure Location
I	V_{ci} -in-00	146.3	73.1	2.4	75.5	V_{ci}	—
	V_{ci} -in-25	146.3	73.1	2.4	75.5	V_{ci}	Out
	V_{ci} -in-50	119.6	59.8	4.4	64.2	V_{ci}	In
	V_{ci} -in-75	85.9	43.0	4.4	47.4	V_{ci}	In
II	V_{ci} -out-00	126.5	63.3	0.0	63.3	V_{ci}	—
	V_{ci} -out-25	126.5	63.3	0.0	63.3	V_{ci}	Out
	V_{ci} -out-50	126.5	63.3	0.0	63.3	V_{ci}	Out
	V_{ci} -out-75	126.5	63.3	0.0	63.3	V_{ci}	Out
III	V_{cw} -00	168.3	84.2	4.2	88.4	V_{cw}	—
	V_{cw} -25	162.0	81.0	4.2	85.2	V_{cw}	In
	V_{cw} -50	139.8	69.9	3.2	73.1	V_{cw}	In
	V_{cw} -75	113.1	56.6	3.2	59.8	V_{cw}	In
IV	V_{ci} -in-50- V_s	168.3	84.1	4.4	88.5	V_{ci}	In

TABLE D.3
Concrete Mix Design Weights per Cubic Yard

Material	Design Weights Per Cubic Yard
Type I Cement (lbs)	500
Fly Ash (lbs)	100
3/4" Coarse Aggregate (lbs)	1850
Fine Aggregate (lbs)	1380
Water (lbs)	240
BASF Glenium 3030 NS Full Range Water Reducer (oz)	9

TABLE D.4
Concrete Mix Batch Weights per Cubic Yard for Series I (V_{ci-in})

Material	Cast 1		Cast 3	
	Truck 1	Truck 2	Truck 1	Truck 2
	$V_{ci-in-00}$	$V_{ci-in-75}$	$V_{ci-in-25}$	$V_{ci-in-50}$
Type I Cement (lbs)	498	499	498	499
Fly Ash (lbs)	97	96	97	98
3/4" Coarse Aggregate (lbs)	1844	1844	1844	1844
Fine Aggregate (lbs)	1451	1448	1447	1444
Water (lbs)	177	179	164	164
BASF Glenium 3030 NS Full Range Water Reducer (oz)	11.8	12	11.8	12
Slump (in.)	5.5	5.5	4.5	5.5

TABLE D.5
Concrete Mix Batch Weights per Cubic Yard for Series II (V_{ci-out})

Material	Cast 1		Cast 3	
	Truck 1	Truck 2	Truck 1	Truck 2
	$V_{ci-out-00}$	$V_{ci-out-75}$	$V_{ci-out-25}$	$V_{ci-in-50}$
Type I Cement (lbs)	499	500	511	498
Fly Ash (lbs)	98	99	98	97
3/4" Coarse Aggregate (lbs)	1844	1844	1844	1844
Fine Aggregate (lbs)	1429	1432	1436	1440
Water (lbs)	159	158	177	178
BASF Glenium 3030 NS Full Range Water Reducer (oz)	12	12	12	12
Slump (in.)	6	4.5	6	6

TABLE D.6
Concrete Mix Batch Weights per Cubic Yard for Series III (V_{cw})

Material	Cast 5 (one truck)		Cast 6 (one truck)	
	V_{cw-00}	V_{cw-75}	V_{cw-25}	V_{cw-50}
Type I Cement (lbs)		498		501
Fly Ash (lbs)		96		98
3/4" Coarse Aggregate (lbs)		1843		1858
Fine Aggregate (lbs)		1440		1440
Water (lbs)		178		161
BASF Glenium 3030 NS Full Range Water Reducer (oz)		12		11.8
Slump (in.)		5.5		5.5

TABLE D.7
Concrete Mix Batch Weights per Cubic Yard for Series IV

Material	Cast 7	
	Truck 1	Truck 2
	V _{ci-in-50-V_s}	V _{ci-out-75-2}
Type I Cement (lbs)	501	501
Fly Ash (lbs)	96	97
3/4" Coarse Aggregate (lbs)	1844	1844
Fine Aggregate (lbs)	1440	1421
Water (lbs)	174	183
BASF Glenium 3030 NS Full Range Water Reducer (oz)	12	12
Slump (in.)	5	7.5

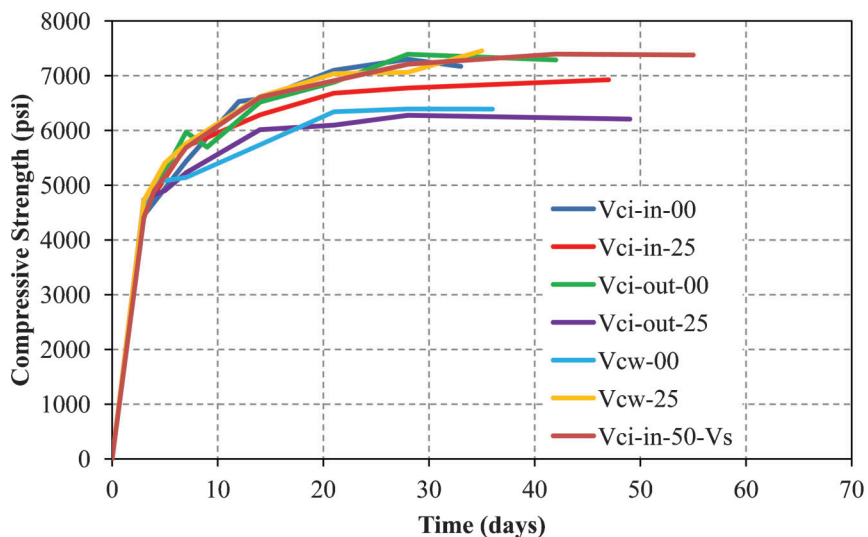


Figure D.31 Compressive strength growth.

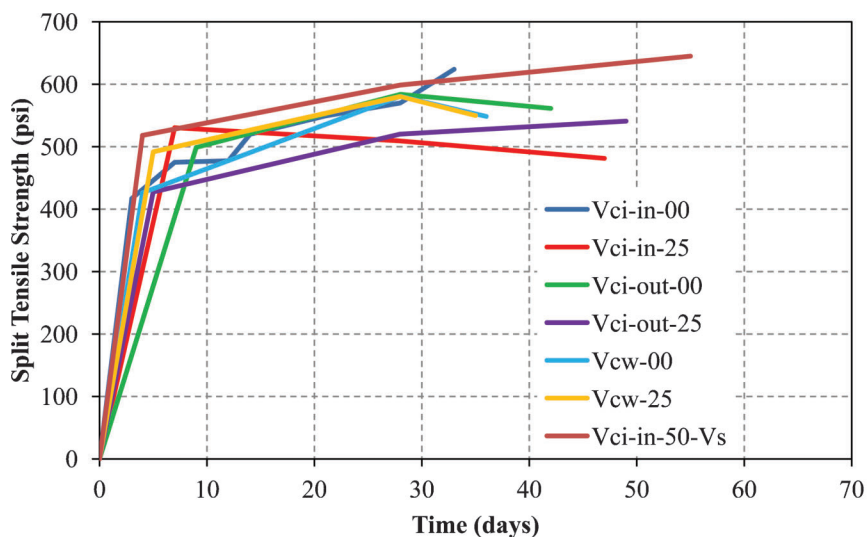


Figure D.32 Split tensile strength growth.

TABLE D.8
Concrete Strengths on Test Day

Series	Specimen ID	Age (days)	f'_c (psi)	f_{cr} (psi)
I	V _{ci} -in-00	33	7,170	620
	V _{ci} -in-25	47	6,930	480
	V _{ci} -in-50	50	6,800	510
	V _{ci} -in-75	36	6,950	610
II	V _{ci} -out-00	42	7,290	560
	V _{ci} -out-25	49	6,210	540
	V _{ci} -out-50	53	6,380	520
	V _{ci} -out-75	45	7,330	560
	V _{ci} -out-75-2	61	6,780	560
III	V _{cw} -00	36	6,390	550
	V _{cw} -25	35	7,450	550
	V _{cw} -50	39	7,130	570
	V _{cw} -75	40	6,380	500
IV	V _{ci} -in-50-V _s	55	7,380	650

each specimen is provided in Table D.8. These strengths are from cylinders cast with the same concrete used to cast each specimen, and therefore represent the actual strength of each specimen. Furthermore, the complete set of compressive and split tensile strength data is provided in Appendix D-2. It should be noted that I-beam casts required one truck.

The final cast for this experimental program included two beams (Table D.7). One of these beams is V_{ci}-in-50-V_s (Series IV), and the other was designed to be identical to the V_{ci}-out-75 specimen from Series II. The only difference in the duplicate specimen (V_{ci}-out-75-2) is in the timing of form removal and transfer for the reasons that are discussed in Section D.7.2. V_{ci}-out-75-2 was added to this final cast because there was room on the casting bed for an additional beam. This specimen is discussed in detail in Section D.7.2.

D.4.2 Prestressing Steel

The prestressing steel used throughout the laboratory investigation was from the same strand pack that was donated by American Spring Wire Corporation which was produced by RettCo Steel, LLC in Newnan, Georgia. This strand is Grade 270, uncoated, seven wire, low-relaxation strand with a nominal diameter of 1/2 in. The nominal cross-sectional area of the strand is 0.153 in.² It is the same strand used in the debonding effectiveness study presented in Chapter 2.

Three samples of this strand were tested in a four post universal testing machine in the Bowen Laboratory. Testing of the strand was in conformance with ASTM A370. The strands were gripped with the same 1/2 in. standard prestressing chucks used in the experimental programs. In addition, standard aluminum foil was wrapped around the ends of the strands before the chucks were installed. Three layers of aluminum foil helped minimize the jaws from biting into strand ends which can cause failure at the grip locations.

Three samples, with approximately 4 ft gage lengths, were tested to failure. The maximum load and stress for each sample

TABLE D.9
Prestressing Strand Tensile Strengths

Sample	Failure Distance From Grip (in.)	Max. Load (lb)	Max. Stress (ksi)
1	7	42,813	279.8
2	0	42,732	279.3
3	0	42,767	279.5
Average:		42,771	279.5

are listed in Table D.9. It should be noted that all samples achieved a maximum stress greater than the 270 ksi nominal strength. In addition, although Samples 2 and 3 failed at the grips, the peak load reached was nearly identical to that of Sample 1, which failed away from the grips. Figure D.33 illustrates the failure of Sample 1 as well as the prestress chuck grip at the failed end.

D.4.3 Mild Steel Transverse Reinforcement

The transverse reinforcement used throughout this testing program consisted of Grade 60 mild steel deformed bars. These bars were manufactured by Gerdau and fabricated by Indiana Steel Fabricating, Inc. located in Indianapolis, Indiana. The yield stress, ultimate stress, and maximum strain for the #3 stirrups used in the V_{ci}-in-50-V_s specimen are provided in Table D.10. The bars were tested in conformance with ASTM A370. The yield stress presented is the stress corresponding to a strain of 0.35% (ACI 318-11 Section 3.5.3.2). This size stirrup (#3) was only used for V_{ci}-in-50-V_s. The rest of the beams with transverse reinforcement used #4 stirrups. However, the #4 stirrups were provided in the specimens to ensure failure outside the transverse reinforced area. Therefore, the tensile properties were not tested.

The stress-strain curves for each #3 sample are illustrated in Figure D.34. The stress was calculated from the load provided by the testing machine, while the entire strain domain was measured using a break-away extensometer supplied by Epsilon Tech. This extensometer has an 8 in. gage length and allows continuation of measurements through rupture preventing potential gage failure by splitting into two pieces. Figure D.35 shows a typical failure of the #3 stirrup test samples. The break-away extensometer is also shown. It is worth noting that the samples consisted of the vertical legs that were cut out of extra stirrups. Each cut was made a minimum of 1 in. away from the end of the radius.

D.4.4 Mild Steel Longitudinal Reinforcement

Grade 60 mild steel longitudinal reinforcement was located in the top of each specimen. Two #3 bars per beam along the entire length were provided for ease of constructing the rebar cages. However, it should be noted that even though stirrups were not included in every specimen, the #3 longitudinal bars were provided in each beam for consistency. Tensile tests of these bars were not performed because they were in the compression zone and their post-yield behavior does not influence the testing program.

D.5 SPECIMEN CONSTRUCTION

The pretensioned beams were constructed at the Bowen Laboratory in seven casts. The casting bed of 56 ft permitted two beams to be constructed per cast. The beams were constructed on the same casting bed and with the same pretensioning abutments as discussed in Section 2.4.

D.5.1 Pretensioning

Jacking of the prestressing strands was carried out in two phases. The first phase included pulling the strands to 2 kips which kept the strands taught allowing strain gages to be installed.



Figure D.33 Prestressing steel test sample.

After strain gage installation, the second phase began. In this phase, the stressing crew tensioned each strand to the full jacking stress. The release stress was targeted at 51.5% (139 ksi) and 54.6% (147.5 ksi) of the ultimate nominal strength of the strands (270 ksi) for the rectangular beams and I-beams, respectively. This corresponds to a release force of 21.3 kips per strand for the rectangular beams and 22.6 kips per strand for the I-beams. The difference in release forces is due to the fact that the losses were expected to be greater in the I-beams than the rectangular beams. Due to seating losses, a jacking force of 24 kips ($0.56f_{pu}$) was initially selected for the first strand of the first set of rectangular beams. This initial jacking force was determined by estimating a strand slip (seating in the chuck) of 0.5 in. over a bed length of 70 ft. The jacking force estimation was checked by monitoring the strain gage and load cell measurements during stressing operations through the following procedure.

While stressing the first strand, the strain measurements at 21.3 kips (desired force at release) were noted. The jacking force was subsequently increased to 24 kips to account for the seating losses as previously mentioned. The jacking force was then slowly released, allowing the strand to slowly and completely seat into the chuck. As the strand was seating into the chuck, the strain measurements continued to drop until the jacking force was zero. At this point, the final strain measurements were compared to the strains noted at 21.3 kips. The strains were too high (corresponding to a strand force of 21.8 kips); therefore, the second strand was stressed to 23 kips. After releasing the jacking force on the second strand, the strains (after seating losses) were in close agreement to the strains noted at 21.3 kips. Therefore, the force remaining in the strand was approximately 21.3 kips. A jacking force of 23 kips was used for the remaining stressing operations for the rectangular beams. The same process was used for the I-beam stressing operations. Based on the seating losses observed for the rectangular beams, a jacking force of 24 kips was initially used. This first trial resulted in strains after seating closely matching the strains noted at 22.6 kips (desired release force for I-beams). Therefore, all strands in the I-beams were stressed to 24 kips. It should be noted that dial gages (stationed at both pretensioning abutments) recorded a maximum total movement (for all stressing operations) of 0.028 in. and 0.037 in. for the rectangular beams and I-beams, respectively. This resulted in a negligible loss of approximately 150 lbs and 200 lbs per strand for rectangular beams and I-beams, respectively. The jacking assembly used for these pretensioned beams was the same used in the debonding effectiveness evaluation (Section 2.4.2).

TABLE D.10
#3 Stirrup Tensile Properties

Sample	Yield Stress (ksi)	Ultimate Stress (ksi)	Maximum Strain
1	74.1	108.0	12.5%
2	73.4	108.7	13.6%
3	74.9	109.3	12.6%
Average:	74.1	108.7	12.9%

D.5.2 Formwork

The formwork was constructed from 3/4 in. plywood and 2 × 4 s. The side forms were constructed with 3/4 in. plywood panels screwed to 2 × 4 ladder frames consisting of vertical studs, a header, and a base board as shown in Figure D.36. The 2 × 4 headers were attached approximately 1 in. from the top edge of the plywood panels to prevent excess concrete build-up during casting operations which simplified screeding. Side forms were attached to the base with lag screws to restrict form movement at the base. Lateral pressures during casting were resisted with two lines of wales made of adjacent 2 × 4 s. A series of 3/4 in. plywood spacers between the 2 × 4 s allowed the network of 1/4 in. steel threaded tie-rods to be installed. The lateral pressure is resisted by the wales which are restrained by the tie-rods. The tie-rods, anchored by steel wedge washers on either end, provide a self-equilibrating form system. In addition, the formwork is supported at each panel splice by means of 2 × 4 cross beams on top as well as 2 × 4 diagonals attached to the base formwork to ensure squareness. The formwork was discontinued in between the two specimens permitting strand cutting at transfer.

D.5.3 Casting

The pretensioned beams discussed in Chapter 3 were constructed in seven casts. A one cubic yard concrete bucket was used to transport the concrete from the truck to the specimens as shown in Figure D.37. As the concrete was being placed (in three lifts), internal vibrators were used to consolidate the mix. After vibrating, the top surface was screeded to the proper level followed by finishing with magnesium hand floats.

The specimens were wet cured for different time periods (Table D.11) based on the rate of strength gain, the availability of a lab technician to cut the strands, and the time to instrument the beams with mechanical strain gage locating disks (Section 2.5). Concrete compressive strengths at the time of transfer are noted. Wet curing was accomplished by covering the surface with wet burlap and plastic to prevent moisture loss. In addition, the burlap was re-wetted every 12–24 hours to maintain curing. After wet curing, the side forms and plastic cylinder molds were removed. The forms were removed to allow placement of the mechanical strain gage locating disks on the concrete surface. However, these locating disks were only installed on the first three casts (six beams) for reasons discussed in Section D.7.2.

Standard 6 × 12 in. cylinders were cast alongside the specimens. The cylinders were consolidated using a small internal vibrator according to ASTM C192. The cylinders were wet cured in the same manner and for the same duration as the specimens.

D.5.4 Strand Release

The prestressing strands were released after curing was discontinued. Each strand was gradually released by heating approximately a 1 ft length back and forth with a torch until all of the seven wires were cut as shown in Figure D.38. The individual wires typically broke two or three at a time, and the specimens slid on the smooth base after all of the strands were cut. The order of

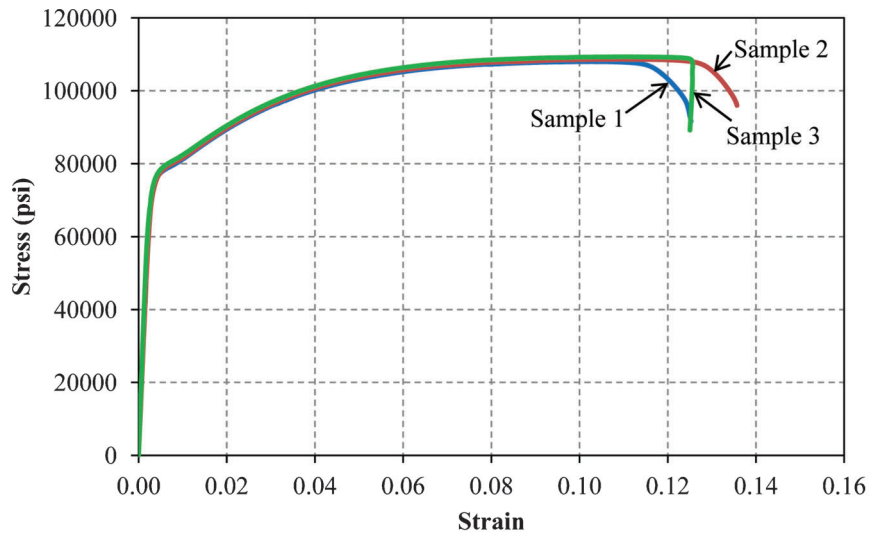


Figure D.34 Stress-strain response of transverse reinforcement.



Figure D.35 Transverse reinforcement test sample.

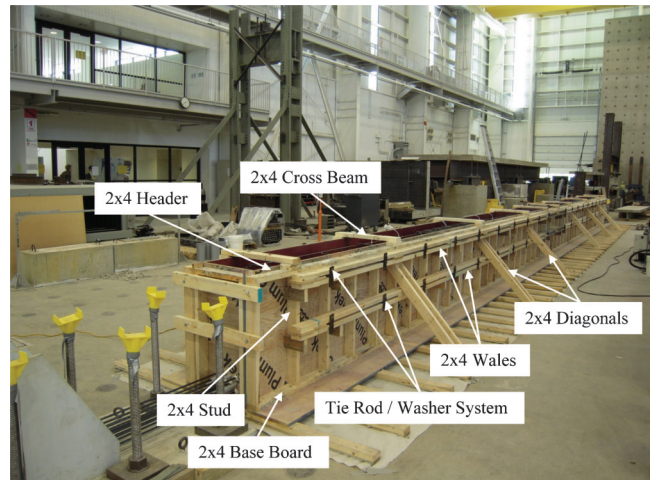


Figure D.36 Formwork.



Figure D.37 Concrete transport during casting operations.

TABLE D.11
Curing and Transfer

Series	Specimen ID	Curing (days)	Transfer (days)	f'_c (psi)
I	V _{ci} -in-00	6	12	6,530
	V _{ci} -in-25	3	7	5,710
	V _{ci} -in-50	3	7	5,760
	V _{ci} -in-75	6	12	6,120
II	V _{ci} -out-00	4	9	5,700
	V _{ci} -out-25	5	5	4,900
	V _{ci} -out-50	5	5	4,880
	V _{ci} -out-75	4	9	6,040
	V _{ci} -out-75-2	4	4	4,350
III	V _{cw} -00	4	4	5,060
	V _{cw} -25	5	5	5,400
	V _{cw} -50	5	5	5,400
	V _{cw} -75	4	4	5,060
IV	V _{ci} -in-50-V _s	4	4	4,910

strand release was top row, middle row, and bottom row from the outside in. After all twelve strands were initially cut at the live end (jacking end). They were then cut at the other abutment (dead end) and finally in between the specimens in the casting line.

D.6 TEST SETUP AND PROCEDURE

D.6.1 Test Setup

The beams were simply supported with a concentrated load applied at midspan as illustrated in Figure D.39. A structural steel test frame tensioned to the strong floor with 300 kips of pretension force was used to resist the applied load from a hydraulic ram (Figure D.39). The pin and roller supports were mounted on top of reinforced concrete pedestals to provide space

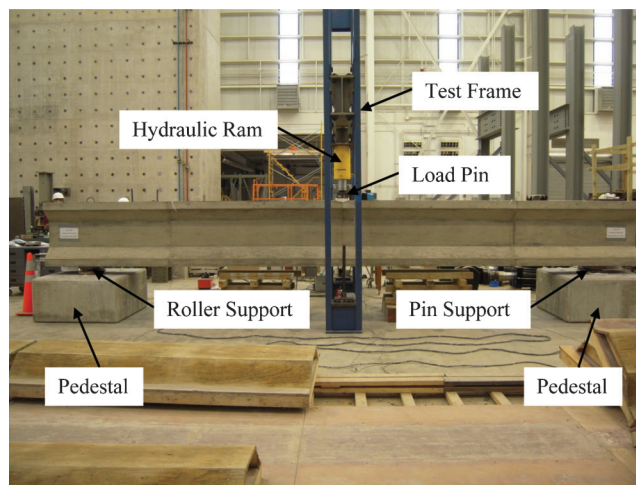


Figure D.39 Test setup.

for deflection and to place the beams at a convenient elevation for testing (Figure D.40). Each support consisted of a 1.5 in. diameter steel rod between two 18 in. long \times 8 in. wide \times 1.5 in. thick steel plates. The plates in the pin support were machine beveled with a slightly larger radius than the rod to allow free rotation without lateral translation. In addition, load was transferred to the beam along a single line with a pin system to apply equal shear forces to both shear spans (Figure D.41). The load pin consisted of a 1.5 in. diameter steel rod between two 18 in. long \times 6 in. wide \times 1.5 in. thick steel plates.

D.6.2 Test Procedure

The beams were statically loaded to failure in 10 kip increments using a hand-operated hydraulic pump. At the end of each load stage, the cracks were outlined, photographs were taken, and support movement measured by the dial gage was noted. If first cracking was heard or observed on the load-deflection plot,



Figure D.38 Strand release.



Roller



Pin

Figure D.40 Supports.

loading was stopped, and an inspection was made to mark any cracks that may have formed. After failure, a crack map was recorded, photographs were taken, and concrete cylinders documenting concrete strength were tested.

D.6.3 Instrumentation

Several types of instrumentation were used in this experimental program. Strain gages were installed on the strands to monitor strains during stressing, before and after transfer, and during testing. During testing, other sensors used include LVDTs, string pots, and a load cell. LVDTs were installed to monitor strand slip at both ends of each beam. The load cell monitored the applied force while string pots were used for beam displacements at the load point (midspan). The instrumentation was nearly identical for all fourteen beams tested in this study. The only difference is that displacements were measured with LVDTs for the first two beams while string pots were used for the rest. All data was

recorded with a Micro Measurements System 7000 data acquisition system controlled by StrainSmart software.

D.6.3.1 Strain Gages

The strain gages used on the prestressing strands were 2 mm gage length, 120 ohm, quarter bridge gages from Texas Measurements. As discussed in Section D.5.1, the strain gages were installed after an initial tension of 2 kips was placed on each strand. This initial tension lifted the strands off the casting bed which allowed for more convenient gage installation. In addition, this initial tension allowed the gages to be placed in their proper locations by taking into account the expected additional elongation due to final stressing. For example, a gage desired at the midspan of the beam closer to the dead end (opposite from the stressing end) required installing it 1.05 in. short of midspan in anticipation of strand elongation during final stressing. The gage at midspan for the beam closer to the live end (stressing end) required installing it 2.65 in. short of midspan in anticipation of the larger elongation at this point.

Strain gage installation materials were supplied by Vishay. The following steps outline the process of strain gage application used in this study. First, the location was cleaned by spraying degreaser onto a gauze pad and wiping the strand thoroughly. Next, conditioner (acid) was applied to a coarse wet/dry sand paper (220 grit) and immediately used to scrub the strand. The same process was repeated using a finer sand paper (400 grit). The area was then wiped clean with a new gauze pad. Then neutralizer (base) was continually applied to the treated area with a Q-tip. While a small pool of neutralizer remained on the strand, a gauze pad was used to wipe the area clean. Subsequently, installation tape was used to place the gage in the proper location, and then folded back to allow application of the bonding agent (M-Bond 200). A small amount of catalyst was brushed onto the back of the gage, and a drop of M-Bond 200 was applied to the proper location on the strand where the gage would be placed. The tape, with the strain gage, was immediately folded down and thumb pressure applied to the gage for approximately two minutes. At least 15 minutes was allowed to pass before removing the installation tape. M-Coat D was then applied over the gage, the leads, and underneath the leads to electrically insulate the strain gage. Then after allowing the M-Coat D to dry for at least 15 minutes, a layer of butyl rubber was applied under the leads and over the entire gage area (including the leads). The butyl rubber was added to provide mechanical protection during casting operations. A layer of silicone caulking was spread over the entire gage area as an additional waterproof barrier. Furthermore, strain relief was added to the strain gage cable by securely fastening a cable tie around the cable and strand immediately adjacent to the gage leads. Finally, each strain gage cable length embedded in concrete was covered with plastic tubing to prevent wire failure at the

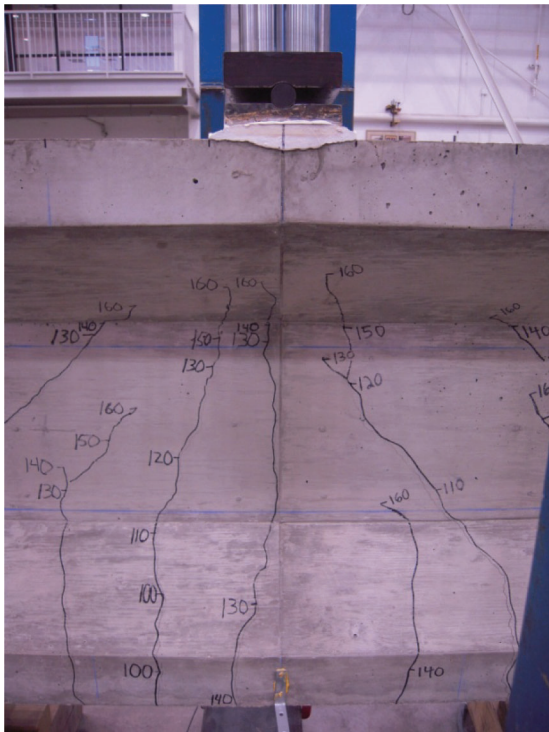


Figure D.41 Load pin.

location of cracks. Two installed strain gages are shown in Figure D.42.

D.6.3.2 LVDTs

LVDTs, each with a range of ± 1 in., were installed at both ends of each beam to measure strand slip. Two of the LVDTs were installed on fully bonded strands (one top, one bottom) while the other two were installed on debonded strands (one top, one bottom) as shown in Figure D.43. The LVDTs on the debonded strands were expected to continually measure strand movement considering that the strands were free in the debonded regions, but the main focus was to monitor any sudden slips that may occur. The LVDTs installed on the fully bonded strands were similarly used to monitor slippage. Considering that they were fully bonded, any movement is indicative of slip.

LVDTs were also used to measure support movement. One LVDT was installed at either support to monitor vertical deformation of the concrete support relative to the laboratory strong floor. These measurements were verified through the use of a mechanical dial gage located at the pin support. Figure D.44 provides an illustration of the support deformation instrumentation setup.

D.6.3.3 String Pots

Two string pots with a range of 25 in. were installed at midspan, one on each side. Reported midspan displacement measurements are the average value of the two string pots at midspan. The string pots were mounted on a steel beam which rested on the strong floor as shown in Figure D.45. It is important to note that the support deformations were negligible; therefore, they were not used to correct the displacements at midspan.

D.6.3.4 Load Cell

A load cell with a maximum load rating of 300 kips was installed directly above the hydraulic ram at midspan to measure the applied load. The load cell is illustrated in Figure D.45.

D.7 TEST RESULTS

The test results are summarized in Table D.12. This table provides the total shear force including self-weight at the formation (and location) of the primary shear crack, V_{test} . The total shear force is comprised of the component from the applied shear, $V_{applied}$, and the shear due to self-weight, $V_{self-weight}$ at the primary shear crack location. The applied load at the formation of



Figure D.42 Strain gage installation.

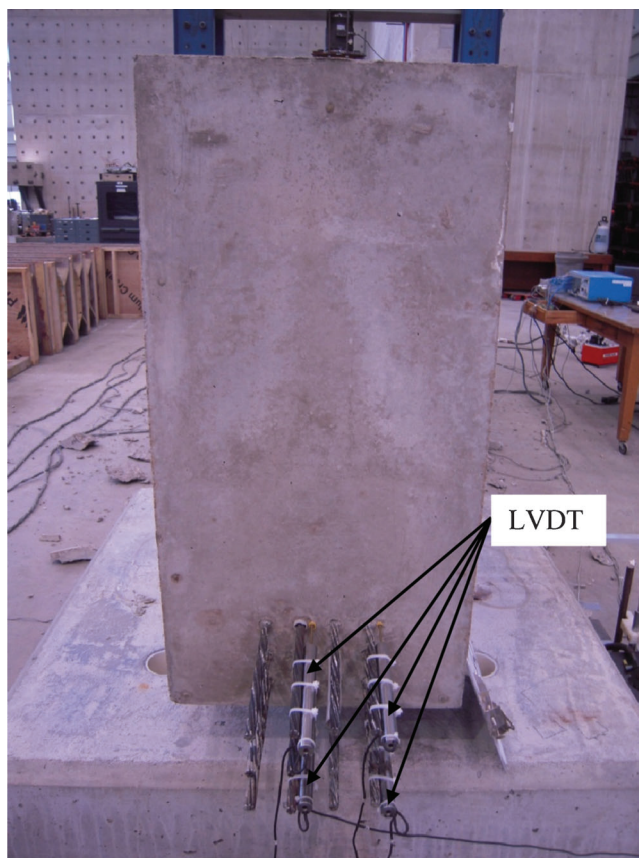


Figure D.43 Strand slip instrumentation.

the primary shear crack, $P_{applied}$, is also given in the table. The primary shear crack location is noted as “In” when inside the debonded region and “Out” when outside the debonded region.

The test results at the point of ultimate failure for each specimen are provided in Table D.13. Shears at ultimate, V_{ult} , also include the shear due to self-weight, $V_{self-weight}$ at the location of failure. It should be noted that the ultimate failure mode and location may not correspond to the mode and location of the primary shear crack formation listed in Table D.12. Therefore, the ultimate failure modes and locations are provided as well.

The reported shears due to self-weight listed in Table D.12 and Table D.13 were calculated based on an assumed unit weight of

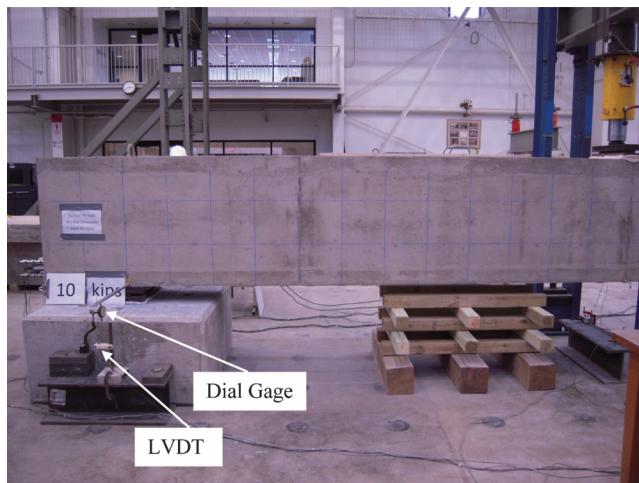


Figure D.44 Support deformation instrumentation.

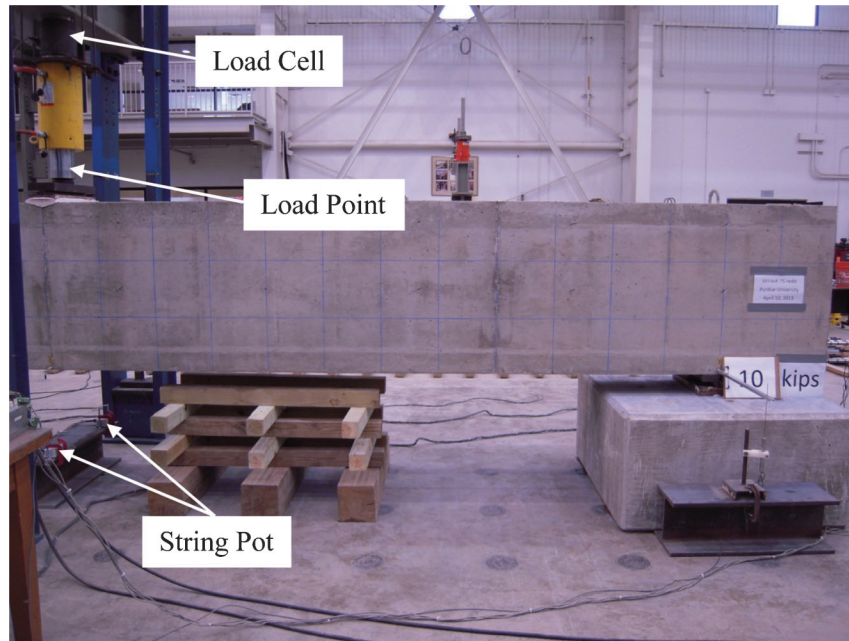


Figure D.45 Instrumentation at midspan.

150 lb/ft³ for prestressed concrete beams. This results in a uniform dead load of 675 lb/ft for the rectangular sections (Series I, II, and IV) and 405 lb/ft for the I-beams (Series III). These uniform dead loads produce shears distributed across each shear span as illustrated in Figure D.46. Sections within a distance $h/2$ (18 in.) from the support are assumed to carry the shear computed at a distance $h/2$ (18 in.) from the support according to ACI 318-11 Section 11.1.3.2. It should be noted that the shears due to self-weight provided in Table D.12 and Table D.13 are outside of the plateau (toward midspan) shown in Figure D.46. That is, each of the failures occurred more than 18 in. from the supports (on the sloped portion of the shear diagram). These shear diagrams were also used in the analytical section (Section D.8).

D.7.1 Series I (V_{ci} -in)

The load-deflection behavior for the V_{ci} -in test series is presented in Figure D.47. The percent of debonded strand is

noted for each test result, and the point at which the primary shear crack formed in the beam is annotated by a circle.

The crack patterns at the formation of the primary shear crack are shown in Figure D.48. It should be noted that the white dashed line in Figure D.48 represents the end of the debonded region, and the thick black outlined crack highlights the critical (primary) shear crack. Photos of the ultimate failures are shown in Appendix D-3.

In general, the load-deflection behavior for each specimen is characterized by three phases. In the first phase, the load-deflection relationship is linear elastic. Furthermore, the linear elastic portions of the load-deflection curves are nearly identical because the specimens were all designed with the same dimensions, concrete strength, and prestressing force (in the fully bonded region). The end of the first phase of behavior is marked by the formation of a flexural crack near midspan for the specimens with 0%, 25%, and 50% debonded strand. Flexural cracking initiated at an applied load of approximately 80 kips for each of these three beams. However, the first crack in V_{ci} -in-75 was a flexure-shear

TABLE D.12
Test Results at Formation of Primary Shear Crack

Series	Specimen ID	P_{applied} (kip)	V_{applied} (kip)	$V_{\text{self-weight}}$ (kip)	V_{test} (kip)	Crack Mode	Crack Location
I	V_{ci} -in-00	170.0	85.0	3.3	88.3	V_{ci}	—
	V_{ci} -in-25	156.0	78.0	4.4	82.4	V_{ci}	In
	V_{ci} -in-50	105.3	52.6	4.4	57.0	V_{ci}	In
	V_{ci} -in-75	60.0	30.0	4.4	34.4	V_{ci}	In
II	V_{ci} -out-00	153.3	76.6	2.7	79.3	V_{ci}	—
	V_{ci} -out-25	147.9	73.9	2.7	76.6	V_{ci}	Out
	V_{ci} -out-50	139.9	69.9	2.7	72.6	V_{ci}	Out
	V_{ci} -out-75	100.0	50.0	6.1	56.1	V_{ci}	In
	V_{ci} -out-75-2	100.2	50.1	6.1	56.2	V_{ci}	In
III	V_{cw} -00	180.2	90.1	3.2	93.3	V_{cw}	—
	V_{cw} -25	180.1	90.1	3.2	93.3	V_{cw}	In
	V_{cw} -50	150.2	75.1	3.2	78.3	V_{cw}	In
	V_{cw} -75	100.2	50.1	3.2	53.3	V_{ci}	In
IV	V_{ci} -in-50- V_s	107.9	53.9	4.4	58.3	V_{ci}	In

TABLE D.13
Test Results at Ultimate Failure

Series	Specimen ID	P _{applied} (kip)	V _{applied} (kip)	V _{self-weight} (kip)	V _{ult} (kip)	Failure Mode	Failure Location
I	V _{ci} -in-00	204.2	102.1	3.3	105.4	V _{ci}	—
	V _{ci} -in-25	205.2	102.6	4.4	107.0	V _{ci}	In
	V _{ci} -in-50	154.9	77.4	4.4	81.8	V _{ci}	In
	V _{ci} -in-75	84.2	42.1	4.4	46.5	V _{ci}	In
II	V _{ci} -out-00	179.2	89.6	2.7	92.3	V _{ci}	—
	V _{ci} -out-25	162.0	81.0	2.7	83.7	V _{ci}	Out
	V _{ci} -out-50	154.4	77.2	2.7	79.9	V _{ci}	Out
	V _{ci} -out-75	100.0	50.0	6.1	56.1	V _{ci}	In
	V _{ci} -out-75-2	100.2	50.1	6.1	56.2	V _{ci}	In
III	V _{cw} -00	204.3	102.2	0.0	102.2	Flexure	—
	V _{cw} -25	208.9	104.5	0.0	104.5	Flexure	Out
	V _{cw} -50	206.9	103.4	0.0	103.4	Flexure	Out
	V _{cw} -75	140.0	70.0	3.2	73.2	V _{ci}	In
IV	V _{ci} -in-50-V _s	182.4	91.2	4.4	95.6	V _{ci}	In

crack that formed at the end of the debonded region at an applied load of 60 kips.

The second phase is characterized by nonlinear behavior after first cracking. A reduced stiffness is observed in this phase for the specimens with 0%, 25%, and 50% debonded strand. The crack patterns spread outward from midspan and upward from the bottom. The end of the second phase is marked by the formation of the primary shear crack. In each of the specimens with debond sheathing, the primary shear crack formed at the end of the debonded region. These cracks were typically followed by a reduction in load. Furthermore, in each specimen, the primary shear crack formed at the end of one debonded region and then, with a slight increase in load, at the end of the other debonded region. It should be noted, however, that there was no observable second phase of behavior for the V_{ci}-in-75 specimen because the first crack that formed was the primary shear crack. Therefore, the end of the first phase for this specimen also marked the end of the second phase.

The third phase of load-deflection behavior represents all behavior after the primary shear cracks formed. During this stage, the load-deflection behavior is typically characterized by an initial increase in stiffness, followed by increasing deflections without increased load capacity (zero stiffness). In this third phase, the

beams begin acting more like tied-arches and less like beams. The cracking pattern generally remained the same throughout this stage. However, the cracks opened wider until the beams completely failed. The specimens with 0%, 25%, and 50% debonded strand failed in shear-compression with the compression zone crushing above the primary flexure-shear crack (Appendix D-3). The V_{ci}-in-75 specimen failed in shear-tension with the fully bonded strands rupturing at the single crack opening (at the end of the debonded region).

The load at which the primary shear crack forms is observed to decrease as the amount of debonding increases as shown in Figure D.47. Figure D.48 illustrates that each primary shear crack initiated at the end of the debonded region, denoted by the white dashed line for the specimens with debonded strand. For the specimen with no debonded strand (0%), the failure location was shifted towards midspan. The dashed line in the 0% specimen is included to allow direct comparison of the crack patterns. There were no debonded strands in this beam. It should be noted that the displacement sensors on the beam labeled “0%” (V_{ci}-in-00) in Figure D.47 went out of range at approximately the peak load. The deflections continued to grow without an increase in load, similar to the load-deflection curve of V_{ci}-in-25; therefore, the load-deflection plot is artificially cut off.

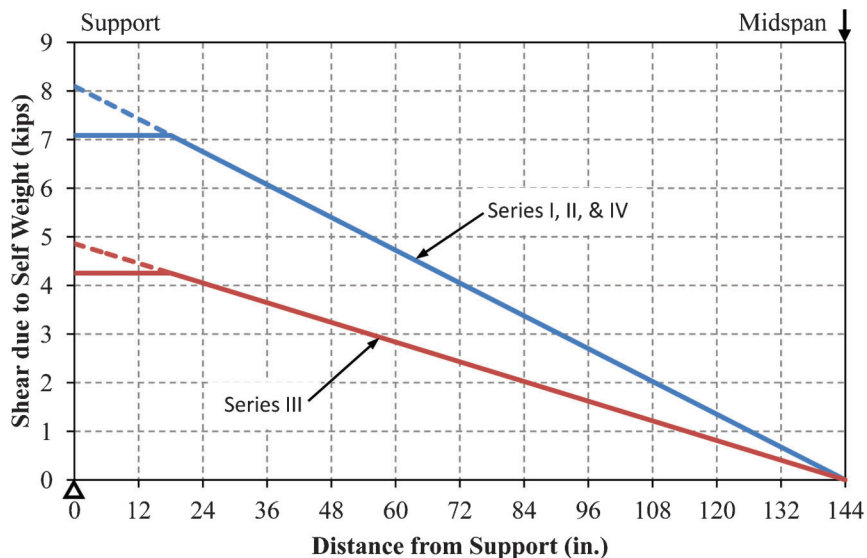


Figure D.46 Shear due to self-weight.

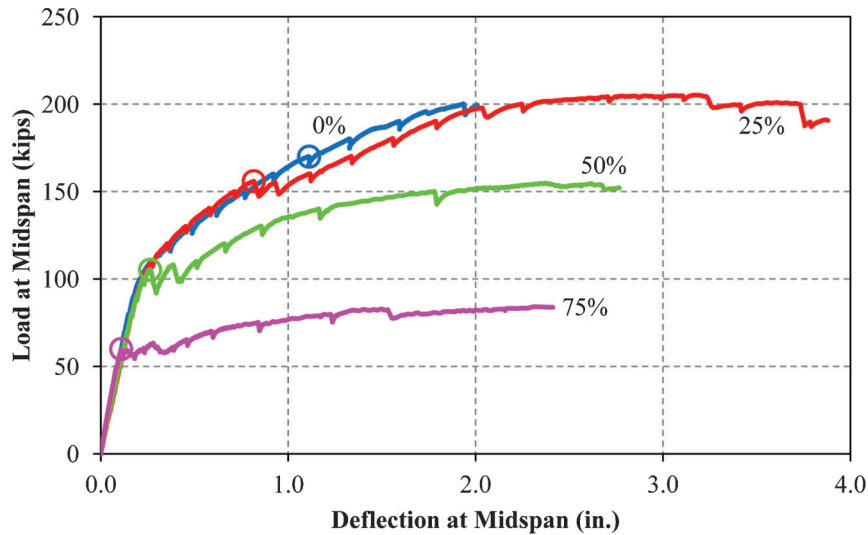


Figure D.47 Load-deflection behavior—Series I (V_{ci} -in).

D.7.2 Series II (V_{ci} -out)

The load-deflection behavior for the V_{ci} -out test series is presented in Figure D.49. The crack patterns at the formation of the primary shear crack are shown in Figure D.50. It should be noted that the end of the debonded region is only shown for V_{ci} -out-75. For the other specimens, the end of the debonded region is outside the photo to the left. The photo of V_{ci} -out-75 includes a series of external stirrups which allowed the specimen to be retested to fail the other shear span. The photo was taken immediately before the crack was closed by tightening the stirrups. Photos of the ultimate failures are shown in Appendix D-3.

In general, the load-deflection behavior for each specimen is characterized by three phases. In the first phase, the load-deflection relationship is linear elastic. Furthermore, the linear elastic portions of the load-deflection curves are nearly identical because the specimens were all designed with the same dimensions, concrete strength, and prestressing force (in the fully bonded region). The end of the first phase of behavior is marked by the formation of a flexural crack near midspan. Flexural cracking initiated at an applied load of approximately 80 kips for each beam.

The second phase is characterized by nonlinear behavior after first cracking. A reduced, but relatively constant, stiffness is observed in this phase. The crack patterns spread outward from

midspan and upward from the bottom. The end of the second phase is marked by the formation of the primary shear crack. Only the V_{ci} -out-75 specimen's primary shear crack formed at the end of the debonded region. The formation of this primary shear crack resulted in the complete failure for V_{ci} -out-75. The primary shear cracks in the other three specimens formed outside the debonded region. These cracks were typically followed by a reduction in load. Furthermore, in each specimen (except V_{ci} -out-75), the primary shear crack formed on one side of midspan and then, with a slight increase in load, on the other side.

The third phase of load-deflection behavior represents all behavior after the primary shear cracks formed. During this stage, the load-deflection behavior is characterized by an initial increase in stiffness, followed by increasing deflections without significantly increased load capacity. In this third phase, the beams acted more like tied-arches and less like beams. The cracking pattern generally remained the same throughout this stage with the cracks opening wider until complete failure. All of the beams in this series failed in shear-compression with the compression zone crushing above the primary flexure-shear crack (Appendix D-3). The third phase of behavior was not observed in the V_{ci} -out-75 specimen due to failure occurring when the primary shear crack formed.

The V_{ci} -out-75 beam behavior was significantly different from the other specimens in that the primary shear crack formed at a

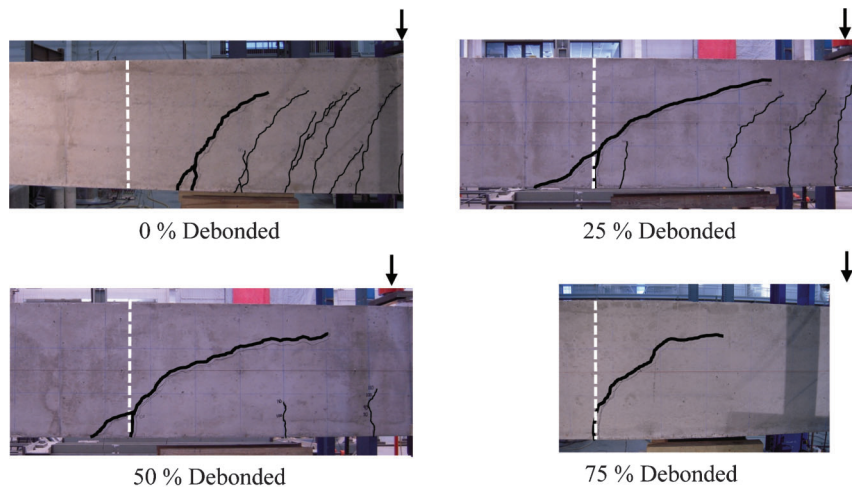


Figure D.48 Primary shear cracks—Series I (V_{ci} -in).

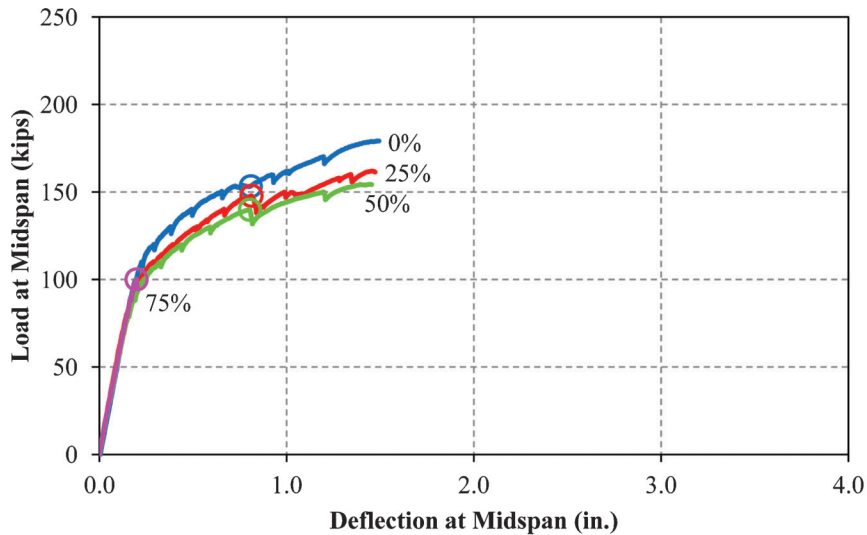


Figure D.49 Load-deflection behavior—Series II (V_{ci} -out).

much lower load. V_{ci} -out-75 failed in flexure-shear, but unlike the other beams in this series, failure initiated from the end of the debonded region as shown in Figure D.50. The predictions in Section D.3.2.3, however, show all four specimens in this series failing at the same load and at the same location (midspan). The beam failed at an applied load of approximately 100 kips which means that the crack formed at the end of the debonded region at a modulus of rupture of approximately $3.0\sqrt{f'_c}$ which is extremely low. The beam first cracked at midspan at a modulus of rupture of approximately $6.3\sqrt{f'_c}$ which is also on the low side. These modulus of ruptures were not expected; therefore, the shear capacity and location of failure was not correctly predicted.

After observing the failure of the V_{ci} -out-75 specimen, it was hypothesized that shrinkage cracks may have formed during the time when the DEMEC locating disks were installed, and could have led to a premature failure. If shrinkage cracks did form, it was believed to be due to the delay between stripping the forms (simultaneously ending the wet curing process) and cutting the strands. During this time, the beam began shrinking but was restrained by the uncut strands. Therefore, there is a possibility that shrinkage cracks formed along the beam which would have closed after transfer of the prestress force, going unnoticed. Some healing of these cracks may have occurred due to the early age of the concrete along with the clamping force from the prestressing. This could explain the low

modulus of ruptures experienced. It should be noted that thin cracks were observed along the top of the beam prior to testing.

To assist in determining if the low capacity and failure location of V_{ci} -out-75 was an outlier, the beam was retested to form the primary shear crack in the other shear span (Figure D.51 and Figure D.52). To retest, however, the failed shear span needed to be reinforced in shear due to the complete loss of concrete capacity to shear resistance. The failed shear span was reinforced with external stirrups consisting of 5/8 in. diameter, Grade B7 threaded rods anchored to back-to-back C3 × 5, A36 steel channels placed at the top and bottom of the beam (Figure D.52). These external stirrups were spaced at 9 in. along the entire failed shear span and tightened until the existing crack was closed.

The load-deflection behavior comparing both shear spans of V_{ci} -out-75 is illustrated in Figure D.51. Primary shear cracks for both shear span failures are shown in Figure D.52. The load-deflection behavior of the north and south shear span tests are quite different as evidenced by Figure D.51. The initial stiffness of the north shear span test diverges almost immediately from the original test (south shear span). Cracking spread outward from midspan and upward during the north shear span test as illustrated in Figure D.52. However, the cracks from the original V_{ci} -out-75 test significantly reduced the overall beam stiffness for the second test. Failures also initiated at the end of the debonded

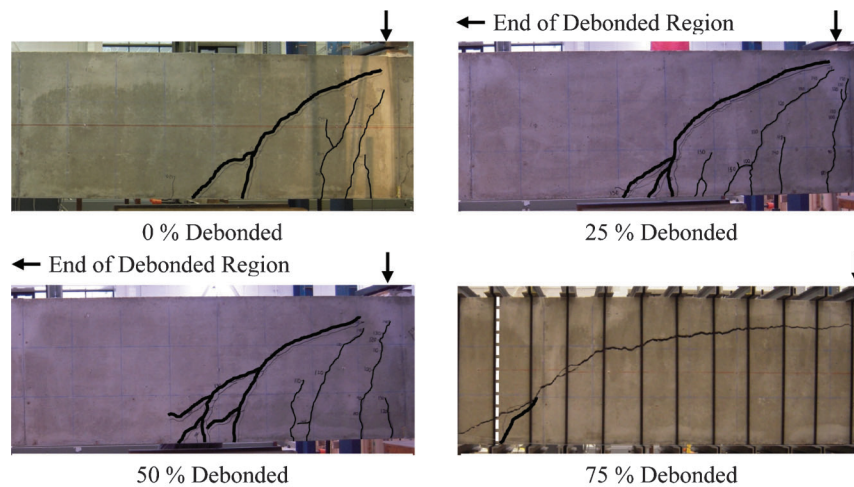


Figure D.50 Primary shear cracks—Series II (V_{ci} -out).

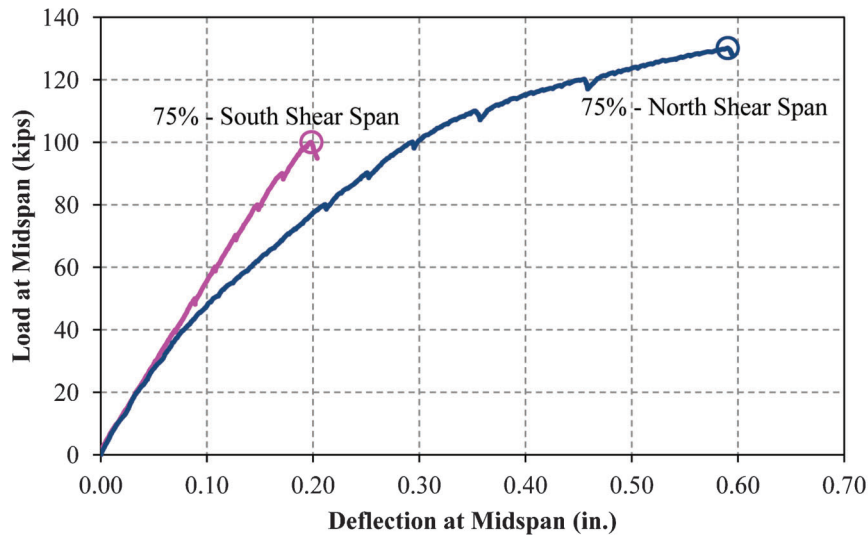


Figure D.51 Load-deflection behavior— V_{ci} -out-75.

region (Figure D.52), but the applied load was significantly higher in the north shear span (130 kips). This difference in capacity may be explainable by shrinkage cracking.

D.7.2.1 Duplicate Test

To test the hypothesis that shrinkage cracks may have weakened V_{ci} -out-75, resulting in a premature failure, a second specimen (V_{ci} -out-75-2) was constructed, but without installing the locating disks. It is worth noting that the locating disks were no longer installed on the specimens (after the first V_{ci} -out-75 beam), and instead, the strands were cut immediately after form removal to reduce the potential for restrained shrinkage cracking. Figure D.53 shows the load-deflection behavior for both V_{ci} -out-

75 specimens. The primary shear crack for both beams is illustrated in Figure D.54.

The behavior of V_{ci} -out-75-2 is nearly identical to V_{ci} -out-75. Both specimens formed flexural cracks at midspan at approximately 80 kips. In addition, the primary shear crack formed at the end of the debonded region at approximately 100 kips for both beams. The only observable difference in the load-deflection behavior, as illustrated in Figure D.53, is that the elastic stiffness of V_{ci} -out-75-2 is slightly less than that of V_{ci} -out-75. The primary shear cracks for both specimens are similar in appearance and location as shown in Figure D.54. Therefore, restrained shrinkage does not appear to be responsible for this unexpected behavior.

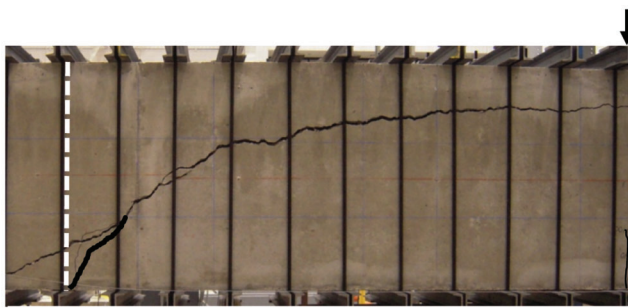
D.7.3 Series III (V_{cw})

The load-deflection behavior for the V_{cw} test series is presented in Figure D.55, and the crack patterns at the formation of the primary shear crack are shown in Figure D.56. The white dashed line in the 0% is included to allow direct comparison of the crack patterns. There were no debonded strands in this beam. Photos of the ultimate failures are shown in Appendix D-3.

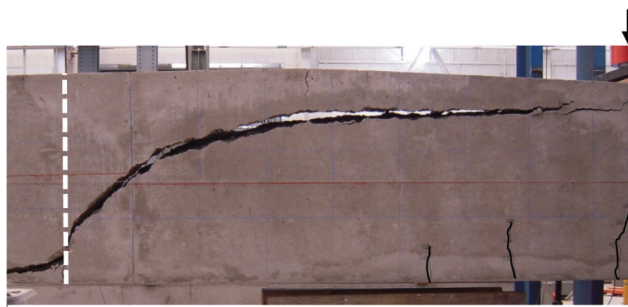
In general, the load-deflection behavior for each specimen is characterized by three phases. In the first phase the load-deflection relationship is linear elastic. Furthermore, the linear elastic portions of the load-deflection curves are nearly identical because the specimens were all designed with the same dimensions, concrete strength, and prestressing force (in the fully bonded region). The end of the first phase of behavior is marked by the formation of a flexural crack near midspan. Flexural cracking initiated at an applied load of approximately 90 kips for each beam.

The second phase is characterized by nonlinear behavior after first cracking. A reduced stiffness is observed in this phase. The crack patterns spread outward from midspan and upward from the bottom. The end of the second phase is marked by the formation of the primary shear crack. The primary shear cracks formed at the end of the debonded region for each specimen (Figure D.56). These cracks were typically followed by a reduction in load. Furthermore, in each specimen, the primary shear crack formed on one side of midspan and then, with a slight increase in load, on the other side. A flexure-shear crack formed at the end of the debonded region for V_{cw} -75. Web-shear cracks formed throughout the debonded region in V_{cw} -00 and V_{cw} -25. A web-shear crack formed at the end of the debonded region in V_{cw} -50.

The third phase of load-deflection behavior represents behavior after the primary shear cracks formed. During this stage, the load-deflection behavior is characterized by an initial increase in



75 % Debonded - S



75 % Debonded - N

Figure D.52 Primary shear cracks— V_{ci} -out-75.

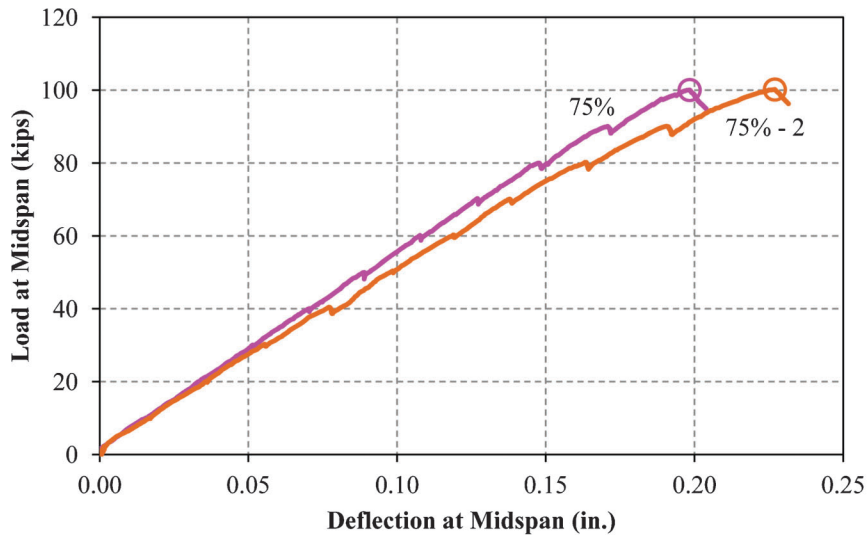


Figure D.53 Load-deflection behavior— V_{ci} -out-75 and V_{ci} -out-75-2.

stiffness, followed by increasing deflections without increased load capacity (zero stiffness). In this third phase, the beams acted more like tied-arches and less like beams. The cracking pattern generally remained the same throughout this stage; however, the cracks opened wider until the beams completely failed. All of the beams in this series, except V_{cw} -75, failed in flexure with concrete crushing at midspan. V_{cw} -75 failed in shear-compression at the end of the debonded region with the compression zone crushing above the primary flexure-shear crack (Appendix D-3).

Similar to the results for the V_{ci} -in series, the load at which the primary shear crack forms decreases as the amount of debonding increases. It should be noted, however, that the load at the formation of the primary shear cracks for V_{cw} -00 and V_{cw} -25 was approximately equal. This is evident from the predictions discussed in Section D.3.3.5

($V_{u, fail, 0.0} = 88.4$ kips and $V_{u, fail, 0.25} = 85.2$ kips). The predicted shear strength profile for V_{cw} -00 (Figure D.25) illustrates that the failure should occur near the support as shown in Figure D.56. The predicted shear strength profile for V_{cw} -25 (Figure D.26) shows that the failure could occur at both ends of the debonded region. This is evident in Figure D.56 where web-shear cracking has simultaneously formed throughout the debonded region.

D.7.4 Series IV: Transverse Reinforcement

Figure D.57 shows the load-deflection behavior for both V_{ci} -in-50 specimens. The primary shear crack for both beams is illustrated in Figure D.58.

The load-deflection behavior is characterized by three phases. In the first phase the load-deflection relationship is linear elastic. Furthermore, the linear elastic portions of the load-deflection curves are nearly identical because the specimens were both designed with the same dimensions, concrete strength, and prestressing force. The end of the first phase of behavior is marked by the formation of a flexural crack near midspan. Flexural cracking initiated at an applied load of approximately 80 kips for both beams.

The second phase is characterized by nonlinear behavior after first cracking. A reduced stiffness is observed in both specimens. The crack patterns spread outward from midspan and upward from the bottom. The end of the second phase is marked by the formation of the primary shear crack. In both specimens the primary shear cracks formed at the end of the debonded region. These cracks were followed by a reduction in load. Furthermore, in both specimens, the primary shear crack formed at the end of one debonded region and then, with a slight increase in load, at the end of the other debonded region.

The third phase of load-deflection behavior represents behavior after the primary shear cracks formed. During this stage, the load-deflection behavior is characterized by an initial increase in stiffness, followed by increasing deflections without increased load capacity (zero stiffness). In this third phase, the beams acted more like tied-arches and less like beams. The cracking pattern generally remained the same throughout this stage; however, the cracks opened wider until the beams completely failed. V_{ci} -in-50 failed in shear-compression with the compression zone crushing above the primary flexure-shear crack. V_{ci} -in-50- V_s failed in shear-tension with the fully bonded strands rupturing at the end of the debonded region immediately after both legs of a stirrup crossing the primary shear crack ruptured. The ultimate failure of V_{ci} -in-50- V_s is shown in Figure D.59. The ultimate failure of every specimen in this testing program is shown in Appendix D-3.

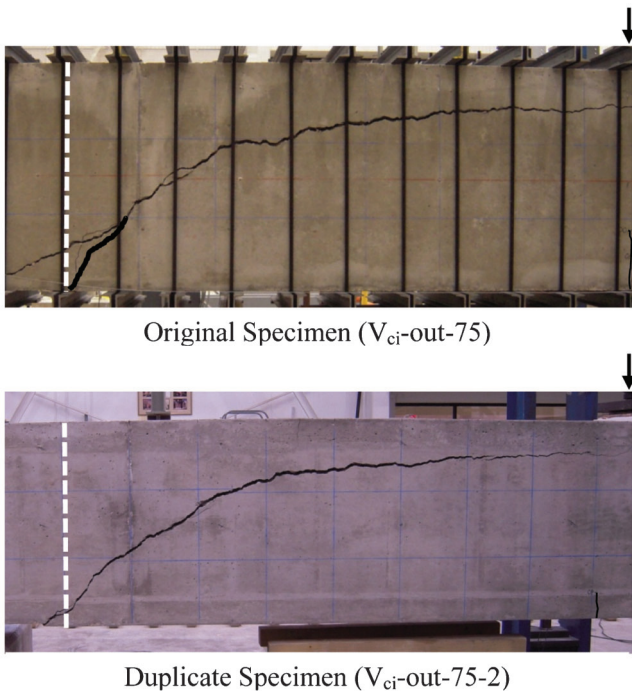


Figure D.54 Primary shear cracks— V_{ci} -out-75 and V_{ci} -out-75-2.

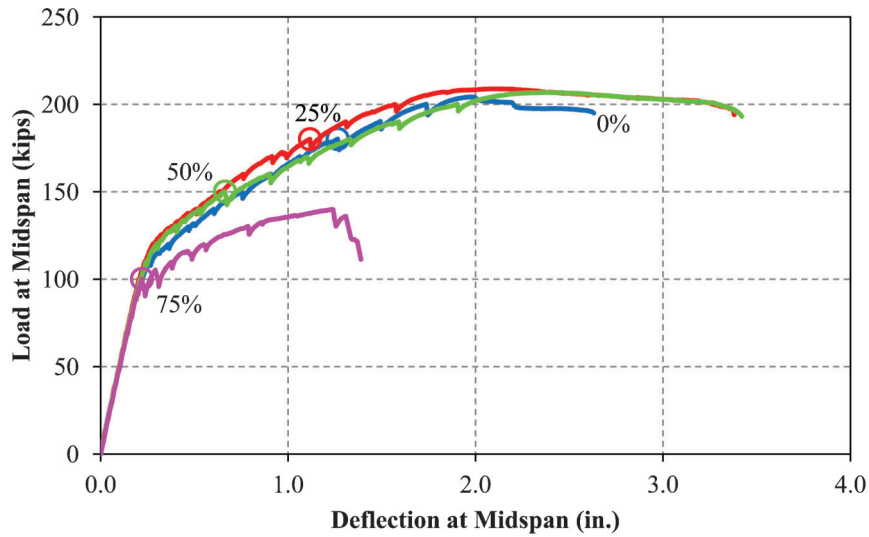


Figure D.55 Load-deflection behavior—Series III (V_{cw}).

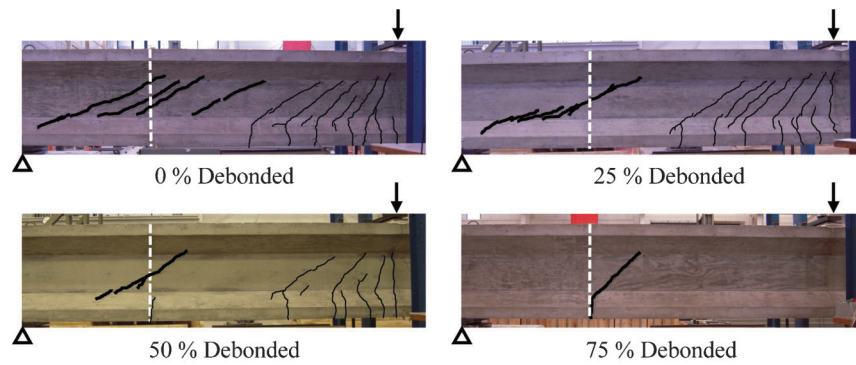


Figure D.56 Primary shear cracks—Series III (V_{cw}).

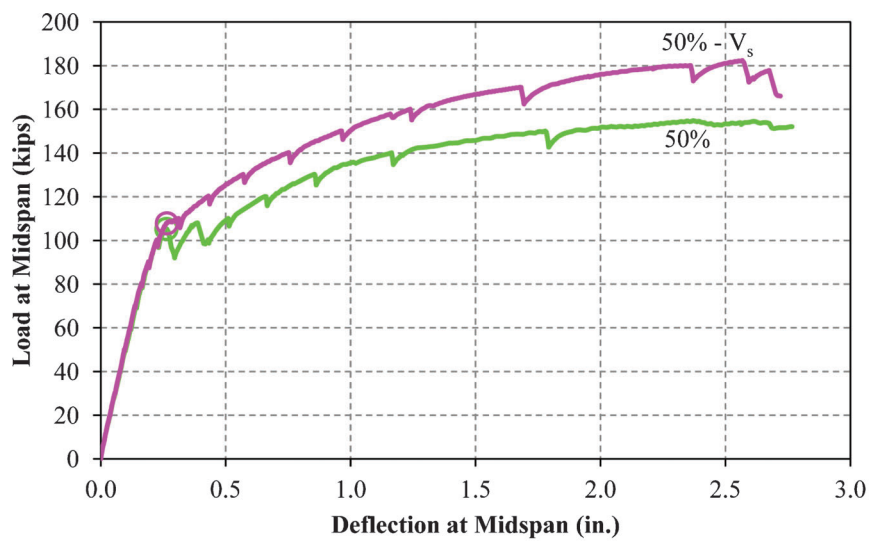


Figure D.57 Load-deflection behavior— V_{ci} -in-50 and V_{ci} -in-50- V_s .

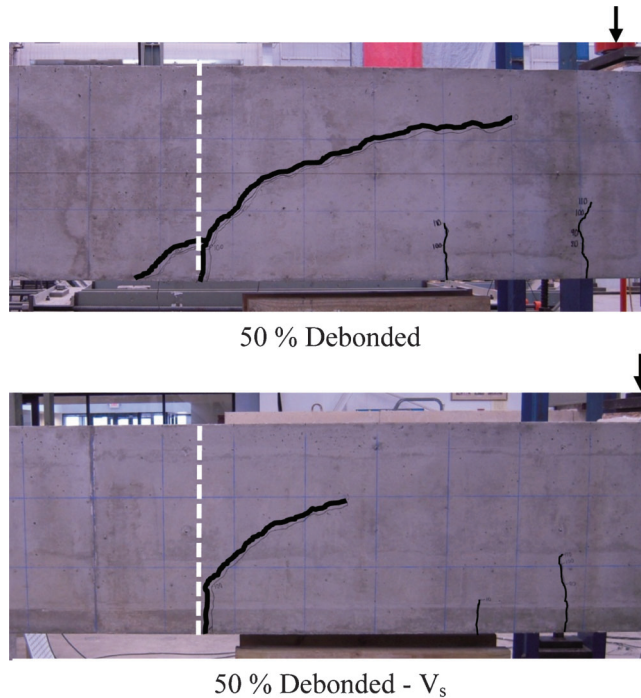


Figure D.58 Primary shear cracks— V_{ci} -in-50 and V_{ci} -in-50- V_s .

Both specimens were characterized by the primary shear crack forming at approximately the same load (Figure D.57). However, the primary shear crack in V_{ci} -in-50- V_s did not propagate as far as in the V_{ci} -in-50 specimen at the time the actual primary shear cracks initiated (Figure D.58). In addition, both beams deflected approximately 2.75 in. at failure, however, V_{ci} -in-50- V_s carried an additional 30 kips of applied load.

D.8 ANALYSIS OF RESULTS

D.8.1 Series I (V_{ci} -in)

Although each beam was able to resist additional load after the primary shear crack formed, it is believed that aggregate interlock and arch action contributed to this additional capacity. Furthermore, these beams would be assumed to have lost their concrete contribution to shear strength (AASHTO Section

5.8.3.4.3 and ACI 318-11 Section R11.4.7). Only the contribution of the transverse reinforcement would be assumed to add capacity after formation of the flexure-shear crack. However, the beams in this series did not have transverse reinforcement in the failure location (Figure D.12). In fact, the beams in this series could have suddenly failed after the formation of the inclined shear crack. In addition, it should be emphasized that the primary shear crack formed at the end of the debonded region in each beam, just as expected in the design phase (Figure D.48). The shear cracks initiated at the ends of the debonded regions, according to the shear analysis methodology described in Section D.2.3.2.1, because the neutral axis, and therefore, flexure-shear strength, is minimized at this location. These low neutral axis depths (at the ends of the debonded regions) are due to the reduced prestress force and longitudinal reinforcement stiffness in combination with relatively high flexural stresses.

The calculated shear capacities for each specimen, V_n , were plotted against the total applied shear, V_u (dead plus superimposed). The applied load was analytically increased for each beam until $V_u \geq V_n$. The location at which this occurs is the location of failure (formation of primary shear crack), and is labeled “ $V_{u,fail}$ ” in each shear strength profile. The flexure-shear strengths are combined with the web-shear strengths for both the bonded and debonded regions to create one comprehensive shear strength profile for each specimen.

The tensile strength, which was used to calculate the web-shear strength, was taken as $6\sqrt{f'_c}$ psi in all analyses. It is important to note that the modulus of rupture, f_r (in psi), was also assumed to be $6\sqrt{f'_c}$ in the development of the initial shear strength profiles, remaining consistent with the design provisions (AASHTO Section 5.4.2.6 and ACI 318-11 Section 11.3.3.1) for the cracking moment calculation. However, after the premature failure of V_{ci} -out-75, the value of the modulus of rupture was reviewed. The flexural crack that started at the end of the debonded region in V_{ci} -out-75 initiated at a much lower moment than expected. The crack initiated at a modulus of rupture of approximately $3\sqrt{f'_c}$. Therefore, to determine the appropriate modulus of rupture, additional analyses were carried out for each specimen, varying the assumed modulus of rupture each time. The upper ($6\sqrt{f'_c}$) and lower ($0\sqrt{f'_c}$) bounds are presented, as well as, an intermediate value ($3\sqrt{f'_c}$). The modulus of rupture was also varied by region of



Figure D.59 Ultimate failure— V_{ci} -in-50- V_s .

the beam to determine if the modulus of rupture was only being reduced in the debonded regions. Therefore, some analyses use a different modulus of rupture in the debonded region as opposed to the central region where all strands are bonded. The shear strength profiles for each modulus of rupture variation are illustrated in Figure D.60 through Figure D.63. All analyses use the concrete compressive strengths on test day provided in Table D.8.

The shear strength profiles for Series I (Figure D.60 through Figure D.63) show that the failure mode (primary shear crack) for each specimen (in all modulus of rupture combinations) is flexure-shear (V_{ci}). The profiles also show that the primary shear crack in V_{ci} -in-25 should form outside the debonded region while the primary cracks in the other two debonded specimens (V_{ci} -in-50 and V_{ci} -in-75) are shown to form at the end of the debonded region. It is important to note that the analytical failures are observed to occur nearly simultaneously inside and outside the debonded region for V_{ci} -in-25 (Figure D.61). In fact, Figure D.61(e) shows that the failures do occur simultaneously inside and outside the debonded region. The shears, V_u , are different due to self-weight.

Changing the modulus of rupture values in the analyses affects the extents of cracked regions as observed in the shear strength profiles. The shear capacities are mostly unaffected as the modulus of rupture is reduced, however, because the section where analytical failure occurs is already cracked when failure is reached. Therefore, reducing the modulus of rupture in sections that would otherwise already be cracked only reduces the cracking moment and increases the extent of cracking. Reducing the modulus of rupture from $6\sqrt{f'_c}$ in the debonded region of V_{ci} -in-75, however, reduced the shear capacity. The capacity was reduced in this specimen because a value of $6\sqrt{f'_c}$ resulted in failure at first cracking. When the modulus was reduced, there was not a jump to failure at first cracking, but rather the section was already cracked.

The critical values from the shear strength profiles are provided in Table D.14 to compare the calculated shear capacities (V_{model}) to the measured shear capacities at the formation of the primary shear crack (V_{test}) for each modulus of rupture combination. The shear capacities from ACI 318 and AASHTO are provided as well. Ratios of measured shear capacities to calculated shear capacities are provided in Table D.15. These ratios allow comparisons between the three different approaches to calculate shear strength. The ACI 318 and AASHTO values in Table D.14 and Table D.15 are presented with and without the lower bound limit (Section D.2.3.2.2 and Section D.2.3.2.3) to determine the validity of the limit. In addition, the modulus of rupture values used in the ACI 318 (Equation D.21) and AASHTO (Equation D.26) calculations for flexure-shear strength were also adjusted to make comparisons with the results from the shear model. It is important to note that all of the shears reported in Table D.14 include the shear due to self-weight. The shear diagram due to self-weight is illustrated in Figure D.46.

The results of these analyses suggest that there are minimal changes in the shear capacities using the shear model as the modulus of rupture is varied. The only exception is in the analyses of the V_{ci} -in-75 specimen which agree well with the test result when the modulus of rupture in the debonded region is reduced below $6\sqrt{f'_c}$. In general, the shear model is able to capture the decreasing trend of shear capacities (including type and location) as the percentage of debonded strand increases.

Conversely, capacities from the ACI 318 and AASHTO procedures for calculating flexure-shear strength (Section D.2.3.2.2 and Section D.2.3.2.3) are mostly unaffected by the percentage of debonded strand and the adjustments of the modulus of rupture. This is due to the fact that the lower bound limit of flexure-shear strength controlled in almost every analysis. Therefore, the ACI 318 and AASHTO approaches (with the lower limit in place) are unable to capture the shear strength of specimens with relatively large percentages of debonded strand (greater than 25%) or specimens that may have a reduced modulus of rupture. When the lower limit is ignored, however, the analytical results are much improved.

In general, the shear strength ratios are observed to decrease as the percentage of debonded strand increases. This is true for the shear strength ratios from all three approaches. Finally, the analytical results using a modulus of rupture of $0\sqrt{f'_c}$ throughout

the entire beam provides conservatism ($V_{test}/V_{calc} > 1$) for all specimens except V_{ci} -in-75 when using the ACI 318 and AASHTO provisions (neglecting the lower limit). It appears that this reduction in conservatism as the percentage of debonded strand is increased may be directly related with the decreasing trend in the modulus of rupture as debonding increases. For the shear model, results are only slightly below 1 for the 50% and 75% case. Overall, the shear model results in the most consistent and conservative calculations of shear strength.

The modulus of rupture values observed for each beam are provided in Table D.16. This table presents the measured modulus of rupture values at the end of the debonded region, labeled "Debond" and at midspan, labeled "Bond." It should be noted that there was no flexural cracking at midspan during the V_{ci} -in-75 test because failure occurred at the end of the debonded region prior to cracking at midspan (Table D.16). A reduction in the measured modulus of rupture is evident in each of the debonded regions relative to the bonded regions. The reduced moduli of rupture is theorized to be due to the damage caused by all of the debonded strand transferring prestressing force at the end of the debonded region when cut. The strand was cut at a relatively early age for the concrete; therefore, the prestressing force may have partially "healed" the damaged concrete at the end of the debonded region resulting in a reduced modulus of rupture.

D.8.2 Series II (V_{ci} -out)

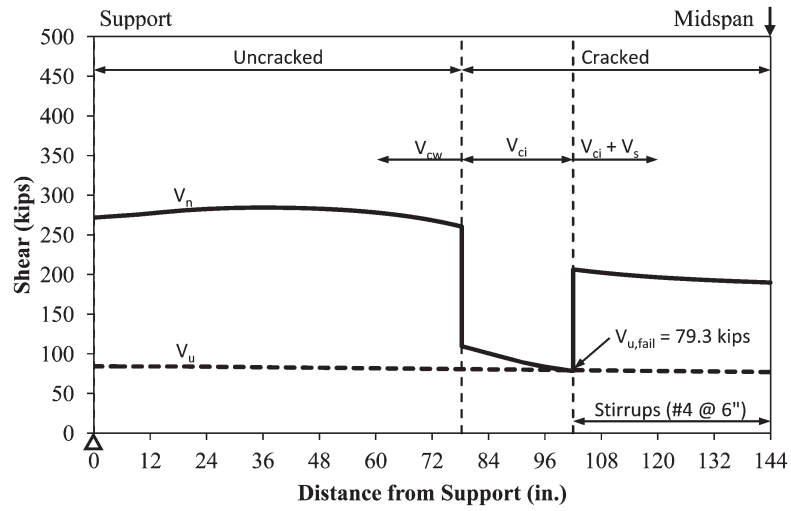
Except for the V_{ci} -out-75 specimen, all of the beams in Series II developed flexure-shear cracks outside the debonded region. These failures are believed to have occurred outside the debonded region due to the lower neutral axis depths near midspan. The high flexural stresses near midspan outweighed the reduced prestress force and longitudinal reinforcement stiffness in the debonded region. Therefore, the failure occurred outside the debonded region, where the neutral axis depths were smaller.

As previously discussed V_{ci} -out-75 failed prematurely and in a different location than expected with failure initiating at the end of the debonded region rather than away from the region. It was originally theorized that this failure could be due to restrained shrinkage cracking. To evaluate this hypothesis, a duplicate beam was constructed and tested (V_{ci} -out-75-2). However, after testing the V_{ci} -out-75-2 beam, it was obvious that the time delay between removing forms and cutting the strands did not contribute to the reduced shear strength. Both beams failed at nearly the same load (Figure D.53) and at the same location (Figure D.54). The only difference in the load-deflection behavior is that the stiffness was slightly lower in the second beam (V_{ci} -out-75-2). This is due to the fact that the concrete strength in the second beam was approximately 8% lower than the original beam (Table D.8). However, it should be emphasized that the same mix was ordered for both beams and the concrete age at testing was similar.

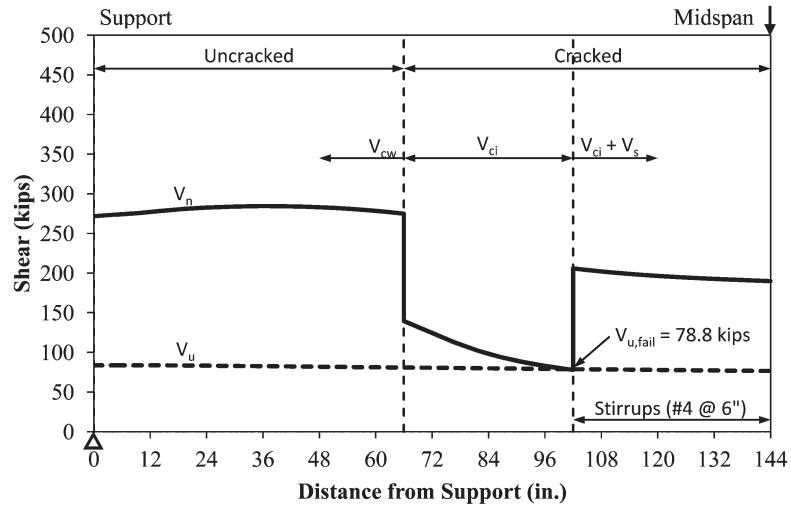
The shear strength profiles for all specimens are illustrated in Figure D.64 through Figure D.68. All analyses use the concrete compressive strengths on test day provided in Table D.8.

The shear strength profiles for Series II (Figure D.64 through Figure D.68) show that the failure mode (primary shear crack) for each specimen (in all modulus of rupture combinations) is flexure-shear (V_{ci}). The profiles also show that the primary shear cracks should form outside the debonded region for each specimen with the exception of V_{ci} -out-75. When the modulus of rupture in the debonded region is reduced below $6\sqrt{f'_c}$, the primary shear crack in V_{ci} -out-75 forms at the end of the debonded region (matching the test results).

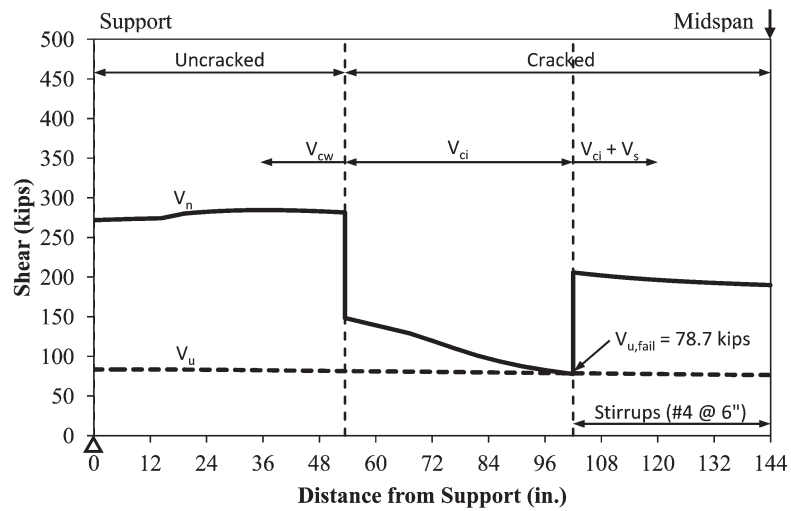
Similar to the shear strength profiles in Series I, changing the modulus of rupture values in the analyses affects the extents of cracking along the beam as observed in the shear strength profiles. Reducing the modulus of rupture in the debonded region of V_{ci} -out-75 and V_{ci} -out-75-2 reduces the shear capacity because they possess a low longitudinal reinforcement stiffness (low neutral axis depth) in the debonded region at flexural cracking. Therefore, when the cracking moment is exceeded at the end of the debonded region, there is not enough compressive area to resist the shear which causes immediate failure. Reducing the modulus of rupture



(a) Upper Bound ($f_{r,bond} = 6\sqrt{f'_c}$)

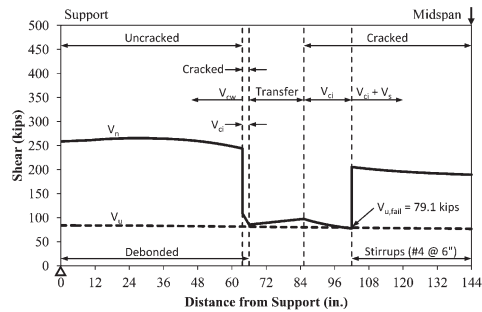


(b) Intermediate ($f_{r,bond} = 3\sqrt{f'_c}$)

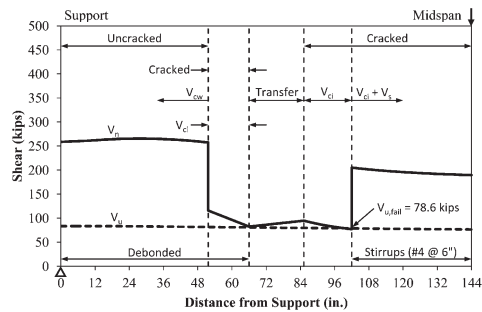


(c) Lower Bound ($f_{r,bond} = 0\sqrt{f'_c}$)

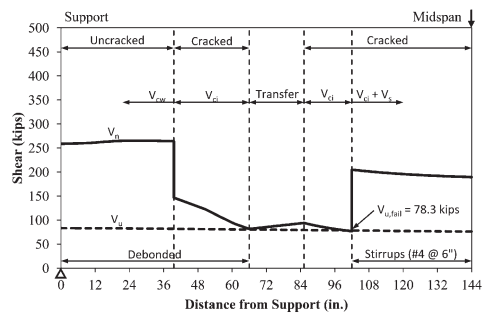
Figure D.60 Shear strength profile for V_{ci} -in-00.



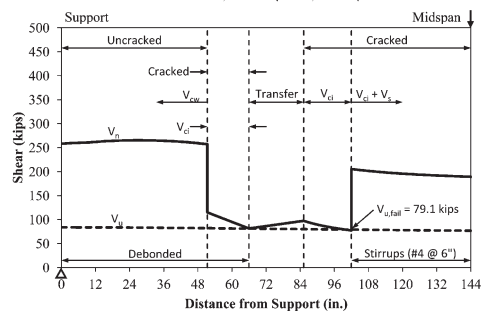
(a) Upper Bound ($f_{r,debond} = 6\sqrt{f'_c}$; $f_{r,bond} = 6\sqrt{f'_c}$)



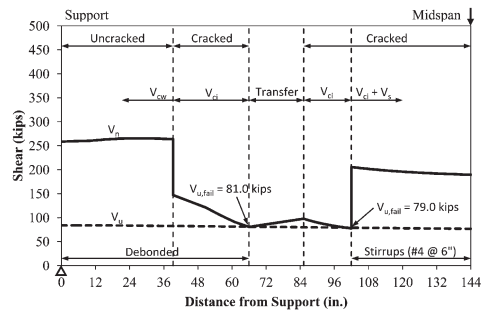
(b) Intermediate ($f_{r,debond} = 3\sqrt{f'_c}$; $f_{r,bond} = 3\sqrt{f'_c}$)



(c) Lower Bound ($f_{r,debond} = 0\sqrt{f'_c}$; $f_{r,bond} = 0\sqrt{f'_c}$)

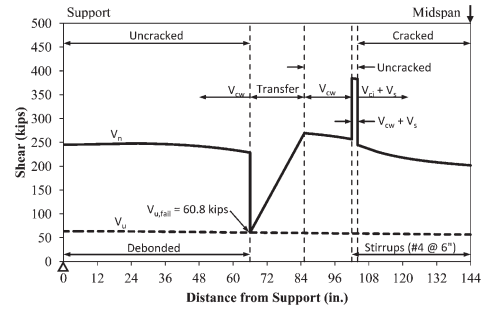


(d) Reduced Debond Strength ($f_{r,debond} = 3\sqrt{f'_c}$; $f_{r,bond} = 6\sqrt{f'_c}$)

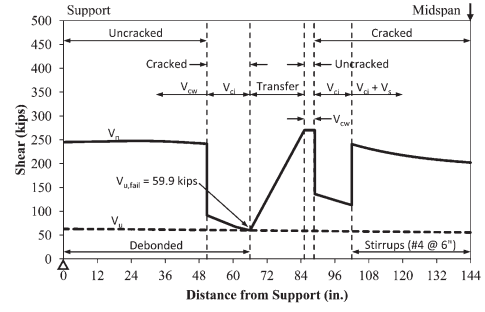


(e) Reduced Debond Strength ($f_{r,debond} = 0\sqrt{f'_c}$; $f_{r,bond} = 6\sqrt{f'_c}$)

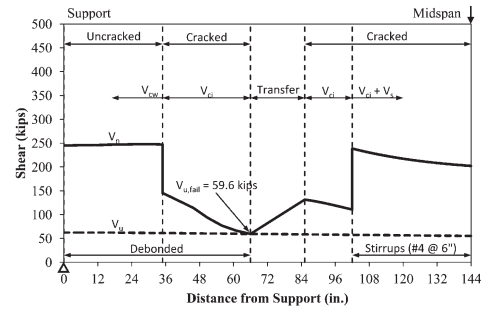
Figure D.61 Shear strength profile for V_{ci} -in-25.



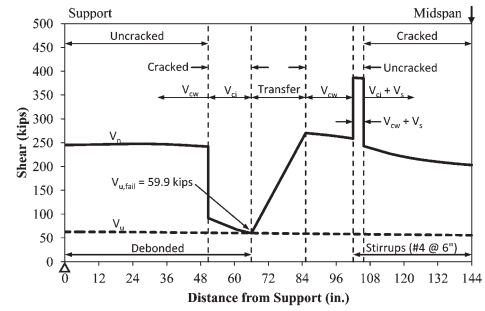
(a) Upper Bound ($f_{r,debond} = 6\sqrt{f'_c}$; $f_{r,bond} = 6\sqrt{f'_c}$)



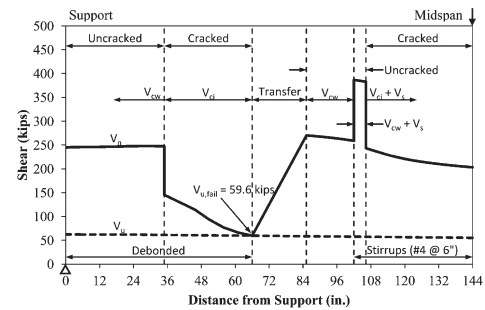
(b) Intermediate ($f_{r,debond} = 3\sqrt{f'_c}$; $f_{r,bond} = 3\sqrt{f'_c}$)



(c) Lower Bound ($f_{r,debond} = 0\sqrt{f'_c}$; $f_{r,bond} = 0\sqrt{f'_c}$)



(d) Reduced Debond Strength ($f_{r,debond} = 3\sqrt{f'_c}$; $f_{r,bond} = 6\sqrt{f'_c}$)



(e) Reduced Debond Strength ($f_{r,debond} = 0\sqrt{f'_c}$; $f_{r,bond} = 6\sqrt{f'_c}$)

Figure D.62 Shear strength profile for V_{ci} -in-50.

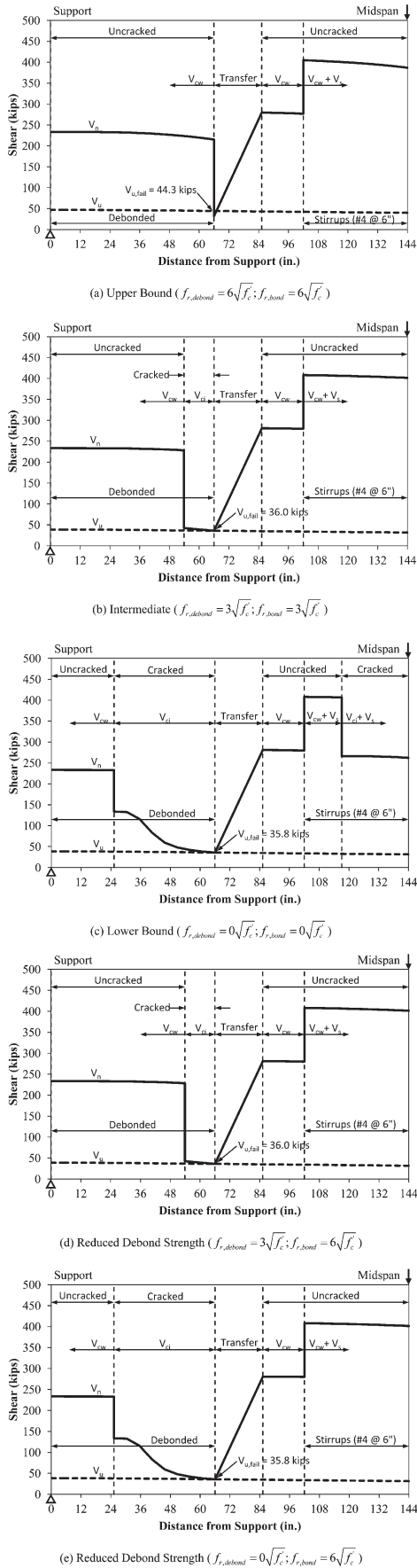


Figure D.63 Shear strength profile for V_{ci} -in-75.

in the debonded region results in a lower cracking moment thereby changing the failure location and reducing the shear capacity in the specimens with 75% debonded strand. It should be noted that the difference in calculated shear strengths for V_{ci} -out-75 and V_{ci} -out-75-2 is due to the difference in concrete strength.

The critical values from the shear strength profiles are provided in Table D.17 to compare the calculated shear capacities (V_{model}) to the measured shear capacities at the formation of the primary shear crack (V_{test}) for each modulus of rupture combination. The shear capacities from ACI 318 and AASHTO are provided as well. Ratios of measured shear capacities to calculated shear capacities are provided in Table D.18. The ACI 318 and AASHTO values in Table D.17 and Table D.18 are presented with and without the lower bound limit on the calculated flexure-shear strength (Section D.2.3.2.2 and Section D.2.3.2.3) to determine the validity of the limit. It is important to note that all of the shears reported in Table D.17 include the shear due to self-weight. The shear diagram due to self-weight is illustrated in Figure D.46.

The results of these analyses suggest that there are minimal changes in the shear capacities (using the shear model) as the modulus of rupture is varied. The exception is in the analyses of V_{ci} -out-75 and V_{ci} -out-75-2 when the modulus of rupture is reduced below $6\sqrt{f_c}$. Conversely, capacities from the ACI 318 and AASHTO procedures for calculating flexure-shear strength (Section D.2.3.2.2 and Section D.2.3.2.3) are completely unaffected by the percentage of debonded strand and the adjustments of the modulus of rupture. This is due to the fact that the lower bound limit of flexure-shear strength controlled in every analysis. When the lower limit is ignored, however, the analytical results are much improved. The analytical results using a modulus of rupture of $0\sqrt{f_c}$ throughout the entire beam provides conservatism ($V_{test}/V_{calc} > 1$) for all specimens except V_{ci} -out-75 when using the ACI 318 and AASHTO provisions (neglecting the lower limit). Using the shear model, consistent and conservative results are obtained when using a modulus of $0\sqrt{f_c}$.

The modulus of rupture values for each beam are provided in Table D.19. There is a distinct reduction in the modulus of rupture in the debonded region relative to the bonded region. The reduced moduli of rupture is theorized to be due to the damage caused by all of the debonded strand transferring prestressing force at the end of the debonded region when cut (Section D.8.1). The reduced modulus of rupture values in the debonded region for Series II (Table D.19) are even more pronounced than the reductions observed in Series I (Table D.16). It should be noted that cracking occurred at the end of the debonded region only for specimens V_{ci} -out-75 and V_{ci} -out-75-2. These results support the use of a reduced modulus of rupture.

D.8.3 Series III (V_{cw})

The primary shear crack formed at the end of the debonded region in each specimen. This is believed to be due to the fact that the beam at the end of the debonded region experiences a combination of reduced prestress forces and relatively high flexural stresses. The increasing flexural stresses increase the principle tensile stresses, enhancing the likelihood of developing web-shear cracks (V_{cw} -00, V_{cw} -25, and V_{cw} -50). On the other hand, increasing flexural stresses reduces the neutral axis, which improves the chances of developing flexure-shear cracks, especially for specimens with a large percentage of debonded strand (V_{cw} -75).

The same combinations of modulus of rupture values were used in the development of the shear strength profiles for Series III (Figure D.69 through Figure D.72) as were used in Series I and II. Although Series III consisted of I-beams designed to fail in web-shear, the same sets of analyses were performed to be consistent. It is important to note that while the values for the modulus of rupture (f_r) were changed, the tensile strength (f_{ct}) used to calculate web-shear strength remained $6\sqrt{f_c}$ throughout all analyses. The same tensile strength was used in each analysis because the assumed damage caused by the debonded strand at transfer would have likely only affected the bottom of the section (where strand is located) and not the web in the middle of the

TABLE D.14
Comparison of Shear Strengths for Series I

Specimen ID	Modulus of Rupture (psi)		V_{test} (kip)	Model	V_{calc} (kip)			
					ACI 318		AASHTO	
					Debond	Bond	Limit	No Limit
V _{ci} -in-00	—	$6\sqrt{f'_c}$	88.3	79.3	87.2	87.2	86.9	86.9
	—	$3\sqrt{f'_c}$		78.8	82.9	77.6	86.9	77.3
	—	$0\sqrt{f'_c}$		78.7	82.9	67.9	86.9	67.6
V _{ci} -in-25		$6\sqrt{f'_c}$	82.4	79.1	86.2	86.2	85.8	85.8
		$3\sqrt{f'_c}$		78.6	81.5	76.7	85.2	76.3
		$0\sqrt{f'_c}$		78.3	81.5	67.2	85.2	66.8
	$3\sqrt{f'_c}$	$6\sqrt{f'_c}$		79.1	86.2	86.2	85.8	85.8
	$0\sqrt{f'_c}$	$6\sqrt{f'_c}$		79.0	81.5	75.0	85.2	75.1
V _{ci} -in-50		$6\sqrt{f'_c}$	57.0	60.8	85.7	85.7	85.3	85.3
		$3\sqrt{f'_c}$		59.9	80.7	73.4	84.3	74.0
		$0\sqrt{f'_c}$		59.6	80.7	58.8	84.3	59.4
	$3\sqrt{f'_c}$	$6\sqrt{f'_c}$		59.9	80.7	73.4	84.3	74.0
	$0\sqrt{f'_c}$	$6\sqrt{f'_c}$		59.6	80.7	58.8	84.3	59.4
V _{ci} -in-75		$6\sqrt{f'_c}$	34.4	44.3	81.6	72.7	85.4	73.7
		$3\sqrt{f'_c}$		36.0	81.6	58.0	85.4	59.0
		$0\sqrt{f'_c}$		35.8	81.6	43.2	85.4	44.3
	$3\sqrt{f'_c}$	$6\sqrt{f'_c}$		36.0	81.6	58.0	85.4	59.0
	$0\sqrt{f'_c}$	$6\sqrt{f'_c}$		35.8	81.6	43.2	85.4	44.3

TABLE D.15
Comparison of Shear Strength Ratios for Series I

Specimen ID	Modulus of Rupture (psi)		V_{test} (kip)	Model	V_{test}/V_{calc}			
					ACI 318		AASHTO	
					Debond	Bond	Limit	No Limit
V _{ci} -in-00	—	$6\sqrt{f'_c}$	88.3	1.11	1.01	1.01	1.02	1.02
	—	$3\sqrt{f'_c}$		1.12	1.07	1.14	1.02	1.14
	—	$0\sqrt{f'_c}$		1.12	1.07	1.30	1.02	1.31
V _{ci} -in-25		$6\sqrt{f'_c}$	82.4	1.04	0.96	0.96	0.96	0.96
		$3\sqrt{f'_c}$		1.05	1.01	1.07	0.97	1.08
		$0\sqrt{f'_c}$		1.05	1.01	1.23	0.97	1.23
	$3\sqrt{f'_c}$	$6\sqrt{f'_c}$		1.04	0.96	0.96	0.96	0.96
	$0\sqrt{f'_c}$	$6\sqrt{f'_c}$		1.04	1.01	1.10	0.97	1.10
V _{ci} -in-50		$6\sqrt{f'_c}$	57.0	0.94	0.67	0.67	0.67	0.67
		$3\sqrt{f'_c}$		0.95	0.71	0.78	0.68	0.77
		$0\sqrt{f'_c}$		0.96	0.71	0.97	0.68	0.96
	$3\sqrt{f'_c}$	$6\sqrt{f'_c}$		0.95	0.71	0.78	0.68	0.77
	$0\sqrt{f'_c}$	$6\sqrt{f'_c}$		0.96	0.71	0.97	0.68	0.96
V _{ci} -in-75		$6\sqrt{f'_c}$	34.4	0.78	0.42	0.47	0.40	0.47
		$3\sqrt{f'_c}$		0.96	0.42	0.59	0.40	0.58
		$0\sqrt{f'_c}$		0.96	0.42	0.80	0.40	0.78
	$3\sqrt{f'_c}$	$6\sqrt{f'_c}$		0.96	0.42	0.59	0.40	0.58
	$0\sqrt{f'_c}$	$6\sqrt{f'_c}$		0.96	0.42	0.80	0.40	0.78

TABLE D.16
Measured Modulus of Ruptures for Series I

Specimen ID	f'_c (psi)	Modulus of Rupture (psi)	
		Debond	Bond x (in.)
V _{ci} -in-00	7,170	—	$6.4\sqrt{f'_c}$
V _{ci} -in-25	6,930	$5.7\sqrt{f'_c}$	$6.5\sqrt{f'_c}$
V _{ci} -in-50	6,800	$4.9\sqrt{f'_c}$	$6.6\sqrt{f'_c}$
V _{ci} -in-75	6,950	$4.0\sqrt{f'_c}$	—

section. All analyses use the concrete compressive strengths on test day provided in Table D.8.

The shear strength profiles for Series III (Figure D.69 through Figure D.72) show that the failure for each specimen (in all modulus of rupture combinations) occurs inside the debonded region. The analytical failures of V_{cw}-00 in Figure D.69 occur near the support. It should be noted, however, that the failure is marked approximately 5 in. from the support because this is the first point along the profile that a shear strength analysis was conducted. Linear interpolation was then used to find the shear capacity at the support. Therefore, it was decided to use the first point in the shear span as the failure location for this specimen.

The critical values from the shear strength profiles are provided in Table D.20 to compare the calculated shear capacities (V_{model}) to the measured shear capacities at the formation of the primary shear crack (V_{test}) for each modulus of rupture combination. The shear capacities from ACI 318 and AASHTO are provided as well. Ratios of measured shear capacities to calculated shear capacities are provided in Table D.21. These ratios allow comparisons between the three different approaches to calculate shear strength. The ACI 318 and AASHTO values in Table D.20 and Table D.21 are presented with and without the lower bound limit on the calculated flexure-shear strength (Section D.2.3.2.2 and Section D.2.3.2.3) to determine the validity of the limit. It is important to note that all of the shears reported in Table D.20 include the shear due to self-weight. The shear diagram due to self-weight is illustrated in Figure D.46.

The results of these analyses show that the shear capacities (using the shear model) are reduced as the modulus of rupture is reduced when the failure type changes from web-shear to flexure-shear. In general, the shear model is able to capture the decreasing trend of shear capacities (including type and location) as the percentage of debonded strand increases. The AASHTO simplified procedure for calculating web-shear strength (Section D.2.3.2.3) is also able to capture this trend, albeit with overly conservative strengths. Capacities from the ACI 318 procedures for calculating web-shear strength (Section D.2.3.2.2) are much closer to the measured shear strengths. This is due to the fact that the web-shear equation in ACI 318 (Equation D.22) provides lower shear strengths than the web-shear equation in AASHTO (Equation D.27). Although the form of the web-shear strength equation is the same in ACI 318 and AASHTO, the coefficient of the first term is different. The first term in the ACI 318 web-shear strength calculation is $3.5\sqrt{f'_c}$ (in psi units), and the first term of the AASHTO equation is $1.9\sqrt{f'_c}$ (in psi units). Furthermore, the effective depth in AASHTO is defined such that it will always be smaller than the ACI 318 defined effective depth (Section D.2.3.2.2 and Section D.2.3.2.3). For these reasons, the web-shear strengths using the AASHTO approach are lower than the ACI 318 approach.

The modulus of rupture values for each beam are provided in Table D.22. This table presents the measured modulus of rupture values at the end of the debonded region, labeled "Debond" and at midspan, labeled "Bond." It should be noted that there was no flexural cracking at the end of the debonded region during the V_{cw}-25 test. In addition, a reduction of the modulus of rupture in the debonded region was observed in V_{cw}-50 and V_{cw}-75. The slightly higher modulus values observed here fit well with the shear strength comparisons of the shear model shown in Table D.20 where modulus values closer to $6\sqrt{f'_c}$ agree well with the test results.

D.8.4 Series IV (Transverse Reinforcement)

V_{ci}-in-50-V_s is believed to have carried additional load after the formation of the primary shear crack due to aggregate interlock, arch action, and transverse reinforcement. This specimen is the only one with transverse reinforcement in the debonded region. Therefore, tests were performed on the #3 stirrup legs to determine the tensile properties (Section D.4.3). The actual yield stress was measured to be 74.1 ksi at a strain of 0.35%. This yield stress was then used in the following analyses of the specimen to develop shear strength profiles for each modulus of rupture combination (Figure D.73). The steel contribution to shear capacity is calculated using the smeared stirrup approach (Section D.2.3.2). All analyses use the concrete compressive strength on test day provided in Table D.8.

The shear strength profiles illustrated in Figure D.73 should be compared with those in Figure D.62 to gain a better understanding of the effects of transverse reinforcement in the debonded region. The failure mode (flexure-shear) and location (end of debonded region) is the same for both sets of analyses. It is clear, however, that the addition of transverse reinforcement in the debonded region (V_{ci}-in-50-V_s) increased the shear capacity and the extents of cracking compared with V_{ci}-in-50.

A modification was made to the calculation of the steel contribution to shear capacity after observing the failure crack in V_{ci}-in-50-V_s. A different calculation for the steel contribution to shear capacity (V_s) was needed that could adequately account for the discrete number of stirrups that would conservatively be crossed and engaged by a flexure-shear crack. An equation matching these criteria came from studies conducted by Frosch (2000) and Tompos and Frosch (2002). This equation (Equation D.32) reduced the horizontal projection of the assumed crack by the development length of the stirrup to ensure that each stirrup used to calculate strength is adequately anchored.

The crack shown in Figure D.74 engaged 2 stirrups instead of the 3.6 stirrups assumed using d/s smeared stirrup calculation from ACI 318. The third stirrup (with 8 in. embedment) is assumed not to be effective because the vertical crack along this stirrup prevents adequate anchorage even though this stirrup only requires 6.5 in. of embedment according to Equation D.34. It should be noted that Equation D.34 is taken from ACI 318-11 Section 12.5 to calculate the development length of hooked bars in tension using the actual yield stress of 74.1 ksi.

$$V_s = A_v f_y N_v \quad (D.32)$$

where:

N_v: number of stirrups crossed by shear crack, truncated integer quantity (Eq. D.33)

$$N_v = INT \left(\frac{d - l_{dv}}{s} \right) \quad (D.33)$$

where:

l_{dv}: development length of shear reinforcement, in. (Eq. D.34)

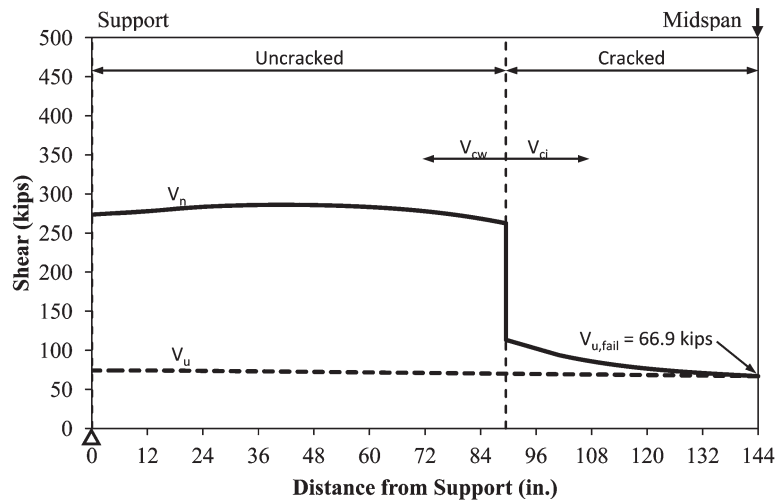
$$l_{dv} = \left(\frac{0.02 f_y}{\sqrt{f'_c}} \right) d_b \quad (D.34)$$

where:

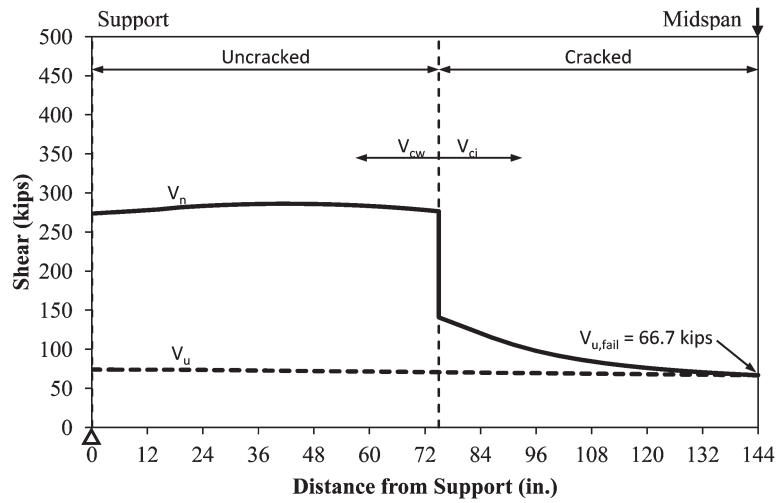
d_b: diameter of stirrup, in.

Shear strength profiles using this alternative approach to calculate the steel contribution to shear capacity are shown in Figure D.75. Two stirrups cross the shear crack according to Equation D.33. It should be noted that two stirrups are assumed to be effective at each section along the entire span length.

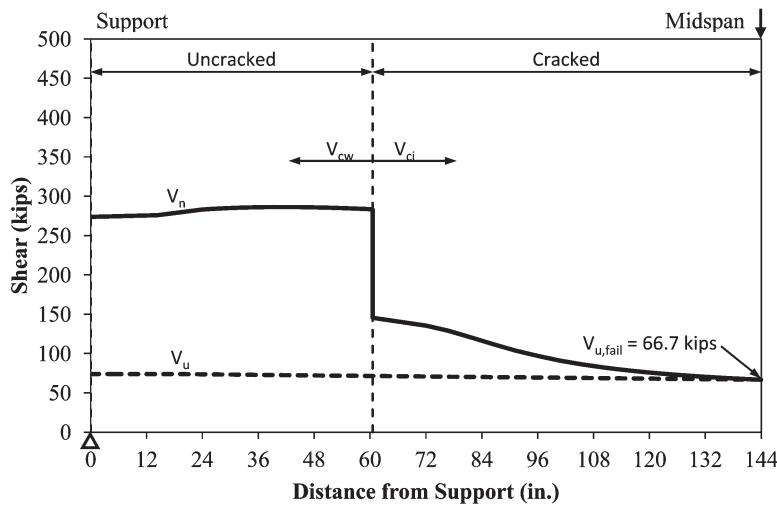
The shear strength profiles for Series IV (Figure D.73 and Figure D.75) show that the failure mode (primary shear crack) for V_{ci}-in-50-V_s (in all modulus of rupture combinations) is flexure-shear (V_{ci}). The profiles also show that the primary shear crack should form inside the debonded region.



(a) Upper Bound ($f_{r,bond} = 6\sqrt{f'_c}$)

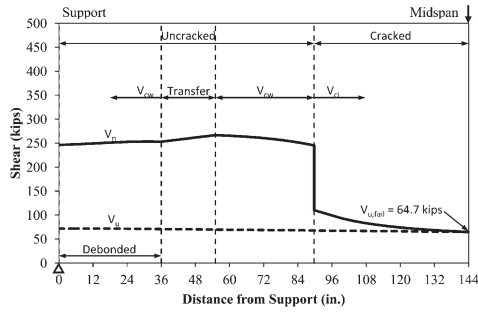


(b) Intermediate ($f_{r,bond} = 3\sqrt{f'_c}$)

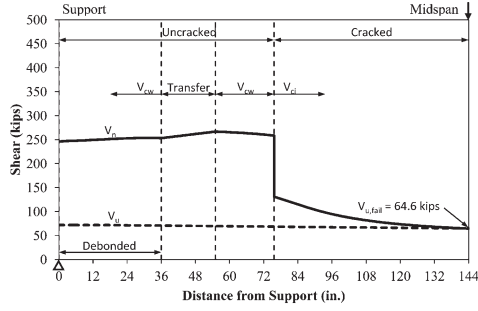


(c) Lower Bound ($f_{r,bond} = 0\sqrt{f'_c}$)

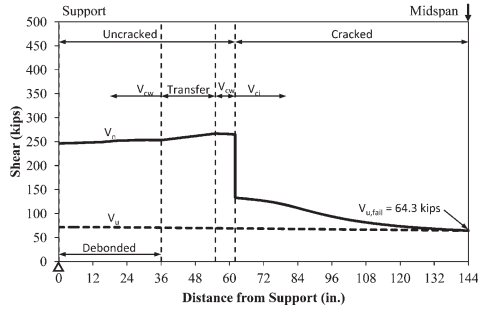
Figure D.64 Shear strength profile for V_{ci} -out-00.



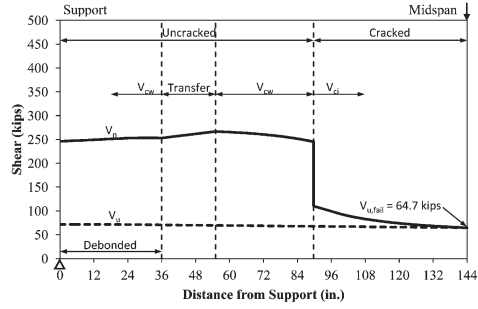
(a) Upper Bound ($f_{r,debond} = 6\sqrt{f'_c}$; $f_{r,bond} = 6\sqrt{f'_c}$)



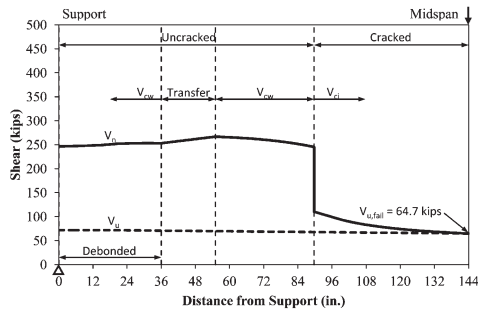
(b) Intermediate ($f_{r,debond} = 3\sqrt{f'_c}$; $f_{r,bond} = 3\sqrt{f'_c}$)



(c) Lower Bound ($f_{r,debond} = 0\sqrt{f'_c}$; $f_{r,bond} = 0\sqrt{f'_c}$)

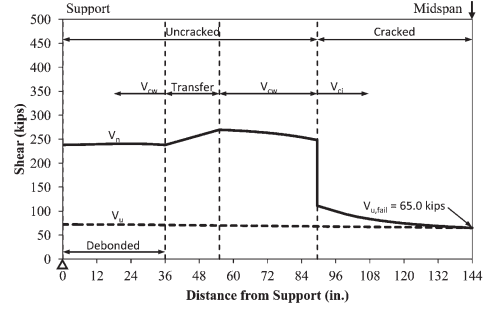


(d) Reduced Debond Strength ($f_{r,debond} = 3\sqrt{f'_c}$; $f_{r,bond} = 6\sqrt{f'_c}$)

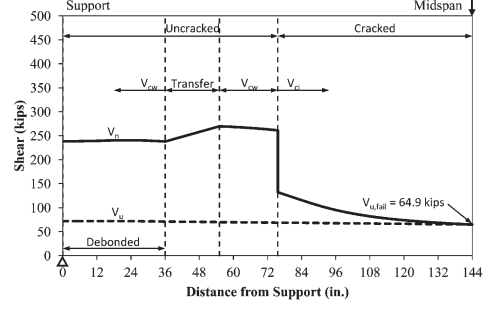


(e) Reduced Debond Strength ($f_{r,debond} = 0\sqrt{f'_c}$; $f_{r,bond} = 6\sqrt{f'_c}$)

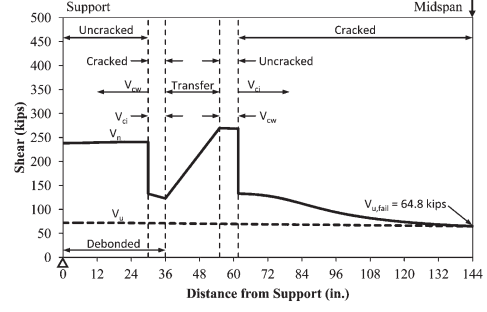
Figure D.65 Shear strength profile for V_{ci} -out-25.



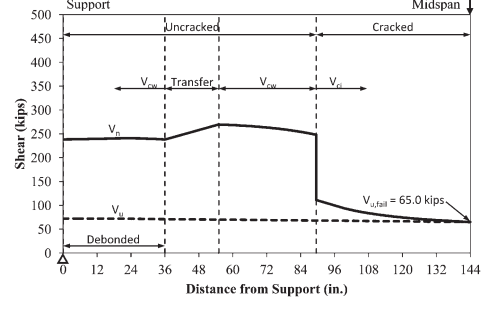
(a) Upper Bound ($f_{r,debond} = 6\sqrt{f'_c}$; $f_{r,bond} = 6\sqrt{f'_c}$)



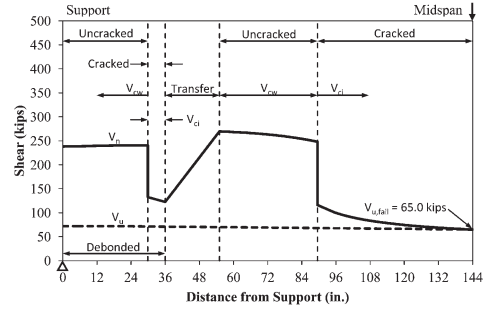
(b) Intermediate ($f_{r,debond} = 3\sqrt{f'_c}$; $f_{r,bond} = 3\sqrt{f'_c}$)



(c) Lower Bound ($f_{r,debond} = 0\sqrt{f'_c}$; $f_{r,bond} = 0\sqrt{f'_c}$)

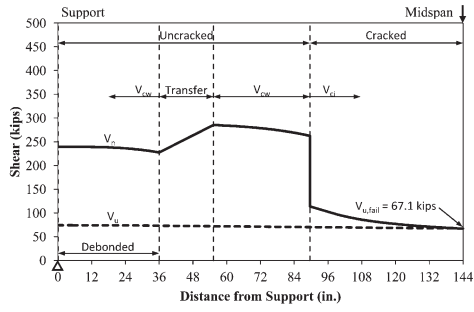


(d) Reduced Debond Strength ($f_{r,debond} = 3\sqrt{f'_c}$; $f_{r,bond} = 6\sqrt{f'_c}$)

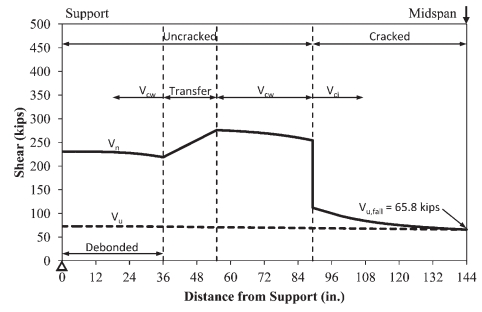


(e) Reduced Debond Strength ($f_{r,debond} = 0\sqrt{f'_c}$; $f_{r,bond} = 6\sqrt{f'_c}$)

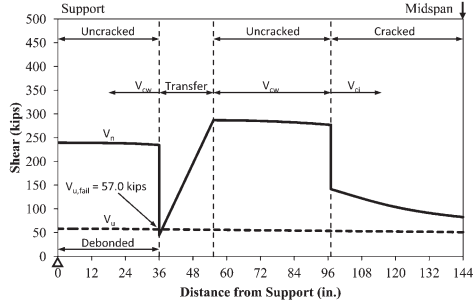
Figure D.66 Shear strength profile for V_{ci} -out-50.



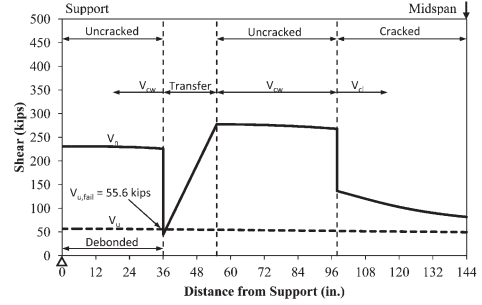
(a) Upper Bound ($f_{r,debond} = 6\sqrt{f'_c}$; $f_{r,bond} = 6\sqrt{f'_c}$)



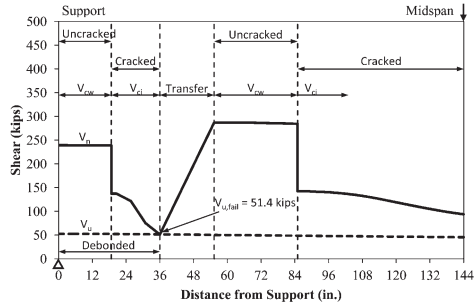
(a) Upper Bound ($f_{r,debond} = 6\sqrt{f'_c}$; $f_{r,bond} = 6\sqrt{f'_c}$)



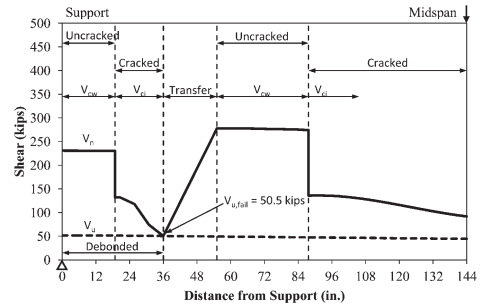
(b) Intermediate ($f_{r,debond} = 3\sqrt{f'_c}$; $f_{r,bond} = 3\sqrt{f'_c}$)



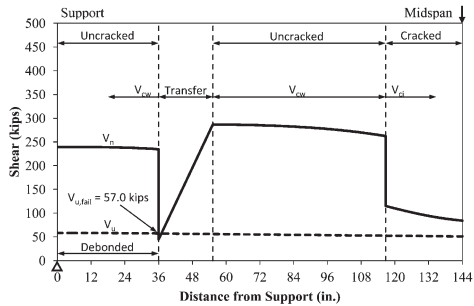
(b) Intermediate ($f_{r,debond} = 3\sqrt{f'_c}$; $f_{r,bond} = 3\sqrt{f'_c}$)



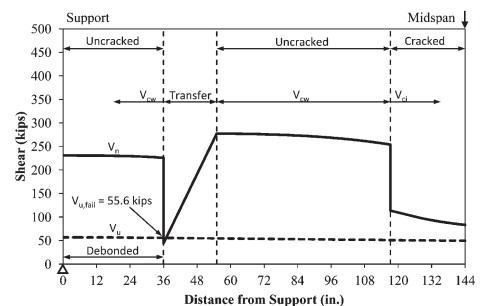
(c) Lower Bound ($f_{r,debond} = 0\sqrt{f'_c}$; $f_{r,bond} = 0\sqrt{f'_c}$)



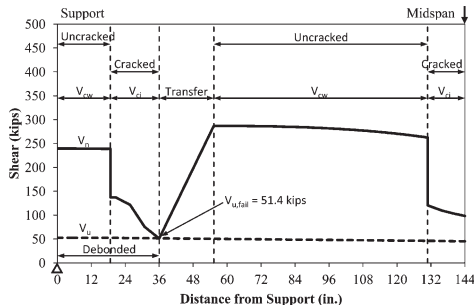
(c) Lower Bound ($f_{r,debond} = 0\sqrt{f'_c}$; $f_{r,bond} = 0\sqrt{f'_c}$)



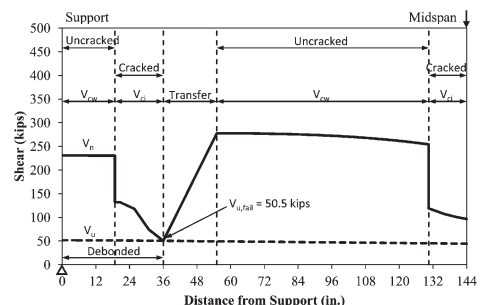
(d) Reduced Debond Strength ($f_{r,debond} = 3\sqrt{f'_c}$; $f_{r,bond} = 6\sqrt{f'_c}$)



(d) Reduced Debond Strength ($f_{r,debond} = 3\sqrt{f'_c}$; $f_{r,bond} = 6\sqrt{f'_c}$)



(e) Reduced Debond Strength ($f_{r,debond} = 0\sqrt{f'_c}$; $f_{r,bond} = 6\sqrt{f'_c}$)



(e) Reduced Debond Strength ($f_{r,debond} = 0\sqrt{f'_c}$; $f_{r,bond} = 6\sqrt{f'_c}$)

Figure D.67 Shear strength profile for V_{ci} -out-75.

Figure D.68 Shear strength profile for V_{ci} -out-75-2.

TABLE D.17
Comparison of Shear Strengths for Series II

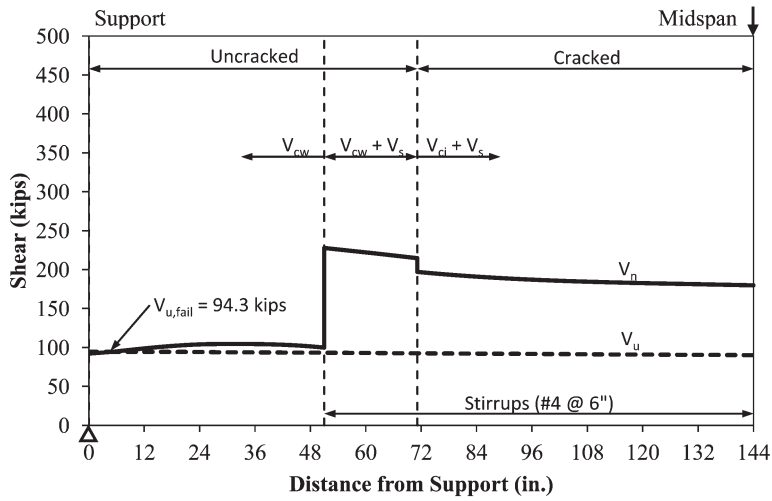
Specimen ID	Modulus of Rupture (psi)		V_{test} (kip)	Model	V_{calc} (kip)			
	Debond	Bond			ACI 318		AASHTO	
					Limit	No Limit	Limit	No Limit
V _{ci} -out-00	—	$6\sqrt{f'_c}$	79.3	66.9	83.6	68.6	87.8	68.4
	—	$3\sqrt{f'_c}$		66.7	83.6	61.7	87.8	61.5
	—	$0\sqrt{f'_c}$		66.7	83.6	54.8	87.8	54.5
V _{ci} -out-25		$6\sqrt{f'_c}$	76.6	64.7	77.2	64.9	79.9	64.3
		$3\sqrt{f'_c}$		64.6	77.2	58.5	79.9	57.9
		$0\sqrt{f'_c}$		64.3	77.2	52.2	79.9	51.6
	$3\sqrt{f'_c}$	$6\sqrt{f'_c}$		64.7	77.2	64.9	79.9	64.3
	$0\sqrt{f'_c}$	$6\sqrt{f'_c}$		64.7	77.2	64.9	79.9	64.3
V _{ci} -out-50		$6\sqrt{f'_c}$	72.6	65.0	78.2	65.5	81.2	65.0
		$3\sqrt{f'_c}$		64.9	78.2	59.0	81.2	58.5
		$0\sqrt{f'_c}$		64.8	78.2	52.6	81.2	52.0
	$3\sqrt{f'_c}$	$6\sqrt{f'_c}$		65.0	78.2	65.5	81.2	65.0
	$0\sqrt{f'_c}$	$6\sqrt{f'_c}$		65.0	78.2	65.5	81.2	65.0
V _{ci} -out-75		$6\sqrt{f'_c}$	56.1	67.1	83.8	68.8	88.0	68.6
		$3\sqrt{f'_c}$		57.0	83.8	61.9	88.0	61.6
		$0\sqrt{f'_c}$		51.4	83.8	58.5	88.0	59.6
	$3\sqrt{f'_c}$	$6\sqrt{f'_c}$		57.0	83.8	68.8	88.0	68.6
	$0\sqrt{f'_c}$	$6\sqrt{f'_c}$		51.4	83.8	58.5	88.0	59.6
V _{ci} -out-75-2		$6\sqrt{f'_c}$	56.2	65.8	80.6	66.8	84.1	66.3
		$3\sqrt{f'_c}$		55.6	80.6	60.1	84.1	59.7
		$0\sqrt{f'_c}$		50.5	80.6	57.0	84.1	58.0
	$3\sqrt{f'_c}$	$6\sqrt{f'_c}$		55.6	80.6	66.8	84.1	66.3
	$0\sqrt{f'_c}$	$6\sqrt{f'_c}$		50.5	80.6	57.0	84.1	58.0

TABLE D.18
Comparison of Shear Strength Ratios for Series II

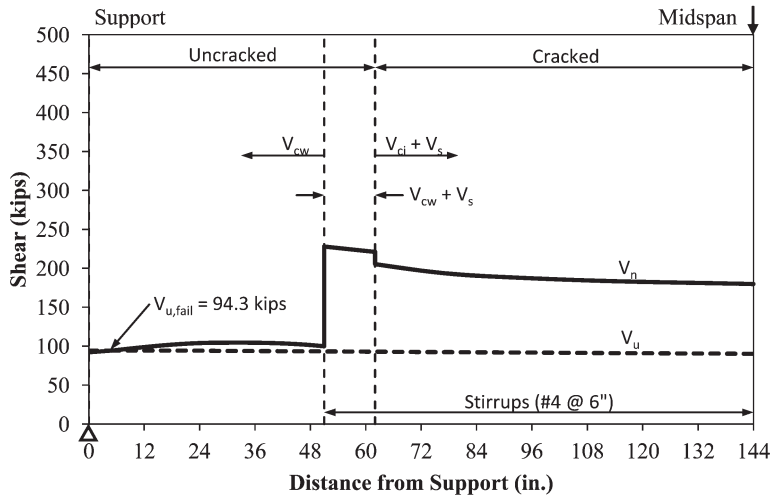
Specimen ID	Modulus of Rupture (psi)		V_{test} (kip)	Model	V_{test}/V_{calc}			
	Debond	Bond			ACI 318		AASHTO	
					Limit	No Limit	Limit	No Limit
V _{ci} -out-00	—	$6\sqrt{f'_c}$	79.3	1.19	0.95	1.16	0.90	1.16
	—	$3\sqrt{f'_c}$		1.19	0.95	1.29	0.90	1.29
	—	$0\sqrt{f'_c}$		1.19	0.95	1.45	0.90	1.46
V _{ci} -out-25		$6\sqrt{f'_c}$	76.6	1.18	0.99	1.18	0.96	1.19
		$3\sqrt{f'_c}$		1.19	0.99	1.31	0.96	1.32
		$0\sqrt{f'_c}$		1.19	0.99	1.47	0.96	1.48
	$3\sqrt{f'_c}$	$6\sqrt{f'_c}$		1.18	0.99	1.18	0.96	1.19
	$0\sqrt{f'_c}$	$6\sqrt{f'_c}$		1.18	0.99	1.18	0.96	1.19
V _{ci} -out-50		$6\sqrt{f'_c}$	72.6	1.12	0.93	1.11	0.89	1.12
		$3\sqrt{f'_c}$		1.12	0.93	1.23	0.89	1.24
		$0\sqrt{f'_c}$		1.12	0.93	1.38	0.89	1.40
	$3\sqrt{f'_c}$	$6\sqrt{f'_c}$		1.12	0.93	1.11	0.89	1.12
	$0\sqrt{f'_c}$	$6\sqrt{f'_c}$		1.12	0.93	1.11	0.89	1.12
V _{ci} -out-75		$6\sqrt{f'_c}$	56.1	0.84	0.67	0.82	0.64	0.82
		$3\sqrt{f'_c}$		0.98	0.67	0.91	0.64	0.91
		$0\sqrt{f'_c}$		1.09	0.67	0.96	0.64	0.94
	$3\sqrt{f'_c}$	$6\sqrt{f'_c}$		0.98	0.67	0.82	0.64	0.82
	$0\sqrt{f'_c}$	$6\sqrt{f'_c}$		1.09	0.67	0.96	0.64	0.94
V _{ci} -out-75-2		$6\sqrt{f'_c}$	56.2	0.85	0.70	0.84	0.67	0.85
		$3\sqrt{f'_c}$		1.01	0.70	0.94	0.67	0.94
		$0\sqrt{f'_c}$		1.11	0.70	0.99	0.67	0.97
	$3\sqrt{f'_c}$	$6\sqrt{f'_c}$		1.01	0.70	0.84	0.67	0.85
	$0\sqrt{f'_c}$	$6\sqrt{f'_c}$		1.11	0.70	0.99	0.67	0.97

TABLE D.19
Measured Modulus of Ruptures for Series II

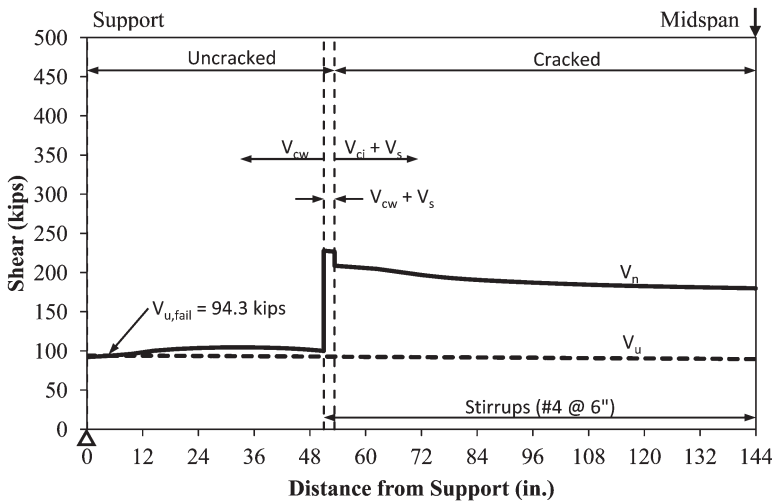
Specimen ID	f'_c (psi)	Modulus of Rupture (psi)	
		Debond	Bond x (in.)
V _{ci} -out-00	7,290	—	$6.3\sqrt{f'_c}$
V _{ci} -out-25	6,210	—	$6.8\sqrt{f'_c}$
V _{ci} -out-50	6,380	—	$6.8\sqrt{f'_c}$
V _{ci} -out-75	7,330	$3.0\sqrt{f'_c}$	$6.3\sqrt{f'_c}$
V _{ci} -out-75-2	6,780	$3.0\sqrt{f'_c}$	$6.5\sqrt{f'_c}$



(a) Upper Bound ($f_{r,bond} = 6\sqrt{f'_c}$)

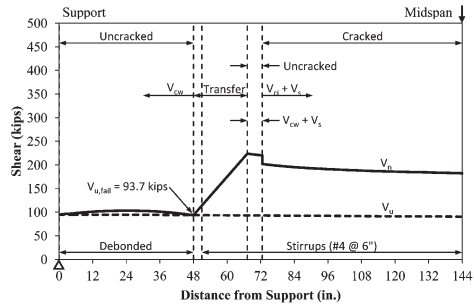


(b) Intermediate ($f_{r,bond} = 3\sqrt{f'_c}$)

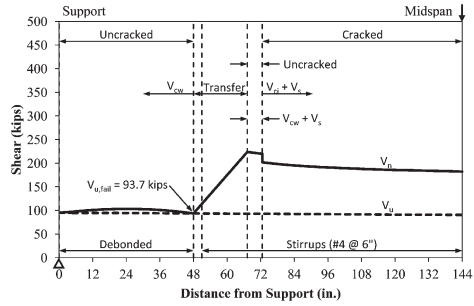


(c) Lower Bound ($f_{r,bond} = 0\sqrt{f'_c}$)

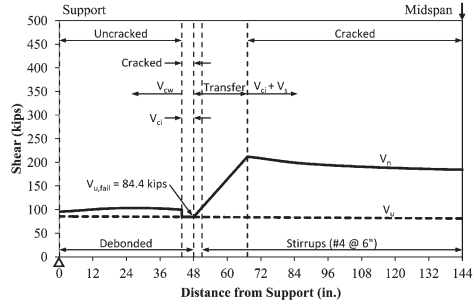
Figure D.69 Shear strength profile for V_{cw} -00.



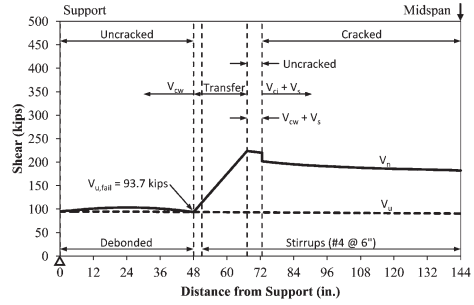
(a) Upper Bound ($f_{r,debond} = 6\sqrt{f'_c}$; $f_{r,bond} = 6\sqrt{f'_c}$)



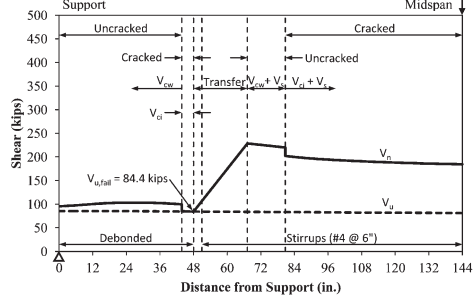
(b) Intermediate ($f_{r,debond} = 3\sqrt{f'_c}$; $f_{r,bond} = 3\sqrt{f'_c}$)



(c) Lower Bound ($f_{r,debond} = 0\sqrt{f'_c}$; $f_{r,bond} = 0\sqrt{f'_c}$)

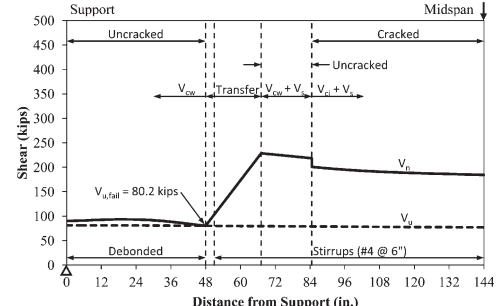


(d) Reduced Debond Strength ($f_{r,debond} = 3\sqrt{f'_c}$; $f_{r,bond} = 6\sqrt{f'_c}$)

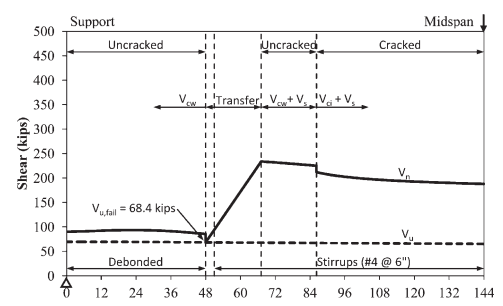


(e) Reduced Debond Strength ($f_{r,debond} = 0\sqrt{f'_c}$; $f_{r,bond} = 6\sqrt{f'_c}$)

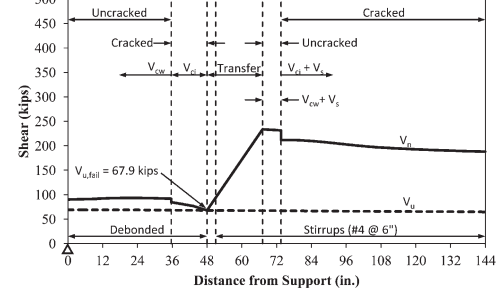
Figure D.70 Shear strength profile for V_{cw} -25.



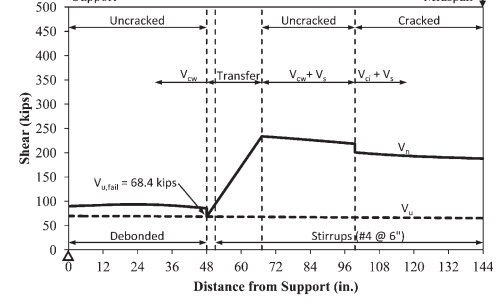
(a) Upper Bound ($f_{r,debond} = 6\sqrt{f'_c}$; $f_{r,bond} = 6\sqrt{f'_c}$)



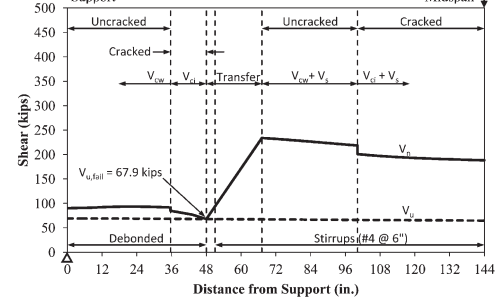
(b) Intermediate ($f_{r,debond} = 3\sqrt{f'_c}$; $f_{r,bond} = 3\sqrt{f'_c}$)



(c) Lower Bound ($f_{r,debond} = 0\sqrt{f'_c}$; $f_{r,bond} = 0\sqrt{f'_c}$)



(d) Reduced Debond Strength ($f_{r,debond} = 3\sqrt{f'_c}$; $f_{r,bond} = 6\sqrt{f'_c}$)



(e) Reduced Debond Strength ($f_{r,debond} = 0\sqrt{f'_c}$; $f_{r,bond} = 6\sqrt{f'_c}$)

Figure D.71 Shear strength profile for V_{cw} -50.

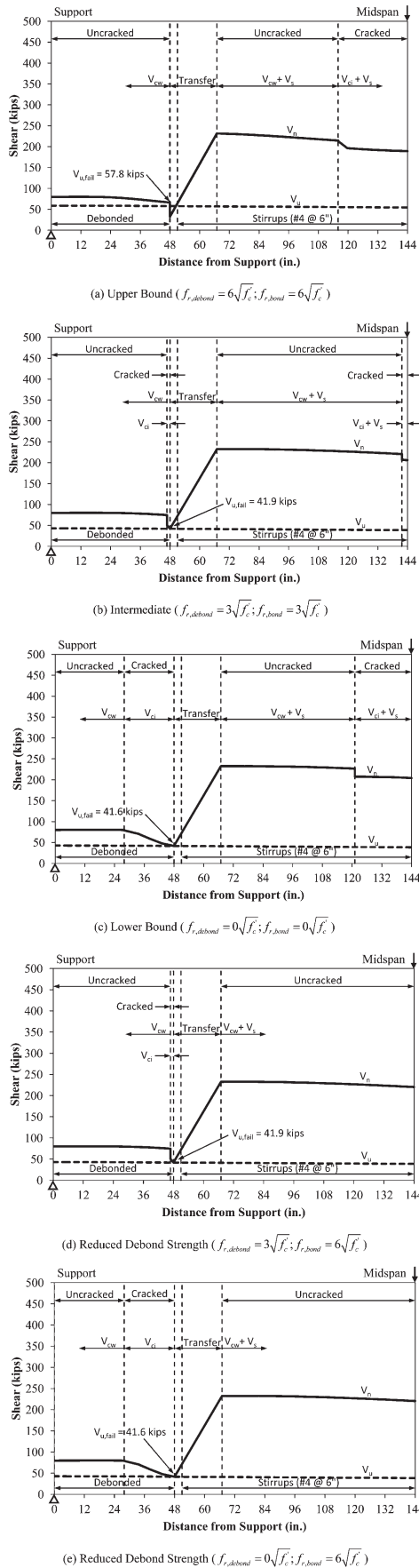


Figure D.72 Shear strength profile for V_{cw} -75.

The critical values from the shear strength profiles are provided in Table D.23 to compare the calculated shear capacities (V_{model}) to the measured shear capacities (V_{test}) at the maximum load observed during the test for each modulus of rupture combination. The shear corresponding to the maximum load is provided because the stirrups provided additional capacity (V_s) beyond that of the concrete contribution (V_c). The shear capacities from ACI 318 and AASHTO are provided as well. These values are the shears at flexural failure (flexure controlled in the ACI 318 and AASHTO analyses). Ratios of measured shear capacities to calculated shear capacities are provided in Table D.24. It is important to note that all of the shears reported in Table D.23 include the shear due to self-weight. The shear diagram due to self-weight is illustrated in Figure D.46.

The results of these analyses suggest that there are almost no changes in the shear capacities (using the shear model) as the modulus of rupture is varied for V_{ci} -in-50- V_s . The slight differences in capacity are a result of the tensile stresses immediately beneath the neutral axis which were accounted for after cracking in the analyses. All tensile stresses in the concrete below the modulus of rupture were considered part of the tensile force contribution when checking equilibrium. It should be noted that the shear capacities calculated by the shear model for V_{ci} -in-50- V_s include the contribution of the transverse reinforcement.

Flexural failure controlled in the ACI 318 and AASHTO approaches. This is due to the fact that the code equations overestimated the contribution of the stirrups to the shear capacity. The actual contribution of the stirrups can be calculated from the shears measured during the testing of V_{ci} -in-50- V_s as the maximum shear force (capacity) minus the concrete contribution to shear capacity. This equation can be written as $V_s = V_u - V_c$ which after substitution of the test values yields: $V_s = 95.6 \text{ kips} - 58.3 \text{ kips} = 37.3 \text{ kips}$. It should be noted that the concrete contribution to shear capacity for V_{ci} -in-50 and V_{ci} -in-50- V_s was 57.0 kips and 58.3 kips, respectively. The slight difference in strength may be attributed to the difference in concrete strength at the time of testing (Table D.8). The ACI 318 equation (Equation D.24) for the steel contribution gives 58.0 kips, and the AASHTO equation yields values between 54.6 kips and 66.4 kips (depending on conditions in Equation D.28). Both codes greatly overestimate the steel contribution to shear capacity. On the other hand, the integer approach developed by Frosch (2000) (Equation D.32) gives 32.6 kips which is a conservative and more accurate representation of the actual steel contribution. The values in Table D.23 and Table D.24 reflect the conservative nature of the integer approach and the unconservative nature of the code equations.

The modulus of rupture values for each beam are provided in Table D.25. This table presents the measured modulus of rupture values at the end of the debonded region, labeled "Debond" and at midspan, labeled "Bond" for V_{ci} -in-50 and V_{ci} -in-50- V_s . It should be noted that a reduction of the modulus of rupture in the debonded region was observed in both beams. The measured modulus of ruptures compare well each other.

D.9 CONCLUSIONS

Fourteen pretensioned beams were constructed, tested, and analyzed to evaluate the effects of strand debonding on shear strength. The following conclusions are made based on the experimental and analytical results:

- As the percentage of debonding increased from 0% to 75%, shear strengths decreased. For V_{ci} at the end of the debonded region (Series I), a 35% reduction in shear strength (at formation of primary shear crack) was observed in the specimen with 50% debonding relative to the specimen with 0% debonding. In increasing the debonded strand to 75%, a 61% reduction in shear strength (at formation of primary shear crack) occurred. For V_{cw} within the debonded region (Series III), a 16% reduction in shear strength (at formation of primary shear crack) was observed in the specimen with 50% debonding relative to the specimen with 0% debonding. Where V_{ci} cracks formed outside the debonded region (Series

TABLE D.20
Comparison of Shear Strengths for Series III

Specimen ID	Modulus of Rupture (psi)		V_{test} (kip)	Model	V_{calc} (kip)			
					ACI 318		AASHTO	
	Debond	Bond			Limit	No Limit	Limit	No Limit
V _{cw} -00	—	$6\sqrt{f'_c}$	93.3	94.3	70.3	70.3	51.2	51.2
	—	$3\sqrt{f'_c}$		94.3	70.3	70.3	51.2	51.2
	—	$0\sqrt{f'_c}$		94.3	70.3	70.3	51.2	51.2
V _{cw} -25		$6\sqrt{f'_c}$	93.3	93.7	74.7	74.7	48.2	48.2
		$3\sqrt{f'_c}$		93.7	74.7	74.7	48.2	48.2
		$0\sqrt{f'_c}$		84.4	74.7	74.7	48.2	48.2
	$3\sqrt{f'_c}$	$6\sqrt{f'_c}$		93.7	74.7	74.7	48.2	48.2
	$0\sqrt{f'_c}$	$6\sqrt{f'_c}$		84.4	74.7	74.7	48.2	48.2
V _{cw} -50		$6\sqrt{f'_c}$	78.3	80.2	66.4	66.4	41.2	41.2
		$3\sqrt{f'_c}$		68.4	66.4	66.4	41.2	41.2
		$0\sqrt{f'_c}$		67.9	57.6	57.6	41.2	41.2
	$3\sqrt{f'_c}$	$6\sqrt{f'_c}$		68.4	66.4	66.4	41.2	41.2
	$0\sqrt{f'_c}$	$6\sqrt{f'_c}$		67.9	57.6	57.6	41.2	41.2
V _{cw} -75		$6\sqrt{f'_c}$	53.3	57.8	56.3	56.3	33.1	33.1
		$3\sqrt{f'_c}$		41.9	48.9	48.9	33.1	33.1
		$0\sqrt{f'_c}$		41.6	32.3	32.3	32.6	32.6
	$3\sqrt{f'_c}$	$6\sqrt{f'_c}$		41.9	48.9	48.9	33.1	33.1
	$0\sqrt{f'_c}$	$6\sqrt{f'_c}$		41.6	32.3	32.3	32.6	32.6

TABLE D.21
Comparison of Shear Strength Ratios for Series III

Specimen ID	Modulus of Rupture (psi)		V_{test} (kip)	Model	V_{test}/V_{calc}			
					ACI 318		AASHTO	
	Debond	Bond			Limit	No Limit	Limit	No Limit
V _{cw} -00	—	$6\sqrt{f'_c}$	93.3	0.99	1.33	1.33	1.82	1.82
	—	$3\sqrt{f'_c}$		0.99	1.33	1.33	1.82	1.82
	—	$0\sqrt{f'_c}$		0.99	1.33	1.33	1.82	1.82
V _{cw} -25		$6\sqrt{f'_c}$	93.3	1.00	1.25	1.25	1.94	1.94
		$3\sqrt{f'_c}$		1.00	1.25	1.25	1.94	1.94
		$0\sqrt{f'_c}$		1.11	1.25	1.25	1.94	1.94
	$3\sqrt{f'_c}$	$6\sqrt{f'_c}$		1.00	1.25	1.25	1.94	1.94
	$0\sqrt{f'_c}$	$6\sqrt{f'_c}$		1.11	1.25	1.25	1.94	1.94
V _{cw} -50		$6\sqrt{f'_c}$	78.3	0.98	1.18	1.18	1.90	1.90
		$3\sqrt{f'_c}$		1.14	1.18	1.18	1.90	1.90
		$0\sqrt{f'_c}$		1.15	1.36	1.36	1.90	1.90
	$3\sqrt{f'_c}$	$6\sqrt{f'_c}$		1.14	1.18	1.18	1.90	1.90
	$0\sqrt{f'_c}$	$6\sqrt{f'_c}$		1.15	1.36	1.36	1.90	1.90
V _{cw} -75		$6\sqrt{f'_c}$	53.3	0.92	0.95	0.95	1.61	1.61
		$3\sqrt{f'_c}$		1.27	1.09	1.09	1.61	1.61
		$0\sqrt{f'_c}$		1.28	1.65	1.65	1.63	1.63
	$3\sqrt{f'_c}$	$6\sqrt{f'_c}$		1.27	1.09	1.09	1.61	1.61
	$0\sqrt{f'_c}$	$6\sqrt{f'_c}$		1.28	1.65	1.65	1.63	1.63

TABLE D.22
Measured Modulus of Ruptures for Series III

Specimen ID	f'_c (psi)	Modulus of Rupture (psi)	
		Debond	Bond x (in.)
V _{cw} -00	6,390	—	$7.7\sqrt{f'_c}$
V _{cw} -25	7,450	—	$8.4\sqrt{f'_c}$
V _{cw} -50	7,130	$5.0\sqrt{f'_c}$	$8.6\sqrt{f'_c}$
V _{cw} -75	6,380	$5.2\sqrt{f'_c}$	$8.3\sqrt{f'_c}$

- II), an 8% reduction in shear strength (at formation of primary shear crack) was observed in the specimen with 50% debonding relative to the specimen with 0% debonding.
- The modulus of rupture was observed to be lower at the end of the debonded region than at midspan (fully bonded region). Values as low as $3\sqrt{f'_c}$ were observed for the Series II specimens with 75% debonding. This corresponds to a 53% reduction in the modulus of rupture relative to midspan. It is theorized that these reduced modulus of rupture values result from damage sustained at the end of the debonded region at transfer (when the strands were cut). As the number of debonded strand increased, the modulus of rupture at the end of the debonded region decreased. In addition, a larger modulus reduction (53%) was observed in the Series II specimens with 75% debonding compared to the Series I specimen with 75% debonding (38%). The shorter debonded length likely resulted in less friction in the sheathing at transfer; therefore, increasing damage.
 - Using the shear model to analyze the beams with a modulus of rupture assumed to be zero throughout the beam (debonded and fully bonded regions) resulted in conservative and consistent calculations of the concrete contribution to shear strength. As shown in Table D.26 the shear model provided an average shear strength ratio of 1.10 and a standard deviation of 0.09 when the modulus was taken as zero ($f_r = 0\sqrt{f'_c}$). Using a modulus of rupture of zero is conservative and allows for variations of the modulus as well as effects of debonding.
 - The ACI 318 and AASHTO approaches provided conservative calculations for web-shear strength (V_{cw}). However, these approaches are unconservative for flexure-shear (V_{ci}) as shown in Table D.26 ($f_r = 0\sqrt{f'_c}$, Limit). There are two problems. First, the lower bound limits are not appropriate for lightly reinforced sections such as what occurs with debonding. Second, the use of a modulus of rupture of $6\sqrt{f'_c}$ is too high for sections with debonded strand. These results indicate that current design expressions cannot be safely used with a high percentage of debonded strand.
 - The ACI 318 and AASHTO approaches for the calculation of flexure-shear strength can be significantly improved if slightly modified. First, the lower bound limits should not be used for sections with debonded strand. Second, the modulus of rupture should be set as $0\sqrt{f'_c}$. Results of this approach are provided in Table D.26 ($f_r = 0\sqrt{f'_c}$, No Limit). It should be noted that the code estimates (using these modifications) for the flexure-shear strength of V_{ci}-in-75 are still unconservative (Table D.26). Therefore, these modifications do not completely solve the problems with these expressions.
 - Transverse reinforcement (#3 at 9 in.) placed in (and surrounding) the debonded region (V_{ci}-in-50-V_s) resulted in a higher shear capacity with more ductility compared to the specimen without transverse reinforcement in the debonded region (V_{ci}-in-50). The shear carried beyond the formation of the primary shear crack in V_{ci}-in-50-V_s was increased by 64%. In addition, cracks widths were controlled until complete failure. For comparison, shear beyond the primary shear crack in V_{ci}-in-50 was increased by 44%. However, extremely wide shear crack widths occurred after primary shear crack formation.
 - The steel contribution to shear capacity (V_s) for V_{ci}-in-50-V_s was overestimated when using the ACI 318 and AASHTO

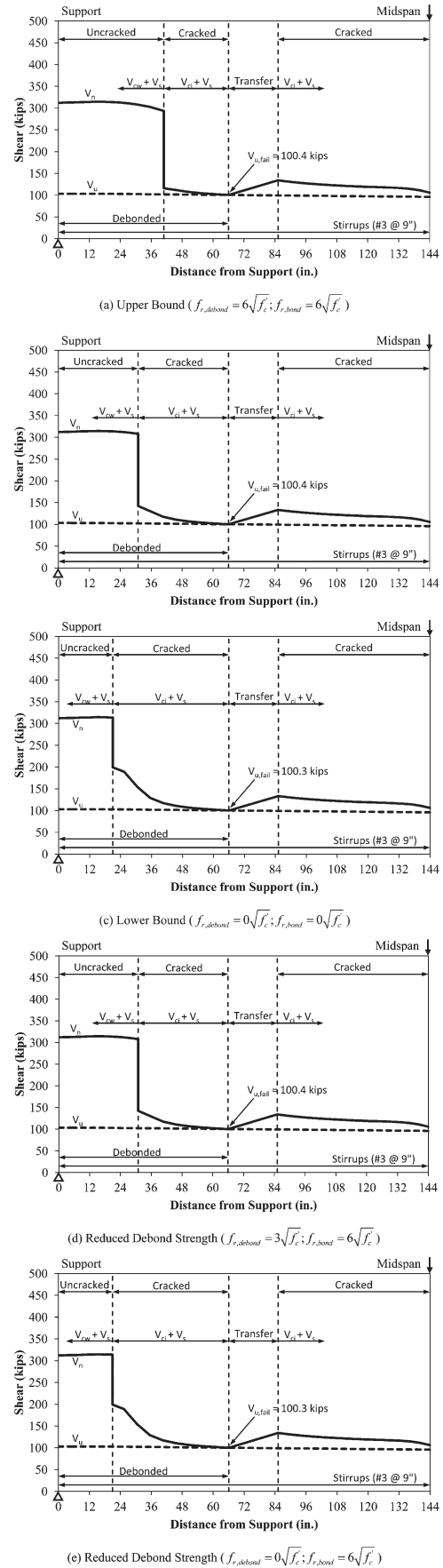


Figure D.73 Shear strength profile for V_{ci}-in-50-V_s.

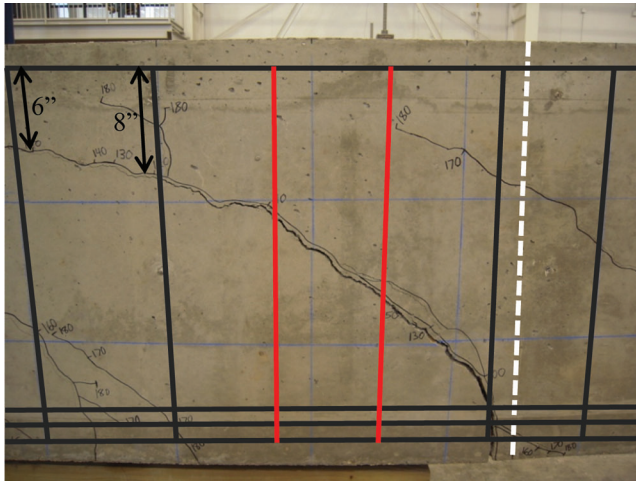


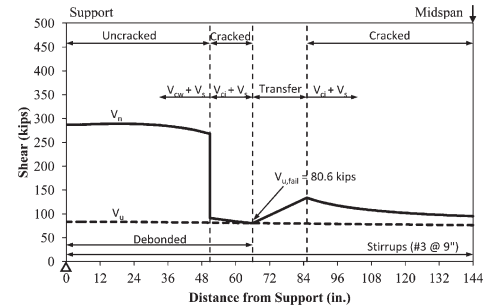
Figure D.74 Stirrup locations for V_{ci} -in-50- V_s .

equations which are smeared stirrup approaches (Table D.26). Test results indicate that only 2 stirrups were effective while the equations suggest 3.6. An equation proposed by Frosch (2000), however, provided a conservative representation of the stirrup contribution by calculating a discrete number of stirrups that a shear crack would likely cross. Using this approach, 2 stirrups are calculated as effective which is in agreement with the test results. This approach is of increased importance when a large stirrup spacing is used such that a small number of stirrups are expected to cross a shear crack.

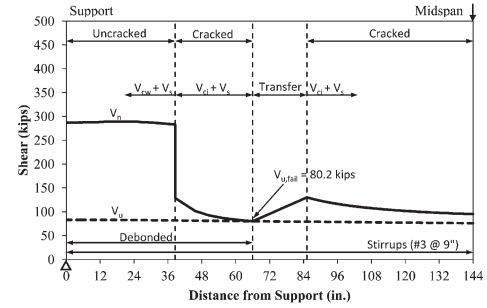
D.10 RECOMMENDATIONS

Based on the test results of this study, the following recommendations are made for pretensioned beams with debonding:

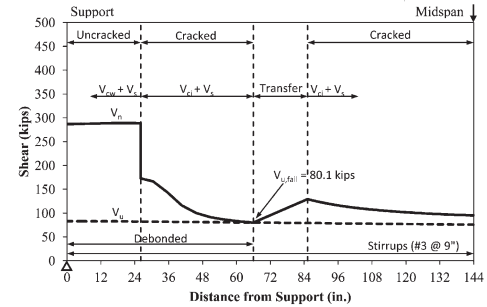
1. Debond sheathing should be staggered so that all debonded strand do not begin transfer at the same location. A significant reduction (53%) in the modulus of rupture was observed when increased numbers of strand were transferred at the same location. The AASHTO LRFD Bridge Design Specifications provide recommendations regarding staggering that are considered reasonable.
2. For the calculation of flexure-shear strength (V_{ci}), it is recommended to:
 - a. Assume a modulus of rupture of zero ($f_r = 0\sqrt{f'_c}$) in the debonded regions. To be conservative, the modulus can be assumed as zero throughout the beam.
 - b. Delete the lower limit if using the ACI 318 or AASHTO shear equations.
3. For the calculation of web-shear strength (V_{cw}), it is recommended to use the alternative method in ACI 318 (principal stress analysis). The ACI 318 required concrete tensile strength of $4\sqrt{f'_c}$ should be used for conservatism. However, if a simplified web-shear strength equation is used, it is recommended to use the ACI 318 equation rather than the AASHTO equation because the AASHTO expression provides overly conservative estimates. It is recommended that the AASHTO expression be modified to agree with the ACI 318 equation.
4. Transverse reinforcement is strongly recommended in all beams. Decreased shear strength provided by debonding can be offset through the proper design of transverse reinforcement. Special consideration should be made when designing beams with wide stirrup spacings. The integer stirrup approach for calculation of shear strength provided by stirrups as provided by Equation D.33 is recommended to ensure sufficient capacity in such beams.



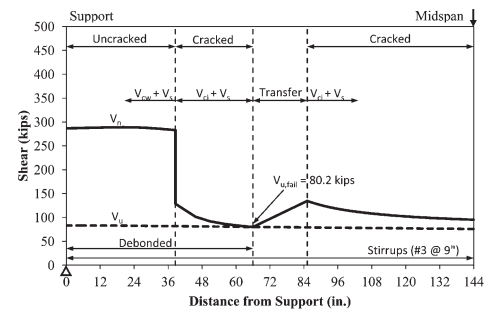
(a) Upper Bound ($f_{r,debond} = 6\sqrt{f'_c}$; $f_{r,bond} = 6\sqrt{f'_c}$)



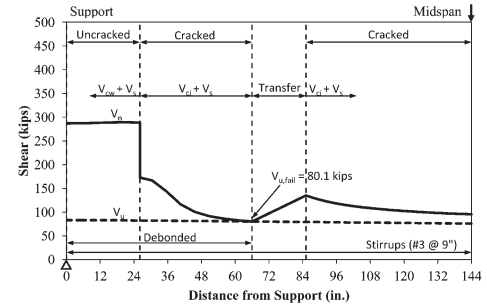
(b) Intermediate ($f_{r,debond} = 3\sqrt{f'_c}$; $f_{r,bond} = 3\sqrt{f'_c}$)



(c) Lower Bound ($f_{r,debond} = 0\sqrt{f'_c}$; $f_{r,bond} = 0\sqrt{f'_c}$)



(d) Reduced Debond Strength ($f_{r,debond} = 3\sqrt{f'_c}$; $f_{r,bond} = 6\sqrt{f'_c}$)



(e) Reduced Debond Strength ($f_{r,debond} = 0\sqrt{f'_c}$; $f_{r,bond} = 6\sqrt{f'_c}$)

Figure D.75 Shear strength profile for V_{ci} -in-50- V_s ; $V_{s,INT}$.

TABLE D.23
Comparison of Shear Strengths for V_{ci} -in-50- V_s

Modulus of Rupture (psi)			V_{calc} (kip)					
			Model		ACI 318*		AASHTO*	
Debond	Bond	V_{test} (kip)	$V_{s,ACI}$	$V_{s,INT}$	Limit	No Limit	Limit	No Limit
	$6\sqrt{f'_c}$	95.6	100.4	80.6	<i>101.5</i>	<i>101.5</i>	<i>101.5</i>	<i>101.5</i>
	$3\sqrt{f'_c}$		100.4	80.2	<i>101.5</i>	<i>101.5</i>	<i>101.5</i>	<i>101.5</i>
	$0\sqrt{f'_c}$		100.3	80.1	<i>101.5</i>	<i>101.5</i>	<i>101.5</i>	<i>101.5</i>
$3\sqrt{f'_c}$	$6\sqrt{f'_c}$		100.4	80.2	<i>101.5</i>	<i>101.5</i>	<i>101.5</i>	<i>101.5</i>
$0\sqrt{f'_c}$	$6\sqrt{f'_c}$		100.3	80.1	<i>101.5</i>	<i>101.5</i>	<i>101.5</i>	<i>101.5</i>

*Values in italics in the ACI 318 and AASHTO columns are shears at end of debonded region corresponding to flexural failure (flexure controls over shear).

TABLE D.24
Comparison of Shear Strength Ratios for V_{ci} -in-50- V_s

Modulus of Rupture (psi)			V_{test}/V_{calc}					
			Model		ACI 318*		AASHTO*	
Debond	Bond	V_{test} (kip)	$V_{s,ACI}$	$V_{s,INT}$	Limit	No Limit	Limit	No Limit
	$6\sqrt{f'_c}$	95.6	0.95	1.19	<i>0.94</i>	<i>0.94</i>	<i>0.94</i>	<i>0.94</i>
	$3\sqrt{f'_c}$		0.95	1.19	<i>0.94</i>	<i>0.94</i>	<i>0.94</i>	<i>0.94</i>
	$0\sqrt{f'_c}$		0.95	1.19	<i>0.94</i>	<i>0.94</i>	<i>0.94</i>	<i>0.94</i>
$3\sqrt{f'_c}$	$6\sqrt{f'_c}$		0.95	1.19	<i>0.94</i>	<i>0.94</i>	<i>0.94</i>	<i>0.94</i>
$0\sqrt{f'_c}$	$6\sqrt{f'_c}$		0.95	1.19	<i>0.94</i>	<i>0.94</i>	<i>0.94</i>	<i>0.94</i>

*Values in italics in the ACI 318 and AASHTO columns use the shears at the end of debonded region corresponding to flexural failure (flexure controls over shear).

TABLE D.25
Measured Modulus of Ruptures for Series IV

Specimen ID	f'_c (psi)	Modulus of Rupture (psi)	
		Debond	Bond x (in.)
V_{ci} -in-50	6,800	$4.9\sqrt{f'_c}$	$6.6\sqrt{f'_c}$
V_{ci} -in-50- V_s	7,380	$4.7\sqrt{f'_c}$	$6.7\sqrt{f'_c}$

TABLE D.26
Comparison of Shear Strength Ratios for Series I, II, and III

Specimen ID	Model	$f_r = 6\sqrt{f'_c}$				$f_r = 0\sqrt{f'_c}$				
		ACI 318		AASHTO		ACI 318		AASHTO		
		Limit	N.L.*	Limit	N.L.*	Limit	N.L.*	Limit	N.L.*	
V_{ci} -in-00	1.11	1.01	1.01	1.02	1.02	1.12	1.07	1.30	1.02	1.31
V_{ci} -in-25	1.04	0.96	0.96	0.96	0.96	1.05	1.01	1.23	0.97	1.23
V_{ci} -in-50	0.94	0.67	0.67	0.67	0.67	0.96	0.71	0.97	0.68	0.96
V_{ci} -in-75	0.78	0.42	0.47	0.40	0.47	0.96	0.42	0.80	0.40	0.78
V_{ci} -out-00	1.19	0.95	1.16	0.90	1.16	1.19	0.95	1.45	0.90	1.46
V_{ci} -out-25	1.18	0.99	1.18	0.96	1.19	1.19	0.99	1.47	0.96	1.48
V_{ci} -out-50	1.12	0.93	1.11	0.89	1.12	1.12	0.93	1.38	0.89	1.40
V_{ci} -out-75	0.84	0.67	0.82	0.64	0.82	1.09	0.67	0.96	0.64	0.94
V_{ci} -out-75-2	0.85	0.70	0.84	0.67	0.85	1.11	0.70	0.99	0.67	0.97
V_{cw} -00	0.99	1.33	1.33	1.82	1.82	0.99	1.33	1.33	1.82	1.82
V_{cw} -25	1.00	1.25	1.25	1.94	1.94	1.11	1.25	1.25	1.94	1.94
V_{cw} -50	0.98	1.18	1.18	1.90	1.90	1.15	1.36	1.36	1.90	1.90
V_{cw} -75	0.92	0.95	0.95	1.61	1.61	1.28	1.65	1.65	1.63	1.63
Average:	1.00	0.92	0.99	1.11	1.19	1.10	1.00	1.24	1.11	1.37
Std. Dev:	0.13	0.26	0.25	0.53	0.48	0.09	0.34	0.24	0.53	0.39

*N.L.=No limit.

APPENDIX D-1. STRAIN PROFILES OVER TIME FOR SPECIMENS IN APPENDIX D

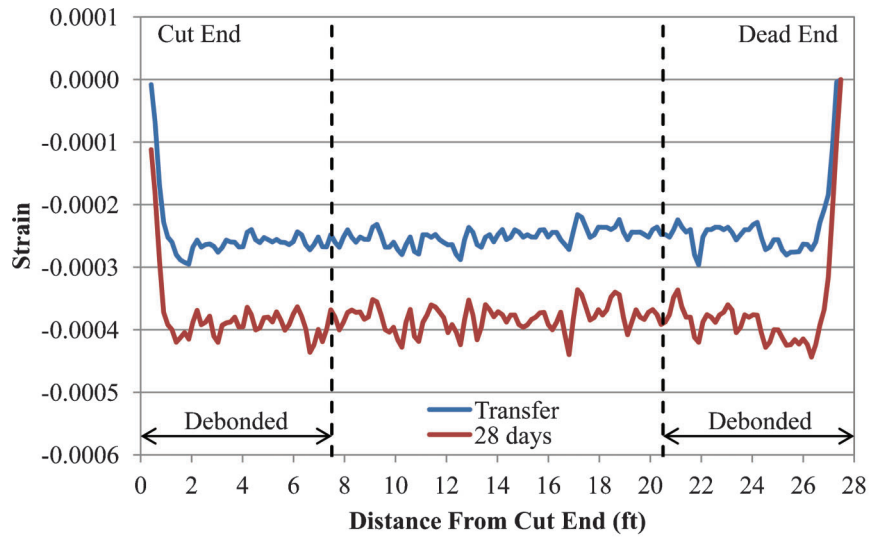


Figure D-1.1 Strain profile over time— V_{ci} -in-00.

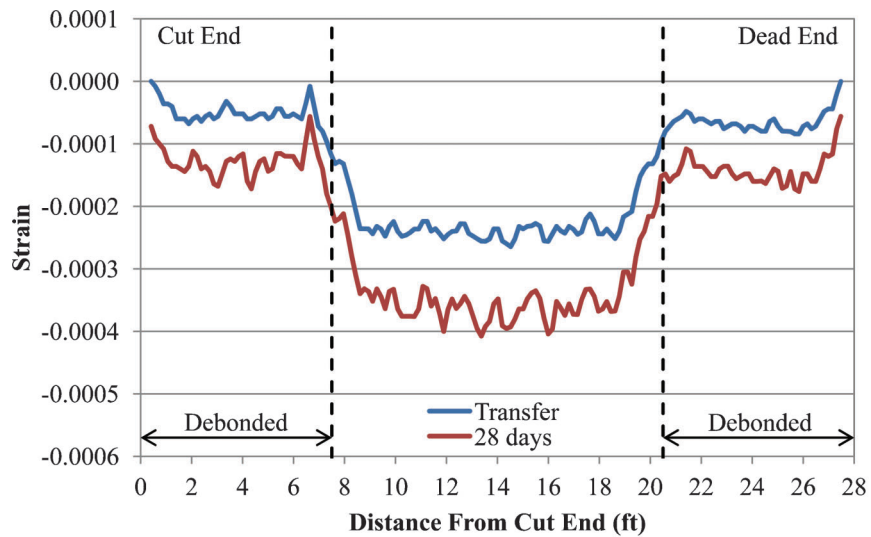


Figure D-1.2 Strain profile over time— V_{ci} -in-75.

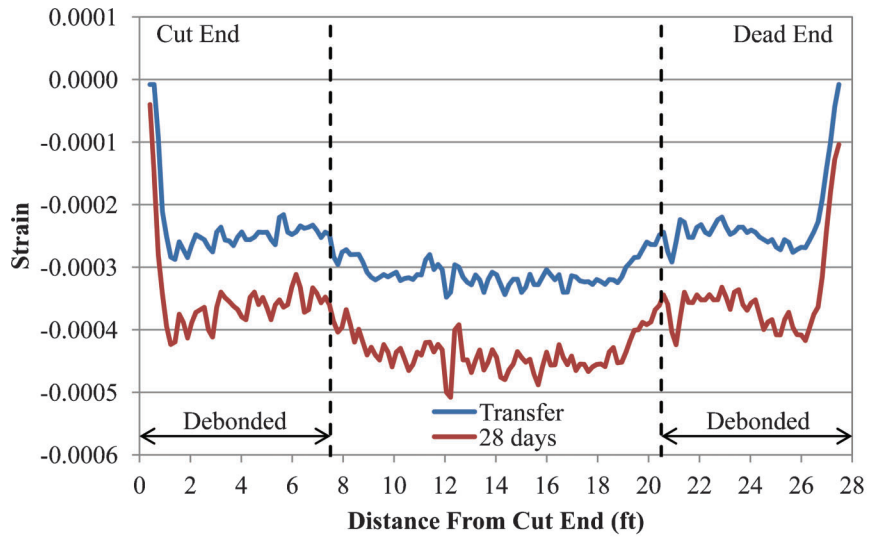


Figure D-1.3 Strain profile over time— V_{ci} -in-25.

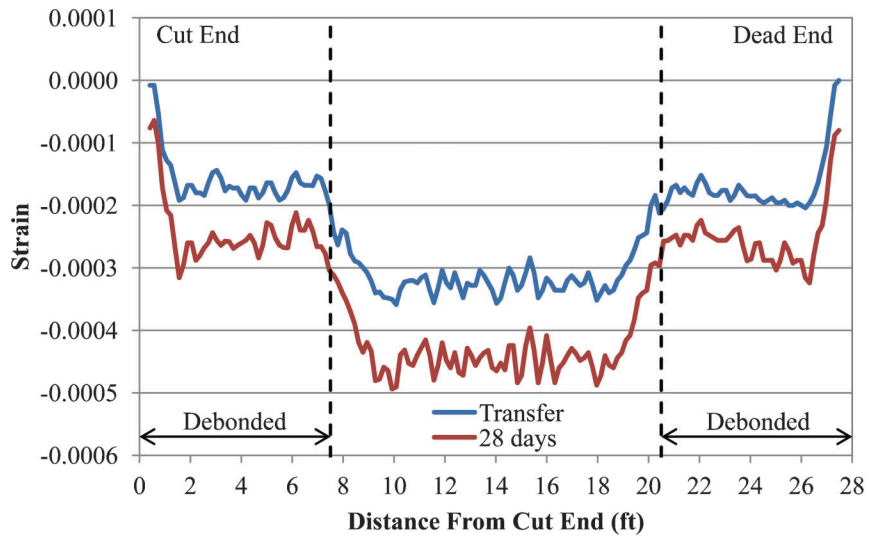


Figure D-1.4 Strain profile over time— V_{ci} -in-50.

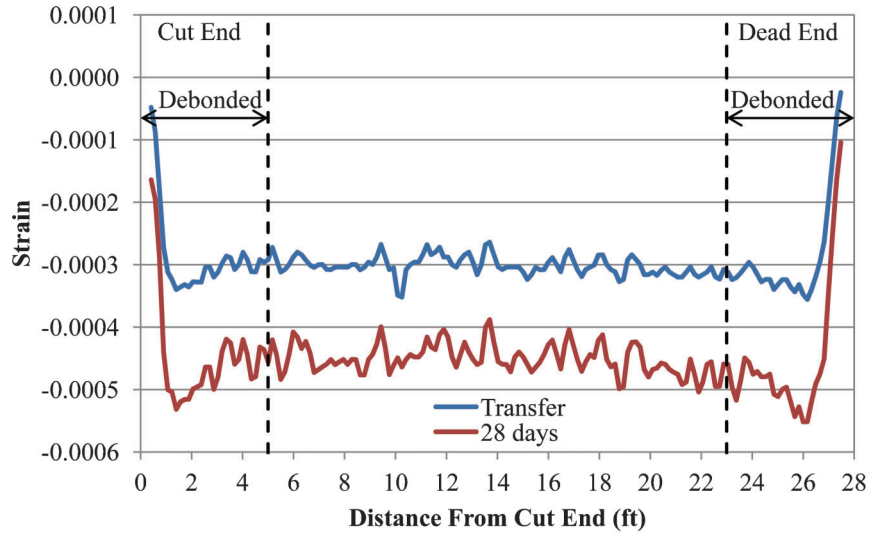


Figure D-1.5 Strain profile over time— V_{ci} -out-00.

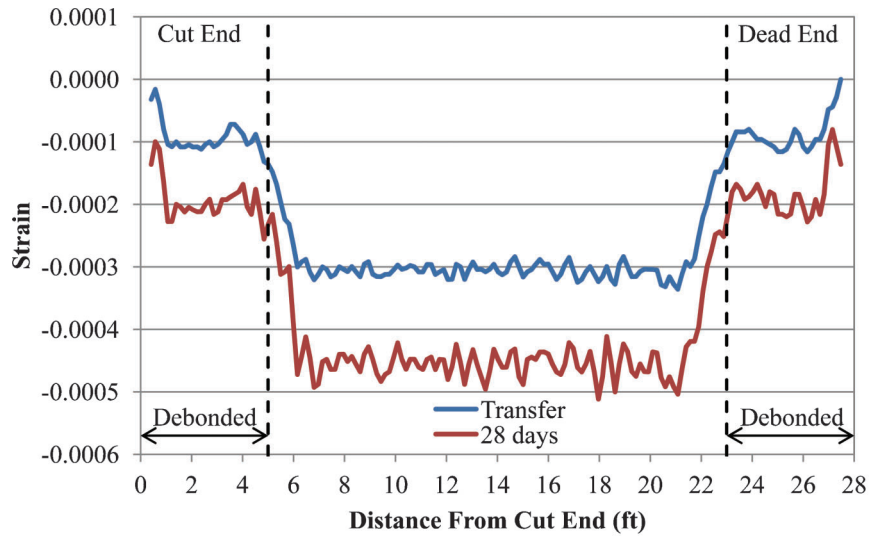


Figure D-1.6 Strain profile over time— V_{ci} -out-75.

APPENDIX D-2. CONCRETE STRENGTHS FOR SPECIMENS IN APPENDIX D

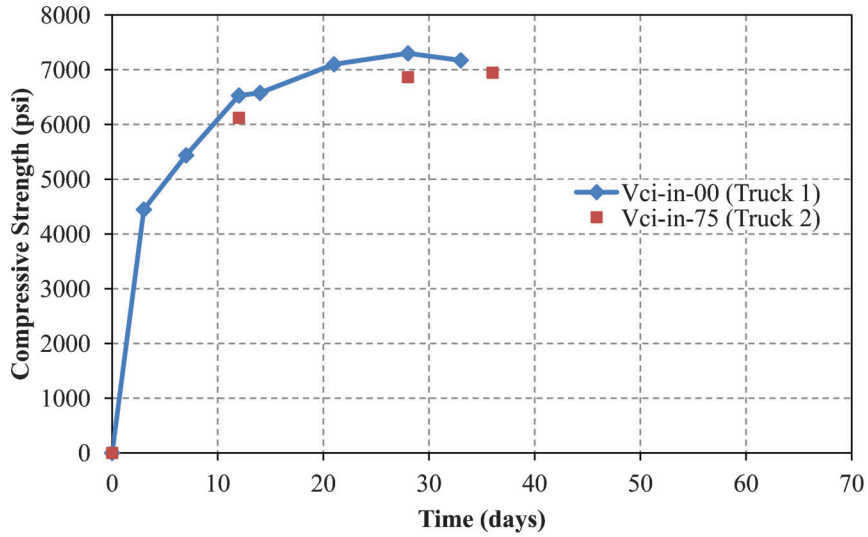


Figure D-2.1 Compressive strength for $V_{ci-in-00}$ and $V_{ci-in-75}$.

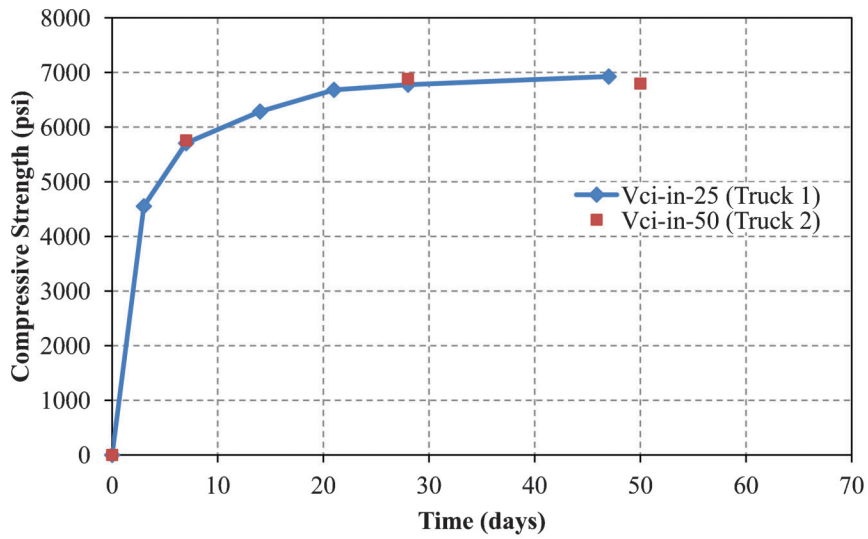


Figure D-2.2 Compressive strength for $V_{ci-in-25}$ and $V_{ci-in-50}$.

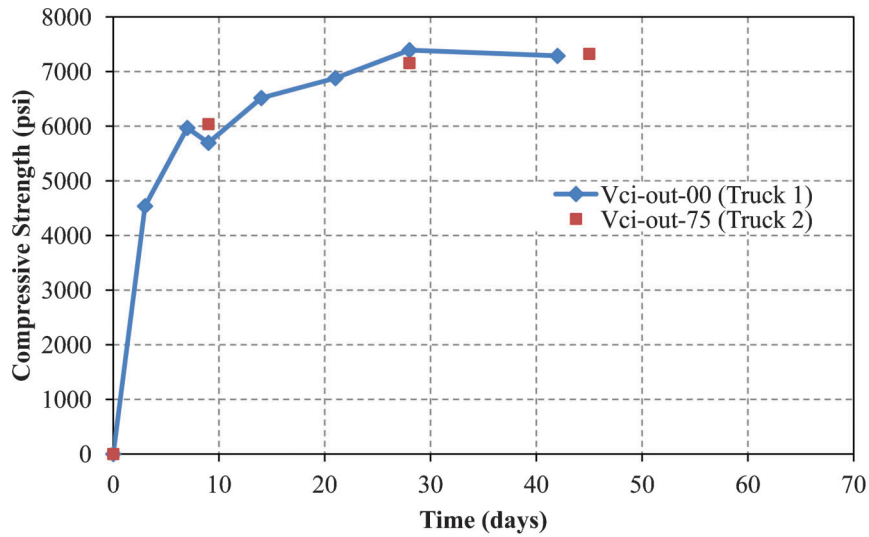


Figure D-2.3 Compressive strength for $V_{ci-out-00}$ and $V_{ci-out-75}$.

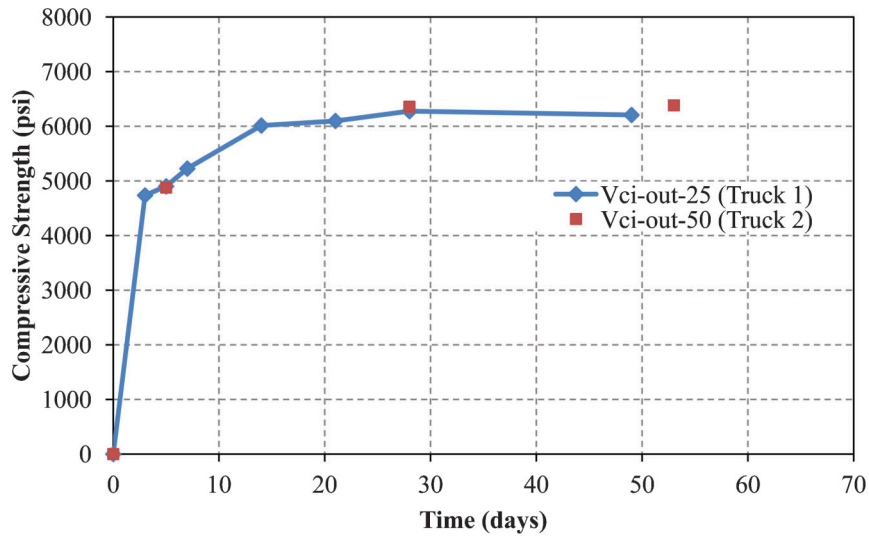


Figure D-2.4 Compressive strength for $V_{ci-out-25}$ and $V_{ci-out-50}$.

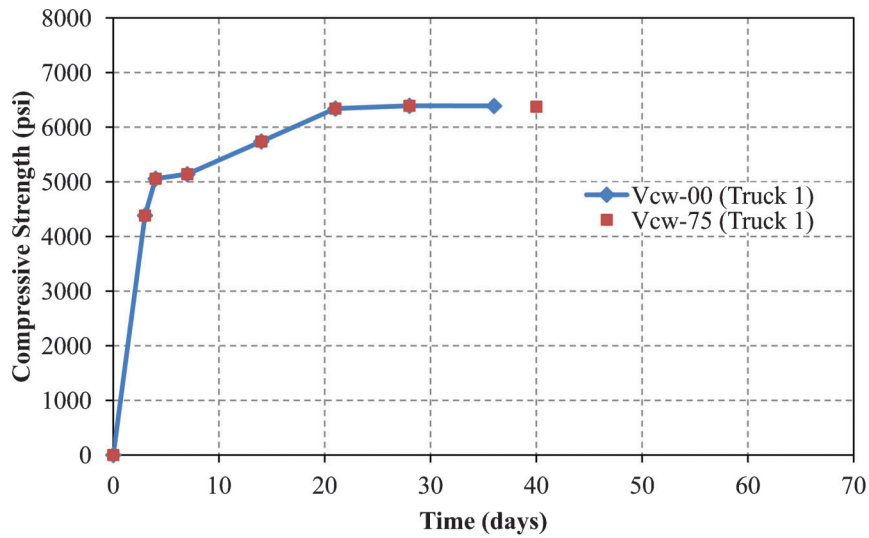


Figure D-2.5 Compressive strength for V_{cw-00} and V_{cw-75} .

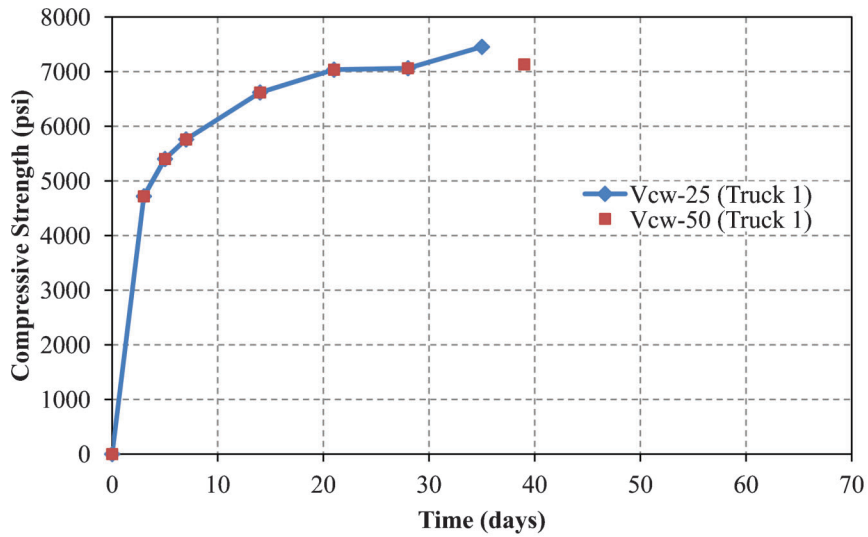


Figure D-2.6 Compressive strength for V_{cw-25} and V_{cw-50} .

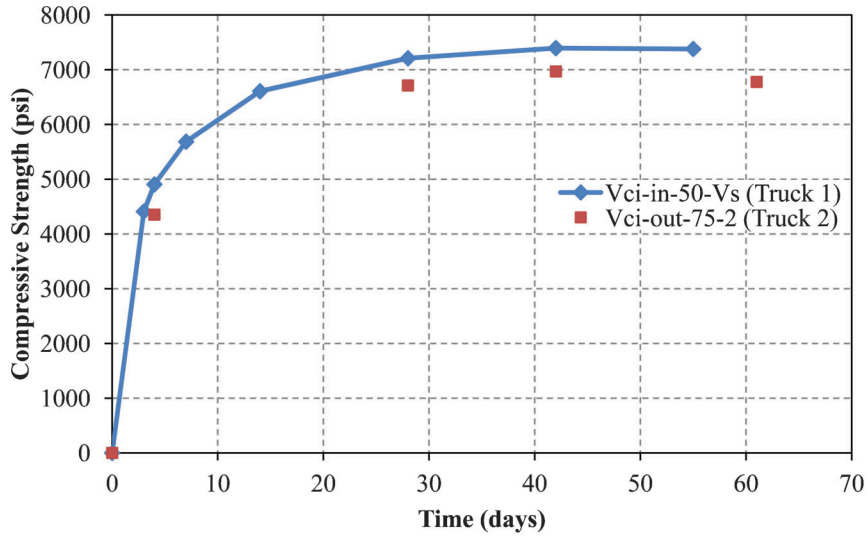


Figure D-2.7 Compressive strength for $V_{ci-in-50-V_s}$ and $V_{ci-out-75-2}$.

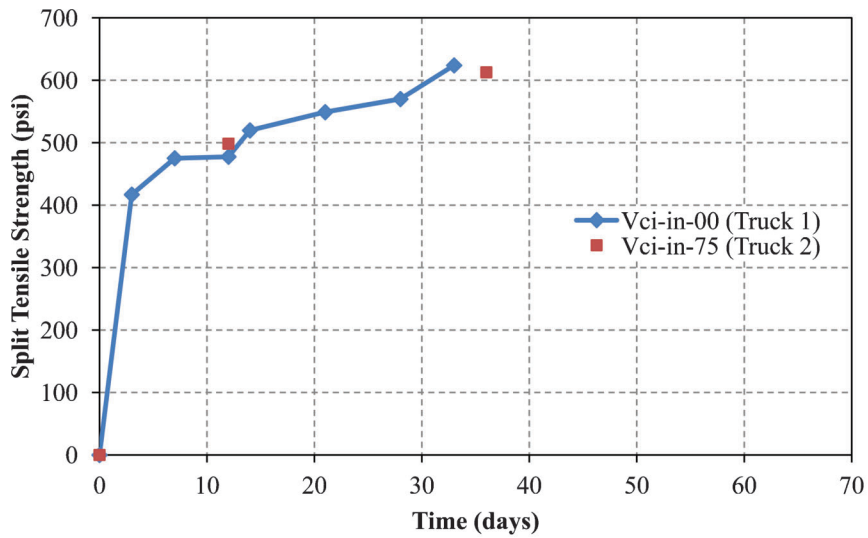


Figure D-2.8 Split tensile strength for $V_{ci-in-00}$ and $V_{ci-in-75}$.

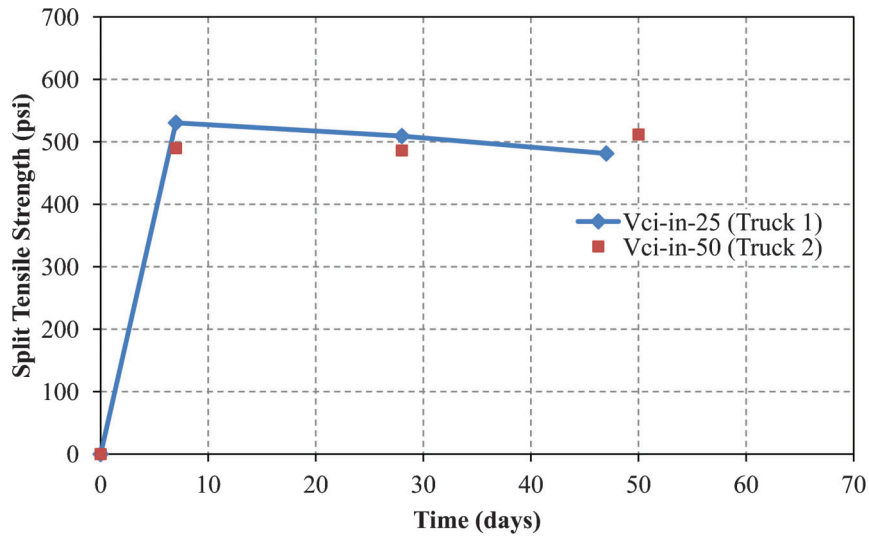


Figure D-2.9 Split tensile strength for $V_{ci-in-25}$ and $V_{ci-in-50}$.

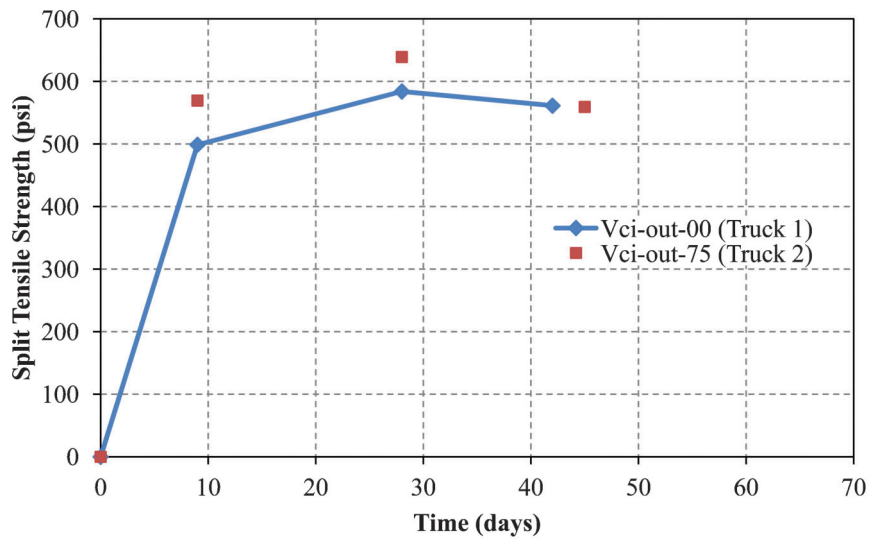


Figure D-2.10 Split tensile strength for $V_{ci-out-00}$ and $V_{ci-out-75}$.

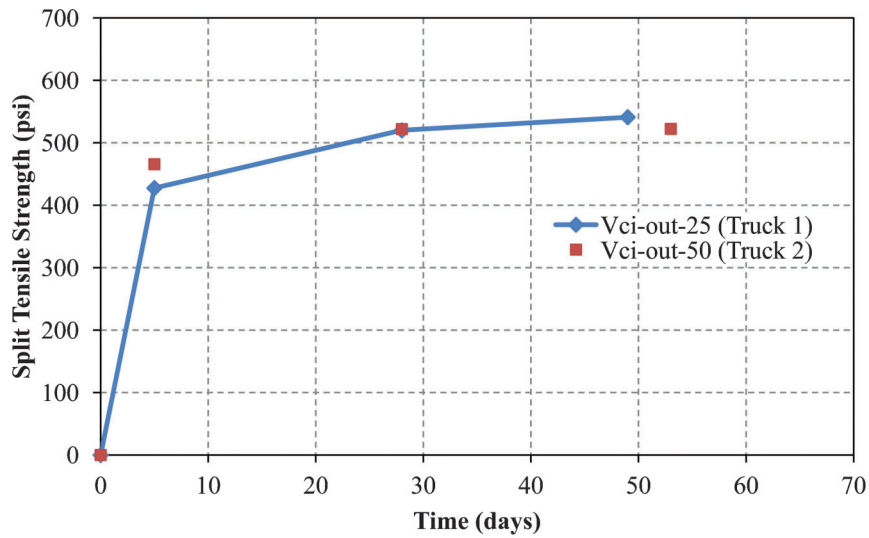


Figure D-2.11 Split tensile strength for $V_{ci-out-25}$ and $V_{ci-out-50}$.

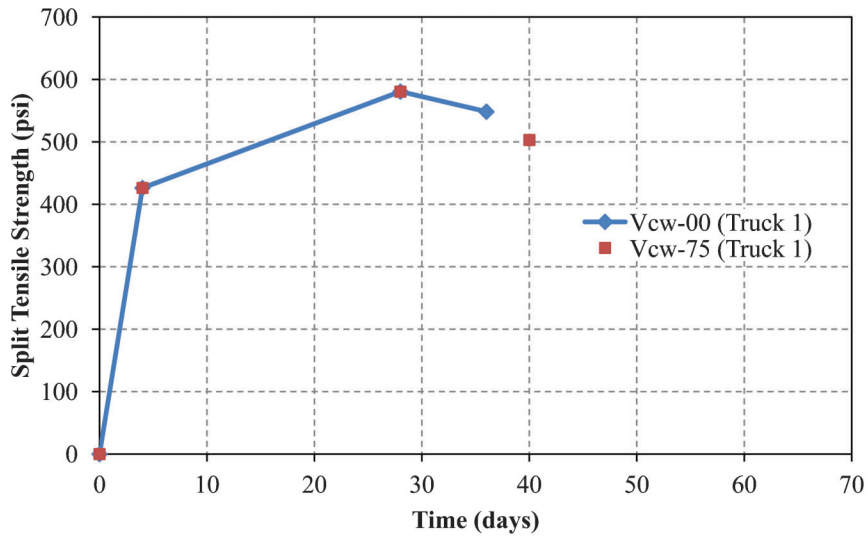


Figure D-2.12 Split tensile strength for V_{cw-00} and V_{cw-75} .

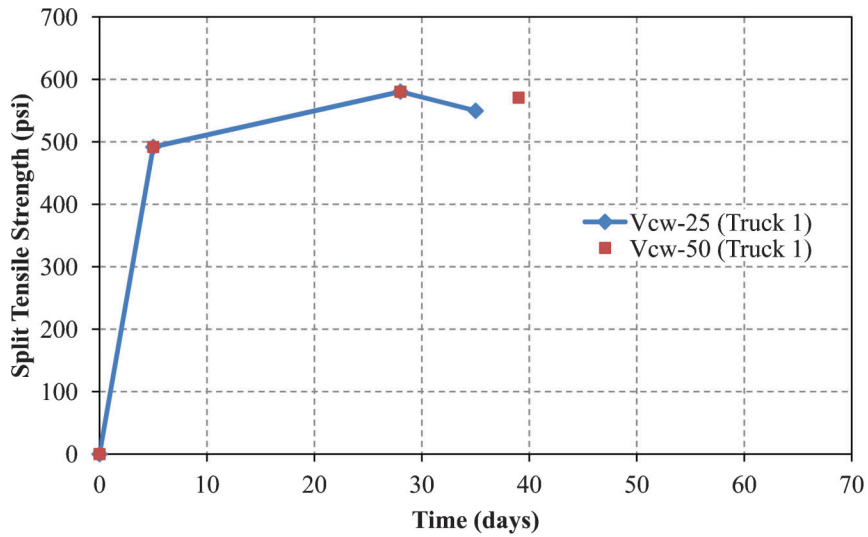


Figure D-2.13 Split tensile strength for V_{cw-25} and V_{cw-50} .

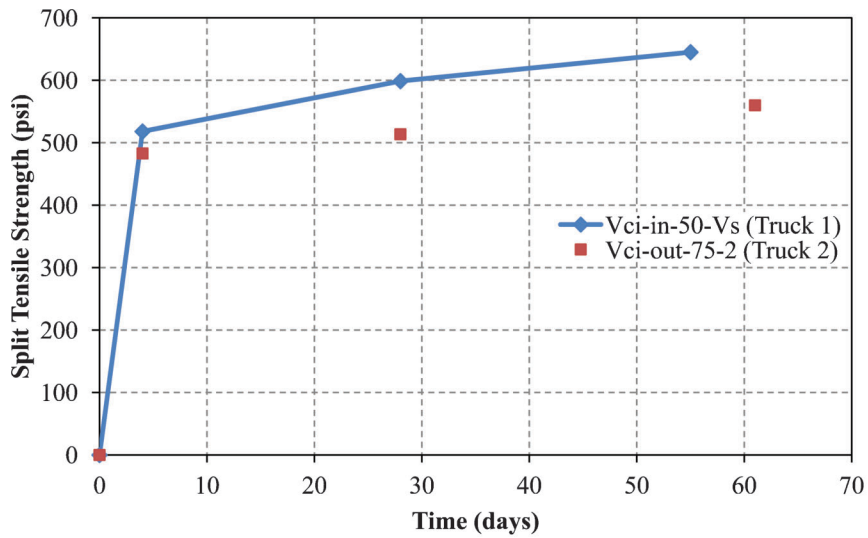


Figure D-2.14 Split tensile strength for $V_{ci-in-50-Vs}$ and $V_{ci-out-75-2}$.

TABLE D-2.1
Average Concrete Compressive Strength Data for Series I (V_{ci-in})

Cast	Specimen ID	Age (days)	f'_c (psi)	Specimen ID	Age (days)	f'_c (psi)
1	$V_{ci-in-00}$ (Truck 1)	3	4,450	$V_{ci-in-75}$ (Truck 2)	—	—
		7	5,440		—	—
		12	6,530		12	6,120
		14	6,580		—	—
		21	7,100		—	—
		28	7,300		28	6,870
		33	7,170	36	6,950	
3	$V_{ci-in-25}$ (Truck 1)	3	4,550	$V_{ci-in-50}$ (Truck 2)	—	—
		7	5,710		7	5,760
		14	6,290		—	—
		21	6,680		—	—
		28	6,780		28	6,880
		47	6,930		50	6,800

TABLE D-2.2
Average Concrete Compressive Strength Data for Series II (V_{ci-out})

Cast	Specimen ID	Age (days)	f'_c (psi)	Specimen ID	Age (days)	f'_c (psi)
2	$V_{ci-out-00}$ (Truck 1)	3	4,540	$V_{ci-out-75}$ (Truck 2)	—	—
		7	5,970		—	—
		9	5,700		9	6,040
		14	6,520		—	—
		21	6,880		—	—
		28	7,390		28	7,160
		42	7,290	45	7,330	
4	$V_{ci-out-25}$ (Truck 1)	3	4,740	$V_{ci-out-50}$ (Truck 2)	—	—
		5	4,900		5	4,880
		7	5,230		—	—
		14	6,010		—	—
		21	6,100		—	—
		28	6,280		28	6,360
		49	6,210	53	6,380	

TABLE D-2.3
Average Concrete Compressive Strength Data for Series III (V_{cw})

Cast	Specimen ID	Age (days)	f'_c (psi)	Specimen ID	Age (days)	f'_c (psi)
5	V_{cw-00} (Truck 1)	3	4,380	V_{cw-75} (Truck 1)	3	4,380
		4	5,060		4	5,060
		7	5,140		7	5,140
		14	5,740		14	5,740
		21	6,340		21	6,340
		28	6,390		28	6,390
		36	6,390	40	6,380	
6	V_{cw-25} (Truck 1)	3	4,720	V_{cw-50} (Truck 1)	3	4,720
		5	5,400		5	5,400
		7	5,760		7	5,760
		14	6,620		14	6,620
		21	7,040		21	7,040
		28	7,060		28	7,060
		35	7,450	39	7,130	

TABLE D-2.4
Average Concrete Compressive Strength Data for Series IV

Cast	Specimen ID	Age (days)	f'_c (psi)	Specimen ID	Age (days)	f'_c (psi)
7	V _{ci} -in-50-V _s (Truck 1)	3	4,410	V _{ci} -out-75-2 (Truck 2)	—	—
		4	4,910		4	4,350
		7	5,690		—	—
		14	6,610		—	—
		28	7,210		28	6,710
		42	7,400		42	6,970
		55	7,380		61	6,780

TABLE D-2.5
Average Concrete Split Tensile Strength Data for All Series

Cast	Specimen ID	Age (days)	f_{ct} (psi)	Specimen ID	Age (days)	f_{ct} (psi)
1	V _{ci} -in-00 (Truck 1)	3	420	V _{ci} -in-75 (Truck 2)	—	—
		7	480		—	—
		12	480		12	500
		14	520		—	—
		21	550		—	—
		28	570		—	—
		33	620		36	610
2	V _{ci} -out-00 (Truck 1)	9	500	V _{ci} -out-75 (Truck 2)	9	570
		28	580		28	640
		42	560		45	560
3	V _{ci} -in-25 (Truck 1)	7	530	V _{ci} -in-50 (Truck 2)	7	490
		28	510		28	490
		47	480		50	510
4	V _{ci} -out-25 (Truck 1)	5	430	V _{ci} -out-50 (Truck 2)	5	470
		28	520		28	520
		49	540		53	520
5	V _{cw} -00 (Truck 1)	4	430	V _{cw} -75 (Truck 1)	4	430
		28	580		28	580
		36	550		40	500
6	V _{cw} -25 (Truck 1)	5	490	V _{cw} -50 (Truck 1)	5	490
		28	580		28	580
		35	550		39	570
7	V _{ci} -in-50-V _s (Truck 1)	4	520	V _{ci} -out-75-2 (Truck 2)	4	480
		28	600		28	510
		55	650		61	560

APPENDIX D-3. PHOTOS OF ULTIMATE FAILURES FOR SPECIMENS IN APPENDIX D



Figure D-3.1 Ultimate failure— V_{ci} -in-00.



Figure D-3.4 Ultimate failure— V_{ci} -in-75.



Figure D-3.2 Ultimate failure— V_{ci} -in-25.



Figure D-3.5 Ultimate failure— V_{ci} -out-00.

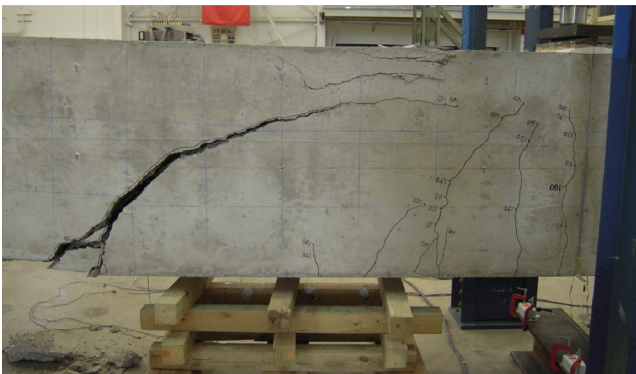


Figure D-3.3 Ultimate failure— V_{ci} -in-50.

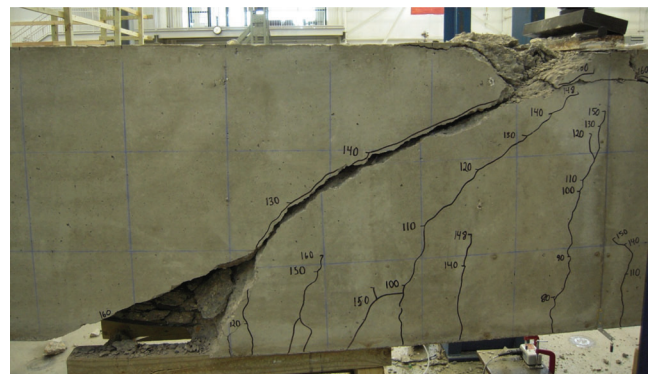


Figure D-3.6 Ultimate failure— V_{ci} -out-25.



Figure D-3.7 Ultimate failure— V_{ci} -out-50.

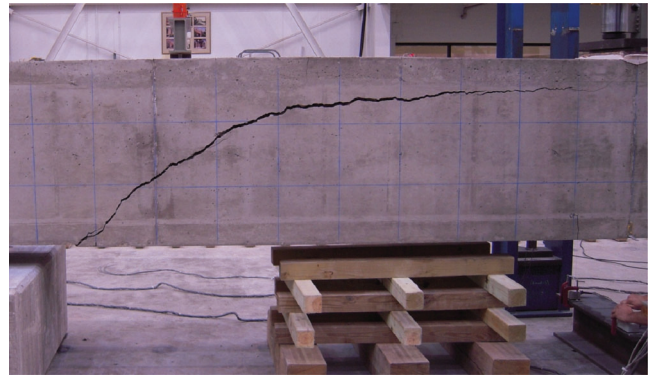


Figure D-3.10 Ultimate failure— V_{ci} -out-75-2.



Figure D-3.8 Ultimate failure— V_{ci} -out-75 (south shear span).



Figure D-3.11 Ultimate failure— V_{cw} -00.



Figure D-3.9 Ultimate failure— V_{ci} -out-75 (north shear span).



Figure D-3.12 Ultimate failure— V_{cw} -25.



Figure D-3.13 Ultimate failure— V_{cw-50} .



Figure D-3.15 Ultimate failure— $V_{ci-in-50-V_s}$.



Figure D-3.14 Ultimate failure— V_{cw-75} .

APPENDIX E. COMPOSITE SECTION EFFECTS ON SHEAR STRENGTH

E.1 INTRODUCTION

To evaluate the influence of different concrete strengths on shear strength in composite sections, an experimental investigation consisting of six reinforced concrete beams was conducted. It is common in composite construction that different concrete strengths are used for the beam and for the deck (U-beams). The question often arises as to what is the appropriate concrete strength for use in shear design. The experimental program was divided into three series. Each series consists of a beam with a low longitudinal reinforcement ratio and a beam with a high reinforcement ratio. The three series are distinguished by the concrete strengths. Series I beams were constructed entirely of normal strength concrete while Series II beams were constructed entirely of high strength concrete. Series III beams were constructed using high strength concrete in the bottom portion and normal strength concrete in the top portion. All six specimens were designed to have the same dimensions and effective depth. This chapter discusses the design, materials, construction, testing, and results of the experimental program.

E.2 SPECIMEN DESIGN

The beams were designed to evaluate the influence of different concrete strengths used in composite members on shear strength. Considering the shear model previously discussed in Chapter 3, it was hypothesized that the concrete compressive strength in the compression zone controls the flexure-shear strength. These tests were designed to evaluate that hypothesis.

The variables that controlled design of the specimens include: shear span-to-depth ratio, concrete strength, and longitudinal reinforcement ratio. The primary variables for the testing program are listed in Table E.1. The notation for the specimen identification is as follows. The first part of the identification “D” represents the “deck” (top portion) concrete followed by its design strength in ksi. The second part “B” represents the “beam” (bottom portion) concrete followed by its design strength in ksi. Finally, the longitudinal reinforcement percentage is provided. Therefore, the D4-B4-0.48 specimen is designed with 4,000 psi concrete and a reinforcement ratio of 0.48%.

It was decided that the test setup would consist of a simply supported, rectangular beam with a concentrated load at midspan as shown in Figure E.1. This setup simplifies analysis by providing a constant and equal shear in both shear spans. The rectangular cross section was selected to isolate the primary variables such that shape does not complicate behavior. A rectangular shape also simplifies analysis and construction. All specimens were designed to fail in flexure-shear according to $V_c = 5\sqrt{f'_c}b_wc$ (Equation 1.1) where the cracked transformed neutral axis depth, c , is calculated using Equation 4.1. The neutral axis depths and corresponding shear strength are included in Table E.1.

TABLE E.1
Test Matrix

Series	Specimen ID	Deck f'_c (psi)	Beam f'_c (psi)	ρ (%)	c (in.)	V_c (kips)
I	D4-B4-0.48	4,000	4,000	0.48	5.1	19.2
	D4-B4-2.40	4,000	4,000	2.40	9.6	36.3
II	D10-B10-0.48	10,000	10,000	0.48	4.1	24.8
	D10-B10-2.40	10,000	10,000	2.40	8.1	48.5
III	D4-B10-0.48	4,000	10,000	0.48	5.1	19.2
	D4-B10-2.40	4,000	10,000	2.40	9.4	41.1

$$c = kd \quad (E.1)$$

where:

k : cracked transformed section factor, Eq. E.2

d : effective depth, in.

$$k = \sqrt{2\rho n + (\rho n)^2} - \rho n \quad (E.2)$$

where:

ρ : longitudinal tension reinforcement ratio, Eq. E.3

n : modular ratio, Eq. E.4

$$\rho = \frac{A_r}{b_w d} \quad (E.3)$$

where:

A_r : area of longitudinal tension reinforcement, in.²

$$n = \frac{E_r}{E_c} \quad (E.4)$$

where:

E_c : modulus of elasticity of concrete, psi

E_r : modulus of elasticity of reinforcement, psi

Design details for all specimens are shown in Figure E.2. All of the specimens have the same concrete dimensions and effective depth. The “Deck” and “Beam” denoted in Figure E.2 represent the top and bottom portions of the specimens, respectively.

E.2.1 Cross Section

Rectangular cross section dimensions were controlled by several variables. The most important cross section dimension is the beam depth. The beam depth was selected to ensure a shear failure while maintaining slender beam behavior (a/d ratio greater than 3.0). Ultimately, a depth was selected that promoted a shear failure while maintaining the steel stresses below yield. The beam width also affects the shear capacity, although the degree of effect is much less than the influence of the beam depth. Therefore, the width was primarily selected to result in a 21 beam depth to width ratio. This selection resulted in a 12 in. wide \times 24 in. deep cross section.

The beams in Series III were designed to create a composite section where the bottom portion represents the beam and the top portion represents the deck. The depth of each was selected so that the neutral axis at cracking was completely inside the deck portion (low concrete strength) in the low longitudinal reinforcement ratio specimen and well within the beam portion (high concrete strength) in the high longitudinal reinforcement ratio specimen. The longitudinal reinforcement was designed with this goal in mind (Section E.2.3). These two neutral axis depth scenarios enable comparisons to be made to assist in determining the appropriate concrete strength that should be used in shear strength calculations. Based on this design objective, a 7 in. deep deck and a 17 in. deep beam as

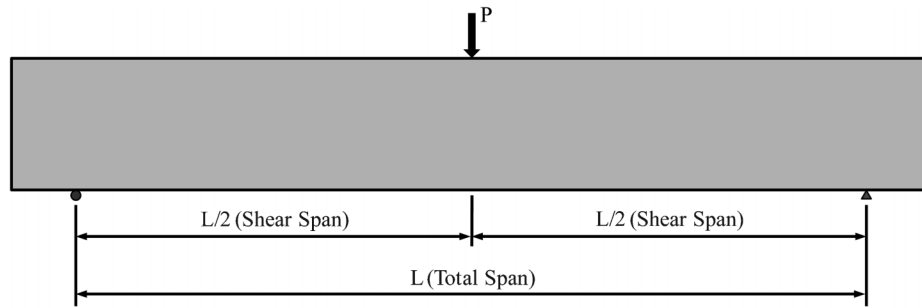


Figure E.1 Support and loading conditions.

illustrated in Figure E.2 were selected. As noted in Table E.1, the neutral axis depth for the 0.48% reinforced specimen is completely within the deck while the depth for the 2.40% reinforced specimen is 2.4 in. below the beam-deck interface.

E.2.2 Concrete Compressive Strength

The concrete compressive strength was selected to provide a typical, nominal concrete strength (4,000 psi) used for bridge deck construction. Prestensioned beams are commonly constructed with high strength concrete to allow release after 24 to 48 hours. The high strengths are needed at an early age in precast production; therefore, the concrete strength when the member is in service is often 8,000 to 10,000 psi. Consequently, 10,000 psi concrete was selected for the beam (bottom) portion.

E.2.3 Longitudinal Reinforcement

The longitudinal reinforcement was selected to result in significantly different neutral axis depths so that the importance of the concrete compressive strength in the compression zone could be evaluated. Furthermore, it was desirable that the reinforcement not yield prior to shear failure; therefore, high strength ($f_y > 100$ ksi) reinforcing steel was selected. The two reinforcement ratios selected to achieve the considerably different neutral axis depths are 0.48% (2 #7 bars) and 2.40% (10 #7 bars). This resulted in the cracked transformed section neutral axis

depths provided in Table E.1. The effective depth was maintained constant so that results could be readily compared.

E.3 MATERIALS

E.3.1 Concrete

The concrete was ordered from Irving Materials, Inc. (IMI) with a target of 4,000 psi and 10,000 psi. The two mixes selected are shown in Table E.2. The selected normal strength mix contained 3/4 in. maximum aggregate size (crushed stone), while the high strength mix consisted of blended aggregate (3/4 in. maximum aggregate size silica stone mixed with pea gravel).

The six specimens were constructed in one cast, requiring one truck for each different strength mix. A slump of 4 in. was requested for each truck and was measured upon arrival at the laboratory. The batch weights and slump for each mix (truck) are included in Table E.3. No water was added to the trucks onsite.

Standard 6 × 12 in. cylinders were cast in plastic molds and cured in the same manner as the test specimens. After the concrete surface hardened, the specimens and cylinders were covered with wet burlap and plastic to prevent moisture loss. Curing of the cylinders was discontinued at the same time that the curing of the specimens was discontinued. Additionally, the cylinder molds were removed when the specimen forms were removed.

Compressive strength was monitored by testing three cylinders in accordance with ASTM C39 at regular intervals (7, 14, 21, 27, and 56 days) including one day which was selected to represent the

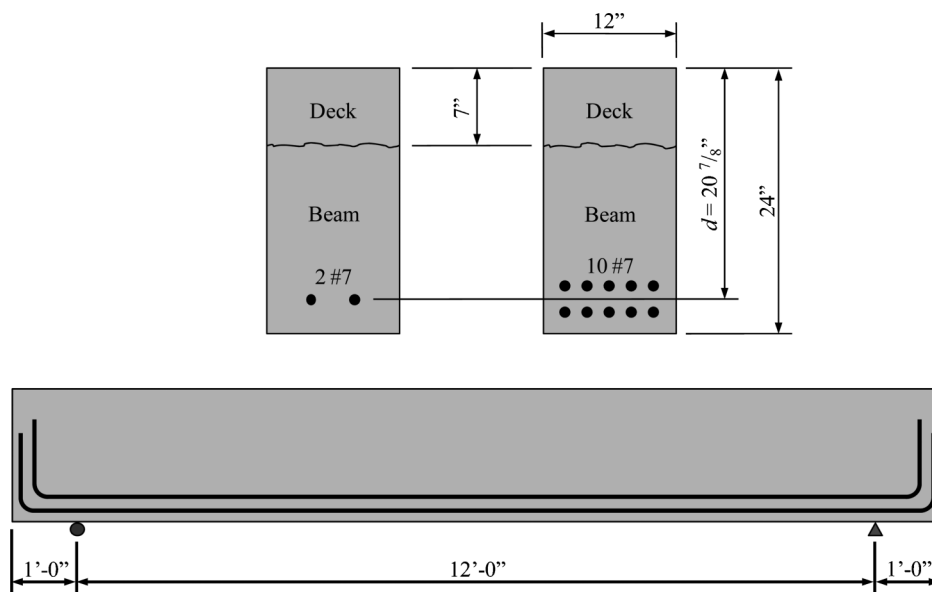


Figure E.2 Specimen designs.

TABLE E.2
Concrete Mix Design Weights per Cubic Yard

Material	Design Weights Per Cubic Yard	
	4,000 psi	10,000 psi
Type I Cement (lbs)	430	658
Fly Ash (lbs)	—	100
3/4" Coarse Aggregate (lbs)	1800	1650
Pea Gravel (lbs)	—	250
Fine Aggregate (lbs)	1540	1200
Water (lbs)	230	168
BASF Glenium 3030 NS Full Range Water Reducer (oz)	8.6	68.2

testing period for all specimens. In addition, split tension cylinders were tested in accordance with ASTM C496 (2011) on the same days as the compression tests. A loading rate of 50,000 lb per minute was used during the compressive cylinder tests along with 70 durometer elastomeric pads. A loading rate of 15,000 lb per minute was used for the split tension tests.

The compressive and split tensile strength growth curves for each mix are shown in Figure E.3 and Figure E.4, respectively. A summary of the compressive and split tensile strength results during the testing phase for each specimen is provided in Table E.4. All of the cylinders were tested on one day which coincided with the middle of the 12 day testing period (Table E.5). Complete compressive and split tensile strength data is provided in Appendix E-1.

E.3.2 Longitudinal Reinforcement

The longitudinal reinforcement consisted of high strength (Grade 100) deformed bars in conformance with ASTM A1035. These bars were manufactured, fabricated, and donated by the MMFX Steel Corporation of America. Two samples of the #7 MMFX bars were tested in conformance with ASTM A370 in a universal testing machine in the Bowen Laboratory. The yield stress (and stress-strain curve) are not presented for these tension samples due to extensometer slipping problems. The ultimate stress (calculated from the load provided by the testing machine) of these samples are listed in Table E.6.

Due to the extensometer slippage encountered in samples tested in the Bowen Laboratory, the yield stress for two tensile samples tested by MMFX are provided in Table E.7. The bars were tested in conformance with ASTM A370. The yield stress presented in Table E.7 is the stress corresponding to a 0.2% offset, and the stress-strain curve for each sample is illustrated in Figure E.5. The elastic limit is approximately 100 ksi. In these tensile tests conducted by MMFX, the extensometer was removed prior to bar rupture to prevent potential gage failure; therefore, the complete stress-strain curve (including the ultimate stress) is not shown. The ultimate stress and 0.2% offset yield stress from the mill certification for the heat of steel used in the testing program is

TABLE E.3
Concrete Mix Batch Weights per Cubic Yard

Material	Batch Weights Per Cubic Yard	
	4,000 psi	10,000 psi
Type I Cement (lbs)	428	655
Fly Ash (lbs)	—	102
3/4" Coarse Aggregate (lbs)	1797	1642
Pea Gravel (lbs)	—	245
Fine Aggregate (lbs)	1582	1233
Water (lbs)	170	119
BASF Glenium 3030 NS Full Range Water Reducer (oz)	8.6	68.7
Slump (in.)	5.5	3

provided in Table E.8. It is important to note that the samples tested by MMFX were from the same heat as the steel used in this testing program (including the test samples in Table E.6). As shown, the ultimate stress from the Bowen tests (Table E.6), and the yield stress from the MMFX tests (Table E.7), is in reasonable agreement with the tensile properties from the mill certification listed in Table E.8.

E.4 SPECIMEN CONSTRUCTION

The reinforced concrete beams were constructed in the Bowen Laboratory using one cast (two trucks). The formwork permitted three sets of casting beds, each with two beams, to be constructed. Each casting bed contained one series of specimens (two beams).

E.4.1 Formwork

The formwork was constructed from 3/4 in. plywood and 2 × 4 s. The side forms were constructed with 3/4 in. plywood panels screwed to 2 × 4 ladder frames consisting of vertical studs, a header, and a base board as shown in Figure E.6. The 2 × 4 headers were attached approximately 1/2 in. from the top edge of the plywood panels to prevent excess concrete build-up during casting operations which simplified screeding. Side forms were attached to the base with lag screws to restrict form movement at the base. Lateral pressures during casting were resisted with several sets of 2 × 4 diagonals attached to the base which also ensured squareness. In addition, the formwork was supported by means of 2 × 4 cross beams on top. The two beams on each casting bed were separated with an interior form wall. This interior form wall was built and attached the same way as the exterior walls. The only difference was the interior wall was covered with plywood on both sides, instead of just one.

E.4.2 Casting

Concrete was poured directly from the truck into the forms as shown in Figure E.7. As the concrete was being placed (in two

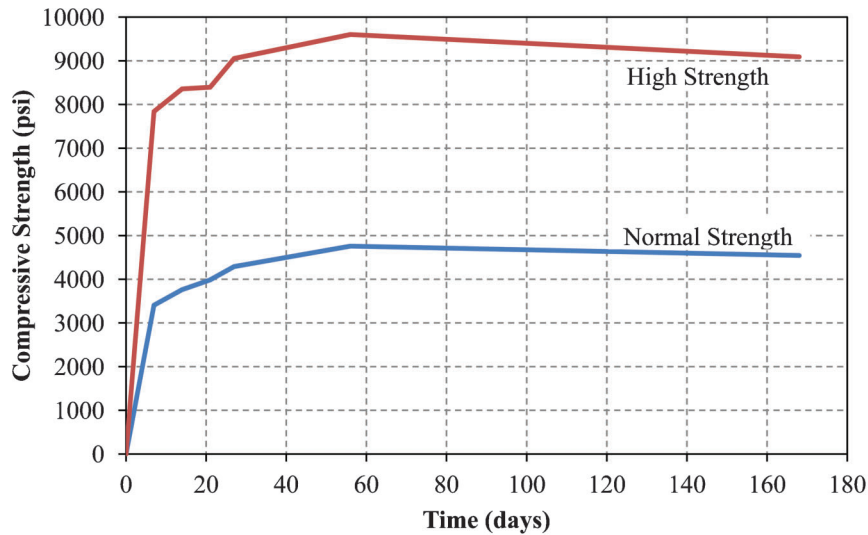


Figure E.3 Compressive strength.

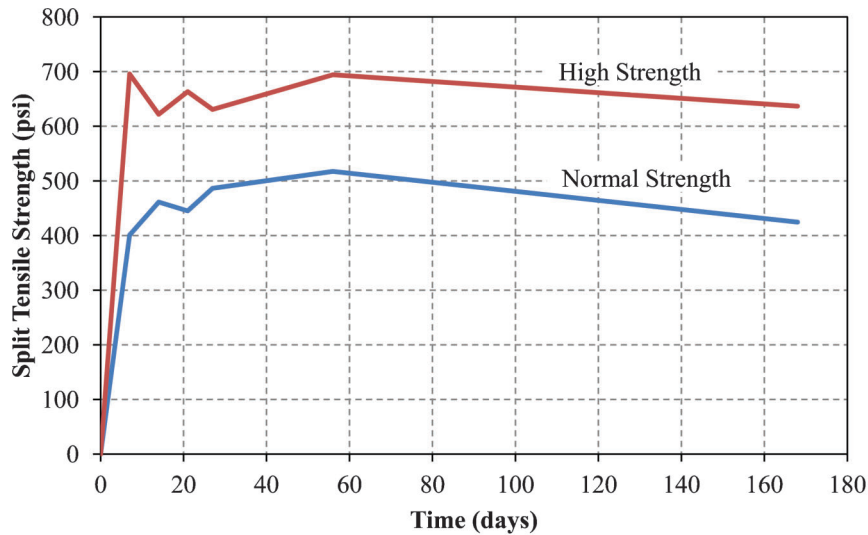


Figure E.4 Split tensile strength.

TABLE E.4
Concrete Strengths During Test Phase

Concrete Mix	Age (days)	(psi)	f_{cr} (psi)
Normal Strength	168	4,550	420
High Strength	168	9,090	640

TABLE E.5
Concrete Age on Test Day

Series	Specimen ID	Age (days)
I	D4-B4-0.48	162
	D4-B4-2.40	164
II	D10-B10-0.48	167
	D10-B10-2.40	169
III	D4-B10-0.48	170
	D4-B10-2.40	174

TABLE E.6
Longitudinal Reinforcement Ultimate Stress (Tested at Bowen Lab)

Sample	Ultimate Stress (ksi)
1	165.8
2	165.3
Average:	165.6

TABLE E.7
Longitudinal Reinforcement Yield Stress (Tested by MMFX)

Sample	Yield Stress (ksi)
1	140.4
2	134.1
Average:	137.3

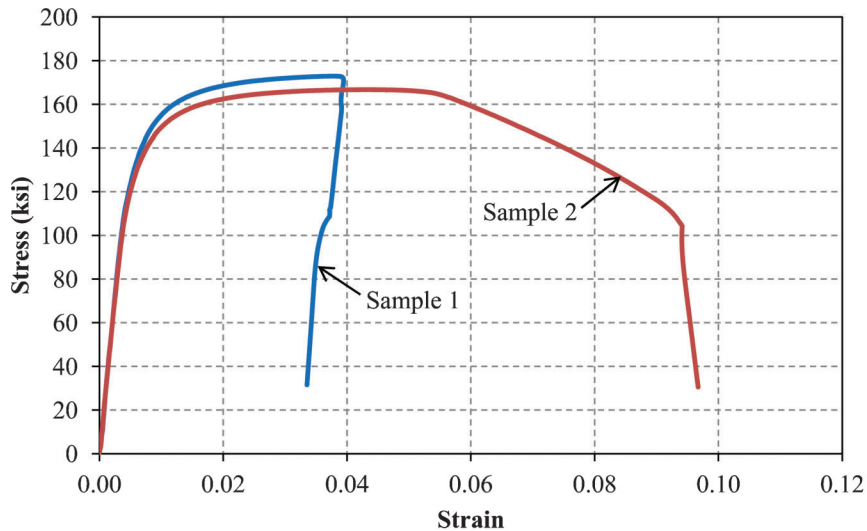


Figure E.5 Stress-strain response of longitudinal reinforcement.

lifts), internal vibrators were used to consolidate the mix. Although each specimen was cast in two lifts, the specimens with composite mixes (Series III) required filling the forms up to 7 in. from the top with the high strength mix and then topping them with the normal strength mix. It is important to note that the concrete from the first truck (high strength mix) was not allowed to harden before the normal strength mix was cast on top. However, the high strength mix was much stiffer than expected during placement operations; therefore, additional vibration was required. During placement, there was concern regarding the quality of the high strength mix considering its stiffness. To ensure monolithic beams in Series III, the vibrators (while vibrating the top layer) were inserted approximately 1 in. into the bottom layer (high strength mix). After vibrating, the top surface was screeded to the proper level followed by finishing with magnesium hand floats.

The specimens were wet cured for seven days. Wet curing was accomplished by covering the surface with wet burlap and plastic to prevent moisture loss. In addition, the burlap was re-wetted every 12–24 hours to maintain curing. After wet curing, the side forms and plastic cylinder molds were removed.

Standard 6 × 12 in. cylinders were cast alongside the specimens. The cylinders were consolidated using a small internal vibrator according to ASTM C192. The cylinders were wet cured in the same manner and for the same duration as the specimens.

E.5 TEST SETUP AND PROCEDURE

E.5.1 Test Setup

The beams were simply supported with a concentrated load applied at midspan as illustrated in Figure E.8. A structural steel test frame tensioned to the strong floor with 200 kips of pretension force was used to resist the applied load from a hydraulic ram (Figure E.8). The pin and roller supports were mounted on top of reinforced concrete pedestals to provide space for deflection and to place the beams at a convenient elevation for testing (Figure E.9). Load was transferred to the beam along a

single line with a pin system to apply equal shear forces to both shear spans (Figure E.10). The pin and roller supports, as well as, the load pin consisted of a 1 in. diameter steel rod between two 12 in. long × 6 in. wide × 0.5 in. thick steel plates.

E.5.2 Test Procedure

The beams were statically loaded to failure using a hand-operated hydraulic pump. The specimens with the low reinforcement ratio (0.48%) were loaded in 5 kip increments while the specimens with the high reinforcement ratio (2.40%) were loaded in 10 kip increments due to the expected difference in shear capacities. At the end of each load stage, the cracks were outlined, and photographs were taken. If first cracking was heard or observed on the load-deflection plot, loading was stopped, and an inspection was made to mark any cracks that may have formed. After failure, a crack map was recorded and photographs were taken.

E.5.3 Instrumentation

Two types of instrumentation were used in this experimental program. A load cell monitored the applied force while string pots were used for beam displacements at the load point (midspan) and

TABLE E.8
Longitudinal Reinforcement Tensile Properties (Mill Certification)

Yield Stress (ksi)	Ultimate Stress (ksi)
134.9	168.2

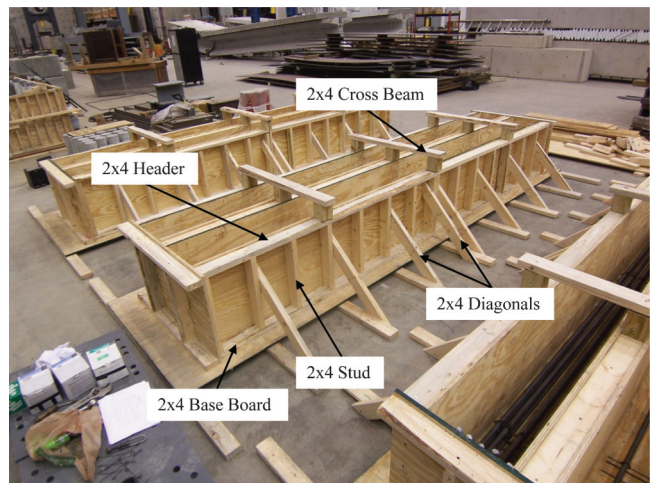


Figure E.6 Formwork.



Figure E.7 Concrete casting operations.

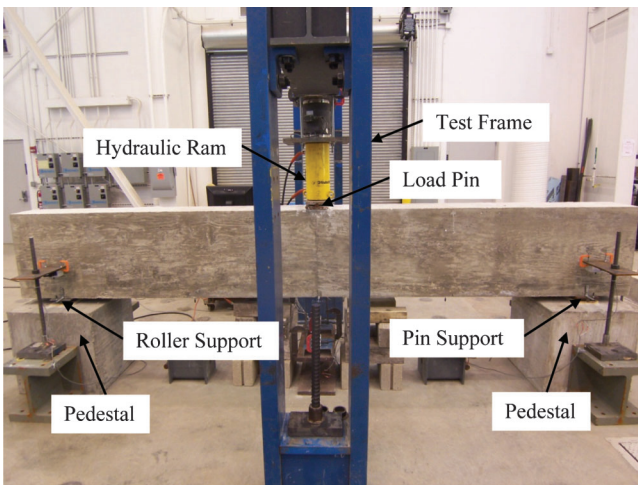


Figure E.8 Test setup.

at quarter points. String pots were also used to measure any support deformation during testing. The instrumentation was identical for all six beams tested in this study. All data was recorded with a Micro Measurements System 7000 data acquisition system controlled by StrainSmart software.

E.5.3.1 String Pots

Two string pots with a range of 25 in. were installed at midspan, one on each side. Reported midspan displacement



Roller



Pin

Figure E.9 Supports.

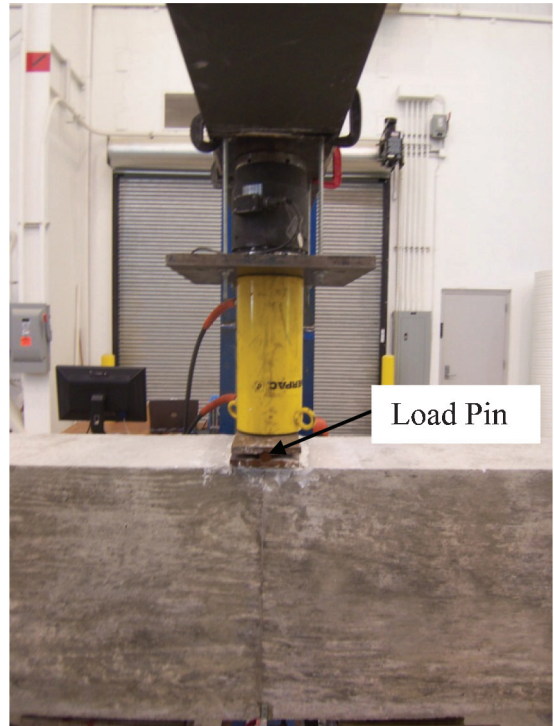


Figure E.10 Load pin.

measurements are the average value of the two string pots at midspan. A 25 in. string pot was also installed at each quarter point. Additionally, two string pots (with a 10 in. range) were installed at each support location. It is important to note that the support deformations were negligible (<0.03 in.); therefore, they were not used to correct the displacements at midspan. The string pots (eight in total) were mounted on steel beams which rested on the strong floor as shown in Figure E.11.

E.5.3.2 Load Cell

A load cell with a maximum load rating of 150 kips was installed directly above the hydraulic ram at midspan to measure the applied load. The load cell is illustrated in Figure E.11.

E.6 TEST RESULTS

The test results are summarized in Table E.9. This table presents the total shear force including self-weight at the formation (and location) of the primary shear crack, V_{test} . The total shear force is comprised of the component from the applied

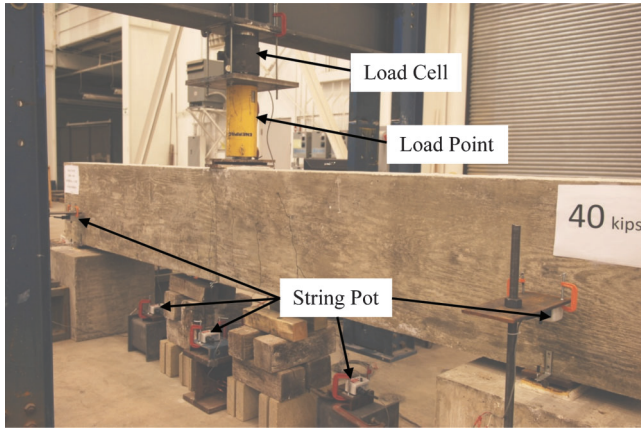


Figure E.11 Instrumentation.

shear, V_{applied} , and the shear due to self-weight, $V_{\text{self-weight}}$ at the failure location. The applied load at failure, P_{applied} , is also provided in the table.

The load-deflection behavior is presented in Figure E.12. The longitudinal reinforcement ratio is noted, and the formation of the primary shear crack is marked by a circle. The crack patterns at the formation of the primary shear crack are shown in Figure E.13 through Figure E.15. Black arrows mark the location of the applied load. In most cases, formation of the primary shear crack denoted complete failure. Photos of the specimens after complete failure are shown in Appendix E-2.

The load-deflection behavior is characterized by two phases. In the first phase, the response is linear elastic. Furthermore, the linear elastic portions of the load-deflection responses are similar because the specimens were each designed with the same dimensions. However, the responses are not identical due to the difference in the transformed section properties which directly affects the elastic stiffness and cracking load. The end of the first phase of behavior is marked by the formation of a flexural crack near midspan.

The second phase is characterized by a reduced, but relatively constant, stiffness following first cracking. The crack patterns spread outward from midspan and upward from the bottom. The end of the second phase is marked by the formation of the primary shear crack which is immediately followed by a reduction in capacity and typically failure of the specimen.

The capacity is approximately doubled as the reinforcement ratio is increased from 0.48% to 2.40% as illustrated in Figure E.12. The crack patterns (Figure E.13 through Figure E.15) show that the primary shear cracks formed at approximately the same location when the reinforcement ratio was the same. In general, the shear cracks in the highly reinforced specimens formed further away from midspan than the lightly reinforced specimens. In addition, cracking in the highly reinforced specimens is more widespread than cracking in the lightly reinforced specimens. It is important to note that the depth of the compression block (area above cracking) is noticeably

larger in the specimens with 2.40% reinforcement than the specimens with 0.48% reinforcement.

E.7 ANALYSIS OF RESULTS

Although both beams within each series had the same dimensions and concrete strength, the load-deflection behavior and shear capacity differ significantly (Figure E.12). The shear capacity of the specimens with the high reinforcement ratio (2.40%) is approximately double the capacity of the specimens with the low reinforcement ratio (0.48%). This difference is believed to be due to the compression area (neutral axis depth) being directly related to the shear capacity. The only design difference between the two specimens in each series is that one specimen had a low reinforcement ratio (0.48%) while the other had a high reinforcement ratio (2.40%). These reinforcement ratios directly affected the neutral axis depths which affects the compressive area available to resist shear stresses. The specimens with the high reinforcement ratio had a larger compressive area after flexural cracking, and therefore, were able to resist higher shear stresses before failure.

Several approaches were used to estimate the shear strength of the specimens. The shear strength according to ACI was calculated as $V_c = 2\sqrt{f'_c}b_vd$ (ACI 318 Section 11.2.1.1). Two AASHTO approaches were used to calculate shear strength. One of these approaches is the simplified procedure (AASHTO Section 5.8.3.4.3) discussed in Section D.2.3.2.3 and was also implemented in the Chapter 3 analysis. This approach shall be referred to as the "simplified" approach. The other AASHTO approach is based on the Modified Compression Field Theory (MCFT). The MCFT expressions (in ksi units) from AASHTO Section 5.8.3.4.2 are provided in Equations E.5 through Equation E.8. In the ACI 318 and AASHTO approaches, the shear strength of the two composite specimens was calculated using the lower concrete strength as typically done in practice. In the highly reinforced composite specimen (D4-B10-2.40), the shear model calculated the shear strength by adding the shear strength provided by the top portion (deck) to the shear strength provided by the fraction of the bottom portion (beam) in the compression zone. All analyses use the concrete compressive strengths measured during the testing phase which are provided in Table E.4.

$$V_c = 0.0316\beta\sqrt{f'_c}b_vd_v \quad (E.5)$$

where:

β : factor indicating ability of diagonally cracked concrete to transmit tension and shear, Eq. E.6

$$\beta = \frac{4.8}{(1 + 750\varepsilon_x)} \frac{51}{39 + s_{xe}} \quad (E.6)$$

where:

ε_x : net longitudinal tensile strain in section at centroid of tensile reinforcement, Eq. E.7

TABLE E.9
Test Results

Series	Specimen ID	P_{applied} (kip)	V_{applied} (kip)	$V_{\text{self-weight}}$ (kip)	V_{test} (kip)
I	D4-B4-0.48	50.3	25.2	0.9	26.1
	D4-B4-2.40	98.3	49.2	1.2	50.4
II	D10-B10-0.48	49.2	24.6	0.9	25.5
	D10-B10-2.40	100.4	50.2	1.2	51.4
III	D4-B10-0.48	53.3	26.7	0.9	27.6
	D4-B10-2.40	110.2	55.1	1.2	56.3

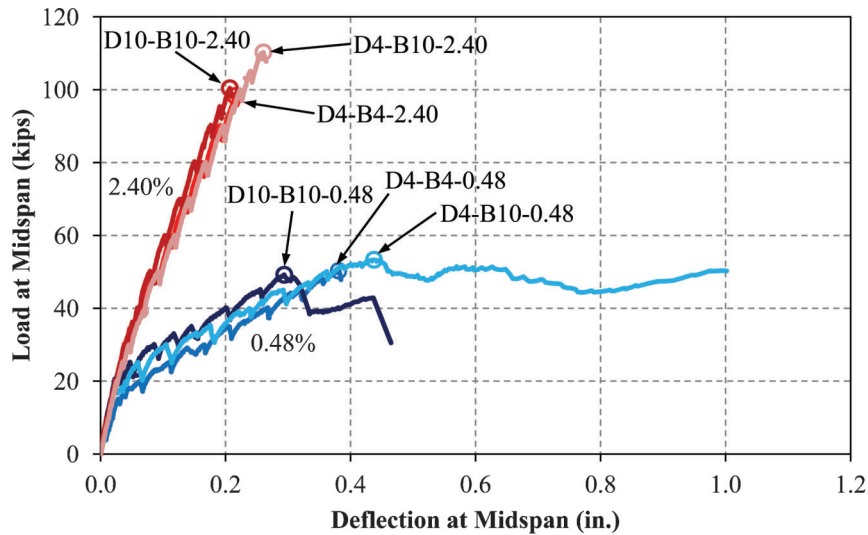


Figure E.12 Load-deflection behavior.

s_{xe} : crack spacing parameter, Eq. E.8

$$\varepsilon_s = \frac{\left(\frac{|M_u|}{d_v} + 0.5N_u + |V_u - V_p| - A_{ps}f_{po} \right)}{E_s A_s + E_p A_{ps}} \quad (E.7)$$

where:

- A_{ps} : area of prestressing steel on flexural tension side, in.²
- A_s : area of nonprestressed steel on flexural tension side, in.²
- E_p : modulus of elasticity of prestressing steel (28,500 ksi)
- E_s : modulus of elasticity of nonprestressed steel (29,000 ksi)
- f_{po} : stress in strand when concrete is cast, ksi
- M_u : factored moment, kip-in.
- N_u : factored axial force (tension: positive, compression: negative), kip
- V_u : factored shear force, kip

$$s_{xe} = s_x \frac{1.38}{a_g + 0.63} \quad (E.8)$$

where:

- a_g : maximum aggregate size, in.
- s_x : lesser of either d_v or maximum distance between longitudinal crack control reinforcement, in.

The calculated shear capacities are compared with the measured shear capacities at the formation of the primary shear crack (V_{test}) in Table E.10. Shear capacities from ACI 318 Section 11.2.1.1 and AASHTO Section 5.8.3.4 are provided as well. Ratios of measured shear capacities to calculated shear capacities are listed in Table E.11. These ratios allow comparisons between four different calculation approaches (shear model, ACI 318, AASHTO simplified, and MCFT from AASHTO). The values in Table E.10 and Table E.11 for the AASHTO simplified approach are presented with and without the lower bound limit (Section D.2.3.2.3) to determine its validity.

The shear model is able to capture the dependence of the shear capacity on the neutral axis depth; therefore, it provided conservative and consistent estimates of the shear capacity. Conversely, the ACI 318 approach is unaffected by the longitudinal reinforcement ratio. In addition, only a small influence is observed using AASHTO's simplified procedure for calculating flexure-shear strength (Section D.2.3.2.3). It is interesting that the

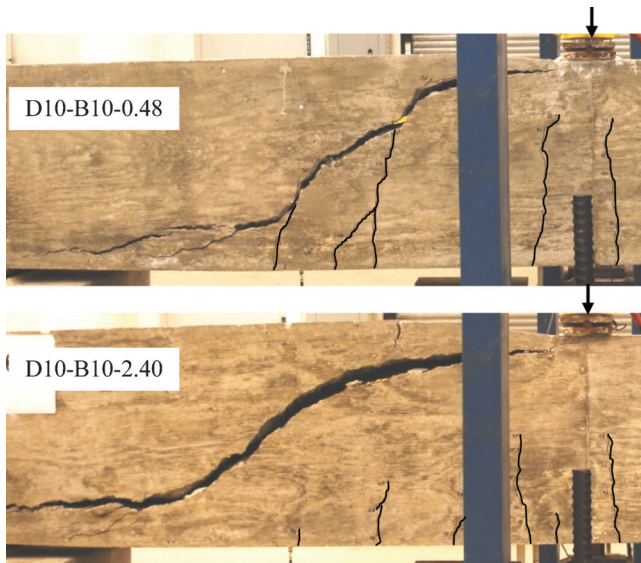


Figure E.13 Primary shear cracks—Series I (4,000 psi).

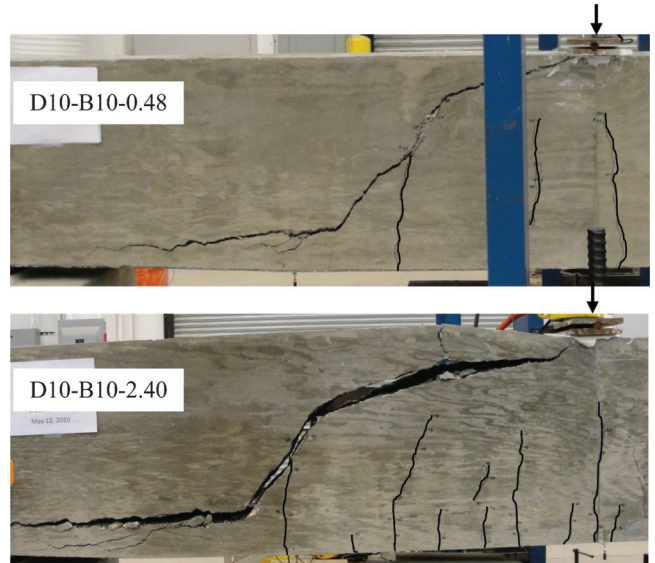


Figure E.14 Primary shear cracks—Series II (10,000 psi).

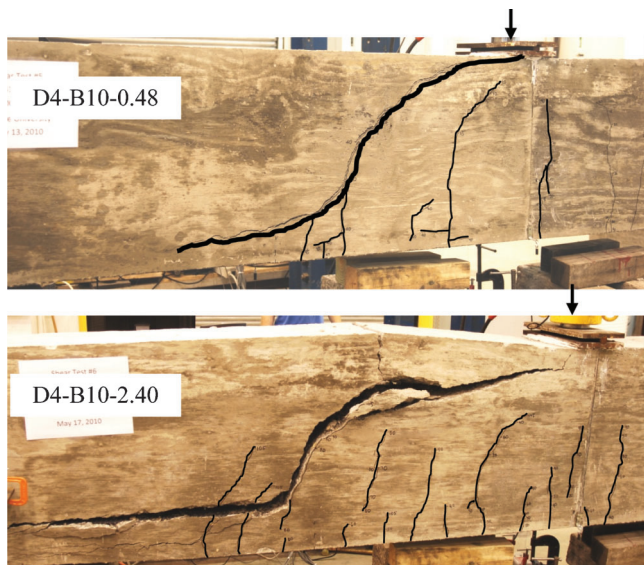


Figure E.15 Primary shear cracks—Series III (composite).

capacities from AASHTO's simplified approach for specimens with a reinforcement ratio of 2.40% are slightly lower than the capacities for specimens with a reinforcement ratio of 0.48%. This behavior of the equation occurs because the effective shear depth (d_v) is lower in the highly reinforced specimens. It is important to

note that the gross section properties were used to calculate the cracking moment for this approach. Similar to the shear model, the MCFT is able to capture the dependence of longitudinal reinforcement stiffness on shear capacity because this approach uses the longitudinal reinforcement stiffness in the calculation of ϵ_s (Equation E.7). It should be noted, however, that the shear model was slightly more consistent in the shear strength estimates. This consistency is evident in the standard deviations of the shear model (0.15) and MCFT (0.21).

Both the shear model and ACI 318 approaches make use of the same square root relationship between the compressive strength and shear strength. The shear model, however, results in a much smaller increase in shear strength when comparing the high strength (10,000 psi) specimens to the normal strength (4,000 psi) specimens. The shear model estimates a 23% average increase in shear strength from the 4,000 psi specimens to the 10,000 psi specimens. ACI 318, on the other hand, estimates a 41% increase for these same specimens. The difference is due to the fact that the neutral axis used by the shear model decreases as the compressive strength increases allowing for a more realistic calculation of shear strength.

Although the average shear capacity from ACI 318 and the AASHTO simplified approach are conservative, several of the ratios listed in Table E.11 are very unconservative. Unconservative capacities using these code approaches are observed in each specimen with the low reinforcement ratio (0.48%). Clearly, low shear capacities observed in the low reinforced specimens are not captured by these current code approaches. It is important to note that the capacities given by the AASHTO simplified approach are conservative in each case when the lower bound limit is ignored. Ignoring the lower bound limit, however, resulted in overly conservative estimates of shear strength in the specimens with a high reinforcement ratio (2.40%).

TABLE E.10
Comparison of Shear Strengths

Series	Specimen ID	V_{test} (kip)	Model	ACI 318	V_{calc} (kip)		
					AASHTO		
					Simplified		MCFT
					Limit	No Limit	
I	D4-B4-0.48	26.1	19.9	33.8	30.1	16.2	20.9
	D4-B4-2.40	50.4	37.8	33.8	28.9	16.0	36.3
II	D10-B10-0.48	25.5	24.1	47.8	44.1	23.7	26.3
	D10-B10-2.40	51.4	47.0	47.8	40.8	22.8	46.1
III	D4-B10-0.48	27.6	19.9	33.8	30.1	19.0	20.9
	D4-B10-2.40	56.3	41.2	33.8	28.9	18.8	36.3

TABLE E.11
Comparison of Shear Strength Ratios

Series	Specimen ID	V_{test} (kip)	Model	ACI 318	V_{test}/V_{calc}		
					AASHTO		
					Simplified		MCFT
					Limit	No Limit	
I	D4-B4-0.48	26.1	1.31	0.77	0.87	1.61	1.25
	D4-B4-2.40	50.4	1.33	1.49	1.74	3.15	1.39
II	D10-B10-0.48	25.5	1.06	0.53	0.58	1.08	0.97
	D10-B10-2.40	51.4	1.09	1.08	1.26	2.25	1.11
III	D4-B10-0.48	27.6	1.39	0.82	0.92	1.45	1.32
	D4-B10-2.40	56.3	1.37	1.67	1.95	2.99	1.55
	Average:		1.26	1.06	1.22	2.09	1.27
	Standard Deviation:		0.15	0.44	0.53	0.85	0.21

E.8 CONCLUSIONS

Six reinforced concrete beams were constructed, tested, and analyzed to evaluate the composite section effects on shear strength. The following conclusions are made based on the experimental program and the analytical phase:

1. The load-deflection behavior of the specimens tested are clearly distinguished by the amount of longitudinal reinforcement. The average shear capacities of the specimens with a high reinforcement ratio (2.40%) were double that of the specimens with a low reinforcement ratio (0.48%).
2. The concrete compressive strength was observed to have almost no impact on the shear strength of the specimens tested in this experimental program. The small differences in test results (8% for the specimens with 0.48% reinforcement and 12% for the specimens with 2.40% reinforcement) are within the scatter expected in the shear test results.
3. The shear model and MCFT conservatively estimated the shear capacity of almost every specimen (Table E.11). It should be noted that the MCFT yielded a slightly unconservative shear strength for D10-B10-0.48. The shear model and MCFT are the only two of the four approaches that incorporate the longitudinal reinforcement stiffness in the calculation of shear strength. The importance of the longitudinal reinforcement ratio is clearly visible in the test results.
4. The effect of the concrete compressive strength in the shear model is also shown to have a reduced impact on shear strength as compared with other methods such as ACI 318. The test results support this minimal influence of the concrete strength on shear strength.
5. Both the ACI 318 and AASHTO simplified approach were unable to conservatively calculate the shear strength of the specimens with a low reinforcement ratio (0.48%) because these code equations do not account for the longitudinal

reinforcement. Shear strength estimates were unconservative in all cases. For the nominal 10,000 psi specimen, $V_{\text{test}}/V_{\text{calc}}$ ratios of 0.53 for ACI 318 and 0.58 for AASHTO were obtained.

6. The AASHTO simplified approach as discussed in Section D.2.3.2.3 conservatively estimated the shear capacity of every specimen when the lower bound limit was ignored. However, for the specimens with a reinforcement ratio of 2.40%, extremely conservative results are obtained with an average $V_{\text{test}}/V_{\text{calc}}=2.8$.

E.9 RECOMMENDATIONS

Based on the results of this study, the following recommendations are provided:

1. For composite sections, the shear strength should be computed using the concrete strength of the compression zone. To simplify design, the section can conservatively be considered as homogenous using the lower strength concrete in the section.
2. The lower bound limit in the AASHTO simplified approach discussed in Section D.2.3.2.3 is not appropriate, particularly for sections with low reinforcement ratios. Therefore, it is recommended that the lower bound limit be eliminated from the AASHTO simplified approach when calculating flexure-shear strength (V_{ci}). In addition, the ACI 318 approach should be used with caution with low reinforcement ratios. Significantly unconservative results are possible.
3. Shear strength should be calculated using either the MCFT approach (general procedure in AASHTO Section 5.8.3.4.2) or the shear model. These approaches conservatively and fairly consistently calculate shear strength accounting for the longitudinal reinforcement ratio and concrete strength.

APPENDIX E-1. CONCRETE STRENGTHS FOR SPECIMENS IN APPENDIX E

TABLE E-1.1
Average Concrete Strength Data for 4,000 psi Concrete Mix

Age (days)	f'_c (psi)	f_{cr} (psi)
7	3,410	400
14	3,760	460
21	3,990	450
27	4,290	490
56	4,760	520
168	4,545	420

TABLE E-1.2
Average Concrete Strength Data for 10,000 psi Concrete Mix

Age (days)	f'_c (psi)	f_{cr} (psi)
7	7,840	700
14	8,360	620
21	8,390	660
27	9,050	630
56	9,600	690
168	9,090	640

APPENDIX E-2. PHOTOS OF ULTIMATE FAILURES FOR SPECIMENS IN APPENDIX E

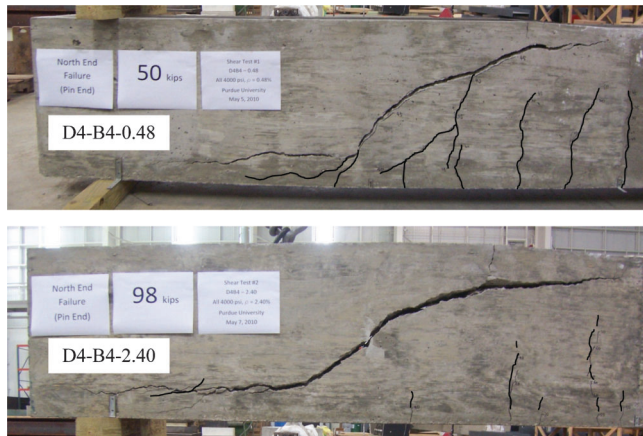


Figure E-2.1 Ultimate failure—Series I (4,000 psi).

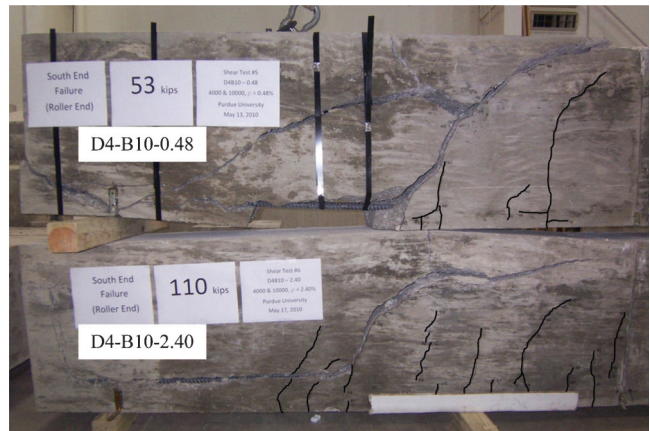


Figure E-2.3 Ultimate failure—Series III (composite).



Figure E-2.2 Ultimate failure—Series II (10,000 psi).

APPENDIX F. INFLUENCE OF U-SHAPE ON SHEAR STRENGTH

F.1 INTRODUCTION

To evaluate the influence of the shape of pretensioned U-beams with debonded strand on shear strength, an experimental investigation was conducted. The experimental program consisted of two half-scale U-beams modeled after the section geometry used on the 21st Street Bridge over I-465 in Indianapolis, Indiana. The specimens were designed to have 50% of the total strands debonded. The beams were also topped with a deck to more closely model behavior of U-beams in service. Both specimens were designed to have the same dimensions, concrete strength, percentage and length of debonding, prestressing force, and prestressing eccentricity. One specimen was designed without transverse reinforcement in the debonded region, while the second specimen included transverse reinforcement throughout the span length. This chapter discusses the analysis, design, materials, construction, testing, and results of the experimental program.

F.2 SPECIMEN DESIGN

Several variables controlled the specimen design and include: length of debonded region (relative to shear span), percentage of debonding, prestressing force, prestressing eccentricity, concrete strength, mild longitudinal reinforcement, and transverse reinforcement. The primary variables for the testing program are listed in Table F.1. Designs also considered cost, construction, and applicable design provisions. It was decided that the test setup would consist of a simply supported beam with a concentrated load at midspan as shown in Figure F.1. The specimens were designed to be loaded with two point loads (one over each web). This setup afforded a simplified analysis by providing constant and equal shear in both shear spans.

F.2.1 U-Beam without Stirrups in Debonded Region (U-50)

This beam was designed to fail in web-shear inside the debonded region. The identifier for this specimen is U-50, where the “50” specifies the percentage of strand debonded, and the “U” indicates that the beam is a U-beam. Design details for U-50 are shown in Figure F.2.

F.2.1.1 Length of Debonded Region and Shear Span

The debonded region was designed to be long enough to ensure that at the end of the debonded region, the flexural stresses were sufficiently large and the neutral axis was small enough to initiate a flexure-shear crack at that section. The length of the debonded region was designed to be 7'-0" from the beam ends. Consideration was also given to developing the fully bonded strands assuming failure initiated at the end of the debonded region. The strands were also designed to be fully developed at midspan. The shear span was adjusted to satisfy these criteria.

F.2.1.2 Cross Section

The cross section dimensions were controlled by the half-scale model of the 21st Street Bridge. However, the web thickness was reduced from 3.75 in. to 3 in. to promote a shear failure. The deck dimensions were chosen to simplify the analysis, construction and testing. Initially, the deck thickness was selected to be 4 in. which is half the thickness of typical Indiana bridge decks. The deck thickness was ultimately designed to be 5 in. to increase the effective depth and prevent a potential flexural failure. Designing the deck width equal to the U-beam width resulted in the entire deck width being considered effective in flexure. It also meant that the deck could be formed without shoring cantilevered sides; therefore, reducing overall cost and construction time. Furthermore, equal beam and deck widths allowed the use of the same testing frame as was used for the specimens in Chapter 3.

F.2.1.3 Strand Pattern

The strand pattern was governed by the hole layout on the pretensioning abutments as well as the bottom flange thickness of the U-beam. It was determined that only one layer of strands would fit in the bottom flange. Therefore, it was desired to maximize the number of strands that would fit in the single row. The hole pattern in the abutments only allowed for six strands. However, two more strands were added through the use of outrigger beams on the back of the abutments which is discussed in more detail in Section F.4.1.

F.2.1.4 Jacking Force

The prestressing stress (after seating losses) was selected based on industry standards ($0.75f_{pu}$), while the jacking force was determined during stressing operations as discussed in Section F.4.1. In addition, the prestressing stress was maximized because of the limited number of strands that could be placed in the section due to beam geometry and pretensioning abutment constraints. A prestressing stress of 202.5 ksi produces a total prestress force of 248 kips after seating losses.

F.2.1.5 Concrete Compressive Strength

The concrete compressive strength was largely controlled by the concrete mix design, which was selected primarily on the basis of constructability. The tight and complex section geometry of the U-beams required that a highly flowable mix be used. Vibrating the bottom flange with internal vibrators would be extremely difficult if the flange and webs were to be cast monolithically. The inner formwork required to cast the U-beams in one cast physically restricts the use of internal vibrators in the bottom flange. These issues resulted in the selection of self-consolidating concrete (SCC) which does not require vibrators to consolidate the mix. A trial batch of an SCC mix developed for the U-beams was delivered by IMI to the Bowen Laboratory to track the compressive and split tensile strengths over time. These strengths were monitored to ensure that the differences between compressive and tensile strengths of the SCC mix over time were similar to conventional concrete. These strengths are provided in Section

TABLE F.1
Test Matrix

Specimen ID	Debonded Strand (%)	Debond Length (ft)	Stirrups	Location of Stirrups
U-50	50	7	#4 @ 6"	Middle
U-50-V _s	50	7	#3 @ 12"	Everywhere

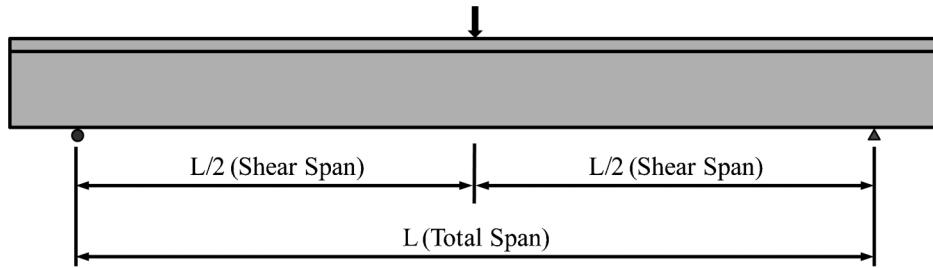


Figure F.1 Support and loading conditions.

F.3.1. The 28 day compressive strength was approximately 7,500 psi; therefore this is the strength that was assumed for design. This strength is also typical of precast, prestressed construction.

F.2.1.6 Mild Longitudinal Reinforcement

The location and quantity of mild longitudinal reinforcement was selected to increase the flexural capacity in the bonded and debonded region in an effort to prevent a flexural failure. Two #5 bars were selected to be placed along the entire length of the beam while two additional #5 bars were placed in the middle region (Figure F.2).

F.2.1.7 Transverse Reinforcement

The location and quantity of transverse reinforcement was selected to promote a shear failure inside the debonded region. Therefore, the middle region (fully bonded region) was reinforced with transverse reinforcement to force the failure to occur outside the fully bonded region and inside the debonded region. The outermost stirrup location was designed to be one effective depth (*d*) outside the debonded region to permit a potential flexure-shear

crack to develop without crossing a stirrup. Ultimately, #4 U-shaped stirrups spaced at 6 in. in the middle region were selected.

F.2.1.8 Deck Reinforcement

The transverse reinforcement for the deck was designed to resist the tensile stresses that result from the point loads creating transverse moments. The point load over each web, combined with the moment arm due to the sloped webs, create these transverse moments. These moments, if not accounted for, could rotate the U-beam webs away from each other. The transverse deck reinforcement resists this moment and acts as a tie between the two U-beam webs. The moment is concentrated at the load points (midspan); however, the reinforcement was provided along the entire deck length to resist restrained shrinkage. One layer of #5 bars spaced at 6 in. was consequently selected for the transverse deck reinforcement.

The longitudinal deck reinforcement was designed to resist shrinkage and temperature effects which resulted in the selection of four #4 bars in one layer. The two outer bars of longitudinal reinforcement in the deck were designed to be tied underneath the top leg of the beam stirrups. This allows the #5 transverse bars to be placed on top of the #4 longitudinal bars (Figure F.2).

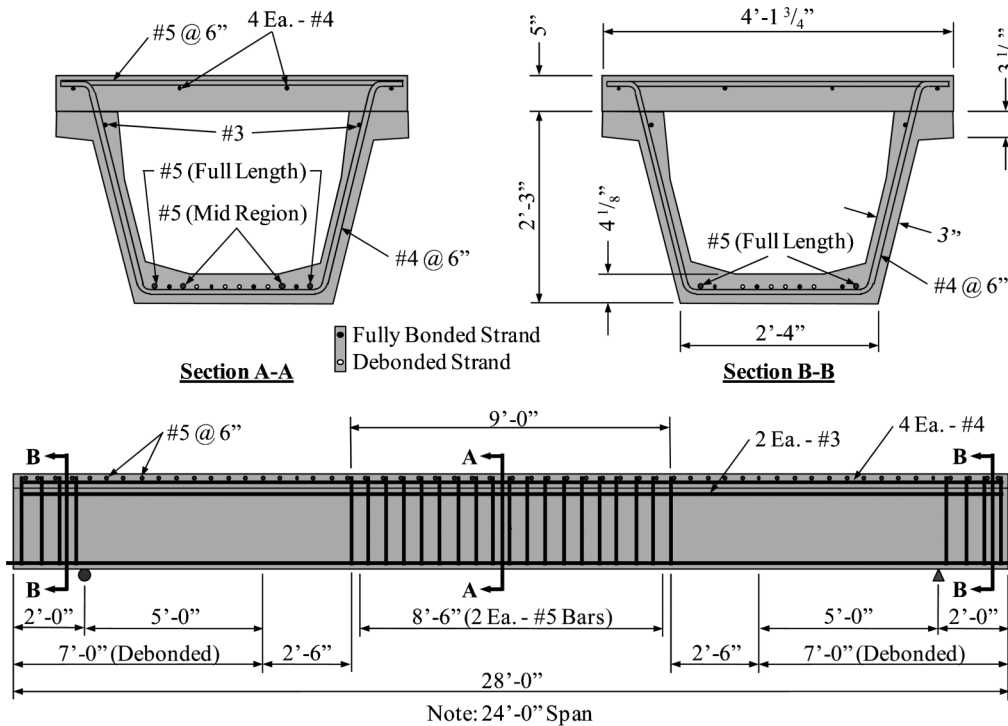


Figure F.2 U-50 specimen.

F.2.1.9 Predicted Shear Strength

The effective shear area was determined using the shear funnel approach discussed in Section D.2.3.2.1. The angles of the shear funnel over each web were determined as the angle created by rotating extensions of the sloped web 45° outward. This results in the shear funnels shown in Figure F.3. It is important to note that while the shear funnel represents the extents of the effective shear area in the analysis, the entire section (including the deck) is assumed effective in flexure.

The following predicted shear strength profiles were created using the shear model discussed in Section D.2.3.2.1. The calculated shear strengths, V_n , were plotted against the total applied shear (dead plus superimposed), V_u as shown in Figure F.4. Due to symmetry, each profile presents the shear over half the beam which is the shear span. The applied load was analytically increased until $V_u \geq V_n$ at any location along the span. The location at which this occurs is the location of failure (formation of primary shear crack) and is labeled “ $V_{u, fail}$ ” in the shear strength profile. The flexure-shear strengths are combined with the web-shear strengths for both the bonded and debonded regions to create one comprehensive shear strength profile. The analyses assume the design concrete strength of 7,500 psi.

It is important to note that the predicted shear strength profile shown in Figure F.4(a) used the original modulus of rupture assumption of $7.5\sqrt{f'_c}$. However, after observing reduced moduli in the testing program discussed in Chapter 3, an additional analysis was conducted assuming a modulus of rupture of zero throughout the beam. The predicted shear strength profile for this reduced modulus of rupture is illustrated in Figure F.4(b).

The predicted shear strength profiles for U-50 (Figure F.4) illustrate that the primary shear crack should form inside the debonded region. In addition, Figure F.4(a) shows a web-shear failure while the analysis using a reduced modulus of rupture shown in Figure F.4(b) results in a flexure-shear failure.

F.2.2 U-Beam with Stirrups throughout Span Length (U-50- V_s)

This beam was designed to fail in flexure-shear outside the debonded region. The identifier for this specimen is U-50- V_s , where the “50” specifies the percentage of strand debonded, and the “U” indicates that the beam is a U-beam. The suffix, “ V_s ” denotes that transverse reinforcement was added in the debonded region. The only design differences between this specimen and the U-50 specimen discussed in Section F.2.1 is the transverse reinforcement. All other variables were held constant in an effort to allow for comparison between the two beams. Design details for U-50- V_s are shown in Figure F.5.

F.2.2.1 Transverse Reinforcement

The transverse reinforcement was selected in an effort to shift the primary shear crack outside the debonded region. Therefore,

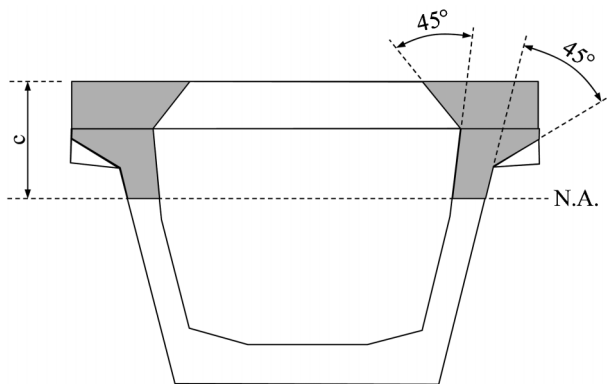


Figure F.3 Effective shear area of U-beam.

#3 U-shaped stirrups were spaced at 12 in. throughout the span length. Enough reinforcement was provided to increase the shear capacity, but to ensure a shear failure. The transverse reinforcement was limited to still produce a shear failure. A shear failure was desirable to allow for evaluation of the shear strength provided by the transverse reinforcement.

F.2.2.2 Predicted Shear Strength

The following predicted shear strength profiles (Figure F.6) were created in the same manner and with the same notation as the shear strength profiles illustrated in Figure F.4. These analyses also assume the design concrete strength of 7,500 psi.

The predicted shear strength profile shown in Figure F.6(a) used the original modulus of rupture assumption of $7.5\sqrt{f'_c}$. However, an additional analysis was conducted assuming a modulus of rupture of zero throughout the beam. The predicted shear strength profile for this reduced modulus of rupture is illustrated in Figure F.6(b).

The predicted shear strength profile shown in Figure F.6(a) assuming the upper bound modulus of rupture for U-50- V_s illustrates that the primary shear crack should form outside the debonded region. However, as illustrated in the shear strength profile in Figure F.6(b), when the modulus of rupture is assumed to be zero, the primary shear crack forms inside (at the end of) the debonded region. Both profiles show that a flexure-shear failure mode (primary shear crack) is expected.

F.2.3 Summary of Predictions

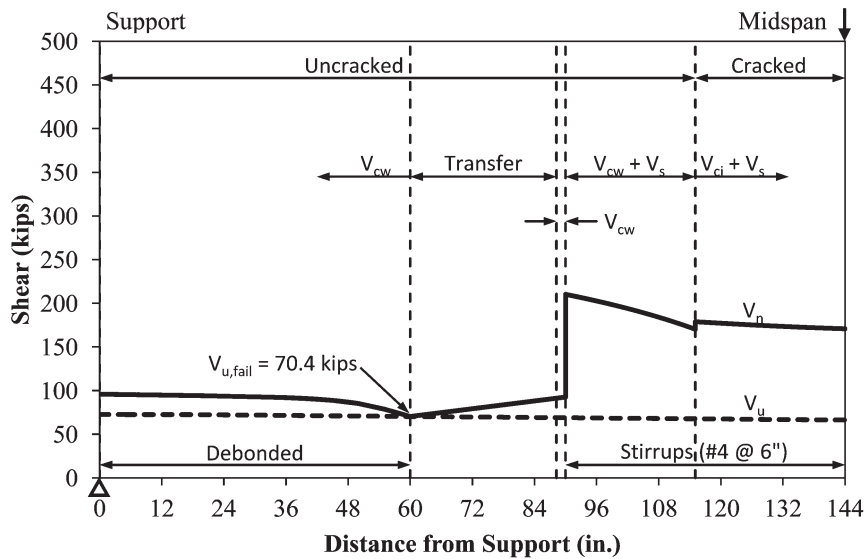
The capacities predicted by the shear model, V_{pred} , are provided in Table F.2. The predicted shear capacities consist of the shear due to applied load, $V_{applied}$, and the shear due to self-weight, $V_{self-weight}$, at each failure location. A uniform load of 589 lb/ft was used to calculate $V_{self-weight}$. It is important to note that the small increase in the predicted shear capacity of U-50- V_s compared to U-50 at a modulus of $7.5\sqrt{f'_c}$ corresponds to an increased load capacity, $P_{applied}$, of 15.5 kips. The difference in predicted failure locations provide the explanation for the difference between the shear and load capacities. Shear from self-weight in U-50 is not present in the U-50- V_s prediction because failure is calculated to occur at midspan while the shear from self-weight in U-50- V_s is 4.1 kips calculated 5 ft from the support. In addition, when assuming a modulus of zero, the difference in shear capacity between the specimens is more evident. Furthermore, both modulus of rupture assumptions result in increased shear strength predictions for U-50- V_s compared to U-50; therefore the specimen designs were expected to allow evaluation of the stirrup contribution to shear strength.

F.3 MATERIALS

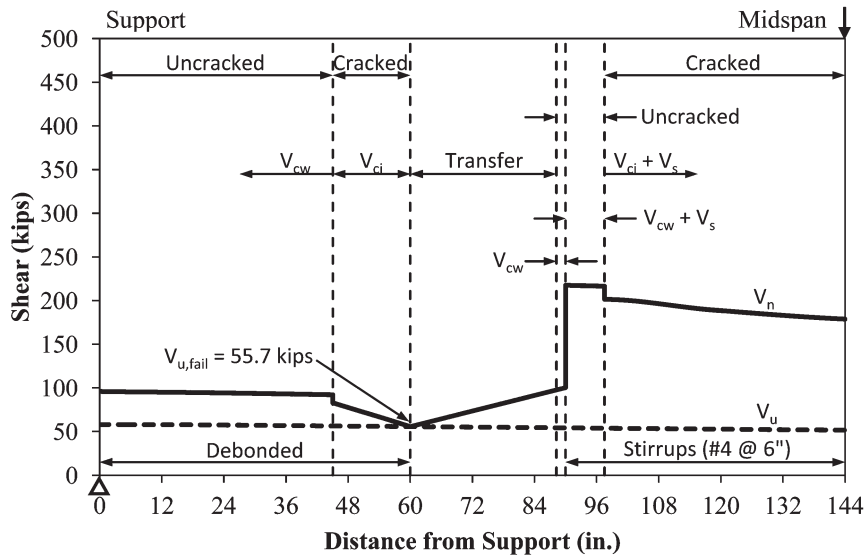
F.3.1 Concrete

The concrete was an SCC mix designed by Irving Materials, Inc. (IMI) based on the constructability of the U-beams. The selected mix consisted of cement and fly ash with a full range water reducing admixture and a viscosity modifying admixture as provided in Table F.3. It should be noted that the selected mix contained 3/8 in. maximum aggregate size (3/8 in. crushed stone). This aggregate was selected to allow concrete placement in the thin webs, as well as, to provide half-scale aggregate for the half-scale beams. Before the mix was confirmed, however, a trial batch was cast to compare the compressive and tensile strengths to a conventional mix (such as that used for the specimens in Chapter 3). The batch weights for the trial batch are included in Table F.4. The compressive and tensile strength history for the trial batch is shown in Figure F.7 and Figure F.8, respectively.

After determining the compressive and tensile strength history for the trial batch, it was decided to construct the U-beams with the same mix. It should be noted that similar ratios of split tensile strength to compressive strength were observed in the trial batch



(a) Upper Bound ($f_{r,debond} = 7.5\sqrt{f'_c}$; $f_{r,bond} = 7.5\sqrt{f'_c}$)



(b) Lower Bound ($f_{r,debond} = 0\sqrt{f'_c}$; $f_{r,bond} = 0\sqrt{f'_c}$)

Figure F.4 Predicted shear strength profiles for U-50.

and the mixes used for the specimens discussed in Chapter 3. A slump flow range of 24–30 in. was requested for the cast and was measured upon arrival at the laboratory. The slump flow was initially measured as 15 in. Therefore, it was decided to add five gallons of water to the truck onsite to increase the flowability of the mix. This resulted in a slump flow of 19 in. (Figure F.9), and it was decided to proceed with the casting operations based on the improved flowability. It is important to note, however, that supplementary full range water reducing admixture was added to the truck after the first beam (U-50-V_s) was cast. This water reducer was added to further improve flowability before casting the second beam (U-50). The slump flow increased to 26 in. after the supplementary water reducer was added (Figure F.10). The final batch weights, including the additional water and water reducer added onsite, and slump flow are included in Table F.5.

The same SCC mix was also used to cast the deck on each U-beam (Table F.6).

Standard 6 × 12 in. cylinders were cast in plastic molds and cured in the same manner as the test specimens. After the concrete surface hardened, the specimens and cylinders were covered with wet burlap and plastic to prevent moisture loss. Curing of the cylinders was discontinued at the same time that curing of the specimens was discontinued. Additionally, the cylinder molds were removed when the specimen forms were removed. The removal of forms and cylinder molds coincided with the discontinuation of wet curing for all three casts (trial batch, U-beams, and decks).

Compressive strength was monitored by testing three cylinders at regular intervals up to 28 days including at the time of release and test day in accordance with ASTM C39 (2012). In addition, split tension cylinders were tested in accordance with ASTM C496

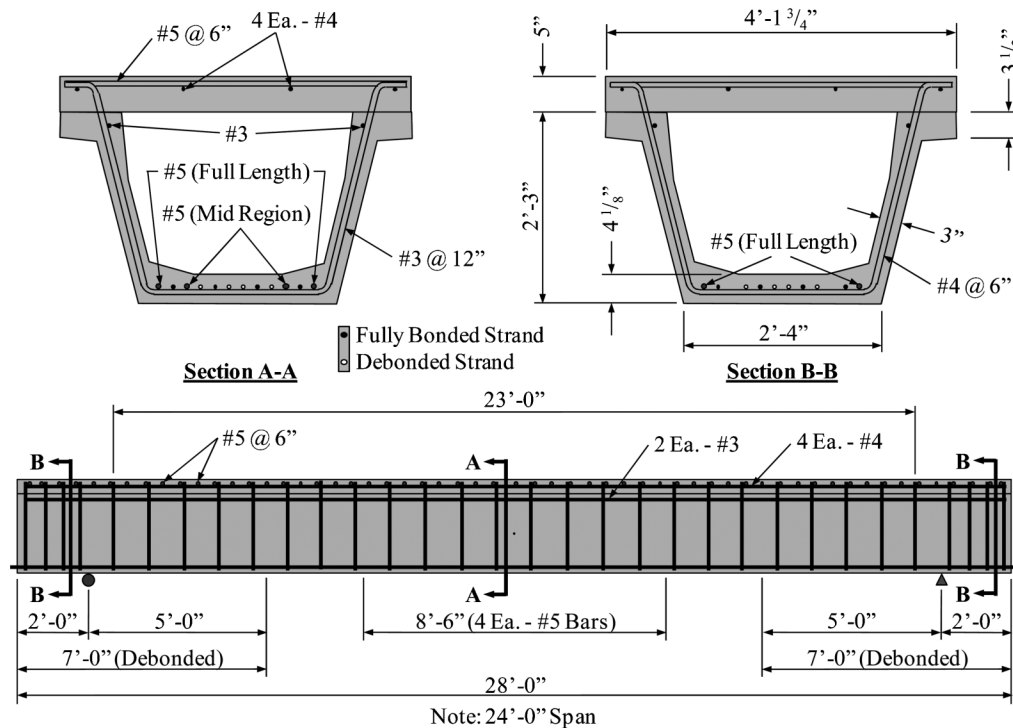


Figure F.5 U-50- V_s specimen.

(2011) at the time of release, 28 days, and test day. Additional cylinders were cast after the supplementary water reducer was added immediately before casting the second U-beam (U-50). Enough cylinders were added to determine the compressive strength at 28 days and compressive and tensile strengths on test day for U-50 to determine if any difference in strength occurred due to the addition of the water reducer.

A loading rate of 50,000 lb per minute was used during the compressive cylinder tests along with 70 durometer elastomeric pads. A loading rate of 15,000 lb per minute was used for the split tension cylinder tests. The compressive and split tensile strength growth curves for each cast are shown in Figure F.11 and Figure F.12, respectively. The trial batch results are also shown for comparative purposes. As shown, similar strengths were achieved in the actual cast. A summary of the compressive strength results on the test day for each specimen is provided in Table F.7. As shown, similar concrete strengths for U-50 and U-50- V_s were achieved even though the mix for U-50 contains slightly more water reducer. It should be noted, however, that a higher strength at 28 days was observed in U-50 (8,980 psi) compared to U-50- V_s (8,270 psi). Furthermore, the complete set of compressive and split tensile strength data is provided in Appendix F-1. It should be noted that while there was no release strength needed for the deck concrete, cylinders at a similar time (five days) were tested for comparison purposes.

F.3.2 Prestressing Steel

The prestressing steel used throughout the laboratory investigation was from the same strand pack that was donated by American Spring Wire Corporation which was produced by RettCo Steel, LLC in Newnan, Georgia. This strand is Grade 270, uncoated, seven wire, low-relaxation strand with a nominal diameter of 1/2 in. The nominal cross-sectional area of the strand is 0.153 in.² The results of tensile tests performed on this strand can be found in Section D.4.2.

F.3.3 Mild Steel Longitudinal Reinforcement

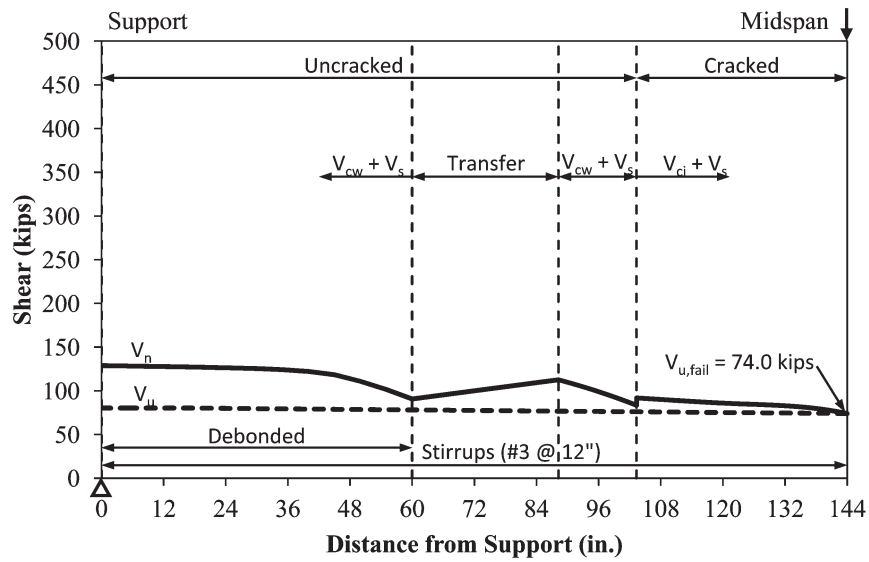
The longitudinal reinforcement used in the U-beam testing program consisted of #5 Grade 60 mild steel deformed bars. These bars were manufactured by Nucor Steel and shipped from Indiana Steel Fabricating, Inc. located in Indianapolis, Indiana to the Bowen Laboratory. The yield stress, ultimate stress, and maximum strain for the #5 bars used in both specimens are provided in Table F.8. The bars were tested in conformance with ASTM A370. The yield stress presented is the stress corresponding to a strain of 0.35% (ACI 318-11 Section 3.5.3.2).

The stress-strain curves for each #5 sample are illustrated in Figure F.13. The stress was calculated from the load provided by the testing machine, while the entire strain domain was measured using the same break-away extensometer as discussed in Section D.4.3. The elastic limit for the three samples is approximately 55 ksi. Figure F.14 shows a typical failure of the #5 test samples. The break-away extensometer is also shown.

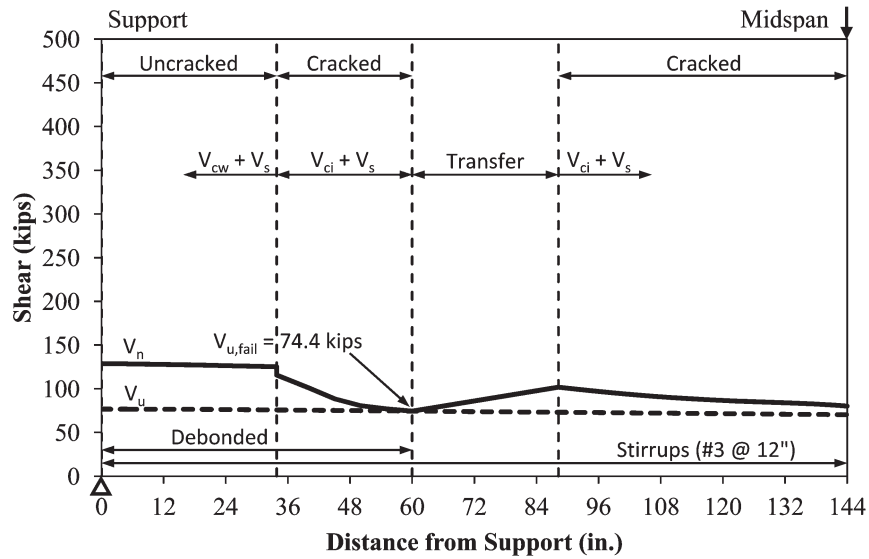
Grade 60 mild steel longitudinal reinforcement was located in the top of each specimen. Two #3 bars per beam along the entire length were provided for ease of constructing the rebar cages. Tensile tests of these bars were not performed because they were placed near the top of the section where compressive stresses (and low tensile stresses) were expected; therefore, their post-yield behavior does not influence the testing program. Deck reinforcement (Grade 60) was not tested for the same reason. It should be noted, however, that the mill certification for the #4 longitudinal deck reinforcement provides a 0.2% offset yield stress of 68.1 ksi and an ultimate stress of 102.3 ksi.

F.3.4 Mild Steel Transverse Reinforcement

The transverse reinforcement used throughout this testing program consisted of Grade 60 mild steel deformed bars. These stirrups were manufactured by Nucor Steel and fabricated by Indiana Steel Fabricating, Inc. The yield stress, ultimate stress,



(a) Upper Bound ($f_{r,debond} = 7.5\sqrt{f'_c}$; $f_{r,bond} = 7.5\sqrt{f'_c}$)



(b) Lower Bound ($f_{r,debond} = 0\sqrt{f'_c}$; $f_{r,bond} = 0\sqrt{f'_c}$)

Figure F.6 Predicted shear strength profiles for U-50- V_s .

TABLE F.2
Predictions

Specimen ID	Modulus of Rupture	P_{applied} (kip)	V_{applied} (kip)	$V_{\text{self-weight}}$ (kip)	V_{pred} (kip)	Failure Mode	Failure Location
U-50	$7.5\sqrt{f'_c}$	132.5	66.3	4.1	70.4	V_{cw}	In
	$0\sqrt{f'_c}$	103.1	51.6	4.1	55.7	V_{ci}	In
U-50- V_s	$7.5\sqrt{f'_c}$	148.0	74.0	0.0	74.0	V_{ci}	Out
	$0\sqrt{f'_c}$	140.6	70.3	4.1	74.4	V_{ci}	In

TABLE F.3
Concrete Mix Design Weights per Cubic Yard

Material	Design Weights Per Cubic Yard
Type I Cement (lbs)	600
Fly Ash (lbs)	150
3/8" Coarse Aggregate (lbs)	1450
Fine Aggregate (lbs)	1400
Water (lbs)	270
Air (oz)	0.75
BASF Glenium 3030 NS Full Range Water Reducer (oz)	90
BASF Rheomac VMA 362 Viscosity Modifying Admixture (oz)	37.5

TABLE F.4
Final Concrete Mix Batch Weights per Cubic Yard for Trial Batch

Material	Batch Weights Per Cubic Yard
Type I Cement (lbs)	600
Fly Ash (lbs)	150
3/8" Coarse Aggregate (lbs)	1450
Fine Aggregate (lbs)	1400
Water (lbs)	270
Air (oz)	0.75
BASF Glenium 3030 NS Full Range Water Reducer (oz)	90
BASF Rheomac VMA 362 Viscosity Modifying Admixture (oz)	37.5

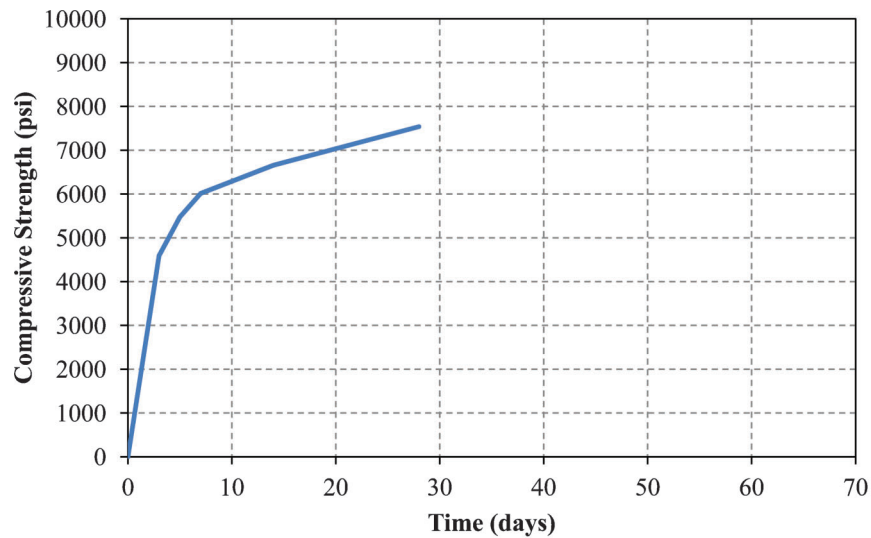


Figure F.7 Compressive strength of trial batch.

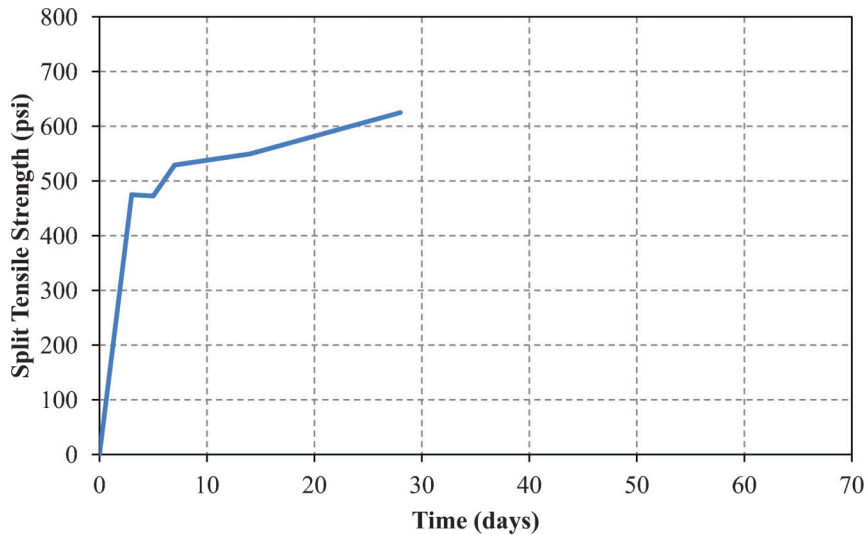


Figure F.8 Split tensile strength for trial batch.

and maximum strain for the #3 stirrups used in U-50-V_s are provided in Table F.9. The samples were tested in conformance with ASTM A370, and the yield stress presented is the stress corresponding to a strain of 0.35%.

The stress-strain curves for the #3 samples are illustrated in Figure F.15. The stress was calculated from the load provided by the testing machine, while the entire strain domain was measured using the break-away extensometer as previously discussed.

Both specimens used #4 stirrups at the ends to resist bursting stresses. In addition, the middle region of U-50 was reinforced with #4 stirrups. The yield stress, ultimate stress, and maximum strain for the #4 stirrups are provided in Table F.10. The samples were tested in conformance with ASTM A370, and the yield stress presented is the stress corresponding to a strain of 0.35%.

The stress-strain curves for the #4 samples are illustrated in Figure F.16. The stress was calculated from the load provided by the testing machine, while the entire strain domain was measured using the break-away extensometer as previously discussed. Figure F.17 shows a typical failure of the transverse reinforcement samples. The break-away extensometer is also shown.

F.4 SPECIMEN CONSTRUCTION

The pretensioned beams were constructed at the Bowen Laboratory in two casts. The U-beams were constructed in the first cast and the decks were cast on top of the U-beams after transfer. The beams were constructed in the same casting bed

and with the same pretensioning abutments as discussed in Section 2.4.

F.4.1 Pretensioning

Jacking of the prestressing strands was carried out in two phases. The first phase included pulling the strands to 2 kips which kept the strands taught allowing strain gages to be installed. After strain gage installation, the second phase began. In this phase, the stressing crew tensioned each strand to the full jacking stress. The release stress was targeted at 75% (202.5 ksi) of the ultimate nominal strength of the strands (270 ksi). This corresponds to a release force of 31 kips per strand. Due to seating losses, a jacking force of 32 kips ($0.77f_{pu}$) was initially selected for the first strand. This initial jacking force was selected to match the jacking force used in the debonding effectiveness prisms (Section 2.4.2) because the same release stress ($0.75f_{pu}$) was desired. The jacking force was checked by monitoring the strain gage and load cell measurements during stressing operations through the following procedure.

While stressing the first strand, the strain measurement at 31 kips (desired force at release) was noted. The jacking force was subsequently increased to 32 kips to account for seating losses as previously mentioned. The jacking force was then slowly released, allowing the strand to slowly and completely seat into the chuck. As the strand was seating into the chuck, the strain measurements continued to drop until the jacking force was zero. At this point,



Figure F.9 Slump flow for U-50-V_s.



Figure F.10 Slump flow for U-50.

TABLE F.5
Final Concrete Mix Batch Weights per Cubic Yard for U-Beams

Material	Batch Weights Per Cubic Yard	
	U-50-V _s	U-50
Type I Cement (lbs)	600	600
Fly Ash (lbs)	149	149
3/8" Coarse Aggregate (lbs)	1457	1457
Fine Aggregate (lbs)	1453	1453
Water (lbs)	187	187
Air (oz)	0.83	0.83
BASF Glenium 3030 NS Full Range Water Reducer (oz)	90	105*
BASF Rheomac VMA 362 Viscosity Modifying Admixture (oz)	37.5	37.5
Slump Flow (in.)	19	26

*This value was estimated by the IMI quality control manager.

TABLE F.6
Final Concrete Mix Batch Weights per Cubic Yard for U-Beam Decks

Material	Batch Weights Per Cubic Yard	
	U-50-V _s	U-50
Type I Cement (lbs)	598	598
Fly Ash (lbs)	146	146
3/8" Coarse Aggregate (lbs)	1449	1449
Fine Aggregate (lbs)	1449	1449
Water (lbs)	197	197
Air (oz)	0.78	0.78
BASF Glenium 3030 NS Full Range Water Reducer (oz)	90	90
BASF Rheomac VMA 362 Viscosity Modifying Admixture (oz)	37.5	37.5
Slump Flow (in.)	20	20

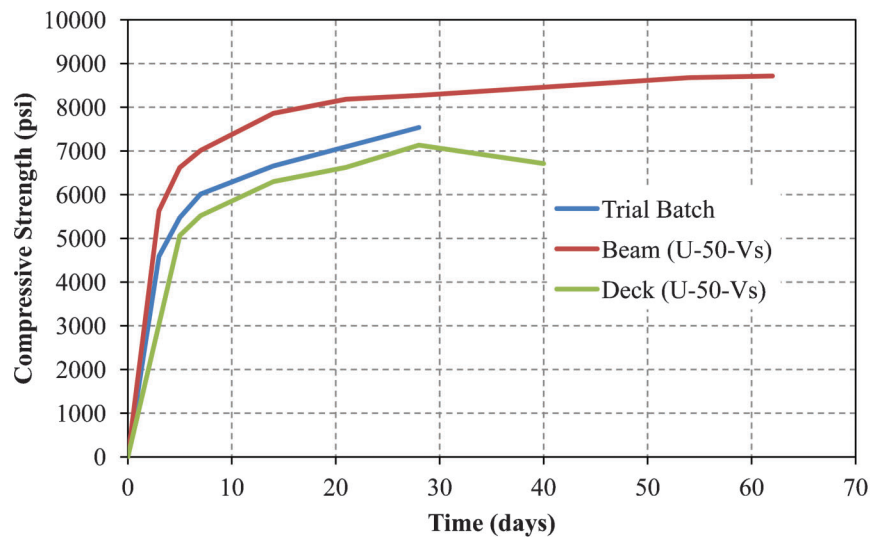


Figure F.11 Compressive strength.

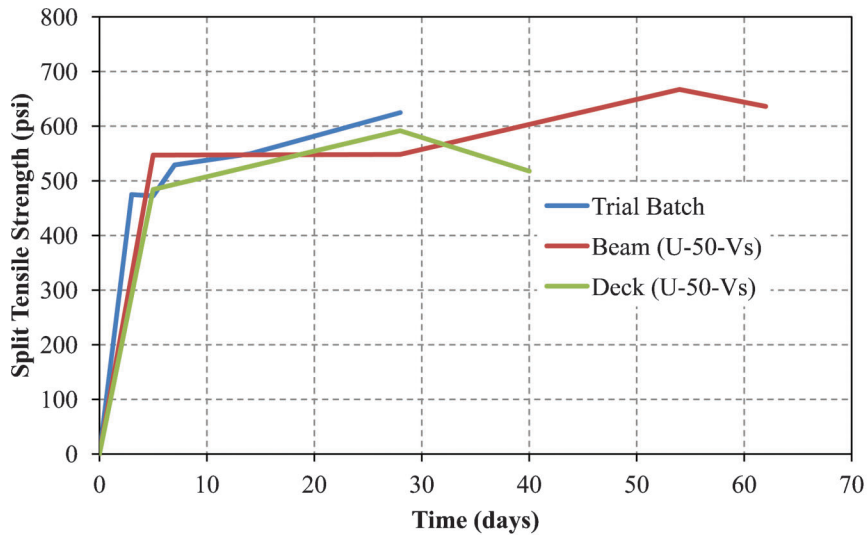


Figure F.12 Split tensile strength.

the final strain measurements were compared to the strains noted at 31 kips. The strains were in close agreement (within 3%); therefore, the force in the strand after seating losses was approximately 31 kips. The remaining strands were tensioned to 32 kips as well. It should be noted that dial gages (stationed at both pretensioning abutments) recorded a maximum total movement (for all stressing operations) of 0.006 in. This resulted in a negligible loss of approximately 30 lbs per strand.

The jacking assembly used for these pretensioned beams was the same used in the debonding effectiveness evaluation (Section 2.4.2) and in the test program discussed in Chapter 3 with one modification. One additional strand was added on either side of the abutments to provide higher prestress forces. To allow placement of two additional strands, an outrigger beam assembly was installed on the backs of both pretensioning abutments. The outrigger assembly consisted of adjacent C3 × 5 (A36) channels with a 1/2 in. spacer plate in between the channels to provide clearance for the strands to pass through as illustrated in Figure F.18. Displacements at the ends of the outrigger beams were monitored by dial gages. The inner strands were tensioned first to lock the outrigger assembly in place before the two outside strands were stressed.

F.4.2 Beam Formwork

The beam formwork was constructed from 3/4 in. plywood, 2 × 4 s, 4 × 4 s, 4 × 6 s, and EPS (expanded polystyrene) foam. All exterior surfaces of the U-beams were formed with wood while the interior surfaces were formed with foam (Figure F.19). The foam was divided into four segments per beam, and the length of each segment matched the adjacent exterior formwork panels. As shown in Figure F.20, a 6 in. deep by 12 in. wide cut was made in the bottom of the foam segments at the beam ends to create a concrete diaphragm that would be positioned directly over each support during testing. The diaphragms were designed to transfer the forces between the bottom flange and webs during testing

while still allowing access inside the U-beams to remove the deck forms.

The exterior side forms were constructed with 3/4 in. plywood panels screwed to 2 × 4 ladder frames consisting of vertical studs, a top plate, and a base board as shown in Figure F.21. Side forms were attached to the base with lag screws to restrict form movement at the base. Lateral pressures during casting were resisted with a wale (on each side of the beam) made of adjacent 2 × 4 s. These are the same wales that were used to cast the specimens discussed in Chapter 3. The lateral pressure is resisted by the wales which are restrained by 4 × 4 columns and 4 × 4 diagonals. In addition, the formwork was laterally supported by 4 × 6 cross beams on top. The cross beams were attached to the 4 × 4 columns with lag screws. These joints were stiffened with 4 × 4 diagonals which were connected to the cross beams and columns with lag screws. The columns, cross beams, and diagonals created structural frames which connected the formwork together.

Vertical plywood side panels were attached to the plywood top plates to form the vertical surface of the top flanges (Figure F.21). These vertical side panels were stiffened with 2 × 4 headers attached to the adjacent 4 × 4 columns.

Each foam segment was positioned inside the exterior formwork and stirrups with a crane, and then 4 × 6 cross beams were inserted between each set of 4 × 4 columns (Figure F.22). Next, the 4 × 6 cross beams were connected to the 4 × 6 stringers on top of the foam segments. The 4 × 6 cross beams were then connected to the 4 × 4 columns once the foam was at the correct elevation. The foam was not supported from the bottom or sides to prevent any additional reinforcement or stress concentrations from steel bolsters or chairs that were not accounted for in design. Therefore, the foam segments were completely suspended from the 4 × 6 cross beams. The foam placement process was repeated for each segment.

The formwork design needed to account for buoyancy forces which result from the volume of concrete displaced by the foam. It

TABLE F.7
Concrete Strengths on Test Day

Cast	Specimen ID	Age (days)	f'_c (psi)	f_{cr} (psi)
Beams	U-50	54	9,020	660
	U-50-V _s	62	8,720	640
Decks	U-50	32	6,890	560
	U-50-V _s	40	6,710	520

TABLE F.8
Longitudinal Reinforcement Tensile Properties

Sample	Yield Stress	Ultimate Stress	Maximum Strain
	(ksi)	(ksi)	
1	62.8	99.5	14.5%
2	63.5	99.7	11.9%
3	63.5	99.6	10.8%
Average:	63.3	99.6	12.4%

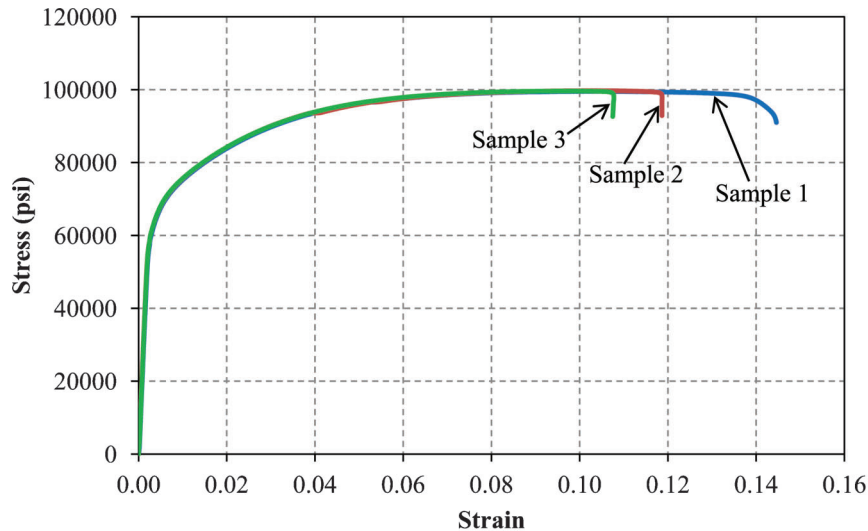


Figure F.13 Stress-strain response of longitudinal reinforcement.

is worth noting that the foam segments were individually wrapped with plastic to prevent water absorption and to aid in foam removal. Buoyant forces were designed to be resisted by the same lateral force resisting system (wood frames) with a few additional components. Two lines of 4 × 6 stringers were used to transfer load from the foam to the frames as shown in Figure F.23. To transfer this load uniformly, however, 2 × 4 ladder form panels were connected to the foam (Figure F.24). A hardboard panel (1/8 in. thick) was first glued down to the top of each foam segment with Gorilla Glue to allow the 2 × 4 form panels to be connected to the foam segments with screws. The form panels were connected to the foam segments, and the 4 × 6 stringers were connected to the form panels with 2 × 4 shear tabs. The cross beams were connected to the 4 × 6 stringers to complete the formwork system and reduce the likelihood of concrete shifting the foam laterally during

concrete placement operations. The columns and lower diagonals were connected to the formwork base with lag screws to prevent the foam from uplifting during casting. It should be noted that a frame was placed at each splice because the interior foam splices and exterior wood form splices were in the same locations. The formwork was discontinued in between the two specimens permitting strand cutting at transfer.

The stirrup layout, before exterior side forms or interior foam segments were installed, is illustrated in Figure F.25. It should be noted that no transverse reinforcement was placed in the end regions of U-50. End zone stirrups were provided, however, to guard against splitting cracks. These end zone stirrups are within 2 ft of the beam ends which is outside of the shear span.

F.4.3 Casting of Beams

Both beams were cast with the same SCC mix from the same truck. Due to the casting bed location on the laboratory floor, a one cubic yard concrete bucket was used to transport the concrete from the truck to the specimens as shown in Figure F.26. The plan was to pour the SCC mix in one web opening allowing the mix to flow through the bottom flange and fill both webs evenly. As the concrete was being placed at the end of the first beam (U-50-V_s), however, the concrete was not filling evenly. Concrete was filling only one web, causing a pressure differential on the internal formwork (foam) which resulted in the foam shifting approximately 1/2 in. towards the unfilled web. Internal vibrators were used to help move the SCC mix from one web to the other. As soon as the first web was filled to the point where the bottom flange was completely full, concrete was placed in the other web. This placement procedure prevented air from becoming trapped in the bottom flange. The same pattern was repeated in approximately six locations along the length of the first beam. After vibrating, the top surface was screeded to the proper level and then roughened with hand rakes while the mix was still plastic.



Figure F.14 Longitudinal reinforcement test sample.

TABLE F.9
#3 Stirrup Tensile Properties

Sample	Yield Stress (ksi)	Max. Stress (ksi)	Max. Strain
1	74.2	109.1	12.7%
2	73.9	108.4	11.6%
3	74.4	108.4	12.7%
Average:	74.2	108.6	12.3%

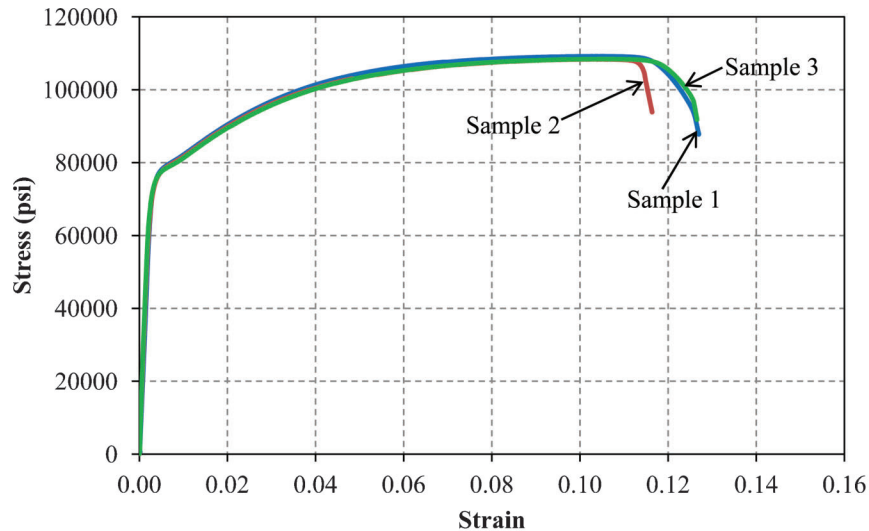


Figure F.15 Stress-strain response of transverse reinforcement for #3 stirrups.

Supplementary water reducer was added to increase the flowability of the mix before the second beam (U-50) was cast. The additional water reducer increased the slump flow from 19 in. for U-50-V_s to 26 in. for U-50, thereby greatly improving placement operations. The increased flowability of the mix allowed both webs to be filled relatively evenly while placing concrete in one web. In addition, no vibration was needed for the second beam. Concrete was placed from end to end, pouring concrete in approximately three locations. Placing concrete from one end to the other prevented air entrapment along the beam length. After the top surface was screeded to the proper level the concrete surface was roughened with hand rakes while the mix was still plastic. The top flanges of both beams were roughened with score lines raked perpendicular to the beam length to promote composite action with the deck.

Standard 6 × 12 in. cylinders were cast alongside the specimens. The cylinders were consolidated using a small internal vibrator according to ASTM C192. The cylinders were wet cured in the same manner and for the same duration as the specimens.

The specimens were wet cured for five days. Wet curing was accomplished by covering the surface with wet burlap and plastic to prevent moisture loss. In addition, the burlap was re-wetted every 12–24 hours to maintain curing. After wet curing, the strands were cut, and then the forms and plastic cylinder molds were removed. The strands were cut before form removal due to the beam geometry and exterior form configuration. Form removal required moving the beams from the casting bed and onto cribbing. The beams were moved to a different location of the laboratory to provide additional space for form removal. The foam segments were also removed resulting in the fully exposed U-beams as shown in Figure F.27.

F.4.4 Strand Release

The prestressing strands were released after curing was discontinued. Each strand was gradually released by heating

TABLE F.10
#4 Stirrup Tensile Properties

Sample	Yield Stress (ksi)	Max. Stress (ksi)	Max. Strain
1	70.5	105.9	15.6%
2	71.6	105.9	13.6%
3	70.1	105.4	13.3%
Average:	70.7	105.7	14.2%

approximately a 1 ft length back and forth with a torch until all of the seven wires were cut. The individual wires typically broke two or three at a time, and the specimens slid on the smooth base after each of the strands were cut. The strands were cut outside to inside to ensure that the outrigger assembly remained stable. After all eight strands were cut at the live end (jacking end), they were cut at the other abutment (dead end) and finally in between the specimens in the casting line.

F.4.5 Deck Formwork

The deck formwork was also constructed from 3/4 in. plywood, 2 × 4 s, 4 × 4 s, and 4 × 6 s. Much of the same formwork from the beam cast was reused for the deck formwork. The 2 × 4 form panels (with the attached 4 × 6 stringers) that were connected to the foam segments were designed as deck formwork as well. The side panels used to form the vertical face of the top flanges of the U-beams were reused to form the vertical face of the decks.

The deck formwork was designed to be removable after casting to ensure that the formwork would not influence the structural behavior of the composite U-beams during testing. Due to the tight spaces that result from casting a deck on top of the U-beams, it was clear that removing forms using the traditional method (manually removing shoring and form panels) would be extremely difficult and dangerous. An alternative formwork and shoring removal technique was designed to simplify and expedite the procedure. The objective was to eliminate all connections from inside the U-beam that require physical attention to remove the forms. A solution was developed which used isolated bearing connections between the deck forms and shoring. Each connection was designed to be isolated with 1/2 in. diameter aluminum rods to allow convenient shoring removal after casting (Figure F.28). To remove the shoring after the deck was cast a cable system was installed that connected each shore line in series. A cable was threaded through both ends of each shoring cross beam with a cable clamp attached behind each cross beam. The design called for complete shoring removal by removing one end wall after casting and then simply pulling the cables to pull the shoring from underneath the deck forms resulting in simplified formwork removal.

The deck forms (with attached 4 × 6 stringers) are supported by the shoring system shown in Figure F.29. A three piece form system was selected to allow form removal. The U-beam section narrows towards the bottom; therefore, a one piece system would become wedged if attempted to be removed. A 1 in. strip of plywood to fill the gap shown in Figure F.29 acted somewhat as a keystone in that once removed the main two formwork panels could be removed.

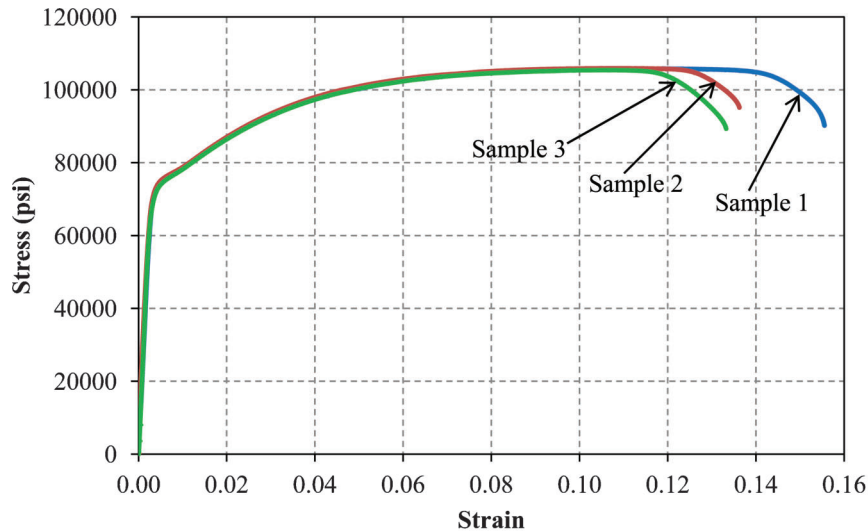


Figure F.16 Stress-strain response of transverse reinforcement for #4 stirrups.

The outer edges of the formwork rest on the sloped inner face of the U-beams. The inner edges of the formwork are supported by a 4 × 4 beam which is supported by short 4 × 4 columns at each shore line. The 4 × 6 stringers rest on 3 × 3 × 1/4 in. steel plates which are supported by two 1/2 in. aluminum rods. The aluminum rods are supported by a flat 4 × 6 cross beam with a hole drilled on either side to allow the cable shown in Figure F.29 to pass through. Below the cross beam is another set of two plates and two aluminum rods. The lower aluminum rods are supported by 3/4 in. high density overlay (HDO) plywood which is connected to two short 4 × 4 columns resting on the flat bottom of the inner surface of the U-beam. This shoring system was successfully proof tested in a compression testing machine at a load level that was three times what was expected during casting. This test also

proved that the cross beam could be removed manually at a load exceeding the tributary deck weight.

As previously discussed, the same side panels (with 2 × 4 headers) that were used to form the vertical face of the U-beam flanges were used to form the vertical face of the decks. To resist the lateral forces on these side panels, the same wood frames from the beam cast were used. The frames, as illustrated in Figure F.30, allow the forces to be transferred down to the base formwork. It should be noted that the lower diagonals were not used for the casting of the decks because the lateral forces were not expected to be nearly as high as in the beam cast. Furthermore, the same end panels were used and connected to the side panels to create a uniform top of deck elevation. The end panels also restrained the lower deck forms from rolling and shifting on the aluminum rods during casting. The end panels, in combination with the inner surface of the U-beams, effectively trapped the lower deck formwork in place during casting.

The deck reinforcement for specimen U-50-V_s is shown in Figure F.31. It is important to note, however, that the deck reinforcement was identical in both specimens.



Figure F.17 Transverse reinforcement test sample.

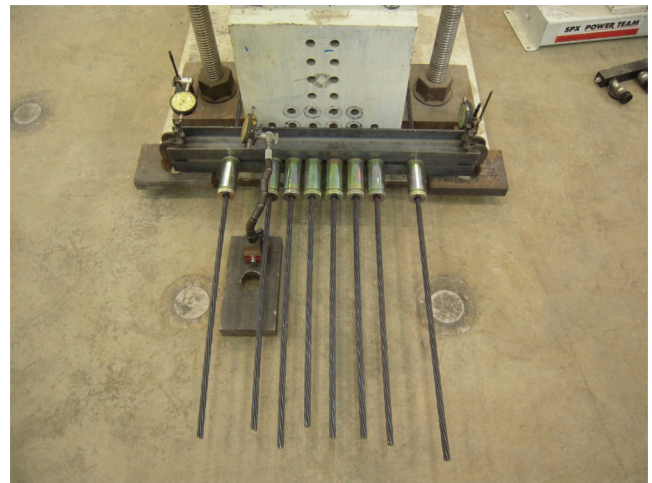


Figure F.18 Prestressing outrigger assembly.

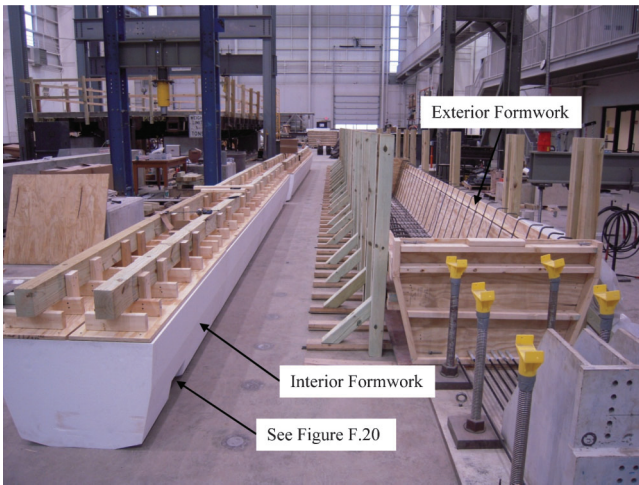


Figure F.19 Interior and exterior formwork.

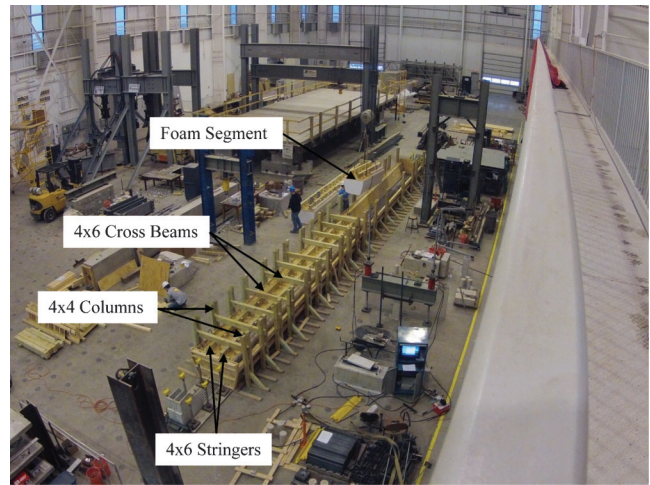


Figure F.22 Placing interior formwork.

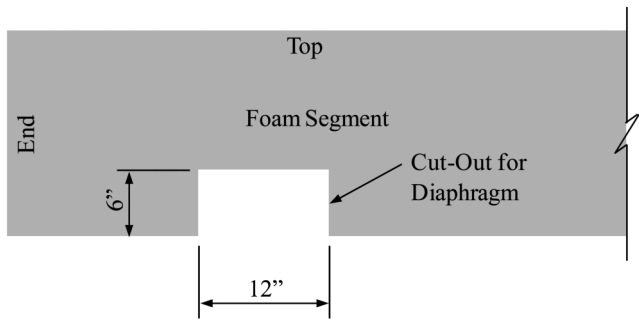


Figure F.20 Foam cut-out for concrete diaphragm.

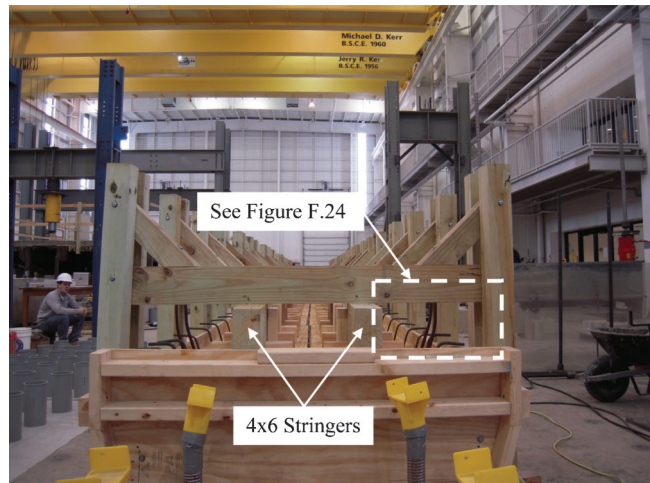


Figure F.23 Buoyancy force resisting system for interior formwork.

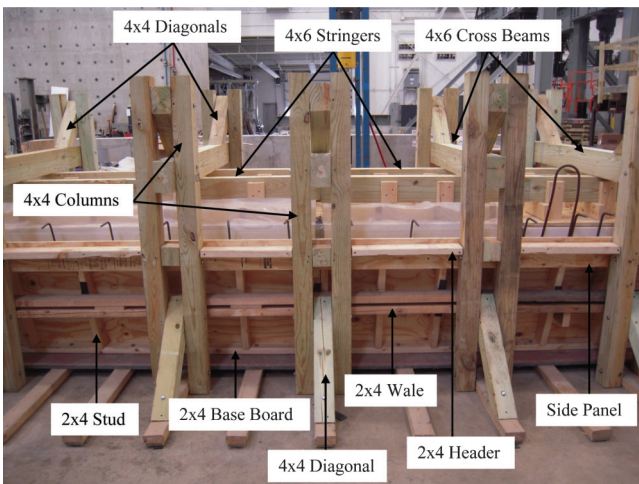


Figure F.21 Lateral force resisting system for exterior formwork.

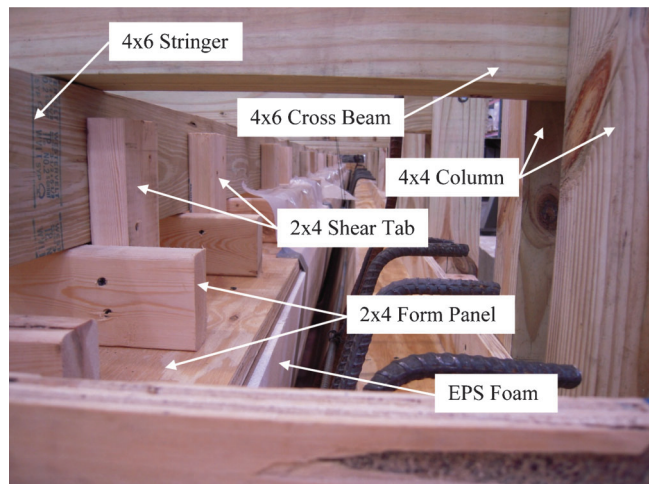


Figure F.24 Detail of buoyancy force resisting system for interior formwork.



U-50



U-50-Vs

Figure F.25 Stirrup layout.



Figure F.26 Concrete placement operations for U-beams.

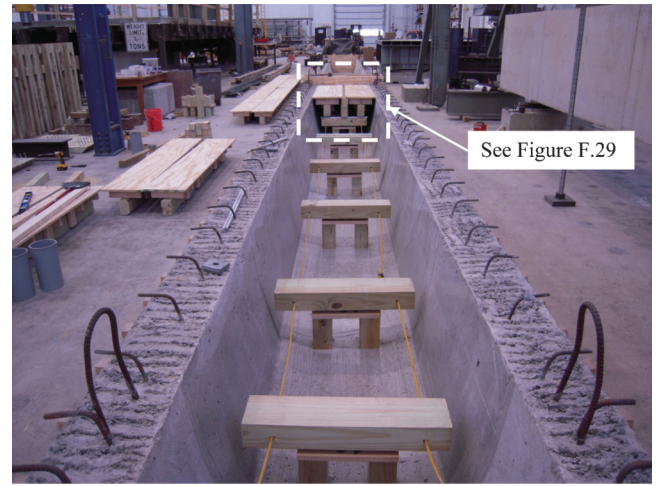


Figure F.28 Deck shoring and formwork.



Figure F.27 U-beams after transfer and form removal.

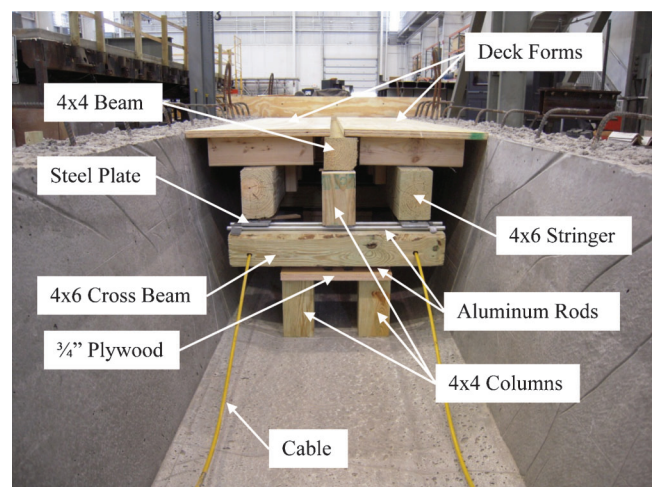


Figure F.29 Deck shoring and formwork detail.



Figure F.30 Lateral force resisting system for deck side panels.

F.4.6 Casting of Decks

Both decks were cast with the same SCC mix as the beams. Due to the casting bed location on the laboratory floor, a one cubic yard concrete bucket was used to transport the concrete from the truck to the specimens as shown in Figure F.32. The deck formwork was filled by placing concrete in approximately four locations along the length of each beam. In addition, due to the nature of the mix, vibration was not necessary. After placing the concrete, the top surface was screeded to the proper level and then finished with magnesium hand floats.

Standard 6 × 12 in. cylinders were cast alongside the specimens. The cylinders were consolidated using a small internal vibrator according to ASTM C192. The cylinders were wet cured in the same manner and for the same duration as the specimens.

The decks, like the beams, were wet cured for five days. Wet curing was accomplished by covering the surface with wet burlap and plastic to prevent moisture loss. In addition, the burlap was re-wetted every 12–24 hours to maintain curing. After wet curing, the forms and plastic cylinder molds were removed.

F.4.7 Removing Deck Shoring and Formwork

The deck shoring and formwork was removed exactly as planned. First, the wood frames and side forms were removed. Second, the end form panels were removed to provide access for



Figure F.31 Deck reinforcement.



Figure F.32 Concrete placement operations for U-beam decks.

removal of the shoring and formwork inside the U-beam (Figure F.33). The shore line shown in Figure F.33 nearest to the end of the beam was removed by hand without the cables due to its proximity to the beam end. Once the first shore line was removed, two people (one person per cable) pulled the cables which immediately pulled all of the shoring from underneath the formwork (Figure F.34). The deck forms hanging from underneath the deck were then easily removed with a pry bar. The form panels and shoring timbers were retrieved after each set of panels were removed from the deck.

F.5 TEST SETUP AND PROCEDURE

F.5.1 Test Setup

The beams were simply supported with a concentrated load applied at midspan as illustrated in Figure F.35. A structural steel test frame tensioned to the strong floor with 300 kips of pretension force was used to resist the applied load from a hydraulic ram (Figure F.35). The pin and roller supports were mounted on top of reinforced concrete pedestals to provide room for deflection and to place the beams at a convenient elevation for testing (Figure F.36). The pin and roller supports consisted of a 1 in. diameter steel rod between two 36 in. long × 6 in. wide × 0.5 in. thick steel plates. In addition, load was transferred to the specimens from a steel transfer beam to a pin system over each



Figure F.33 Deck shoring and formwork before removal.



Figure F.34 Deck shoring removal.

web to apply equal shear forces to both shear spans (Figure F.37). Each load pin consisted of a 1 in. diameter steel rod between two 12 in. long \times 6 in. wide \times 0.5 in. thick steel plates.

F.5.2 Test Procedure

The beams were statically loaded to failure using a hand-operated hydraulic pump in 10 kip increments. At the end of each load stage, the cracks were outlined, photographs were taken, and support movement measured by a dial gage was noted. Deck slip was monitored at each load step by checking a dial gage mounted at the beam-deck interface at each beam end. If first cracking was heard or observed on the force-deflection plot, loading was stopped, and an inspection was made to mark any cracks that may have formed. After failure, a crack map was recorded, photographs were taken, and concrete cylinders documenting concrete strength were tested.

F.5.3 Instrumentation

Several types of instrumentation were used in this experimental program. Strain gages were installed on the strands to monitor strains during stressing, before and after transfer, and during testing. During testing, other sensors used include LVDTs, string pots, and a load cell. LVDTs were installed to monitor strand slip at both ends of each beam. The load cell monitored the applied

force while string pots were used for beam displacements at the load point (midspan). Identical instrumentation was used for the testing of both U-beams. All data was recorded using a Micro Measurements System 7000 data acquisition system controlled by StrainSmart software.

F.5.3.1 Strain Gages

The strain gages used on the prestressing strands were the same type and installed using the same procedure as those discussed in Chapter 3.

F.5.3.2 LVDTs

Four LVDTs, each with a range of ± 1 in., were installed at each end to measure strand slip. Two of the LVDTs were installed on fully bonded strands while the other two were installed on debonded strands as shown in Figure F.38. The LVDTs on the debonded strands were expected to continually measure strand movement considering that the strands were free in the debonded regions, but the main focus was to monitor any sudden slips that may occur. The LVDTs installed on the fully bonded strands were similarly used to monitor slippage. Considering that they were fully bonded, any movement is indicative of slip.

LVDTs were also used to measure support movement. One LVDT was installed at either support to monitor vertical deformation of the concrete support relative to the laboratory strong floor. These measurements were verified through the use of a mechanical dial gage located at the pin support. Figure F.39 provides an illustration of the support deformation instrumentation setup.

F.5.3.3 String Pots

Two string pots with a range of 25 in. were installed at midspan, one on each side. Reported midspan displacement measurements are the average value of the two string pots at midspan. The string pots were mounted on a steel beam which rested on the strong floor as shown in Figure F.40. It is important to note that the support deformations were negligible; therefore, they were not used to correct the displacements at midspan.

F.5.3.4 Load Cell

A load cell with a maximum load rating of 300 kips was installed directly above the hydraulic ram at midspan to measure the applied load. The load cell is illustrated in Figure F.40.

F.6 TEST RESULTS

The test results are summarized in Table F.11. This table provides the total shear force including self-weight at the formation (and location) of the primary shear crack, V_{test} . The total shear force is comprised of the component from the applied shear, $V_{applied}$, and the shear due to self-weight, $V_{self-weight}$ at the primary shear crack location. The applied load at failure, $P_{applied}$, is also provided. The primary shear crack location is noted as “In” when inside the debonded region and “Out” when outside the debonded region.

The test results at the point of ultimate failure for each specimen are provided in Table F.12. Shears at ultimate, V_{ult} , also include the shear due to self-weight, $V_{self-weight}$ at the location of failure. It should be noted that the ultimate failure location may not correspond to the location of the primary shear crack formation listed in Table F.11.

The load-deflection behavior for both specimens is presented in Figure F.41. The point at which the primary shear crack formed in the beam is annotated by a circle. The crack patterns at the formation of the primary shear crack are shown in Figure F.42. It should be noted that the white dashed line in Figure F.42

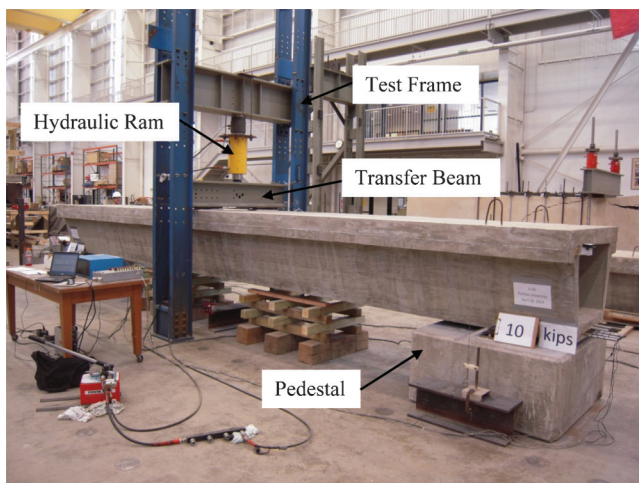


Figure F.35 Test setup.



Roller



Pin

Figure F.36 Supports.

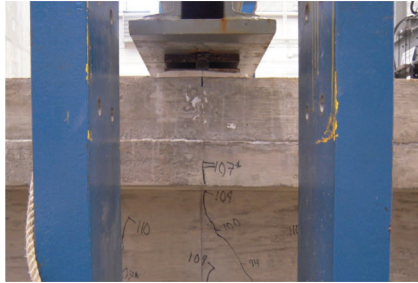


Figure F.37 Load pins.

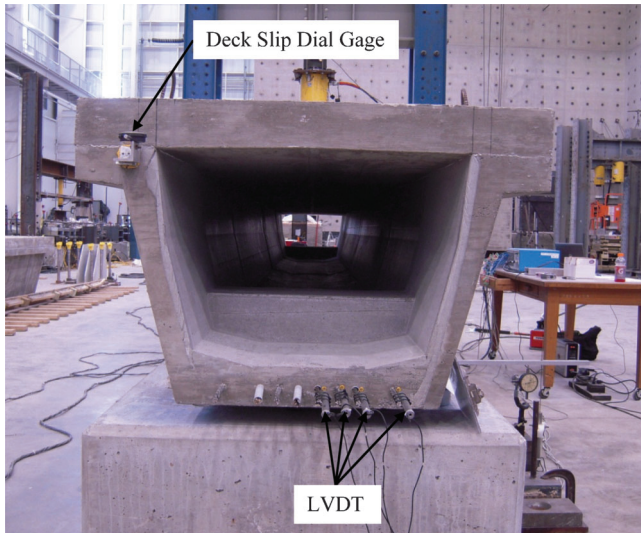


Figure F.38 Strand slip instrumentation.

represents the end of the debonded region, and the thick black outlined crack highlights the critical (primary) shear crack.

The load-deflection behavior of both specimens is characterized by three phases. In the first phase, the load-deflection relationship is linear elastic. Furthermore, the linear elastic portion of the force-deflection responses are nearly identical because the specimens were both designed with the same dimensions, concrete strength, and prestressing force. The end of the first phase of behavior is marked by the formation of a flexural crack near midspan. Flexural cracking initiated at an applied load of approximately 96 kips for U-50 and approximately 93 kips for U-50-V_s.

The second phase is characterized by nonlinear behavior after first cracking. A reduced stiffness is observed in both specimens. The crack patterns spread outward from midspan and upward from the bottom. The end of the second phase is marked by the formation of the primary shear crack. In both specimens, the primary shear cracks formed at the end of the debonded region. These cracks were followed by a reduction in capacity. Furthermore, in both specimens, the primary shear crack formed at the end of one debonded region and then, with a slight increase in load, at the end of the other debonded region. The primary shear crack formed at a slightly lower shear in U-50-V_s (56.8 kips) than U-50 (59.1 kips).

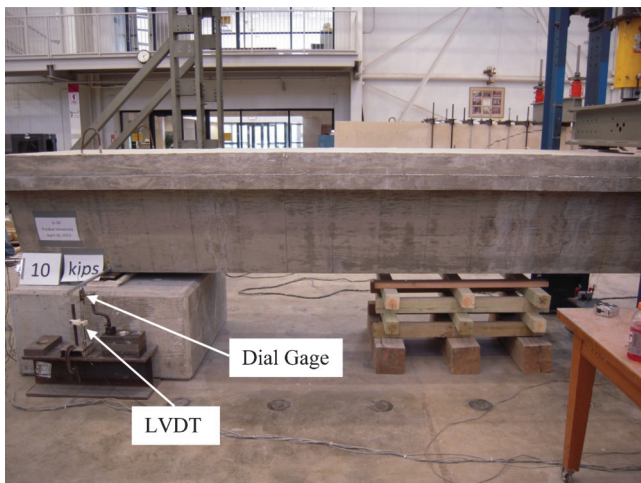


Figure F.39 Support deformation instrumentation.

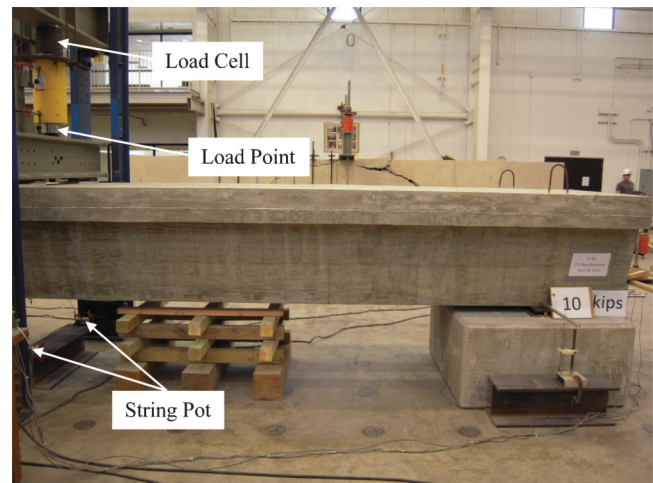


Figure F.40 Instrumentation at midspan.

TABLE F.11
Test Results at Formation of Primary Shear Crack

Specimen ID	P_{applied} (kip)	V_{applied} (kip)	$V_{\text{self-weight}}$ (kip)	V_{test} (kip)	Crack Mode	Crack Location
U-50	109.9	55.0	4.1	59.1	V_{ci}	In
U-50- V_s	105.4	52.7	4.1	56.8	V_{ci}	In

TABLE F.12
Test Results at Ultimate Failure

Specimen ID	P_{applied} (kip)	V_{applied} (kip)	$V_{\text{self-weight}}$ (kip)	V_{ult} (kip)	Failure Mode	Failure Location
U-50	120.1	60.0	4.1	64.1	V_{ci}	In
U-50- V_s	126.4	63.2	1.5	64.7	V_{ci}	Out

The third phase of the load-deflection behavior represents behavior that occurred after formation of the primary shear crack. During this stage, the load-deflection behavior is characterized by another stiffness reduction as new cracks formed and existing cracks widened and extended. For U-50, the cracking pattern generally remained the same throughout this stage. However, the cracks opened wider until the beam completely failed. U-50 failed in shear-compression with one of the webs completely falling out of the beam immediately after failure (Figure F.43). The cracks in U-50- V_s continued to open wider in the third phase. This specimen was able to endure nearly four times as much deflection as its counterpart (U-50). Complete failure was not achieved in U-50- V_s because the steel transfer beam became unstable and globally rotated due to the large beam deflections. Several extremely large cracks were visible as shown in Figure F.44.

In both specimens, the primary shear crack formed at approximately the same load (Figure F.41). However, the primary shear crack in U-50- V_s did not propagate as far as in the U-50 specimen at the time of formation and its orientation was more inclined (Figure F.42). In addition, a greater reduction in load occurred in U-50 immediately after the formation of the primary shear crack as compared with the behavior of U-50- V_s . Finally, U-50- V_s exhibited a higher overall load capacity as illustrated in Figure F.41.

F.7 ANALYSIS OF RESULTS

F.7.1 U-50

The primary shear cracks formed at the end of the debonded region in U-50 (Figure F.42). The shear cracks initiated at the ends of the debonded regions, according to the shear model described in Section D.2.3.2.1, because the neutral axis, and therefore, flexure-shear strength, is minimized at this location. These low neutral axis depths (at the ends of the debonded regions) are due to the combination of the reduced prestress force and longitudinal reinforcement stiffness in combination with relatively high flexural stresses. It should be emphasized that the predicted shear strength profile using a modulus of rupture of $7.5\sqrt{f'_c}$ shows the expected failure location to be at the end of the debonded region (Figure F.4).

The calculated shear capacities, V_n , were plotted against the total applied shear, V_u (dead plus superimposed). The applied load was analytically increased until $V_u \geq V_n$. The location at which this occurs is the location of failure (formation of primary shear crack), and is labeled " $V_{u, \text{fail}}$ " in each shear strength profile. The flexure-shear strengths are combined with the web-shear strengths for both the bonded and debonded regions to create one comprehensive shear strength profile. The same combinations of modulus of rupture values as considered in Chapter 3 were used to

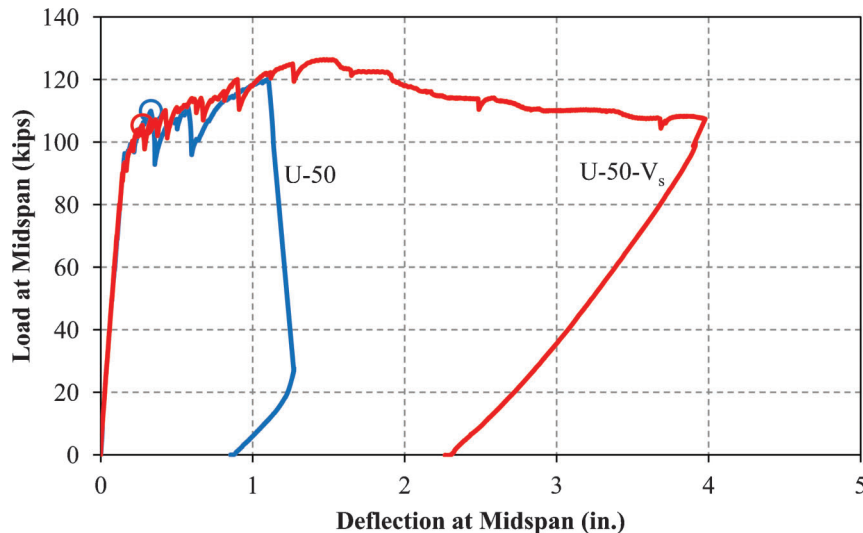


Figure F.41 Load-deflection behavior—U-beams.

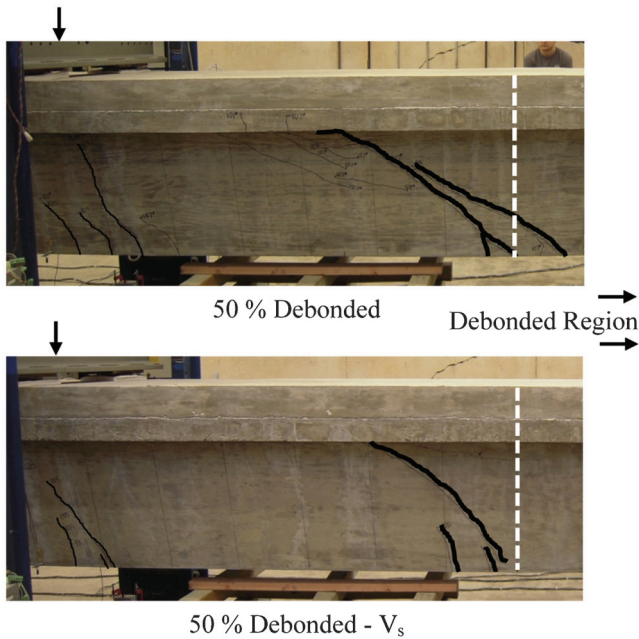


Figure F.42 Primary shear cracks—U-beams.

evaluate the influence of the modulus of rupture on the calculated values (Figure F.45). All analyses use the concrete compressive strengths on test day as presented in Table F.7.

The shear strength profiles for U-50 (Figure F.45) show that the failure mode (primary shear crack) in all modulus of rupture combinations, except one, is flexure-shear (V_{ci}). The only exception is in the analysis with the original modulus of rupture ($6\sqrt{f'_c}$ throughout beam) where a web-shear failure occurs. The profiles also show that the primary shear crack should form at the end of the debonded region. Changing the modulus of rupture values in the analyses affects the extents of cracked regions as observed in the shear strength profiles. Reducing the modulus of rupture from $6\sqrt{f'_c}$ to $3\sqrt{f'_c}$ in the debonded region reduced the shear capacity and changed the failure mode from web-shear to flexure-shear. Reducing the modulus of rupture from $3\sqrt{f'_c}$ to $0\sqrt{f'_c}$ in the debonded region further reduces the shear capacity. The capacity was further reduced in Figure F.45(c) and Figure F.45(e) because a modulus of $3\sqrt{f'_c}$ results in failure at first cracking. When the modulus was reduced to $0\sqrt{f'_c}$, there was not a jump to failure at first cracking but rather the section was already cracked at this location.



Figure F.43 Complete failure—U-50.



Figure F.44 Cracks at conclusion of test—U-50- V_s .

The critical values from the shear strength profiles are provided in Table F.13 to compare the calculated shear capacities (V_{model}) to the measured shear capacities at the formation of the primary shear crack (V_{test}) for each modulus of rupture combination. The shear capacities from ACI 318 and AASHTO are provided as well. Ratios of measured shear capacities to calculated shear capacities are provided in Table F.14. These ratios allow comparisons between the three different approaches to calculate shear strength. The ACI 318 and AASHTO values in Table F.13 and Table F.14 are presented with and without the lower bound limit (Section D.2.3.2) to determine its validity.

The results of these analyses show that the shear model is able to capture the shear strength, failure location, and failure mode when the modulus of rupture in the debonded region is reduced below $6\sqrt{f'_c}$. At a value of $3\sqrt{f'_c}$, the calculated values agree almost exactly with the test results. The ACI 318 approach yielded a conservative and accurate shear strength when assuming a modulus of $0\sqrt{f'_c}$ in the debonded region. The other shear capacities in Table F.13 calculated using ACI 318 are unconservative. It is important to note that the AASHTO approach provided conservative results for each analysis because web-shear strength controlled for each analysis. This is due to fact that the web-shear expression in AASHTO provides lower values than the web-shear strength in ACI 318 as discussed in Section D.8.3. In addition the lower limit does not control for any analysis in ACI 318 or AASHTO.

F.7.2 U-50- V_s

U-50- V_s carried more load than U-50 because U-50- V_s contained stirrups throughout the span length. It is important to note, however, that the large stirrup spacing is believed to have limited the potential shear capacity. The wide crack shown in Figure F.44 only crosses one stirrup instead of the 2.5 stirrups assumed in design using d/s .

The primary shear cracks formed at the end of the debonded region in U-50- V_s (Figure F.42). The shear cracks initiated at the ends of the debonded regions because the neutral axis, and therefore, flexure-shear strength, is minimized at this location. Although the primary shear cracks formed at the end of the debonded region, the transverse reinforcement strengthened the region and forced the failure mechanism towards midspan where higher flexural stresses resulted in reduced neutral axis depths.

The steel contribution to shear capacity is calculated using the same smeared stirrup approach given by ACI 318-11 Section 11.4.7.2. The actual yield stress of 74.2 ksi provided in Section F.3.4 was used in the V_s calculation for U-50- V_s . Shear strength profiles (Figure F.46) were created for each of the same modulus of rupture values used in all the previous analyses. All analyses use

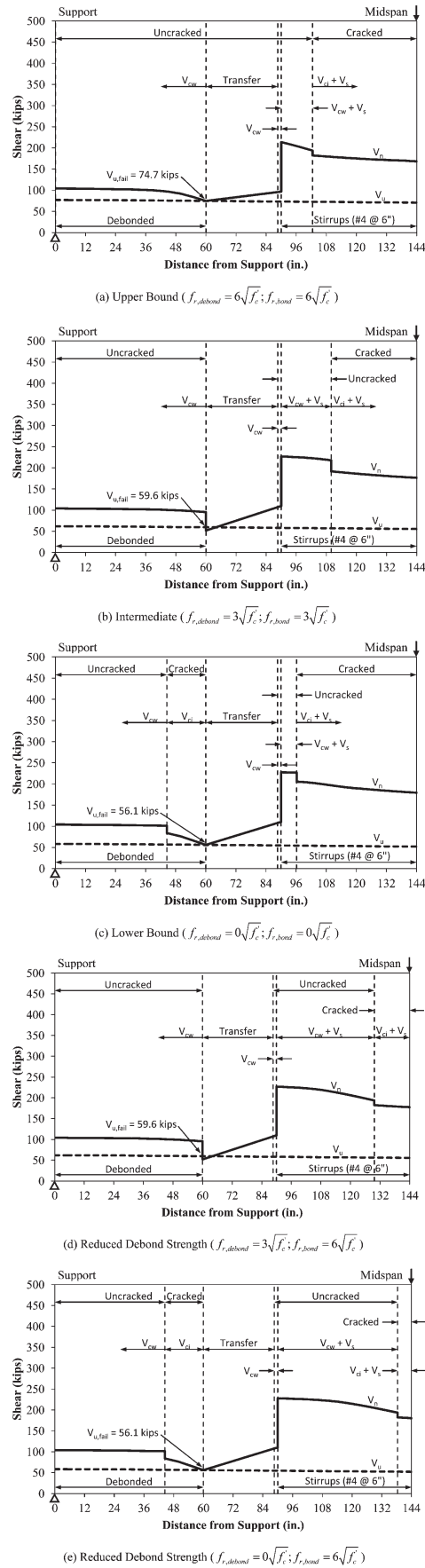


Figure F.45 Shear strength profile for U-50.

the concrete compressive strengths on test day provided in Table F.7.

The shear strength profiles for U-50- V_s (Figure F.46) show that the failure mode (primary shear crack) in all modulus of rupture combinations is flexure-shear (V_{ci}). The profiles also show that the primary shear crack should form at the end of the debonded region. The shear capacities are mostly unaffected as the modulus of rupture is reduced, however, because the section where analytical failure occurs is already cracked when failure is reached. Therefore, reducing the modulus of rupture in sections that would otherwise already be cracked only reduces the cracking moment and increases the extent of cracking. Overall, the calculated shear strengths overestimated the shear strength of the section.

The crack shown in Figure F.47 only engaged one stirrup instead of the 2.5 stirrups assumed using the d/s smeared stirrup calculation from ACI 318. Using the same integer stirrup approach discussed in Section D.8.3, only one stirrup is calculated to be effective. This agrees with what was observed in the test. It should be noted that although there is a 6 in. embedment of a second stirrup crossing the crack as shown in Figure F.47, the required development length is 6.8 in. using Equation 3.34 (as shown below) considering the actual yield stress of 74.2 ksi.

$$l_{dv} = \left(\frac{0.02f_y}{\sqrt{f'_c}} \right) d_b = \left[\frac{0.02(74,200)}{\sqrt{6,710}} \right] (0.375) = 6.8 \text{ in.}$$

Only one stirrup is assumed to be effective at each section along the entire span length as calculated using Equation 3.33 (shown below). It should be noted, however, that two stirrups are assumed to be effective if a yield stress of 60 ksi is assumed. Shear strength profiles using this integer approach to calculate the steel contribution to shear capacity are presented in Figure F.48.

$$N_v = INT \left(\frac{d - l_{dv}}{s} \right) = INT \left(\frac{30 - 6.8}{12} \right) = INT(1.9) = 1$$

The shear strength profiles for U-50- V_s (Figure F.48) with the integer stirrup approach show that the failure mode in all modulus of rupture combinations is flexure-shear (V_{ci}) at the end of the debonding except for the case where the modulus of rupture of $6\sqrt{f'_c}$ is assumed. For that case, a flexure-shear failure (V_{ci}) is calculated to occur at midspan. The shear capacities are mostly unaffected as the modulus of rupture is reduced because the section where analytical failure occurs is already cracked when failure is reached. As previously noted, reducing the modulus of rupture in sections that would otherwise already be cracked only reduces the cracking moment and increases the extent of cracking.

The critical values from the shear strength profiles are provided in Table F.15 to compare the calculated shear capacities (V_{model}) to the measured shear capacities (V_{test}) for each modulus of rupture combination. The shear corresponding to the maximum load is provided because the stirrups provided additional capacity (V_s) beyond that of the concrete contribution (V_c). The shear capacities from ACI 318 and AASHTO are provided as well. Ratios of measured shear capacities to calculated shear capacities are provided in Table F.16.

The modulus of rupture for each specimen is provided in Table F.17. This table presents the measured modulus of rupture values at the end of the debonded region, labeled "Debond" and at midspan, labeled "Bond" for U-50 and U-50- V_s . It should be noted that a reduction of the modulus of rupture in the debonded region was observed in both beams. The measured modulus of rupture values compare well each other. Overall, the measured modulus of rupture values are very low even for the fully bonded section. It should be noted that these moduli were calculated considering the entire section.

The results of these analyses show that the shear model (with the integer stirrup approach for the steel contribution) is able to capture the shear strength and failure mode when the modulus of rupture in the debonded region is reduced below $6\sqrt{f'_c}$. It should be noted that the failure location was not calculated correctly. The failure crack shown in Figure F.44 was located closer to midspan. This difference in location may be explained by the shear crack

TABLE F.13
Comparison of Shear Strengths for U-50

Modulus of Rupture (psi)		V_{test} (kip)	Model	V_{calc} (kip)			
Debond	Bond			ACI 318		AASHTO	
				Limit	No Limit	Limit	No Limit
	$6\sqrt{f'_c}$	59.1	74.7	69.1	69.1	40.3	40.3
	$3\sqrt{f'_c}$		59.6	69.1	69.1	40.3	40.3
	$0\sqrt{f'_c}$		56.1	56.4	56.4	40.3	40.3
$3\sqrt{f'_c}$	$6\sqrt{f'_c}$		59.6	69.1	69.1	40.3	40.3
$0\sqrt{f'_c}$	$6\sqrt{f'_c}$		56.1	56.4	56.4	40.3	40.3

angles. The angles were flatter closer to the debonding location and oriented more vertical closer to midspan. Therefore, the shear cracks closer to the debonding location likely crossed more stirrups than the wide (failure) crack adjacent to midspan. The analyses which produced the shear strength profiles in Figure F.48, however, assumed that one stirrup was effective at each section in the shear span. If different amounts of stirrups are considered effective throughout the shear span (two in the debonded region and one in the fully bonded region) then the shear model calculates a shear failure at midspan. This results in a shear capacity of 66.1 kips ($V_{calc}/V_{test}=0.98$). It should be emphasized that the integer stirrup approach provides conservative and accurate estimates of shear strength without modification (Table F.16).

The ACI 318 and AASHTO approaches provided unconservative shear capacities due to the unconservative nature of the steel contribution (V_s) in specimens with widely spaced stirrups. Even the shear model yielded unconservative results when combined with the smeared stirrup approach employed by ACI 318 and AASHTO.

F.8 CONCLUSIONS

Two pretensioned U-beams were constructed, tested, and analyzed to evaluate the effects of strand debonding and shape on shear strength. The following conclusions are made based on the experimental program and the analytical phase:

1. Low modulus of rupture values were observed for these specimens, especially at the end of the debonded region. On average, the modulus of rupture was $4.6\sqrt{f'_c}$ at midspan and $2.1\sqrt{f'_c}$ at the end of debonding. Therefore, debonding 50% of the strand resulted in a 54% reduction in the modulus. This was higher than observed for the rectangular section in Appendix D, where 50% debonding resulted in a 26% reduction in the modulus.
2. The shear model was shown to be capable of conservatively estimating the concrete contribution to shear strength of U-beams regardless of its complex geometry. The model resulted in a V_{test}/V_{calc} ratio of 1.05 using $f_r=0\sqrt{f'_c}$. The

shear funnel approach using 45 degree angles captured the overall shear behavior.

3. The ACI 318 and AASHTO approaches to calculate the concrete contribution to shear capacity provided conservative estimates of shear strength when the modulus of rupture was taken as zero ($f_r=0\sqrt{f'_c}$) in the debonded region. V_{test}/V_{calc} ratios of 1.05 for ACI 318 and 1.47 for AASHTO were computed.
4. Adding transverse reinforcement in the debonded region provided additional shear capacity as well as improved ductility. With the addition of #3 at 12 in., the shear capacity was increased 20% beyond the shear at the formation of the primary shear crack. Shear crack widths were controlled and failure was not brittle. The transverse reinforcement also forced the shear failure to occur outside the debonded region. Shear beyond the primary shear crack (9% increase) was also carried in the specimen without transverse reinforcement in the debonded region. An extremely brittle failure, however, was observed for this specimen.
5. The wide stirrup spacing led to unconservative estimates of the stirrup contribution to shear capacity when using code expressions which use the smeared stirrup approach. This approach estimated 2.5 stirrups would cross the shear crack while the test results indicate only 1 stirrup crossed the crack. The integer stirrup approach, on the other hand, provided accurate estimates of the stirrup contribution indicating that only 1 stirrup would be effective.

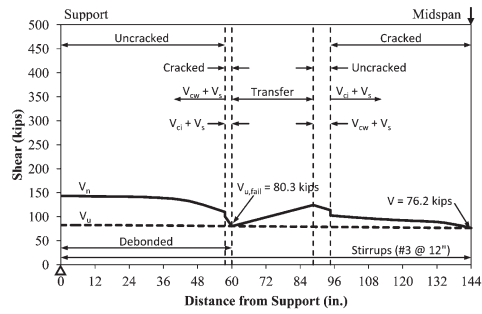
F.9 RECOMMENDATIONS

The following recommendation, in addition to those made in Appendix D, is made for pretensioned U-beams:

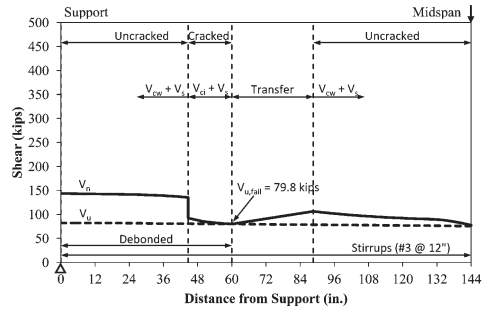
- The shear funnel should be used to calculate the effective shear area when using the shear model. To simplify the geometry, the effective shear area can conservatively be based on the web width.

TABLE F.14
Comparison of Shear Strength Ratios for U-50

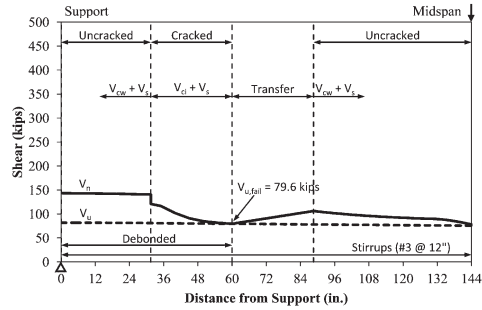
Modulus of Rupture (psi)		V_{test} (kip)	Model	V_{test}/V_{calc}			
Debond	Bond			ACI 318		AASHTO	
				Limit	No Limit	Limit	No Limit
	$6\sqrt{f'_c}$	59.1	0.79	0.86	0.86	1.47	1.47
	$3\sqrt{f'_c}$		0.99	0.86	0.86	1.47	1.47
	$0\sqrt{f'_c}$		1.05	1.05	1.05	1.47	1.47
$3\sqrt{f'_c}$	$6\sqrt{f'_c}$		0.99	0.86	0.86	1.47	1.47
$0\sqrt{f'_c}$	$6\sqrt{f'_c}$		1.05	1.05	1.05	1.47	1.47



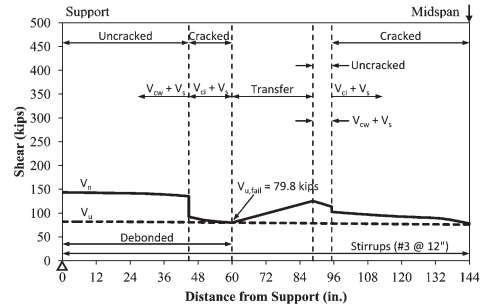
(a) Upper Bound ($f_{r,debond} = 6\sqrt{f'_c}$; $f_{r,bond} = 6\sqrt{f'_c}$)



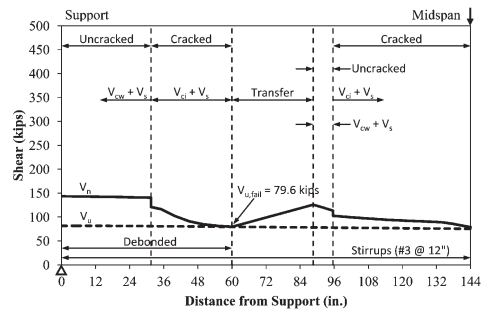
(b) Intermediate ($f_{r,debond} = 3\sqrt{f'_c}$; $f_{r,bond} = 3\sqrt{f'_c}$)



(c) Lower Bound ($f_{r,debond} = 0\sqrt{f'_c}$; $f_{r,bond} = 0\sqrt{f'_c}$)



(d) Reduced Debond Strength ($f_{r,debond} = 3\sqrt{f'_c}$; $f_{r,bond} = 6\sqrt{f'_c}$)



(e) Reduced Debond Strength ($f_{r,debond} = 0\sqrt{f'_c}$; $f_{r,bond} = 6\sqrt{f'_c}$)

Figure F.46 Shear strength profile for U-50-V_s.

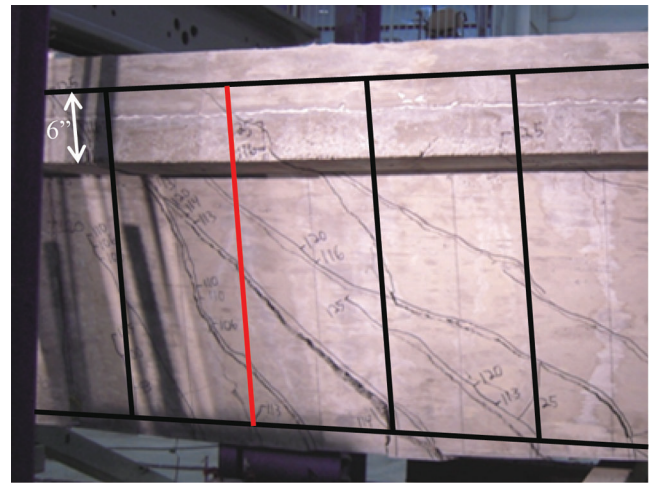
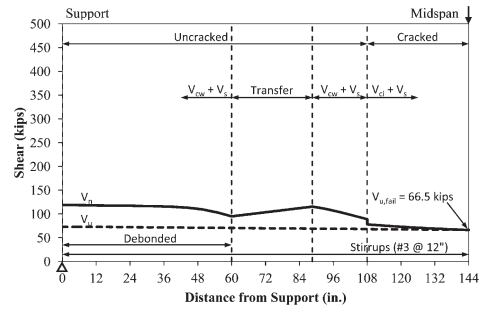
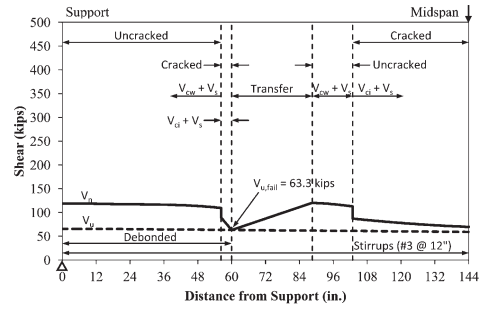


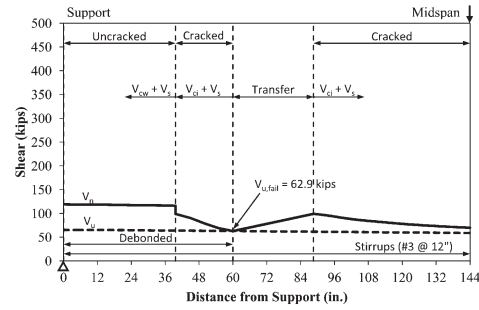
Figure F.47 Stirrup locations for U-50-V_s.



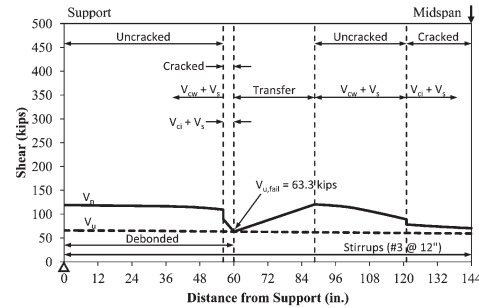
(a) Upper Bound ($f_{r,debond} = 6\sqrt{f'_c}$; $f_{r,bond} = 6\sqrt{f'_c}$)



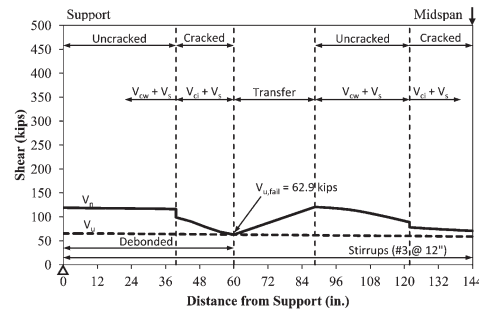
(b) Intermediate ($f_{r,debond} = 3\sqrt{f'_c}$; $f_{r,bond} = 3\sqrt{f'_c}$)



(c) Lower Bound ($f_{r,debond} = 0\sqrt{f'_c}$; $f_{r,bond} = 0\sqrt{f'_c}$)



(d) Reduced Debond Strength ($f_{r,debond} = 3\sqrt{f'_c}$; $f_{r,bond} = 6\sqrt{f'_c}$)



(e) Reduced Debond Strength ($f_{r,debond} = 0\sqrt{f'_c}$; $f_{r,bond} = 6\sqrt{f'_c}$)

Figure F.48 Shear strength profile for U-50-V_S; V_{S,INT.}

TABLE F.15
Comparison of Shear Strengths for U-50-V_s

Modulus of Rupture (psi)			V _{calc} (kip)					
			Model		ACI 318*		AASHTO	
Debond	Bond	V _{test} (kip)	V _{s,ACI}	V _{s,INT}	Limit	No Limit	Limit	No Limit
	6√f' _c	64.7	80.3	66.5	<i>84.1</i>	<i>84.1</i>	78.7	78.7
	3√f' _c		79.8	63.3	<i>84.1</i>	<i>84.1</i>	78.7	78.7
	0√f' _c		79.6	62.9	<i>84.1</i>	<i>84.1</i>	78.7	78.7
3√f' _c	6√f' _c		79.8	63.3	<i>84.1</i>	<i>84.1</i>	78.7	78.7
0√f' _c	6√f' _c		79.6	62.9	<i>84.1</i>	<i>84.1</i>	78.7	78.7

*Values in italics in the ACI 318 columns are shears at end of debonded region corresponding to flexural failure (flexure controls over shear).

TABLE F.16
Comparison of Shear Strength Ratios for U-50-V_s

Modulus of Rupture (psi)			V _{test} /V _{calc}					
			Model		ACI 318*		AASHTO	
Debond	Bond	V _{test} (kip)	V _{s,ACI}	V _{s,INT}	Limit	No Limit	Limit	No Limit
	6√f' _c	64.7	0.81	0.97	<i>0.77</i>	<i>0.77</i>	0.82	0.82
	3√f' _c		0.81	1.02	<i>0.77</i>	<i>0.77</i>	0.82	0.82
	0√f' _c		0.81	1.03	<i>0.77</i>	<i>0.77</i>	0.82	0.82
3√f' _c	6√f' _c		0.81	1.02	<i>0.77</i>	<i>0.77</i>	0.82	0.82
0√f' _c	6√f' _c		0.81	1.03	<i>0.77</i>	<i>0.77</i>	0.82	0.82

*Values in italics in the ACI 318 columns use the shears at the end of debonded region corresponding to flexural failure (flexure controls over shear).

TABLE F.17
Measured Modulus of Ruptures for U-Beams

Specimen ID	f' _c (psi)	Modulus of Rupture (psi)	
		Debond	Bond x (in.)
U-50	9,020	2.2√f' _c	4.6√f' _c
U-50-V _s	8,720	1.9√f' _c	4.5√f' _c

APPENDIX F-1. CONCRETE STRENGTHS FOR SPECIMENS IN APPENDIX F

TABLE F-1.1
Average Concrete Strength Data for Trial Batch

Age (days)	f'_c (psi)	f_{cr} (psi)
3	4,590	480
5	5,470	470
7	6,010	530
14	6,660	550
28	7,540	630

TABLE F-1.3
Average Concrete Strength Data for U-Beam Decks (One Truck)

Age (days)	U-50-V _s (Deck)		U-50 (Deck)	
	f'_c (psi)	f_{cr} (psi)	f'_c (psi)	f_{cr} (psi)
5	5,060	480	5,060	480
7	5,520	—	5,520	—
14	6,300	—	6,300	—
21	6,620	—	6,620	—
28	7,130	590	7,130	590
32	—	—	6,890	560
40	6,710	520	—	—

TABLE F-1.2
Average Concrete Strength Data for U-Beams

Age (days)	U-50-V _s		U-50	
	f'_c (psi)	f_{cr} (psi)	f'_c (psi)	f_{cr} (psi)
3	5,630	—	—	—
5	6,620	550	—	—
7	7,010	—	—	—
14	7,860	—	—	—
21	8,180	—	—	—
28	8,270	550	8,980	—
54	8,680	670	9,020	660
62	8,720	640	—	—

About the Joint Transportation Research Program (JTRP)

On March 11, 1937, the Indiana Legislature passed an act which authorized the Indiana State Highway Commission to cooperate with and assist Purdue University in developing the best methods of improving and maintaining the highways of the state and the respective counties thereof. That collaborative effort was called the Joint Highway Research Project (JHRP). In 1997 the collaborative venture was renamed as the Joint Transportation Research Program (JTRP) to reflect the state and national efforts to integrate the management and operation of various transportation modes.

The first studies of JHRP were concerned with Test Road No. 1—evaluation of the weathering characteristics of stabilized materials. After World War II, the JHRP program grew substantially and was regularly producing technical reports. Over 1,500 technical reports are now available, published as part of the JHRP and subsequently JTRP collaborative venture between Purdue University and what is now the Indiana Department of Transportation.

Free online access to all reports is provided through a unique collaboration between JTRP and Purdue Libraries. These are available at: <http://docs.lib.purdue.edu/jtrp>

Further information about JTRP and its current research program is available at: <http://www.purdue.edu/jtrp>

About This Report

An open access version of this publication is available online. This can be most easily located using the Digital Object Identifier (doi) listed below. Pre-2011 publications that include color illustrations are available online in color but are printed only in grayscale.

The recommended citation for this publication is:

Wesson, M. D., Pavelchak, M. A., Frosch, R. J., & Kreger, M. E. (2014). *Improving the design of U-beams for Indiana* (Joint Transportation Research Program Publication No. FHWA/IN/JTRP-2014/07). West Lafayette, IN: Purdue University. <http://dx.doi.org/10.5703/1288284315501>